

Rediscovering a lost homeland
of ancient Europeans p. 499

Boron nitride pumps
out the heat p. 555

The genomics of schizophrenia
in South Africa p. 569

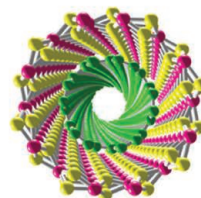
Science

\$15
31 JANUARY 2020
sciencemag.org

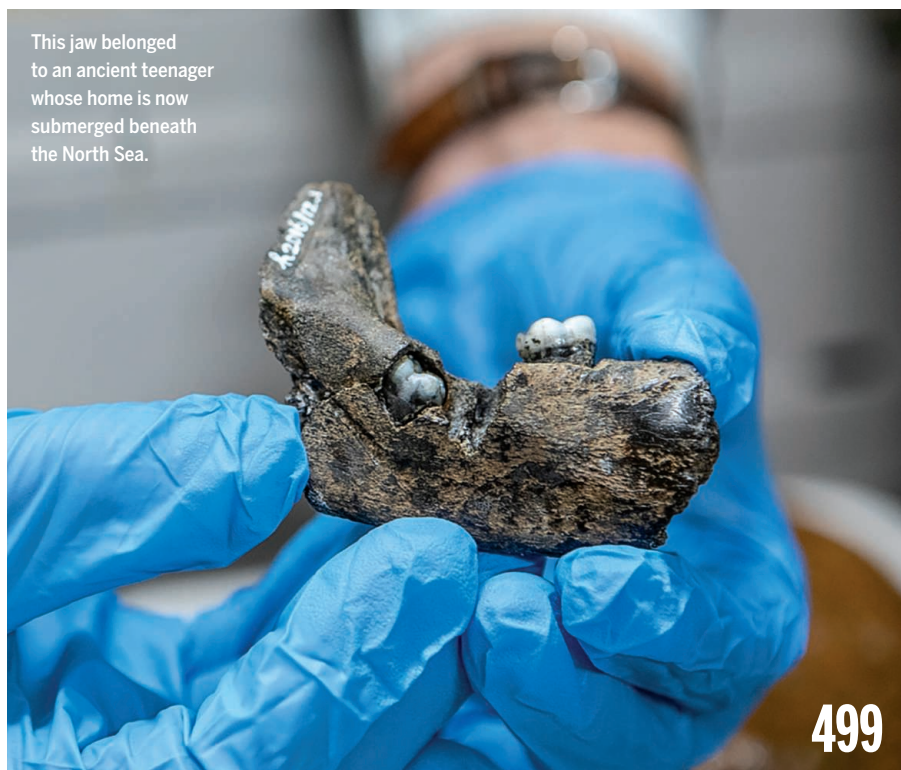
AAAS

SAFEGUARDING BEE HEALTH

Engineered bee symbionts kill
Varroa mites pp. 504 & 573



This jaw belonged to an ancient teenager whose home is now submerged beneath the North Sea.



499

NEWS

IN BRIEF

490 News at a glance

IN DEPTH

492 New coronavirus threat galvanizes scientists

As China outbreak spreads worldwide, researchers probe its origins and how to fight it *By J. Cohen*

494 After Brexit, a long road to mend ties with Europe

U.K. scientists want to join EU research program, but Europe may balk *By K. Kupferschmidt*

495 Black holes caught in the act of swallowing stars

Dozens of tidal disruption events found in galaxy surveys shed light on violent events *By D. Clery*

496 Electricity turns garbage into high-quality graphene

Method could supply graphene in bulk, opening new uses *By R. F. Service*

496 Monkey facility in China lures neuroscientist

Animal rights conflict spurs move of major German lab *By G. Vogel*

497 Africans, too, carry Neanderthal genetic legacy

Ancient Europeans took Neanderthal DNA back to Africa *By M. Price*

498 Screen for childhood trauma triggers debate

Testing across California could have unexpected downsides, critics say *By E. Underwood*

FEATURES

499 Europe's lost frontier

Aided by dedicated amateurs and new methods, scientists reconstruct a now-submerged ancient landscape—and the people who lived there *By A. Curry*

INSIGHTS

PERSPECTIVES

504 A microbiome silver bullet for honey bees

A genetically engineered honey bee gut bacterium knocks down two major bee threats *By R. J. Paxton*

REPORT p. 573

506 Nested hybrid nanotubes

Material made with atom-thin tubular crystals portends the creation of inventive nanodevices

By Y. Gogotsi and B. I. Yakobson

RESEARCH ARTICLE p. 537

507 Liquid but not contactless

The endoplasmic reticulum makes molecular contact with membraneless organelles *By B. Kornmann and K. Weis*

RESEARCH ARTICLE p. 527

509 Stitching two chiral centers with one catalyst

A single catalyst joins alkyl groups with control over stereochemistry of both fragments

By J. Xu and M. P. Watson

REPORT p. 559

510 Monitoring neuronal health

A multiscale imaging approach reveals a neuroimmune communication pathway

By A. Nimmerjahn

RESEARCH ARTICLE p. 528

512 Unpicking the proteome in single cells

Single-cell mass spectrometry will help reveal mechanisms that underpin health and disease *By N. Slavov*

DEPARTMENTS

489 Editorial

Envision a future, make it so *By Sudip Parikh*

594 Working Life

Avoiding immigration limbo *By Jaivime Evaristo*

Science Staff	486
AAAS News & Notes	520
Science Careers	591

POLICY FORUM

514 Progress in natural capital accounting for ecosystems

Global statistical standards are being developed *By L. Hein et al.*

BOOKS ET AL.

516 Game over

A high-stakes game of battleship helped turn the tide in World War II's Battle of the Atlantic *By S. L. Pettyjohn*

517 Profits, prejudice, and plant patents

A journalist investigates a surprising act of espionage *By H. A. Curry*

LETTERS

518 Agricultural lands key to mitigation and adaptation

By R. D. Harrison and A. Gassner

518 Response

By M. D. Morecroft et al.

519 Cancel cuts to Graduate Research Fellowships

By G. Muller-Parker et al.

RESEARCH

IN BRIEF

522 From *Science* and other journals

REVIEW

525 Cancer immunotherapy

Neoadjuvant checkpoint blockade for cancer immunotherapy *S. L. Topalian et al.*

REVIEW SUMMARY; FOR FULL TEXT: [DX.DOI.ORG/10.1126/SCIENCE.AAX0182](https://doi.org/10.1126/SCIENCE.AAX0182)

RESEARCH ARTICLES

526 Neuroscience

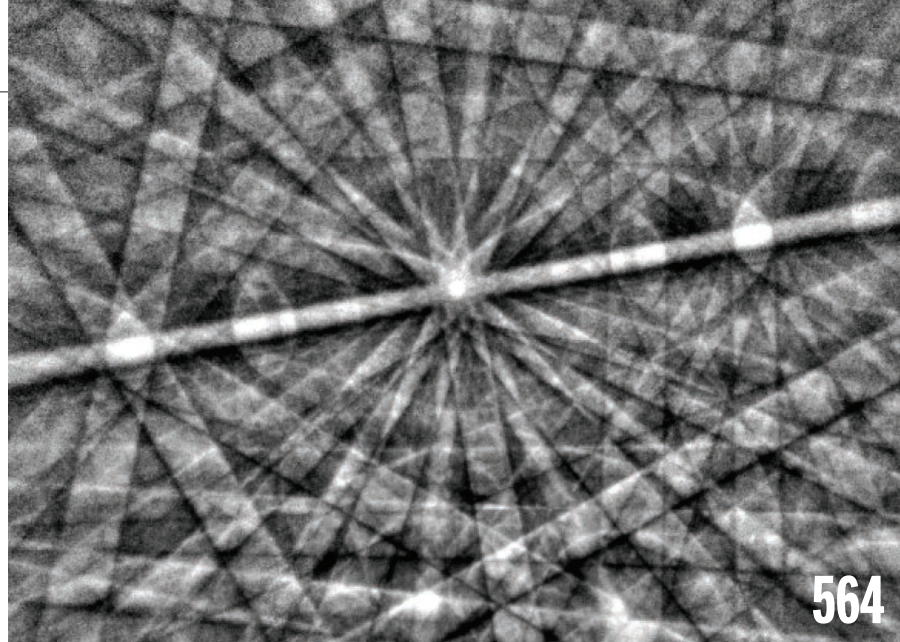
Monosomes actively translate synaptic mRNAs in neuronal processes

A. Biever et al. RESEARCH ARTICLE SUMMARY; FOR FULL TEXT: [DX.DOI.ORG/10.1126/SCIENCE.AAY4991](https://doi.org/10.1126/SCIENCE.AAY4991)

527 Cell biology

Endoplasmic reticulum contact sites regulate the dynamics of membraneless organelles *J. E. Lee et al.*

RESEARCH ARTICLE SUMMARY; FOR FULL TEXT: [DX.DOI.ORG/10.1126/SCIENCE.AAY7108](https://doi.org/10.1126/SCIENCE.AAY7108) PERSPECTIVE p. 507

**528 Cellular neuroscience**

Microglia monitor and protect neuronal function through specialized somatic purinergic junctions *C. Cserép et al.*

PERSPECTIVE p. 510

537 Nanomaterials

One-dimensional van der Waals heterostructures *R. Xiang et al.*

PERSPECTIVE p. 506

542 Catalysis

Highly active cationic cobalt(II) hydroformylation catalysts *D. M. Hood et al.*

549 Neuroscience

Local D2- to D1-neuron transmodulation updates goal-directed learning in the striatum *M. Matamalas et al.*

REPORTS

555 Thermal conductivity

Ultrahigh thermal conductivity in isotope-enriched cubic boron nitride *K. Chen et al.*

559 Organic chemistry

Catalyst-controlled doubly enantioconvergent coupling of racemic alkyl nucleophiles and electrophiles *H. Huo et al.*

PERSPECTIVE p. 509

564 Crystallography

Crystal symmetry determination in electron diffraction using machine learning *K. Kaufmann et al.*

569 Human genetics

Genetics of schizophrenia in the South African Xhosa *S. Gulsuner et al.*

PODCAST

573 Bee health

Engineered symbionts activate honey bee immunity and limit pathogens *S. P. Leonard et al.*

PERSPECTIVE p. 504

577 Gravitation

Lense–Thirring frame dragging induced by a fast-rotating white dwarf in a binary pulsar system *V. Venkatraman Krishnan et al.*

580 Molecular biology

N⁶-methyladenosine of chromosome-associated regulatory RNA regulates chromatin state and transcription *J. Liu et al.*

586 Cancer

Therapeutic targeting of preleukemia cells in a mouse model of *NPM1* mutant acute myeloid leukemia *H. J. Uckelmann et al.*

ON THE COVER



Focus-stacked photograph of a *Varroa* mite on the abdomen of a honey bee. *Varroa* mites are major pests that weaken honey bee colonies by parasitizing bees and spreading viral disease. Researchers have genetically engineered bacterial gut symbionts of bees to kill these mites and boost bee resistance to RNA viruses, an approach that may eventually support honey bee health. See pages 504 and 573. *Image: Alexander Wild*

SCIENCE (ISSN 0036-8075) is published weekly on Friday, except last week in December, by the American Association for the Advancement of Science, 1200 New York Avenue, NW, Washington, DC 20005. Periodicals mail postage (publication No. 484460) paid at Washington, DC, and additional mailing offices. Copyright © 2020 by the American Association for the Advancement of Science. The title SCIENCE is a registered trademark of the AAAS. Domestic individual membership, including subscription (12 months): \$165 (\$74 allocated to subscription). Domestic institutional subscription (51 issues): \$2148; Foreign postage extra: \$98. First class, airmail, student, and emeritus rates on request. Canadian rates with GST available upon request. GST #125488122. Publications Mail Agreement Number 1069624. Printed in the U.S.A. Change of address: Allow 4 weeks, giving old and new addresses and 8-digit account number. Postmaster: Send change of address to AAAS, P.O. Box 96178, Washington, DC 20090-6178. Single-copy sales: \$15 each plus shipping and handling available from backissues.sciencemag.org; bulk rate on request. Authorization to reproduce material for internal or personal use under circumstances not falling within the fair use provisions of the Copyright Act can be obtained through the Copyright Clearance Center (CCC), www.copyright.com. The identification code for Science is 0036-8075. Science is indexed in the Reader's Guide to Periodical Literature and in several specialized indexes.

Editor-in-Chief Holden Thorp, hthorp@aaas.org

Executive Editor Monica M. Bradford

Editors, Research Valda Vinson, Jake S. Yeston Editor, Insights Lisa D. Chong

DEPUTY EDITORS Julia Fahrenkamp-Uppenbrink (UK), Stella M. Hurlley (UK), Phillip D. Szurmi, Sacha Vignieri **SR. EDITORIAL FELLOW** Andrew M. Sugden (UK) **SR. EDITORS** Gemma Alderton (UK), Caroline Ash (UK), Brent Grocholski, Pamela J. Hines, Paula A. Kiberstis, Marc S. Lavine (Canada), Steve Mao, Ian S. Osborne (UK), Beverly A. Purnell, L. Bryan Ray, H. Jesse Smith, Keith T. Smith (UK), Jelena Stajic, Peter Stern (UK), Valerie B. Thompson, Brad Wible, Laura M. Zahn **ASSOCIATE EDITORS** Michael A. Funk, Priscilla N. Kelly, Tage S. Rai, Seth Thomas Scanlon (UK), Yury V. Suleymanov **LETTERS EDITOR** Jennifer Sills **LEAD CONTENT PRODUCTION EDITORS** Harry Jach, Lauren Kmeck **CONTENT PRODUCTION EDITORS** Amelia Beyna, Jeffrey E. Cook, Chris Filiatreau, Julia Katris, Nida Masiulis, Suzanne M. White **SR. EDITORIAL COORDINATORS** Carolyn Kyle, Beverly Shields **EDITORIAL COORDINATORS** Aneera Dobbins, Joi S. Granger, Jeffrey Hearn, Lisa Johnson, Maryrose Madrid, Ope Martins, Shannon McMahon, Jerry Richardson, Alana Warne, Alice Whaley (UK), Anita Wynn **PUBLICATIONS ASSISTANTS** Jeremy Dow, Alexander Kief, Ronnel Navas, Hilary Stewart (UK), Brian White **EXECUTIVE ASSISTANT** Jessica Slater **ASI DIRECTOR, OPERATIONS** Janet Clements (UK) **ASI SR. OFFICE ADMINISTRATOR** Jessica Waldoock (UK)

News Editor Tim Appenzeller

NEWS MANAGING EDITOR John Travis **INTERNATIONAL EDITOR** Martin Enserink **DEPUTY NEWS EDITORS** Elizabeth Culotta, Lila Guterman, David Grimm, Eric Hand (Europe), David Malakoff **SR. CORRESPONDENTS** Daniel Clerly (UK), Jon Cohen, Jeffrey Mezin, Elizabeth Pennisi **ASSOCIATE EDITORS** Jeffrey Brinard, Catherine Maticic **NEWS REPORTERS** Adrian Cho, Jennifer Couzin-Frankel, Jocelyn Kaiser, Kelly Servick, Robert F. Service, Erik Stokstad, Paul Voosen, Meredith Wadman **INTERNS** Eva Frederick, Rodrigo Perez Ortega **CONTRIBUTING CORRESPONDENTS** Warren Cornwall, Ann Gibbons, Mara Hvistendahl, Sam Kean, Eli Kintisch, Kai Kupferschmidt (Berlin), Andrew Lawler, Mitch Leslie, Eliot Marshall, Virginia Morell, Dennis Normile (Shanghai), Elisabeth Pain (Careers), Charles Pillar, Michael Price, Tania Rabesandratana (Barcelona), Emily Underwood, Gretchen Vogel (Berlin), Lizzie Wade (Mexico City) **CAREERS** Donisha Adams, Rachel Bernstein (Editor), Katie Langin (acting editor) **COPY EDITORS** Julia Cole (Senior Copy Editor), Cyra Master (Copy Chief) **ADMINISTRATIVE SUPPORT** Meagan Welland

Creative Director Beth Rakouskas

DESIGN MANAGING EDITOR Marcy Atarod **GRAPHICS MANAGING EDITOR** Alberto Cuadra **PHOTOGRAPHY MANAGING EDITOR** William Douthitt **WEB CONTENT STRATEGY MANAGER** Kara Estelle-Powers **SENIOR DESIGNER** Chrystal Smith **DESIGNER** Christina Aycock **GRAPHICS EDITOR** Nirja Desai **INTERACTIVE GRAPHICS EDITOR** Xing Liu **SENIOR SCIENTIFIC ILLUSTRATORS** Valerie Altounian, Chris Bickel **SCIENTIFIC ILLUSTRATOR** Alice Kitterman **SENIOR GRAPHICS SPECIALISTS** Holly Bishop, Nathalie Cary **SENIOR PHOTO EDITOR** Emily Petersen **PHOTO EDITOR** Kaitlyn Dolan

Chief Executive Officer and Executive Publisher Sudip Parikh

Publisher, Science Family of Journals Bill Moran

DIRECTOR, BUSINESS SYSTEMS AND FINANCIAL ANALYSIS Randy Yi **DIRECTOR, BUSINESS OPERATIONS & ANALYSIS** Eric Knott **DIRECTOR OF ANALYTICS** Enrique Gonzales **MANAGER, BUSINESS OPERATIONS** Jessica Tierney **SENIOR BUSINESS ANALYST** Cory Lipman, Meron Kebede **FINANCIAL ANALYST** Alexander Lee **ADVERTISING SYSTEM ADMINISTRATOR** Tina Burks **SENIOR SALES COORDINATOR** Shirley Young **DIGITAL/PRINT STRATEGY MANAGER** Jason Hillman **QUALITY TECHNICAL MANAGER** Marcus Spiegler **ASSISTANT MANAGER DIGITAL/PRINT** Rebecca Doshi **SENIOR CONTENT SPECIALISTS** Steve Forrester, Jacob Hedrick, Antoinette Lord, Lori Murphy **DIGITAL PRODUCTION MANAGER** Lisa Stanford **CONTENT SPECIALIST** Kimberley Oster **ADVERTISING PRODUCTION OPERATIONS MANAGER** Deborah Tompkins **DESIGNER, CUSTOM PUBLISHING** Jeremy Huntsinger **SR. TRAFFIC ASSOCIATE** Christine Hall **SPECIAL PROJECTS ASSOCIATE** Sarah Dhere

ASSOCIATE DIRECTOR, BUSINESS DEVELOPMENT Justin Sawyers **GLOBAL MARKETING MANAGER** Allison Pritchard **DIGITAL MARKETING MANAGER** Aimee Aponte **JOURNALS MARKETING MANAGER** Shawana Arnold **MARKETING ASSOCIATES** Tori Velasquez, Mike Romano, Ashley Hylton **DIGITAL MARKETING SPECIALIST** Asleigh Rojanavongse **SENIOR DESIGNER** Kim Huynh

DIRECTOR AND SENIOR EDITOR, CUSTOM PUBLISHING Sean Sanders **ASSISTANT EDITOR, CUSTOM PUBLISHING** Jackie Oberst

DIRECTOR, PRODUCT & PUBLISHING DEVELOPMENT Chris Reid **DIRECTOR, BUSINESS STRATEGY AND PORTFOLIO MANAGEMENT** Sarah Whalen **ASSOCIATE DIRECTOR, PRODUCT MANAGEMENT** Kris Bishop **SR. PRODUCT ASSOCIATE** Robert Koepke **DIGITAL PRODUCT STRATEGIST** Michael Hardesty **SPJ ASSOCIATE** Samantha Bruno Fuller

DIRECTOR, INSTITUTIONAL LICENSING Iquo Edim **ASSOCIATE DIRECTOR, RESEARCH & DEVELOPMENT** Elisabeth Leonard **MARKETING MANAGER** Kess Knight **SENIOR INSTITUTIONAL LICENSING MANAGER** Ryan Rexroth **INSTITUTIONAL LICENSING MANAGER** Marco Castellani **MANAGER, AGENT RELATIONS & CUSTOMER SUCCESS** Judy Lillibridge **SENIOR OPERATIONS ANALYST** Lana Guz **FULFILLMENT COORDINATOR** Melody Stringer **SALES COORDINATOR** Josh Haverlock

DIRECTOR, GLOBAL SALES Tracy Holmes **US EAST COAST AND MID WEST SALES** Stephanie O'Connor **US WEST COAST SALES** Lynne Stickrod **US SALES MANAGER, SCIENCE CAREERS** Claudia Paulsen-Young **US SALES REP, SCIENCE CAREERS** Tracy Anderson **ASSOCIATE DIRECTOR, ROW** Roger Gonçalves **SALES REP, ROW** Sarah Lelarge **SALES ADMIN ASSISTANT, ROW** Bryony Cousins **DIRECTOR OF GLOBAL COLLABORATION AND ACADEMIC PUBLISHING RELATIONS**, ASIA Xiaoying Chu **ASSOCIATE DIRECTOR, INTERNATIONAL COLLABORATION** Grace Yao **SALES MANAGER** Danny Zhao **MARKETING MANAGER** Kilo Lan ASCA CORPORATION, JAPAN Kaoru Sasaki (Tokyo), Miyuki Tani (Osaka) **COLLABORATION/CUSTOM PUBLICATIONS/JAPAN** Adarsh Sandhu

DIRECTOR, COPYRIGHT, LICENSING AND SPECIAL PROJECTS Emilie David **RIGHTS AND LICENSING COORDINATOR** Jessica Adams **RIGHTS AND PERMISSIONS ASSOCIATE** Elizabeth Sandler **CONTRACTS AND LICENSING ASSOCIATE** Lili Catlett

MAIN HEADQUARTERS

Science/AAAS
1200 New York Ave. NW
Washington, DC 20005

SCIENCE INTERNATIONAL

Clarendon House
Clarendon Road
Cambridge, CB2 8FH, UK

SCIENCE CHINA

Room 1004, Culture Square
No. 59 Zhongguancun St.
Haidian District, Beijing, 100872

SCIENCE JAPAN

ASCA Corporation
Sibaura TY Bldg. 4F, 1-14-5
Shibaura Minato-ku
Tokyo, 108-0073 Japan

EDITORIAL

science_editors@aaas.org

NEWS

science_news@aaas.org

INFORMATION FOR AUTHORS

sciencemag.org/authors/
science-information-authors

REPRINTS AND PERMISSIONS

sciencemag.org/help/
reprints-and-permissions

MEDIA CONTACTS

scipak@aaas.org
SciencePodcast@aaas.org
ScienceVideo@aaas.org

MULTIMEDIA CONTACTS

SciencePodcast@aaas.org
ScienceVideo@aaas.org

INSTITUTIONAL SALES

sciencemag.org/librarian

PRODUCT ADVERTISING

& CUSTOM PUBLISHING
advertising.sciencemag.org/
products-services
science_advertising@aaas.org

CLASSIFIED ADVERTISING

advertising.sciencemag.org/
science-careers
advertise@sciencecareers.org

JOB POSTING CUSTOMER SERVICE

employers.sciencecareers.org
support@sciencecareers.org

MEMBERSHIP AND INDIVIDUAL

SUBSCRIPTIONS
sciencemag.org/subscriptions

MEMBER BENEFITS

aaas.org/membercentral

AAAS BOARD OF DIRECTORS

CHAIR Margaret A. Hamburg
PRESIDENT Steven Chu
PRESIDENT-ELECT Claire M. Fraser
TREASURER Carolyn N. Ainslie
INTERIM CHIEF EXECUTIVE OFFICER
Alan Leshner
BOARD Cynthia M. Beall
May R. Berenbaum
Rosina M. Bierbaum
Ann Bostrom
Stephen P. A. Fodor
S. James Gates, Jr.
Laura H. Greene
Kaye Husbands Fealing
Maria Klawe
Robert B. Millard
William D. Provine

BOARD OF REVIEWING EDITORS (Statistics board members indicated with \$)

Adriano Aguzzi, U. Hospital Zürich
Takuzo Aida, U. of Tokyo
Leslie Aiello, Wenner-Gren Foundation
Judith Allen, U. of Manchester
Sebastian Amigorena, Institut Curie
James Analytis, U. of California, Berkeley
Paola Ariotta, Harvard U.
Johan Auwerx, EPFL
David Awschalom, U. of Chicago
Clare Baker, U. of Cambridge
Nenad Ban, ETH Zürich
Franz Bauer, Pontificia Universidad Católica de Chile
Ray H. Baughman, U. of Texas at Dallas
Peter Bearman, Columbia U.
Carlo Beenakker, Leiden U.
Yasmine Belkaid, NIAID, NIH
Philip Benfey, Duke U.
Gabriele Bergers, VIB
Bradley Bernstein, Mass. General Hospital
Alessandra Biffi, Harvard Med. School
Peer Bork, EMBL
Chris Bowler, Ecole Normale Supérieure
Ian Boyd, U. of St. Andrews
Emily Brodsky, U. of California, Santa Cruz
Ron Brookmeyer, U. of California, Los Angeles (\$) **Christian Büchel, UKE Hamburg**
Dennis Burton, Scripps Research
Carter Tribble Butts, U. of California, Irvine
György Buzsáki, New York U. School of Med.
Blanche Capel, Duke U.
Annamarie Carlton, U. of California, Irvine
Nick Chater, U. of Warwick
Zhijian Chen, UT Southwestern Med. Ctr.
Ib Chorkendorff, Denmark TU
James J. Collins, MIT
Robert Cook-Deegan, Arizona State U.
Alan Cowman, Walter & Eliza Hall Inst.
Carolyn Coyne, U. of Pittsburgh
Roberta Croce, VU Amsterdam
Jeff L. Dangl, U. of North Carolina
Tom Daniel, U. of Washington
Chiara Daraio, Caltech
Nicolas Daughas, U. of Chicago
Frans de Waal, Emory U.
Claude Desplan, New York U.
Sandra Díaz, Universidad Nacional de Córdoba
Ulrike Diebold, TU Wien
Hong Ding, Inst. of Physics, CAS
Jennifer Dionne, Stanford U.
Dennis Discher, U. of Penn.
Gerald Dorn, Washington U. in St. Louis
Jennifer A. Doudna, U. of California, Berkeley
Bruce Dunn, U. of California, Los Angeles
William Dunphy, Caltech
Christopher Dye, U. of Oxford
Todd Ehlers, U. of Tübingen
Jennifer Eiseleff, Johns Hopkins U.
Tim Elston, U. of North Carolina
Andrea Encalada, U. San Francisco de Quito
Nader Engheta, U. of Penn.
Karen Ersche, U. of Cambridge
Barry Everitt, U. of Cambridge
Vanessa Ezenwa, U. of Georgia
Michael Feuer, The George Washington U.
Toren Finkel, U. of Pittsburgh Med. Ctr.
Gwen Flowers, Simon Fraser U.
Peter Fratzl, Max Planck Inst. Potsdam
Elaine Fuchs, Rockefeller U.
Eileen Furlong, EMBL
Jay Gallagher, U. of Wisconsin
Daniel Geschwind, U. of California, Los Angeles
Karl-Heinz Glassmeier, TU Braunschweig
Ramon Gonzalez, U. of South Florida
Elizabeth Grove, U. of Chicago
Nicolas Gruber, ETH Zürich
Kip Guy, U. of Kentucky College of Pharmacy
Taekjip Ha, Johns Hopkins U.
Christian Haass, Ludwig Maximilians U.
Sharon Hammes-Schiffer, Yale U.
Wolf-Dietrich Hardt, ETH Zürich
Louise Harra, U. College London
Jian He, Clemson U.
Carl-Philipp Heisenberg, IST Austria
Ykä Helariutta, U. of Cambridge
Janet G. Hering, Eawag
Hans Hilgenkamp, U. of Twente
Kai-Uwe Hinrichs, U. of Bremen
David Hodell, U. of Cambridge
Lora Hooper, UT Southwestern Med. Ctr.
Fred Hughson, Princeton U.
Randall Hulet, Rice U.
Auke Ijspeert, EPFL
Akiko Iwasaki, Yale U.
Stephen Jackson, USGS and U. of Arizona
Kai Johnson, EPFL
Peter Jonas, IST Austria
Matt Kaerberlein, U. of Washington
William Kaelin Jr., Dana-Farber Cancer Inst.
Daniel Kammen, U. of California, Berkeley
V. Naray Kim, Seoul Nat. U.
Robert Kingston, Harvard Med. School
Nancy Knowlton, Smithsonian Institution
Etienne Koechlin, Ecole Normale Supérieure
Alexander Kolodkin, Johns Hopkins U.

Thomas Langer, U. of Cologne
Mitchell A. Lazar, U. of Penn.
Ottoline Leyser, U. of Cambridge
Wendell Lim, U. of California, San Francisco
Marcia C. Linn, U. of California, Berkeley
Jianguo Liu, Michigan State U.
Luis Liz-Marzán, CIC biomaGUNE
Jonathan Losos, Washington U. in St. Louis
Ke Lu, Chinese Acad. of Sciences
Christian Lüscher, U. of Geneva
Fabiennne Mackay, U. of Melbourne
Anne Magurran, U. of St. Andrews
Oscar Marin, King's College London
Charles Marshall, U. of California, Berkeley
Christopher Marx, U. of Idaho
Geraldine Masson, CNRS
C. Robertson McClung, Dartmouth College
Rodrigo Medellín, U. of Mexico
Graham Medley, London School of Hygiene & Tropical Med.
Jane Memmott, U. of Bristol
Edward Miguel, U. of California, Berkeley
Tom Misteli, NCI, NIH
Yasushi Miyashita, U. of Tokyo
Alison Motsinger-Reif, NC State U. (\$) **Daniel Nettie, Newcastle U.**
Daniel Neumark, U. of California, Berkeley
Beatriz Noheida, U. of Groningen
Helga Nowotny, Austrian Council
Rachel O'Reilly, U. of Warwick
Harry Orr, U. of Minnesota
Pilar Ossorio, U. of Wisconsin
Andrew Oswald, U. of Warwick
Isabella Pagano, Istituto Nazionale di Astrofisica
Margaret Palmer, U. of Maryland
Elizabeth Levy Paluck, Princeton U.
Jane Parker, Max Planck Inst. Cologne
Giovanni Parmigiani, Dana-Farber Cancer Inst. (\$) **Samuel Pfaff, Salk Inst. for Biological Studies**
Julie Pfeiffer, UT Southwestern Med. Ctr.
Matthieu Piel, Institut Curie
Kathrin Plath, U. of California, Los Angeles
Martin Plenio, Ulm U.
Katherine Pollard, U. of California, San Francisco
Elvira Poloczanska, Alfred-Wegener-Inst.
Julia Pongratz, Ludwig Maximilians U.
Philippe Poulin, CNRS
Jonathan Pritchard, Stanford U.
Félix A. Rey, Institut Pasteur
Trevor Robbins, U. of Cambridge
Joeri Rogelj, Imperial College London
Amy Rosenzweig, Northwestern U.
Mike Ryan, U. of Texas at Austin
Mitsunori Saitou, Kyoto U.
Shimon Sakaguchi, Osaka U.
Miquel Salmeron, Lawrence Berkeley Nat. Lab
Nitish Samarth, Penn. State U.
Jürgen Sandkühler, Med. U. of Vienna
Alexander Schlier, Harvard U.
Wolfram Schlenker, Columbia U.
Susannah Scott, U. of California, Santa Barbara
Rebecca Sear, London School of Hygiene & Tropical Med.
Vladimir Shalaeff, Purdue U.
Jie Shan, Cornell U.
Beth Shapiro, U. of California, Santa Cruz
Jay Shendure, U. of Washington
Steve Sherwood, U. of New South Wales
Brian Shiochet, U. of California, San Francisco
Robert Siliciano, Johns Hopkins U. School of Med.
Lucia Sivilotti, U. College London
Alison Smith, John Innes Centre
Richard Smith, U. of North Carolina (\$) **Mark Smyth, QIMR Berghofer**
Pam Soltis, U. of Florida
John Speakman, U. of Aberdeen
Tara Spire-Jones, U. of Edinburgh
Allan C. Spradling, Carnegie Institution for Science
V. S. Subrahmanian, U. of Maryland
Ira Tabas, Columbia U.
Sarah Teichmann, U. of Cambridge
Rocio Titaniuk, Princeton U.
Shubha Tota, Tata Inst. of Fundamental Research
Wim van der Putten, Netherlands Inst. of Ecology
Reinhold Veugeler, KU Leuven
Bert Vogelstein, Johns Hopkins U.
Kathleen Vohs, U. of Minnesota
David Wallach, Weizmann Inst. of Science
Jane-Ling Wang, U. of California, Davis (\$) **David Waxman, Fudan U.**
Jonathan Weissman, U. of California, San Francisco
Chris Wikle, U. of Missouri (\$) **Terrie Williams, U. of California, Santa Cruz**
Ian A. Wilson, Scripps Research (\$) **Yu Xie, Princeton U.**
Jan Zaanen, Leiden U.
Kenneth Zaret, U. of Penn. School of Med.
Jonathan Zehr, U. of California, Santa Cruz
Xiaowei Zhuang, Harvard U.
Maria Zuber, MIT

Envision a future, make it so

In February, the American Association for the Advancement of Science (AAAS, the publisher of *Science*) and the scientific community will come together in Seattle, Washington, for the 2020 AAAS annual meeting under the theme of *Envisioning Tomorrow's Earth*. This convergence of a vast geographically dispersed community comes at a time of great opportunity and challenge.

These are my first weeks as the new chief executive officer of AAAS and executive publisher of the *Science* family of journals. As part of the leadership of the world's largest multidisciplinary scientific society and nonprofit publisher, I will put my energy, skills, and passion to work in service to our mission of advancing science and serving society. I join a multitude of members who also believe that this is not a moment for stewards, but for leaders. We envision tomorrow's Earth to be a place where our children and their descendants will see science as a key to good decision-making, be awed by the fundamental discoveries under their feet and in the night sky, and be inspired to imagine the future that they want and take action to make it so. As the father of three school-aged children, I am completely committed to this vision.

In the pages of *Science* and elsewhere, we see the extraordinary advances of our era: the potential to not just treat, but cure diseases; computing and technology advances that may serve as the basis for life-improving products; and deepening understanding of the universe through exquisite images of objects in the outer reaches of the solar system and beyond. But we also see that the percentage of Americans who believe that vaccines are unsafe continues to grow; that new technologies raise transcendent questions around privacy and access; and that a small, but substantial and growing number believe Earth is flat.

These challenges to the relationship between science and society are most consequential when they become entangled with policy-making. Many examples face us today, from human germline gene editing to

climate change. With the consequences so far-reaching, science must be integral to decision-making at every policy table and kitchen table.

AAAS must take on the critical topics of our time. We will lead when appropriate and collaborate with like-minded organizations always. As a voice for all sciences, AAAS must take a leadership role in issues that affect the entire scientific enterprise. Areas where you will see AAAS's commitment include global engagement. As more nations take their rightful place at the frontiers of science, a global scientific culture is evolving that must incorporate the best from all and value integrity, inclusivity, and ingenuity. We will continue to invigorate the

**"...this is not
a moment for
stewards,
but for leaders."**

United States as a welcoming crossroads where the best and brightest scientists converge to build the future while protecting science from unacceptable influence and unethical appropriation of intellectual property and ideas. AAAS will also advocate for safeguarding the scientific ecosystem for diverse voices and inclusivity and leverage the power of all great minds. AAAS will continue to be a leading voice for ensuring that evidence-based science is at the

decision-making table at the international, national, and local levels to address preeminent challenges like climate change. And we will always stand up for investments in science and science education. On issues specific to individual disciplines, AAAS will collaborate and coordinate its activities with the leading organizations in that space. We look to our members for input, guidance, and leadership and encourage others to join in strengthening society's relationship with science.

This is a pivotal moment. Rarely have the opportunities for progress been as exciting, yet the challenges so existential. We must rise to the challenges of our time to ensure that the next generation has the opportunity to rise to theirs.

I look forward to *Envisioning Tomorrow's Earth* and to the privilege of working with all of you.

—Sudip Parikh



Sudip Parikh
is the chief executive officer of the American Association for the Advancement of Science (AAAS) and executive publisher of the *Science* journals.
sparikh@aaas.org

“Wake up, America! Wake up, world!”

Jerry Brown, former governor of California and executive chair of the Bulletin of the Atomic Scientists, as the group moved up its Doomsday Clock to 100 seconds until midnight, the closest ever, because of threats from military conflict and climate change.

IN BRIEF

Edited by Jeffrey Brainard



A microbiologist studies the H5N1 avian influenza virus in a biosafety lab.

INFECTIOUS DISEASE

Biosecurity panel to consider openness

A U.S. advisory committee last week agreed to review how to balance security and transparency in research that tweaks risky pathogens in ways that could make them more dangerous to humans. Gain-of-function research that makes pathogens more potent or likely to spread in people could help experts prepare for pandemics. But critics worry that a labmade virus could escape and cause an outbreak. The critics want more transparency, noting that more than 1 year ago, a Department of Health and Human Services (HHS) panel that weighs the risks and benefits of such experiments approved new work on the H5N1 bird flu virus in secret (*Science*, 15 February 2019, p. 676). At last week's meeting of a separate federal committee that offers guidance for such research—the National Science Advisory Board for Biosecurity, which includes academic scientists—HHS officials said they were open to greater disclosure. But meeting participants also noted that the emergence of a new virus in China (p. 492) underscores the need for prompt approvals. The board is to develop recommendations by early summer.

China ties snare Harvard chemist

FOREIGN INFLUENCE | The chair of Harvard University's chemistry department was arrested and charged this week with lying to authorities about his involvement in China's Thousand Talents Program, which recruits foreign scientists. Charles Lieber has received more than \$15 million in U.S. federal research funding since 2008 for his lab's work in nanoscience, according to prosecutors. From 2012 to 2017, he also participated in the Thousand Talents Program, which paid him up to \$50,000 monthly plus additional living expenses and more than \$1.5 million to establish a lab at Wuhan University of Technology, the U.S. Attorney's Office in Boston said. Lieber told investigators in 2018 and 2019 he had never been asked to participate in the program, the office said. He is one of the highest profile researchers to be caught up in a wide-ranging U.S. government effort to crack down on what officials have alleged is a systematic effort by China to take unfair advantage of federally funded research. In a similar case, Turab Lookman, a theoretical physicist at Los Alamos National Laboratory, last week pleaded guilty to denying his participation in China's program. Neither Lookman nor Lieber has been accused of espionage.

Creationist leads Brazil agency

LEADERSHIP | Brazilian scientists are up in arms about the appointment of a creationist advocate to head CAPES, the federal agency responsible for regulating all graduate-level programs at Brazilian universities. Benedito Guimarães Aguiar Neto, appointed CAPES director on 24 January, previously served as the rector of Mackenzie Presbyterian University. The private religious school in São Paulo supports intelligent design (ID), an argument without scientific basis that presents creationist critiques of Charles Darwin's theory of evolution. The university hosted the second Congress on Intelligent Design in October 2019, and Aguiar Neto recently said ID should be introduced in Brazil's basic education curricula as “a counterpoint to the theory of evolution.” Brazilian President Jair Bolsonaro enjoys strong support from Brazil's evangelical Christians, many of whom advocate the teaching of creationism in schools.



Wandering albatrosses float near a toothfish longline fishing vessel.

CONSERVATION

Seabirds outfitted to spot lawbreakers

A new type of eye in the sky is on the lookout for illegal fishers on the ocean. Vessels of a certain size are required to broadcast their locations to avoid collisions, but some turn off satellite transponders so they can break fishing laws. But the crews continue to use radar to avoid obstacles, and albatrosses fitted with small radar scanners can detect the signals, researchers report this week in the *Proceedings of the National Academy of Sciences*. Albatrosses are attracted to fishing vessels,

where they prey on fish. The authors taped scanners to the feathers of 169 albatrosses on three remote islands in the southern Indian Ocean. They estimate that up to one-third of vessels in the southern Indian Ocean are sailing incognito, backing concerns about illegal fishing. In the future, the large patrolling seabirds might help guide fishing enforcement. The birds might also aid conservation of their own species, many of which are listed as threatened, in part because of illegal fishing operations.

EU court backs data releases

DRUG DEVELOPMENT | The European Union's highest court last week upheld decisions by the European Medicines Agency to publish corporate data submitted in applications for drug approvals. Two drugmakers, Merck and PTC Therapeutics, had challenged the disclosures, arguing that they revealed confidential information and could give competitors an unfair advantage. But on 22 January, the European Court of Justice upheld the agency's requirements for transparency, ruling that exceptions should be allowed only if a company can prove that disclosure might cause it concrete harm.

WHO's vaping stand raises ire

PUBLIC HEALTH | New warnings about vaping issued last week by the World Health Organization (WHO) prompted strong pushback from public health experts in the United Kingdom, who charged that WHO

was spreading "blatant misinformation" about the potential risks and benefits of e-cigarettes. The pointed exchange comes amid growing controversy over the hazards of e-cigarettes and their value in smoking cessation. U.K. public health officials have generally supported regulated vaping products as a safer alternative to traditional cigarettes. In contrast, WHO's admonitions echo those voiced by the U.S. Centers for Disease Control and Prevention (CDC). After an outbreak of severe lung disease that's still being investigated and is linked to tetrahydrocannabinol-containing e-cigarettes, CDC now recommends that e-cigarettes of all kinds "never be used by youths."

Michigan suspends provost

#METOO | The University of Michigan (UM), Ann Arbor, last week placed Provost Martin Philbert on administrative leave and began an investigation after receiving on 16 and 17 January "several allegations of sexual misconduct" against him. Philbert,

a toxicologist, studied the effects of nerve toxins on the brain and worked to develop early detection methods for brain cancer. He was dean of the UM School of Public Health before he was made provost in 2017.

TB work resumes in North Korea

PUBLIC HEALTH | A critical lifeline for combatting infectious diseases in North Korea is being restored. On 23 January, the Global Fund to Fight AIDS, Tuberculosis, and Malaria announced an agreement with the North Korean government to spend \$41.7 million over 3 years on efforts against tuberculosis (TB)—including multidrug-resistant strains—and malaria. North Korea has one of the world's highest TB rates, and its stockpile of first-line TB drugs was expected to run out by summer. The agreement reverses the Global Fund's much-criticized decision in 2018 to suspend operations in North Korea; the fund had cited the difficulty of managing grants in the country's "unique operating environment."



An ambulance crosses a deserted bridge in Wuhan, China, which has been cordoned off from the outside world.

INFECTIOUS DISEASES

New coronavirus threat galvanizes scientists

As China outbreak spreads worldwide, researchers probe its origins and how to fight it

By Jon Cohen

Barely 1 month after Chinese health authorities reported the first cases of a mysterious new pneumonia in the city of Wuhan, the world may be on the cusp of a new pandemic. As *Science* went to press, the number of confirmed cases of the novel coronavirus, dubbed 2019-nCoV, had shot up to more than 4500, most of them in mainland China but more than 80 in 17 other countries and territories. China has quarantined 35 million people in Wuhan and several other cities in a desperate attempt to slow the spread of the virus. But as the case numbers keep soaring, the realization has set in that it may be too late to have much impact.

Even seasoned epidemiologists are astonished at the virus's dizzying spread. Early estimates of the number of infected people—thought to far exceed the number of confirmed cases—became obsolete overnight. “Our original results are NO LONGER VALID,” University of Hong Kong epidemiologist Gabriel Leung tweeted on 22 January, 1 day after his group had posted its first mathematical model of the epidemic. Leung is now estimating that Wuhan alone had 43,590 infections by 25 January—and that the number is doubling every 6 days. “How widespread does this go?” asks Marion Koopmans, a virologist at Erasmus Medical

Center. “This deserves our full attention.”

Early this week, the World Health Organization (WHO) had not yet declared the outbreak a Public Health Emergency of International Concern (PHEIC), the loudest alarm the agency can sound. In meetings on 22 and 23 January, a special WHO committee that includes Koopmans was divided on whether a PHEIC was warranted, in part because there was no evidence the disease was spreading between people outside of China. But by 28 January, several countries had reported local human-to-human transmission, which may change the equation.

So far 2019-nCoV appears to be milder than its cousin, severe acute respiratory syndrome (SARS), which had a mortality rate of 10%. Only 106 deaths have been recorded to date. But hundreds more people are seriously ill, and their fate is unclear. And countless other questions remain. Scientists don't know how long the incubation period lasts or whether infected people who show no symptoms can transmit the virus. China's state-run news agency Xinhua reported on 26 January that a seemingly healthy man appeared to have infected “a few colleagues.” If asymptomatic people frequently infect others, it could vastly complicate efforts to contain 2019-nCoV.

The virus's explosive spread has been met by an unprecedented rush by scientists to uncover its origins, find treatments, and develop vaccines that could save millions

of lives if the world really does face a pandemic. Here are some of the ways researchers are attempting to better understand 2019-nCoV and reduce its harm.

WHERE DID THE VIRUS COME FROM?

Almost certainly from animals, but when and how are mysteries. Genetic analyses are starting to yield some clues. Chinese researchers first shared a genomic sequence of 2019-nCoV on 11 January. Labs in China and abroad have since announced nearly three dozen additional sequences of the virus—“a stellar job,” Koopmans says.

A team led by Shi Zheng-Li of the Wuhan Institute of Virology reported on 23 January that 2019-nCoV's sequence was 96.2% identical to that of a bat coronavirus and 79.5% identical to the SARS coronavirus. That doesn't mean 2019-nCoV jumped directly from bats to humans, says evolutionary biologist Kristian Andersen of Scripps Research. SARS, for example, probably moved from bats to civets—sold as a delicacy in many markets—to humans.

From the start, the Huanan Seafood Wholesale Market in Wuhan—which sold mammals as well as fish—was considered a likely source of the outbreak because most of the early patients had visited it. On 27 January, Xinhua reported that researchers have found evidence of the new coronavirus in 33 of 585 environmental samples

taken at the market on 1 January—the day it was closed—and on 12 January. They all came from the western end, which had a concentration of booths selling wildlife.

That indicates the market played a role in spreading the virus, says Daniel Lucey, an infectious disease specialist at Georgetown University—but he says other data suggest it wasn't the origin. The first known patient became ill on 1 December 2019 and had no links to the market, according to a paper published by Chinese researchers in *The Lancet* on 24 January that offered details about the first 41 patients in Wuhan. In that group, 12 others also had no links to the market. Lucey contends the virus was already circulating silently among humans before it contaminated the seafood market, possibly by infected animals, humans, or both.

The genomic data cannot pinpoint the origin, but they do show that the jump from animals to humans happened recently, Koopmans says. An analysis of the first 30 publicly posted sequences shows they differ from each other by no more than seven nucleotides (see graphic, right). Using these differences and presumed mutation rates, several groups have calculated that the virus began to spread around mid-November 2019—which supports the thesis that spread may have occurred before any of the cases linked to the market. One group put the origin of the outbreak as early as 18 September 2019.

Bin Cao, a pulmonary specialist at Capital Medical University in Beijing and the corresponding author of *The Lancet* article, agrees the story is more complicated than many thought. “Now it seems clear that [the] seafood market is not the only origin of the virus,” he wrote in an email to *Science*. “But to be honest, we still do not know where the virus came from now.”

COULD EXISTING DRUGS WORK?

It may take years to develop treatments specifically designed for 2019-nCoV, but researchers hope existing drugs can help. Wuhan's Jin Yintan Hospital has already launched a randomized, controlled trial of the anti-HIV drug combination of lopinavir and ritonavir, according to the report in *The Lancet*. The duo targets the protease enzyme used by HIV to copy itself, and it might thwart the coronavirus's protease as well. There's a precedent from the SARS outbreak: In a nonrandomized trial published in 2004, researchers saw an “apparent improved outcome” from the same two protease inhibitors, combined with a third drug, ribavirin, in SARS patients.

Saudi Arabia is now conducting a trial with the same protease inhibitors, combined with interferon beta-1b, against Middle East respiratory syndrome (MERS), a coronavirus distantly related to SARS and 2019-nCoV that is occasionally spread by camels. But in a recent mouse study by Ralph Baric of the University of North Carolina, Chapel Hill, this cocktail had lackluster results against MERS.

The same study showed better outcomes for remdesivir, an experimental drug made by Gilead and previously tested against Ebola that interferes with the viral polymerase enzyme. Remdesivir combined with interferon slowed viral replication in MERS-infected mice, and their lung function im-

proved. In real life, new vaccines have never been developed fast enough to have a significant impact on an emerging virus. But in the case of 2019-nCoV, scientists are trying to work at Hollywood speed.

The Coalition for Epidemic Preparedness Innovations (CEPI), a nonprofit formed in 2016 to fund and shepherd the development of new vaccines against emerging infectious diseases, has already given two companies and an academic group a total of \$12.5 million to develop 2019-nCoV vaccines. The efforts began hours after Chinese researchers first published a viral sequence 3 weeks ago.

One is a collaboration between the U.S. National Institute of Allergy and Infectious Diseases (NIAID) and U.S. biotech Moderna, which makes vaccines by converting viral sequences into messenger RNA (mRNA). (When injected into the body, mRNA causes the body to produce a viral protein, which triggers immune responses.) Moderna and NIAID have worked on a vaccine against MERS that consists of mRNA coding for a protein on the viral surface called the spike; in theory, all the team needs to do now is swap in the genetic sequence for 2019-nCoV's spike.

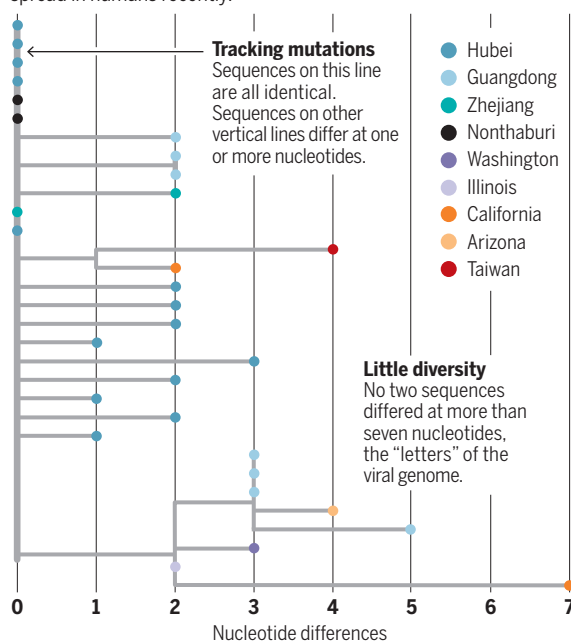
CEPI funded a second company, Inovio, to produce vaccines that work in a similar way but are made of DNA. It, too, has a template for a 2019-nCoV vaccine: another candidate MERS vaccine that relies on the spike protein. CEPI's third grant went to researchers at the University of Queensland who are developing a vaccine made of viral proteins produced in cell cultures. Vaccine projects are also underway in mainland China, Hong Kong, Belgium, and Germany. Once candidate vaccines are available, researchers will test them in animals, then seek approval for phase I human trials. “We're building the airplane as we're flying,” says Inovio CEO Joseph Kim.

NIAID Director Anthony Fauci says the first clinical trial of the Moderna vaccine could start within 3 months. In the best-case scenario, Barney Graham, who leads the project for NIAID, says the Moderna vaccine could be ready for larger, real-world efficacy tests in humans by summer. Even if it works, mass-producing it or any other vaccine quickly would present a huge challenge.

With luck, however, the outbreak will fade by summer, and with it the urgency of having a vaccine at the ready. “Nobody knows what's going to happen,” says Stéphane Bancel, Moderna's CEO. “We're all hoping we'll never need this vaccine.” ■

Genomes offer clues about virus's past

A phylogenetic tree of viral sequences from dozens of patients shows very few differences between them, indicating the new virus began to spread in humans recently.



proved. “Remdesivir has had activity against every coronavirus we’ve tested, and I’d be surprised if it didn’t have activity against” 2019-nCoV, says co-author Mark Denison, a virologist at Vanderbilt University.

Development of entirely new treatments has started as well. U.S. biotech Regeneron is trying to identify monoclonal antibodies effective against 2019-nCoV, as it did previously for MERS and Ebola. The ideal treatment for 2019-nCoV may well be a drug like remdesivir plus monoclonal antibodies, Denison says. “The idea of using those in combination would have profoundly good prospects.”

CAN VACCINES BE DEVELOPED IN TIME?

In the stock pandemic movie, scientists develop a vaccine just in time to save the

EUROPE

After Brexit, a long road to mend ties with Europe

U.K. scientists want to join EU research program, but Europe may balk

By Kai Kupferschmidt

After one referendum, two snap elections, and more than 3 years of dithering and debate, the United Kingdom this week becomes the first country ever to withdraw from the European Union. But rather than marking the end of a process, Brexit will start another clock: an 11-month transition during which the U.K. and Europe will negotiate their future relationship on everything from trade to immigration to clinical trials. “We’re not out of the woods yet,” says Martin Smith, a policy manager at the Wellcome Trust, a U.K. charity.

For researchers, the top issue is U.K. participation in Europe’s research program, Horizon Europe, which will run from 2021 to 2027. At about €90 billion, it is likely to be the bloc’s biggest ever. U.K. researchers now receive about £1.5 billion per year from the current 7-year program, Horizon 2020, and during the transition, they will get the remaining year of grant money owed under the scheme. To join Horizon Europe, however, the United Kingdom will have to pay to access it in the same way as 16 other non-EU countries, including Switzerland, Norway, and Israel.

Although U.K. and EU scientists both want such a deal, European politicians may use it as a bargaining chip in trickier negotiations, such as over border arrangements, says James Wilsdon, a science policy specialist at the University of Sheffield. “In what possible sense is it in [Europe’s] interest to stitch up a neat package on science and put a bow on it for London?” Indeed, the EU research commissioner, Mariya Gabriel, indicated in an interview this month that the European Union would not offer a separate deal on research.

If the United Kingdom is left out of Horizon Europe, the impact will be unequal, says Graeme Reid, a science policy researcher at University College London. Money from Horizon 2020 amounts to just 3% of total U.K. R&D spending overall, but in some disciplines, such as archaeology

and software engineering, it is more than 30%. The loss of those funds “is going to make the research base in this country look like a Swiss cheese: It’s going to be solid overall but will have holes punched in it in unpredictable places,” Reid says.

In November 2019, the U.K. government released a report, co-authored by Reid, on options if it does not join Horizon Europe. The report called for mimicking some aspects of the European program—such as

concerns for the clinical trials her organization supports in the United Kingdom. Now that an exit deal is in place, she isn’t as worried as before about the delivery of experimental medicines for ongoing trials. But she fears Brexit’s long-term fallout will make the United Kingdom a less attractive place for clinical trials.

Much depends on whether the United Kingdom ends up outside a new European system for clinical trials that it helped shape. The system allows trial leaders to apply for approval only once, through a central portal, rather than through multiple national bodies. If the U.K. no longer participates, EU researchers may not want to include U.K. patients in pan-EU clinical trials, or may avoid leading trials in the nation, Ball says. “This extra layer of burden will disincentivize people,” she says.

Researchers also fear that the flow of data between the U.K. and Europe may be choked off. The European Union’s general data protection regulation, a 2018 law, allows data to be freely exchanged between the United Kingdom and other EU countries. Once the transition period ends, however, the European Commission’s Directorate-General for Justice and Consumers will have to declare U.K. data protection as “adequate” for free exchanges to continue. “If arrangements for that aren’t put in place by the end of the year, then lots of things will start to grind to a halt,” Smith says.

The U.K. government, meanwhile, has tried to allay researchers’ concerns by announcing its intention to increase spending on research to 2.4% of gross domestic product, putting U.K. spending near the top for developed countries. “We won’t know how much of this is theater over substance for a while,” Wilsdon says. The next budget, set to be announced on 11 March, will give a clearer sense of what will happen, he says. “If they start to really put proper extra money behind all of this rhetorical commitment, then that will further water down opposition and concern over the European funding question.” ■



creating an organization that disburses long-term grants, like the European Research Council—but not all. “We think we should start again and optimize around U.K. interests,” he says.

Making sure EU scientists are free to live and work in the United Kingdom is also a priority, Smith says. “Mobility will be a big part of what we’re interested in in the next 11 months.” Prime Minister Boris Johnson this week announced new fast-track visas for researchers that will begin on 20 February. There will be no cap on them, and they will be managed by UK Research and Innovation instead of the Home Office.

Cat Ball, head of policy at the Association of Medical Research Charities, has



Models suggest black holes can stretch devoured stars into long streamers.

ASTROPHYSICS

Black holes caught in the act of swallowing stars

Dozens of tidal disruption events found in galaxy surveys shed light on violent events

By **Daniel Clery**

At the center of nearly every galaxy lies a monster, a giant black hole millions or even billions of times heavier than the Sun. Some, known as quasars or active galactic nuclei, shine brightly from across the universe as they continuously devour surrounding gas. But most are dormant, lurking invisibly for thousands of years—until a star passes too close and is ripped to shreds. That triggers a monthslong tidal disruption event (TDE), which can shine as brightly as a supernova.

Until a few years ago, astronomers had spotted only a handful of TDEs. But now, a new generation of wide-field surveys is catching more of them soon after they start—yielding new insights into the violent events and the hidden population of black holes that drives them.

“We’re still in the trenches, trying to understand the physical mechanisms powering these emissions,” says Suvi Gezari of the University of Maryland, College Park. Earlier this month at the annual meeting of the American Astronomical Society in Honolulu, Gezari presented an analysis of 39 TDEs: 22 from recent years and 17 detected in the first 18 months of operation of the Zwicky Transient Facility (ZTF), a 1.2-meter survey telescope in California.

In the standard TDE picture, the gravity of the black hole shreds an approaching star into strands like spaghetti. The black hole immediately swallows half the star’s matter while the rest arcs away in long streamers. These rapidly fall back and settle into an accretion disk that steadily feeds material into the black hole, growing so hot that it emits copious x-rays.

An x-ray mapping satellite spotted the first TDEs in the 1990s. Now, optical surveys like the ZTF are picking up the fast-changing events and capturing telltale details of the visible glow. They are also alerting other observatories, such as NASA’s Swift telescope, to make follow-up observations at ultraviolet and x-ray wavelengths.

The fingerprints of certain gases in the spectra of the visible light can reveal what kind of star went down the black hole’s maw. Gezari and her colleagues found that the TDE spectra fell into three classes, dominated by hydrogen, helium, or a mixture of gases. Hydrogen likely signals large, young stars, whereas helium events could point to the cores of older stars whose hydrogen shells were stripped away—perhaps by an earlier brush with the black hole. She says the proportions reveal something about the populations of stars at the very centers of galaxies, at distances from Earth that would otherwise be impossible to probe.

If astronomers could turn the light into a reading of how quickly material is being sucked in, they might be able to determine a black hole’s mass—something usually estimated crudely by measuring the size of its galaxy. For that, however, “We need to understand the astrophysics of the process with greater clarity,” says Tsvi Piran of the Hebrew University of Jerusalem. For a few TDEs, astronomers have been able to compare the rise and fall of the visible glow with x-ray measurements made from space—and puzzlingly, the two don’t match. The x-rays often flare irregularly, appear late, or are absent altogether.

The x-rays could be steady but obscured by a cloud of gas, hundreds of times bigger than the black hole, that forms from a backlog of

material, says Kate Alexander of the Harvard-Smithsonian Center for Astrophysics. “It’s like the black hole gets indigestion because it eats too much too fast.” Piran thinks it’s more likely that the x-rays are generated in bursts, as clumps of matter fall into the black hole. Either way, astronomers aren’t ready to glean a black hole’s mass from a TDE’s brilliance.

Theory does suggest black holes can become too massive to trigger TDEs. Above a mass of 100 million suns, black holes should swallow stars whole rather than tearing them apart as they approach. So far, all of the growing number of TDEs come from smaller galaxies, suggesting the limit is real.

TDEs could even provide a window into a more elusive black hole characteristic: its spin. Dheeraj Pasham of the Massachusetts Institute of Technology has studied the soft x-ray emissions of three TDEs that pulse in semiregular beats. He says similar, higher frequency beats have been observed coming from smaller, stellar-mass black holes, and he suspects the pulsing reflects the black hole’s spin. Constraints on this property could help solve an enduring mystery: whether giant black holes form by slowly accreting stellar matter over their lifetime—a process expected to produce a fast spin—or by merging with the giant black holes from other galactic cores, which would result in a slower spin. An x-ray survey of many TDEs could reveal which process dominates.

With the tally of captured TDEs growing fast, and hundreds or even thousands of discoveries per year expected from new surveys, researchers are hopeful that the events will answer more questions. “My dream is for TDEs to be some kind of ruler or scale for black hole mass,” Gezari says. “We’re not there yet but we’re getting closer.” ■

MATERIALS SCIENCE

Electricity turns garbage into high-quality graphene

Method could supply graphene in bulk, opening new uses

By Robert F. Service

Awonder material could soon become a bulk commodity. Researchers at Rice University report in *Nature* this week that they can zap virtually any source of solid carbon, from food scraps to car tires, and turn it into graphene—sheets of carbon atoms prized for use in high-strength plastic and flexible electronics. Current techniques yield tiny amounts of picture-perfect graphene or up to tons of less-prized graphene chunks; the new method already produces grams per day of near-pristine graphene in the lab, and researchers are now scaling it up to kilograms per day.

“This work is pioneering from a scientific and practical standpoint,” says Ray Baughman, a chemist at the University of Texas, Dallas, as it promises graphene cheap enough to strengthen asphalt or paint. “I wish I had thought of it.” Already the Rice team has founded a company, Universal Matter, to commercialize the waste-to-graphene process.

With atom-thin sheets of carbon atoms arranged like chicken wire, graphene is stronger than steel, conducts electricity and heat better than copper, and can serve as an impermeable barrier. But since its 2004 discovery, high-quality graphene—in single sheets or a few stacked layers—has remained expensive to make and purify on an industrial scale. That’s not a problem for making diminutive devices such as transistors and light-emitting diodes. But current techniques, which make graphene by depositing it from a vapor, are too costly for high-volume applications. And higher throughput approaches, such as peeling graphene from chunks of graphite, pro-

duce flecks composed of up to 50 graphene layers that are not ideal for most applications.

In 2014, James Tour, a chemist at Rice, and his colleagues found they could make a more pure form of graphene—each piece just a few layers thick—by zapping a form of amorphous carbon called carbon black with a laser. Brief pulses heated the carbon to more than 3000 kelvins, snapping the bonds between carbon atoms. As the carbon cooled, it coalesced into graphene. But the approach used a lot of energy to make tiny quantities.

Then, Luong Xuan Duy, one of Tour’s graduate students, read that other researchers had created metal nanoparticles by zapping a material with electricity, creating the same brief blast of heat as the laser. So Duy put a dash of carbon black in a glass vial and zapped it with 400 volts for up to 200 milliseconds. Initially he got junk. But after tweaks, he saw a yellowish white flash, indicating the temperature in the vial was about 3000 kelvins. Chemical tests revealed he had produced graphene.

It was a type of graphene ideal for bulk uses: “turbostatic” graphene, with its layers at all angles atop one another. “That’s a good thing,” Duy says. In water or other solvents, turbostatic graphene remains suspended instead of clumping, allowing each fleck to interact with the composite it’s added to.

“This will make it a very good material for applications,” says Monica Craciun, a materials physicist at the University of Exeter. In 2018, she and her colleagues reported that adding graphene to concrete more than doubled its compressive strength. Tour’s team saw much the same result. When it added just 0.05% by weight of flash-produced graphene to concrete, the compressive strength rose 25%; graphene added to polydimethylsiloxane, a common plastic, boosted its strength by 250%. Other research suggests it can improve the durability of asphalt and paint.

These applications would require high-quality graphene by the ton. Fortunately, the starting point for flash graphene could hardly be cheaper or more abundant: Virtually any organic matter, including coffee grounds, food scraps, old tires, and plastic bottles, can be vaporized to make the material. “We’re turning garbage into graphene,” Duy says. ■



An electric jolt provides abundant graphene in a flash.



Nikos Logotheitis

ANIMAL RESEARCH

Monkey facility in China lures neuroscientist

Animal rights conflict spurs move of major German lab

By Gretchen Vogel

A prominent neuroscientist whose lab in Germany was targeted by animal rights activists is heading to China, where he says he will be freer to pursue research on macaques and other monkeys. Nikos Logotheitis, one of the directors at the Max Planck Institute for Biological Cybernetics in Tübingen, also says leaders of the Max Planck Society did not defend him strongly enough when he faced the activists and subsequent legal problems in Germany.

“I would still consider staying here [in Tübingen], continuing with rodents,” he says, while doing primate work elsewhere. But Germany’s widespread skepticism of animal research and his disappointment with Max Planck “made this impossible.”

Logotheitis, who studies the brain’s visual system, told colleagues last week that several group leaders from his department will move in the coming months to a new International Center for Primate Brain Research (ICPBR) in Shanghai. Logotheitis will co-direct the center with neuroscientist Poo Mu-Ming, scientific director of the Chinese Academy of Sciences’s Center for Excellence in Brain Science and Intelligence Technology; he will follow after remaining lab members finish their projects. ICPBR will house as many as 6000 nonhuman pri-

PHOTOS: (TOP TO BOTTOM) MARIJAN MURAT/PICTURE ALLIANCE/DPA/AP IMAGES, JEFF FITLOW/RICE UNIVERSITY

mates, including many transgenic monkeys. Poo hopes it will become an international destination for primate neurobiology, akin to CERN for the particle physics community.

"Scientifically it's incredible," Logothetis says. "They have excellent groups working with CRISPR and genetic engineering." And, he adds, the acceptance of nonhuman primate research by authorities and the public in China is much higher than in Europe. They "know that no other brain (besides that of humans themselves) can be a true help in making progress."

The move is another sign that China's investment in neuroscience research, especially involving primates, is paying off, says Stefan Treue, director of the German Primate Center. "China has made incredible progress in an unbelievably short period of time. That is the positive side of a political system that is able to move very quickly."

For nearly 2 decades Logothetis worked primarily with macaques, sometimes implanting electrodes in their brains. In 2014, a German TV program broadcast footage from an undercover animal rights activist showing one animal lame and vomiting and another with blood on its head. Logothetis and colleagues denied any wrongdoing and said the video was misleading and staged. But it triggered an investigation, including a police raid on offices at the institute. Logothetis received death threats. In 2015, he said he would stop work with primates.

Initial legal investigations found no violation of animal regulations at his lab. But in 2017, a Tübingen prosecutor charged that Logothetis and two colleagues had violated Germany's animal protection laws by waiting too long to euthanize ill monkeys. Max Planck removed Logothetis from direct oversight of animal research at the lab. All charges against him and his colleagues were later dropped and the society lifted all restrictions on his leadership. During the episode, major neuroscience organizations published open letters critical of Max Planck's handling of the situation.

Max Planck spokesperson Christina Beck says Logothetis had already informed the society of his move, but not the specific timing. "It's a pity that the vital discussion about whether such research should be left up only to China has been overshadowed by the 2014 case," she says.

Logothetis has been in negotiations with Poo since at least 2018. All five group leaders in his department plan to move with him, he says, along with about half of the roughly 40 current lab members. Other international researchers are considering ICPBR, he adds, including several in Germany. ■

With reporting by Dennis Normile in Shanghai.

HUMAN EVOLUTION

Africans, too, carry Neanderthal genetic legacy

Ancient Europeans took Neanderthal DNA back to Africa

By **Michael Price**

For 10 years, geneticists have told the story of how Neanderthals—or at least their DNA sequences—live on in today's Europeans, Asians, and their descendants. Not so in Africans, the story goes, because modern humans and our extinct cousins interbred only outside of Africa. A new study overturns that notion, revealing an unexpectedly large amount of Neanderthal ancestry in modern populations across Africa. It suggests much of that DNA came from Europeans migrating back into Africa over the past 20,000 years.

"That gene flow with Neanderthals exists in all modern humans, inside and outside of Africa, is a novel and elegant finding," says anthropologist Michael Petraglia of the Max Planck Institute for the Science of Human History. The work, reported in this week's issue of *Cell*, could also help clear up a mysterious disparity: why East Asians appear to have more Neanderthal ancestry than Europeans.

As members of *Homo sapiens* spread from Africa into Eurasia some 70,000 years ago, they met and mingled with Neanderthals. Researchers knew that later back-migrations of Europeans had introduced a bit of Neanderthal DNA into African populations, but previous work suggested it was a just a smidgen. In contrast, modern Europeans and East Asians apparently inherited about 2% of their DNA from Neanderthals.

Previous efforts simply assumed that Africans largely lacked Neanderthal DNA. To get more reliable numbers, Princeton University evolutionary biologist Joshua Akey compared the genome of a Neanderthal from Russia's Altai region in Siberia, sequenced in 2013, to 2504 modern genomes uploaded to the 1000 Genomes Project, a catalog of genomes from around the world that includes five African subpopulations. The researchers then calculated the probability that each stretch of DNA was inherited from a Neanderthal ancestor.

The researchers found that African individuals on average had significantly

more Neanderthal DNA than previously thought—about 17 megabases (Mb) worth, or 0.3% of their genome. They also found signs that a handful of Neanderthal genes may have been selected for after they entered Africans' genomes, including genes that boost immune function and protect against ultraviolet radiation.

The results jibe with as-yet-unpublished work by Sarah Tishkoff, an evolutionary geneticist at the University of Pennsylvania. She told *Science* she has also found higher-than-expected levels of apparent Neanderthal DNA in Africans.

The best fit model for where Africans got all this Neanderthal DNA suggests about half of it came when Europeans—

who had Neanderthal DNA from previous matings—migrated back to Africa in the past 20,000 years. The model suggests the rest of the DNA shared by Africans and the Altai Neanderthal might not be Neanderthal at all: Instead, it may be DNA from early modern humans that was simply retained in both Africans and Eurasians—and was picked up by Neanderthals, per-

haps when moderns made a failed migration from Africa to the Middle East more than 100,000 years ago.

Akey's study might help explain another "head scratcher," says computer biologist Kelley Harris of the University of Washington, Seattle. Studies had suggested East Asians have 20% more Neanderthal DNA than Europeans, she notes. "Europe is where Neanderthal remains are found, so why wouldn't Europeans have more Neanderthal ancestry than any other group?"

By suggesting that Europeans introduced Neanderthal sequences into Africa, the new study points to an explanation: Researchers previously assumed that Neanderthal sequences shared by Europeans and Africans were modern and subtracted them out. After correcting for that bias, the new study found similar amounts of Neanderthal DNA in Europeans and Asians—51 and 55 Mb, respectively. It's a "convincing and elegant" explanation, Harris says. ■

"Gene flow with Neanderthals exists in all modern humans, inside and outside of Africa ..."

Michael Petraglia,

Max Planck Institute for the Science of Human History

PUBLIC HEALTH

Screen for childhood trauma triggers debate

Testing across California could have unexpected downsides, critics say

By Emily Underwood

On 1 January, California became the first U.S. state to screen for adverse childhood experiences (ACEs)—early life hardships such as abuse, neglect, and poverty, which can have devastating health consequences in later life. The project is not just a public health initiative, but a vast experiment. State officials aim to cut the health impacts of early life adversity by as much as half within a generation. But critics say the health benefits of screening are unproven, and it could create demand for services the state cannot provide.

The \$160 million initiative applies to 7 million children on Medi-Cal, California's insurance for low-income people. Health care providers who complete 2 hours of online training are encouraged to screen children up to age 18 for ACEs. The questionnaire, filled out by children's caregivers or teenagers themselves, includes 10 categories of ACEs, such as domestic violence, neglect, and substance abuse, with questions such as "Has your child ever seen or heard a parent/caregiver being screamed at, sworn at, insulted or humiliated by another adult?" and "Have you ever felt unsupported, unloved and/or unprotected?"

If a child has a worrying score, the provider is instructed to give information about helpful resources such as food stamps or housing assistance, discuss how trauma and stress affect the developing body and brain, and, if necessary, make referrals to specialists, such as psychologists.

"The overwhelming body of data ... tells us that early detection and early intervention improves outcomes" for children with high ACEs scores, says California Surgeon General Nadine Burke Harris, who is leading the initiative. "We have the science to act."

Burke Harris notes that toxic stress can set a child on a lifelong trajectory of ill health. A 1998 study by researchers at Kaiser Permanente, for example, found that of 9500 adults, those who remembered high numbers of ACEs had a four- to 12-fold increased risk of alcoholism, drug abuse, depression, and suicide attempts. A follow-

up study of more than 17,000 people found that those who recalled six or more ACEs died 20 years earlier than people who reported none. To try to stem the toll, Medi-Cal also pays for adults to be screened for ACEs, so that doctors can recommend treatments for stress-related conditions such as addiction and depression.

The evidence that ACEs affect health in adulthood is "pretty indisputable," says Aric Prather, a psychologist at the University of California, San Francisco (UCSF). But some researchers caution that the California screen could have unintended consequences. Because state law requires providers to report child abuse and neglect, David Finkelhor, director of the Crimes

many ACEs is also quite scant, Finkelhor says—especially if the trauma was not recent and the child shows no symptoms. "It's not clear to me that [we should treat] a kid who was abused 5 or 6 years ago but doesn't have symptoms or problems."

To test the screen and find out what interventions work, pediatrician Dayna Long of UCSF is running a clinical trial of the new screen with 550 families. Researchers know that those with a stable, supportive caregiver are more resistant to the negative health effects of ACEs, so supporting caregivers is a top priority, she says. And other pilot studies suggest basic services such as food and shelter, counseling, and instruction in techniques such as meditation can also help children overcome trauma.

Yet California may not be capable of providing such wraparound services to all who need them. If doctors start to refer all Medi-Cal enrollees with a history of ACEs to specialists, it could "open a floodgate," Prather says. On the other hand, he says, the program could underscore the need "to ensure the safety of our youngest and most vulnerable" and prompt California to develop new services.

For researchers, Prather says, the screening program offers a chance to study why some people are more resilient to ACEs, and how different adverse experiences affect the brain and body. The state plans to fund studies with \$9 million from the private-public California Initiative to Advance Precision Medicine. "My hope is that as we start to generate data as a state, there's an investment in both the quality and rigor of science so that we can continue to drive policy," Long says. "Ultimately, we want to be able to look across the generations and ask, 'How did we do?'"

How will Burke Harris know whether her state's ambitious plan to reduce childhood trauma has worked? One measure is money, she says. In 2013, for example, ACEs cost Californians \$10.5 billion, she and her colleagues report this week in *PLOS ONE*. If spending on ACEs-related conditions such as asthma, depression, and heart disease falls in coming years, she says, she will count the effort as a success. ■



California aims to reduce childhood trauma's harmful health effects.

against Children Research Center at the University of New Hampshire, Durham, worries that screening could "tremendously increase the number of minor or unnecessary referrals to the child protection system." Burke Harris says that pilot studies haven't shown a significant uptick in such reports, but the state is monitoring for that. "We take those concerns seriously."

Finkelhor points out that many ambitious screening projects have failed to show benefit, and some actually caused harm. Universal domestic violence screenings for women, for example, haven't been shown to improve health or quality of life, he says—perhaps because providers don't know how to help those who report abuse. The evidence about what to do for a child with

A sharp-eyed collector spotted this translucent flint blade—crafted by hunter-gatherers about 8000 years ago—on a Dutch beach.



EUROPE'S LOST FRONTIER

Aided by dedicated amateurs and new methods, scientists reconstruct a now-submerged ancient landscape—and the people who lived there

By **Andrew Curry**, in *Monster, the Netherlands*; Photography by **Manon Bruininga**

On a clear, windy autumn afternoon last October, Willy van Wingerden spent a few free hours before work walking by the sea not far from the Dutch town of Monster. Here, in 2013, the cheerful nurse found her first woolly mammoth tooth. She has since plucked more than 500 ancient artifacts from the broad, windswept beach known as the Zandmotor, or “sand engine.” She has found Neanderthal tools made of river cobbles, bone fishhooks, and human remains thou-

sands of years old. Once, she plucked a tar-covered Neanderthal tool from the water’s edge, earning a co-author credit in the *Proceedings of the National Academy of Sciences (PNAS)* a few months ago.

“Sun, wind, rain, snow—I’m here 5 or 6 days a week,” she says. “I find something every day, almost.”

Van Wingerden’s favorite beachcombing spot is no ordinary stretch of sand. Nearly half a kilometer wide, the beach is made of material dredged from the sea bottom 13 kilometers offshore and dumped on the

existing beach in 2012. It’s a €70 million experimental coastal protection measure, its sands designed to spread over time to shield the Dutch coast from sea-level rise. And the endeavor has made 21 million cubic meters of Stone Age soil accessible to archaeologists.

That soil preserves traces of a lost world. During the last ice age, sea levels were 70 meters lower, and what is now the North Sea between Great Britain and the Netherlands was a rich lowland, home to modern humans, Neanderthals, and even

earlier hominins. It all disappeared when glaciers melted and sea level rose about 8500 years ago.

That vast continental shelf has been a blank spot on the map of prehistoric Europe because archaeologists can't mount traditional excavations underwater. Now, thanks to the Zandmotor and construction work on a harbor extension in nearby Rotterdam, van Wingerden and a dedicated cadre of amateur beachcombers are amassing an impressive collection of artifacts

will make a huge difference to our understanding of prehistory," retired University of York archaeologist Geoff Bailey says.

CLAD IN A BRIGHT YELLOW windbreaker and blue rubber boots, van Wingerden kept her eyes on the sand as she crunched across razor clamshells and bits of driftwood. To the south, the cranes of Rotterdam harbor—Europe's largest port—were just visible on the horizon. To the north, oversize kites bobbed in the sky, pulling kitesurfers along



Willy van Wingerden has found hundreds of ancient artifacts on beaches near her home in the Netherlands.

from that vanished landscape. Scientists on both sides of the North Sea are applying precise new methods to date the artifacts and sequence any genetic traces, as well as mapping the sea floor and analyzing sediment cores. The effort is bringing to light the landscape and prehistory of a lost homeland of ancient Europeans.

The finds show that the region was an inviting place in the few thousand years before it vanished, with forests and river valleys rich in game. "It's not a blank area, it's not a land bridge, it's probably one of the best areas for hunter-gatherers in Europe," says Vincent Gaffney, an archaeologist at the University of Bradford.

The dark, cold waters that now hide the region add to its allure because they preserve organic material for DNA analysis and radiocarbon dating better than on land. And the techniques now being tested to explore the area could aid research on submerged landscapes elsewhere, such as Beringia, the vanished land between Asia and North America inhabited by the first Americans. "It really is a pioneer field and

far below. "Sometimes things are on dry sand; sometimes they're near the water," van Wingerden said of her finds. "There's really no logic to it."

Fifty thousand years ago, the landscape looked different. Doggerland—which University of Exeter archaeologist Bryony Coles named in the 1990s after the Dogger Banks, a productive North Sea fishing spot—extended from Amsterdam up to Scotland and southern Norway. The region once encompassed at least 180,000 square kilometers of dry land, four times the size of the Netherlands today (see map, p. 501). But until the Zandmotor was built in 2011, archaeologists had glimpsed only the outlines of Doggerland. Fishermen had dragged up isolated bones, tusks, and stone tools.

In calmer seas, archaeologists might have dived to the sea floor for follow-up searches. But the rough, cold, murky waters of the North Sea, crisscrossed with busy shipping lanes, ruled that out.

"The technology [to explore the sea floor] wasn't available, nobody knew what

might have survived sea-level rise, and it all seemed hopelessly expensive and useless," Bailey says. Archaeologists were also reluctant to be seen chasing after "lost continents," he adds, lest they be associated with fringe theories such as Atlantis.

That's changing fast, thanks in part to beachcombers like van Wingerden. In his office at the National Museum of Antiquities, archaeologist Luc Amkreutz opens his email and scrolls through messages, some just hours old. "This morning a fisherman sent in photos of an elk antler with a shaft hole," he says, opening an attachment. "It just goes on and on."

Using email and a WhatsApp group with the straightforward name "Stone Age Finds," Amkreutz and Marcel Niekus, an independent archaeologist, keep in constant contact with amateurs scouring beaches all along the Dutch coast. The archaeologists help identify prehistoric artifacts from photos and get access to dozens of specimens in exchange. "We're easy to approach, and people can bring us finds," Amkreutz says.

Other researchers are reaping similar bonanzas. In late 2018, Leiden University Medical Center archaeogeneticist Eveline Altena was part of a research group that invited van Wingerden and other amateurs to an open house, asking them to bring human bones for identification. The response was overwhelming: In a single day, beachcombers brought more than 50 human skeletal fragments, many suitable for dating and DNA analysis. "Now, we're getting new fragments on a weekly basis," she says. "I can't keep up anymore."

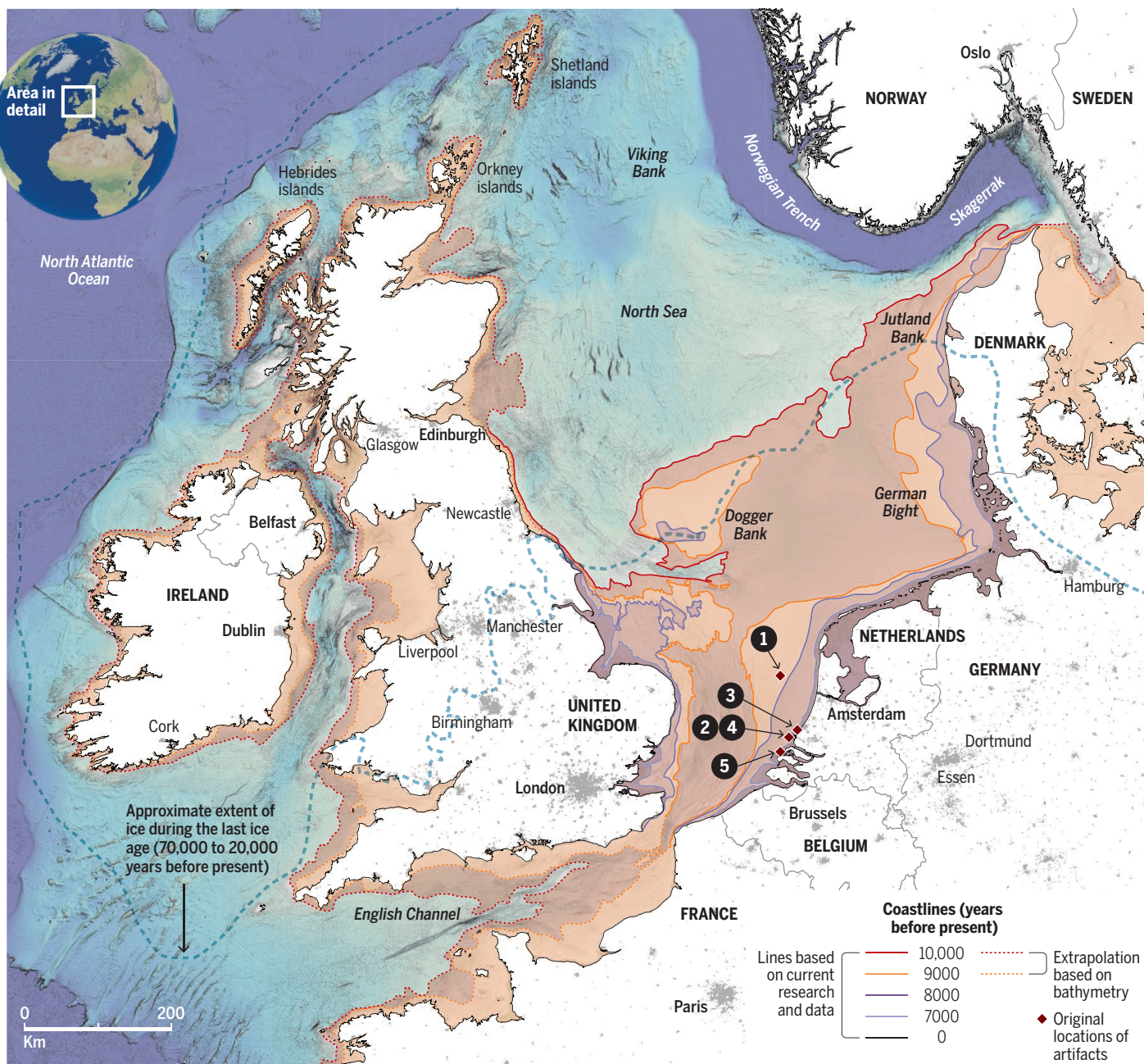
In 2015, van Wingerden found a flint flake with a gob of tar stuck to one end to form a simple handle. Niekus and Amkreutz recognized it as a Neanderthal hand tool at least 50,000 years old. Chemical analysis helped show how Neanderthals used complex methods to process birch bark into tar, as a team including Niekus, Amkreutz, and van Wingerden reported in *PNAS*.

Archaeologists can't know exactly where on the sea floor an artifact found on the beach originated, so the context they prize is missing. But because coastal reclamation efforts such as the Zandmotor dredge from specific locations, archaeologists know the artifacts' sources to within a few kilometers. "There are complete cemeteries being sucked up and sprayed on beaches," Amkreutz says. "Even though these finds aren't in their original find spot, they can say something about a huge area."

Those findings suggest several phases of occupation. Tools and other relics 800,000 years old or more harken back to when this part of Europe was likely occupied by

A vanished landscape

Over the millennia, Doggerland has been an icy wasteland, verdant valleys and forests, and now the bottom of the cold North Sea. Various kinds of humans have adapted to all these changes, with *Homo antecessor*, Neanderthals, and *H. sapiens* likely making use of the land's bounty at different times.



1 Large flint core ax, 9000 to 6000 B.C.E.
Found in a fisher's net in the 1980s, this ax was shaped and used by Mesolithic European hunter-gatherers.



2 Barbed bone points, 9000 to 6000 B.C.E.
Found in sand and gravel recovered from off the Dutch coast, these points likely helped humans bag fish and birds in Doggerland's rich wetlands.



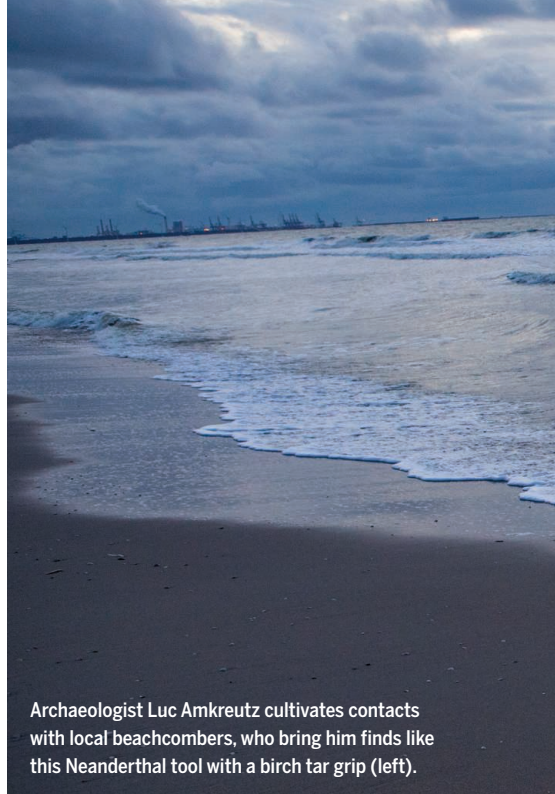
3 Neanderthal flake with birch tar grip
About 50,000 years ago, a Neanderthal used a complex process to make birch tar and affix it to the point.



4 Perforated antler ax, 9000 to 6000 B.C.E.
This shaft for an ax, crafted by early European hunter-gatherers, dates to the final millennia before Doggerland sank below the North Sea.



5 Neanderthal hand ax
Found in sediments dredged off the Dutch coast south of Rotterdam, this stone tool may be 250,000 years old. Part of a Neanderthal bone was found nearby.



Archaeologist Luc Amkreutz cultivates contacts with local beachcombers, who bring him finds like this Neanderthal tool with a birch tar grip (left).

Homo antecessor, an early human thought by many researchers to be an evolutionary dead end. One set of footprints, found in a layer of compressed sand on a beach in the United Kingdom and dated by its geological context, recorded children and adults apparently migrating across a mudflat.

Long cold spells then covered parts of the region in ice. About 100,000 years ago, small, hardy bands of Neanderthals arrived on the trail of megafauna such as mammoths and woolly rhinoceros. Hundreds of tools and a lone skull fragment offer evidence of a population living on the fringes of habitable Europe, resourceful enough to eke out a living in small groups under what Amkreutz calls “extreme” conditions on the edge of glaciers.

Neanderthals died out about 45,000 years ago—about when anatomically modern humans entered Europe. A few flint tools, found among stones dredged from the sea floor to create artificial sea walls for the Rotterdam harbor, suggest *H. sapiens* may have been active in Doggerland even as early as 40,000 years ago, when it was still an icy steppe. (More conclusive tools have turned up in the United Kingdom and Belgium, on each side of Doggerland.) About 20,000 years ago, a severe cold spell made the entire region too cold to be habitable.

But the end of the last ice age, about 15,000 years ago, brought a brief idyll: Pollen samples, DNA evidence, and fossilized wood fragments recovered from the sea floor suggest a fertile landscape of forests and rivers, with plentiful birds, fish, and mammals. Human remains and finely worked stone, bone, and antler tools suggest modern humans

made the most of the area, occupying it even as rising waves transformed large parts into a coastal wetland.

The seafloor bones are filling in the picture of Europe’s genetic past. Studies of ancient and modern DNA indicate that certain groups of hunter-gatherers entered northern Europe from the south and east perhaps about 14,000 years ago, after much of the ice had melted; modern European populations still carry their genetic legacy.

The trove of human bones that amateurs turned over to Altena for sampling promises to add to the picture. Of the bones amassed in June 2019, 90 were well-preserved enough for radiocarbon dating and DNA analysis. Altena and researchers from the Max Planck Institute for the Science of Human History (SHH) in Jena, Germany, identified teeth and bones between 8000 and 10,000 years old, when modern human hunter-gatherers occupied Doggerland. They have started to extract DNA, and so far have recovered it from more than five individuals. “In some ways the context is limited, but we can still do so much more than anyone ever expected,” Altena says.

Drawn from the outer limits of hunter-gatherer expansion in the fringes of Europe at that time, those samples “are fascinating,” says Cosimo Posth, an SHH geneticist. He notes that the DNA could illuminate how these early populations mixed with others in Europe.

MOST DOGGERLAND FINDS have been accidental. A long-term goal is to learn enough about the past landscape so researchers

can go to sea and look for sites instead of waiting for evidence to wash ashore. “Until you have reliable maps, you can’t do much,” Gaffney says. “We’re dealing with a completely unexplored country we can’t visit.”

More than 10 years ago, Gaffney set out to do the next-best thing, persuading oil, gas, and wind power companies to pass on data gathered in seismic surveys done to plan offshore oil and gas wells. Initial maps were coarse, but over the past several years, Gaffney and colleagues used €2.5 million in funding from the European Research Council to deploy side-scan sonar and other undersea imaging technologies to make their own maps, in what they call the Europe’s Lost Frontiers project. Maps in hand, the researchers looked for ancient areas suited to human habitation.

More than a decade of work paid off last year when Gaffney and Belgian researchers headed to the Brown Banks, about 50 kilometers off the U.K. coast. Mapping had suggested that between 7000 and 13,000 years ago, the spot was an elevated area 30 kilometers long, overlooking a river.

Researchers aboard the Belgian research vessel *Belgica* took core samples, scooped up sediment, and made “grabs” with a metal claw. Among the finds were traces of a fossilized forest 32 meters beneath the waves, including tree roots, terrestrial snail shells, and peat—plus a small flint flake and part of a broken flint hammerstone shaped by hunter-gatherers. “We went to the place where we thought [human artifacts] would be and recovered them,” Gaffney says. “That’s a first.”



Putting those maps together with the sheer number of samples emerging from the North Sea, researchers are beginning to answer a question particularly relevant to humanity's future: What do people do when sea levels rise?

About 8500 years ago, a massive freshwater lake in North America called Lake Agassiz, formed by melting glaciers, drained suddenly into the sea. What had been gradual sea-level rise accelerated, and seas rose a few meters within decades. Doggerland transformed from a temperate, forested plain into an estuarial wetland dotted by drier highlands. Core samples collected along river valleys by the Lost Frontiers team traced the flooding, amounting to a "transect through time," Gaffney says.

To explore the impact on people, Amkreutz analyzed dozens of human bones dragged up by fishing boats as well as finds plucked off the Zandmotor and other Dutch beaches. He traced the bones to 18 offshore sites around the prehistoric Rhine River estuary and dated them with radiocarbon to a precision of about 100 years; all were about 8500 years old.

He and Niekus then used chemical signatures from collagen preserved in dozens of the bones to analyze what people in Mesolithic Doggerland were eating before and during that transition. As the landscape changed, the diet of its residents did, too, shifting from land animals to freshwater fish. "It shows their flexibility in the face of climate change," Amkreutz says. "They didn't leave as sea levels rose; they changed their diet."

Eventually, that, too, came to an end. On the basis of sediments and computer models, researchers think a tsunami originating off modern-day Norway around 6150 B.C.E. devastated Doggerland with waves at least 10 meters high. Soon the landscape vanished as global sea levels continued to rise.

At his lab at the University of Warwick, Robin Allaby is tracing the changes by searching 60 of the core samples collected by Gaffney and his team for what's called environmental DNA, shed into water and soil by ancient species. The team scoops up and analyzes all the DNA in a sample, using next-generation sequencing methods that capture millions of DNA fragments, and compares it with libraries of known genomes. "The surprising thing is just how much DNA is still down there," Allaby says. The results chronicle changes in Doggerland's ecosystems as seas rose.



This 13,000-year-old skull fragment of a modern human was fished up off Rotterdam, the Netherlands.

In the older, earlier layers, "We can see quite a broad range of DNA that's clearly terrestrial," he says. Allaby has picked out terrestrial species, including bears, boars, birds, spiders, and mosquitoes. He has identified plant species, too, including hazel and linden trees and meadow grasses. "It's obviously a lowland, very fertile and probably more attractive than the British uplands and adjacent Europe," he says.

Higher up, in the younger core samples, the DNA tells a tale of inexorable transformation. "We can see the rise of an estuarine environment and a slow switch to marine taxa," Allaby says, as bears and boars give way to sea grasses and fish.

Researchers say the techniques being pioneered or perfected in the North Sea could be applied to far-flung hot spots of human migration, including Beringia and the waters that surround the archipelagos of Oceania. "There are big questions about human dispersal and development which can only be answered by looking at submerged landscapes," Bailey says. "These same landscapes were probably good places to provide stepping stones into new territory."

At the end of van Wingerden's afternoon walk, all she had to show for 2 hours of searching were a few pieces of animal bone and a wide smile. But the next day, her luck turned. Tucked in among a pile of seashells, she found a carefully worked tool with characteristic Neanderthal handiwork, dating back at least 45,000 years: one more piece of a lost landscape, rediscovered. ■

Andrew Curry is a journalist in Berlin.

INSIGHTS

PERSPECTIVES



MICROBIAL ENGINEERING

A microbiome silver bullet for honey bees

A genetically engineered honey bee gut bacterium knocks down two major bee threats

By **Robert J. Paxton**

The western honey bee (*Apis mellifera*) brings tangible benefits to humans as an important pollinator and insights into social evolution as a model organism. Yet, despite close scientific scrutiny, it is under global threat from a range of

stressors (1) that are unlikely to diminish with global change. Chief among these are pests and pathogens, remedies to which are either ineffective, short-term, expensive, or impractical. On page 573 of this issue, Leonard *et al.* (2) reveal a hidden microbiological key to fight these pests and pathogens: genetically modified honey bee gut bacteria tailored to

induce host RNA interference (RNAi)-based defense (3) that is effective, long-term, potentially cheap, and easy to apply. This important approach may not only provide a solution to many of the honey bee's woes, it also offers a new functional genomic toolkit with which to dissect the molecular intricacies of honey bees and their societies.

PHOTO: CYRIL RUOSO/MINDEN PICTURES

Pests and pathogens threaten a major pollinator, the honey bee (*Apis mellifera*).

Originally brought to the Americas by early European settlers, the honey bee is now globally distributed and indispensable in agriculture. Yet its success—and intercontinental transport—has been accompanied by the spread of its numerous pests and pathogens, foremost among which are the exotic *Varroa destructor* (hereafter “varroa”) ectoparasitic mite and deformed wing virus (DWV), a killer pathogen transmitted by varroa mites (4). The varroa-DWV nexus is widely blamed for increased honey bee mortality across the temperate world and both mite and virus are nowadays ubiquitous, infecting more or less every hive (5); colony collapse is the outcome. Current treatments include a range of natural and synthetic miticides to kill varroa or high-tech solutions that induce a natural innate host defense mechanism,

within hosts. This approach seems to offer bees sustainable protection from varroa or DWV. Could this be a silver bullet for the honey bee?

RNAi is a biological process found in most eukaryotes that regulates endogenous as well as exogenous (foreign) RNA, such as that of viruses. Introducing exogenous double-stranded RNA (dsRNA) into a host cell causes that cell’s molecular machinery to degrade like-sequenced RNA. This can reduce the expression of a corresponding host gene (so-called gene “knockdown”) or lead to the destruction of a viral RNA, resulting in viral control (3). But there is a catch—dsRNA is expensive to produce in large quantities, inherently unstable, and difficult to direct into host cells, where it is needed.

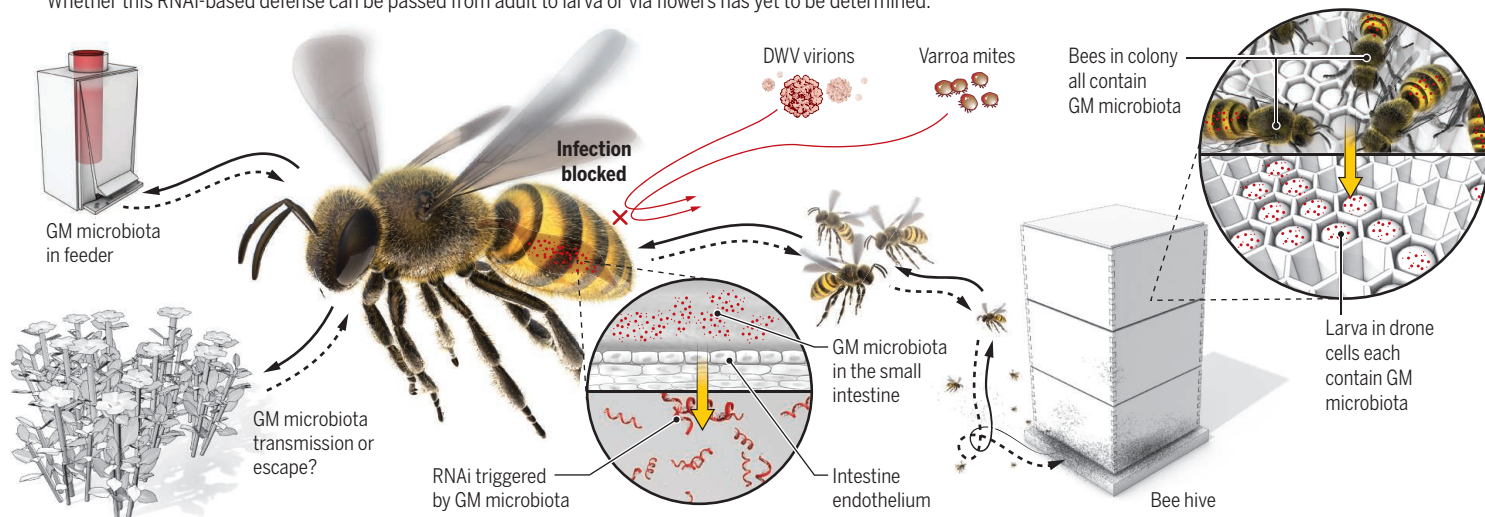
Whitten *et al.* (8) demonstrated that an insect’s gut bacteria—its microbiome—can be engineered to express copious dsRNA in a stable manner that acts systemically in

Leonard *et al.*’s laboratory-based experiments used handfuls of worker honey bees. The next step is to scale up with full-sized colonies, which contain up to 50,000 individuals, to demonstrate field-realistic feasibility. Furthermore, during spring and summer, varroa mites exert their most serious effects when feeding on honey bee pupae, upon which they also reproduce and to which they efficiently transmit DWV. If the honey bee larval microbiome reflects that of the adult, then a mechanism of delivery of RNAi from adult to larva exists, though whether RNAi-based varroa-virus defense can be passed on from larva to ensuing pupa awaits confirmation.

Leonard *et al.* also wisely advocate for further research to improve dsRNA production and transfer from gut bacteria to honey bee and to optimize the design of the genetically engineered target RNA sequence. Target sequence is of particular relevance for RNA viruses, such as DWV, because of

Improving honey bee survival

Symbiotic bee gut bacteria were genetically modified (GM) to release specific RNA that triggers an immune response in the host involving RNA interference (RNAi). Once RNAi was activated, honey bees survived infection by a particular virus or parasitic mite. Whether this RNAi-based defense can be passed from adult to larva or via flowers has yet to be determined.



RNAi, to reduce pathogen (including viral) burden (6). But the former has limited efficacy because mites soon evolve resistance; moreover, miticides can enter the human food chain through contamination of honey. The latter, by contrast, has proven effective in controlling DWV (7) but is expensive and the benefits are temporary—on the order of days or weeks. Now, Leonard *et al.* have genetically modified one honey bee gut bacterium, *Snodgrassella alvi*, thereby refining a system to induce RNAi

insect hosts. Leonard *et al.* have perfected this approach by engineering *S. alvi* to express varroa or viral genes and feeding the engineered bacteria to honey bees. When the corresponding varroa or viral dsRNA was produced by the ingested bacteria (and then taken up by the host—in the case of varroa, even passed on to mites feeding on honey bee tissue), the host’s RNAi machinery was activated to destroy those RNA sequences—self-destruction in the case of varroa. Thus, when treated honey bees were subsequently challenged with varroa or DWV, mites died and viral replication was suppressed: a major breakthrough in their control (see the figure).

their extremely high mutation rates (9). DWV itself comes in two widely distributed genotypes, A and B, the latter of which exhibits higher virulence (10) and is currently spreading across honey bee populations in the United States (11). Methods to optimize sequences that more efficiently target viral RNA [e.g., (12)] and that of other pathogens are likely to improve protection offered by Leonard *et al.*’s approach.

However, the major ethical issue of gene escape needs to be addressed before engineered bacteria are applied to honey bees in the field. The honey bee gut harbors a species-specific and astoundingly consistent core set of bacteria, its microbiome

Institute for Biology, Martin Luther University Halle-Wittenberg, Hoher Weg 8, 06120 Halle (Saale), Germany. Email: robert.paxton@zoologie.uni-halle.de

(13), which Leonard *et al.* demonstrated to be shared among nestmates while grooming and cleaning. This theoretically facilitates the treatment of an entire colony's workforce (and potentially those of neighboring hives) while limiting the probability that genetically modified microbiota colonize other animals. But bacteria are renowned for horizontal gene transfer. From an ecological perspective, the consequences of gene escape need to be scrutinized and the potential for release robustly evaluated. From an evolutionary perspective, high mutation rates confer considerable adaptive potential on RNA viruses, and the consequences of RNAi treatment for the evolution of virulence also warrant attention.

Although sociality—like that exhibited by honey bees—is a very successful ecological strategy, many social insects are invasive pests, such as fire ants (*Solenopsis invicta*) and Formosan termites (*Coptotermes formosanus*) in the southern United States. Could the silver bullet be turned onto these pest species by genetically modifying their core microbiota for effective, species-specific biocidal control? Research is still needed to determine whether their gut microbiota are highly conserved yet differ from those of native ants and termites.

Other major problems facing honey bees include insecticide (mis)use and loss of flower-rich habitat (1, 6). Honey bee gut bacteria engineered to alter host expression of genes involved in detoxification or pollen digestion might go some way to resolving these problems, too. As well as promising insights into fundamental aspects of biology, Leonard *et al.*'s approach has great potential to improve bee—and even our own—health (14). ■

REFERENCES AND NOTES

1. D. Goulson, E. Nicholls, C. Botias, E. L. Rotheray, *Science* **347**, 1255957 (2015).
2. S. P. Leonard *et al.*, *Science* **367**, 573 (2020).
3. K. Kupferschmidt, *Science* **341**, 732 (2013).
4. L. Wilfert *et al.*, *Science* **351**, 594 (2016).
5. S. J. Martin, L. E. Brettell, *Annu. Rev. Virol.* **6**, 49 (2019).
6. C. M. Grozinger, M. L. Flenniken, *Annu. Rev. Entomol.* **64**, 205 (2019).
7. S. D. Desai, Y. J. Eu, S. Whyard, R. W. Currie, *Insect Mol. Biol.* **21**, 446 (2012).
8. M. M. A. Whitten *et al.*, *Proc. Biol. Sci.* **283**, 20160042 (2016).
9. E. C. Holmes, *The Evolution and Emergence of RNA Viruses* (Oxford Univ. Press, 2009).
10. D. P. McMahon *et al.*, *Proc. Biol. Sci.* **283**, 20160811 (2016).
11. E. V. Ryabov *et al.*, *Sci. Rep.* **7**, 17447 (2017).
12. S. Gago-Zachert *et al.*, *Nucleic Acids Res.* **47**, 9343 (2019).
13. W. K. Kwong, N. A. Moran, *Nat. Rev. Microbiol.* **14**, 374 (2016).
14. K. J. Chua, W. C. Kwok, N. Aggarwal, T. Sun, M. W. Chang, *Curr. Opin. Chem. Biol.* **40**, 8 (2017).

ACKNOWLEDGMENTS

The author is supported by the German Research Foundation DFG Pa 632/10.

10.1126/science.aba6135

MATERIALS SCIENCE

Nested hybrid nanotubes

Material made with atom-thin tubular crystals portends the creation of inventive nanodevices

By Yury Gogotsi¹ and Boris I. Yakobson²

From the Stone Age to the Silicon Age, humans have crafted tools by carving them out of large pieces of material, such as bones or silicon crystals. In the nanotechnology era, scientists began creating—atomic layer by atomic layer—materials, building blocks, structures, or even entire devices that do not exist in nature but offer new combinations of properties. On page 537 of this issue, Xiang *et al.* (1) report on the synthesis of one-dimensional (1D) van der Waals heterostructures that stack in ways reminiscent of traditional Russian dolls.

Atoms-small zero-dimensional (0D), atom-thin 1D, and two-dimensional (2D) materials were first made from carbon (fullerenes, nanotubes, graphene) and later from other elements and compounds. With the current availability of numerous 2D materials, it is possible to combine them into heterostructures by mechanical transfer, self-assembly in solution, or vapor-phase growth. Mixing and matching 2D crystals with different properties produces van der Waals-bonded stacks with new functionalities (2). Unlike 2D layers, 0D cages and 1D tubules are topologically protected from being stack-nested and, until recently, were difficult to grow.

Xiang *et al.* created 1D heterostructures by depositing perfect boron nitride (BN) or molybdenum disulfide (MoS₂) shells onto single-walled carbon nanotubes. Unlike the results of early attempts to produce 1D heterostructures (3), the outer shells of BN and MoS₂ are single-crystalline seamless perfect cylinders. Moreover, the authors showed that a couple of layers of BN and then a layer of MoS₂ can be grown on a carbon tube, creating stacked tubular structures (see the figure).

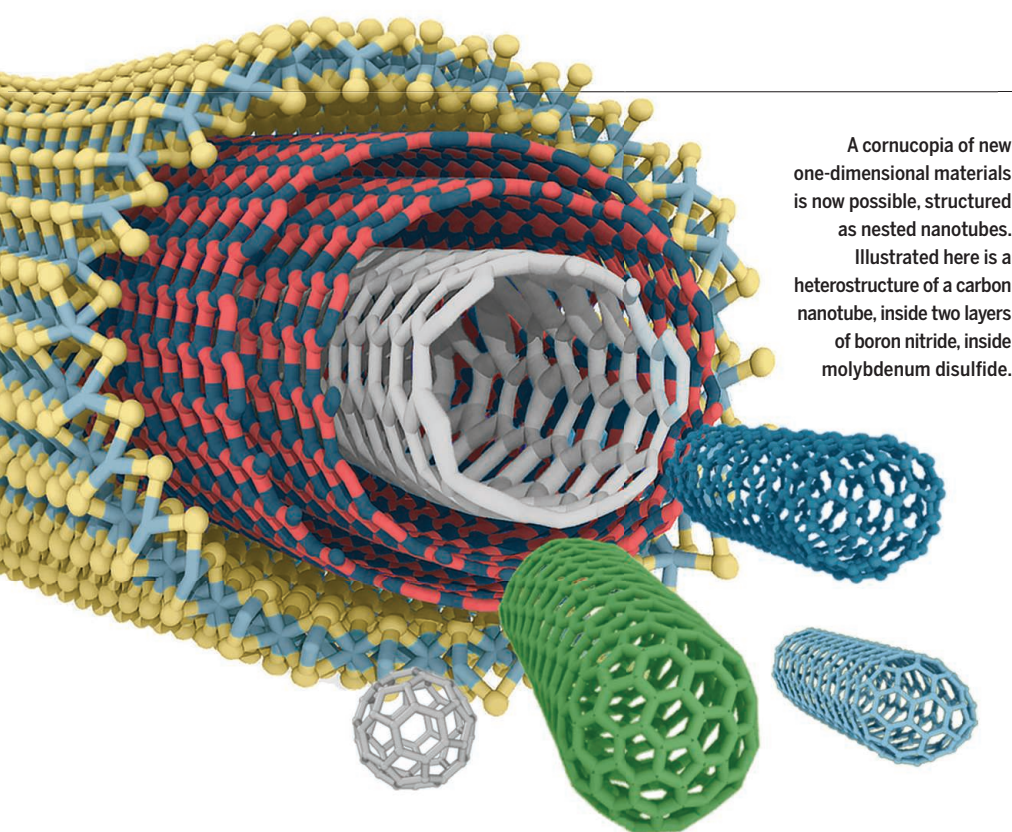
Scientists have envisioned 1D heterostructures in theory, but until now, synthetic attempts have produced only disordered shells on multiwall nanotubes (3). The chemical vapor deposition (CVD)-based growth method demonstrated by Xiang *et al.* extends the concept of van der Waals heterostructures to 1D

coaxial materials. This opens up an entirely new realm of 1D heterostructures. Beyond BN and MoS₂, other transition metal dichalcogenides (MoS₂-like compounds of metal with sulfur, selenium, or tellurium) and borides (such as TiB₂), oxides, and potentially carbides and nitrides (4) can be grown by CVD on carbon nanotube cores. Carbon nitride, silicene, borophene (5), and other materials made as 2D layers might be added as well, including predicted nanotubes that have not yet been produced [e.g., MXenes (6)]. Although Xiang *et al.* used single-walled nanotubes as a template, their available double- and triple-wall analogs offer a larger diameter (*d*) and lower curvature (1/*d*), which ease overgrowth by heterolayers. Also, the core tubes of noncarbon compositions [e.g., BN or dichalcogenides (7)] can be tried for coaxial growth. The combination of insulator BN with carbon tubes (which, depending on their chirality, can be either semiconducting or metallic) might result in new electronic functionalities, leading to versatile nanodevices and even nanoscale machines.

The newly described synthesis of 1D heterostructures has several implications for future research. The surface-to-surface templating, rather than atom-to-atom epitaxy, supports 1D tubular crystal growth; this might also be true for syntheses of many 2D materials wherein the interactions between crystalline layers are too weak to support the growth of new crystalline layers well-aligned with the substrate (epitaxy). Recently, it was shown that strong lateral interactions at the layers' edges alone are sufficient to guide planar BN growth on metals (8) without registry to the substrate; this growth shares similarities with that observed by Xiang *et al.* in which the outer shell can grow in a crystal direction that is different from that of the core nanotube. Moreover, no catalyst was present at the growing edge during nanotube shell growth in the study of Xiang *et al.* Again, this approach is transferable to planar 2D heterostructures. A further notable aspect of the new study is the role of curvature, which adds strain energy ($\sim h^2/d^2$) to the chemical potential of added atoms; this suppresses growth, on nanometer-thin core tubes, of both very narrow tubes and more rigid shells of greater thickness (*h*), as seen with MoS₂.

Not merely a fascinating concept, nested

¹Department of Materials Science and Engineering and A. J. Drexel Nanomaterials Institute, Drexel University, Philadelphia, PA 19104, USA. ²Department of Materials Science and Nano-Engineering and Department of Chemistry, Rice University, Houston, TX 77005, USA. Email: gogotsi@drexel.edu; bij@rice.edu



A cornucopia of new one-dimensional materials is now possible, structured as nested nanotubes. Illustrated here is a heterostructure of a carbon nanotube, inside two layers of boron nitride, inside molybdenum disulfide.

1D heterostructures offer tangible benefits. The oxidation or chemical resistance of carbon nanotubes can be improved by the protective BN sheath (1, 3). A plethora of opportunities arises when stacking 1D crystals coaxially, such as interesting 1D physics in heterostructure electronics. The hybrid shells of 1D heterostructures can be chosen with an electronic band alignment such that interlayer excitons—electrically neutral, short-lived particles normally caused by light—become favored even in the ground state, reaching Bose-Einstein condensation into an excitonic superfluid (9). This enables scientists to build low-power logic devices or direct-current electrical transformers.

Furthermore, the strain gradient from the outer to the inner surface of the tube curvature leads to flexoelectric polarization (10) and a voltage shift inside the tube, which changes the offset of electron energy bands from straddling to staggered. This enables charge separation under light, which gives rise to an electrical current at the junction of the coaxial shells and along the tubes. New devices such as tunneling diodes and transistors can be fabricated with heterostructures of semiconducting, dielectric, or metallic coaxial nanotubes.

All of the materials studied by Xiang *et al.*—graphitic carbon, MoS₂, and BN—are widely used as solid lubricants in their planar 2D state. The lack of intershell registry between the disparate materials suggests negligible friction (superlubricity) (11). This property invites the use of 1D heterostructures as nanoscale bearings (12), which brings scientists a step closer to tiny gears and other nano-

machines (13). However, before the industry realizes such applications, it must overcome certain challenges, such as the ability to grow 1D heterostructures in forests (nanotubes vertically aligned on a substrate), in large quantities in fluidized bed reactors, or in a predetermined location on a silicon chip.

The prospect of developing 1D materials of various compositions can motivate a combinatorial exploration guided by density functional theory computations or artificial intelligence models that predict the best synthesis protocols for 1D heterostructures with attractive properties. This in turn might lead to a new wave of interest in nanotubes, which have been overshadowed in the past decade by 2D materials and their heterostructures. Flat, planar stacks of 2D materials now can retain one dimension only, while having another fold onto itself. Even in “Flatland” the world turns out to be round. ■

REFERENCES AND NOTES

1. R. Xiang *et al.*, *Science* **367**, 537 (2020).
2. K. S. Novoselov *et al.*, *Science* **353**, aac9439 (2016).
3. L. L. Chen *et al.*, *J. Am. Ceram. Soc.* **87**, 147 (2004).
4. Y. Gogotsi, B. Anasori, *ACS Nano* **13**, 8491 (2019).
5. A. J. Mannix, Z. Zhang, N. P. Guisinger, B. I. Yakobson, M. C. Hersam, *Nat. Nanotechnol.* **13**, 444 (2018).
6. A. N. Enyashin, A. L. Ivanovskii, *Comput. Theor. Chem.* **989**, 27 (2012).
7. R. Tenne, *Nat. Nanotechnol.* **1**, 103 (2006).
8. K. V. Bets *et al.*, *Nano Lett.* **19**, 2027 (2019).
9. S. Gupta *et al.*, arXiv 1908.07513 (16 August 2019).
10. T. Dumitrică *et al.*, *Chem. Phys. Lett.* **360**, 182 (2002).
11. Y. Song *et al.*, *Nat. Mater.* **17**, 894 (2018).
12. J. Cumings, A. Zettl, *Science* **289**, 602 (2000).
13. K. E. Drexler, *Nanosystems* (Wiley, 1992).

ACKNOWLEDGMENTS

B.I.Y. thanks K. Bets (supported by NSF grant CBET-1605848) for help with computer graphics simulations.

10.1126/science.aba6133

CELL BIOLOGY

Liquid but not contactless

The endoplasmic reticulum makes molecular contact with membraneless organelles

By Benoît Kornmann¹ and Karsten Weis²

In the past decade, the understanding of cellular organization has undergone two major paradigm shifts. On the one hand, it was demonstrated that membrane-bound compartments exchange their contents not only through vesicular transport but also by means of direct membrane tethering at specific contact sites (1), revealing a new layer of connectivity in eukaryotic cells. On the other hand, the discovery of membraneless organelles, such as processing bodies (P-bodies) and stress granules, has revealed that proteins and RNAs can self-assemble and condense into liquid-like droplets through weak and multivalent interactions (2). This indicates that the cytosol is not a randomly dispersed soup of macromolecules but that it is subcompartmentalized. On page 527 of this issue, Lee *et al.* (3) bring these two exciting fields together by showing that a membrane-bound organelle, the endoplasmic reticulum (ER), contacts at least two membraneless compartments, P-bodies and stress granules, and influences their behavior.

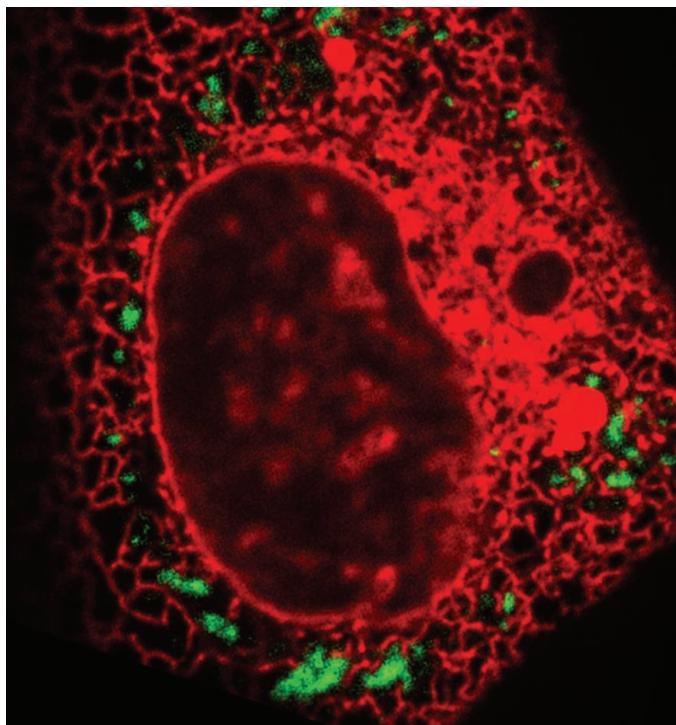
By imaging live human cells expressing markers for the ER and for membraneless organelles, Lee *et al.* found that P-bodies and stress granules were in contact with the ER much more frequently than expected by chance (see the photo). Membraneless organelles are biomolecular condensates that form by coalescence of macromolecules. P-bodies and stress granules are archetypical membraneless organelles found in the cytoplasm of eukaryotic cells. Membraneless organelles also occur in the nucleus, including the nucleolus (4), a factory for ribosome assembly, and Cajal bodies that function in small RNA processing. Interactions within membraneless organelles are driven by low-affinity, multivalent protein-protein, RNA-protein, and RNA-RNA interactions. These weak interactions cause

¹Department of Biochemistry, University of Oxford, Oxford OX1 3QU, UK. ²Institute of Biochemistry, ETH Zurich, 8093 Zurich, Switzerland. Email: benoit.kornmann@bioch.ox.ac.uk

phase separation but do not lead to a fixed position or stoichiometry of the components within the organelle, unlike in a classical protein complex (2). Current models posit that P-bodies store messenger RNAs (mRNAs) that are not actively translated, whereas stress granules serve a similar purpose but only form when a stress represses translation.

Membrane contact sites are established and maintained by protein complexes that tether two membranes stably and keep organelles in proximity for hours. Lee *et al.* found that most of the interactions between the ER and P-bodies or stress granules are stable, akin to membrane contact sites. This raises numerous questions. What is the molecular nature of the tethering between the ER and membraneless organelles? One possibility is that liquid droplets attach to the ER through translating mRNAs and ribosomes bound to the ER surface. However, P-bodies and stress granules appear to repress translation and exclude ribosomes. Furthermore, inhibition of ER translation did not detach P-bodies from the ER. Therefore, the specific nature of the interactions between ER tubules and P-bodies or stress granules implies the existence of a dedicated machinery, currently unknown, that serves as molecular glue between these structures.

What is the role of attaching RNA-containing membraneless organelles to the ER? Connection between the ER and P-bodies seems to be evolutionary conserved from yeast to mammals (5, 6). Moreover, in yeast, the nucleolus is tethered to the ER-derived nuclear membrane (4, 7). Although their physiological role is unclear, the evolutionary conservation of contacts between ER and membraneless organelles suggests that this is important. Organelle tethering is largely considered to create a platform that allows the exchange of metabolites and information. For example, the proximity between organelles allows transporters to shuttle hydrophobic lipid molecules from one membrane to the other through the hydrophilic cytosol. Organelle proximity also allows exchange of calcium ions from one compartment (for example, the ER) to another (for example, mitochondria), with minimal disturbance of cytosolic calcium concentration (1). Because substantial translation occurs at the ER and because P-bodies and stress granules



In human cells, the endoplasmic reticulum (red) forms stable contacts with stress granules (green) and processing bodies (P-bodies; not shown).

can be sites of mRNA storage, Lee *et al.* speculated that these connections serve to exchange mRNAs from the droplet, where they are translationally silent, to their site of expression on the ER. However, the P-body and stress granule transcriptomes (5, 6, 8) are not obviously enriched in mRNAs that are destined to be translated at the ER (that is, mRNAs encoding secreted proteins). Future experiments will likely reveal whether such mRNAs are enriched in droplets attached to the ER; whether tethering facilitates the transition from translationally silent to active, and vice versa; and whether specific regulatory processes govern the handover of mRNAs from P-bodies to ER according to cellular needs.

An interesting observation by Lee *et al.* unveils one potential role of the ER-droplet tether: Liquid droplets undergo division at sites where ER tubules are present. This parallels the previous discovery by the same laboratory that the sites of division for two membrane-bound organelles, the endosomes and the mitochondria (9, 10), are also characterized by the nearby presence and perhaps tethering of ER tubules. This suggests that contacting the ER is a prerequisite for liquid droplets to split. Conventional liquid droplets do not split spontaneously. However, in the dynamic cytoplasm, could ER motion simply apply mechanical forces onto membraneless organelles, causing their division? Mechanical forces appear to be an important factor

in deciding where and when mitochondrial division take place. Actin filaments nucleated at the ER were shown to be particularly important for mitochondrial fission (11), and mechanical forces are sufficient to cause this phenomenon (12). It is thus conceivable that the ER-nucleated actin filaments could forcibly divide membraneless organelles. Alternatively, the surface of the ER membrane may act like a surfactant that helps to disperse membraneless organelles. The ER membrane is charged, and specific ER-localized proteins might influence local ionic strength, which could trigger local dissolution of liquid droplets. Or, perhaps the ER recruits a specific division machinery. Because division of a liquid droplet requires energy, candidate fission enzymes include adenosine triphosphatases (ATPases) such as molecular chaperones or members

of the DEAD-box family (13, 14), which are enriched in P-bodies and stress granules.

As for mitochondria and endosomes, the advantage of making droplet fission coincide with the ER is unknown and requires further investigation. Does it prevent membraneless organelles from getting entangled with the ER? Or, perhaps the ER is involved in controlling droplet numbers for other reasons. To answer these questions, it will be essential to uncover the molecular machines that connect the ER to P-bodies and stress granules and mediate organelle fission. ■

REFERENCES AND NOTES

1. B. Kornmann, C. Ungermann, *Biochim. Biophys. Acta Mol. Cell Res.* **1864**, 1435 (2017).
2. A. A. Hyman *et al.*, *Annu. Rev. Cell Dev. Biol.* **30**, 39 (2014).
3. J. E. Lee *et al.*, *Science* **367**, eaay7108 (2020).
4. C. P. Brangwynne *et al.*, *Proc. Natl. Acad. Sci. U.S.A.* **108**, 4334 (2011).
5. C. Wang *et al.*, *eLife* **7**, e29815 (2018).
6. C. Kilchert *et al.*, *Mol. Biol. Cell* **21**, 2624 (2010).
7. K. Mekhail *et al.*, *Nature* **456**, 667 (2008).
8. A. Hubstenberger *et al.*, *Mol. Cell* **68**, 144 (2017).
9. M. J. Hoyer *et al.*, *Cell* **175**, 254 (2018).
10. J. R. Friedman *et al.*, *Science* **334**, 358 (2011).
11. F. Korobova *et al.*, *Science* **339**, 464 (2013).
12. S. C. J. Helle *et al.*, *eLife* **6**, e30292 (2017).
13. M. Hondele *et al.*, *Nature* **573**, 144 (2019).
14. S. Jain *et al.*, *Cell* **164**, 487 (2016).

ACKNOWLEDGMENTS

B.K. is an investigator of the Wellcome Trust (grant 214291/Z/18/Z). K.W. is supported by the Swiss National Science Foundation (project number 31003A_179275). The authors thank E. Dufresne for discussions on droplet behavior.

10.1126/science.aba3771

Stitching two chiral centers with one catalyst

A single catalyst joins alkyl groups with control over stereochemistry of both fragments

By **Jianyu Xu** and **Mary P. Watson**

Transition metal-based catalysts can chaperone carbon-carbon (C-C) bond formation between an electrophilic and a (usually) nucleophilic partner. Reactions such as the palladium (Pd)-based Suzuki-Miyaura cross-coupling rival amide-bond formation in frequency of use (1). Such Pd-based cross-couplings join unsaturated carbon atoms, as in aryl-aryl couplings, but many recent efforts have focused on alkyl-alkyl cross-couplings (2). Chiral nickel (Ni)-based catalysts have enabled both efficient C-C bond formation as well as control over the stereochemistry of a stereocenter on the electrophilic-partner alkyl group. Similar control has only been demonstrated for a single cyclic nucleophilic partner, and this nucleophile has also been needed for the selective formation of stereocenters on both alkyl fragments. On page 559 of this issue, Huo *et al.* (3) demonstrate that a single chiral Ni catalyst can join two alkyl groups with high levels of control over the orientations of the neighboring stereocenters.

Alkyl-alkyl bonds are found in most synthetic targets of pharmaceutical and agrichemical interest, but forming these linkages remains challenging in many synthetic contexts (4). Classic alkylation reactions that proceed through canonical S_N1 and S_N2 mechanisms have several drawbacks, including the need for harsh carbon nucleophiles and specific steric requirements, the presence of competitive elimination pathways, and a dearth of opportunities for controlling the stereochemistry of the products. By changing the reaction mechanism, transition-metal catalysis can overcome these limitations but presents its own challenges. In particular, the alkylmetal intermediates can decompose through competitive pathways to form alkenes instead of

the desired cross-coupling products. Such decomposition pathways are theoretically possible with each alkyl reagent, so alkyl-alkyl couplings have double the potential for this fate.

Through appropriate choice of ligand and control of the redox potentials of the catalyst, these undesired reactions can be mitigated. Zultanski and Fu demonstrated that alkyl electrophiles could be used effectively in cross-couplings (5). This work, along with studies by other groups, established that these reactions proceed through a mecha-

nism distinct from Pd-catalyzed aryl-aryl couplings. The alkyl electrophiles are activated through single-electron transfer to form configurationally unstable radical intermediates. Recognizing that this instability presented the opportunity for having the catalyst control which radical proceeds, Fischer and Fu demonstrated that chiral ligands can induce asymmetry in these cross-couplings (6). This approach allowed both enantiomers of a chiral electrophile to be converted stereoconvergently to a single enantiomer of the product (see the figure, top).

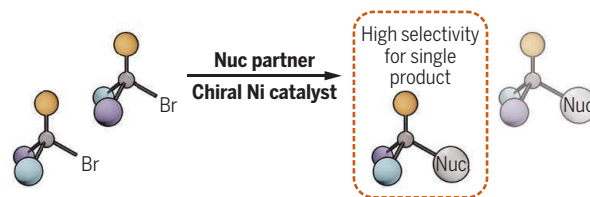
By contrast, the development of a stereoconvergent cross-coupling of a racemic chiral alkyl nucleophile has proven more challenging. Although such methods have been developed to form alkyl-vinyl and alkyl-aryl bonds (7), only a single alkyl nucleophile had been successfully used in stereoconvergent alkyl-alkyl cross-couplings. In the coupling of this nucleophile, the chiral catalyst differentiated a methylene (CH_2) versus a *tert*-butyl carbamate (NBoc) in a cyclic substrate (8).

The method of Huo *et al.* overcomes this restriction by using acyclic β -zincated amide nucleophiles and a Ni catalyst equipped with a chiral bidentate ligand (see the figure, middle). The authors hypothesize that the bidentate nature of the ligand enables coordination of the substrate amide to Ni and that this coordination allows differentiation of two alkyl groups. The variation possible within this family of β -zincated amides is notable and shows a broad tolerance for many different functional groups.

In addition to this dramatic advance in the nucleophilic partner, Huo *et al.* demonstrate a solution to an even greater challenge in alkyl-alkyl cross-couplings. The coupling of two secondary alkyl groups has proven difficult, and only limited examples have been reported. The increased steric demand of both alkyl groups often prevents them from being effectively loaded onto the Ni catalyst. With a related Ni catalyst, again equipped with a bidentate ligand, Huo *et al.* coupled two second-

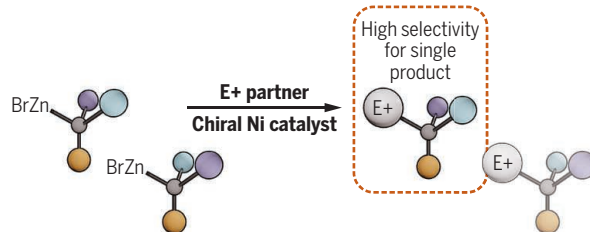
Orienting alkyl-alkyl cross-couplings

Carbon-carbon bond formation between chiral alkyl centers (bearing different groups shown in color; Br, bromine; Zn, zinc) with nickel (Ni) catalysts is extended to a variety of nucleophile (Nuc) partners.



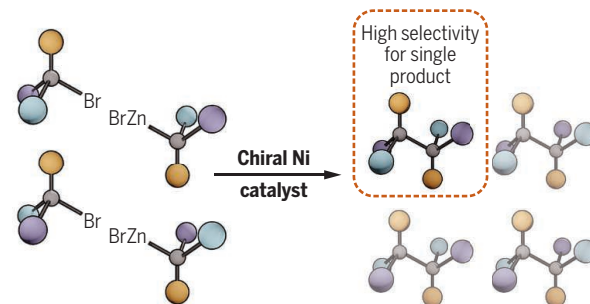
Chiral electrophilic partners

In prior alkyl-alkyl cross-couplings, both enantiomers of a chiral electrophile (E^+) were converted to a single orientation of product.



Chiral nucleophilic partners

Huo *et al.* now show that a chiral catalyst is effective in stereoconvergent couplings of a whole family of chiral nucleophilic partners.



Double control

The catalyst delivers one stereoisomer of the four possibilities.

Department of Chemistry and Biochemistry,
University of Delaware, Newark, DE 19716, USA.
Email: mpwatson@udel.edu

ary alkyl groups. Moreover, when they used a propargylic bromide as the electrophilic partner, the products were obtained in high yields and with high selectivity for a single orientation. The catalyst delivers one stereoisomer of the four possibilities (see the figure, bottom). This type of doubly stereoconvergent cross-coupling has only been achieved once before and only worked for the cyclic pyrrolidine nucleophile described above (9).

The synthetic implications of this approach are exciting. In synthesis courses, students are taught to “retrosynthetically” disconnect target molecules into simpler intermediates by “clearing” stereocenters through bond disconnections (10). The opportunity to clear two stereocenters and disconnect the molecule into two much simpler racemic starting materials is powerful. Although this method requires the products to have amide and alkyne groups, these are ripe for elaboration and derivatization through straightforward manipulations.

In addition, the limits of this strategy are not yet defined. Deeper understanding of the mechanism and the role of the amide in coordinating the catalyst will help define the other groups that can be used to organize the key catalytic intermediates and transition states, along with the lengths of the tether that are effective. Given the importance of all-carbon quaternary stereocenters, there will be a demand to increase the size limits of the alkyl groups and to explore whether a single catalyst can cross-couple tertiary alkylating agents to set vicinal stereocenters in which one or both are quaternary (11). Last, a catalyst has been discovered to deliver only one of the two possible diastereomers. Given that each diastereomer may elicit a different biological response, it will be of interest to see if a complementary catalyst can be discovered to deliver the other diastereomer in equally high enantiomeric excess and yield (12). ■

REFERENCES AND NOTES

1. D. G. Brown, J. Boström, *J. Med. Chem.* **59**, 4443 (2016).
2. J. Choi, G. C. Fu, *Science* **356**, eaaf7230 (2017).
3. H. Huo, B. J. Gorsline, G. C. Fu, *Science* **367**, 559 (2020).
4. G. C. Fu, *ACS Cent. Sci.* **3**, 692 (2017).
5. S. L. Zultanski, G. C. Fu, *J. Am. Chem. Soc.* **135**, 624 (2013).
6. C. Fischer, G. C. Fu, *J. Am. Chem. Soc.* **127**, 4594 (2005).
7. A. H. Cherney, N. T. Kadunce, S. E. Reisman, *Chem. Rev.* **115**, 9587 (2015).
8. C. J. Cordier, R. J. Lundgren, G. C. Fu, *J. Am. Chem. Soc.* **135**, 10946 (2013).
9. X. Mu, Y. Shibata, Y. Makida, G. C. Fu, *Angew. Chem. Int. Ed.* **56**, 5821 (2017).
10. E. J. Corey, X.-M. Cheng, *The Logic of Chemical Synthesis* (Wiley, 1995).
11. Z. Wang, H. Yin, G. C. Fu, *Nature* **563**, 379 (2018).
12. S. Krautwald, E. M. Carreira, *J. Am. Chem. Soc.* **139**, 5627 (2017).

ACKNOWLEDGMENTS

NIH (R35 GM131816) is gratefully acknowledged.

10.1126/science.aba4222

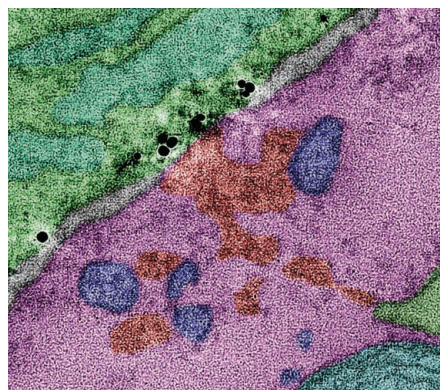
NEUROSCIENCE

Monitoring neuronal health

A multiscale imaging approach reveals a neuroimmune communication pathway

By Axel Nimmerjahn

Neurodegenerative disorders, most commonly stroke, Alzheimer's disease, and Parkinson's disease, affect millions of people worldwide (1). Despite their different etiologies, a frequent feature of neurodegenerative disorders is the persistent activation of the innate immune system (2). Controlling this inflammatory response in a way that positively affects clinical outcomes for cognition and behavior is a current major challenge and requires deeper understanding of the cellular and molecular mechanisms that govern neuroimmune interactions. On page 528 of this issue, Cserép *et al.* (3) identify a pathway through



A microglial process (green) with P2Y purinoceptor 12 (black) contacts a neuron cell body (pink) in mouse.

which microglia, the innate immune sensors of the central nervous system (CNS), monitor and influence neuronal health.

Microglia are damage sensors for the CNS. They continually surveil the parenchyma with highly motile processes and rapidly respond to tissue disturbances. However, the cellular and molecular mechanisms that control this structural and functional plasticity remain incompletely understood (4, 5). Much attention has focused on the interaction between microglial processes and neuronal synapses; this work has uncovered their important roles in activity-dependent synaptic plasticity and

synapse elimination in health and neurodegenerative disorders (6). However, much less attention has focused on microglial interactions with other cell compartments, including the soma (cell body), where most of a neuron's function is controlled. Cserép *et al.* show that targeted contact of microglial processes with neuronal somas (see the photo) is a prevalent feature of the mouse and human brain, rooted in specialized ultrastructure, and provides neuroprotection after injury. Inhibiting this protective response results in increased cell loss.

The death of a sufficient number of neurons can have devastating consequences for quality of life, as is evident in patients living with the effects of stroke, Parkinson's disease, or spinal cord injury. Furthermore, given the limited regenerative capacity of the CNS, neurons and their thousands of synaptic connections are typically not replaced when these cells die prematurely (7). A key role of immune sentinels such as microglia is to protect neurons against intrinsic and extrinsic threats, such as disruption of the blood-brain barrier (which restricts extravasation of blood-borne substances into the brain) or viral infection. If the threat cannot be eliminated or contained and a neuron becomes critically injured or dysfunctional, microglia face a difficult decision: Should resources be directed toward rescuing this cell, or should the cell be removed to prevent further damage to neighboring and connected neurons? To help guide this cell fate decision, microglia rely on a number of soluble and membrane-bound signals (8).

One important messenger in this context is adenosine triphosphate (ATP) and its metabolites, including adenosine diphosphate (ADP). High extracellular concentrations of ATP and ADP generated by injured and stressed cells are detected by purinergic receptors, including P2Y purinoceptor 12 (P2Y12 receptor), that are expressed on microglia. Thus, high extracellular ATP and ADP concentrations constitute a “find me” signal that guides microglia to the site of tissue damage. Lower concentrations of ATP are generally released under physiological conditions—for example, as a neurotransmitter at synapses (4, 5). The study of Cserép *et al.* shows that the activity-dependent release of ATP from anatomical specializations on neuronal somas

Waitt Advanced Biophotonics Center, Salk Institute for Biological Studies, La Jolla, CA 92037, USA.
Email: animmerj@salk.edu

PHOTO: CSERÉP ET AL. (3)

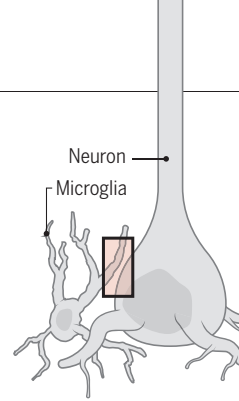
is a ubiquitous feature of cortical and deep brain regions and serves to continually communicate with nearby microglia.

These “somatic purinergic junctions” comprise a distinct combination of proteins and organelles, including mitochondria, reticular membrane structures, intracellular tethers, vesicle-like membrane structures, and clusters of the voltage-gated potassium channel Kv2.1 (see the figure). Kv2.1 clusters localize to the soma and proximal dendrites of excitatory and inhibitory neurons, and functionally tether the plasma membrane to the endoplasmic reticulum, thereby providing sites of endocytosis and exocytosis (9). The authors show that ATP released through this machinery, and likely converted to ADP in the extracellular space, attracts microglial processes and controls their contact duration in a P2Y12 receptor-dependent manner. Junctional contact by microglial processes correlated with the amount of nicotinamide adenine dinucleotide (NADH) in nearby neuronal mitochondria, which suggests active communication, albeit through an unknown mechanism. Because P2Y12 receptor inhibition reduced contact lifetime but did not prevent cellular interactions, additional factors may regulate microglial sampling.

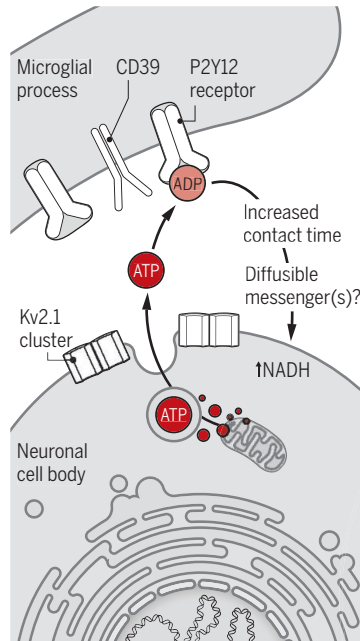
Cserép *et al.* investigated how the microglia-neuron interaction is altered in disease. After inducing middle cerebral artery occlusion (MCAo) in mice, which causes ischemia as well as neuron stress and injury (as occurs in stroke), they found that microglia in penumbral regions markedly increased the process coverage of stressed but morphologically intact neurons hours after reperfusion. This was inhibited by administration of the P2Y12 receptor antagonist PSB0739 before or immediately after MCAo, resulting in a larger region of neuron damage. Additionally, they show that ischemia led to degradation of the purinergic junctions in neurons, including mitochondrial fragmentation and Kv2.1 declustering. Increased microglial process coverage was also found in post-mortem stroke patient tissue.

Microglia protect neurons

During homeostasis, low amounts of ATP released from active neurons are converted to ADP and detected by microglial processes through P2Y12 receptors, leading to increased contact time with cell bodies and NADH in neurons. After neuronal injury, high concentrations of extracellular ATP increase coverage by microglial processes that protect viable neurons from cell death, although the precise mechanisms remain unknown.

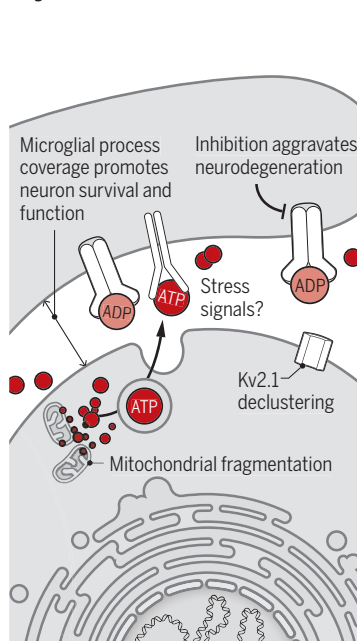


Homeostasis



ADP, adenosine diphosphate; ATP, adenosine triphosphate; Kv2.1, voltage-gated potassium channel 2.1; NADH, nicotinamide adenine dinucleotide; P2Y12 receptor, P2Y purinoceptor 12.

Dysfunction



Although P2Y12 receptor-mediated signaling in the microglial response to injury is important, the findings of Cserép *et al.* raise the question of what role the purinergic junctions play at different time points after stroke. Initially, neuronal hyperexcitability likely causes massive ATP release that attracts microglia to stressed neurons. However, as purinergic junctions disintegrate and ATP concentration drops, the mechanisms that sustain microglial contact remain unknown. Changes in extracellular ATP and ADP concentration are likely insufficient, and they may not allow microglia to discriminate neurons that can be rescued. Instead, such discrimination likely involves the integration of a variety of soluble and membrane-bound factors, including those derived from mitochondrial stress. Microglial ensheathment likely provides neuroprotection through various mechanisms, such as limiting the exposure of neurons to excitotoxic substances (e.g., high glutamate concentrations or leaked blood plasma components), controlling the ion flux of neurons, or providing them with trophic factors.

The identification by Cserép *et al.* of somatic purinergic junctions broadens our knowledge of the mechanistic basis underlying neuroimmune communication in the CNS. Alterations in this pathway may have implications for other disorders. For example, Kv2.1 declustering occurs in response to neuronal hyperactivity (9) and may therefore modulate neuron-microglia communication in epilepsy or neuropathic pain. Additionally, the neuroprotective abilities of microglia are likely impaired by dysregulation of their function during aging or neurodegenerative disease. Recent genetic analyses have revealed that many of the genes associated with the risk of neurodegenerative diseases are expressed in the CNS predominantly or exclusively by microglia (e.g., in Alzheimer's disease, which is associated with prominent down-regulation of P2Y12 receptor expression) (6).

Perhaps the most important question is how this new knowledge can be translated into better treatments. In stroke, the timing and route of drug administration can make the difference between protective and detrimental treatment outcomes (10). Better understanding of this spatiotemporal interaction will facilitate the design of treatments that either augment the beneficial effects or reduce the pathogenic effects of immune responses, ultimately improving the lives of patients. ■

REFERENCES AND NOTES

1. GBD 2016 Neurology Collaborators, *Lancet Neurol.* **18**, 459 (2019).
2. J. Stephenson *et al.*, *Immunology* **154**, 204 (2018).
3. C. Cserép *et al.*, *Science* **367**, 528 (2020).
4. P. Izquierdo, D. Attwell, C. Madry, *Trends Neurosci.* **42**, 278 (2019).
5. E. M. York, L.-P. Bernier, B. A. MacVicar, *Dev. Neurobiol.* **78**, 593 (2018).
6. M. W. Salter, B. Stevens, *Nat. Med.* **23**, 1018 (2017).
7. S. Grade, M. Götz, *NPJ Regen. Med.* **2**, 29 (2017).
8. G. Lemke, *Nat. Rev. Immunol.* **19**, 539 (2019).
9. B. Johnson, A. N. Leek, M. M. Tamkun, *Channels* **13**, 88 (2019).
10. K. E. Sandoval, K. A. Witt, *Neurobiol. Dis.* **32**, 200 (2008).

ACKNOWLEDGMENTS

Thanks to G. S. Shadel and G. Lemke for discussions. Supported by NIH grants NS108034, NS103522, and NS112959 (to A.N.) and CA014195 (to the Salk Institute).

10.1126/science.aba4472

SYSTEMS BIOLOGY

Unpicking the proteome in single cells

Single-cell mass spectrometry will help reveal mechanisms that underpin health and disease

By **Nikolai Slavov**

Recently, the throughput of single-cell RNA-sequencing (transcriptomics) and genomics technologies has increased more than a 1000-fold. This increase has powered new analyses: Whereas traditional analysis of bulk tissue averages all differences between the diverse cells comprising such samples, single-cell analysis characterizes each individual cell and thus has enabled the discovery and classification of previously unknown cell states. Yet, the nucleic-acid-based technologies are effectively blind to an important group of biological regulators: proteins. Fortunately, emerging mass-spectrometry (MS) technologies that identify and quantify proteins promise to deliver similar gains to single-cell protein analysis. These proteomic technologies will enable high-throughput investigation of key biological questions, such as signaling mechanisms based on protein binding, modifications, and degradation, that have long remained elusive.

The abundance and activity of many proteins are regulated by degradation and posttranslational modifications (PTMs) that cannot be inferred from genomic and transcriptomic measurements. Moreover, genomic and transcriptomic sequencing cannot report directly on protein-protein interactions and protein localization, which are critical for numerous signaling pathways (1–3). The extracellular matrix surrounding each cell is composed of proteins whose chemical and physical properties, such as stiffness, can also play vital roles in regulating cellular behavior, including proliferation, migration, metastasis, and aging (4). Yet, current single-cell sequencing tools provide little information about the protein composition and biological roles of the extracellular matrix (3–5). Thus, methodologies are needed that can directly analyze a broad repertoire of intracellular, membrane-bound, and extracellular proteins at the single-cell level.

Single-cell protein analysis has a long history, but the conventional technologies have relatively limited capabilities (6, 7).

Most proteomics methods, such as mass cytometry, cellular indexing of transcriptomes and epitopes by sequencing, RNA expression and protein sequencing, and CO-Detection by indEXing, rely on antibodies to detect select protein epitopes and can analyze only a few dozen proteins per cell (6) (see the figure). However, many antibodies have low specificity for their targets, which results in nonspecific protein detection. Indeed, fewer than a third of more than a thousand antibodies tested in multiple laboratories bind specifically to their cognate targets (6). As a result, ~\$800 million is wasted worldwide annually on purchasing nonspecific antibodies and even more on experiments following up flawed hypotheses based on these nonspecific antibodies (8). Although some highly specific and well-validated antibodies can be useful to analyze a few proteins across many cells, the low specificity and limited throughput of the current generation of single-cell protein analytical methods pose challenges for understanding the interactions and functions of proteins at single-cell resolution.

These challenges are being addressed by emerging technologies for analyzing single cells by MS without the use of antibodies, such as Single Cell ProtEomics by MS (SCoPE-MS) and its second generation, SCoPE2. These methods allow the quantification of thousands of proteins across hundreds of single-cell samples (9, 10) (see the figure). A key driver of this progress was the development of multiplexed experimental designs in which proteins from single cells and from the total cell lysate of a small group of cells (called carrier proteins) are barcoded and then combined (9, 10). With this design, the carrier proteins reduce the loss of proteins from single cells adhering to equipment surfaces while simultaneously enhancing peptide identification.

Other key drivers of progress include methods for clean and automated sample preparation, for which there is preliminary evidence (11), as well as rigorous computational approaches that incorporate additional peptide features, such as retention time, to determine peptide sequences from limited sample quantities (12). Further technological developments can increase the accuracy of quantification and numbers of analyzed cells by 100- to 1000-fold while affording quantification of protein modi-

fications at single-cell resolution (7). For example, the carrier protein approach (9) can be extended to quantify PTMs by using a carrier composed of peptides with PTMs while avoiding the need to enrich modified proteins from single cells and, thus, enrichment-associated protein losses.

Although current methods can quantify proteins present at ~50,000 copies per cell (which is the median protein abundance in a typical human cell), increased efficiency of peptide delivery to MS analyzers, e.g., by increasing the time over which peptide ions (proteins are fragmented into peptides and ionized in MS analysis) are sampled (7, 13), will increase sensitivity to proteins present at only 1000 copies per cell. In general, the emerging technologies offer a trade-off between quantifying low-abundance proteins with increased accuracy or quantifying more proteins. This trade-off can be mitigated by simultaneously sampling multiple peptides (7). Over the next few years, improvements in sample preparation, peptide separation and ionization, and instrumentation are likely to afford quantification of more than 5000 proteins across thousands of single cells, while targeted approaches are poised to enable analysis of even low-abundance proteins of interest (7).

MS methods have the potential to measure not merely the abundance and PTMs of proteins in single cells, but also their complexes and subcellular localization. When proteins form a complex, polypeptide chains from different proteins can get close enough to be cross-linked by small molecules. Because only proteins in the complex are likely to be cross-linked, the abundance of such peptides can report directly on complex formation and composition. Some cross-linked peptide pairs are observed only with specific complex conformations, and thus these pairs can be useful in distinguishing active and inactive complexes. Furthermore, if a protein complex is close to organelles, targeted MS analysis of cross-linked peptides between the complex and organelle-specific proteins may report on the subcellular localization. Such analysis has not yet been applied to single-cell MS, but is likely to be feasible.

Realizing these exciting prospects requires concerted effort and community standards devoted to ensuring that hype does not overshadow scientific rigor. For

Department of Bioengineering and Barnett Institute, Northeastern University, Boston, MA, USA.
Email: nslavov@neu.edu, nslavov@alum.mit.edu

example, systematic artifacts, such as contaminant proteins introduced to single-cell samples during their preparation or chromatographic separation, may result in reproducible measurements. Despite their reproducibility, such measurements do not reflect protein abundances in single cells. If reproducibility is misinterpreted as accuracy, the resulting errors may erode the credibility of this emerging field.

Single-cell proteomics will find many applications in biomedical research. Some applications, such as classifying cell states and cell types, overlap with those of single-cell RNA sequencing. Other applications can only be achieved by measuring proteins. For example, the development of cells for regenerative therapies through the rational engineering of directed differentiation

processes that lead to the desired cell types and then simulating them by using agonists and/or antagonists. Whereas single-cell RNA sequencing can identify the cells of interest, the amounts of messenger RNA are poor surrogates for the signaling activities mediated by protein modifications, such as phosphorylation or protein cleavage (2, 15). Single-cell proteomics could provide a robust means to characterize such signaling dynamics.

Another potential application is the identification of the sets of molecular interactions leading from a genotype or a stimulus to a phenotype of interest. This goal presents a substantial challenge in part because interacting molecules within a pathway are rarely measured across a large range of phenotypic states to constrain cellular network models. This limitation is particularly evi-

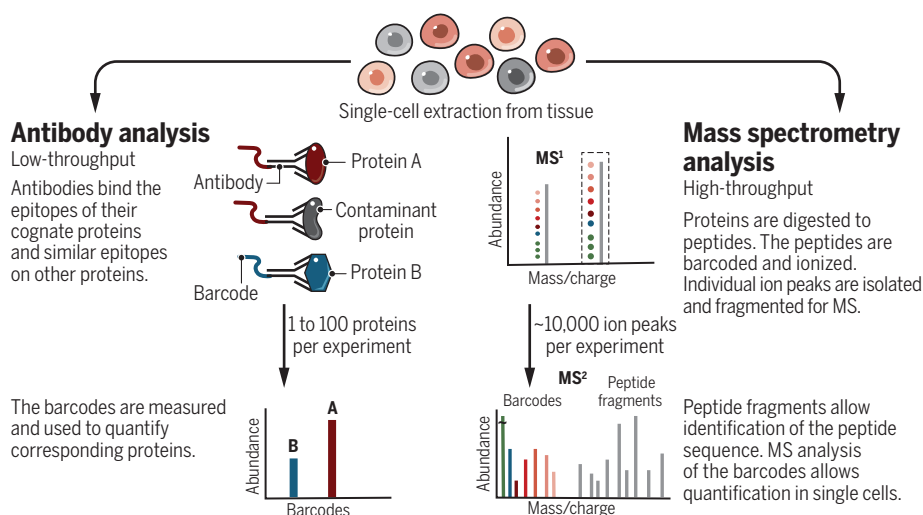
Next-generation single-cell protein analytical technologies will reduce these assumptions and thus increase the validity of inferred mechanisms. If proteins, RNAs, DNA, and metabolites are measured across tens of thousands of individual cells, it may be possible to identify direct molecular interactions without the need to make assumptions about basic aspects of the pathway. Next-generation single-cell analysis is poised to generate just this type of data, which should underpin systems-level understanding of intracellular and extracellular regulatory mechanisms.

Single-cell proteomics may also have clinical applications. Protein measurements from limited clinical samples are attractive because they afford direct measurements of deregulated signaling pathways that drive disease. Furthermore, measuring protein concentrations allows the development of assays to test therapies that induce protein degradation, which are among the most rapidly growing therapeutic modalities (15). Additionally, protein assays may be more robust than RNA-sequencing assays because protein concentrations are less noisy and proteins degrade more slowly than RNAs. Moreover, the cost of protein analysis will decrease proportionately with increased multiplexing (7, 11).

The latest generation of nucleic acid-based single-cell analytical methods has opened the door to describing the varied and complex constellation of cell states that exist within tissue. The next generation of proteomics-based methods will complement current methods while shifting the emphasis from description toward functional characterization of these cell states. ■

Single-cell protein analysis

Traditional methods identify and quantify a limited number of proteins based on antibodies barcoded with DNA sequences, fluorophores, or transition metals. Emerging single-cell mass-spectrometry (MS) methods will allow high-throughput analysis of proteins and their posttranslational modifications, interactions, and degradation.



may benefit from single-cell proteomics. Although there has been much progress in developing directed differentiation protocols for certain cell types, these efforts tend to rely on trial-and-error approaches (14). Many of the resulting protocols remain relatively inefficient: Only a fraction of the cells differentiate into the desired cell type, and such cells may not fully recapitulate the desired physiological phenotypes (14).

Next-generation single-cell proteomics analysis offers an alternative to this trial-and-error approach. If the signaling events (usually mediated by protein interactions and PTMs) that guide cell differentiation during normal development can be identified, it should be possible to recapitulate such signaling in induced pluripotent stem cells. This would require identifying the signaling

dependent for proteins and their PTMs (1–3). Yet, proteins are key regulators in cells; models that ignore them cannot capture molecular mechanisms involving protein interactions. For example, the absence of direct protein measurements compromises the ability to study signaling networks because most of the key regulatory variables are missing from the data. Currently, when proteins and their PTMs are measured in bulk tissues, they have been analyzed in a few tens to a few hundreds of samples (2, 3). Analyzing so few samples tends to require assumptions about the specific sets of interactions and functional dependencies that occur between interacting proteins and molecules. Such assumptions fundamentally underpin the inferred biological mechanisms and undermine their validity (3).

REFERENCES AND NOTES

1. D. M. Sabatini, *Proc. Natl. Acad. Sci. U.S.A.* **114**, 11818 (2017).
2. A. Franks, E. Airolidi, N. Slavov, *PLOS Comput. Biol.* **13**, e1005535 (2017).
3. Y. Liu, A. Beyer, R. Aebersold, *Cell* **165**, 535 (2016).
4. M. Segel et al., *Nature* **573**, 130 (2019).
5. A. J. Cote et al., *Nat. Commun.* **7**, 10865 (2016).
6. E. Levy, N. Slavov, *Essays Biochem.* **62**, 595 (2018).
7. H. Specht, N. Slavov, *J. Proteome Res.* **17**, 2565 (2018).
8. A. Bradbury, A. Plückthun, *Nature* **518**, 27 (2015).
9. B. Budnik et al., *Genome Biol.* **19**, 161 (2018).
10. V. Marx, *Nat. Methods* **16**, 809 (2019).
11. H. Specht et al., *bioRxiv* (2019). 10.1101/665307
12. A. T. Chen, A. Franks, N. Slavov, *PLOS Comput. Biol.* **15**, 1 (2019).
13. R. G. Huffman et al., *J. Proteome Res.* **18**, 2493 (2019).
14. F. W. Pagliuca et al., *Cell* **159**, 428 (2014).
15. P. P. Chamberlain, L. G. Hamann, *Nat. Chem. Biol.* **15**, 937 (2019).

ACKNOWLEDGMENTS

N.S. is an inventor on patent application 16/251,039. N.S. is supported by a New Innovator Award from the National Institute of General Medical Sciences (award no. DP2GM123497).

10.1126/science.aaz6695

POLICY FORUM

ECONOMICS AND THE ENVIRONMENT

Progress in natural capital accounting for ecosystems

Global statistical standards are being developed

By **Lars Hein, Kenneth J. Bagstad, Carl Obst, Bram Edens, Sjoerd Schenau, Gem Castillo, Francois Soulard, Claire Brown, Amanda Driver, Michael Bordt, Anton Steurer, Rocky Harris, Alejandro Caparrós**

Reversing the ongoing degradation of the planet's ecosystems requires timely and detailed monitoring of ecosystem change and uses. Yet, the System of National Accounts (SNA), first developed in response to the economic crisis of the 1930s and used by statistical offices worldwide to record economic activity (for example, production, consumption, and asset accumulation), does not make explicit either inputs from the environment to the economy or the cost of environmental degradation (*1, 2*). Experimental Ecosystem Accounting (EEA), part of the System of Environmental-Economic Accounting (SEEA), has been developed to monitor and report on ecosystem change and use, using the same accounting approach, concepts, and classifications as the SNA (*3*). The EEA is part of the statistical community's response to move SNA measurement "beyond gross domestic product (GDP)." With the first generation of ecosystem accounts now published in 24 countries, and with a push to finalize a United Nations (UN) statistical standard for ecosystem accounting by 2021, we highlight key advances, challenges, and opportunities.

PROGRESS TO DATE

Led by the UN Statistical Commission (UNSC) and involving statistical offices from all continents, international organizations such as the European Commission and the World Bank, and several hundred scientists and nongovernmental organization representatives, the SEEA is the world's leading natural capital accounting approach. The SEEA includes two parts: the Central Framework (CF), adopted as a statistical standard by the UNSC in 2012 (*4*), and the EEA framework (not yet a standard), first published in 2014 (*5*). In an accounting sense, the CF extends the asset

boundary of the SNA (in physical, not monetary, terms), whereas the EEA also extends the production and consumption boundary. The CF measures emissions, stocks and uses of individual natural resources, and transactions related to environmental management. The CF is used, in particular, to report on water; energy, including oil and natural gas reserves; mineral ores; and emissions to air. The EEA provides a framework for measuring ecosystems and their uses and recognizes that ecosystems generate multiple types of services (provisioning, regulating, and cultural). By broadening measures of production, consumption, income, and asset value, ecosystems' contributions to society become visible. Furthermore, in recognition of the spatial heterogeneity of ecosystems, the EEA uses maps for analytical and reporting purposes. The EEA includes individual accounts recording: the extent of different ecosystem types, their condition, physical and monetary flows of ecosystem services, and the monetary value of ecosystem assets. Additionally, the EEA includes thematic accounts for land, water, carbon, and biodiversity (*6*). Countries typically compile the most policy-relevant accounts first. Because of their spatial nature, the EEA can report by ecosystem types, watersheds, or administrative units.

To maintain consistency with the SNA, monetary valuation in the SEEA is based on exchange prices—prices at which goods, services, or assets are or could be transacted. Monetary values in the SEEA thus complement those provided in the SNA and can be used to analyze the contribution of natural capital to the economy or compare the costs of ecosystem degradation with increases in economic output, among others.

EEA accounts have now been published in 24 countries [see the figure and supplementary materials (SM), section 1]. The United Kingdom (*7*) and the Netherlands (*8*) have published the most comprehensive accounts to date. Both countries' accounts include detailed maps and physical and monetary accounting tables. In Australia, several accounts have been published at the national and local scale (*9*). In Andalusia (Spain), ecosystem service accounts have

been compiled and environmental income assessed (*10*). In South Africa, national ecosystem accounts have been developed for the extent and condition of rivers (*11*). Supranational accounts have been developed for the European Union (*12*). In Organisation for Economic Co-operation and Development (OECD) countries, national governments financed the compilation of accounts, whereas in many developing countries, donors have contributed, either directly or through UN or World Bank programs. Statistical agencies differ in their capacity to analyze ecosystems and their services and have often collaborated with specialized research institutes and universities.

POLICY APPLICATIONS

A key feature of the accounts is to show ecosystems' contributions to the economy. For example, the contributions of nature recreation and tourism and crop provisioning services to the economy are relatively high in the United Kingdom and the Netherlands (*7, 8*). This reflects both the relative contribution of ecosystems to the tourism sector and agriculture and the economic importance of these activities. Per-hectare monetary values are around 50% higher in the Netherlands. This is mainly due to broader coverage for the service "recreation and tourism."

EEA accounts can inform various natural resource management decisions (*13*). In the Netherlands, for example, EEA accounts show that in peat areas used for dairy farming, the combined costs of maintaining infrastructure and controlling water levels and carbon dioxide emissions considerably exceed farmers' profits. This has led to new policies aimed at reducing drainage in peatlands and converting farmland back to natural ecosystems (*14*). In Indonesia, local governments have responsibility for land-use planning but often lack spatial information on forest extent, condition, and use. Accounts can facilitate local government efforts to plan, implement, monitor, and enforce forest management policies, provided that statistical offices make high-resolution spatial data available.

The accounts can enhance transparency and fairness of ecosystem use. For example, information is often lacking on rents resulting from the exploitation of ecosystems (for example, for timber extraction or plantation agriculture). EEA accounts show these rents in a spatially explicit manner, providing an objective basis for their taxation. The EEA also allows trends in ecosystem extent, condition, and use to be monitored, including UN Sustainable Development Goals indicators. The EEA accounts can provide comprehensive and objective baseline data

See supplementary materials for author affiliations.
Email: lars.hein@wur.nl

Countries that have compiled SEEA EEA accounts

Some countries have published all accounts that they have compiled, and others have published only some. China, Japan, and the United States have compiled accounts but not published them (see supplementary materials, section 1). The scope and resolution of the accounts vary between countries. The figure presents a snapshot—countries continue to compile and publish accounts. SEEA, System of Environmental-Economic Accounting; EEA, Experimental Ecosystem Accounting.



for private-sector natural capital accounting, for example, with the Natural Capital Protocol. This allows businesses to better understand their impacts and dependency on natural capital.

CHALLENGES AND OPPORTUNITIES

Ecosystem accounts published to date vary in scope and level of (spatial) detail. This reflects differences in budget, technical capacity, and data between countries, with notable constraints in developing countries. Compiling the full suite of ecosystem accounts requires substantial data and use of multiple biophysical models (see SM, section 2). The Netherlands ecosystem accounts provide 90 policy-relevant indicators, derived from various datasets and models. They indicate, for example, how small landscape elements such as hedgerows contribute to crop production by maintaining pollinator populations.

Institutional challenges occur, for instance, in relation to integrating data from different agencies: Data may be in incompatible formats, or there may be a reluctance to share it. Furthermore, the SEEA has a different measurement approach compared with some existing reporting systems (for example, carbon reporting under the UN Framework Convention on Climate Change). Collaboration between government institutes holding different datasets facilitates enhanced data integration and greater commonality in terminology and definitions (13).

Some technical challenges remain. For instance, the diversity of ecosystems makes

selection of ecosystem condition and biodiversity indicators challenging. In South African and Australian accounts, ecosystem condition has been defined in relation to pre-European settlement conditions, which is not useful for western Europe with its long ecosystem-use history. Challenges also exist in valuing nonmarket ecosystem services such as water regulation and air filtration.

The EEA's inherent limitations should be considered when the accounts are used in policy-making. The EEA accounts produced to date do not include indicators for ecosystem resilience or consider probabilities of sudden future collapses of overexploited ecosystems (15). Furthermore, exchange prices of ecosystem services reflect current pricing mechanisms and market conditions. Given that the SEEA does not record the welfare generated by using natural capital (2), it is imperative that monetary values in the EEA are not interpreted as representing "the value of nature" (see SM, section 3).

Several ongoing efforts address remaining challenges to the global implementation of the EEA. The UNSC is working with scientists and statisticians toward establishing a statistical standard for the EEA by 2021. Working groups have been established to address remaining technical issues, including defining metrics expressing ecosystem condition, biodiversity, and the capacity of ecosystems to supply services and valuing nonmarket ecosystem services (for instance, on the basis of simulated exchange values). Through various scientific efforts connected

to the EEA, such as the Earth Observation for Ecosystem Accounting initiative of the Group on Earth Observations, tests are being done to examine how ecosystem extent, condition, and regulating services can be modeled across large countries or even continents at high resolution using data from remote-sensing and global datasets. Increasingly, machine-learning techniques are used, for instance, to assess the impacts of ecosystem changes on hydrological cycles and the availability of water for people. Social media posts can be used to analyze recreation in ecosystems, for example. The EEA is making large datasets available to a variety of users, and global, high-resolution modeling of critical ecosystem characteristics and services will facilitate easier uptake of the EEA in developing countries.

The EEA allows consistent (over time and between countries), comprehensive, and high-resolution analysis and reporting on ecosystems and their use. The EEA accounts do not capture all connections between people and nature and have limited capacity to consider ecosystem complexities such as thresholds and feedbacks. These caveats need to be clearly articulated when EEA accounts are published. Nonetheless, the EEA considerably enhances the scope and accuracy of information available in support of ecosystem management, facilitating better management of global natural capital. ■

REFERENCES AND NOTES

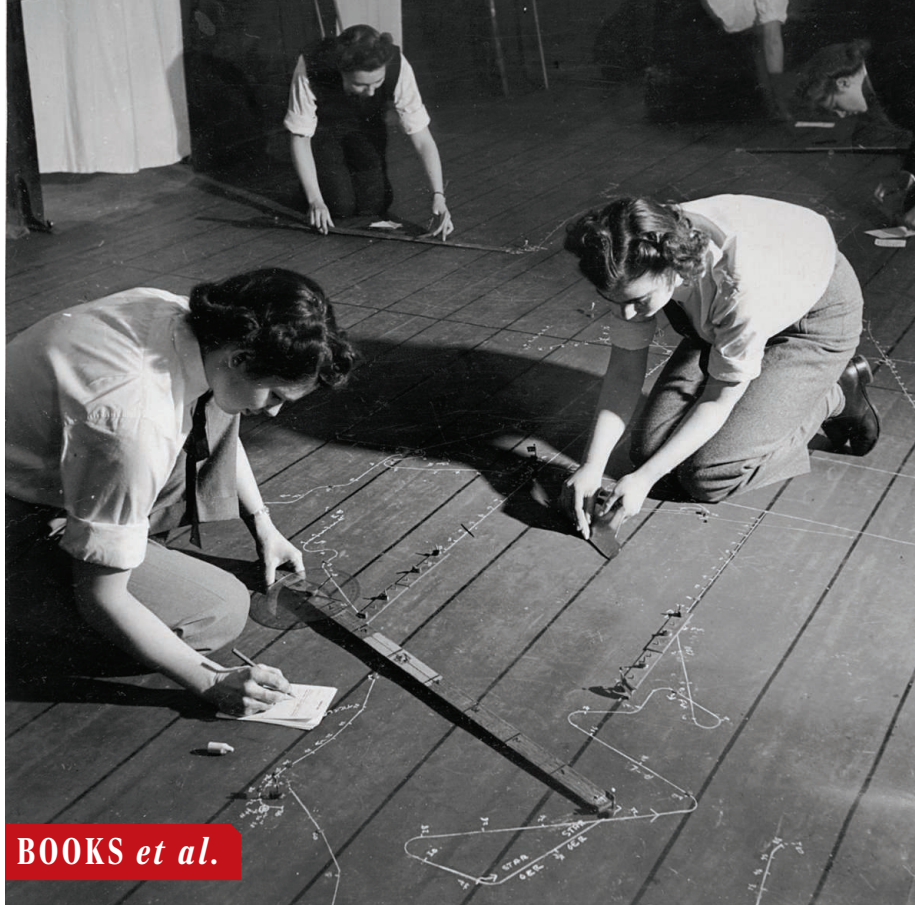
1. J. Stiglitz, J. Fitoussi, M. Duran, *Beyond GDP: Measuring What Counts for Economic and Social Performance* (OECD Publishing, 2018).
2. D. W. Jorgenson, *J. Econ. Lit.* **56**, 867 (2018).
3. UN et al., *The System of National Accounts*, 2008 (UN, 2009).
4. UN et al., "System of environmental-economic accounting 2012: Central framework" (UN, 2014).
5. UN et al., "System of environmental-economic accounting: Experimental ecosystem accounting" (UN, 2014).
6. UN, "Technical Recommendations in support of the SEEA Experimental Ecosystem Accounting" (UN, 2019).
7. ONS (Office for National Statistics), "UK natural capital accounts: 2019" (ONS, 2019).
8. Horlings et al., "Experimental monetary valuation of ecosystem services and assets in the Netherlands" (Report, Statistics Netherlands and Wageningen University and Research, 2019).
9. H. Keith et al., *Nat. Ecol. Evol.* **1**, 1683 (2017).
10. P. Campos et al., *Ecol. Econ.* **157**, 218 (2019).
11. J. L. Nel, A. Driver, "National river ecosystem accounts for South Africa" (South African National Biodiversity Institute, Pretoria, 2015).
12. S. Vallecillo et al., "Ecosystem services accounting—Part II Pilot accounts for crop and timber provision, global climate regulation and flood control" (JRC technical reports, Publications Office of the European Union, 2019).
13. G. Bright et al., *Oxf. Rev. Econ. Policy* **35**, 88 (2019).
14. Government of the Netherlands, "National Climate Agreement" (2019).
15. C. Folke et al., *Ecol. Soc.* **21**, 41 (2016).

ACKNOWLEDGMENTS

The views expressed in this article are those of the authors and do not necessarily reflect the policies of the UN or the European Union.

SUPPLEMENTARY MATERIALS

science.sciencemag.org/content/367/6477/514/suppl/DC1
10.1126/science.aaz8901



Members of the Women's Royal Naval Service trace the paths of hypothetical British and German vessels.

BOOKS *et al.*

WAR GAMES

Game over

A high-stakes game of battleship helped turn the tide in World War II's Battle of the Atlantic

By **Stacie L. Pettyjohn**

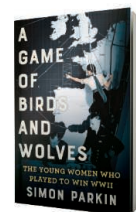
In *A Game of Birds and Wolves*, journalist Simon Parkin reports on a long overlooked piece of World War II's Battle of the Atlantic, focusing on a war game that helped the British counter Nazi U-boats threatening Britain's vital sea lines.

The first part of the book will be familiar to war scholars and history buffs, offering an overview of German Admiral Karl Doenitz's plan to use a fleet of U-boats to cut off commerce to the United Kingdom, which the island nation needed to stay in the war. Although a similar strategy had been tried unsuccessfully in World War I, Doenitz believed that improved communications would enable groups of U-boats to operate together,

like a wolf pack, and allow them to coordinate and defeat escorted convoys.

Doenitz's plan, devised in 1937, was not realized until June 1940, when Germany's occupation of France gave it Atlantic bases. Nazis called this the "happy time" because their U-boats roamed the seas with impunity, sinking civilian vessels carrying cargo and, notably, the passenger ship *SS City of Benares*, which was carrying 90 children fleeing the United Kingdom. (Parkin's vivid description of the *Benares*'s fate is, at times, a distraction from the larger narrative.) According to Parkin, this success was largely due to bold tactics developed by German Captain Otto Kretschmer, who launched night attacks within the columns of a convoy, firing torpedoes at point-blank range, then submerging until the convoy dispersed.

In January 1942, Winston Churchill enlisted Captain Gilbert Roberts to lead a small organization—the Western Approaches Tactical Unit (WATU)—charged with identifying U-boat tactics, developing effective countermeasures, and teaching British sailors to use new countermaneuvers. Lacking competent men to staff WATU, Roberts turned to the Women's Royal Naval Service (known as the "Wrens"), which assigned women who had a "keen mind for numbers" to build and run a game modeling a two-sided tactical fight between British escorts and German U-boats.



A Game of Birds and Wolves
Simon Parkin
Little, Brown, 2020.
336 pp.

During this game, the two sides maneuvered their respective vessels, dropped depth charges, and fired torpedoes on a linoleum floor, where each 10-inch square represented one nautical mile. The British team commanded their escorts from behind white sheets designed to limit their line of sight to replicate the view from a ship's bridge. While British ships were outlined in conspicuous white chalk, the U-boats were marked in green, rendering them invisible. Throughout the game, the Wrens measured and marked the ships' movements, provided intelligence, guided discussions, and played as the German team. Roberts presided over the game and the postgame discussion.

Parkin nicely highlights how this war game was used for multiple purposes at different times during the war. Roberts and the Wrens first used the game to uncover Kretschmer's tactical innovation, for example. They then used it to develop and test countermeasures. Additionally, the game was used to teach skeptical audiences the superiority of WATU's countermeasures when compared with existing tactics. By the war's end, nearly 5000 sailors had taken WATU's weeklong course covering four different battle scenarios.

The book's third and final section details the apex of the war at sea, when British convoys used WATU-developed tactics and, bolstered by aircraft and naval support groups, fended off the largest wolf-pack attacks of World War II. After 41 U-boats were sunk in May 1943, the Battle of the Atlantic turned decisively toward the Allies.

A Game of Birds and Wolves is extensively researched and well written, and it tells an engrossing story of a little-known topic. Still, war gamers and those interested in the role of women in war games are likely to be disappointed. The book's actual discussion of war games is relegated to a relatively small section in the middle of the book, and Parkin's protagonists are Doenitz and Roberts. A dearth of firsthand accounts from the Wrens hampered Parkin's research, and the women are rendered in broad strokes as a supporting cast of characters.

Sadly, the Wrens were an anomaly, reflecting a brief moment when women were war gamers out of necessity, operating in a field that to this day is dominated by men. Yet gender diversity has been shown to yield better and more innovative solutions in such settings, and achieving it should be a priority. ■

The reviewer is director of Project AIR FORCE's Strategy and Doctrine Program and codirector of the Center for Gaming, RAND Corporation, Arlington, VA 22202, USA. Email: spettyjo@rand.org

10.1126/science.aba2874

INTELLECTUAL PROPERTY

Profits, prejudice, and plant patents

A journalist investigates a surprising act of espionage

By **Helen Anne Curry**

For many of us, the idea of industrial espionage conjures up secreted factory blueprints, copied chemical formulas, and hacked computer systems. It calls to mind the high tech and highly trained, the stuff of spy novels and James Bond films. It does not evoke Iowa cornfields—at least, no more than a few scattered ears of corn missed by a mechanical harvester might suggest vulnerable trade secrets.

Yet some seeds are a source of intense competition and controversy, and they feature prominently among the many purported and confirmed objects of economic theft. In the United States, seed companies have complained about having their products “stolen” by competitors since the very earliest days of commercial breeding and industrial seed production. Before governments began allowing patents on plants, it was easy—and legal—to reproduce and profit from others’ plant varieties simply by harvesting and selling their seeds. Breeders developed various strategies for preventing this, from special pricing to contracts to trademarks to producing F1 (first-generation) hybrids, but it was not until the advent of state-enforced protections on a wide range of agricultural crops in the 1970s that selling someone else’s seeds became a crime.

In 2016, the conviction of a Florida physicist on charges of conspiring to steal trade secrets confirmed that seed theft had also become, at least to those who influence U.S. federal policies and procedures, a national security threat. The scientist, Mo Hailong (also known as Robert Mo), pled guilty to having assisted a Chinese company in acquiring corn seed lines owned by the transnational seed behemoths Monsanto and DuPont Pioneer.

The reviewer is at the Department of History and Philosophy of Science, University of Cambridge, Cambridge CB2 3RH, UK, and is the author of *Evolution Made to Order: Plant Breeding and Technological Innovation in Twentieth-Century America* (University of Chicago Press, 2016). Email: hac44@cam.ac.uk

The journalist and former *Science* correspondent Mara Hvistendahl explores the history of Mo’s strange and, ultimately, sad career as an industrial operative in her third book, *The Scientist and the Spy*. Although Mo could be either the scientist or the spy alluded to in the title, he is hardly the real subject of the book. Hvistendahl convincingly casts Mo as a “pawn in an international struggle” between China and the United States.

The U.S. Federal Bureau of Investigation (FBI) spared little expense in developing a case against Mo. A 2-year period saw 73 agents devote time to the effort, 17,000 emails intercepted, hundreds of hours of

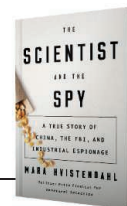


Iowa cornfields were the target of industrial espionage in 2016.

audio recorded and transcribed, and more. All of this was done to defend the intellectual property of two extremely profitable, world-leading agribusinesses—“American industry”—against the haphazardly organized incursions of an expanding Beijing-based animal feed corporation that did not even have the expertise in place to efficiently exploit stolen seeds—“unfair foreign competition.”

To understand why the U.S. government devotes a substantial amount of taxpayer dollars to investigating and litigating on behalf of Monsanto—a company that not only is in possession of an aggressive legal division but also, at the time of Mo’s activities, was under investigation by the U.S. Justice Department for potential violation

The Scientist and the Spy:
A True Story of China, the
FBI, and Industrial Espionage
Mara Hvistendahl
Riverhead Books,
2020. 331 pp.



of antitrust law—one really needs to appreciate global politics.

Hvistendahl considers factors that range from the FBI’s post-Cold War refashioning, which contributed to a new narrative of industrial espionage as a national security threat, to the effects that greater meat consumption in China have had on demand for feed corn and, therefore, seed corn. The consolidation of agribusiness features prominently as well, a factor that both explains, and is explained by, the dogged defense of patents on corn and other crop varieties described above.

If there is a subplot that makes this book essential reading, especially for those working in the sciences today, it is Hvistendahl’s documentation of the disturbing effects that the too-vigorous pursuit of industrial spies has had on Chinese scientists and engineers in the United States. For nearly two decades, the FBI and other U.S. agencies have expounded an account of China’s espionage strategy in which the Chinese government is said to rely on “a dispersed network of nontraditional collectors” rather than professional agents. This vision of a “human wave” of students, scientists, and engineers...who gather intelligence ad hoc” wrongly implicates all ethnic Chinese working in the United States as potential spies for the Communist Party.

Hvistendahl provides evidence that this characterization, which evokes old racist fears of “the yellow peril,” not only is fundamentally inaccurate with respect to China’s state-led spy operations but also produces racially motivated suspicion, hostility, and harm. Wrongful investigations have ruined careers and lives.

Is American industry really at risk? Or is it values such as tolerance, openness, and justice that are truly in danger? Hvistendahl’s foray through cornfields and courtrooms eschews easy answers to these questions, yet her vivid observations and incisive analyses will leave readers well equipped to arrive at their own conclusions. ■

10.1126/science.aba0297



Adaptations to
smallholder farms
can contribute to
climate resilience.

Edited by Jennifer Sills

Agricultural lands key to mitigation and adaptation

In their Review “Measuring the success of climate change adaptation and mitigation in terrestrial ecosystems” (13 December 2019, p. eaaw9256), M. D. Morecroft *et al.* ignored the role of agricultural land. Although the carbon density of agricultural ecosystems is lower than for forests, the land area available (~22.2 million km²) (1) and the fact that they are actively managed make them an important mitigation opportunity (1).

Globally, cropland soils could sequester an additional 0.90 to 1.85 gigatons of carbon (Gt C) per year (2), approximately equivalent to the current emissions resulting from land-use change (2). Across the European Union, it has been estimated that agroforestry could sequester 1.6 Gt C per year, or approximately 37% of the European Union’s annual emissions (3). Globally, agroforestry accounts for ~34 Gt C (1).

Interventions such as agroforestry and integrated soil fertility management also deliver substantial adaptation benefits (4). Morecroft *et al.*’s coverage of adaptation was almost entirely focused on the co-benefits for biodiversity conservation. Livelihoods were barely mentioned. Especially in the tropics, severe climatic events, such as storms, droughts, and floods, interact with poverty to cause major humanitarian disasters [e.g., (5)].

Adaptation for the world’s approximately 500 million smallholder farmers (6) means

increasing incomes, diversifying crops and income sources, and enhancing resilience through improved management of soils and other natural resources. Moreover, habitat protection and ecological restoration alone will not suffice to conserve biodiversity. It is imperative that agricultural lands are managed in a way that conserves biodiversity, through increasing trees on farms and adopting agroecological approaches to crop management.

Rhett D. Harrison^{1*} and Anja Gassner²

¹World Agroforestry, Lusaka, Zambia. ²World Agroforestry, International Rice Research Institute, Laguna, Philippines.

*Corresponding author. Email: r.harrison@cgiar.org

REFERENCES AND NOTES

1. R. J. Zomer *et al.*, *Sci. Rep.* **6**, 29987 (2016).
2. R. J. Zomer, D. A. Bossio, R. Sommer, L. V. Verchot, *Sci. Rep.* **7**, 15554 (2017).
3. J. Aertsens, L. De Nocker, A. Gobin, *Land Use Pol.* **31**, 584 (2013).
4. A. Lavell *et al.*, in *Managing the Risks of Extreme Events and Disasters to Advance Climate Change Adaptation: Special Report of the Intergovernmental Panel on Climate Change* (Cambridge University Press, 2012); pp. 25–64.
5. R. Maclean, “Cyclone Idai: More than 1000 feared dead in Mozambique” (2019); www.theguardian.com/world/2019/mar/18/cyclone-idai-death-toll-climbs-over-120-in-mozambique-and-zimbabwe.
6. S. K. Lowder *et al.*, *World Dev.* **78**, 16 (2016).

COMPETING INTERESTS

A.G. is supported by the International Climate Initiative (IKI) of the Federal Ministry for the Environment, Nature Conservation and Nuclear Safety (BMU).

10.1126/science.aba6211

Response

Our Review deliberately focuses on climate change adaptation and mitigation in natural and semi-natural ecosystems. As Harrison and Gassner point out,

agricultural land is also critical for adaptation and mitigation, and we welcome the opportunity to broaden the discussion. A variety of mitigation measures can be applied in cropped systems (1–3), ranging from changing management practices within present systems, including applying fertilizer more efficiently and increasing soil carbon, to changing whole agricultural systems, such as adopting agroforestry. We agree that agricultural, nature-based solutions can deliver a range of benefits for adaptation and biodiversity as well as mitigation, food production, and livelihoods.

One of our Review’s key messages is the importance of taking an “integrated view of mitigation, adaptation, biodiversity, and the needs of people.” We suggest a list of questions to determine the suitability of potential nature-based solutions based on a range of criteria in which the needs of people are integral alongside those of biodiversity. These questions are as valid for agro-ecosystems as they are for more natural systems. However, the balance of priorities will be different in determining what constitutes success, with food supply and livelihoods critical in agricultural systems.

A key challenge is to identify the most appropriate strategies for land use and management in different places. There is evidence that increasing agricultural productivity is achievable in ways that support biodiversity as well as people (4). There is also evidence that increasing yields in some areas while protecting and restoring ecosystems elsewhere provides multiple benefits, including for climate change mitigation (5). There is a clear case for the

protection of existing natural ecosystems, but whether it is better to restore cropland to semi-natural ecosystems or support ongoing agriculture in any particular place will depend on a wide range of criteria. Decisions of this sort need to be made within the broader context of sustainable development and at a range of levels to account for both local needs and national targets for greenhouse gas emissions reductions. A clear focus on what constitutes success in its fullest sense and how to measure it is essential to keep all decision-making grounded and practical.

Michael D. Morecroft^{1,2*}, Simon Duffield¹, Mike Harley³, James W. Pearce Higgins^{4,5}, Nicola Stevens^{6,7}, Olly Watts⁸, Jeanette Whitaker⁹

¹Natural England, York, YO1 7PX, UK.

²Environmental Change Institute, University of Oxford, OX1 3QY, UK.

³Climate Resilience, Stamford, PE9 4AU, UK.

⁴British Trust for Ornithology, Thetford, Norfolk, IP24 2PU, UK.

⁵Conservation Science Group, Department of Zoology, Cambridge University, Cambridge, CB2 3QZ, UK.

⁶Department of Zoology and Botany, Stellenbosch University, Stellenbosch, 7600, South Africa.

⁷Present address: Environmental Change Institute, University of Oxford, OX1 3QY, UK.

⁸Royal Society for the Protection of Birds, Sandy, SG19 2DL, UK.

⁹UK Centre for Ecology & Hydrology, Lancaster Environment Centre, Lancaster, LA1 4AP, UK.

*Corresponding author.

Email: mike.morecroft@naturalengland.org.uk

REFERENCES AND NOTES

1. B. W. Griscom *et al.*, *Proc. Natl. Acad. Sci. U.S.A.* **114**, 11645 (2017).
2. K. Paustian *et al.*, *Nature* **532**, 49 (2016).
3. P. Smith, J. Price, A. Molotoks, R. Warren, Y. Malhi, *Philos. Trans. R. Soc. A Math. Phys. Eng. Sci.* **376**, 20160456 (2018).
4. J. Pretty *et al.*, *Nat. Sustain.* **1**, 441 (2018).
5. A. Balmford *et al.*, *Nat. Sustain.* **1**, 477 (2018).

10.1126/science.aba7577

Cancel cuts to Graduate Research Fellowships

The National Science Foundation plans to decrease its Graduate Research Fellowship Program (GRFP) awards, which support graduate students pursuing degrees in science, technology, engineering, and mathematics (STEM) and STEM education fields, to only 1600 in upcoming competitions (1). No supporting evidence or rationale has been provided. Such cuts would likely have a disproportionate effect on women and underrepresented minorities. After the doubling of fellowships to 2000 awards in 2010, women and underrepresented minorities made substantial and sustainable gains that have grown over time (2). In the 2018 GRFP competition, nearly 58% of awardees were women, and 23% (461 individuals) identified as underrepresented minorities (3). A 20%

cut in new fellowships risks narrowing the participation of these groups in the U.S. scientific workforce, especially in STEM leadership roles.

Cutting the number of GRFP awards poses a threat to U.S. leadership in science and innovation. It signals to the “best and brightest” (4) U.S. citizens that their talents are valued less in the STEM workforce than in lucrative fields such as management or finance. Although the U.S. population grew by 5.8% between 2010 and 2018 (5), the number of awards has remained at 2000 for the past 10 years. This would be defensible from a policy standpoint if employment in science and engineering sectors were flat; however, such employment is steadily rising (6). The United States should be increasing federal fellowships for its citizens, not decreasing them.

We urge NSF and elected leaders to cancel the cuts. GRFP recruits a diverse pool of talented early-career STEM students from a broad range of scientific fields, educational institutions, geographic regions, and economic circumstances. However, sustaining this public good demands publicly available data and a thoughtful approach to the mix of federal funding mechanisms used to support graduate students. We call for experts in graduate education and STEM workforce development to convene and consider evidence-based policies for nurturing student-centered research and innovation in the United States (7).

Gisèle Muller-Parker^{1*}, Susan Brennan², Erick C. Jones³

¹Retired from National Science Foundation, Lewes, DE 19958, USA.

²Department of Psychology, Stony Brook University, Stony Brook, NY 11794–2500, USA.

³College of Engineering, University of Texas Arlington, Arlington, TX 76017, USA.

*Corresponding author. Email: gmullerp@gmail.com

REFERENCES AND NOTES

1. NSF, Graduate Research Fellowship Program Solicitation: NSF 19-590 (2019); www.nsf.gov/pubs/2019/nsf19590/nsf19590.pdf.
2. G. Muller-Parker, S. E. Brennan, E. C. Jones, *GradEdge: Insights Grad Educ Res.* **9**, 4 (2020).
3. NSF, “NSF announces Graduate Research Fellowships for 2018,” News Release 18-022 (2018); www.nsf.gov/news/news_summ.jsp?cntn_id=245024.
4. R. B. Freeman, “Investing in the best and brightest: Increased fellowship support for American scientists and engineers” (Brookings Discussion Paper 2006-09, 2006).
5. U.S. Census Bureau, “Monthly population estimates for the United States: April 1, 2010 to December 1, 2020 (NA-EST2019-01)” (2019); www.census.gov/data/tables/time-series/demo/popest/2010s-national-total.html#par_textimage_2011805803.
6. National Science Board Science and Engineering Indicators, U.S. S&E workforce: Definition, size, and growth (2018).
7. National Academies of Sciences, Engineering, and Medicine, *Graduate STEM Education for the 21st Century* (The National Academies Press, Washington, DC, 2018).

10.1126/science.aba6660

AAAS Travels

Members and friends of AAAS are invited to join AAAS Travels on fascinating trips to all 7 continents!

The Sikkim & Darjeeling HIMALAYAS



May 16-30, 2020

Join us to explore the amazing landscapes and flora of Sikkim & the Darjeeling Himalayas! Visit botanic gardens, orchid gardens, the Yumthang “Valley of the Flowers”, the Shingba Rhododendron Sanctuary and much more. Also view Kanchenjunga, the 3rd highest peak in the world.

\$4,295 pp twin share + air

ARMENIA & the REPUBLIC of GEORGIA



May 26-June 11, 2020

Nestled in the Caucasus Mountains east of the Black Sea are the charming and fascinating countries of Armenia and Georgia. Discover ancient monasteries, unique plants, spectacular vistas of biblical Mount Ararat, plus parks and cities in Georgia which edges the Black Sea.

\$4,995 pp twin Share + air

For a detailed brochure, please call (800) 252-4910

All prices are per person twin share + air



BETCHART EXPEDITIONS Inc.

17050 Montebello Rd

Cupertino, California 95014

Email: AAASInfo@betchartexpeditions.com

www.betchartexpeditions.com



AAAS Kavli Awards: 75 years of top science journalism

Evolution of the program accurately reflected changes in reporting and the world

By **Michaela Jarvis**

From awarding its first competitive prize in a field of just 137 U.S. newspaper entries, to this year's 75th-anniversary contest that may draw as many as a thousand entries from around the world, the program now known as the AAAS Kavli Science Journalism Awards has kept pace with a dramatically changing media landscape while continuing to promote superior science journalism.

"I don't know of another journalism award that has played the same role in setting and maintaining an international standard of excellence," said Robert Lee Hotz of *The Wall Street Journal*, who is a three-time winner and a member of the Managing Committee for the awards.

Today, in a political environment that has been damaging to journalism, the awards perform a crucial function, said Laura Helmuth, health, science, and environment editor for *The Washington Post*. "The most important value they uphold is truth—of real information in a world of misinformation, of verifiable facts in an age of people falsely calling truth 'fake news,'" said Helmuth, who has been a long-time judge for the contest. "Science and journalism are both based

in honesty and transparency," she said, "and using journalism to interrogate science is a powerful combination that lets readers know how the world works."

Established in 1945, the awards were the idea of Robert D. Potter, who was the president of the National Association of Science Writers. Through an associate, Potter secured the sponsorship of the Westinghouse Educational Foundation and helped arrange for the American Association for the Advancement of Science to independently administer the awards. In its inaugural year, the program presented citations to 13 prominent reporters who had been pioneers in U.S. science journalism. The first competitive award, selected among 137 entries in 1946, went to James G. Chesnutt of *The San Francisco Call-Bulletin*.

Special activities to celebrate the 75th anniversary of the awards will be held 14 to 15 February at the AAAS Annual Meeting, which is taking place this year at the Washington State Convention Center in Seattle. The Kavli Foundation luncheon and media roundtable at noon on 14 February, showcasing the work of the current award winners and the anniversary of the awards, will be hosted by Hotz. That evening, at 7 to 10 p.m., the AAAS Kavli Science Journalism Awards reception and ceremony will be held at the Pacific Science Center and will be hosted by Alan Boyle of GeekWire. A wine-and-cheese reception in honor of the 75th anniversary—open to general attendees of the Annual Meeting as well as its Newsroom registrants—will be held the next day, 15 February, at 4 to 5 p.m.

Launched at the dawn of the atomic age, a key goal of the awards program in its early years was to encourage closer cooperation between reporters and scientists in explaining dramatic new advances in science and engineering to the public.

The first judges for the contest were not only journalists but also politicians and academics, and the awards program actually had



Chris Schmidt (left) and Julia Cort of NOVA, Joe Palca of NPR, Laura Helmuth of *The Washington Post*, and Robert Lee Hotz of *The Wall Street Journal*.

PHOTOS (TOP TO BOTTOM, THEN COUNTERCLOCKWISE): STEVE RINGMAN/THE SEATTLE TIMES/TAKEN UNDER NOAA PERMIT 21348; COURTESY NOVA/WGBH; COURTESY NOVA/WGBH; COURTESY OF JOE PALCA; AAAS; AAAS

A resident orca, subject of a Gold Award-winning series by *The Seattle Times*, breaches in Puget Sound.

a goal—in addition to promoting broader public understanding of science—of fostering the relationships of science writers and their sources. James B. Conant, president of AAAS in 1946 (and also president of Har-

vard University) noted at the time that “the purpose of the [George Westinghouse Science Writing] awards is to assist in developing closer cooperation between news writers and scientists.”

“The ties between the reporters and those they covered were pretty chummy in the early days, when the awards were very much aimed at describing science as an emerging force in American life,” said Earl Lane, executive director of the awards. “Over the years, the approach became more probing,” he said. “The judging panels are now composed exclusively of science journalists, and the winning entries often describe not only the underlying science but also its impact on society.”

Among the early judges were some big names: critic H.L. Mencken (1947–1948), *Saturday Review* editor Norman Cousins (1949–1951) and *Esquire* Editor Harold Hayes (1963). Dixy Lee Ray was recruited to judge in 1972, one year before she was appointed chair of the United States Atomic Energy Commission by President Nixon, but she was a no-show. Astronomer Carl Sagan was also a no-show, after being recruited to judge in 1976.

By that year, the program had expanded to include not only newspapers but also magazines, which had been added early on, in 1947. Radio and television debuted in 1981. In 2001, the dramatic shift to a digital format that was starting to overtake journalism was reflected in a new online award category.

“The platforms for disseminating good science journalism have changed over the years, and the awards have adapted to those changes,” said NPR’s Joe Palca, who has said of the award he won in 1997, “It was the award you most wanted to win if you considered yourself a serious science journalist.”

Many of the best-known names in science journalism have won the awards—among them Natalie Angier, Deborah Blum, Ira Flatow, Atul Gawande, and Elizabeth Kolbert. Some of the winners were just starting careers and went on to further success in science journalism after having been honored with the AAAS Kavli award.

“I didn’t think I was doing science writing,” said Hotz, referring in a 2018 interview to the work that won him his first award in 1977. “I was just doing the daily news. [The award] was a bolt from the blue, and it was a moment of discovery.”

In 2009, the Kavli Foundation granted the awards program a \$2 million endowment, assuring its long-term future, and the awards were renamed the AAAS Kavli Science Journalism Awards. The foundation doubled its endowment in 2015, allowing the program to go global and accept entries from journalists around the world. It also expanded the program to include two awards in each of the contest’s eight categories. The current categories are Large Newspaper, Small Newspaper, Magazine, Video Spot News/Feature Reporting (20 min or less), Video In-Depth Reporting (more than 20 min), Audio, Online, and Children’s Science News.

In the first year of the international contest, 1158 entries arrived from 44 countries, which was almost twice as many entries as the year before. The program handled the deluge by recruiting senior science journalists who had been AAAS Kavli award judges or members of the Managing Committee to help screen the many entries before passing them on to the Washington-area scientists who volunteer to screen the submissions for scientific accuracy. The program also recruited international judges from *The Guardian*, *Nature*, and the German news agency Deutsche Presse-Agentur to join the judging panels.

“At that time,” said Hotz, “the award went from a signature national award to one that celebrates the best science journalism of the entire globe. It was transformative, and really opened up the influence of the award.”

2019 AAAS Kavli Science Journalism Award winners

Strong local reporting on the status of Puget Sound’s killer whales, the degradation of soils in a region of France, air quality in Utah, and the impact of an Idaho nuclear research facility are among the winning entries for the 2019 AAAS Kavli Science Journalism Awards.

The judges also honored a NOVA program on “The Next Pompeii,” BBC audio reports on the development of technology that enabled astronauts to land on the moon, and a trio of stories by Sharon Begley for *STAT* on how fierce loyalty to the prevailing hypothesis on the origin of Alzheimer’s disease likely has hampered progress toward a cure. The winners:

LARGE NEWSPAPER

Gold Award

Lynda Mapes, Steve Ringman, Ramon Dompör, Emily Eng, and Lauren Frohne, *The Seattle Times*

Silver Award

Nathaniel Herzberg, *Le Monde (Paris)*

SMALL NEWSPAPER

Gold Award

Erica Evans, *Deseret News (Salt Lake City)*

Silver Award

Amy Joi O’Donoghue, *Deseret News (Salt Lake City)*

MAGAZINE

Gold Award

Maryn McKenna, *The New Republic*

Silver Award

Tom Whipple, *The Times Magazine (London)*

VIDEO

Spot News/Feature Reporting:

Gold Award

Mairead Dundas and Marina Bertsch, *France 24*

Silver Award

Agnes Walton, Lee Doyle, Arielle Duhaime-Ross, and Ruben Davis, *VICE News Tonight*

In-Depth Reporting:

Gold Award

Duncan Bulling, Caterina Turroni, Richard Bradley, and Chris Schmidt,

NOVA production by Lion Television for WGBH in association with ARTE France

Silver Award

Henry Fraser, Carlo Massarella, and Dan Kendall, *Windfall Films for Smithsonian Networks and the BBC, in association with NHK, Canal +, and Welt24*

ONLINE

Gold Award

Sharon Begley, *STAT*

Silver Award

Nicholas Kusnetz, *InsideClimate News*

AUDIO

Gold Award

Rory Galloway and Geoff Marsh, *BBC Radio 4*

Silver Award

Andrew Luck-Baker, Kevin Fong, Rami Tzabar, and Chris Browning, *BBC World Service*

CHILDREN’S SCIENCE NEWS

Gold Award

Lindsay Patterson, Marshall Escamilla, and Sara Robberson Lentz, *Tumble Science Podcast for Kids*

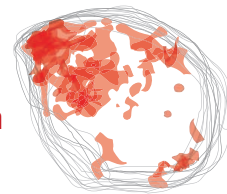
Silver Award

Sharon Oosthoek, *Science News for Students*

For more information on the winning entries, go to sjawards.aaas.org.

There have been multiple winners recently from the United Kingdom, Canada, Germany, and France. There also have been winners from China, Australia, South Africa, Sweden, Denmark, the Netherlands, Switzerland, and Ireland. There were 1116 entries from 47 countries for the 2019 contest.

Through it all, the AAAS Kavli awards continue to promote the value of both science reporting and science itself. As Julia Cort and Chris Schmidt, co-executive producers of *NOVA* for PBS, put it: “In an age when reporting and expertise are the target of ideological attack, the recognition offered by the awards highlights the importance of evidence-based storytelling. The awards help to promote scientific inquiry as a critically important activity in our society.”



IN SCIENCE JOURNALS

Edited by Michael Funk

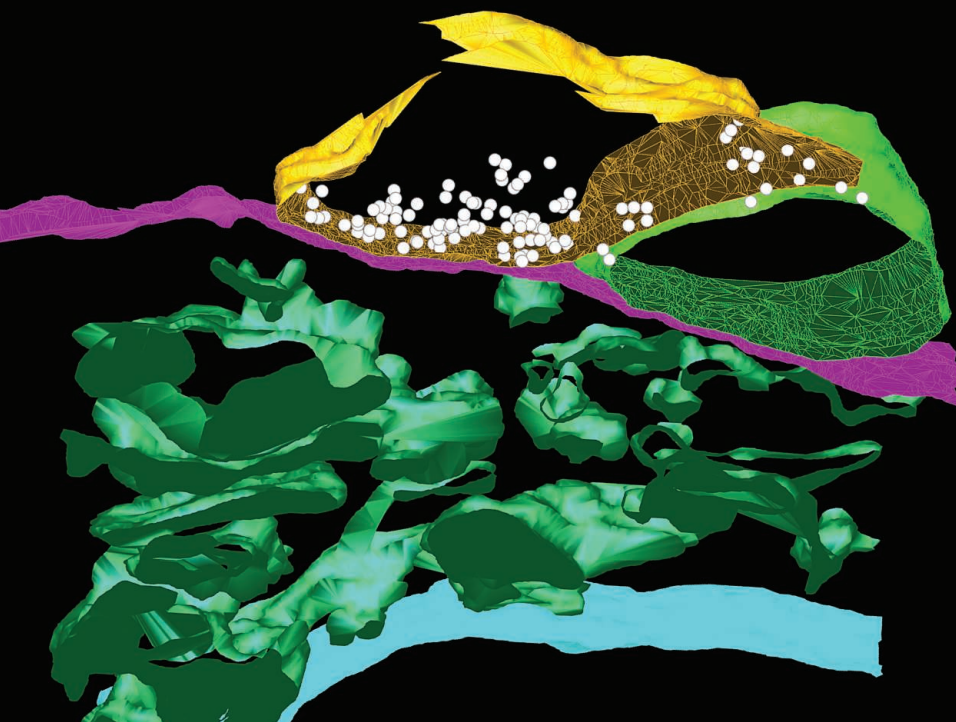
CELLULAR NEUROSCIENCE

Microglia take control

Changes in the activity of microglia, the primary immune cells of the central nervous system, are linked with major human diseases, including stroke, epilepsy, psychiatric disorders, and neurodegeneration. Cserép *et al.* identified a specialized morphofunctional communication site between microglial processes and neuronal cell bodies in the mouse and the human brain (see the Perspective by Nimmerjahn). These junctions are formed at specific areas of the neuronal somatic membranes and possess a distinctive nanoarchitecture and specialized molecular composition linked to mitochondrial signaling. The junctions appear to provide a major site for microglia-neuron communication and may help to mediate the neuroprotective effects of microglia after acute brain injury. —SMH

Science, this issue p. 528; see also p. 510

Three-dimensional electron tomography reconstruction of a microglial cell–neuron junction



GRAVITATION

Pulsar timing detects frame dragging

Frame dragging is a predicted phenomenon in general relativity, whereby a rotating mass drags the surrounding spacetime around with it. Venkatraman Krishnan *et al.* analyzed timing observations of PSR J1141–6545, a young pulsar in a binary orbit with a white dwarf. Modeling the arrival times of the radio pulses showed a long-term drift in the orbital parameters. After considering possible contributions to this drift, they concluded that it is dominated by frame dragging (the Lense-Thirring effect) of the rapidly spinning white dwarf. These observations verify a prediction of general relativity

and provide constraints on the evolutionary history of the binary system. —KTS

Science, this issue p. 577

HUMAN GENETICS

African schizophrenia genetic variants

The genetics of schizophrenia have predominately been studied in populations of European and Asian descent. However, studies in Africans, who host the greatest degree of human genetic diversity, have lagged. Examining the exomes of more than 1800 Xhosa individuals from South Africa, about half of which have been diagnosed with schizophrenia, Gulsuner *et al.* identified both rare and common genetic variants associated with

the disease. They found that the genetic architecture of schizophrenia in Africans generally reflects that of Europeans but that the greater genetic variation in Africa provides more power to detect relationships of genes to phenotypes. —LMZ

Science, this issue p. 569

CANCER

Taking preventive measures

Recent technological advances have made it possible to detect, in healthy individuals, premalignant blood cells that are likely to progress to hematologic cancer. These advances in early detection have fueled interest in “cancer interception,” the idea that drugs designed to treat

advanced cancer might also be useful for cancer prevention. Uckelmann *et al.* now provide support for this concept in a study of mice genetically predisposed to develop acute myeloid leukemia. Early administration of an epigenetic therapy that had previously been shown to have anticancer activity in advanced leukemia models was able to eliminate preleukemia cells and extend survival of the mice. —PAK

Science, this issue p. 586

BIOCHEMISTRY

When the most popular are not the best

Understanding the specificity and sensitivity of antibodies is important for interpreting

experimental data generated with these reagents. Frohner *et al.* found that monoclonal antibodies raised against the catalytic subunit of protein phosphatase 2A, one of which is used in a commercial assay kit, were sensitive to posttranslational modifications and cross-reacted with related phosphatases (see the Focus by Janes). Schüchner *et al.* found that the recognition of Myc-tagged proteins by a widely used Myc-specific monoclonal antibody varied depending on sequences adjacent to the tag. These studies highlight the need for careful validation of antibody-based assays. —AMV

Sci. Signal. **13**, eaax6490, eaaz8130, eaax9730 (2020).

SOCIAL SCIENCE

Resilient misinformation in a crisis

Countering the public's belief in false or unsupported claims may require more than corrective, factual information. Carey *et al.* analyzed results from a nationally representative survey in Brazil and show that corrective information campaigns did not reduce commonly held conspiracy theories relating to Zika and failed to effect preventive behavior for yellow fever. Efforts to counter misperceptions about the Zika virus also had the unintended consequence of reducing the accuracy of other beliefs about the disease. This work demonstrates the resilience of public health misperceptions and the need for tested strategies to combat such erroneous information. —AC

Sci. Adv. **10**.1126/sciadv.aaw7449 (2020).

THERMAL CONDUCTIVITY

A cool way to use isotopes

Thermal management of electronics requires materials that can efficiently remove heat. Several promising materials have been found recently, but diamond remains the bulk material with the highest thermal conductivity. Chen *et al.* found that isotopically pure cubic

boron nitride has an ultrahigh thermal conductivity, 75% that of diamond. Using only boron-11 or boron-10 allows the crystal vibrations that carry heat to move more efficiently through the material. This property could be exploited for better regulating the temperature of high-power devices. —BG

Science, this issue p. 555

ORGANIC CHEMISTRY

Convergent coupling

Metal-catalyzed coupling of two flat aromatic rings is one of the most versatile and widely applied chemical reactions. Efforts to extend this protocol to alkyl-alkyl coupling are complicated by the prospect of forming two different three-dimensional configurations at each carbon center, corresponding to four possible products. Huo *et al.* now report that a chiral nickel catalyst can convergently link two mirror-image pairs of alkyl reactants into just one product (see the Perspective by Xu and Watson). The specific reaction couples propargylic halides to zinc-activated aliphatic amides. —JSY

Science, this issue p. 559; see also p. 509

CRYSTALLOGRAPHY

Speedy crystallography

Electron backscatter diffraction is one standard technique for determining crystal structure, typically of materials or geological samples. However, this method requires structural guesses and user input that are often time consuming or incorrect. Kaufmann *et al.* developed a general methodology using a convoluted neural network that automatically determines the crystal structure quickly and with high accuracy. After the network is exposed to a training set, it can identify the crystal structure without any additional input most of the time, providing a method for eliminating some of the guesswork from crystal structure determination. —BG

Science, this issue p. 564

IN OTHER JOURNALS

Edited by **Caroline Ash**
and **Jesse Smith**



PUBLIC HEALTH

Causal evidence for effects of driving on health

Driving is associated with reduced physical activity and weight gain, but identifying a causal link is difficult because people typically choose to drive or not. Anderson *et al.* tracked the health of citizens in Beijing, China, who entered into a randomized lottery for a permit to be eligible to own a car. By taking advantage of this natural experiment, the authors found that lottery winners used less public transit, walked less, cycled less, and, among older adults, gained weight. These results have implications for the health consequences of increased automobile use, particularly in cities. —TSR *BMJ* **367**, 16491 (2019).

Older drivers in Beijing, China, gain more weight than their nondriving counterparts.

CANCER IMMUNOLOGY

MAIT cells and tumor immunity

Mucosal-associated invariant T (MAIT) cells are immune cells that recognize host microbial metabolites presented by major histocompatibility complex

class I-related protein 1 (MR1). During bacterial infection, activation of MAIT cells leads to the elimination of the infected cells. However, the role of MAIT cells in other disease states is less clear. For example, MAIT cells have been reported to be present in human tumors, but the



FAT METABOLISM

Signals from lipid hydrolysis

An exploration of how lipolysis is coupled to mitochondrial changes that increase oxidative capacity may reveal how a Mediterranean diet is beneficial. Najt *et al.* found that monounsaturated fatty acids (MUFAs) released by lipolysis bound to the protein perilipin 5, which carried them to the nucleus. MUFAs also bound to the deacetylase sirtuin 1 (SIRT1), which is implicated in the health span—improving effects of caloric restriction. MUFA binding increased SIRT1 activity toward certain substrates. Foods like nuts, avocados, and olive oil all provide MUFAs in the diet, and these effects could in part underlie their beneficial properties. —LBR

Mol. Cell 10.1016/j.molcel.2019.12.003 (2020).

Eating a selection of foods that are high in monounsaturated fatty acids is beneficial for health.

physiological relevance has not been explored. Yan *et al.* studied two different experimental mouse tumor models and found that MAIT cells promoted lung metastasis by quashing natural killer cell activity. The researchers could block this effect and reduce metastasis by using inhibitory antibodies against MR1. Targeting the MAIT cell–MR1 axis may represent an emerging strategy for cancer immunotherapy. —PNK

Cancer Discov. 10, 124 (2020).

CELL BIOLOGY

The cellular architecture of ERAD

Endoplasmic reticulum (ER)–associated degradation (ERAD) is an evolutionarily conserved quality control mechanism whereby misfolded proteins are removed from the ER and degraded in the cytosol by the ubiquitin-proteasome system. Many ERAD-mediating proteins have been identified, but their spatial organization within the cell is less well established. Albert *et al.* used in situ cryo-electron tomography to image the native molecular landscape within *Chlamydomonas* cells. They found that ERAD proteins concentrated within

~200-nanometer cytosolic foci that contacted the ER membrane away from the ER-Golgi interface. The ribosome-excluding ERAD microcompartments consisted of a core of clustered proteasomes surrounded by Cdc48. Within these clusters, active proteasomes appeared to engage directly with substrates at the ER membrane, a function thought to be performed by Cdc48. In live-cell imaging experiments, the proteasome clusters were seen to form dynamically, possibly by liquid-liquid phase separation. This dynamic, but well-defined, architecture of ERAD machinery likely contributes to efficient protein quality control. —SMH

Proc. Natl. Acad. Sci. U.S.A. 117, 1069 (2020).

NEUROSCIENCE

Fast and slow recycling of synaptic vesicles

The function of microtubules and filamentous actin in mature synapses is not fully understood. Using confocal and stimulated emission depletion microscopy on a giant auditory synapse of the rat nervous system, termed the calyx of Held, Babu *et al.* found that microtubules extended into

terminal swellings and were partially colocalized with synaptic vesicles. Depolymerization of microtubules in calyceal terminals prolonged the recovery of excitatory postsynaptic currents from short-term depression, whereas fast recovery from short-term depression was prolonged by depolymerization of filamentous actin. These results reveal distinct contributions of filamentous actin and microtubules to synaptic neurotransmission and indicate that these cytoskeletal elements independently contribute to different aspects of the recycling of synaptic vesicles. —PRS

J. Neurosci. 40, 131 (2020).

QUANTUM GASES

Probing a quantum emulsion

Ultracold atomic gases with strongly repulsive interactions can be a useful model system for studying the emergence of itinerant ferromagnetism. However, the same atoms that can order magnetically are also prone to pairing into loosely bound molecules. If an atomic system is suddenly placed in a strongly interacting regime, both processes occur and an inhomogeneous,

phase-separated state consisting of unpaired and paired atoms can form. Scazza *et al.* studied this state with a variety of probes. The data were consistent with the formation of a quantum emulsion consisting of polarized domains coexisting with paired atoms. The state was stabilized by low temperatures and strong interactions. —JS

Phys. Rev. A 101, 013603 (2020).

MEMBRANE PROTEINS

Simulating deformation

Biological membranes are jam-packed with proteins and enzymes that exert forces, both static and dynamic, on their adjacent lipids and can cause local and global changes in membrane curvature. Zhou *et al.* used large-scale molecular dynamics simulations to understand how the membranes around a small-molecule transporter deform as the protein undergoes motions coupled to transport. By comparing different states of the transporter, the authors found that the lipids move with the transport domains, causing local deformations of ~10 angstroms in an area of ~1000 square angstroms at a cost of 6 to 7 kilocalories per mole. —MAF

eLife 8, e50576 (2019).

NEUROSCIENCE

A learning mechanism in the striatum

An intriguing characteristic of the striatum is the random spatial distribution and high degree of intermingling between expression of dopamine receptor types 1 (D1) and 2 (D2) within striatal projection neurons (SPNs). The resulting highly entropic mosaic extends through a homogeneous space and is mostly devoid of histological boundaries. The rules established locally by D1- and D2-expressing SPNs (D1-SPNs and D2-SPNs) are thus likely critical in defining how functional territories develop throughout the striatum. Matamalas *et al.* found that activated D2-SPNs access and modify developing behavioral programs encoded by regionally defined ensembles of transcriptionally active D1-SPNs. This process is slow because it depends on the molecular integration of additive neuromodulatory signals. However, with time, it creates the regional functional boundaries that are necessary to identify and shape specific learning in the striatum. —PRS

Science, this issue p. 549

SYSTEMS BIOLOGY

Single-cell protein profiling

Single-cell DNA and RNA sequencing can describe numerous aspects of cell state, but such techniques cannot assess the functional effectors of cells: proteins. In a Perspective, Slavov discusses the advances in single-cell mass spectrometry techniques that allow protein profiling, including characterization of protein modifications and potentially complex composition and subcellular localization. Although there are limitations to this emerging technology, single-cell proteomics may add to the characterization of cellular components and provide functional information about signaling

networks in homeostasis and disease. —GKA

Science, this issue p. 512

CANCER IMMUNOTHERAPY

Presurgical immune checkpoint blockade

Checkpoint blockade immunotherapy using antibodies that inhibit the programmed cell death 1 (PD-1) or cytotoxic T lymphocyte-associated protein 4 (CTLA-4) pathways has resulted in unprecedented clinical outcomes for certain cancers such as melanoma. Topalian *et al.* review advances in neoadjuvant (presurgical) immunotherapy as an important next step for enhancing the response of early-stage tumors to immune checkpoint blockade. They highlight the mechanistic rationale for neoadjuvant immunotherapy and recent neoadjuvant clinical trials based on anti-PD-1 or anti-PD-1 ligand 1 (anti-PD-L1) therapy. Pathological assessment criteria that may provide early on-treatment biomarkers to predict patient response are also discussed. —PNK

Science, this issue p. 525

NEUROSCIENCE

Monosomes translate proteins in neurons

Like all other cells, neurons use different proteins to process information and respond to stimuli. To meet the huge demands for new proteins in their large and complex cell volume, neurons have moved the protein templates—messenger RNAs (mRNAs)—and the protein synthesis machines—ribosomes—out to synapses to make proteins locally. During protein synthesis, multiple ribosomes can form a structure known as a polysome, which produces multiple protein copies from a single mRNA. Working in rodent preparations, Biever *et al.* found that solitary, mRNA-associated ribosomes, or

monosomes, are a substantial source of proteins in neuronal processes. Many synaptic proteins are made on single ribosomes, which may solve the problem of limited space in tiny synaptic compartments. —SMH

Science, this issue p. 526

CELL BIOLOGY

ER regulates stress granule fission

A hallmark of eukaryotic cells is the ability to compartmentalize essential reactions into membrane-bound and membraneless organelles. Membrane-bound organelles form networks through transport vesicles and interorganellar contact sites. The endoplasmic reticulum (ER) has emerged as a network hub and forms physical connections with nearly every membrane-bound organelle. Lee *et al.* now identify another class of ER contact sites that appear to help regulate the biogenesis and fission of membraneless ribonucleoprotein (RNP) granules (see the Perspective by Kornmann and Weis). Live-cell fluorescence microscopy of human cells revealed that ER tubule dynamics are spatially and temporally coupled to the fission site of two types of RNP granules, processing bodies (P-bodies) and stress granules. —SMH

Science, this issue p. 527;
see also p. 507

CATALYSIS

Charging up cobalt for hydroformylation

Hydroformylation reactions are applied at massive scale in the chemical industry to transform olefins into aldehydes. The original catalysts were neutral cobalt complexes. Hood *et al.* now report that positively charged cobalt complexes, stabilized by chelating phosphine ligands, show higher activities at lower pressures

than their neutral counterparts, approaching the activities of precious rhodium catalysts. These charged catalysts are particularly adept at accelerating the reactions of internal olefins while avoiding decomposition. Spectroscopic studies implicate the involvement of 19-electron intermediates in the catalytic cycle. —JSY

Science, this issue p. 542

NANOMATERIALS

Growing coaxial nanotubes

Heterostructures of highly crystalline two-dimensional materials such as graphene, hexagonal boron nitride (hBN), and molybdenum disulfide (MoS₂) are now routinely assembled from films or grown as layers. Xiang *et al.* report the growth of one-dimensional analogs of these heterostructures on single-walled carbon nanotubes (SWCNTs) through a chemical vapor deposition (see the Perspective by Gogotsi and Yakobson). Single-crystalline monolayers or multilayers of hBN or MoS₂ were grown that maintained the electrical conductivity of the SWCNT. A monolayer of MoS₂ was grown on a trilayer of hBN that encapsulated a SWCNT. —PDS

Science, this issue p. 537;
see also p. 506

BEE HEALTH

Inducing immune bee genes

Honey bees are prone to parasitism by the *Varroa* mite, which is a vector for several bee pathogens. However, honey bees are also host to the symbiotic gut bacterium *Snodgrassella alvi*. Leonard *et al.* engineered *S. alvi* to produce double-stranded RNA (dsRNA)—a stimulus for insect RNA interference defense responses—from a plasmid containing two inverted promoters

tagged with a fluorescent label (see the Perspective by Paxton). This dsRNA module can be targeted to interfere with specific bee genes as well as crucial viral and mite genes. The authors found that gene expression could be blocked for at least 15 days as the symbionts established in the bees' guts and continuously expressed the dsRNA constructs. *S. alvi* with specifically targeted plasmids not only suppressed infection with deformed wing virus but also effectively reduced *Varroa* mite survival. —CA

Science, this issue p. 573;
see also p. 504

MOLECULAR BIOLOGY

A new layer of transcriptional control

*N*⁶-methyladenosine (m⁶A) is the most abundant messenger RNA modification in almost all eukaryotes. Liu *et al.* now show that m⁶A is also cotranscriptionally added onto various chromosome-associated regulatory RNAs (carRNAs) in mammalian cells. Disruption of m⁶A modification of these RNAs increases their abundance and promotes gene transcription by increasing the chromatin accessibility. Thus, m⁶A serves as a switch to regulate carRNA levels by tuning nearby chromatin state and downstream transcription. —SYM

Science, this issue p. 580

TUBERCULOSIS

Translating TB

Mycobacterium tuberculosis can cause tuberculosis (TB) in humans, although the majority of infected individuals naturally control infection and never show symptoms. To better understand immune control of *M. tuberculosis*, Ahmed *et al.* compared a number of gene expression datasets from infected humans and different animal models. Differences in gene expression between samples linked to either disease control or progression revealed potentially beneficial shared pathways.

Some pathways were tested by examining *M. tuberculosis* infection in gene-deficient inbred mice. These results highlight how focusing on commonalities in TB infection can lead to new insights for treating TB. —LP
Sci. Transl. Med. **12**, eaay0233 (2020).

REVIEW SUMMARY

CANCER IMMUNOTHERAPY

Neoadjuvant checkpoint blockade for cancer immunotherapy

Suzanne L. Topalian*, Janis M. Taube, Drew M. Pardoll

BACKGROUND: Immunotherapies that target the interaction of programmed death 1 (PD-1) with its ligands, PD-L1 and PD-L2, have ushered in the modern oncology era. The PD-1 pathway is a key mediator of local immunosuppression in the tumor microenvironment (TME) but can also modulate T cell priming against tumor antigens in secondary lymphoid tissues. In advanced inoperable cancers refractory to other treatments, drugs that block the PD-1 receptor on lymphocytes or the PD-L1 ligand on tumor and/or immune cells [anti-PD-(L)1] can mediate tumor regression. Although anti-PD-(L)1 treatment is broadly active and is regarded as a “common denominator” for cancer therapy, many tumors demonstrate *de novo* or acquired resistance. Using anti-PD-(L)1 therapies in the neoadjuvant (presurgical) setting, when the tumor is potentially “resectable for cure,” presents a potential solution. There is ample oncologic precedent for this approach with presurgical chemotherapies in breast and lung cancer, as-

sociating pathologic response with improved long-term clinical outcomes. Our Review focuses on the development of neoadjuvant immunotherapies in the era of PD-1 pathway blockade, highlighting particular considerations for immunological mechanisms, clinical development, and pathologic response assessments.

ADVANCES: The immunologic effects of the PD-1 pathway on T cell priming, effector function, and exhaustion suggest distinct mechanisms underlying neoadjuvant immunotherapy versus chemotherapy. Whereas neoadjuvant chemotherapy can “debulk” tumors preoperatively, neoadjuvant immunotherapy aims to enhance systemic immunity against tumor antigens, eliminating micrometastatic tumor deposits that would otherwise be the source of postsurgical relapse. Furthermore, neoadjuvant PD-(L)1 blockade while the primary tumor is in place, as opposed to adjuvant therapy directed only against micrometastatic disease after re-

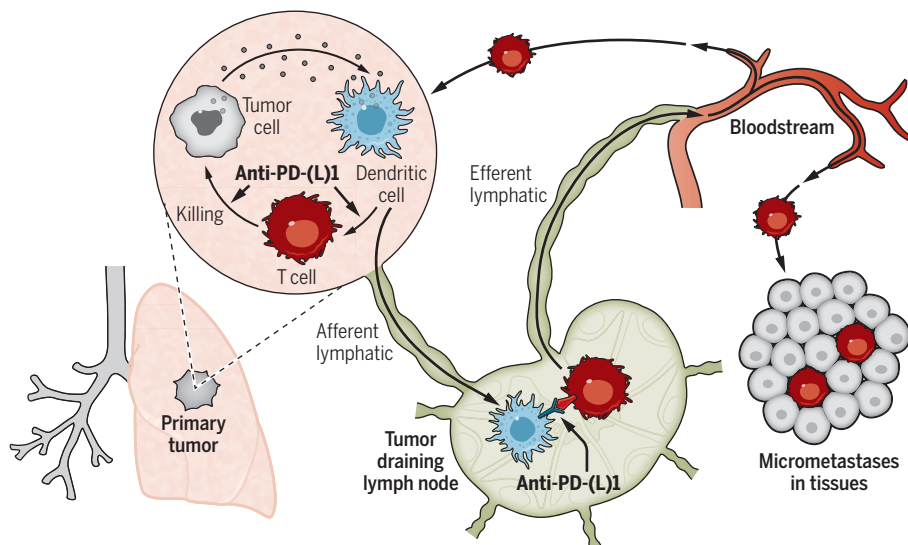
section, leverages higher levels of endogenous tumor antigen present in the primary tumor to enhance T cell priming.

We discuss scientific evidence that supports two different but not mutually exclusive models by which neoadjuvant PD-(L)1 blockade may promote systemic antitumor immunity. First, anti-PD-(L)1 rejuvenates tumor-specific cytotoxic T cells that already reside in the

TME, causing their activation, proliferation, and trafficking to micrometastatic deposits. Second, tumor-draining lymph nodes (TDLN) appear to be the focal point for anti-PD-(L)1 activity, where dendritic cell presentation of tumor antigens to T cells is enhanced; these tumor-specific T cells then enter the bloodstream and migrate to tumor sites. The destruction of micrometastases is central to the notion that neoadjuvant PD-1 blockade should result in enhanced relapse-free and overall survival in operable patients who would otherwise relapse after surgery alone.

There is a strong rationale for evaluating neoadjuvant immunotherapy across tumor types. Presurgical drug administration provides abundant on-therapy tissue for in-depth mechanistic and biomarker studies. We discuss data from recent clinical trials of neoadjuvant anti-PD-(L)1 that show that pathologic tumor regression can outpace radiographic regression and demonstrate the involvement of diverse cellular subsets in this process.

OUTLOOK: At present, more than 100 clinical trials of neoadjuvant anti-PD-(L)1 blockade, as monotherapy or combination therapy, are ongoing or planned. Combining anti-PD-1 with anti-CTLA-4 (cytotoxic T lymphocyte-associated protein 4), or with multidrug chemotherapies for triple-negative breast and lung cancer, has yielded substantial pathologic response rates that are encouraging but require longer follow-up. Next-generation trials may help assign patients to postsurgical observation or intervention depending on the degree of pathologic response, similar to the precedent established with non-immunologic neoadjuvant therapies in breast cancer. Tumors resected after neoadjuvant immunotherapy provide sufficient materials for in-depth scientific interrogations that are expected to further illuminate mechanisms of response and resistance, revealing pathways and molecules that can be cotargeted in new treatment combinations to increase the efficacy of anti-PD-(L)1 therapy. ■



Two potential mechanisms for the enhancement of systemic antitumor T cell immunity after neoadjuvant PD-(L)1 blockade. PD-(L)1 blockade could result in the “in situ” expansion of tumor-specific T cell clones already within the tumor microenvironment. This expansion and activation is largely driven by PD-L1- and PD-L2-expressing dendritic cells in the tumor. Tumor-specific tumor-infiltrating lymphocytes may represent naïve T cells or T cells that have already been “primed” to tumor antigen before PD-1 pathway blockade. In addition, tumor antigen-containing dendritic cells that originate in the tumor pick up tumor antigens and traffic to the tumor-draining lymph nodes, where they present antigens either ineffectively or in a tolerogenic fashion to tumor-specific T cells. PD-(L)1 blockade could act at this point, enhancing productive stimulation of tumor-specific T cells or partially reversing tolerance induction. Activated T cells enter the circulation by way of efferent lymphatics and then egress into tissues.

The list of author affiliations is available in the full article online.

*Corresponding author. Email: stopali1@jhmi.edu
Cite this article as S. L. Topalian *et al.*, *Science* 367, eaax0182 (2020). DOI: 10.1126/science.aax0182

REVIEW

CANCER IMMUNOTHERAPY

Neoadjuvant checkpoint blockade for cancer immunotherapy

Suzanne L. Topalian^{1,2*}, Janis M. Taube^{2,3}, Drew M. Pardoll^{2,4}

Cancer immunotherapies that target the programmed cell death 1 (PD-1):programmed death-ligand 1 (PD-L1) immune checkpoint pathway have ushered in the modern oncology era. Drugs that block PD-1 or PD-L1 facilitate endogenous antitumor immunity and, because of their broad activity spectrum, have been regarded as a common denominator for cancer therapy. Nevertheless, many advanced tumors demonstrate *de novo* or acquired treatment resistance, and ongoing research efforts are focused on improving patient outcomes. Using anti-PD-1 or anti-PD-L1 treatment against earlier stages of cancer is hypothesized to be one such solution. This Review focuses on the development of neoadjuvant (presurgical) immunotherapy in the era of PD-1 pathway blockade, highlighting particular considerations for biological mechanisms, clinical trial design, and pathologic response assessments. Findings from neoadjuvant immunotherapy studies may reveal pathways, mechanisms, and molecules that can be cotargeted in new treatment combinations to increase anti-PD-1 and anti-PD-L1 efficacy.

The advent of immunotherapies that target the interaction of programmed cell death 1 (PD-1) with its major ligands, PD-L1 and PD-L2, has ushered in the modern oncology era (1). The PD-1 pathway is a key mediator of local immunosuppression in the tumor microenvironment (TME). In advanced inoperable cancers, blocking this pathway by inhibiting the PD-1 receptor on immune cells, or the PD-L1 ligand on tumor and/or immune cells, can mediate the rejection of established cancers that are refractory to other therapeutic modalities. To date, three monoclonal antibodies that block PD-1 (pembrolizumab, nivolumab, and cemiplimab) and three that block PD-L1 (atezolizumab, durvalumab, and avelumab) have been approved for use by the U.S. Food and Drug Administration (FDA) across 17 different types of advanced unresectable cancers, in the first- and/or later-line treatment settings. The antitumor effects of these drugs are remarkably consistent, with major response rates for individual tumor types running the gamut between ~15 and ~65%. A higher likelihood of response has been associated with various biological factors, including tumor mutational burden, PD-L1 protein expression, and oncogenic virus integration (2–5). Because of the broad activity spectrum of these drugs, PD-1 pathway blockade is regarded as a “common denominator” for cancer therapy. Nevertheless, in many patients, tumors demonstrate

de novo or acquired resistance to anti-PD-1 or –PD-L1 [anti-PD-(L)1] treatment; furthermore, some cancer types are particularly resistant to this treatment approach (such as pancreatic and prostate cancer). Ongoing clinical and basic scientific research efforts aim to overcome these limitations. Using anti-PD-(L)1 therapies against earlier stages of cancer is hypothesized to be one solution.

The clinical efficacy of anti-PD-(L)1 drugs, coupled with a relatively modest rate of serious side effects (10 to 20% of patients), supports the testing of these drugs against earlier stages of cancer. Recent retrospective analyses showed that in the advanced metastatic treatment setting, patients with lower tumor burdens were more likely to experience long-term survival after anti-PD-1 therapy (6, 7). This suggests that postoperative (adjuvant) anti-PD-1 therapy directed against residual micrometastatic disease in cancer types known to be responsive to anti-PD-1 might prolong relapse-free survival (RFS) and overall survival (OS). In surgically resectable metastatic melanoma (stages IIIA to IV), randomized phase 3 clinical trials demonstrated the efficacy of adjuvant anti-PD-1 therapy, leading the FDA to approve nivolumab and pembrolizumab for this indication (8, 9). Because a proportion of these patients would have been cured by surgery alone, special attention was paid to risk:benefit considerations in clinical trial design. Protocol-eligible patients were at substantial risk for tumor relapse after potentially curative surgery, according to clinicopathologic staging (10).

The neoadjuvant (presurgical) application of immunotherapy occurs at an even earlier stage of cancer development, when cancer is considered potentially “resectable for cure.” There is ample precedent for this approach with the

presurgical administration of chemotherapy in breast cancer and lung cancer, for which pathologic response is associated with improved long-term outcomes (RFS and OS) (11, 12). There is also some experience with neoadjuvant immunotherapies from the era before anti-PD-1 treatment, such as anti-CTLA-4 (cytotoxic T lymphocyte-associated protein 4) treatment for bladder cancer and melanoma (13, 14) and a cancer vaccine combined with chemoradiation for pancreatic cancer (15). This Review will focus on the development of neoadjuvant immunotherapies in the era of PD-1 pathway blockade, highlighting distinct considerations for biological mechanisms, clinical development, and immune-related pathologic response assessment.

Mechanistic rationale for neoadjuvant immunotherapies based on anti-PD-1

The known immunologic effects of the PD-1 pathway on T cell priming, effector functions, and exhaustion suggest a clinical utility for neoadjuvant checkpoint blockade based on mechanisms different than neoadjuvant chemotherapy. Although neoadjuvant chemotherapy is used to “debulk” tumors preoperatively, the hypothesis that launched the current wave of neoadjuvant immunotherapy trials posits that this form of treatment will enhance the systemic T cell response to tumor antigens (Fig. 1). This systemic response is predicted to result in enhanced detection and killing of micrometastatic tumor deposits disseminated beyond the resected tumor, which are ultimately the source of postsurgical relapse. A key corollary to this hypothesis is that neoadjuvant PD-1 blockade while the primary tumor is in place, as opposed to adjuvant therapy directed only against micrometastatic disease after resection, will leverage the higher levels of endogenous tumor antigen present in the primary tumor to enhance T cell priming. Essentially, the higher tumor antigen load present in the body in the context of neoadjuvant therapy relative to postresection adjuvant therapy will hypothetically result in presentation to and thus priming of more tumor-specific T cells circulating systemically.

This hypothesis was directly tested preclinically by Liu, Teng, and colleagues (16) using two spontaneously metastasizing transplantable mouse breast cancer models. When the 4T1.2 and E0771 breast cancer lines are established in mammary fat pad, the primary tumor seeds metastatic cells to distant sites. The metastases are not initially observable but ultimately grow and kill the mice within 30 days after implantation, regardless of whether the primary tumor is removed. Immunotherapy with anti-PD-1, anti-PD-1 plus an agonistic antibody directed against CD137 (a tumor necrosis factor receptor family costimulatory receptor), or regulatory T cell (T_{reg} cell) depletion was given

¹Department of Surgery, Johns Hopkins University School of Medicine, Baltimore, MD 21287, USA. ²Bloomberg-Kimmel Institute for Cancer Immunotherapy, Sidney Kimmel Comprehensive Cancer Center, Baltimore, MD 21287, USA.

³Department of Dermatology, Johns Hopkins University School of Medicine, Baltimore, MD 21287, USA. ⁴Department of Oncology, Johns Hopkins University School of Medicine, Baltimore, MD 21287, USA.

*Corresponding author. Email: stopali1@jhmi.edu

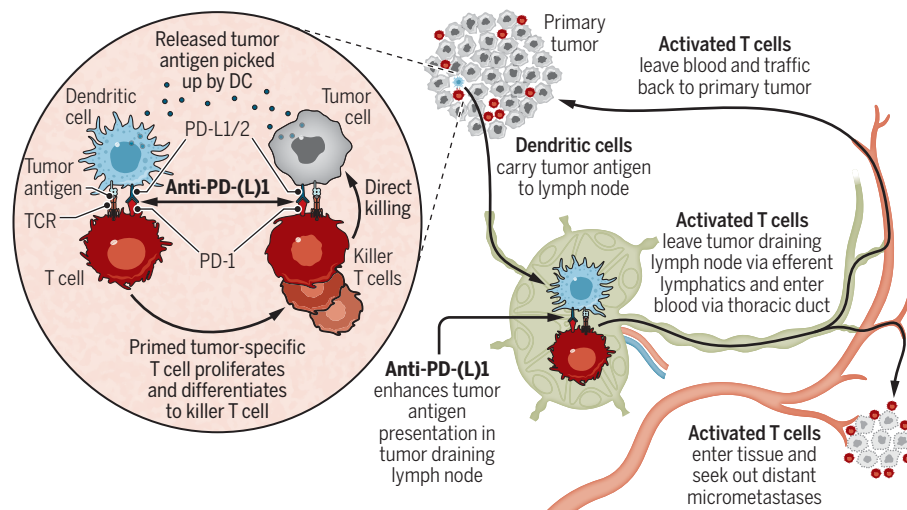


Fig. 1. Two potential mechanisms for the enhancement of systemic antitumor T cell immunity after neoadjuvant PD-1 blockade. PD-1 blockade could result in the “in situ” expansion of tumor-specific T cell clones already within the tumor microenvironment (left). This expansion and activation is largely driven by PD-L1- and PD-L2-expressing dendritic cells in the tumor. Tumor-specific tumor-infiltrating lymphocytes (TILs) may represent naïve T cells or T cells that have already been “primed” to tumor antigen (84) before PD-1 pathway blockade. In addition, tumor antigen-containing DCs originating in the tumor pick up tumor antigens and traffic to the tumor-draining lymph nodes, where they present antigens either ineffectively or in a tolerogenic fashion to tumor-specific T cells. PD-1 blockade could act at this point, enhancing productive stimulation of tumor-specific T cells or partially reversing tolerance induction. Activated T cells enter the circulation by way of efferent lymphatics and then egress into tissues.

either before surgical removal of the primary tumor (neoadjuvant) or afterward (adjuvant). Survival was significantly better with neoadjuvant versus adjuvant immunotherapy, even when treatment commenced at the same time after tumor implantation. Enhanced survival was associated with greater numbers of tumor-specific CD8⁺ T cells in the lungs and blood and enhanced cytokine production in response to an endogenous retroviral antigen expressed by tumor cells, indicating that systemic antitumor immunity had been generated. In follow-up studies, these authors showed that a specific interval between the initiation of neoadjuvant immunotherapy and surgery was critical for the enhanced systemic antitumor effect. Performing surgery too soon after immunotherapy initiation, or waiting too long, diminished the neoadjuvant effect (17). Although it is difficult to temporally compare mouse and human data, these studies highlight the importance of systematically exploring the optimal duration of neoadjuvant immunotherapy in clinical trials.

In comparing the two immune checkpoint pathways targeted by FDA-approved therapeutic antibodies—CTLA-4 and PD-1—CTLA-4 is viewed as a “master” checkpoint. It restricts the initial priming of T cells (naïve or memory) in secondary lymphoid organs by antagonizing the master costimulatory signal, CD28, which shares the same ligands with CTLA-4 (CD80 and CD86) (18–22). CTLA-4 was originally thought to restrain early T cell receptor (TCR)/

CD28-mediated activation of conventional CD4⁺ T cells (T_{conv} cells) (23–25), whereas PD-1 is thought to predominantly restrain CD8⁺ effector T cell (T_{eff} cell) responses in peripheral tissues (26–28). For these reasons, the primary mechanism of action for PD-1 blockade in cancer immunotherapy is generally thought to be unleashing tumor-specific cytotoxic T cells that already reside in the TME before treatment (Fig. 1) (29). Part and parcel of this “unleashed activity” by both CTLA-4 and PD-1 pathway inhibition [collectively termed checkpoint inhibition (CPI)] is the proliferation of tumor-specific T cells in the TME. Nonetheless, true intratumoral proliferation of tumor-specific T cells upon PD-1 blockade has not yet been proven in humans, although it has been surmised from findings of increased clonality of TCRs in melanomas after anti-PD-1 therapy (30). Findings of an enhanced density of T cell infiltrates in resected tumors after neoadjuvant anti-PD-1 therapy are compatible with, but do not prove, intratumoral stimulation of T cells. Because these studies do not address the antigen-specificity of the expanded clones, it is not known whether they have any specificity for tumor antigens or whether they are “bystander cells” with specificities irrelevant to the tumor.

A number of elegant mouse studies clearly demonstrate an intratumoral dendritic cell (DC)-T cell presentation axis (Fig. 1, left). Labeling and intravital imaging studies show

that CD103⁺ DCs with DC2 markers ingest tumor antigen and can present antigenic peptides when isolated and cocultured with antigen-specific T cells (31). A recent study by Garriss, Pettit, and colleagues using intravital imaging provided evidence that DCs could present tumor antigen to T cells within the tumor itself (32). This intratumoral presentation involved DC-T cell cross-talk in which T cell responses depended on interleukin-12 (IL-12) produced by DCs in response to interferon- γ (IFN- γ) production by T cells. In some models, cross-talk between intratumoral natural killer (NK) cells and DCs amplified the ultimate activation of antitumor T cell responses within the TME (33). Siddiqui *et al.* showed that Tcf1⁺ antigen-experienced T cells within the TME are the primary pool of tumor-specific T cells activated by CPI (34).

Beyond the evidence for direct priming of T cell responses by DCs within the primary tumor, there is mounting evidence that tumor-draining lymph nodes (TDLN) are also a key site for tumor antigen presentation to tumor-specific T cells and that this process is enhanced by PD-1 pathway blockade. Over a decade ago, Chen, Pardoll, and colleagues demonstrated PD-1 expression emerging on the surface of T cells within 12 hours of first contact with antigen, by the time of first cell division in the lymph node (35, 36). Induction of anergy in autoreactive T cells through self-antigen presentation in the lymph node was partially mitigated in mice in which PD-L1 or PD-1 was knocked out (KO mice), or through antibody blockade (35–37). Tumors are known to induce immune tolerance to their own antigens (38). One could imagine from these findings that increased antitumor immunity after neoadjuvant anti-PD-1 therapy is generated not only within the TME, which possesses multiple metabolic (such as glucose and glutamine deprivation, hypoxia, and indoleamine-pyrrole 2,3-dioxygenase) and cytokine-based (such as transforming growth factor- β) general inhibitory mechanisms, but also at the level of TDLN by reversing tolerogenic antigen presentation (Fig. 1). Direct evidence that tumor antigens are brought to TDLN has come recently through a number of experimental strategies, including fluorescence labeling of tumors, engineering of tumors to express model neoantigens recognized by cognate TCR-transgenic T cells, analysis of DC subsets in tumor and TDLN by means of flow cytometry and single-cell RNA-sequencing, and DC-specific KO mice. In mouse models, Krummel and colleagues demonstrated that CD103⁺ migratory DCs (CD141⁺ in humans) could carry tumor antigen to TDLN and cross-present it to CD8⁺ T cells. These DCs were CD8⁺ and resembled the classical DCs that efficiently cross-present antigens to CD8⁺ T cells. By contrast, there was no evidence for tumor antigen-carrying macrophages in lymph nodes (39).

The trafficking of DCs carrying tumor antigen to TDLN was also demonstrated by Salmon *et al.* (40). They provided experimental evidence for classical DC (cDC) presentation of tumor antigen in TDLN. The absence of cDCs resulted in failure of CD8⁺ T cells to enter into the tumor parenchyma after anti-PD-1 treatment, suggesting that intratumoral T cell expansion was due to trafficking of T cells first activated in TDLN back into the tumor rather than primary intratumoral expansion. Using similar DC-specific conditional KO mice as those of Salmon *et al.*, Liu *et al.* (41) showed that DCs were necessary for successful neoadjuvant immunotherapy. A caveat in the interpretation of these studies is that DCs are absent from birth in DC KO mice, and thus the failure of anti-PD-1 to generate antitumor effects could be due to tumor-specific T cells never being “primed” to a Tcf1⁺ state (memory or exhausted) from which PD-1 pathway blockade could effect “reinvigoration.”

Although these studies confirm that DC presentation of tumor antigens to tumor-specific T cells is important in the antitumor effects of CPI, the relative roles of intratumoral versus TDLN antigen presentation and priming of tumor-specific T cells has yet to be completely resolved. The demonstration that intratumoral DCs contain tumor antigen and the capacity to present it to antigen-specific T cells in vitro does not prove that presentation to T cells is occurring within the tumor, as opposed to within the TDLN, to which DCs traffic once they express CCR7. Defining the location of DC antigen presentation in vivo is in fact quite difficult. The primary experimental approach to determining the role of lymph node priming of tumor-specific T cells has used the sphingosine 1-phosphate (S1P) receptor inhibitor FYT720, which blocks the egress of T cells out of the lymph node through efferent lymphatics. Results with FYT720 have been contradictory in various animal models of cancer. Fransen *et al.* showed that FYT720 treatment abrogates the antitumor efficacy of anti-PD-1 treatment (42). By contrast, other groups have found that FYT720 treatment after tumor establishment does not inhibit accumulation of tumor-specific T cells in the tumor nor mitigate antitumor immune responses; this evidence favors intratumoral T cell priming as the predominant mechanism (33, 34). However, this pharmacologic technique for inhibition of T cell egress from the lymph node is not as clean as a genetic knockout. Early studies showed that although FYT720 rapidly diminishes numbers of circulating lymphocytes, depletion is not complete; circulating T cells are reduced to ~20% of control levels, and thus, lymph node-primed T cells can still leak out into the blood after the initiation of FYT720 treatment (43). Additionally, FYT720 effects were analyzed in the primary tumor implant, not in systemic micro-

metastases, the latter of which are most relevant for the ultimate clinical value of neoadjuvant CPI. The only experimentally defined way for T cells in tissues (including the primary tumor in situ) to migrate systemically is to first traffic to draining lymph nodes through afferent lymphatics and then enter the bloodstream through efferent lymphatics. Thus, T cells activated in the primary tumor through intratumoral DC presentation upon neoadjuvant CPI would ultimately need to pass through TDLN, where they might further encounter tumor antigen-presenting DCs before entering the blood by way of the efferent lymphatic vessels.

Mechanistically, an important outcome of enhanced priming of tumor-specific T cells by DCs is to change not only the activation state but ultimately the clonal dynamics of tumor-specific T cells. Studies of clonal dynamics in neoadjuvant CPI clinical trials are discussed below, and recent analyses in mouse models and in non-neoadjuvant clinical settings are beginning to shed light on this subject. Recently, Yost, Chang, and colleagues showed that after anti-PD-1 therapy of basal cell and cutaneous squamous cell carcinomas, T cell clonal expansion was due to new clones “appearing” in the TME rather than expansion of clones already in the tumor before initiation of anti-PD-1 therapy; these findings suggest that either clones not present initially in the tumor traffic into the tumor upon anti-PD-1 treatment (memory T cells from lymph nodes) or that subdominant T cell clones present intratumorally below the detection limit before treatment are selectively expanded (44). A caveat in this work is that the tumor specificity of the T cell clones is not known based on the TCR-sequencing data presented. However, in a neoadjuvant study of anti-PD-1 treatment in humans with non-small cell lung cancer (NSCLC), the frequency of validated neoantigen-specific T cell clones decreased substantially (roughly 10-fold) in the tumor 4 weeks after treatment initiation, whereas these same clones were increasing in the periphery (45). At the time of surgery, these clones were found at highest frequency in TDLN.

More direct evidence that anti-PD-1 treatment can expand “subdominant” T cell clones has also been reported. Kamphorst *et al.* reported that tumor killing by reinvigorated intratumoral tumor-specific T cells after PD-1 blockade may enable de novo T cell priming against new epitopes (46). Furthermore, it has been shown that anti-PD-1 treatment may allow subdominant T clones that could not be detected at baseline to be reinvigorated. Memarnejadian *et al.* showed in a mouse tumor model that anti-PD-1 treatment promotes epitope spreading in antitumor CD8⁺ T cell reactivity by preventing the fratricidal death of subdominant clones to relieve immunodomination (47).

Continued elucidation of these processes is central to the notion that neoadjuvant PD-

1 blockade will clinically result in enhanced relapse-free survival, a critical determinant of overall survival in operable patients who would otherwise relapse at distant sites after resection of the primary tumor alone.

Clinical trials assessing neoadjuvant immunotherapies based on anti-PD-(L)1

Basic laboratory research has predicted the potential for neoadjuvant PD-1 pathway blockade to potentiate antitumor immunity in a productive and enduring way. Through ongoing clinical research, we are now learning whether and how these observations might translate in patients with cancer. Special considerations for clinical translation are centered on risk:benefit expectations in patient populations among which a proportion would be cured by surgery alone, although biomarkers are currently lacking to identify individuals destined to benefit. In general, neoadjuvant cancer therapies offer several potential clinical advantages, including tumor reduction before surgery and the ability to assess pathologic response as an early surrogate marker for RFS and OS. They also provide adequate tissue availability on-therapy for in-depth scientific studies to explore drug mechanism-of-action and efficacy biomarkers. However, these advantages must be weighed against the potential disadvantages of tumor progression during the neoadjuvant treatment period and the occurrence of drug-related adverse events resulting in undue surgical delay, either of which could lead to loss of a surgical option.

To date, published reports of neoadjuvant anti-PD-1-based immunotherapies have centered on relatively small investigator-initiated clinical trials with a rich correlative scientific component. In 2018, Forde *et al.* presented the first literature report of neoadjuvant anti-PD-1 therapy, describing an investigator-initiated phase 2 trial of nivolumab in 21 patients with high-risk (stages I to IIIA) NSCLC (45). Although all subjects were deemed “resectable for cure” by a surgical expert, the risk of post-surgical relapse and death within 5 years was estimated to be 50 to 80%. In this study, previously untreated patients received nivolumab preoperatively for a brief 4-week period. Surgery was then carried out according to standard practice, resecting the primary tumor mass along with surrounding normal lung tissue and TDLN. The treatment regimen was found to be safe, with no surgical delays, no unanticipated toxicities, one treatment-related grade 3 adverse event, and one patient who was found to have an unresectable tumor intraoperatively. Particularly revealing was a comparison of tumor response assessments conducted radiographically, with computerized tomographic (CT) scans at baseline and just before surgery, or histologically by examining the surgical specimen for evidence of pathologic response. Although partial radiographic

Table 1. Anti-PD-1-based neoadjuvant therapy trials in melanoma. AJCC, American Joint Commission on Cancer (10). Stage III, regional lymph node metastases; stage IIIB/C, macroscopic regional lymph node metastases; stage IV, disseminated metastases. ORR, objective response rate (complete + partial responses) based on radiographic and clinical assessments according to RECIST1.1 (83). pCR, pathologic complete response; MPR, major pathologic response, $\leq 10\%$ viable tumor cells remaining; pPR, pathologic partial response, $\leq 50\%$ viable tumor cells remaining. AE, treatment-related adverse event (toxicity).

ClinicalTrials.gov identifier (citation)	NCT02519322 (49)	NCT02437279 (50)	NCT02434354 (51)	NCT02977052 (52)
Phase of trial	2	1b	1b	2
Randomization	Monotherapy versus combination therapy	Neoadjuvant versus adjuvant therapy	Not done	Three different combination therapy regimens
Number of evaluable patients	23	20	29	86*
AJCC stage	III to IV	IIIB/C	III to IV	IIIB/C
Treatment period	Preop 8 to 9 weeks + postop 6 months	Preop 6 weeks + postop 6 weeks; or 12 weeks postop only	Preop 3 weeks + postop 1 year	Preop 6 weeks
Anti-PD-1 monotherapy†				
ORR	25%	Not done	Not provided	Not done
Pathologic response‡	25% pCR		30% = pCR + MPR	
Grade ≥ 3 AEs	8%		Not provided	
Anti-PD-1 + anti-CTLA-4 combination therapy§				
ORR	73%	50%	Not done	35 – 63%
Pathologic response‡	45% pCR	78% = pCR + MPR + pPR		65-80% = pCR + MPR + pPR
Grade ≥ 3 AEs	73%	90%		20-50%
Risk:benefit	Trial stopped early because of safety concerns.	Only 10% of patients completed therapy, due to toxicity.	Treatment safe and moderately effective.	6 weeks nivolumab 3 mg/kg + ipilimumab 1 mg/kg identified as optimal regimen.
Immunologic correlates of response	Radiographic response associated with higher tumor PD-L1 expression at baseline, and higher CD8 T cell density, lymphoid gene expression, and TCR clonality in tumor at 3 to 4 weeks.	Relapse-free survival associated with pathologic response; higher PD-L1, CD3, B2M, and IFN- γ -related gene expression in baseline tumor; and greater number of newly detected tumor-resident T cell clones in the peripheral blood at week 6.	Relapse-free survival associated with pathologic response; higher expression of genes reflecting T cell activation and IFN- γ signaling in baseline tumor; brisk TILs with increased exhausted T cells (EOMES ^{hi} , Tbet ^{lo}) and decreased proliferating T _{reg} cells in tumor at week 3; and gene expression reflecting intratumoral angiogenesis and B cells.	Relapse-free survival associated with pathologic response and higher IFN- γ gene expression signature in baseline tumor.

*An extension cohort of approximately 100 patients who will receive the selected optimal neoadjuvant regimen provides for limited surgery in patients achieving a pCR or MPR on biopsy.

†Anti-PD-1, nivolumab in (49) and pembrolizumab in (51).

‡In specimens resected after neoadjuvant therapy.

§Anti-PD-1 (nivolumab) plus anti-CTLA-4 (ipilimumab).

responses (defined as $\geq 30\%$ decrease in the sum of tumor diameters) were observed in only 2 of 21 (10%) patients, major pathologic responses at the primary tumor site ($\leq 10\%$ viable tumor cells remaining) were seen in 9 of 20 (45%) operable cases. Thus, conventional radiographic studies underestimated the extent and rapidity of pathologic responses, which were characterized by an influx of immune cells and proliferative fibrosis, which is consistent

with an immunological mechanism. The degree of pathologic response significantly correlated with tumor mutational burden and with the computationally predicted neoantigen burden. Furthermore, an in-depth study of one patient revealed that neoantigen-specific T cell clones that were present intratumorally and in TDLN expanded in the peripheral blood during preoperative nivolumab therapy; these clones persisted in the periphery for weeks after tumor

resection. This example appears to recapitulate findings from mouse tumor models of neoadjuvant immunotherapy described above, supporting the notion that neoadjuvant immunotherapy can amplify systemic antitumor immunity and that these effects may persist even after surgical removal of the primary tumor and regional lymph nodes. A follow-up analysis of T cell clonal dynamics from this study showed that pathologic response was correlated with

posttreatment increases in the peripheral blood of clones that were highly represented in pre-treatment tumor biopsies, further supporting the notion that peripheral mobilization of intratumoral T cells is correlated with intratumoral response (48). As mentioned above, these results do not distinguish the anatomic location of tumor-specific T cell activation through neoadjuvant PD-1 pathway blockade.

Four reports of neoadjuvant immunotherapy regimens in resectable melanoma have illustrated opportunities to further deepen our mechanistic understanding of immune checkpoint blockade while underlining the practical challenges of balancing risk and benefit in clinical trial design (Table 1) (49–52). These melanoma reports represent the largest neoadjuvant anti-PD-1 immunotherapy literature in a single cancer type to date. In two studies by Amaria *et al.* and Blank *et al.*, high rates of radiographic and pathologic response were achieved by combining nivolumab (anti-PD-1) with ipilimumab (anti-CTLA-4) for 8 to 9 weeks preoperatively (49, 50); this drug combination was already FDA-approved as a standard of care in advanced unresectable melanoma (53). However, efficacy in the neoadjuvant setting came at the cost of high rates of severe toxicities, which limited the conduct of these trials. Severe toxicity rates in the neoadjuvant treatment population appeared to exceed those previously documented in the advanced unresectable melanoma patient population; the investigators hypothesized that this might reflect a heightened impact of combined PD-1/CTLA-4 blockade in patients with earlier cancers and intact immune systems. By contrast, a study by Huang *et al.* using pembrolizumab (anti-PD-1) monotherapy for only 3 weeks preoperatively showed a lower rate of side effects but also a lower response rate (51). Subsequently, a trial reported by Rozeman *et al.*, testing three randomized combination treatment arms, yielded a modified dosing regimen of nivolumab plus ipilimumab that had a substantial response rate and fewer severe toxicities (52). Preliminary evidence from these melanoma trials suggests that RFS may be prolonged in patients achieving a substantial pathologic response, compared with those with minimal or no pathologic response (51, 52). These results, requiring validation in larger trials, suggest that pathologic response after neoadjuvant immunotherapy may be an early surrogate marker for long-term clinical outcomes, similar to the general experience with neoadjuvant chemotherapies in breast and lung cancer (11, 12).

The anti-PD-1-based neoadjuvant trials in melanoma, although relatively small, also proffered preliminary evidence for baseline and on-treatment tumor biomarkers associated with radiographic response, pathologic response, and/or RFS (Table 1). Response markers, including increased densities of tumor-infiltrating

T cells and IFN- γ -related gene expression signatures at baseline and on treatment, were subsequently also reported in a study of pembrolizumab in muscle-invasive bladder cancer (54). The melanoma trial by Blank *et al.* comparing neoadjuvant versus adjuvant regimens of anti-PD-1 plus anti-CTLA-4 found a greater expansion of tumor-resident T cell clones in the peripheral blood of patients enrolled on the neoadjuvant arm (50). These preliminary findings in small groups of patients mirrored preclinical studies in a mouse breast cancer models (described above) that showed superior tumor control and persistence of peripheral tumor-specific T cells with neoadjuvant compared with adjuvant immunotherapy, although they await validation in larger randomized trials (16). Similarly, a randomized trial of neoadjuvant versus adjuvant anti-PD-1 (pembrolizumab) in recurrent glioblastoma showed significantly improved RFS and OS in the neoadjuvant group, whose resection specimens were characterized by enhanced IFN- γ -related gene expression profiles and PD-L1 expression and whose on-treatment blood specimens showed expansion of T cell clones that were also found intratumorally (55). Another study in glioblastoma, which combined neoadjuvant plus adjuvant anti-PD-1 (nivolumab), found increased intratumoral chemokine gene expression, activated CD8 T cells, and TCR diversity in on-treatment tumor specimens compared with tumors from patients who did not receive anti-PD-1 treatment (56). The systemic persistence of tumor-associated or tumor-reactive T cells suggests that a period of continued immunotherapy after surgery may further boost these immune responses and avert tumor relapse. In melanoma, for which two adjuvant anti-PD-1 therapies are already approved as standards of care, these regimens have been added to the design of some neoadjuvant immunotherapy trials (Table 1).

Surgeons are crucial clinical partners for medical oncologists and pathologists in the development of neoadjuvant immunotherapies, not only for determining the candidacy of individual patients, general guidelines for patient selection, and optimal preoperative treatment intervals but also for addressing new challenges that arise from early experience with these regimens. For example, tumors that regress rapidly or completely during the neoadjuvant treatment interval may be difficult to locate intraoperatively. This has led some investigators to suggest interventional placement of radiographic tumor markers before commencing neoadjuvant immunotherapy (57). Furthermore, if an aggressive or cosmetically disfiguring surgery would have been recommended in the absence of neoadjuvant therapy, would the same surgical approach still be required for tumors exhibiting a major response to neoadjuvant treatment? Some have suggested that surgery

could be avoided entirely in the setting of a clinically and radiographically documented complete response (52), or that limited surgical interventions could be used in patients whose on-treatment tumor biopsies show a complete or major pathologic response (for example, as provided in an extension cohort of NCT02977052) (Table 1). These issues, some of which were not foreseen before the advent of active neoadjuvant immunotherapies, are the subject of ongoing and future investigations.

Pathologic response assessment

In oncology drug development, the gold-standard endpoint for assessing therapeutic benefit is OS, which is usually determined in large randomized trials conducted over several years. However, with the rapid development of neoadjuvant immunotherapy regimens, it would be advantageous for the field, and most importantly for patients, to identify an early indicator of long-term benefit. Pathologic response is a candidate early surrogate endpoint for OS and RFS, which might allow for expedient resulting of clinical trials, redirecting ongoing trials in real time, and making rational therapeutic decisions for individual patients.

Pathologic response criteria for neoadjuvant cancer therapy were first developed in the context of chemotherapy as a parameter portending clinical outcomes. Pathologic complete response (pCR), the most stringent criterion, is defined as the absence of any viable tumor in the definitive surgical resection specimen. It has been variably defined to refer only to the primary tumor site or to include assessment of TDLN (11). pCR has been correlated with OS in patients who received chemotherapy for muscle-invasive bladder cancer, gastric or gastroesophageal junction cancers, breast cancer, and NSCLC, with average pCR rates of 28.6, 7, 21, and 8%, respectively. (58–61) Although informative for those patients achieving a pCR, this readout misses a potential opportunity to prognosticate and make treatment decisions for the vast majority of patients. To that end, “major pathologic response” (MPR), describing a treatment effect resulting in $\leq 10\%$ residual viable tumor (RVT), was proposed as an alternative endpoint (62). However, retrospective studies have suggested that OS correlates with a much larger spectrum of RVT, implying that if assessments beyond pCR and MPR could be performed, prognostication could potentially be available for all patients (12, 63).

To date, pCR and MPR are the most commonly used metrics for assessing response to neoadjuvant immunotherapy, although differences exist both within and across tumor types as to how these pathologic criteria have been assessed. For example, some studies of neoadjuvant immunotherapy in melanoma grouped patients as having a pCR, “near pCR” (MPR, $\leq 10\%$ RVT), “partial pathologic response” (pPR,

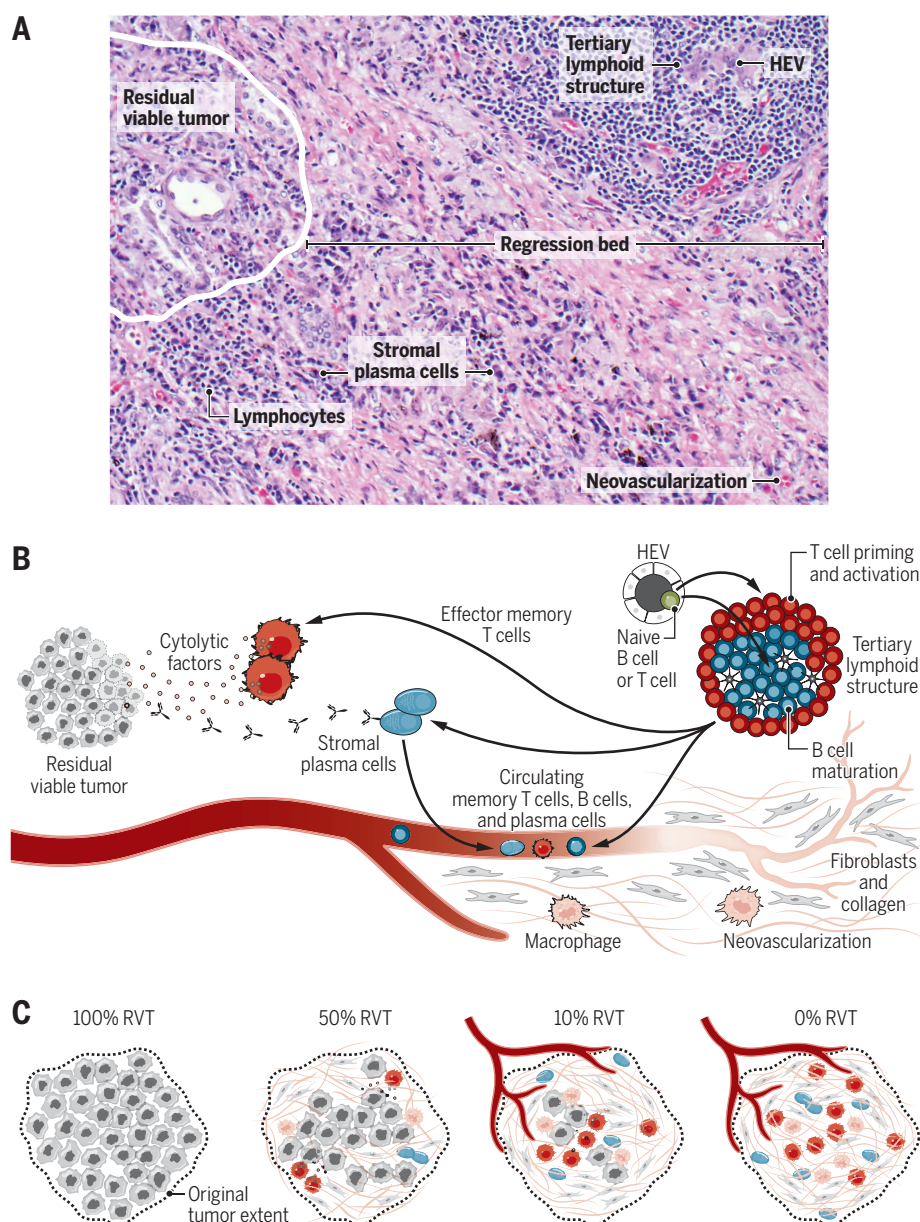


Fig. 2. Immune-mediated tumor regression. (A) Representative photomicrograph from a definitive surgical resection specimen from a patient with NSCLC responding to neoadjuvant immunotherapy. Hematoxylin and eosin staining was used, with 100× original magnification. HEV, high endothelial venule. (B) Schematic of the tumor bed immunoarchitecture, displaying features consistent with both T cell- and B cell-mediated local antitumor immune responses. The regression bed—the area where the tumor used to be—is characterized by hallmarks of tissue repair and wound healing, such as neovascularization and proliferative fibrosis. (C) Percent RVT using irPRC is calculated by the surface area of the RVT/surface area of the tumor bed. The tumor bed surface area includes RVT + tumor-associated stroma + necrosis + regression bed. Schematics show examples of 100, 50, 10 (MPR), and 0% (pCR) RVT.

≤50% RVT), or “no pathologic response” (>50% RVT) (64), whereas others focused only on pCR as a readout (Table 1). A study of neoadjuvant anti-PD-1 for patients with muscle-invasive bladder cancer used pCR as a primary endpoint, with pathologic down-staging as a secondary endpoint (54); a study on glioblastoma multiforme reported “observable tissue-

based and clinical treatment effects” but did not formally score pathologic response (55); and the initial report of neoadjuvant anti-PD-1 in NSCLC reported pCR and MPR at the primary tumor site but used a chemotherapy scoring system available at that time (12, 45). Optimal pathologic response thresholds correlating with long-term clinical outcomes remain

to be determined as data from ongoing neoadjuvant immunotherapy trials mature. Ultimately, informative pathologic response thresholds may vary by tumor type (65). It will be necessary to collect and report data regarding %RVT in a uniform and reproducible fashion to allow for valid cross-study comparisons.

Recently, immune-related pathologic response criteria (irPRC) have been developed with the aim of assessing the full spectrum of response to immunotherapy in the complete resection specimen—that is, scoring 0 to 100% RVT at 10% intervals (66). This approach, first described in the context of neoadjuvant anti-PD-1 monotherapy in NSCLC (45), has been extended to include other tumor types, tumors from multiple anatomic locations, and combination treatment regimens based on anti-PD-1 (67). The ability to assess regional lymph nodes as well as the primary tumor site provides additional information regarding treatment response; excluding regional lymph nodes from pathologic response assessments may alter long-term outcome correlations (11, 45). Some neoadjuvant immunotherapies are now being tested in cancer types in which the primary tumor is often surgically absent at the time that immunotherapy commences, such as melanoma and Merkel cell carcinoma (57, 68). In these cases, neoadjuvant immunotherapy is directed against resectable metastases in lymph nodes and/or distant organ sites. This has necessitated the development of pathologic response scoring systems that evaluate response in metastatic sites with or without an accompanying primary tumor (64, 66, 67). New scoring systems that assess the full spectrum of potential pathologic response will require educating pathologists in academic centers as well as in the community. This will be particularly important as neoadjuvant immunotherapies become standard of care.

In addition to emphasizing pathologic assessment of the entire surgical specimen, irPRC recognize the distinct histologic characteristics of anti-PD-1-based treatment response (Fig. 2). Accurate identification of the regression bed has been shown to lead to more reproducible assessments of %RVT than historical scoring systems that do not detail this component (66, 67). The features of this zone may also provide important insights into the mechanism of action of immune checkpoint inhibitors. They include activation of diverse immune cell types such as lymphocytes, macrophages, and plasma cells associated with tertiary lymphoid structures (TLS); the stigmata of organized tumor cell death; and features of tissue repair, such as proliferative fibrosis and neovascularization (66). It is recognized that TLS support the organization of antitumor B cell and T cell responses, and an appreciation of their role in this setting could potentially be leveraged therapeutically, such as by using

chemokines or even synthetic scaffolds to induce TLS formation in otherwise “noninflamed” tumors (69). High expression of genes associated with angiogenesis and B cell receptor pathways was associated with prolonged RFS after neoadjuvant anti-PD-1 therapy in a melanoma study (Table 1) (51), supporting the histologic description of a tumor regression bed that extends beyond a simple T cell signature. The potential role of B-lineage cells in tumor rejection after anti-PD-1 therapy has been relatively understudied. The expansion of B cells after anti-PD-1 therapy is consistent with the original basic functional description of the PD-1 pathway (70); however, their increased detection in the TME does not necessarily equate with a requirement for tumor rejection. Additional research will be needed to define the potential role of B cells in tumor regression and to determine whether their contributions may be tumor type or context dependent (56, 71, 72). The above-described features of robust inflammation and fibrosis in responding tumors have been shown to account for apparent discrepancies between radiographic and pathologic response assessments after neoadjuvant immunotherapy (45, 52, 66, 73). Such discrepancies may depend on the kinetics of anti-PD-1 response in certain tumor types, in the context of the neoadjuvant treatment interval before radiographic restaging and surgery.

In cases in which definitive surgical resection after neoadjuvant immunotherapy would result in serious functional or cosmetic consequences—for example, locally advanced gynecologic or genitourinary carcinomas, or scalp or facial tumors—it is possible that on-treatment biopsies could be used to assess therapeutic response by using the above-described irPRC. These criteria, originally developed for assessing response to neoadjuvant anti-PD-1-based immunotherapies, have recently been applied to core needle tumor biopsies taken from patients with advanced unresectable cancers while receiving the same therapies. In a melanoma study, such assessments have already been shown to correlate with 5-year OS (73), suggesting the potential for innovations in pathologic evaluation to allow for prognostication, therapeutic decision making, and organ sparing. Association of irPRC with OS in this latter scenario supports the concept that irPRC may ultimately be correlated with long-term patient outcomes in the neoadjuvant setting. Over time, more advanced imaging tools may also become available to capitalize on the observed features of the regression bed or otherwise more accurately reflect the residual tumor burden.

Future development

More than 100 clinical trials of neoadjuvant anti-PD-(L)1 therapy are now ongoing in diverse tumor types, in which anti-PD-(L)1 is administered as monotherapy or in combination

with other immunotherapies, radiation therapy, chemotherapy, kinase inhibitors, tumor-targeted antibodies, or endocrine or metabolic modulators [reviewed in (74, 75)]. Treatment combinations designed to recruit more immune cells into the tumor—such as intratumoral therapies (oncolytic viruses or interferon pathway agonists), cancer vaccines, and kinase inhibitors—hold promise. Furthermore, treatment combinations with increased antitumor efficacy might accelerate response kinetics, thus shortening the optimal presurgical treatment interval. The first wave of neoadjuvant trials has emphasized cancer types in which anti-PD-(L)1 mono- or combination therapies have already shown some efficacy in the advanced metastatic disease setting, hypothesizing that applying these treatments earlier in the course of cancer evolution will be beneficial. Early reports of safety and substantial PCR rates from neoadjuvant combinations of anti-PD-1 with anti-CTLA-4 (52), or with multidrug chemotherapies for triple-negative breast cancer (76, 77) or NSCLC (78), are encouraging but require longer follow-up for assessment of clinical efficacy endpoints. Next-generation trials may assign patients to postsurgical observation or intervention depending on the degree of pathologic response, similar to the precedent established with nonimmunologic neoadjuvant therapies in breast cancer (79).

Although conventional computerized tomographic imaging at early time points on neoadjuvant therapy often underestimates the extent of pathologic changes occurring in tumor tissues, advanced methods for CT image analysis and interpretation are currently under evaluation and may provide previously unidentified on-treatment markers of response to guide clinical decision-making (80, 81). Furthermore, nuclear imaging with positron emission tomography (PET) may operationalize markers specific for immune cells, checkpoint molecules, or metabolic processes associated with neoadjuvant treatment response or resistance (82).

Tumor specimens obtained after neoadjuvant immunotherapy provide a rich source of materials for in-depth scientific interrogations that are expected to further illuminate mechanism of action for anti-PD-1 drugs. A surprisingly high B cell component observed in responding tumors has drawn attention to the potential role of this cell type in cooperating to mediate anti-PD-1 responses. The quantity of tissue obtained at surgery will allow much more extensive single-cell analyses of on-therapy immune responses within the TME, as well as analyses of residual viable tumor cells, which have been overlooked in many studies. It will be of great interest in the future to better understand the particular characteristics of these two compartments with regard to immunoarchitecture, cytokine signatures, and cellular functional states, including tumor cell

signaling and immune evasion mechanisms in cases with residual tumor. Findings from such studies may reveal pathways, mechanisms, and molecules that can be cotargeted in new treatment combinations to increase the efficacy of anti-PD(L)1 drugs.

REFERENCES AND NOTES

1. S. L. Topalian, C. G. Drake, D. M. Pardoll, Immune checkpoint blockade: A common denominator approach to cancer therapy. *Cancer Cell* **27**, 450–461 (2015). doi: [10.1016/j.ccell.2015.03.001](https://doi.org/10.1016/j.ccell.2015.03.001); pmid: 25858804
2. M. Yarchoan, A. Hopkins, E. M. Jaffee, Tumor mutational burden and response rate to PD-1 inhibition. *N. Engl. J. Med.* **377**, 2500–2501 (2017). doi: [10.1056/NEJMc1713444](https://doi.org/10.1056/NEJMc1713444); pmid: 29262275
3. S. L. Topalian et al., Safety, activity, and immune correlates of anti-PD-1 antibody in cancer. *N. Engl. J. Med.* **366**, 2443–2454 (2012). doi: [10.1056/NEJMoa1200690](https://doi.org/10.1056/NEJMoa1200690); pmid: 22658127
4. P. T. Nghiem et al., PD-1 blockade with pembrolizumab in advanced Merkel-cell carcinoma. *N. Engl. J. Med.* **374**, 2542–2552 (2016). doi: [10.1056/NEJMoa1603702](https://doi.org/10.1056/NEJMoa1603702); pmid: 27093365
5. S. L. Topalian, J. M. Taube, R. A. Anders, D. M. Pardoll, Mechanism-driven biomarkers to guide immune checkpoint blockade in cancer therapy. *Nat. Rev. Cancer* **16**, 275–287 (2016). doi: [10.1038/nrc.2016.36](https://doi.org/10.1038/nrc.2016.36); pmid: 27079802
6. S. L. Topalian et al., Five-year survival and correlates among patients with advanced melanoma, renal cell carcinoma, or non-small cell lung cancer treated with nivolumab. *JAMA Oncol.* **5**, 1411–1420 (2019). doi: [10.1001/jamaoncol.2019.1287](https://doi.org/10.1001/jamaoncol.2019.1287); pmid: 31343665
7. C. Robert et al., Pembrolizumab versus ipilimumab in advanced melanoma (KEYNOTE-006): Post-hoc 5-year results from an open-label, multicentre, randomised, controlled, phase 3 study. *Lancet Oncol.* **20**, 1239–1251 (2019). doi: [10.1016/S1470-2045\(19\)30388-2](https://doi.org/10.1016/S1470-2045(19)30388-2); pmid: 31345627
8. J. Weber et al., Adjuvant nivolumab versus ipilimumab in resected stage III or IV melanoma. *N. Engl. J. Med.* **377**, 1824–1835 (2017). doi: [10.1056/NEJMoa1709030](https://doi.org/10.1056/NEJMoa1709030); pmid: 28891423
9. A. M. M. Eggermont et al., Adjuvant pembrolizumab versus placebo in resected stage III melanoma. *N. Engl. J. Med.* **378**, 1789–1801 (2018). doi: [10.1056/NEJMoa1802357](https://doi.org/10.1056/NEJMoa1802357); pmid: 29658430
10. J. E. Gershenwald et al., Melanoma staging: evidence-based changes in the American Joint Committee on Cancer eighth edition cancer staging manual. *CA: Cancer J Clin* **67**, 472–492 (2017).
11. P. Cortazar et al., Pathological complete response and long-term clinical benefit in breast cancer: The CTNeoBC pooled analysis. *Lancet* **384**, 164–172 (2014). doi: [10.1016/S0140-6736\(13\)62422-8](https://doi.org/10.1016/S0140-6736(13)62422-8); pmid: 24529560
12. A. Pataer et al., Histopathologic response criteria predict survival of patients with resected lung cancer after neoadjuvant chemotherapy. *J. Thorac. Oncol.* **7**, 825–832 (2012). doi: [10.1097/JTO.0b013e318247504a](https://doi.org/10.1097/JTO.0b013e318247504a); pmid: 22481232
13. B. C. Carthon et al., Preoperative CTLA-4 blockade: Tolerability and immune monitoring in the setting of a presurgical clinical trial. *Clin. Cancer Res.* **16**, 2861–2871 (2010). doi: [10.1158/1078-0432.CCR-10-0569](https://doi.org/10.1158/1078-0432.CCR-10-0569); pmid: 20460488
14. A. A. Tarhini et al., Immune monitoring of the circulation and the tumor microenvironment in patients with regionally advanced melanoma receiving neoadjuvant ipilimumab. *PLOS ONE* **9**, e87705 (2014). doi: [10.1371/journal.pone.0087705](https://doi.org/10.1371/journal.pone.0087705); pmid: 24498358
15. E. R. Lutz et al., Immunotherapy converts nonimmunogenic pancreatic tumors into immunogenic foci of immune regulation. *Cancer Immunol. Res.* **2**, 616–631 (2014). doi: [10.1158/2326-6066.CIR-14-0027](https://doi.org/10.1158/2326-6066.CIR-14-0027); pmid: 24942756
16. J. Liu et al., Improved efficacy of neoadjuvant compared to adjuvant immunotherapy to eradicate metastatic disease. *Cancer Discov.* **6**, 1382–1399 (2016). doi: [10.1158/2159-8290.CD-16-0577](https://doi.org/10.1158/2159-8290.CD-16-0577); pmid: 27663893
17. J. Liu et al., Timing of neoadjuvant immunotherapy in relation to surgery is crucial for outcome. *Oncol Immunology* **8**, e1581530 (2019). doi: [10.1080/2162402X.2019.1581530](https://doi.org/10.1080/2162402X.2019.1581530); pmid: 31069141
18. D. J. Lenschow, T. L. Walunas, J. A. Bluestone, CD28/B7 system of T cell costimulation. *Annu. Rev. Immunol.* **14**, 233–258 (1996). doi: [10.1146/annurev.immunol.14.1.233](https://doi.org/10.1146/annurev.immunol.14.1.233); pmid: 8717514

19. C. E. Rudd, A. Taylor, H. Schneider, CD28 and CTLA-4 coreceptor expression and signal transduction. *Immunol. Rev.* **229**, 12–26 (2009). doi: [10.1111/j.1600-065X.2009.00770.x](https://doi.org/10.1111/j.1600-065X.2009.00770.x); pmid: [19426212](https://pubmed.ncbi.nlm.nih.gov/19426212/)
20. G. J. Freeman *et al.*, Cloning of B7-2: A CTLA-4 counter-receptor that costimulates human T cell proliferation. *Science* **262**, 909–911 (1993). doi: [10.1126/science.7694363](https://doi.org/10.1126/science.7694363); pmid: [7694363](https://pubmed.ncbi.nlm.nih.gov/7694363/)
21. P. S. Linsley *et al.*, CTLA-4 is a second receptor for the B cell activation antigen B7. *J. Exp. Med.* **174**, 561–569 (1991). doi: [10.1084/jem.174.3.561](https://doi.org/10.1084/jem.174.3.561); pmid: [1714933](https://pubmed.ncbi.nlm.nih.gov/1714933/)
22. P. S. Linsley *et al.*, Human B7-1 (CD80) and B7-2 (CD86) bind with similar avidities but distinct kinetics to CD28 and CTLA-4 receptors. *Immunity* **1**, 793–801 (1994). doi: [10.1016/S1074-7613\(94\)80021-9](https://doi.org/10.1016/S1074-7613(94)80021-9); pmid: [7534620](https://pubmed.ncbi.nlm.nih.gov/7534620/)
23. E. A. Tivol *et al.*, Loss of CTLA-4 leads to massive lymphoproliferation and fatal multiorgan tissue destruction, revealing a critical negative regulatory role of CTLA-4. *Immunity* **3**, 541–547 (1995). doi: [10.1016/1074-7613\(95\)90125-6](https://doi.org/10.1016/1074-7613(95)90125-6); pmid: [7584144](https://pubmed.ncbi.nlm.nih.gov/7584144/)
24. P. Waterhouse *et al.*, Lymphoproliferative disorders with early lethality in mice deficient in CtlA-4. *Science* **270**, 985–988 (1995). doi: [10.1126/science.270.5238.985](https://doi.org/10.1126/science.270.5238.985); pmid: [7481803](https://pubmed.ncbi.nlm.nih.gov/7481803/)
25. G. Q. Phan *et al.*, Cancer regression and autoimmunity induced by cytotoxic T lymphocyte-associated antigen 4 blockade in patients with metastatic melanoma. *Proc. Natl. Acad. Sci. U.S.A.* **100**, 8372–8377 (2003). doi: [10.1073/pnas.1533209100](https://doi.org/10.1073/pnas.1533209100); pmid: [12826605](https://pubmed.ncbi.nlm.nih.gov/12826605/)
26. H. Nishimura *et al.*, Autoimmune dilated cardiomyopathy in PD-1 receptor-deficient mice. *Science* **291**, 319–322 (2001). doi: [10.1126/science.291.5502.319](https://doi.org/10.1126/science.291.5502.319); pmid: [11209085](https://pubmed.ncbi.nlm.nih.gov/11209085/)
27. H. Nishimura, M. Nose, H. Hiai, N. Minato, T. Honjo, Development of lupus-like autoimmune diseases by disruption of the PD-1 gene encoding an ITIM motif-carrying immunoreceptor. *Immunity* **11**, 141–151 (1999). doi: [10.1016/S1074-7613\(00\)80089-8](https://doi.org/10.1016/S1074-7613(00)80089-8); pmid: [10485649](https://pubmed.ncbi.nlm.nih.gov/10485649/)
28. H. Dong *et al.*, B7-H1 determines accumulation and deletion of intrahepatic CD8(+) T lymphocytes. *Immunity* **20**, 327–336 (2004). doi: [10.1016/S1074-7613\(04\)00050-0](https://doi.org/10.1016/S1074-7613(04)00050-0); pmid: [15030776](https://pubmed.ncbi.nlm.nih.gov/15030776/)
29. J. M. Taube *et al.*, Colocalization of inflammatory response with B7-H1 expression in human melanocytic lesions supports an adaptive resistance mechanism of immune escape. *Sci. Transl. Med.* **4**, 127ra37 (2012). doi: [10.1126/scitranslmed.3003689](https://doi.org/10.1126/scitranslmed.3003689); pmid: [22461641](https://pubmed.ncbi.nlm.nih.gov/22461641/)
30. P. C. Tumeh *et al.*, PD-1 blockade induces responses by inhibiting adaptive immune resistance. *Nature* **515**, 568–571 (2014). doi: [10.1038/nature13954](https://doi.org/10.1038/nature13954); pmid: [25428505](https://pubmed.ncbi.nlm.nih.gov/25428505/)
31. M. L. Broz *et al.*, Dissecting the tumor myeloid compartment reveals rare activating antigen-presenting cells critical for T cell immunity. *Cancer Cell* **26**, 638–652 (2014). doi: [10.1016/j.ccr.2014.09.007](https://doi.org/10.1016/j.ccr.2014.09.007); pmid: [25446897](https://pubmed.ncbi.nlm.nih.gov/25446897/)
32. C. S. Garriss *et al.*, Successful anti-PD-1 cancer immunotherapy requires T cell-dendritic cell crosstalk involving the cytokines IFN- γ and IL-12. *Immunity* **49**, 1148–1161.e7 (2018). doi: [10.1016/j.immuni.2018.09.024](https://doi.org/10.1016/j.immuni.2018.09.024); pmid: [30552023](https://pubmed.ncbi.nlm.nih.gov/30552023/)
33. K. C. Barry *et al.*, A natural killer-dendritic cell axis defines checkpoint therapy-responsive tumor microenvironments. *Nat. Med.* **24**, 1178–1191 (2018). doi: [10.1038/s41591-018-0085-8](https://doi.org/10.1038/s41591-018-0085-8); pmid: [29942093](https://pubmed.ncbi.nlm.nih.gov/29942093/)
34. I. Siddiqui *et al.*, Intratumoral Tcf1⁺PD-1⁺CD8⁺ T cells with stem-like properties promote tumor control in response to vaccination and checkpoint blockade immunotherapy. *Immunity* **50**, 195–211.e10 (2019). doi: [10.1016/j.immuni.2018.12.021](https://doi.org/10.1016/j.immuni.2018.12.021); pmid: [30635237](https://pubmed.ncbi.nlm.nih.gov/30635237/)
35. M. V. Goldberg *et al.*, Role of PD-1 and its ligand, B7-H1, in early fate decisions of CD8 T cells. *Blood* **110**, 186–192 (2007). doi: [10.1182/blood-2006-12-062422](https://doi.org/10.1182/blood-2006-12-062422); pmid: [17392506](https://pubmed.ncbi.nlm.nih.gov/17392506/)
36. F. Tsuchida *et al.*, Interaction between B7-H1 and PD-1 determines initiation and reversal of T-cell anergy. *Blood* **110**, 180–185 (2007). doi: [10.1182/blood-2006-11-060087](https://doi.org/10.1182/blood-2006-11-060087); pmid: [17289811](https://pubmed.ncbi.nlm.nih.gov/17289811/)
37. B. T. Fife *et al.*, Interactions between PD-1 and PD-L1 promote tolerance by blocking the TCR-induced cost signal. *Nat. Immunol.* **10**, 1185–1192 (2009). doi: [10.1038/ni.1790](https://doi.org/10.1038/ni.1790); pmid: [19783989](https://pubmed.ncbi.nlm.nih.gov/19783989/)
38. K. Staveley-O'Carroll *et al.*, Induction of antigen-specific T cell anergy: An early event in the course of tumor progression. *Proc. Natl. Acad. Sci. U.S.A.* **95**, 1178–1183 (1998). doi: [10.1073/pnas.95.3.1178](https://doi.org/10.1073/pnas.95.3.1178); pmid: [9448305](https://pubmed.ncbi.nlm.nih.gov/9448305/)
39. E. W. Roberts *et al.*, Critical role for CD103(+) /CD141(+) dendritic cells bearing CCR7 for tumor antigen trafficking and priming of T cell immunity in melanoma. *Cancer Cell* **30**, 324–336 (2016). doi: [10.1016/j.ccr.2016.06.003](https://doi.org/10.1016/j.ccr.2016.06.003); pmid: [27424807](https://pubmed.ncbi.nlm.nih.gov/27424807/)
40. H. Salmon *et al.*, Expansion and activation of CD103(+) dendritic cell progenitors at the tumor site enhances tumor responses to therapeutic PD-L1 and BRAF inhibition. *Immunity* **44**, 924–938 (2016). doi: [10.1016/j.immuni.2016.03.012](https://doi.org/10.1016/j.immuni.2016.03.012); pmid: [27096321](https://pubmed.ncbi.nlm.nih.gov/27096321/)
41. J. Liu *et al.*, Batf3⁺ DCs and type I IFN are critical for the efficacy of neoadjuvant cancer immunotherapy. *Oncotarget* **8**, e1546068 (2018). doi: [10.1080/2162402X.2018.1546068](https://doi.org/10.1080/2162402X.2018.1546068); pmid: [30713806](https://pubmed.ncbi.nlm.nih.gov/30713806/)
42. M. F. Franssen *et al.*, Tumor-draining lymph nodes are pivotal in PD-1/PD-L1 checkpoint therapy. *JCI Insight* **3**, e124507 (2018). doi: [10.1172/jci.insight.124507](https://doi.org/10.1172/jci.insight.124507); pmid: [30518694](https://pubmed.ncbi.nlm.nih.gov/30518694/)
43. S. Thangada *et al.*, Cell-surface residence of sphingosine 1-phosphate receptor 1 on lymphocytes determines lymphocyte egress kinetics. *J. Exp. Med.* **207**, 1475–1483 (2010). doi: [10.1084/jem.20091343](https://doi.org/10.1084/jem.20091343); pmid: [20584883](https://pubmed.ncbi.nlm.nih.gov/20584883/)
44. K. E. Yost *et al.*, Clonal replacement of tumor-specific T cells following PD-1 blockade. *Nat. Med.* **25**, 1251–1259 (2019). doi: [10.1038/s41591-019-0522-3](https://doi.org/10.1038/s41591-019-0522-3); pmid: [31359002](https://pubmed.ncbi.nlm.nih.gov/31359002/)
45. P. M. Forde *et al.*, Neoadjuvant PD-1 blockade in resectable lung cancer. *N. Engl. J. Med.* **378**, 1976–1986 (2018). doi: [10.1056/NEJMoa1716078](https://doi.org/10.1056/NEJMoa1716078); pmid: [29658848](https://pubmed.ncbi.nlm.nih.gov/29658848/)
46. A. O. Kamphorst *et al.*, Rescue of exhausted CD8 T cells by PD-1-targeted therapies is CD28-dependent. *Science* **355**, 1423–1427 (2017). doi: [10.1126/science.aaf0683](https://doi.org/10.1126/science.aaf0683); pmid: [28280249](https://pubmed.ncbi.nlm.nih.gov/28280249/)
47. A. Memarnejad *et al.*, PD-1 blockade promotes epitope spreading in antitumor CD8⁺ T cell responses by preventing fratricidal death of subdominant clones to relieve immunodominance. *J. Immunol.* **199**, 3348–3359 (2017). doi: [10.4049/jimmunol.1700643](https://doi.org/10.4049/jimmunol.1700643); pmid: [28939757](https://pubmed.ncbi.nlm.nih.gov/28939757/)
48. J. Zhang *et al.*, Compartmental analysis of T cell clonal dynamics as a function of pathologic response to neoadjuvant PD-1 blockade in resectable non-small cell lung cancer. *Clin. Cancer Res.* clincanres.2931.2019; Epub ahead of print (2019). doi: [10.1158/1078-0432.CCR-19-2931](https://doi.org/10.1158/1078-0432.CCR-19-2931); pmid: [31754049](https://pubmed.ncbi.nlm.nih.gov/31754049/)
49. R. N. Amaria *et al.*, Neoadjuvant immune checkpoint blockade in high-risk resectable melanoma. *Nat. Med.* **24**, 1649–1654 (2018). doi: [10.1038/s41591-018-0197-1](https://doi.org/10.1038/s41591-018-0197-1); pmid: [30297909](https://pubmed.ncbi.nlm.nih.gov/30297909/)
50. C. U. Blank *et al.*, Neoadjuvant versus adjuvant ipilimumab plus nivolumab in macroscopic stage III melanoma. *Nat. Med.* **24**, 1655–1661 (2018). doi: [10.1038/s41591-018-0198-0](https://doi.org/10.1038/s41591-018-0198-0); pmid: [30297911](https://pubmed.ncbi.nlm.nih.gov/30297911/)
51. A. C. Huang *et al.*, A single dose of neoadjuvant PD-1 blockade predicts clinical outcomes in resectable melanoma. *Nat. Med.* **25**, 454–461 (2019). doi: [10.1038/s41591-019-0357-y](https://doi.org/10.1038/s41591-019-0357-y); pmid: [30804515](https://pubmed.ncbi.nlm.nih.gov/30804515/)
52. E. A. Rozeman *et al.*, Identification of the optimal combination dosing schedule of neoadjuvant ipilimumab plus nivolumab in macroscopic stage III melanoma (OPACIN-neo): A multicentre, phase 2, randomised, controlled trial. *Lancet Oncol.* **20**, 948–960 (2019). doi: [10.1016/S1470-2045\(19\)30151-2](https://doi.org/10.1016/S1470-2045(19)30151-2); pmid: [31160251](https://pubmed.ncbi.nlm.nih.gov/31160251/)
53. J. Larkin *et al.*, Combined nivolumab and ipilimumab or monotherapy in untreated melanoma. *N. Engl. J. Med.* **373**, 23–34 (2015). doi: [10.1056/NEJMoa1504030](https://doi.org/10.1056/NEJMoa1504030); pmid: [26027431](https://pubmed.ncbi.nlm.nih.gov/26027431/)
54. A. Necchi *et al.*, Pembrolizumab as neoadjuvant therapy before radical cystectomy in patients with muscle-invasive urothelial bladder carcinoma (PURE-01): An open-label, single-arm, phase II study. *J. Clin. Oncol.* **36**, 3353–3360 (2018). doi: [10.1200/JCO.18.01148](https://doi.org/10.1200/JCO.18.01148); pmid: [30343614](https://pubmed.ncbi.nlm.nih.gov/30343614/)
55. T. F. Cloughesy *et al.*, Neoadjuvant anti-PD-1 immunotherapy promotes a survival benefit with intratumoral and systemic immune responses in recurrent glioblastoma. *Nat. Med.* **25**, 477–486 (2019). doi: [10.1038/s41591-018-0337-7](https://doi.org/10.1038/s41591-018-0337-7); pmid: [30742122](https://pubmed.ncbi.nlm.nih.gov/30742122/)
56. K. A. Schalper *et al.*, Neoadjuvant nivolumab modifies the tumor immune microenvironment in resectable glioblastoma. *Nat. Med.* **25**, 470–476 (2019). doi: [10.1038/s41591-018-0339-5](https://doi.org/10.1038/s41591-018-0339-5); pmid: [30742120](https://pubmed.ncbi.nlm.nih.gov/30742120/)
57. R. N. Amaria *et al.*, Neoadjuvant systemic therapy in melanoma: Recommendations of the International Neoadjuvant Melanoma Consortium. *Lancet Oncol.* **20**, e378–e389 (2019). doi: [10.1016/S1470-2045\(19\)30332-8](https://doi.org/10.1016/S1470-2045(19)30332-8); pmid: [31267972](https://pubmed.ncbi.nlm.nih.gov/31267972/)
58. F. Petrelli *et al.*, Correlation of pathological complete response with survival after neoadjuvant chemotherapy in bladder cancer treated with cystectomy: A meta-analysis. *Eur. Urol.* **65**, 350–357 (2014). doi: [10.1016/j.eururo.2013.06.049](https://doi.org/10.1016/j.eururo.2013.06.049); pmid: [23849998](https://pubmed.ncbi.nlm.nih.gov/23849998/)
59. Z. Li *et al.*, Correlation of pathological complete response with survival after neoadjuvant chemotherapy in gastric or gastroesophageal junction cancer treated with radical surgery: A meta-analysis. *PLOS ONE* **13**, e0189294 (2018). doi: [10.1371/journal.pone.0189294](https://doi.org/10.1371/journal.pone.0189294); pmid: [29370182](https://pubmed.ncbi.nlm.nih.gov/29370182/)
60. L. Spring *et al.*, Pathologic complete response after neoadjuvant chemotherapy and long-term outcomes among young women with breast cancer. *J. Natl. Compr. Canc. Netw.* **15**, 1216–1223 (2017). doi: [10.6004/jnccn.2017.0158](https://doi.org/10.6004/jnccn.2017.0158); pmid: [28982747](https://pubmed.ncbi.nlm.nih.gov/28982747/)
61. G. Mouillet *et al.*, Pathologic complete response to preoperative chemotherapy predicts cure in early-stage non-small-cell lung cancer: Combined analysis of two IFCT randomized trials. *J. Thorac. Oncol.* **7**, 841–849 (2012). doi: [10.1097/JTO.0b013e31824c7d92](https://doi.org/10.1097/JTO.0b013e31824c7d92); pmid: [22722786](https://pubmed.ncbi.nlm.nih.gov/22722786/)
62. M. D. Hellmann *et al.*, Pathological response after neoadjuvant chemotherapy in resectable non-small-cell lung cancers: Proposal for the use of major pathological response as a surrogate endpoint. *Lancet Oncol.* **15**, e42–e50 (2014). doi: [10.1016/S1470-2045\(13\)70334-6](https://doi.org/10.1016/S1470-2045(13)70334-6); pmid: [24384493](https://pubmed.ncbi.nlm.nih.gov/24384493/)
63. W. F. Symmans *et al.*, Measurement of residual breast cancer burden to predict survival after neoadjuvant chemotherapy. *J. Clin. Oncol.* **25**, 4414–4422 (2007). doi: [10.1200/JCO.2007.10.6823](https://doi.org/10.1200/JCO.2007.10.6823); pmid: [17785706](https://pubmed.ncbi.nlm.nih.gov/17785706/)
64. M. T. Tetzlaff *et al.*, Pathological assessment of resection specimens after neoadjuvant therapy for metastatic melanoma. *Ann. Oncol.* **29**, 1861–1868 (2018). doi: [10.1093/annonc/mdy226](https://doi.org/10.1093/annonc/mdy226); pmid: [29945191](https://pubmed.ncbi.nlm.nih.gov/29945191/)
65. Y. Qu *et al.*, Pathologic assessment after neoadjuvant chemotherapy for NSCLC: Importance and implications of distinguishing adenocarcinoma from squamous cell carcinoma. *J. Thorac. Oncol.* **14**, 482–493 (2019). doi: [10.1016/j.jtho.2018.11.017](https://doi.org/10.1016/j.jtho.2018.11.017); pmid: [30503889](https://pubmed.ncbi.nlm.nih.gov/30503889/)
66. T. R. Cottrell *et al.*, Pathologic features of response to neoadjuvant anti-PD-1 in resected non-small-cell lung carcinoma: A proposal for quantitative immune-related pathologic response criteria (irPRC). *Ann. Oncol.* **29**, 1853–1860 (2018). doi: [10.1093/annonc/mdy218](https://doi.org/10.1093/annonc/mdy218); pmid: [29982279](https://pubmed.ncbi.nlm.nih.gov/29982279/)
67. J. E. Stein *et al.*, Pan-tumor pathologic scoring of response to PD-(L)1 blockade. *Clin. Cancer Res.* 10.1158/1078-0432.CCR-19-2379 (2019). doi: [10.1158/1078-0432.CCR-19-2379](https://doi.org/10.1158/1078-0432.CCR-19-2379); pmid: [31672770](https://pubmed.ncbi.nlm.nih.gov/31672770/)
68. S. L. Topalian *et al.*, Nivolumab (Nivo) as neoadjuvant therapy in patients with resectable Merkel cell carcinoma (MCC) in CheckMate 358. *J. Clin. Oncol.* **36**, 9505–9505 (2018). doi: [10.1200/JCO.2018.36.15_suppl.9505](https://doi.org/10.1200/JCO.2018.36.15_suppl.9505)
69. C. Sautès-Fridman, F. Petitprez, J. Calderaro, W. H. Fridman, Tertiary lymphoid structures in the era of cancer immunotherapy. *Nat. Rev. Cancer* **19**, 307–325 (2019). doi: [10.1038/s41568-019-0144-6](https://doi.org/10.1038/s41568-019-0144-6); pmid: [31092904](https://pubmed.ncbi.nlm.nih.gov/31092904/)
70. T. Okazaki, A. Maeda, H. Nishimura, T. Kurosaki, T. Honjo, PD-1 immunoreceptor inhibits B cell receptor-mediated signaling by recruiting src homology 2-domain-containing tyrosine phosphatase 2 to phosphotyrosine. *Proc. Natl. Acad. Sci. U.S.A.* **98**, 13866–13871 (2001). doi: [10.1073/pnas.231486598](https://doi.org/10.1073/pnas.231486598); pmid: [11698646](https://pubmed.ncbi.nlm.nih.gov/11698646/)
71. W. Damsky *et al.*, B cell depletion or absence does not impede anti-tumor activity of PD-1 inhibitors. *J. Immunother. Cancer* **7**, 153 (2019). doi: [10.1186/s40425-019-0613-1](https://doi.org/10.1186/s40425-019-0613-1); pmid: [31200747](https://pubmed.ncbi.nlm.nih.gov/31200747/)
72. J. Griss *et al.*, B cells sustain inflammation and predict response to immune checkpoint blockade in human melanoma. *Nat. Commun.* **10**, 4186 (2019). doi: [10.1038/s41467-019-12160-2](https://doi.org/10.1038/s41467-019-12160-2); pmid: [31519915](https://pubmed.ncbi.nlm.nih.gov/31519915/)
73. J. E. Stein *et al.*, Major pathologic response on biopsy (MPRbx) in patients with advanced melanoma treated with anti-PD-1: Evidence for an early, on-therapy biomarker of response. *Ann. Oncol.* **30**, 589–596 (2019). doi: [10.1093/annonc/mdz019](https://doi.org/10.1093/annonc/mdz019); pmid: [30689736](https://pubmed.ncbi.nlm.nih.gov/30689736/)
74. E. Z. Keung, E. U. Ukponmwan, A. P. Cogdill, J. A. Wargo, The rationale and emerging use of neoadjuvant immune checkpoint blockade for solid malignancies. *Ann. Surg. Oncol.* **25**, 1814–1827 (2018). doi: [10.1245/s10434-018-6379-8](https://doi.org/10.1245/s10434-018-6379-8); pmid: [29500764](https://pubmed.ncbi.nlm.nih.gov/29500764/)
75. J. S. O'Donnell, E. P. Hoefsmit, M. J. Smyth, C. U. Blank, M. W. L. Teng, The promise of neoadjuvant immunotherapy and surgery for cancer treatment. *Clin. Cancer Res.* **25**, 5743–5751 (2019). doi: [10.1158/1078-0432.CCR-18-2641](https://doi.org/10.1158/1078-0432.CCR-18-2641); pmid: [31040150](https://pubmed.ncbi.nlm.nih.gov/31040150/)
76. R. Nanda *et al.*, Pembrolizumab plus standard neoadjuvant therapy for high-risk breast cancer (BC): Results from I-SPY 2. *J. Clin. Oncol.* **35**, 506–506 (2017). doi: [10.1200/JCO.2017.35.15_suppl.506](https://doi.org/10.1200/JCO.2017.35.15_suppl.506)
77. P. Schmid *et al.*, KEYNOTE-522: Phase III study of pembrolizumab (pembro) + chemotherapy (chemo) vs placebo

- (pbo) + chemo as neoadjuvant treatment, followed by pembrolizumab (pbo) as adjuvant treatment for early triple-negative breast cancer (TNBC). *Ann. Oncol.* **30**, v851–v934 (2019). doi: [10.1093/annonc/mdz394.003](https://doi.org/10.1093/annonc/mdz394.003)
78. M. Provencio-Pulla *et al.*, Neoadjuvant chemo/immunotherapy for the treatment of stages IIIA resectable non-small cell lung cancer (NSCLC): A phase II multicenter exploratory study—NADIM study-SLCG. *J. Clin. Oncol.* **36**, 8521 (2018). doi: [10.1200/JCO.2018.36.15_suppl.8521](https://doi.org/10.1200/JCO.2018.36.15_suppl.8521)
 79. T. M. Prowell, J. A. Beaver, R. Pazdur, Residual disease after neoadjuvant therapy—developing drugs for high-risk early breast cancer. *N. Engl. J. Med.* **380**, 612–615 (2019). doi: [10.1056/NEJMp1900079](https://doi.org/10.1056/NEJMp1900079); pmid: [30763188](https://pubmed.ncbi.nlm.nih.gov/30763188/)
 80. R. Sun *et al.*, A radiomics approach to assess tumour-infiltrating CD8 cells and response to anti-PD-1 or anti-PD-L1 immunotherapy: An imaging biomarker, retrospective multicohort study. *Lancet Oncol.* **19**, 1180–1191 (2018). doi: [10.1016/S1470-2045\(18\)30413-3](https://doi.org/10.1016/S1470-2045(18)30413-3); pmid: [30120041](https://pubmed.ncbi.nlm.nih.gov/30120041/)
 81. S. Trebeschi *et al.*, Predicting response to cancer immunotherapy using non-invasive radiomic biomarkers. *Ann. Oncol.* **30**, 998–1004 (2019). doi: [10.1093/annonc/mdz108](https://doi.org/10.1093/annonc/mdz108); pmid: [30895304](https://pubmed.ncbi.nlm.nih.gov/30895304/)
 82. M. N. McCracken, R. Tavaré, O. N. Witte, A. M. Wu, Advances in PET detection of the antitumor T cell response. *Adv. Immunol.* **131**, 187–231 (2016). doi: [10.1016/bs.ai.2016.02.004](https://doi.org/10.1016/bs.ai.2016.02.004); pmid: [27235684](https://pubmed.ncbi.nlm.nih.gov/27235684/)
 83. E. A. Eisenhauer *et al.*, New response evaluation criteria in solid tumours: Revised RECIST guideline (version 1.1). *Eur. J. Cancer* **45**, 228–247 (2009). doi: [10.1016/j.ejca.2008.10.026](https://doi.org/10.1016/j.ejca.2008.10.026); pmid: [19097774](https://pubmed.ncbi.nlm.nih.gov/19097774/)
 84. Y. Simoni *et al.*, Bystander CD8⁺ T cells are abundant and phenotypically distinct in human tumour infiltrates. *Nature* **557**, 575–579 (2018). doi: [10.1038/s41586-018-0130-2](https://doi.org/10.1038/s41586-018-0130-2); pmid: [29769722](https://pubmed.ncbi.nlm.nih.gov/29769722/)

ACKNOWLEDGMENTS

The authors thank L. Beswick (Johns Hopkins University School of Medicine) for editorial assistance. **Funding:** We gratefully acknowledge research support from NCI R01 CA142779 (to S.L.T., J.M.T., and D.M.P.), the Cancer Research Institute/Stand Up To Cancer-Immunology Translational Cancer Research Grant AACR-DT1012 (to D.M.P.), Bristol-Myers Squibb (S.L.T., J.M.T., and D.M.P.), the Barney Family Foundation (S.L.T.), Moving for Melanoma of Delaware (S.L.T.), the Laverna Hahn Charitable Trust (S.L.T.), the Melanoma Research Alliance (J.M.T.), the Harry J. Lloyd Charitable Trust (J.M.T.), the Emerson Collective

Foundation (J.M.T.), the Mark Foundation for Cancer Research (J.M.T. and D.M.P.), and the Johns Hopkins Bloomberg-Kimmel Institute for Cancer Immunotherapy (S.L.T., J.M.T., and D.M.P.). **Authors' contributions:** All authors participated in the writing and final approval of this article. **Competing interests:** D.M.P. and S.L.T. report stock and other ownership interests from Aduro Biotech, Compugen, DNAtrix, Dragonfly Therapeutics, Ervaxx, Five Prime Therapeutics, FLX Bio, Jounce Therapeutics, Potenza Therapeutics, Tizona Therapeutics, and WindMIL; consulting or advisory role with AbbVie, Amgen, Bayer, Compugen, DNAtrix, Dragonfly Therapeutics, Dynavax, Ervaxx, Five Prime Therapeutics, FLX Bio, Immunocore, Immunomic Therapeutics, Janssen Oncology, MedImmune, Merck, Tizona Therapeutics, and Wind MIL; research funding from Bristol-Myers Squibb, Compugen, and Potenza Therapeutics; patents, royalties, and other intellectual property from Aduro Biotech, Bristol-Myers Squibb, and Immunomic Therapeutics; and travel, accommodations, and expenses from Bristol-Myers Squibb and Five Prime Therapeutics. J.M.T. reports receiving equipment and reagents from Akoya Biosciences; grants and personal fees from Bristol-Myers Squibb; and personal fees from Merck, Astra Zeneca, and Amgen.

10.1126/science.aax0182

RESEARCH ARTICLE SUMMARY

NEUROSCIENCE

Monosomes actively translate synaptic mRNAs in neuronal processes

Anne Biever*, Caspar Glock*, Georgi Tushev, Elena Ciirdaeva, Tamas Dalmay, Julian D. Langer, Erin M. Schuman†

INTRODUCTION: RNA sequencing and in situ hybridization have revealed the presence of an unexpectedly high number of RNA species in neuronal dendrites and axons, and many studies have documented the local translation of proteins in these compartments. During messenger RNA (mRNA) translation, multiple ribosomes can occupy an individual mRNA (a complex called a polysome), resulting in the generation of multiple copies of the encoded protein. Polysomes, usually recognized in electron micrographs as a cluster of three or more ribosomes, have been detected in neuronal dendrites but are surprisingly infrequent given the diversity of mRNAs present in dendrites and axons. In neuronal processes, the features and mechanisms of translation have not been explored in detail, in part because of the relative inaccessibility of dendrites and axons. In this study, we investigated how a diverse set of neuronal proteins might be synthesized from

a limited population of polysomes present in small synaptic volumes.

RATIONALE: To accommodate their complex morphology, neurons localize mRNAs and ribosomes near synapses to produce proteins locally. Yet a relative scarcity of polysomes (considered the active sites of translation) detected in electron micrographs of neuronal processes has suggested a rather limited capacity for local protein synthesis. To visualize the capacity for local protein production in vivo, we profiled actively translating mRNAs in rodent hippocampal neuronal processes. To access neuronal compartments, we microdissected the neuropil and somata layer from the CA1 region of hippocampal slices, generating samples enriched in dendrites and/or axons versus cell bodies. Polysome profiling of microdissected regions was used to determine the association of axonal and/or dendritic and somatic transcripts, respectively, with mono-

somes or polysomes. Ribosome footprinting was then used to assess the translational activity of monosomes (single ribosomes) and polysomes. Bioinformatic analyses were used to determine the features of monosome-preferring transcripts as well as the families of protein groups that were encoded by monosome-preferring transcripts. We also compared the monosome-to-polysome (M/P) preference of transcripts between the somata and neuropil. To estimate the abundance of proteins encoded by monosome- and polysome-preferring transcripts, we measured protein levels in the neuropil by using mass spectrometry-based proteomics.

RESULTS: In the adult rodent brain, we detected substantial levels of ongoing protein synthesis in the synaptic neuropil (a region

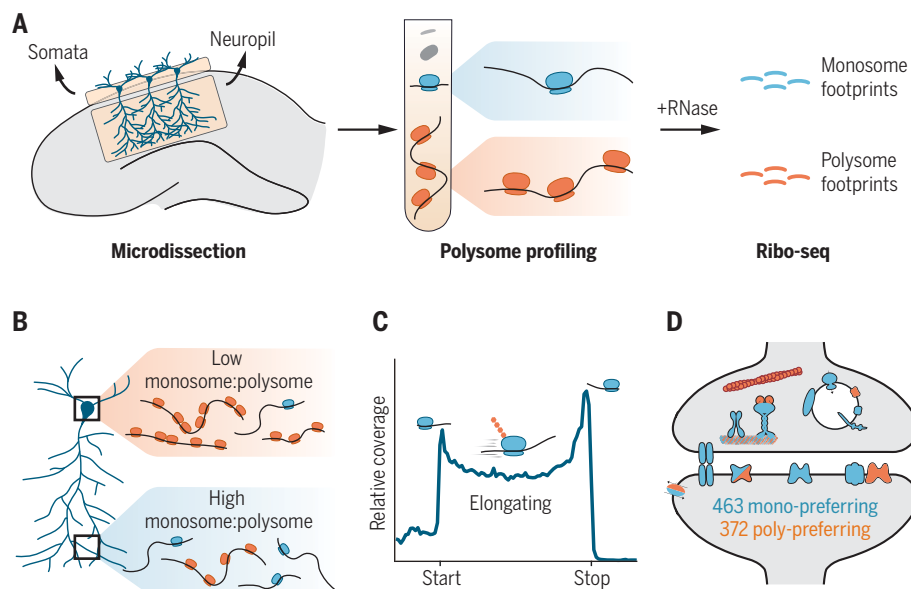
ON OUR WEBSITE

Read the full article at <http://dx.doi.org/10.1126/science.aay4991>

enriched in neuronal axons and dendrites) in vivo and provide direct evidence for the preferential translation of a high number of both pre and postsynaptic transcripts by mono-

somes. The monosomes were in the process of active polypeptide elongation in dendrites and axons. Most transcripts exhibited a similar M/P preference in both somata and neuropil, suggesting that ribosome occupancy is often an intrinsic feature of the transcript. Several transcripts exhibited a preference for monosomes or polysomes that switched depending on the compartment; these mRNAs encoded some synaptic plasticity-related proteins. Overall, neuropil transcripts exhibited a preference for monosome translation. Monosome-preferring transcripts encoded a full range of low- to high-abundance proteins in the neuropil.

CONCLUSION: In this study, we investigated the translational landscape in neuronal processes and identified local translation on 80S monosomes as an important source of synaptic proteins. Neuropil-localized transcripts exhibited a greater monosome preference than somatic transcripts, potentially allowing for the production of a more diverse set of proteins from a limited pool of available ribosomes at synapses. This finding thus bridges the gap between the relative paucity of visualized translational machinery in neuronal processes and actual measurements of local translation. Given the spatial limitations within dendritic spines and axonal boutons, synaptic activity could also regulate monosome translation to diversify the local proteome with spatial and temporal precision. ■



Monosomes translate synaptic mRNAs in the neuropil. (A) Polysome profiling followed by monosome (cyan) or polysome (orange) footprinting (Ribo-seq) in microdissected somata (enriched in cell bodies) or neuropil (enriched in dendrites and/or axons) from rodent brain slices. (B) Transcripts localized to dendrites and/or axons were predominantly associated with monosomes. (C) Monosomes were in the process of active polypeptide elongation. (D) Neuropil monosome-preferring transcripts (cyan) often encoded synaptic proteins.

The list of author affiliations is available in the full article online.

*These authors contributed equally to this work.

†Corresponding author. Email: erin.schuman@brain.mpg.de
Cite this article as A. Biever *et al.*, *Science* 367, eaay4991 (2020). DOI: 10.1126/science.aay4991

RESEARCH ARTICLE

NEUROSCIENCE

Monosomes actively translate synaptic mRNAs in neuronal processes

Anne Bieber^{1*}, Caspar Glock^{1*}, Georgi Tushev¹, Elena Ciirdaeva¹, Tamas Dalmay¹, Julian D. Langer^{1,2}, Erin M. Schuman^{1†}

To accommodate their complex morphology, neurons localize messenger RNAs (mRNAs) and ribosomes near synapses to produce proteins locally. However, a relative paucity of polysomes (considered the active sites of translation) detected in electron micrographs of neuronal processes has suggested a limited capacity for local protein synthesis. In this study, we used polysome profiling together with ribosome footprinting of microdissected rodent synaptic regions to reveal a surprisingly high number of dendritic and/or axonal transcripts preferentially associated with monosomes (single ribosomes). Furthermore, the neuronal monosomes were in the process of active protein synthesis. Most mRNAs showed a similar translational status in the cell bodies and neurites, but some transcripts exhibited differential ribosome occupancy in the compartments. Monosome-preferring transcripts often encoded high-abundance synaptic proteins. Thus, monosome translation contributes to the local neuronal proteome.

RNA sequencing (RNA-seq) and in situ hybridization have revealed the presence of an unexpectedly high number of RNA species in the CA1 neuropil (a region enriched in neuronal axons and dendrites) (1, 2), and many studies have documented the local translation of proteins in dendrites and/or axons (3–5). During messenger RNA (mRNA) translation, multiple ribosomes can occupy an individual mRNA (a complex known as a polysome), resulting in the generation of multiple copies of the encoded protein. Polysomes, usually recognized in electron micrographs as a cluster comprising three or more ribosomes, have been detected in neuronal dendrites (6, 7). Given the diversity of mRNAs present, polysomes are relatively infrequent in dendrites and axons [e.g., <0.5 polysomes per micrometer (7)]. In neuronal processes, the features and mechanisms of translation have not been explored in detail, partly because of the relative inaccessibility of the dendrites and axons in the neuropil. In particular, it is not clear how diverse proteins might be synthesized from a limited population of polysomes present in small synaptic volumes.

Monosomes are the predominant ribosome population in neuronal processes

To visualize the capacity for protein synthesis in the neuropil in vivo, we labeled the de novo proteome using puromycylation (8). We infused puromycin directly into the lateral ventricle of mice, waited 10 min, and then visualized newly synthesized proteins in hippocampal

pyramidal neurons by coimmunofluorescence labeling of nascent protein (anti-puromycin antibody) and CA1 pyramidal neurons (anti-wolframin antibody; Wfs1). As expected, we detected an intense nascent protein signal in the somata layer (stratum pyramidale), comprising the cell bodies of pyramidal neurons (Fig. 1A and fig. S1A). Additionally, strong nascent protein was evident throughout the dendrites of pyramidal neurons in the neuropil (stratum radiatum) (Fig. 1A and fig. S1A). Co-injection of a protein synthesis inhibitor (anisomycin) abolished the nascent protein signal. Because of the very short window of metabolic labeling, these data indicate that protein synthesis also occurs in dendrites in vivo.

Polysome profiling is a biochemical fractionation method that allows one to examine the degree of ribosome association of a transcript—that is, association with a monosome (single ribosome) or a polysome (multiple ribosomes loaded on an mRNA) (9). Using polysome profiling, we examined the ribosome occupancy of transcripts in the hippocampus by comparing somata and neuropils that were microdissected from ex vivo adult rat hippocampal slices (area CA1) (Fig. 1B). Immunoblot analysis confirmed that the microdissected neuropil was strongly de-enriched for neuronal cell bodies (fig. S1, B and C). We obtained a typical polysome profile with two ribosomal subunit peaks (40S and 60S), one monosome (single ribosome, 80S) peak, and multiple polysome peaks. No signs of altered polysome integrity (such as a shift toward lower ribosome occupancy) were observed. We assessed the relative association of transcripts with monosomes or polysomes [monosome/polysome

(M/P) ratio; see Materials and methods section] in the somata and neuropil by measuring the area under the curve (AUC) of the corresponding absorbance peaks. Although a large proportion of mRNAs was associated with polysomes in the somata (Fig. 1C), the M/P ratio was more than twice as high in the neuropil (Fig. 1, D and E). The increased M/P ratio observed in the neuropil resulted from a decrease in polysome abundance when compared to the somata (fig. S1D). As expected, the M/P ratios in whole (nonmicrodissected) hippocampi (0.56 ± 0.04), comprising cell bodies and neuronal processes, occupied a position between the values obtained for the somata (0.30 ± 0.03) and neuropil (0.76 ± 0.19) (fig. S1E and Fig. 1, C and D), confirming that the microdissection procedure did not disrupt polysome stability.

To confirm the difference in the M/P ratios between somata and neuronal projections, we used a well-established in vitro system to enrich for cell bodies and neuronal processes (10). Rat neurons were cultured on microporous membranes, allowing the dendrites and axons (but not cell bodies) to extend to the area beneath the membrane (Fig. 1F and fig. S1, F to I). After 21 days in vitro, we harvested the cell bodies and dendrites and/or axons separately and again conducted polysome profiling. Consistent with the microdissected slice data, the M/P ratio was significantly higher in neurites than in cell bodies, owing to an increase and a decrease in the number of monosomes and polysomes in the neurite layer, respectively (Fig. 1, G to I, and fig. S1J).

Monosomes actively elongate transcripts in the synaptic neuropil

In mammalian cells, polysomes are thought to represent the translationally active ribosome population (11–13). By contrast, monosomes, reflecting single ribosomes detected on transcripts, are presumed to represent the isolation of protein synthesis initiation and termination events but not active protein synthesis (i.e., the elongation of the polypeptide chain) (11–13). We compared the translational status of somatic or neuropil-localized monosomes and polysomes by using ribosome profiling to precisely map the position of the ribosome(s) along the mRNA (14) (Fig. 2A). Monosomal or polysomal fractions from the rat neuropil or somata were collected; the purity of fractionation was independently demonstrated by the lack of polysome or monosome peaks on sucrose gradient profiles from isolated monosomal and polysomal fractions, respectively (fig. S2). After polysome profiling, ribosomal fractions were digested and monosome or polysome footprint libraries were prepared. After sequencing three replicates of monosome and polysome footprint libraries and aligning the reads to a reference genome (alignment

¹Max Planck Institute for Brain Research, Frankfurt, Germany.

²Max Planck Institute of Biophysics, Frankfurt, Germany.

*These authors contributed equally to this work.

†Corresponding author. Email: erin.schuman@brain.mpg.de

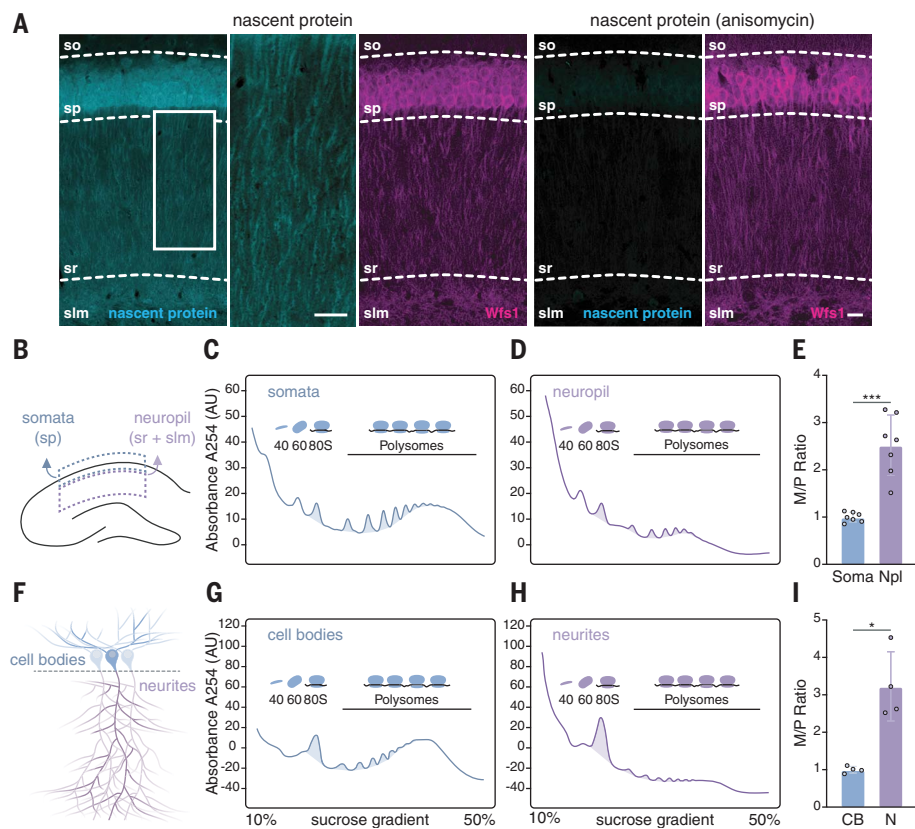


Fig. 1. Monosomes are the major ribosome population in neuronal processes. (A) Immunofluorescence labeling of the nascent protein metabolic label (cyan) and the CA1 pyramidal neuron marker Wfs1 (purple) in hippocampal sections from mice that received a brief infusion of puromycin without (left) or with the protein synthesis inhibitor anisomycin (right) into the lateral ventricle. Scale bar, 20 μ m. A higher-magnification image of the nascent protein signal in the boxed dendritic region is shown. Scale bar, 50 μ m. so, stratum oriens; sp, stratum pyramidale; sr, stratum radiatum; slm, stratum lacunosum moleculare. (B) Scheme of a hippocampal slice showing the regions (somata and neuropil) that were microdissected for subsequent polysome profiling. Representative polysome profiles (C and D) and comparison of the monosome/polysome (M/P) ratios (E) of the microdissected somata (Soma, blue; M/P = 0.30 ± 0.03) or neuropil (Npl, purple; M/P = 0.76 ± 0.19) ($n = 7$ biological replicates). Areas measured to calculate the M/P ratios are shaded (see Materials and methods). *** $P \leq 0.001$, Welch's t test. AU, arbitrary units. (F) Scheme showing cortical neurons grown on a microporous membrane enabling the separation of cell bodies and neurites for polysome profiling. Representative polysome profiles (G and H) and M/P ratios (I) of the cell body (CB, blue) or neurite layer (N, purple) ($n = 4$ replicates). Areas measured to calculate the M/P ratios are shaded. * $P \leq 0.05$, Welch's t test. Error bars in (E) and (I) indicate SDs.

statistics shown in fig. S3A), the classical ribosome profiling quality metrics were assessed (fig. S3). As expected, the monosome and polysome footprints peaked at a length of ~31 nucleotides (representing the area occupied by the ribosome; fig. S3, B and C) and exhibited a depletion of read densities in the untranslated regions (UTRs) and introns (fig. S3, D and E). The ribosome profiling libraries were highly reproducible between replicates, as shown by the very small within-group variance (fig. S3F) and Pearson correlation coefficients >0.95 for the majority of the samples (fig. S3G). The neuropil monosome and polysome translomes also overlapped with the previously published neuropil de novo proteome (15) (fig. S3H).

We examined the positions of the RNA footprints obtained from neuropil monosomes (Fig. 2B) or polysomes (Fig. 2C) across the open reading frame (ORF) of transcripts. Both the monosome and polysome footprint coverages peaked at the 5' ORF (near or at the translation initiation site); monosome footprints decreased more sharply than polysome footprints over the first 25% of the ORF before reaching a plateau. Only the monosome sample exhibited a pronounced enrichment of footprint reads around the stop codon, presumably reflecting the position of terminating ribosomes. This pattern is in good agreement with previously published metagenome analyses of monosome and polysome footprint densities in yeast (16), thus

confirming the purity of isolated monosomal and polysomal fractions. Surprisingly, however, a large fraction of monosome footprints occupied the center of the ORF, demonstrating that the localized monosomes were engaged in peptide elongation. A similar pattern was evident for the monosome (and polysome) footprint coverage in the somata (fig. S4, A and B) and the whole (nonmicrodissected) hippocampus (fig. S4, C and D; representative polysome profile shown in fig. S1E). Thus, the mid-ORF monosome footprints were not a result of altered polysome integrity during the microdissection procedure.

Because the somata and neuropil include neurons as well as glia and interneurons (fig. S5A), we developed a strategy to investigate the translational status of monosomes and polysomes in hippocampal excitatory neurons. We identified the translome (ribosome-associated mRNAs) of select hippocampal excitatory neuron populations by combining RiboTag immunoprecipitation (RiboTag-IP) (17) with RNA-seq (fig. S5, B and C). Using differential expression analysis (18), we identified transcripts enriched in the RiboTag-IP from hippocampi of Camk2Cre::RiboTag mice (fig. S5, D and E) or microdissected somata (fig. S5, D and F) and neuropils (fig. S5, D and G) of Wfs1Cre::RiboTag mice (19). Combining the three datasets, we obtained a comprehensive list of 5069 mRNAs (neuronal transcripts) selectively translated in cell bodies and processes of excitatory hippocampal neurons (fig. S5H). The relative enrichment and de-enrichment of neuronal genes and glia- and/or interneuron-related genes, respectively, were validated using a previously published dataset (fig. S5I) (20). These data were used to obtain a filtered list of neuronal footprint reads in monosome or polysome libraries from the somata and neuropil (Fig. 2D). Again, a significant fraction of neuronal transcripts displayed coverage in the elongating portion of the ORF in the monosome and the polysome samples of both neuropil (fig. S6, A and B) and somata (fig. S6, C and D). The neuropil-derived monosome (Fig. 2E) and polysome (fig. S6E) footprints exhibited three-nucleotide phasing throughout the ORF, reflecting the characteristic codon-by-codon translocation of the ribosome on its mRNA (14). Thus, both monosomes and polysomes contribute to the active elongation of transcripts localized to neuronal processes.

Neuropil monosomes translate synaptic transcripts

To measure the degree to which a neuropil-localized transcript is translated by monosomes or polysomes, we focused on ribosomes that were undergoing elongation but not initiation or termination by using footprints aligned to the center of the ORF (see Materials

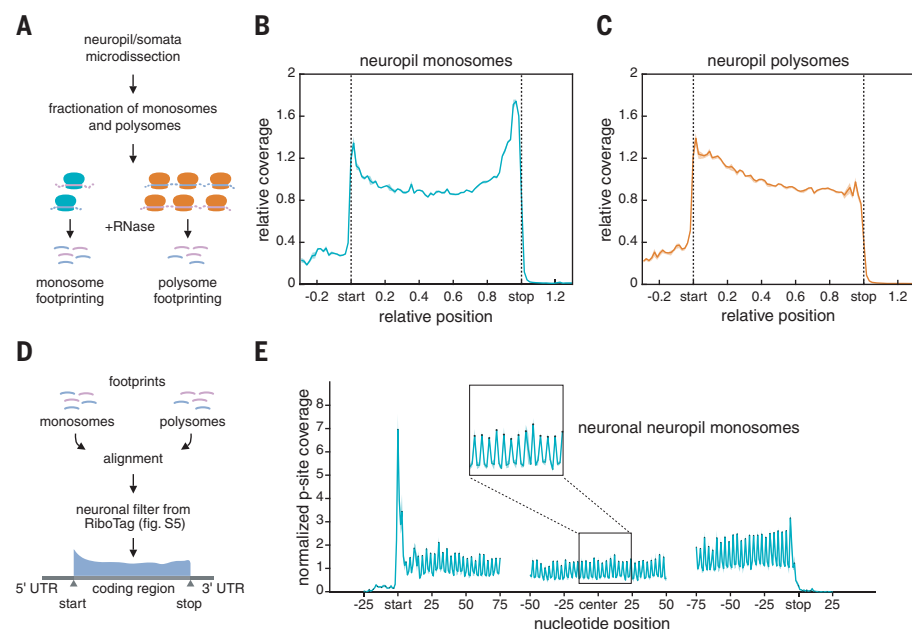


Fig. 2. Neuronal monosomes actively elongate transcripts in the neuropil. (A) Experimental workflow. Somata or neuropil fractions were obtained, monosomes and polysomes were isolated by polysome profiling, and ribosome profiling was performed on isolated fractions. (B and C) Metagene analyses showing the footprint density throughout the transcript ORF in the neuropil monosomes (B) or polysomes (C). The average relative normalized coverage is plotted per nucleotide position, and the standard deviation is shaded ($n = 3$ replicates). Genes were individually normalized. (D) To assess the translational status of neuronal monosomes or polysomes, only reads classified as “neuronal” (fig. S5) were retained for further analysis. (E) Metagene analyses showing the P-site coverage of neuronal transcripts in the neuropil monosome sample. The average normalized coverage is plotted per nucleotide position around the 5' end (start), central portion (center), and 3' end (stop) of the ORF. The standard deviation is shaded ($n = 3$ replicates).

and methods) in the monosome and polysome footprint libraries. Using differential expression analysis (18), we identified localized neuronal transcripts preferentially translated by either monosomes or polysomes. In the neuropil, we found 463 transcripts significantly enriched in the monosome fraction versus 372 transcripts enriched in the polysome fraction (Fig. 3A and table S1). By contrast, a greater number of transcripts exhibited a significant enrichment on polysomes in the somata (fig. S7A and table S1). When we examined the neuropil footprint pattern across individual transcripts, we identified transcripts that displayed increased monosome (e.g., *Kif1a*; Fig. 3B) or polysome (e.g., *Camk2a*; Fig. 3C) footprint coverage throughout the entire ORF. There was also a large proportion of transcripts (e.g., *Slc17a7*; Fig. 3D) that exhibited equal coverage in monosome and polysome footprint libraries.

Footprints from monosome-enriched mRNAs exhibited strong three-nucleotide periodicity, reflecting the stepwise movement of active individual ribosomes during the elongation of this transcript subset (Fig. 3E). During translation elongation, however, ribosomes can pause as a result of local RNA structures, the presence of rare codons, interactions between

nascent chains, or association with trans-regulatory factors (21–24). The predominant association of an mRNA with monosomes could thus result from increased pausing at individual codons when compared with the same mRNA's association with polysomes. To test this for the 463 monosome-enriched transcripts, we computed a pause score by comparing the normalized footprint coverage at individual codons in the monosome and polysome samples (see Materials and methods). We found that most codons did not exhibit significant differences in pausing between the monosome and polysome libraries (Fig. 3F). To further investigate the translational activity status of monosome-preferring transcripts, we used harringtonine (an initiation inhibitor) to analyze a time series of ribosome run-off during elongation (25) in hippocampal cultures. Metagene analysis revealed a progressive loss of ribosomes from the 5' end of monosome-preferring transcripts after the harringtonine treatments (fig. S8). Thus, monosome-preferring transcripts are actively elongated and do not exhibit differential pausing when associated with single or multiple ribosomes.

What transcript properties influence the neuropil M/P preference? We detected a posi-

tive correlation between the neuropil M/P preference and ORF length, 3'UTR folding energy, and 5'UTR length (fig. S9A and table S1). On the other hand, a negative correlation was observed between the M/P ratio and the mean of the typical decoding rate (MTDR) index [an estimate of the elongation efficiency (26)], GC content, codon adaptation index (CAI), and initiation rate (fig. S9A and table S1). We also observed an overrepresentation of upstream ORF-containing transcripts (73 mRNAs) among monosome-enriched genes (fig. S9B). Although a previous study in yeast reported that monosomes occupy nonsense-mediated mRNA decay (NMD) targets (27), no relationship was found between the neuropil M/P preference of transcripts and their likelihood of classification as NMD targets (fig. S9C). The fine-tuning of translation rates may allow for the optimization of the nascent polypeptide folding during protein synthesis (28, 29). We thus explored how the M/P preference related to the structural complexity of the encoded polypeptide. Indeed, an increased number of secondary structures (α helix and β strand) were predicted for monosome-preferring transcripts (fig. S9D). Furthermore, monosome-preferring transcripts encoded proteins displaying longer structural domains (fig. S9E).

To examine whether particular protein function groups are encoded by monosome- versus polysome-preferring transcripts in the neuropil, we used gene ontology (GO) (Fig. 4A; see fig. S7B for the somata). Monosome-preferring transcripts exhibited a more significant association with GO terms such as “synapse,” “vesicle,” or “dendritic tree” than did polysome-preferring transcripts in the neuropil. In accordance with this finding, synaptic genes [SynGO annotation (30)] displayed higher mean M/P ratios compared with nonsynaptic genes (fig. S10, A and B). Polysome-preferring transcripts often encoded proteins involved in actin cytoskeleton remodeling (Fig. 4, A and B). Because functional and morphological changes in synapses rely on the dynamic actin cytoskeleton remodeling (31), polysome translation may be required to supply synapses with high copy numbers of cytoskeletal proteins. Thus, in dendrites and axons, a significant proportion of transcripts important for synaptic function are principally translated by monosomes.

Dissecting neuronal monosome translation

To address whether the M/P preference is intrinsic to the transcript or influenced by its environment (i.e., its subcellular localization), we compared the relative M/P enrichment of each transcript in the neuropil and somata. We observed a high correlation (coefficient of determination $R^2 = 0.6$) between the somata and neuropil M/P ratios, indicating

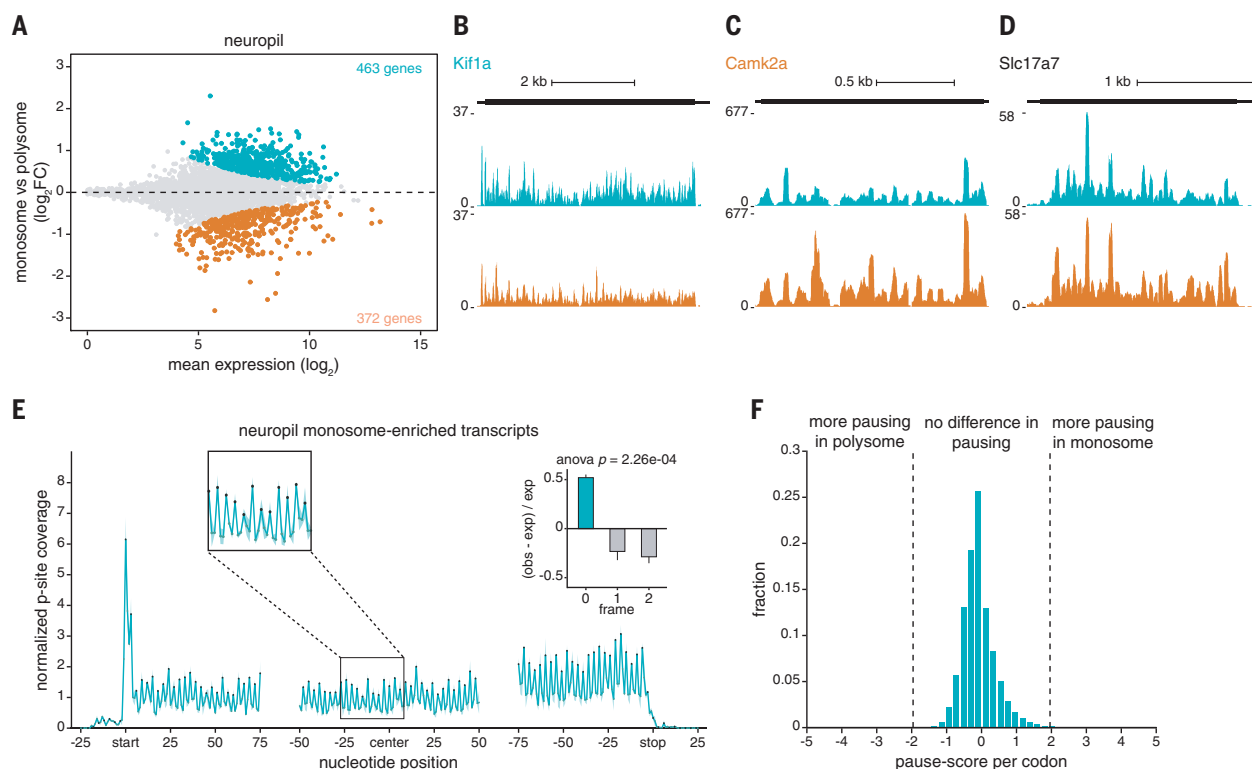


Fig. 3. Monosomes predominate on a subset of transcripts in dendrites and axons. (A) MA plot showing transcripts with significantly enriched monosome (cyan) or polysome (orange) footprint coverage in the central portion of the ORF (region spanning 15 codons from the start site to 5 codons before the stop site). DESeq2 was used for analysis, with a threshold of 0.05 on the adjusted P value (see Materials and methods). Gray dots denote nonenriched transcripts. (B to D) Genome browser views representing the average monosome (top) or polysome (bottom) footprint coverage for three transcripts: *Kif1a* (B), *Camk2a* (C), and *Slc17a7* (D). The y axis indicates the number of normalized reads. (E) Metagenesis analysis showing the monosome P-site coverage of transcripts that exhibit significant monosome enrichment in the neuropil. The average normalized coverage is plotted per nucleotide position

around the 5' end (start), central portion (center), and 3' end (stop) of the ORF. The standard deviation is shaded ($n = 3$ replicates). The inset shows the observed (obs)–to–expected (exp) ratio of the footprint distribution in different reading frames. $P = 2.26 \times 10^{-4}$, ANOVA. (F) A pause score was computed for each codon located in the elongating ORF portion of the 463 monosome-enriched transcripts: pause score (z-score-like) = (normalized footprint coverage in monosome library – normalized footprint coverage in polysome library)/(normalized footprint coverage in polysome library) $^{1/2}$ ($n = 3$ replicates). The graph shows the fraction of codons per pause score. Dashed lines highlight pause score values of ± 1.96 ($P = 0.05$), values between these lines represent codons exhibiting similar coverage in monosome and polysome libraries.

that a large proportion of transcripts prefer the same type of ribosome occupancy in both compartments (Fig. 5A, monosome-enriched in quadrant I or polysome-enriched in quadrant III). An overlap of the genes classified as monosome- or polysome-preferring in the somata (fig. S7A) and neuropil (Fig. 3A) revealed that many but not all genes exhibited a similar preference between compartments (fig. S11, A and B). Using DESeq2 (18), we identified transcripts that exhibited significant differences in the M/P ratio between somata and neuropil (Fig. 5A and table S1). Only a handful of transcripts (e.g., *Arc*; Fig. 5B) exhibited a significantly lower M/P ratio in the neuropil than in the somata (Fig. 5A, purple dots, and Fig. 5C). The majority of transcripts (e.g., *Serpini1*; Fig. 5D) with differential ribosome occupancy between compartments displayed significantly elevated M/P fold changes in the neuropil (Fig. 5A, cyan dots, and Fig. 5E). Overall, we observed a shift

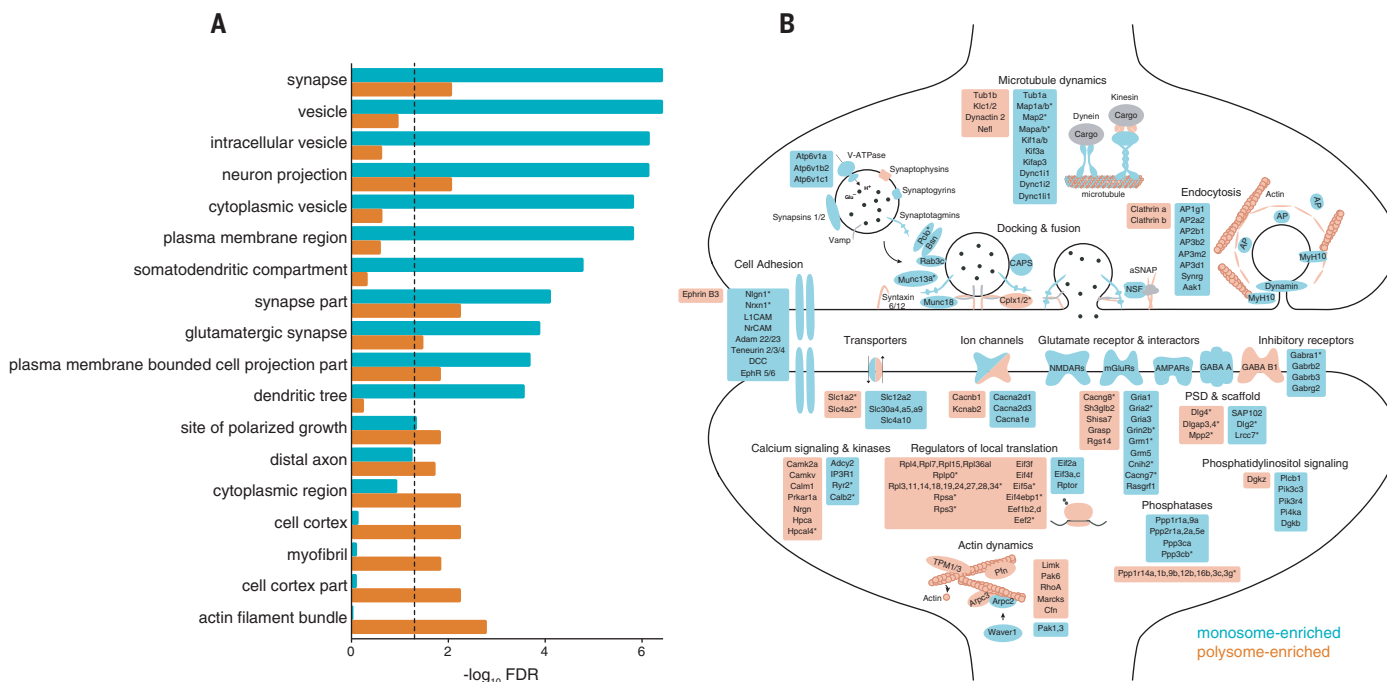
toward a higher monosome preference in the neuropil (Fig. 5F and fig. S11C), which could result, at least in part, from a lower ribosome abundance in the neuropil than in the somata (fig. S12, A and B).

Notably, we also identified some transcripts with opposing M/P ratios between somata and neuropil (i.e., monosome-preferring in one compartment and polysome-preferring in the other), some of which were key regulators of synaptic plasticity (Fig. 5A, quadrants II and IV; fig. S12, C and D; and table S1) (32–41). Thus, neuropil-localized transcripts are, in general, more likely to be translated on monosomes than somatic transcripts.

Monosome translation contributes to the neuropil proteome

Individual synapses are small independent information processing units, each endowed with their own complement of proteins, ranging in copy numbers from tens to a thousand

or so (42, 43). We observed that previously published protein copy numbers in the rat presynapse (Fig. 6A) (43) and postsynapse (Fig. 6B) (42) were poorly correlated with the neuropil M/P preference. To understand the contribution of monosome and polysome translation to the overall proteome composition, we conducted mass spectrometry of neuropil proteins (see Materials and methods) and estimated their absolute protein abundances using iBAQ (intensity-based absolute quantification) (44) (fig. S13A). As might be expected, we observed higher median iBAQ values for proteins encoded by polysome-preferring transcripts when compared with proteins encoded by monosome-preferring transcripts (Fig. 6C; see fig. S14A for the somata). When we examined the relationship between the abundance of neuropil proteins and their respective M/P ratios, however, we observed a surprisingly weak correlation ($R^2 = 0.021$; P value = 2.944×10^{-11} ; Fig. 6D;



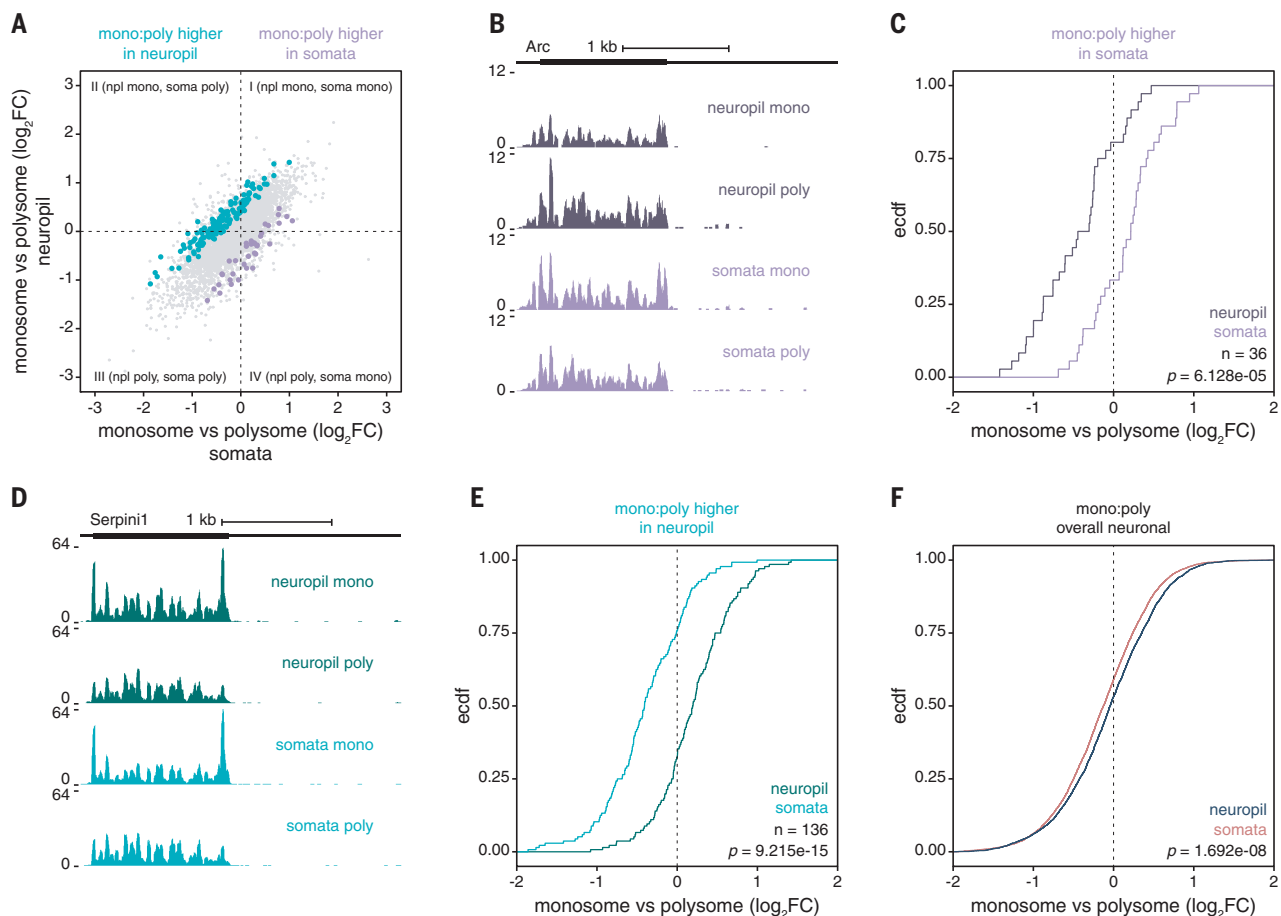


Fig. 5. Localization influences the translational status of selective transcripts.

(A) M/P \log_2 fold changes (FC) in the neuropil (y axis) versus the somata (x axis). The majority of transcripts exhibited correlated ($R^2 = 0.6$, $P < 2.2 \times 10^{-16}$) M/P enrichments between both compartments. Colored dots highlight transcripts that exhibit significantly increased (cyan, $n = 136$ replicates) or decreased (purple, $n = 36$ replicates) M/P \log_2 fold changes in the neuropil compared with the somata. DESeq2 was used for analysis, with a threshold of 0.05 on the adjusted P value (see Materials and methods). Numerals represent the different quadrants. Gray dots denote transcripts that do not exhibit significant changes in M/P \log_2 fold changes between compartments. (B and C) Example (*Arc*) (B) and cumulative distribution frequency of

the M/P \log_2 fold changes (C) of transcripts exhibiting significantly higher M/P ratios in the somata (purple) compared with the neuropil (dark purple). $P = 6.128 \times 10^{-5}$, Kolmogorov-Smirnov test. ecdf, empirical cumulative distribution function.

(D and E) Example (*Serpini1*) (D) and cumulative distribution frequency of the M/P \log_2 fold changes (E) of transcripts exhibiting significantly higher M/P ratios in the neuropil (dark cyan) compared to the somata (cyan). $P = 9.215 \times 10^{-15}$, Kolmogorov-Smirnov test. (F) Cumulative distribution frequency depicting the M/P \log_2 fold changes of all neuronal genes [cyan, purple, and gray dots in (A)] in the somata (red) and neuropil (blue), indicating an overall tendency toward higher M/P ratios in the neuropil. $P = 1.692 \times 10^{-8}$, Kolmogorov-Smirnov test.

have been reported to move within cells at an average speed of $2 \mu\text{m/s}$ (53), and potentially greater mobility of translating monosomes may allow them to patrol and serve a larger number of synapses. Given that one polysome translates a single mRNA resulting in multiple copies of a single protein, the relative scarcity of ribosomes imposes constraints on both the timing and diversity of locally synthesized proteins. Neuropil-localized transcripts exhibited a greater monosome preference than somatic transcripts, potentially allowing for the production of a more diverse set of proteins from a limited pool of available ribosomes at synapses.

Monosome-preferring transcripts encoded proteins that span a broad range of abundances in the neuropil. Because many synap-

tic proteins are present at very low copy numbers within the pre- and postsynaptic compartments [e.g., AMPA receptors; estimated ~15 to 20 per postsynaptic density (PSD)] (54), their local translation by single ribosomes may suffice to maintain or even alter synaptic activity. We also uncovered a subset of monosome-preferring transcripts that encode surprisingly high-abundance proteins, including the scaffolding proteins Bsn and Dlg3. This subset also exhibited increased RNA levels and translation rates within the neuropil. These features might underlie the ability of these monosome-preferring transcripts to encode abundant proteins. On the other hand, predominant polysome translation was observed for key signaling, scaffolding, or cytoskeletal proteins (e.g., Camk2a, PSD95,

and actin), which are present at very high copy numbers within synapses (54). Many studies investigating translational control in synaptic plasticity or neurological disorders have focused their analysis on transcripts that cosediment with polysomes (9, 55–57). Given that monosomes are key contributors to the neuronal translome, focusing on polysome-associated transcripts may provide an incomplete picture of translational regulation.

Most transcripts exhibited a similar M/P preference in both the somata and neuropil, suggesting that ribosome occupancy is often an intrinsic feature of the transcript. Consistent with this finding, we detected a positive correlation between M/P ratio and ORF length, in agreement with previous studies reporting decreased ribosome density and

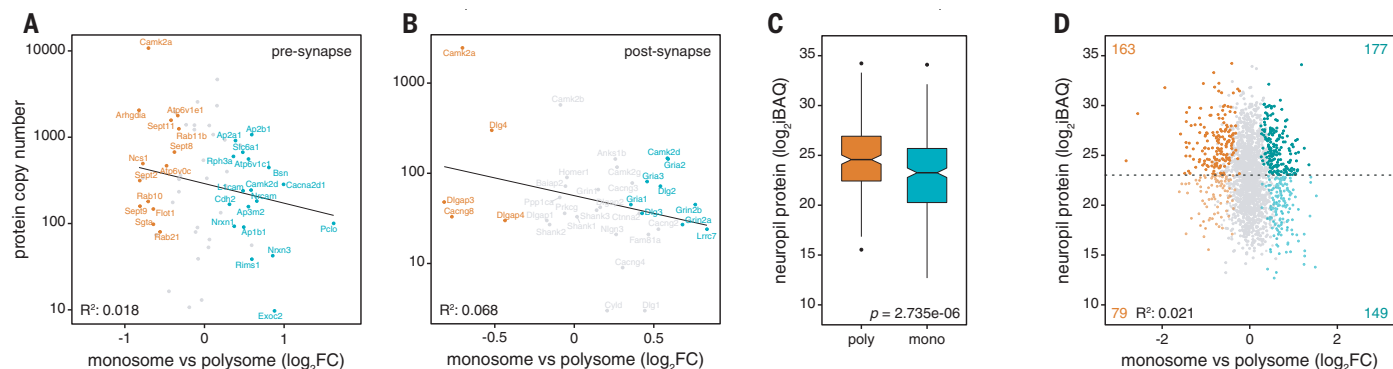


Fig. 6. Monosome translation can contribute to the maintenance of the local proteome. (A and B) M/P fold changes in the neuropil were not correlated with the copy numbers of some key presynaptic (43) (A) and postsynaptic proteins (42) (B). Regression lines and corresponding adjusted R^2 values are represented (presynapse $P = 0.1488$, postsynapse $P = 0.07145$). (C) Box plots of protein (log₂ iBAQ) measurements in the neuropil for monosome-enriched (mono, cyan) or polysome-enriched (poly, orange) genes. $P = 2.735 \times 10^{-6}$, Wilcoxon rank-sum test. Of 463 and 372 monosome- and polysome-preferring transcripts in the neuropil, 326 and 242, respectively, passed the stringent proteomics filtering criteria (see Materials and methods). (D) Scatter plot of the protein abundance (log₂ iBAQ) versus M/P fold changes for monosome-enriched (cyan), polysome-enriched (orange), and nonenriched (gray) genes ($R^2 = 0.021$, $P = 2.944 \times 10^{-11}$). The dashed line indicates the mean log₂ iBAQ value. Monosome-preferring transcripts encoding proteins with abundances greater than average are highlighted by dark cyan dots (mono-high). (E and F) The local proteome correlates with the local transcriptome and translome. Scatter plots of the protein abundance (log₂ iBAQ) versus RNA (log₂ TPM) ($R^2 = 0.26$, $P < 2.2 \times 10^{-16}$) (E) and translation rate (obtained from total footprints, without biochemical fractionation) ($R^2 = 0.33$, $P < 2.2 \times 10^{-16}$) (F) measurements for all neuronal genes are shown. Monosome-preferring genes encoding high-abundance proteins are highlighted by dark cyan dots.

protein production for long ORFs (58–60). In part, this observation can be explained by reduced initiation rates of longer transcripts [correlation coefficient $r = -0.29$; P value $< 2.2 \times 10^{-16}$; see also (61)]. Contrasting observations, however, have been made in yeast, where monosomes preferentially occupy short ORFs (27). This discrepancy might be explained by differences in the translational regulatory mode between organisms, such as an expansion in the UTR length and/or complexity during evolution from lower to higher eukaryotes (2, 62, 63).

We also observed that monosome-preferring transcripts were often subject to a negative translational regulation, with moderate initiation and elongation kinetics. Notably, proteins predominantly encoded by monosome-preferring transcripts were not only longer but also structurally more complex. A “quality mode” slow translation of the monosome-preferring transcripts might allow the fine-tuning of cotranslational folding events, ensuring the functionality and preventing the aggregation of the encoded proteins. On the other hand, we found that polysome-preferring transcripts displayed increased initiation and elongation rates, allowing a more efficient translation. Polysome-preferring transcripts may

thus encode proteins of lower structural complexity, which require less de novo protein folding fidelity, potentially allowing their translation in a fast “productivity mode” (28, 29).

Some transcripts exhibited a differential M/P preference between the somata and neuropil. Neurons differentially localize 5′ and/or 3′ UTR isoforms between subcellular compartments (64). Because these cis-regulatory mRNA elements regulate initiation efficiency (62, 63), neurons may fine-tune their M/P preference through selective targeting of competitive UTR isoforms between compartments. Notably, *Arc*, a previously reported natural NMD target that contains 3′UTR introns (65), was monosome-preferring in the somata but polysome-preferring in the neuropil. According to the model proposed by Giorgi *et al.* (65), *Arc* may be silenced by NMD in the somata, whereas in the neuropil, synaptic activity could trigger its release from NMD, resulting in a translational up-regulation (i.e., polysome translation).

Alternatively, differences in the monosome preference between somata and neuropil could also arise from differential localization or activity of specific translational regulators, including RNA-binding proteins (RBPs) (66, 67), microRNAs (68, 69), initiation and elongation

factors (57), or the ribosome itself (70). For instance, the RBP FMRP is thought to inhibit the translation of selective transcripts in neuronal processes by pausing the translocation of polysomes or by directly interacting with the RNA-induced silencing complex (71, 72). Synaptic activity has also been reported to regulate the local translational machinery through changes in the phosphorylation status of initiation and elongation factors (57). Thus, local activity-induced signaling events may also control the flow of ribosomes on an mRNA and dictate its M/P preference.

A rapid up-regulation in the number of polysomes has been observed in electron micrographs of dendritic shafts and spines after synaptic plasticity induction (7). Our data show that, for many transcripts, monosome translation is the preferred mode of protein synthesis in neuronal processes and presumably satisfies the local demands under basal conditions. The formation of polysomes, however, could be required to supply synapses with de novo plasticity-related proteins in response to stimulation. We identified transcripts that prefer the predominant ribosome population present in either somata (polysomes) or neuropil (monosomes) and thus

represent candidates that may shift toward higher polysome occupancy in response to synaptic stimulation. Furthermore, given the spatial limitations within dendritic spines and axonal boutons, synaptic activity could also regulate monosome translation to diversify the local proteome with spatial and temporal precision.

Materials and methods

Experimental procedures

Animals

Homozygous RiboTag Rpl22^{HA/HA} mice (The Jackson Laboratory, 011029) were crossed with Camk2Cre (The Jackson Laboratory, 005359) or Wfs1CreERT mice (The Jackson Laboratory, 009103). Male 8-week-old C57Bl/6, Wfs1CreERT::RiboTag, and Camk2Cre::RiboTag mice were housed in standard cages and fed standard lab chow and water ad libitum. Male Wfs1CreERT::RiboTag mice were treated for 3 days with tamoxifen [100 mg/kg, intraperitoneally (i.p.), Sigma], dissolved in sunflower oil/ethanol (10/1) to a final concentration of 10 mg/ml and used 1 week later for immunostaining or IP studies (19).

Adult male 4-week-old Sprague Dawley SPF (specific pathogen-free; Charles River Laboratories) rats were housed on a 12/12-hour light/dark cycle with food and water ad libitum until euthanasia. Timed pregnant SPF (Charles River Laboratories) females were housed in the institute's animal facility for 1 week on a 12/12-hour light/dark cycle with food and water ad libitum until the litter was born. Cultured neurons were derived from P0 (postnatal day 0) Sprague-Dawley rat pups (CD Crl:CD, both male and female, RRID: RGD 734476). Pups were euthanized by decapitation.

The housing and euthanasia procedures involving animal treatment and care were conducted in conformity with the institutional guidelines that are in compliance with national and international laws and policies (DIRECTIVE 2010/63/EU; German animal welfare law; FELASA guidelines). The animals were euthanized according to annex 2 of § 2 Abs. 2 Tierschutz-Versuchstier-Verordnung. Animal numbers were reported to the local authority (Regierungspräsidium Darmstadt, approval numbers: V54-19c20/15-F126/1020 and V54-19c20/15-F126/1023).

Hippocampal tissue collection and microdissection

After sacrifice, the heads of 4-week-old male rats (for polysome/ribosome profiling experiments) or 8-week-old male mice [for translating ribosome IP (RiboTag) experiments] were immediately immersed in liquid nitrogen for 6 s to cool the brains. The brains were removed and the hippocampi were rapidly dissected on an ice-cooled disk. Hippocampal

slices (500 μ m) were prepared in a drop of ice-cold RNase-free phosphate-buffered saline (PBS) containing 100 μ g/ml cycloheximide using a manual tissue slicer (Stoelting). Each slice was immediately passed to a second experimenter who microdissected the CA1 somatic and the neuropil layer at 0° to 4°C on a cold plate (TCP50, Thermoelectrics) in a drop of ice-cold RNase-free PBS containing 100 μ g/ml cycloheximide. To ensure the purity of the microdissected neuropil, only slices located in the middle portion of the dorsoventral axis of the hippocampus were used (approximately six slices per hippocampus). Somata and neuropil sections were immediately snap-frozen after their dissection and kept at -80°C until lysis. The microdissection procedure described here maintained the polysome integrity in the somata and neuropil regions. By contrast, signs of ribosome run-off were observed when the microdissection was carried out after 1 hour of slice recovery in artificial cerebrospinal fluid (1, 2).

Primary hippocampal and cortical cultures

Dissociated rat hippocampal or cortical neurons were prepared from P0 day-old rat pups, as previously described (73). For hippocampal cultures, neurons were plated at a density of 31.250 cells/cm² onto 100-mm culture dishes and cultured for 21 days in vitro (DIV) in pre-conditioned growth medium (Neurobasal-A supplemented with B27 and GlutaMAX, 30% glia-culture supernatant, 15% cortex-culture supernatant). Cortical neurons were plated at a density of 100.000 cells/cm² onto poly-D-lysine-coated 75-mm, 3- μ m-pore polycarbonate membrane culture inserts (Corning 3420). At 1 DIV, AraC was added to a final concentration of 5 μ M. After 2 days, medium was exchanged to preconditioned growth medium and neurons were cultured until 21 DIV. All cultures were maintained in a humidified incubator at 37°C and 5% CO₂. The sex of animals from which the cells were obtained was not determined.

Run-off experiment in primary hippocampal culture

At 24 hours before drug treatment, cell medium was adjusted to 8 ml per dish. Harringtonine (LKT Laboratories) was added to a final concentration of 2 μ g/ μ l from a 2-mg/ml stock in 100% ethanol. Cells were returned to the incubator at 37°C for 30 or 90 s. Cycloheximide was added to a final concentration of 100 μ g/ml from a stock of 50 mg/ml in 100% ethanol. After drug addition, cells were returned in the incubator at 37°C for 1 min. After the incubation with cycloheximide, the cells were immediately placed on ice and washed twice with ice-cold PBS plus 100 μ g/ml cycloheximide and lysed in polysome lysis buffer as described

below. Total footprint libraries were prepared as described below.

Immunolabeling of cortical neurons cultured on membrane inserts

At 21 DIV, a part of the membrane was excised, briefly submerged in PBS, and fixed for 20 min in PFA (4% paraformaldehyde in PBS pH 7.5). Cells were permeabilized with 0.5% Triton X-100 in PBS supplemented with 4% goat serum for 15 min and blocked with blocking buffer (4% goat serum in PBS) for 1 hour. Dendrites were stained using an anti-MAP2 antibody (SySy 188004, 1/1000) in blocking buffer overnight at 4°C. After washing the cells three times for 5 min in PBS, the secondary antibody (ThermoFisher A488 A-11073, 1/1000) was incubated in blocking buffer for 45 min at room temperature. Cells were washed three times for 5 min in PBS with DAPI (4',6'-diamidino-2-phenylindole) added to the second wash. Membranes were mounted on glass slides using Aqua-Poly/Mount and imaged from the top (cell body layer) or bottom (neurite layer).

Tagged ribosome immunoprecipitation

Hemagglutinin (HA)-tagged ribosome IP of hippocampi from male Camk2Cre::RiboTag or somata/neuropil sections from male Wfs1Cre::RiboTag mice was performed as described previously (17, 74), with slight modifications. Tissue sections were homogenized in a glass homogenizer containing ice-cold RiboTag lysis buffer [50 mM Tris pH 7.4, 100 mM KCl, 12 mM MgCl₂, 1% NP40, 1 mM DTT, 20 U/ml SUPERaseIN® RNase inhibitor (Ambion), 200 U/ml RNasin (Promega), 100 μ g/ml cycloheximide, 10 U/ml TurboDNase, and protease inhibitor cocktail (Roche)]. After triturating the lysate 10 times using a 23-gauge syringe, samples were chilled on ice for 10 min and cleared by centrifugation at 16,100g for 10 min. Ten percent of the supernatant was kept as an input. HA IP was performed by incubation of the remaining supernatant with 5 μ l of anti-HA antibody (abcam ab9110) overnight at 4°C with gentle rotation. Incubation of the samples with magnetic beads (Dynabeads protein G, Invitrogen), washes, and elution were performed according to (74). Total RNA was extracted from both the input and immunoprecipitated ribosome-mRNA complexes using the RNeasy MinElute kit (Qiagen). RNA integrity was assessed using the Agilent RNA 6000 Pico kit.

Lysate preparation for polysome and ribosome profiling

Tissue: Rat tissue samples were homogenized in polysome lysis buffer [20 mM Tris pH 7.5, 150 mM NaCl, 5 mM MgCl₂, 24 U/ml TurboDNase, 100 μ g/ml cycloheximide, 1 mM DTT, 1% Triton X-100, and protease inhibitor

cocktail (Roche)] (25) by douncing in a glass homogenizer. For the experiments including RNase inhibitors, the polysome lysis buffer was supplemented with 200 U/ml RNase inhibitors (Promega). After triturating the lysate 10 times using a 23-gauge syringe, samples were chilled on ice for 10 min and cleared by two centrifugations at 16,100g for 6 min.

Neuronal culture: At 21 DIV, rat cortical primary neurons were washed twice in ice-cold PBS supplemented with 100 µg/ml cycloheximide. Neurons were collected with a scraper in polysome lysis buffer [20 mM Tris pH 7.5, 150 mM NaCl, 5 mM MgCl₂, 24 U/ml TurboDNase, 100 µg/ml cycloheximide, 1 mM DTT, protease inhibitor cocktail (Roche), and 8% glycerol]. After scraping, the lysates were supplemented with Triton X100 to a final concentration of 1% and chilled on ice for 10 min. After triturating the lysates 10 times using a 23-gauge syringe, samples were chilled on ice for 10 min and then cleared by centrifugation at 16,100g for 10 min.

Polysome profiling

Samples were loaded onto 6-ml 10 to 50% sucrose density gradients that were prepared w/v in the following gradient buffer: 20 mM Tris pH 7.5, 150 mM NaCl, 5 mM MgCl₂, 100 µg/ml cycloheximide, and 1 mM DTT. For polysome profiling from neuronal cultures, the gradient buffer was supplemented with 8% glycerol. To ensure proper RNase digestion during ribosome profiling on the sucrose gradient fractions, RNase inhibitors were omitted from the polysome lysis buffer. RNase-free reagents were used and samples were handled on ice during the entire procedure. The similarity of the neuropil polysome profiles in the presence or absence of RNase inhibitors indicated that this procedure did not affect RNA integrity (fig. S15). Gradients were centrifuged for 2 hours 45 min at 36,000 revolutions per minute (rpm) at 4°C in a SW41 Ti swing-out rotor. Polysome profiling was performed using a density gradient fractionation system (Brandel) with upward displacement and continuous monitoring at 254 nm using a UA-6 detector. The AUC of individual absorbance peaks was quantified. A M/P ratio was calculated by relating the monosome AUC to the sum of the AUCs of all polysome peaks. Somata and neuropil polysome profiles loaded with an equal amount of RNA were used for representation and the comparisons of the monosome or polysome AUC separately between compartments. Fractions of 125 µl corresponding to the monosome or the polysome peaks were collected and combined in a monosome and polysome pool, respectively.

Monosome and polysome footprint isolation

For the whole-hippocampus monosome and polysome footprinting, three replicates were

used, each comprising the hippocampi from three rats, yielding ~150 µg of RNA. For the somata and neuropil monosome and polysome footprinting, three replicates were used, each comprising a pool of microdissected tissue from 55 rats, yielding ~110 µg of RNA. For each replicate, microdissected tissue was lysed as described above, and aliquots containing 20 or 10 µg of RNA were retained for total ribosome footprinting and total RNA-seq, respectively. The remaining lysate was loaded onto 10 to 50% sucrose gradients and centrifuged as described above. To prevent masking of the ribosome peaks by myelin (75), each replicate was loaded onto two to three gradients, and monosome or polysome fractions from different gradients were pooled after polysome profiling. A volume of M/P fraction containing 10 µg (hippocampi) or 2 to 5 µg (somata/neuropil) of RNA was diluted with gradient buffer and digested with 7.5 U/µg RNA of RNase I (Epicentre), rotating for 45 min at 24°C (a range of RNase I concentrations was tested beforehand to optimize the digestion conditions; table S1). Nuclease digestion reactions were promptly cooled and spun, and 10 µl of SUPERaseIN*RNase inhibitor was added. Samples were then layered onto a 34% sucrose cushion, prepared w/v in gradient buffer supplemented with 20 U/µl of SUPERaseIN*RNase inhibitor. 80S particles were pelleted by centrifugation in a SW55Ti rotor for 3 hours 30 min at 55,000 rpm at 4°C.

Total ribosome footprint isolation

Neuropil lysates from three biological replicates (see section “Monosome and polysome footprint isolation”) containing 20 µg of RNA were digested with 0.5 U/µg RNase I (Epicentre), shaking for 45 min at 400 rpm at 24°C (76). Nuclease digestion reactions were promptly cooled and spun, and 10 µl of SUPERaseIN*RNase inhibitor was added. Samples were then layered onto a 34% sucrose cushion, prepared w/v in gradient buffer supplemented with 20 U/µl of SUPERaseIN*RNase inhibitor. 80S particles were pelleted by centrifugation in a SW55Ti rotor for 3 hours 30 min at 55,000 rpm at 4°C.

Ribosome footprint library preparation

Footprint libraries were prepared according to (76) with the following modifications: After RNA extraction from the ribosomal pellet, rRNAs were depleted using the Ribo-Zero Magnetic Gold Mammalian kit (Illumina), followed by footprint purification using the RNA Clean & Concentrator-5 kit (Zymo). Footprint fragments were purified by polyacrylamide gel electrophoresis (PAGE) on a 15% tris-borate EDTA (TBE)-urea gel, and fragments from 26 to 34 nucleotides were isolated. After footprint dephosphorylation and

linker ligation, the ligation reaction was depleted of unligated linker by incubation with 0.5 µl of 5' yeast deadenylase 10 U/µl (NEB) and 0.5 µl of RecJ exonuclease 10 U/µl (Epicentre) for 45 min at 30°C. In addition, ligation products were purified by PAGE, purification on a 15% TBE-urea gel. Reverse transcription was performed as described previously, with the following modification: The reverse transcription reaction was directly incubated with 2 µl of exonuclease I (NEB) at 37°C for 1 hour followed by 15 min at 80°C. cDNA was gel purified by PAGE on a 15% TBE-urea gel. After circularization, circDNA was submitted to an additional rRNA depletion using 14 custom biotinylated rat rRNA oligos (table S1) according to (77). After amplification, the libraries were run on an 8% nondenaturing TBE gel, and 160-base pair (bp) products were isolated and characterized using the Agilent High Sensitivity DNA assay. Libraries were sequenced on an Illumina NextSeq500, using a single-end, 52-bp run.

RNA isolation and library preparation

RNA was isolated from tissue lysates using the Direct-zol RNA micro prep kit (Zymo). RNA integrity was assessed using the Agilent RNA 6000 Nano kit. Rat neuropil total RNA-seq libraries were prepared starting from ~200 ng of total RNA using the TruSeq stranded total RNA library prep gold kit (Illumina). For the input/IP samples from Camk2Cre::RiboTag hippocampi or Wfs1Cre::RiboTag somata and neuropil, mRNA-seq libraries were prepared, starting from ~100 ng of total RNA, using the TruSeq stranded mRNA library prep kit (Illumina). Libraries were sequenced on an Illumina NextSeq500, using a single-end, 75-bp run.

rRNA-to-total RNA percentage

Total RNA was isolated from rat somata and neuropil ($n = 4$) as described above and measured using the Agilent RNA 6000 Nano kit. The ratio of rRNA to total RNA was obtained by summing the 18S rRNA and 28S rRNA percentages of total RNA calculated by the Agilent Bioanalyzer.

Immunoblotting

Neurite and cell body layers were collected in ice-cold PBS and centrifuged, and pellets were lysed in lysis buffer (1% Triton X-100, 0.5% SDS in PBS) supplemented with TurboDNase 24 U/ml at 70°C for 15 min. Lysates were cleared by centrifugation and stored at -80°C until use. Somata and neuropil lysates were prepared in polysome buffer. Lysates were resolved by SDS-PAGE in 4 to 12% Bis-Tris gels (Invitrogen) and analyzed by immunoblotting using far-red fluorescent dyes and a Licor Odyssey scanner [mouse anti-NeuN (1/1000, MAB377); rabbit anti-bActin (1/2000, ab8227); anti-mouse IR800

(1/5000, Licor); anti-rabbit IR680 (1/5000, Licor)]. Protein levels in bands of interest were quantified using ImageJ (NIH). Western blot normalization was conducted according to the Revert Total Protein Stain (Licor) manufacturer's instructions.

Mass spectrometry data acquisition

Three replicates of rat neuropil were micro-dissected as described above. Tissue pieces were snap-frozen and kept at -80°C until lysis. Tissue pieces were lysed in 4% Chaps, 8 M urea, 0.2 M Tris HCl, and 1 M NaCl. All samples were digested, reduced, and alkylated according to a previously published filter-aided ample preparation protocol (78). Dried peptide pellets were stored at -20°C until liquid chromatography–tandem mass spectrometry (LC-MS/MS) analysis. Proteolytic digests were analyzed via Nano-LC-MS/MS on an Ultimate 3000 nanoUPLC (Thermo Fisher Scientific, Bremen) coupled to a Orbitrap Fusion Lumos (Thermo Fisher Scientific, Bremen).

After dissolving the dried peptides in 20 μL of 0.1% FA in 5% acetonitrile, samples were separated using an Acclaim pepmap C18 column (50 cm by 75 μm , particle size: 2 μm) after trapping on an Acclaim pepmap C18 pre-column (2 cm by 75 μm , particle size: 3 μm). Trapping was performed for 6 min with a flow rate of 6 $\mu\text{L}/\text{min}$ using a loading buffer (98/2 water/acetonitrile with 0.05% trifluoroacetic acid). Peptides were then eluted and separated on the analytical column at a flow rate of 300 nL/min with the following gradient: from 4 to 33% B in 150 min, 33 to 48% B in 20 min, 48 to 90% B in 1 min, and constant 90% for 13 min (buffer A: 0.1% FA in water, buffer B: 0.1% FA in 80/20 acetonitrile/water). All LC-MS-grade solvents were purchased from Honeywell/Riedel del Hæn.

Peptides eluting from the column were ionized online using a Nano Flex ESI source and analyzed with an Orbitrap Fusion Lumos mass spectrometer in data-dependent mode. Survey scans were acquired over the mass/charge ratio range of 350 to 1400 in the Orbitrap (maximum injection time: 50 s, automatic gain control (AGC), fixed at 2×10^5 and $R = 120,000$) and sequence information was acquired by a “Top-Speed” method with a fixed cycle time of 2 s for the survey and after MS/MS scans. MS/MS scans were performed on the most abundant precursors exhibiting a charge state from two to five with an intensity minimum of 5×10^3 . Selected precursors were isolated in the quadrupole at 1.4 Da and fragmented using higher-energy C-trap dissociation at normalized collision energy = 30%. For MS/MS, an AGC of 10^4 and a maximum injection time of 300 s were used. Resulting fragments were detected in the ion trap using the rapid scan mode. The dynamic exclusion was set to 30 s with a mass tolerance of

10 parts per million (ppm). All samples were measured in technical triplicates.

Intracerebroventricular puromycin administration

Mice ($n = 3$ per group) were anesthetized with isoflurane (induction: 4%, maintenance: 2%) in oxygen-enriched air (Oxymat 3, Weinmann, Hamburg, Germany) and fixed in a stereotaxic frame (Kopf Instruments, Tujunga, USA). Core body temperature was maintained at 37.5°C by a feedback-controlled heating pad (FHC, Bowdoinham, ME, USA). Analgesia was provided by local injection of ropivacain under the scalp (Naropin, AstraZeneca, Switzerland) and systemic injection of metamizol (100 mg/kg, i.p., Novalgin, Sanofi) and meloxicam (2 mg/kg, i.p., Metacam, Boehringer-Ingelheim, Ingelheim, Germany) (79). A stainless steel 26-gauge guide cannula (PlasticsOne, Roanoke, VA) was implanted vertically toward the right lateral ventricle (A/P: -0.22 mm, M/L: 1 mm, D/V: -2 mm). Guide cannulas were fixed onto the skull with instant adhesive (Ultra Gel, Henkel, Düsseldorf, Germany) and dental cement (Paladur, Heraeus, Hanau, Germany). An obturator was inserted into each guide cannula and remained in place until the drug infusion when it was removed and replaced with an injector that extended 0.5 mm beyond the tip of the guide cannula. After surgery recovery, 3 μL of puromycin solution (9 mg/mL, 10% DMSO/90% saline) or vehicle were infused for 1 min into the cannula through polyethylene tubing using an infusion pump (Stoelting) (80). The protein synthesis inhibitor control received an infusion of 3 μL of anisomycin (25 $\mu\text{g}/\mu\text{L}$, initially dissolved in 3 N HCl and brought to pH 7.3 by addition of 3 N NaOH) (81, 82). At 30 min after the anisomycin infusion, mice were infused with 3 μL of puromycin (9 mg/mL) supplemented with 75 μg of anisomycin. After drug infusions, the tubing remained in place for one extra minute to ensure proper delivery of the solution. All mice were previously handled to ensure proper immobility during intracerebroventricular administration. At 10 min after puromycin infusion, mice were transcardially perfused as described below.

Immunolabeling of hippocampal slices

After anesthesia with isoflurane, mice were rapidly euthanized and transcardially perfused for 1 min with PBS followed by 2 min with 4% (w/v) paraformaldehyde in PBS. Brains were post-fixed overnight in the same solution and stored at 4°C . Sections of 30- μm thickness were cut with a vibratome (Leica) and stored at 4°C in PBS until they were processed for immunofluorescence. Hippocampal sections were identified using a mouse brain atlas, and sections including -1.34 to -2.06 mm from bregma were included in the analysis.

Hippocampal sections from Wfs1Cre::RiboTag and Camk2Cre::RiboTag mice were processed as follows: Free-floating sections were rinsed three times for 10 min with PBS. After 15 min incubation in 0.2% Triton X-100 in PBS, sections were rinsed in PBS again and blocked for 1 hour in a solution of 3% BSA in PBS. Finally, they were incubated for 72 hours at 4°C in 1% BSA, 0.15% Triton X-100 with the anti-HA antibody (abcam Ab9110, 1/500).

In vivo puromycylated brain slices were immunostained as described previously (80). Briefly, sections were incubated for 20 min with coextraction buffer [50 mM Tris-HCl, pH 7.5, 5 mM MgCl_2 , 25 mM KCl, protease inhibitor cocktail (Roche), and 0.015% digitonin (Wako Chemicals)]. After three rinses with PBS, sections were incubated for 72 hours at 4°C with puromycin (Milipore MAB E343, 1/1000) and Wfs1 (Proteintech 11558-1-AP, 1/1000) antibodies in a solution containing 0.05% saponin, 10 mM glycine, and 5% fetal bovine serum in PBS. After primary antibody incubation, sections were rinsed three times for 10 min in PBS and incubated overnight at 4°C with the secondary antibody (ThermoFisher A546 A-11030, A647 A-21245, 1/500). Sections were rinsed three times for 10 min in PBS and mounted in Aqua-Poly/Mount.

Fluorescence imaging was performed with an LSM880 confocal microscope (Zeiss) using a 20x air objective (Plan Apochromat 20x/0.8 M27) with appropriate excitation laser lines and spectral detection windows. Laser power and detector gain were adjusted to avoid saturated pixels. Imaging conditions were held constant within experiments. Single images were acquired at the same depth. For better visualization, brightness and contrast were adjusted. Processing was kept constant between conditions. The brightness and contrast of the zoom-in was additionally enhanced for better visualization.

Data analyses

Proteomics data analysis

Raw data were processed using the Max Quant software version 1.6.2.2 (83). MS/MS spectra were searched against the UniprotKB database from *Rattus norvegicus* (36080 entries, downloaded on 21 December 2017) and additionally against a database containing common mass spectrometry contaminations using the probabilistic based algorithm from the Andromeda search engine. The set of stringent constraints allowed only peptides with full tryptic specificity allowing N-terminal cleavage to proline and up to two missed cleavages. Carbamidomethylation of cysteine was set as a fixed modification. Oxidation of methionine and acetylation of the protein N terminus were set as variable modifications. Minimum peptide length was set to seven amino acids. The first search was performed with 20-ppm

precursor tolerance for mass recalibration, and the main search mass tolerance was set to 4.5 ppm. The fragment mass tolerance was 0.5 Da, and the “match between runs” option was enabled. Peptides and proteins were identified on the basis of a 1% false discovery rate (FDR) with the use of a decoy strategy, and only those protein groups identified with at least one unique peptide were used for further analysis.

Proteomics postprocessing

The Perseus package v1.6.2.2 (84) was used for further bioinformatic analysis of the resulting expression data from MaxQuant. Before further processing, decoy and contaminant database hits as well as proteins only identified using modified peptides (“identified by site”) were excluded. Additionally, only those protein groups identified in at least two of three technical replicates and in two of three biological replicates were considered for further analysis.

Footprint genome and transcriptome alignment

Adapters were removed with Cutadapt v1.15 (85) (–cut 1 –minimum-length 22 –discard-untrimmed –overlap 3 –e 0.2). An extended unique molecular identifier was constructed from the two random nucleotides from the RT primer and the five random nucleotides from the linker and added to the description line using a custom Perl script. Trimmed reads that aligned to rat noncoding RNA were removed using Bowtie2 v2.3.4.3 (86) (–very-sensitive). Remaining reads were aligned to the rat genome (rn6) with the split-aware aligner STAR v2.6.1a (87) (–twopassMode Basic –twopassreadsN -1 –seedSearchStartLmax 15 –outSJfilterOverhangMin 15 8 8 8 –outFilterMismatchNoverReadLmax 0.1). When required, STAR –quantMode was used to retrieve transcript coordinates. Transcriptome alignments were used for all analyses, except for differential expression and genomic feature analysis. The STAR genome index was built using annotation downloaded from the UCSC table browser (88). Polymerase chain reaction duplicates were suppressed using a custom Perl script, and alignments flagged as secondary alignment were filtered out.

RNA genome alignment

Adapters and low-quality nucleotides were removed with Cutadapt v1.15 (85) (–minimum-length 25 –netseq-trim=20). Reads were aligned to the rat (rn6) or the mouse (mm10) genome with STAR v2.6.1a (87).

Assigning footprint reads to genomic features

Genomic feature coordinates [coding sequence (CDS), 3'UTR, 5'UTR, intron] were downloaded from the UCSC table browser as BED files (88).

Bedtools v2.26.0 (89) was used to first convert BAM files into the BED format and then identify reads overlapping with the individual features.

Counting and differential expression analysis

M/P ratios: Counts per gene were calculated from reads mapped to the genome using featureCounts v1.6.3 (90). Only a single transcript isoform, with the highest possible APPRIS score (91), was considered per gene. Only footprint reads aligned to the central portion of the ORF—by convention, 15 codons from the start until 5 codons before the stop codon—were counted (76). Raw counts were fed into DESeq2 (18) for differential expression analysis. Log fold change (LFC) shrinkage was used to generate more accurate log₂ fold-change estimates (92). To test if the M/P fold-change differs across compartments, an interaction was added to the design formula. In this analysis, unshrunk log₂ fold changes were used.

RiboTag-IP-to-input ratios: Counts per gene were calculated from reads mapped to the genome using featureCounts v1.6.3 (90). All transcript isoforms were considered. Raw counts were fed into DESeq2, and LFC shrinkage was used.

Classification of neuronal genes

A classifier to identify excitatory neuron-enriched genes was developed. The union of genes with significantly enriched RiboTag-IP to input fold changes (threshold of 0.05 on the adjusted *P* value and a 30% enrichment) was formed from the three RiboTag experiments (Hippocampus Camk2Cre::RiboTag, somata/neuropil Wfsr1Cre::RiboTag).

Classification of NMD targets

Genes with the Ensembl biotype annotation “nonsense_mediated_decay” or “retained_intron” were classified as possible NMD targets.

Translation rate calculations

The translation rate was computed from three biological replicates of neuropil/somata total ribosome footprinting, as previously described in (25). In brief, the number of footprint reads in the gene's CDS was divided by its CDS length in kilobases. This value was then normalized to the total number of footprint reads mapping to any region of the gene. Only reads with a minimum of 10 raw reads in all footprint libraries were used for analysis.

Translational efficiency calculations

Translational efficiency was computed from three biological replicates of neuropil total ribosome footprinting. The translational efficiency of a gene was calculated as the ratio of normalized footprint reads [transcripts

per million (TPM)] to normalized RNA-seq reads (TPM).

Integration of proteomic and transcriptomic data

Protein and RNA data were matched as described in (93). A protein centric view was taken. For each protein in the protein group, the corresponding RNA measures in TPM or the corresponding translation rates were summed and the mean of the corresponding monosome to polysome log₂ fold change was determined. In a functional group, at least half of the genes had to be classified as “neuronal” to pass the RiboTag filter. A functional group was determined as “monosome enriched” or “polysome enriched” if more than half of its transcripts were classified as “monosome enriched” or “polysome enriched,” respectively. In all other cases, the functional group was classified as “nonenriched.”

Metagene analysis

Metagene plots represent the accumulated footprint coverage over the length-normalized ORF. The normalized footprint coverage was generated for each gene (footprint coverage divided by the average codon coverage). Edge positions were defined relative to the ORF start and stop codons and divided into 100 bins. Each gene contributed with its average normalized footprint coverage per bin.

Harringtonine depletion profile analysis

ORF footprint coverages per gene were generated for each time point. Analysis was performed on well-translated genes with at least 0.1 reads per codon. Profiles were scaled by the average coverage between codons 400 and 450. Transcripts shorter than 460 codons were excluded from the analysis. For each time point, the metagene profiles were smoothed in 30-codon windows and normalized to the 0-s time point. Only transcripts with a monosome preference in both hippocampal culture and tissue were considered.

Three-nucleotide periodicity analysis

First, the P-site offset was defined for individual footprint lengths. For this, all reads spanning the ORF start were used, and the most probable offset from the start and end of the read was defined for each length. Second, the P-site position per read was determined on the basis of its length and the previously defined offset. All P-site positions were projected for 100 nucleotides around the ORF start, stop, and center. The P-site coverage of each gene was normalized to its average footprint coverage. The nucleotide coverage at frame positions 0, 1, and 2 was assessed. To determine if the observed frame fraction differed from the expected frame

fraction, a one-way analysis of variance (ANOVA) was performed. A significant *P* value rejects the null hypothesis that all frames exhibit the expected P-site coverage.

Genome browser track visualization

Footprint coverage was visualized as custom tracks on the UCSC Genome Browser (94). Footprint alignments were converted into BedGraph files (<https://genome.ucsc.edu/goldenPath/help/bedgraph.html>) using Bedtools v2.26.0.

Gene ontology analysis

GO enrichment of monosome- or polysome-preferring genes was performed using the R package clusterProfiler (95) with a Benjamini-Hochberg multiple testing adjustment and a FDR cutoff of 0.05, using all expressed neuronal genes in the neuropil or somata as background, respectively. The simplify function with a cutoff of 0.7 was used to remove redundancy from enriched GO terms.

Correlation between the M/P fold change and transcript attributes

DNA sequences were extracted from the rat (rn6) genome. Only genes with valid values for all transcript attributes were used for analysis. The length of 3'UTRs and 5'UTRs was set to a minimum of 10 nts.

GC content: The GC content was assessed by counting the number of G or C bases in the sequence and then dividing by the number of bases in the predicted 5'UTR, CDS, or 3'UTR.

Minimum free energy (MFE): The ViennaRNA package version 2.0 with RNAfold was used to calculate the MFE per 5'UTR or 3'UTR sequence (96). A method described by Trotta (97) was adapted to normalize MFE units to the sequence length. The sequence length was restricted to a maximum of 500 nucleotides in proximity to the start and stop codons.

Codon adaptation index: CAI values in the neuropil were obtained for neuronal genes only, following the procedure described in (98).

Initiation rate: The initiation rate per gene was calculated on the basis of the neuropil total ribosome footprint and RNA coverage, as previously described (99). In short, the initiation rate depends on the translational efficiency (defined as described above), CDS length, average time for a ribosome to traverse the CDS, and normalized ribosome occupancy in the initial 10 codons of the CDS. The average elongation rate was assumed to be 4 codons/s (53). A ξ value of 0.0084 was determined from the best-fit line to the average ribosome density of a transcript (from polysome profiling) versus its translational efficiency (from ribosome profiling and RNA-seq).

Mean typical decoding rate: A per-gene MTDR was calculated on the basis of the neuropil total ribosome footprint coverage, as previously described in (26). In short, each

amino acid decoding time was defined as a convolution of an average decoding time (a Gaussian component with the parameters μ and σ) and a pausing decoding time (an exponential component with the parameter λ). A model-fitting procedure was used to deconvolve the two distributions and identify the three parameters per amino acid. The geometric mean of all average decoding times (μ) was calculated to determine the per-gene MTDR.

Upstream open reading frame (uORF)

To identify transcripts containing uORFs, neuropil total ribosome footprint libraries from three replicates were used. Only genes with annotated 5'UTRs were considered. A string match algorithm was used to identify sequences within annotated 5'UTRs that are flanked by canonical in-frame start and stop codons. Only sequences with a minimum length of three codons and at least 10 raw footprints in all three replicates were considered as uORFs.

Prediction of protein secondary structure and protein domains

Appris transcript isoforms were translated into amino acid sequences and used to predict secondary structures and protein domains. Porter 5 was used to predict protein secondary structures in three classes (α helix, β strand, and coil) (100). Spans of coils were defined as unstructured, whereas helices and strands were defined as structured sequences. Transitions from structured to unstructured, and vice versa, were counted and normalized to the sequence length. Protein domains were predicted using InterProScan5 based on the Pfam database (101). Functional domains per protein were merged into unique regions, and their average length was compared between monosome- and polysome-enriched genes.

Codon pause score analysis

For each codon located in the elongating ORF portion (15 codons from the start until 5 codons before the stop codon) of neuropil monosome-enriched genes, a pause score was calculated based on a z -score-like quantity: pause score = (normalized footprint coverage in monosome library - normalized footprint coverage in polysome library)/(normalized footprint coverage in polysome library)^{1/2}.

REFERENCES AND NOTES

1. I. J. Cajigas *et al.*, The local transcriptome in the synaptic neuropil revealed by deep sequencing and high-resolution imaging. *Neuron* **74**, 453–466 (2012). doi: [10.1016/j.neuron.2012.02.036](https://doi.org/10.1016/j.neuron.2012.02.036); pmid: 22578497
2. G. Tushev *et al.*, Alternative 3' UTRs Modify the Localization, Regulatory Potential, Stability, and Plasticity of mRNAs in Neuronal Compartments. *Neuron* **98**, 495–511.e6 (2018). doi: [10.1016/j.neuron.2018.03.030](https://doi.org/10.1016/j.neuron.2018.03.030); pmid: 29656876
3. J. M. Cioni, M. Koppers, C. E. Holt, Molecular control of local translation in axon development and maintenance. *Curr. Opin. Neurobiol.* **51**, 86–94 (2018). doi: [10.1016/j.conb.2018.02.025](https://doi.org/10.1016/j.conb.2018.02.025); pmid: 29549711

4. C. Glock, M. Heumüller, E. M. Schuman, mRNA transport & local translation in neurons. *Curr. Opin. Neurobiol.* **45**, 169–177 (2017). doi: [10.1016/j.conb.2017.05.005](https://doi.org/10.1016/j.conb.2017.05.005); pmid: 28633045
5. A. S. Hafner, P. G. Donlin-Asp, B. Leitch, E. Herzog, E. M. Schuman, Local protein synthesis is a ubiquitous feature of neuronal pre- and postsynaptic compartments. *Science* **364**, eaau3644 (2019). doi: [10.1126/science.aau3644](https://doi.org/10.1126/science.aau3644); pmid: 31097639
6. L. E. Ostroff, J. C. Fiala, B. Allwardt, K. M. Harris, Polyribosomes redistribute from dendritic shafts into spines with enlarged synapses during LTP in developing rat hippocampal slices. *Neuron* **35**, 535–545 (2002). doi: [10.1016/S0896-6273\(02\)00785-7](https://doi.org/10.1016/S0896-6273(02)00785-7); pmid: 12165474
7. L. E. Ostroff *et al.*, Shifting patterns of polyribosome accumulation at synapses over the course of hippocampal long-term potentiation. *Hippocampus* **28**, 416–430 (2018). doi: [10.1002/hipo.22841](https://doi.org/10.1002/hipo.22841); pmid: 29575288
8. E. K. Schmidt, G. Clavarino, M. Ceppi, P. Pierre, SUNSET, a nonradioactive method to monitor protein synthesis. *Nat. Methods* **6**, 275–277 (2009). doi: [10.1038/nmeth.1314](https://doi.org/10.1038/nmeth.1314); pmid: 19305406
9. C. Bagni, L. Mannucci, C. G. Dotti, F. Amaldi, Chemical stimulation of synaptosomes modulates alpha -Ca2+/calmodulin-dependent protein kinase II mRNA association to polysomes. *J. Neurosci.* **20**, RC76 (2000). doi: [10.1523/JNEUROSCI.20-10.0004.2000](https://doi.org/10.1523/JNEUROSCI.20-10.0004.2000); pmid: 10783400
10. M. M. Poon, S. H. Choi, C. A. Jamieson, D. H. Geschwind, K. C. Martin, Identification of process-localized mRNAs from cultured rodent hippocampal neurons. *J. Neurosci.* **26**, 13390–13399 (2006). doi: [10.1523/JNEUROSCI.3432-06.2006](https://doi.org/10.1523/JNEUROSCI.3432-06.2006); pmid: 17182790
11. J. R. Warner, P. M. Knopf, The discovery of polyribosomes. *Trends Biochem. Sci.* **27**, 376–380 (2002). doi: [10.1016/S0968-0004\(02\)02126-6](https://doi.org/10.1016/S0968-0004(02)02126-6); pmid: 12114027
12. J. R. Warner, P. M. Knopf, A. Rich, A multiple ribosomal structure in protein synthesis. *Proc. Natl. Acad. Sci. U.S.A.* **49**, 122–129 (1963). doi: [10.1073/pnas.49.1.122](https://doi.org/10.1073/pnas.49.1.122); pmid: 13998950
13. J. R. Warner, A. Rich, The Number of Soluble Rna Molecules on Reticulocyte Polyribosomes. *Proc. Natl. Acad. Sci. U.S.A.* **51**, 1134–1141 (1964). doi: [10.1073/pnas.51.6.1134](https://doi.org/10.1073/pnas.51.6.1134); pmid: 14215634
14. N. T. Ingolia, S. Ghaemmaghami, J. R. Newman, J. S. Weissman, Genome-wide analysis in vivo of translation with nucleotide resolution using ribosome profiling. *Science* **324**, 218–223 (2009). doi: [10.1126/science.1168978](https://doi.org/10.1126/science.1168978); pmid: 19213877
15. J. J. Hodas *et al.*, Dopaminergic modulation of the hippocampal neuropil proteome identified by biorthogonal noncanonical amino acid tagging (BONCAT). *Proteomics* **12**, 2464–2476 (2012). doi: [10.1002/pmic.201200112](https://doi.org/10.1002/pmic.201200112); pmid: 22744909
16. J. W. Charlton, K. C. Hunt, J. Frydman, Cotranslational signal-independent SRP preloading during membrane targeting. *Nature* **536**, 224–228 (2016). doi: [10.1038/nature19309](https://doi.org/10.1038/nature19309); pmid: 27487213
17. E. Sanz *et al.*, Cell-type-specific isolation of ribosome-associated mRNA from complex tissues. *Proc. Natl. Acad. Sci. U.S.A.* **106**, 13939–13944 (2009). doi: [10.1073/pnas.0907143106](https://doi.org/10.1073/pnas.0907143106); pmid: 19666516
18. M. I. Love, W. Huber, S. Anders, Moderated estimation of fold change and dispersion for RNA-seq data with DESeq2. *Genome Biol.* **15**, 550 (2014). doi: [10.1186/s13059-014-0550-8](https://doi.org/10.1186/s13059-014-0550-8); pmid: 25516281
19. L. Ceolin *et al.*, Cell Type-Specific mRNA Dysregulation in Hippocampal CA1 Pyramidal Neurons of the Fragile X Syndrome Mouse Model. *Front. Mol. Neurosci.* **10**, 340 (2017). doi: [10.3389/fnmol.2017.00340](https://doi.org/10.3389/fnmol.2017.00340); pmid: 29104533
20. A. Zeisel *et al.*, Cell types in the mouse cortex and hippocampus revealed by single-cell RNA-seq. *Science* **347**, 1138–1142 (2015). doi: [10.1126/science.1241934](https://doi.org/10.1126/science.1241934); pmid: 25700174
21. G. Kramer, D. Boehringer, N. Ban, B. Bukau, The ribosome as a platform for co-translational processing, folding and targeting of newly synthesized proteins. *Nat. Struct. Mol. Biol.* **16**, 589–597 (2009). doi: [10.1038/nsmb.1614](https://doi.org/10.1038/nsmb.1614); pmid: 19491936
22. J. B. Plotkin, G. Kudla, Synonymous but not the same: The causes and consequences of codon bias. *Nat. Rev. Genet.* **12**, 32–42 (2011). doi: [10.1038/nrg2899](https://doi.org/10.1038/nrg2899); pmid: 21102527
23. K. C. Stein, J. Frydman, The stop-and-go traffic regulating protein biogenesis: How translation kinetics controls proteostasis. *J. Biol. Chem.* **294**, 2076–2084 (2019). doi: [10.1074/jbc.REV118.002814](https://doi.org/10.1074/jbc.REV118.002814); pmid: 30504455

24. T. E. Graber *et al.*, Reactivation of stalled polyribosomes in synaptic plasticity. *Proc. Natl. Acad. Sci. U.S.A.* **110**, 16205–16210 (2013). doi: [10.1073/pnas.1307747110](#); pmid: [24043809](#)
25. N. T. Ingolia, L. F. Lareau, J. S. Weissman, Ribosome profiling of mouse embryonic stem cells reveals the complexity and dynamics of mammalian proteomes. *Cell* **147**, 789–802 (2011). doi: [10.1016/j.cell.2011.10.002](#); pmid: [22056041](#)
26. A. Dana, T. Tuller, The effect of tRNA levels on decoding times of mRNA codons. *Nucleic Acids Res.* **42**, 9171–9181 (2014). doi: [10.1093/nar/gku646](#); pmid: [25056313](#)
27. E. E. Heyer, M. J. Moore, Redefining the Translational Status of 80S Monosomes. *Cell* **164**, 757–769 (2016). doi: [10.1016/j.cell.2016.01.003](#); pmid: [26871635](#)
28. D. Balchin, M. Hayer-Hartl, F. U. Hartl, In vivo aspects of protein folding and quality control. *Science* **353**, aac4354 (2016). doi: [10.1126/science.aac4354](#); pmid: [27365453](#)
29. J. Zhao, B. Qin, R. Nikolay, C. M. T. Spahn, G. Zhang, Translatomics: The Global View of Translation. *Int. J. Mol. Sci.* **20**, 212 (2019). pmid: [30626072](#)
30. F. Koopmans *et al.*, SynGO: An Evidence-Based, Expert-Curated Knowledge Base for the Synapse. *Neuron* **103**, 217–234.e4 (2019). doi: [10.1016/j.neuron.2019.05.002](#); pmid: [31171447](#)
31. R. P. Tas, L. C. Kapitein, Exploring cytoskeletal diversity in neurons. *Science* **361**, 231–232 (2018). doi: [10.1126/science.aat5992](#); pmid: [30026215](#)
32. A. J. Silva, C. F. Stevens, S. Tonegawa, Y. Wang, Deficient hippocampal long-term potentiation in alpha-calcium-calmodulin kinase II mutant mice. *Science* **257**, 201–206 (1992). doi: [10.1126/science.1378648](#); pmid: [1378648](#)
33. G. L. Lyford *et al.*, Arc, a growth factor and activity-regulated gene, encodes a novel cytoskeleton-associated protein that is enriched in neuronal dendrites. *Neuron* **14**, 433–445 (1995). doi: [10.1016/0896-6273\(95\)90299-6](#); pmid: [7857651](#)
34. T. Bacaj, M. Ahmad, S. Jurado, R. C. Malenka, T. C. Südhof, Synaptic Function of Rab11Fip5: Selective Requirement for Hippocampal Long-Term Depression. *J. Neurosci.* **35**, 7460–7474 (2015). doi: [10.1523/JNEUROSCI.1581-14.2015](#); pmid: [25972173](#)
35. P. B. Allen, A. T. Greenfield, P. Svenningsson, D. C. Haspelagh, P. Greengard, Phactr3 1-4: A family of protein phosphatase 1 and actin regulatory proteins. *Proc. Natl. Acad. Sci. U.S.A.* **101**, 7187–7192 (2004). doi: [10.1073/pnas.0401673101](#); pmid: [15107502](#)
36. H. Wang *et al.*, Norbin is an endogenous regulator of metabotropic glutamate receptor 5 signaling. *Science* **326**, 1554–1557 (2009). doi: [10.1126/science.1178496](#); pmid: [20007903](#)
37. B. Tewes *et al.*, Synthetic microRNA-mediated downregulation of Nogo-A in transgenic rats reveals its role as regulator of synaptic plasticity and cognitive function. *Proc. Natl. Acad. Sci. U.S.A.* **110**, 6583–6588 (2013). doi: [10.1073/pnas.1217665110](#); pmid: [23576723](#)
38. Y. Fan, X. Tang, E. Vitriol, G. Chen, J. Q. Zheng, Actin capping protein is required for dendritic spine development and synapse formation. *J. Neurosci.* **31**, 10228–10233 (2011). doi: [10.1523/JNEUROSCI.0115-11.2011](#); pmid: [21752999](#)
39. G. G. Farias, C. M. Guardia, R. De Pace, D. J. Britt, J. S. Bonifacio, BORC/kinesin-1 ensemble drives polarized transport of lysosomes into the axon. *Proc. Natl. Acad. Sci. U.S.A.* **114**, E2955–E2964 (2017). doi: [10.1073/pnas.1616363114](#); pmid: [28320970](#)
40. I. H. Kim, H. Wang, S. H. Soderling, R. Yasuda, Loss of Cdc42 leads to defects in synaptic plasticity and remote memory recall. *eLife* **3**, e02839 (2014). doi: [10.7554/eLife.02839](#); pmid: [25006034](#)
41. P. W. Beesley, R. Herrera-Molina, K. H. Smalla, C. Seidenbecher, The Neurexins adhesion molecules: Key regulators of neuronal plasticity and synaptic function. *J. Neurochem.* **131**, 268–283 (2014). doi: [10.1111/jnc.12816](#); pmid: [25040546](#)
42. M. S. Lowenthal, S. P. Markey, A. Dosemeci, Quantitative mass spectrometry measurements reveal stoichiometry of principal postsynaptic density proteins. *J. Proteome Res.* **14**, 2528–2538 (2015). doi: [10.1021/acs.jproteome.5b00109](#); pmid: [25874902](#)
43. B. G. Wilhelm *et al.*, Composition of isolated synaptic boutons reveals the amounts of vesicle trafficking proteins. *Science* **344**, 1023–1028 (2014). doi: [10.1126/science.1252884](#); pmid: [24876496](#)
44. N. Nagaraj *et al.*, Deep proteome and transcriptome mapping of a human cancer cell line. *Mol. Syst. Biol.* **7**, 548 (2011). doi: [10.1038/msb.2011.81](#); pmid: [22068331](#)
45. K. M. Harris, R. J. Weinberg, Ultrastructure of synapses in the mammalian brain. *Cold Spring Harb. Perspect. Biol.* **4**, a005587 (2012). doi: [10.1101/cshperspect.a005587](#); pmid: [22357909](#)
46. K. S. Kosik, Life at Low Copy Number: How Dendrites Manage with So Few mRNAs. *Neuron* **92**, 1168–1180 (2016). doi: [10.1016/j.neuron.2016.11.002](#); pmid: [28009273](#)
47. T. Shigeoka *et al.*, Dynamic Axonal Translation in Developing and Mature Visual Circuits. *Cell* **166**, 181–192 (2016). doi: [10.1016/j.cell.2016.05.029](#); pmid: [27321671](#)
48. T. J. Younts *et al.*, Presynaptic Protein Synthesis Is Required for Long-Term Plasticity of GABA Release. *Neuron* **92**, 479–492 (2016). doi: [10.1016/j.neuron.2016.09.040](#); pmid: [27764673](#)
49. J. N. Bourne, K. E. Sorra, J. Hurlburt, K. M. Harris, Polyribosomes are increased in spines of CA1 dendrites 2 h after the induction of LTP in mature rat hippocampal slices. *Hippocampus* **17**, 1–4 (2007). doi: [10.1002/hipo.20238](#); pmid: [17094086](#)
50. V. Tatavarty *et al.*, Single-molecule imaging of translational output from individual RNA granules in neurons. *Mol. Biol. Cell* **23**, 918–929 (2012). doi: [10.1091/mbc.e11-07-0622](#); pmid: [22219377](#)
51. K. M. Harris, J. K. Stevens, Dendritic spines of CA1 pyramidal cells in the rat hippocampus: Serial electron microscopy with reference to their biophysical characteristics. *J. Neurosci.* **9**, 2982–2997 (1989). doi: [10.1523/JNEUROSCI.09-08-02982.1989](#); pmid: [2769375](#)
52. L. E. Ostroff *et al.*, Accumulation of Polyribosomes in Dendritic Spine Heads, But Not Bases and Necks, during Memory Consolidation Depends on Cap-Dependent Translation Initiation. *J. Neurosci.* **37**, 1862–1872 (2017). doi: [10.1523/JNEUROSCI.3301-16.2017](#); pmid: [28087764](#)
53. C. Wang, B. Han, R. Zhou, X. Zhuang, Real-Time Imaging of Translation on Single mRNA Transcripts in Live Cells. *Cell* **165**, 990–1001 (2016). doi: [10.1016/j.cell.2016.04.040](#); pmid: [27153499](#)
54. M. Sheng, E. Kim, The postsynaptic organization of synapses. *Cold Spring Harb. Perspect. Biol.* **3**, a005678 (2011). doi: [10.1101/cshperspect.a005678](#); pmid: [22046028](#)
55. D. Panja *et al.*, Two-stage translational control of dentate gyrus LTP consolidation is mediated by sustained BDNF-TrkB signaling to MNK. *Cell Rep.* **9**, 1430–1445 (2014). doi: [10.1016/j.celrep.2014.10.016](#); pmid: [25453757](#)
56. G. M. Schratz, E. A. Nigh, W. G. Chen, L. Hu, M. E. Greenberg, BDNF regulates the translation of a select group of mRNAs by a mammalian target of rapamycin-phosphatidylinositol 3-kinase-dependent pathway during neuronal development. *J. Neurosci.* **24**, 7366–7377 (2004). doi: [10.1523/JNEUROSCI.1739-04.2004](#); pmid: [15317862](#)
57. W. S. Sossin, M. Costa-Mattoli, Translational Control in the Brain in Health and Disease. *Cold Spring Harb. Perspect. Biol.* **11**, a032912 (2018). pmid: [30082469](#)
58. L. Ciandrini, I. Stansfield, M. C. Romano, Ribosome traffic on mRNAs maps to gene ontology: Genome-wide quantification of translation initiation rates and polysome size regulation. *PLoS Comput. Biol.* **9**, e1002866 (2013). doi: [10.1371/journal.pcbi.1002866](#); pmid: [23382661](#)
59. L. D. Fernandes, A. P. S. Moura, L. Ciandrini, Gene length as a regulator for ribosome recruitment and protein synthesis: Theoretical insights. *Sci. Rep.* **7**, 17409 (2017). doi: [10.1038/s41598-017-1618-1](#); pmid: [29234048](#)
60. M. K. Thompson, W. V. Gilbert, mRNA length-sensing in eukaryotic translation: Reconsidering the “closed loop” and its implications for translational control. *Curr. Genet.* **63**, 613–620 (2017). doi: [10.1007/s00294-016-0674-3](#); pmid: [28028558](#)
61. D. E. Weinberg *et al.*, Improved Ribosome-Footprint and mRNA Measurements Provide Insights into Dynamics and Regulation of Yeast Translation. *Cell Rep.* **14**, 1787–1799 (2016). doi: [10.1016/j.celrep.2016.01.043](#); pmid: [26876183](#)
62. K. Leppek, R. Das, M. Barna, Functional 5' UTR mRNA structures in eukaryotic translation regulation and how to find them. *Nat. Rev. Mol. Cell Biol.* **19**, 158–174 (2018). doi: [10.1038/nrm.2017.103](#); pmid: [29165424](#)
63. C. Mayr, Regulation by 3'-Untranslated Regions. *Annu. Rev. Genet.* **51**, 171–194 (2017). doi: [10.1146/annurev-genet-120116-024704](#); pmid: [28853924](#)
64. C. E. Holt, K. C. Martin, E. M. Schuman, Local translation in neurons: Visualization and function. *Nat. Struct. Mol. Biol.* **26**, 557–566 (2019). doi: [10.1038/s41594-019-0263-5](#); pmid: [31270476](#)
65. C. Giorgi *et al.*, The EJC factor eIF4AIII modulates synaptic strength and neuronal protein expression. *Cell* **130**, 179–191 (2007). doi: [10.1016/j.cell.2007.05.028](#); pmid: [17632064](#)
66. J. C. Darnell, J. D. Richter, Cytoplasmic RNA-binding proteins and the control of complex brain function. *Cold Spring Harb. Perspect. Biol.* **4**, a012344 (2012). doi: [10.1101/cshperspect.a012344](#); pmid: [22723494](#)
67. A. Zappulo *et al.*, RNA localization is a key determinant of neurite-enriched proteome. *Nat. Commun.* **8**, 583 (2017). doi: [10.1038/s41467-017-00690-6](#); pmid: [28928394](#)
68. S. Sambandan *et al.*, Activity-dependent spatially localized miRNA maturation in neuronal dendrites. *Science* **355**, 634–637 (2017). doi: [10.1126/science.aaf8995](#); pmid: [28183980](#)
69. K. T. Thomas, C. Gross, G. J. Bassell, microRNAs Sculpt Neuronal Communication in a Tight Balance That Is Lost in Neurological Disease. *Front. Mol. Neurosci.* **11**, 455 (2018). doi: [10.3389/fnmol.2018.00455](#); pmid: [30618607](#)
70. N. R. Genuth, M. Barna, The Discovery of Ribosome Heterogeneity and Its Implications for Gene Regulation and Organismal Life. *Mol. Cell* **71**, 364–374 (2018). doi: [10.1016/j.molcel.2018.07.018](#); pmid: [30075139](#)
71. J. C. Darnell *et al.*, FMRP stalls ribosomal translocation on mRNAs linked to synaptic function and autism. *Cell* **146**, 247–261 (2011). doi: [10.1016/j.cell.2011.06.013](#); pmid: [21784246](#)
72. R. S. Muddashetty *et al.*, Reversible inhibition of PSD-95 mRNA translation by miR-125a, FMRP phosphorylation, and mGluR signaling. *Mol. Cell* **42**, 673–688 (2011). doi: [10.1016/j.molcel.2011.05.006](#); pmid: [21658607](#)
73. G. Aakalu, W. B. Smith, N. Nguyen, C. Jiang, E. M. Schuman, Dynamic visualization of local protein synthesis in hippocampal neurons. *Neuron* **30**, 489–502 (2001). doi: [10.1016/S0896-6273\(01\)00295-1](#); pmid: [11395009](#)
74. E. Puighermanal *et al.*, Anatomical and molecular characterization of dopamine D1 receptor-expressing neurons of the mouse CA1 dorsal hippocampus. *Brain Struct. Funct.* **222**, 1897–1911 (2017). doi: [10.1007/s00429-016-1314-x](#); pmid: [27678395](#)
75. W. P. Lou, A. Baser, S. Klüßmann, A. Martin-Villalba, In vivo interrogation of central nervous system translation by polyribosome fractionation. *J. Vis. Exp.* **2014**, e51255 (2014). doi: [10.3791/51255](#); pmid: [24835574](#)
76. N. J. McGlinchy, N. T. Ingolia, Transcriptome-wide measurement of translation by ribosome profiling. *Methods* **126**, 112–129 (2017). doi: [10.1016/j.ymeth.2017.05.028](#); pmid: [28579404](#)
77. N. T. Ingolia, G. A. Brar, S. Rouskin, A. M. McGeachy, J. S. Weissman, The ribosome profiling strategy for monitoring translation in vivo by deep sequencing of ribosome-protected mRNA fragments. *Nat. Protoc.* **7**, 1534–1550 (2012). doi: [10.1038/nprot.2012.086](#); pmid: [22836135](#)
78. J. R. Wiśniewski, A. Zougman, N. Nagaraj, M. Mann, Universal sample preparation method for proteome analysis. *Nat. Methods* **6**, 359–362 (2009). doi: [10.1038/nmeth.1322](#); pmid: [19377485](#)
79. E. Abs *et al.*, Learning-Related Plasticity in Dendrite-Targeting Layer 1 Interneurons. *Neuron* **100**, 684–699.e6 (2018). doi: [10.1016/j.neuron.2018.09.001](#); pmid: [30269988](#)
80. A. Biever *et al.*, PKA-dependent phosphorylation of ribosomal protein S6 does not correlate with translation efficiency in striatonigral and striatopallidal medium-sized spiny neurons. *J. Neurosci.* **35**, 4113–4130 (2015). doi: [10.1523/JNEUROSCI.3288-14.2015](#); pmid: [25762659](#)
81. A. E. Power, D. J. Berla, J. L. McGaugh, O. Steward, Anisomycin infused into the hippocampus fails to block “reconsolidation” but impairs extinction: The role of re-exposure duration. *Learn. Mem.* **13**, 27–34 (2006). doi: [10.1101/lm.91206](#); pmid: [16452651](#)
82. J. Remaud *et al.*, Anisomycin injection in area CA3 of the hippocampus impairs both short-term and long-term memories of contextual fear. *Learn. Mem.* **21**, 311–315 (2014). doi: [10.1101/lm.033969.113](#); pmid: [25171422](#)
83. J. Cox, M. Mann, MaxQuant enables high peptide identification rates, individualized p.p.b.-range mass accuracies and proteome-wide protein quantification. *Nat. Biotechnol.* **26**, 1367–1372 (2008). doi: [10.1038/nbt.1511](#); pmid: [19029910](#)
84. S. Tyanova *et al.*, The Perseus computational platform for comprehensive analysis of (prote)omics data. *Nat. Methods* **13**, 731–740 (2016). doi: [10.1038/nmeth.3901](#); pmid: [27348712](#)

85. M. Martin, Cutadapt removes adapter sequences from high-throughput sequencing reads. *EMBnet.journal* **17**, 10–12 (2011). doi: [10.14806/embnet.17.1.200](https://doi.org/10.14806/embnet.17.1.200)
86. B. Langmead, S. L. Salzberg, Fast gapped-read alignment with Bowtie 2. *Nat. Methods* **9**, 357–359 (2012). doi: [10.1038/nmeth.1923](https://doi.org/10.1038/nmeth.1923); pmid: [22388286](https://pubmed.ncbi.nlm.nih.gov/22388286/)
87. A. Dobin et al., STAR: Ultrafast universal RNA-seq aligner. *Bioinformatics* **29**, 15–21 (2013). doi: [10.1093/bioinformatics/bts635](https://doi.org/10.1093/bioinformatics/bts635); pmid: [23104886](https://pubmed.ncbi.nlm.nih.gov/23104886/)
88. D. Karolchik et al., The UCSC Table Browser data retrieval tool. *Nucleic Acids Res.* **32**, D493–D496 (2004). doi: [10.1093/nar/gkh103](https://doi.org/10.1093/nar/gkh103); pmid: [14681465](https://pubmed.ncbi.nlm.nih.gov/14681465/)
89. A. R. Quinlan, I. M. Hall, BEDTools: A flexible suite of utilities for comparing genomic features. *Bioinformatics* **26**, 841–842 (2010). doi: [10.1093/bioinformatics/btq033](https://doi.org/10.1093/bioinformatics/btq033); pmid: [20110278](https://pubmed.ncbi.nlm.nih.gov/20110278/)
90. Y. Liao, G. K. Smyth, W. Shi, featureCounts: An efficient general purpose program for assigning sequence reads to genomic features. *Bioinformatics* **30**, 923–930 (2014). doi: [10.1093/bioinformatics/btt656](https://doi.org/10.1093/bioinformatics/btt656); pmid: [24227677](https://pubmed.ncbi.nlm.nih.gov/24227677/)
91. J. M. Rodriguez et al., APPRIS 2017: Principal isoforms for multiple gene sets. *Nucleic Acids Res.* **46**, D213–D217 (2018). doi: [10.1093/nar/gkx997](https://doi.org/10.1093/nar/gkx997); pmid: [29069475](https://pubmed.ncbi.nlm.nih.gov/29069475/)
92. A. Zhu, J. G. Ibrahim, M. I. Love, Heavy-tailed prior distributions for sequence count data: Removing the noise and preserving large differences. *Bioinformatics* **35**, 2084–2092 (2019). doi: [10.1093/bioinformatics/bty895](https://doi.org/10.1093/bioinformatics/bty895); pmid: [30395178](https://pubmed.ncbi.nlm.nih.gov/30395178/)
93. J. Cox, M. Mann, 1D and 2D annotation enrichment: A statistical method integrating quantitative proteomics with complementary high-throughput data. *BMC Bioinformatics* **13** (Suppl. 16), S12 (2012). doi: [10.1186/1471-2105-13-S16-S12](https://doi.org/10.1186/1471-2105-13-S16-S12); pmid: [23176165](https://pubmed.ncbi.nlm.nih.gov/23176165/)
94. W. J. Kent et al., The human genome browser at UCSC. *Genome Res.* **12**, 996–1006 (2002). doi: [10.1101/gr.229102](https://doi.org/10.1101/gr.229102); pmid: [12045153](https://pubmed.ncbi.nlm.nih.gov/12045153/)
95. G. Yu, L. G. Wang, Y. Han, Q. Y. He, clusterProfiler: An R package for comparing biological themes among gene clusters. *OMICS* **16**, 284–287 (2012). doi: [10.1089/omi.2011.0118](https://doi.org/10.1089/omi.2011.0118); pmid: [22455463](https://pubmed.ncbi.nlm.nih.gov/22455463/)
96. R. Lorenz et al., ViennaRNA Package 2.0. *Algorithms Mol. Biol.* **6**, 26 (2011). doi: [10.1186/1748-7188-6-26](https://doi.org/10.1186/1748-7188-6-26); pmid: [22115189](https://pubmed.ncbi.nlm.nih.gov/22115189/)
97. E. Trott, On the normalization of the minimum free energy of RNAs by sequence length. *PLOS ONE* **9**, e113380 (2014). doi: [10.1371/journal.pone.0113380](https://doi.org/10.1371/journal.pone.0113380); pmid: [25405875](https://pubmed.ncbi.nlm.nih.gov/25405875/)
98. R. Jansen, H. J. Bussemaker, M. Gerstein, Revisiting the codon adaptation index from a whole-genome perspective: Analyzing the relationship between gene expression and codon occurrence in yeast using a variety of models. *Nucleic Acids Res.* **31**, 2242–2251 (2003). doi: [10.1093/nar/gkg306](https://doi.org/10.1093/nar/gkg306); pmid: [12682375](https://pubmed.ncbi.nlm.nih.gov/12682375/)
99. A. K. Sharma et al., A chemical kinetic basis for measuring translation initiation and elongation rates from ribosome profiling data. *PLOS Comput. Biol.* **15**, e1007070 (2019). doi: [10.1371/journal.pcbi.1007070](https://doi.org/10.1371/journal.pcbi.1007070); pmid: [31120880](https://pubmed.ncbi.nlm.nih.gov/31120880/)
100. M. Torrisi, M. Kaleel, G. Pollastri, Deeper Profiles and Cascaded Recurrent and Convolutional Neural Networks for state-of-the-art Protein Secondary Structure Prediction. *Sci. Rep.* **9**, 12374 (2019). doi: [10.1038/s41598-019-48786-x](https://doi.org/10.1038/s41598-019-48786-x); pmid: [31451723](https://pubmed.ncbi.nlm.nih.gov/31451723/)
101. P. Jones et al., InterProScan 5: Genome-scale protein function classification. *Bioinformatics* **30**, 1236–1240 (2014). doi: [10.1093/bioinformatics/btu031](https://doi.org/10.1093/bioinformatics/btu031); pmid: [24451626](https://pubmed.ncbi.nlm.nih.gov/24451626/)
102. J. A. Vizcaino et al., 2016 update of the PRIDE database and its related tools. *Nucleic Acids Res.* **44**, D447–D456 (2016). doi: [10.1093/nar/gkv1145](https://doi.org/10.1093/nar/gkv1145); pmid: [26527722](https://pubmed.ncbi.nlm.nih.gov/26527722/)
103. schumanlab, schumanlab/ribotools: ribotools_monosomes, version v1.0, Zenodo (2019). doi: [10.5281/zenodo.3579508](https://doi.org/10.5281/zenodo.3579508)

ACKNOWLEDGMENTS

We thank D. Vogel for assistance with the preparation of cultured neurons; M. Heumüller and J. J. Letzkus for assistance with the intracerebroventricular injections; I. Wüllenweber and F. Rupprecht for assistance with the proteomics analysis; N. T. Ingolia and

M. J. McGlinchy (Department of Molecular and Cellular Biology, University of California, Berkeley) for advice on bioinformatic analysis of footprint libraries; and E. Valjent (IGF, CNRS, INSERM, University of Montpellier) for providing the Wfs1Cre transgenic mice. **Funding:** A.B. is supported by an EMBO long-term postdoctoral fellowship (EMBO ALTF 331-2017). E.M.S. is funded by the Max Planck Society, an Advanced Investigator award from the European Research Council (grant 743216), DFG CRC 1080: Molecular and Cellular Mechanisms of Neural Homeostasis, and DFG CRC 902: Molecular Principles of RNA-based Regulation. **Author contributions:** A.B. and C.G. designed and conducted experiments and analyzed results. G.T. analyzed results. E.C. and T.D. conducted experiments. J.D.L. acquired the proteomics data. E.M.S. designed experiments and supervised the project. A.B. and E.M.S. wrote the manuscript, and all authors edited the manuscript. **Competing interests:** The authors declare no competing interests. **Data and material availability:** All data are available in the main text or the supplementary materials. The accession number for the raw sequencing data reported in this paper is NCBI BioProject: PRJNA550323. The mass spectrometry proteomics data are deposited at the ProteomeXchange Consortium via PRIDE ([102](https://www.ebi.ac.uk/pride/)) partner repository with the dataset identifier PXD016552. All bioinformatic tools used in this study are contained in one modular C++ program called RiboTools. The source code and further notes on the algorithms can be found on our GitHub repository ([103](https://github.com/schumanlab/ribotools)). Other analysis scripts and codes are available upon request.

SUPPLEMENTARY MATERIALS

science.sciencemag.org/content/367/6477/eaay4991/suppl/DC1
Figs. S1 to S15
Table S1

[View/request a protocol for this paper from Bio-protocol.](#)

24 June 2019; resubmitted 29 October 2019

Accepted 18 December 2019

[10.1126/science.aay4991](https://doi.org/10.1126/science.aay4991)

RESEARCH ARTICLE SUMMARY

CELL BIOLOGY

Endoplasmic reticulum contact sites regulate the dynamics of membraneless organelles

Jason E. Lee, Peter I. Cathey, Haoxi Wu, Roy Parker, Gia K. Voeltz*

INTRODUCTION: The cytoplasm contains an unconventional class of organelles that concentrate specific factors and resources without a limiting membrane. These membraneless organelles include ribonucleoprotein (RNP) granules such as processing bodies (P-bodies, or PBs) and stress granules. PBs and stress granules are composed of nontranslating messenger RNAs (mRNAs) and associated proteins and are thought to provide discrete biochemical environments for regulating the translation and/or degradation of mRNA. In contrast to membrane-bound organelles, very little is known about what extrinsic and intrinsic factors regulate the fusion and fission of membrane-less organelles. Recently, an unexpected role for the endoplasmic reticulum (ER) has been observed in regulating the biogenesis of other membrane-bound organelles at contact sites where the two organelles are tethered and closely apposed. ER contact sites can allow the direct exchange of

macromolecules and serve as a platform for the recruitment of machineries that regulate organelle biogenesis, division, and trafficking. Here, we found that ER contact sites can also regulate the biogenesis and fission of two types of membraneless organelles, PBs and stress granules.

RATIONALE: To determine the extent to which PBs, a conserved cytoplasmic membraneless organelle, are tethered to the ER in animal cells, we used live-cell fluorescence microscopy to simultaneously track the spatiotemporal dynamics of the ER and PBs. To overcome the diffraction limits associated with light microscopy, we designed a reversible ER-PB contact assay using probes attached to the ER and PBs that emit a high-intensity fluorescence signal when the probes are close enough to dimerize. Because ER morphology and RNP granule biogenesis are tightly linked to mRNA translation, we systematically evaluated the relationships

between ER morphology, RNP granule biogenesis, and mRNA translation by assessing endogenous PB numbers in response to altering ER shape and translational capacity and to the induction of cytosolic and ER stress. Because

ON OUR WEBSITE

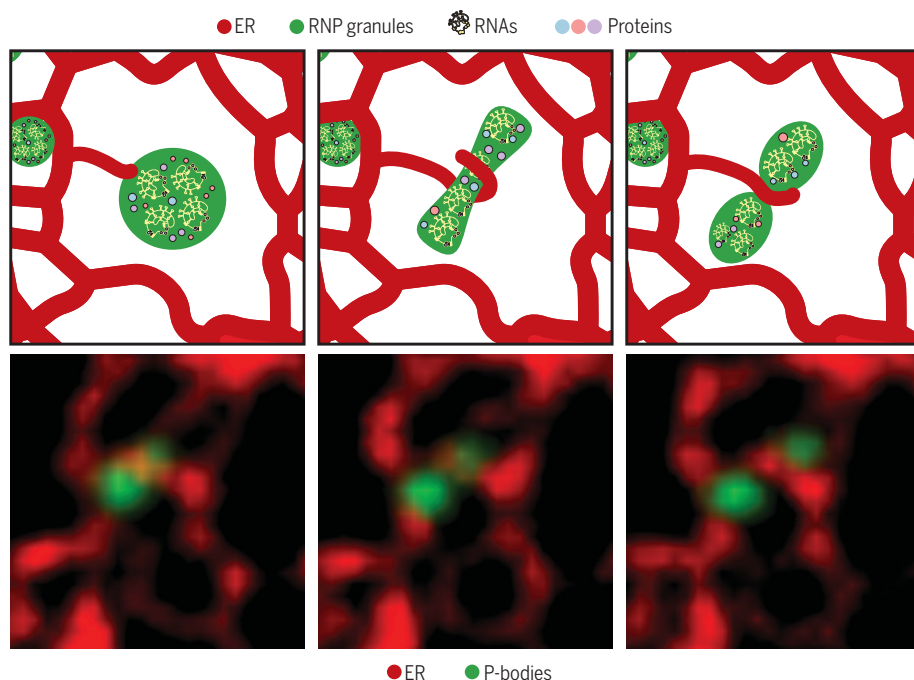
Read the full article at <http://dx.doi.org/10.1126/science.aay7108>

PBs and stress granules are dynamic organelles that undergo fission and fusion reactions akin to membrane-bound organelles, we used live-cell fluorescence microscopy

to score the spatiotemporal relationship between the position of RNP granule division and contact sites with ER tubules.

RESULTS: Using multiple measures, we found that a population of PBs were tethered to the ER in human cells. ER shape exerted profound effects on PB numbers and ER-PB contact. Conditions that promoted expansion of peripheral ER tubules and a reduction in peripheral ER cisternae increased PB numbers and ER-PB contact. Conversely, conditions that promoted an expansion of ER cisternae dramatically decreased PB numbers. The effect of ER shape on PB abundance was likely a reflection of the relative translational capacity of the ER domains. Owing to differences in ribosome density, smooth ER tubules are presumed to have a lower translational capacity than rough ER cisternae. Conditions that locally enhanced the translational capacity of the ER by increasing ER cisternae, such as ER stress, also reduced the number of PBs. Conversely, conditions that globally inhibited mRNA translation (NaAsO₂ and puromycin) suppressed the effects of ER shape on PB abundance. Thus, ER contact sites affected the proliferation of PBs under basal and translationally repressed conditions. Furthermore, ER contact sites also affected the mysterious PB fission process. Live-cell imaging revealed that dynamic ER tubules define the position where PB and stress granule division occurs. These data mirror the spatiotemporal role of ER tubule contact domains that drive the constriction and division of membrane-bound organelles like endosomes and mitochondria.

CONCLUSION: Here, we found that the ER contains contact site domains that are capable of tethering both membraneless and membrane-bound organelles. ER structure and translational capacity has effects on PB biogenesis. Furthermore, the fission of cytoplasmic RNP granules appears to represent an active process that can be driven by ER contact sites, analogous to the division of membrane-bound organelles. ■



Endoplasmic reticulum tubules are a component of the ribonucleoprotein granule fission machinery.

Membraneless RNP granules undergo fission and fusion similar to membrane-bound organelles. A cartoon (top) and the corresponding live-cell fluorescent images (bottom; at 0-, 5-, and 10-s time points, from left to right) of a PB (green) undergoing division at a position where an ER tubule is crossing (red).

The list of author affiliations is available in the full article online.

*Corresponding author. Email: gia.voeltz@colorado.edu
Cite this article as J. E. Lee *et al.*, *Science* 367, eaay7108 (2020). DOI: 10.1126/science.aay7108

RESEARCH ARTICLE

CELL BIOLOGY

Endoplasmic reticulum contact sites regulate the dynamics of membraneless organelles

Jason E. Lee¹, Peter I. Cathey^{1,2}, Haoxi Wu¹, Roy Parker^{2,3}, Gia K. Voeltz^{1,2*}

Tethered interactions between the endoplasmic reticulum (ER) and other membrane-bound organelles allow for efficient transfer of ions and/or macromolecules and provide a platform for organelle fission. Here, we describe an unconventional interface between membraneless ribonucleoprotein granules, such as processing bodies (P-bodies, or PBs) and stress granules, and the ER membrane. We found that PBs are tethered at molecular distances to the ER in human cells in a tunable fashion. ER-PB contact and PB biogenesis were modulated by altering PB composition, ER shape, or ER translational capacity. Furthermore, ER contact sites defined the position where PB and stress granule fission occurs. We thus suggest that the ER plays a fundamental role in regulating the assembly and disassembly of membraneless organelles.

The endoplasmic reticulum (ER) forms membrane contact sites (MCSs) with other membrane-bound organelles to control their composition and distribution throughout the cell (1, 2). MCSs provide an alternative to vesicle-based interorganelle exchange by forming a conduit between two organelles that allows for rapid exchange of resources like lipids and calcium (1–7). ER-organelle MCSs also provide a platform for the recruitment of machineries that regulate bidirectional organelle trafficking on microtubules and help to define the position of organelle division (8–14). In addition to membrane-bound organelles, the cytoplasm is further compartmentalized through condensation of cytosolic macromolecules into a variety of membraneless organelles that differ in function, composition, and number (15, 16). Because the biogenesis and maintenance of membrane-bound organelles are controlled by ER MCSs, we speculated that the dynamics of membraneless organelles might also be regulated by an additional class of ER contact sites.

Ribonucleoprotein (RNP) granules, such as processing bodies (P-bodies, or PBs) and stress granules, are membraneless organelles with distinct structures that are conserved from yeast to animal cells (15, 16). PBs and stress granules are formed from translationally inactive pools of messenger RNAs (mRNAs) and associated proteins and exclude the translation machinery (17). PBs are constitutive structures that are enriched for specific proteins involved in mRNA silencing, decapping, and decay (18–21). Conversely, stress granules are transient structures that form when translation is

restricted (22). Stress granules are enriched with RNA binding proteins and some translation initiation factors and contain most mRNAs with a bias toward enriching for longer mRNAs (23, 24). Thus, PBs and stress granules appear to be long- and short-term holding sites for mRNAs poised to be released into the translation pathway depending on cytoplasmic cues like metabolism and translation capacity. Given the ER-localized translation of mRNA encoding proteins that enter the secretory pathway (25–27) and the stress-dependent release of ER-localized mRNA (28), there could also be RNP granules that store mRNAs for translation reinitiation at the ER membrane.

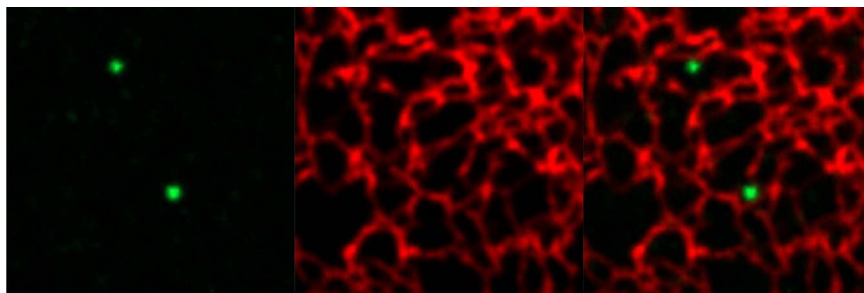
PB dynamics are coupled to ER tubule dynamics in human cells

PBs are an ideal membraneless organelle to begin studies on the interface between the ER and membraneless organelles because PBs are constitutively present in all tested interphase cells and because PBs can grow, shrink, fuse, and undergo fission akin to membrane-bound organelles (17, 29). Two lines of evidence obtained in the budding yeast *Saccharomyces*

cerevisiae suggest that PB biogenesis could be regulated by ER contact sites. First, immunogold-labeled PBs have been observed adjacent to the ER in electron micrographs, and second, PB factors can sediment with the ER in sucrose gradients (19, 21). We thus set out to test the hypothesis that PBs are tethered to the tubular ER network in animal cells using immunofluorescence analysis. A human osteosarcoma (U-2 OS) cell line was fixed and immunolabeled with antibodies against a general luminal ER protein (calreticulin, red) and a PB component [enhancer of decapping (Edc3), green] (Fig. 1, A and B). The colocalization of PBs over the ER network was measured by Mander's coefficient. A large subset of PBs colocalized with ER tubules. As a control, we rotated the ER image 90° and could then see that only a small percentage of PBs overlapped with the ER by chance (Fig. 1, A and B). Thus, a population of endogenous PBs may be bound to the ER network in animal cells.

We next used live-cell imaging to examine the extent to which PBs remained tethered to the ER over time, similar to experiments done to show that the ER is tethered to membrane-bound organelles (9). The tubular ER network is very dynamic. Thus, sustained contact between an individual PB and ER tubules over time suggests that the two organelles are tethered to each other. We collected 2-min movies of U-2 OS cells transiently transfected with fluorescent markers for the ER (mCh-KDEL) and three separate PB markers (GFP-Dcp2, GFP-Dcp1a, and GFP-Dcp1b; GFP, green fluorescent protein) (Fig. 1C, Movie 1, and fig. S1). PB contact with the ER was binned into three categories: The PB contacts the ER for (i) less than 20 s or not at all, (ii) at least 20 s but less than 2 min, and (iii) the entire 2-min movie.

Approximately one-third to one-half of exogenously tagged PBs stably associated with the ER throughout the 2-min movie depending on whether GFP-Dcp2 (39.1 ± 3.9%), GFP-Dcp1a (33.5 ± 5.0%), or GFP-Dcp1b (50.3 ± 4.7%) was expressed (Fig. 1E). By comparison, cells overexpressing GFP-Dcp1b contained fourfold more



Movie 1. Live-cell tracking of the ER and PBs. Time-lapse movie corresponding to Fig. 1C showing the ER (red) labeled with mCh-KDEL and PBs (green) labeled with GFP-Dcp2. Frames were captured every 5 s over the course of 2 min.

¹Department of Molecular, Cellular, and Developmental Biology, University of Colorado, Boulder, CO, USA. ²Howard Hughes Medical Institute, University of Colorado, Boulder, CO, USA. ³Department of Biochemistry, University of Colorado, Boulder, CO, USA.

*Corresponding author. Email: gia.voeltz@colorado.edu

PBs (~40 PBs per cell, Fig. 1D), and this led to an increase in the percentage of PBs that were associated with the ER ($80.4 \pm 3.1\%$) (fig. S1, A to C). Thus, a substantial subset of PBs are tethered to the ER, and PB-ER contact is sensitive to PB composition and abundance.

Nanoscale resolution of ER-PB contact using reversible dimerization-dependent fluorescent proteins in living cells

The live-cell tracking of PBs with ER tubules over time strongly suggested that the two organelles are tethered. Because previous descrip-

tions of RNP granules suggest that they are surrounded by a liquid phase (30, 31), we aimed to test whether ER tubules contact PBs at molecular distances that are reminiscent of typical MCSs (10 to 30 nm) (1, 2). Because 30 nm is below the resolution limit of our microscope, we used dimerization-dependent fluorescent protein (ddFP) domains (32) to resolve molecular contact between the ER and PBs in live cells (Fig. 2A). We fused the core (GB) domain to a PB marker (Dcp1b) and the red fluorescence-capable (RA) domain to an ER marker (Sec61 β) such that red fluorescence will signal that the two organelles are close enough for the two tags to dimerize (Fig. 2A). The ddFP system is attractive for assessing contact sites in live cells because the interactions between ddFP domains are reversible (32). We captured 2-min movies of U-2 OS cells exogenously expressing PB (GFP-Dcp2) and ER (BFP-KDEL; BFP, blue fluorescent protein) markers together with the ddFP system and binned PBs into three categories: (i) PBs with no ddFP signal, (ii) PBs with ddFP signal for at least one frame of the 2-min movie, and (iii) PBs with ddFP signal for the entire 2-min movie (Fig. 2, C and D, and Movies 2 and 3).

Nearly half of the PBs maintained stable contact sites with the ER through the duration of the movie ($46.3 \pm 5.0\%$) (Fig. 2B). The frequency of stable PB-ER contact sites was similar to the qualitative tracking of two organelles in live-cell movies (Fig. 1E). The PBs in category (ii) also revealed that PBs can be recruited to and released from the ER (Fig. 2D, inset 1, and Movie 2).

PB biogenesis is dependent on ER morphology and the translational capacity of the ER

PB and stress granules store translationally inactive mRNAs (15–17). The rough ER is bound by ribosomes and is a major site of translation, translocation, and protein folding in the cell (25–28). Electron microscopy and tomography have revealed that cisternal ER sheets have approximately fivefold higher ribosome density than ER tubules (33, 34). Conversely, ER tubules are functionally linked to phospholipid and sterol synthesis, calcium homeostasis, and the formation of ER-organelle MCSs (1, 2). Because rough cisternal ER is indicative of ER translational capacity, we tested whether altering peripheral ER shape would affect PB biogenesis.

First, ER tubules were increased at the expense of cisternal ER by overexpressing the ER tubule-generating protein reticulon-4a (Rtn4a) (35), which led to a twofold increase in PBs compared with that in control cells expressing a general ER membrane marker, mCh-Sec61 β (Fig. 3, A and B). Converting cisternal ER into tubules also led to an increase in ER-PB contact (Fig. 3, C to E). Next, we performed *RTN4* gene ablation by CRISPR-Cas9 in U-2 OS

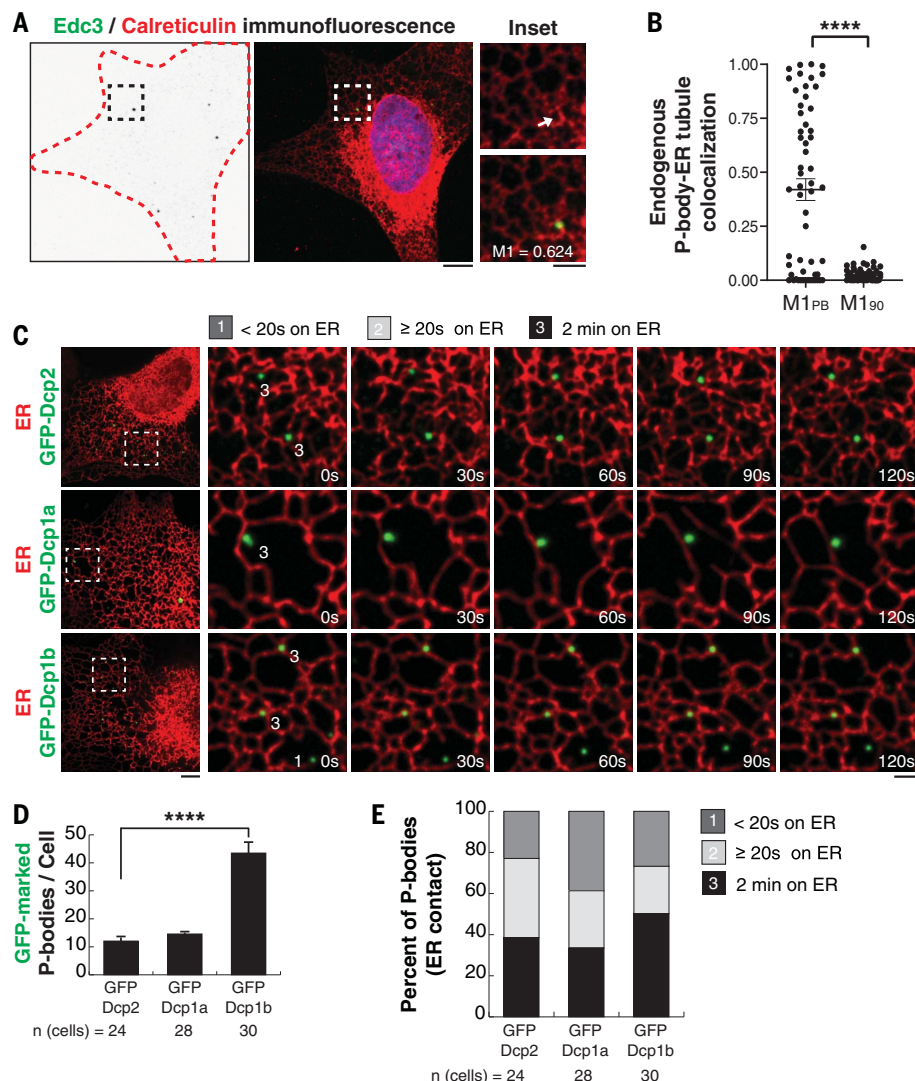


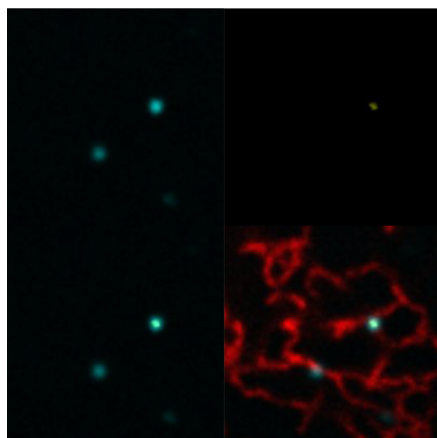
Fig. 1. A subset of PBs colocalize and track with ER tubules in human cells. (A) Representative images of immunofluorescence (IF) studies performed in U-2 OS cells against Edc3 and calreticulin to label PBs (green) and ER (red), respectively. Edc3 IF gray-scale images were inverted to highlight Edc3 puncta (left), Edc3 IF in green merged with the nuclear stain Hoechst in blue (middle), and the middle panels merged with calreticulin IF in red (right). (B) The level of colocalization between endogenous PBs and ER tubules was determined by calculating the Mander's coefficient of PBs within regions of interest (ROIs) with resolvable ER tubules ($M1_{PB}$) and tested for significance using the Kolmogorov-Smirnov test by comparing $M1_{PB}$ to the Mander's coefficient after the ER ROI was rotated 90° ($M1_{90}$). Fifty-six ROIs were analyzed out of 50 cells from three biological replicates. The error bar indicates SEM. (C) Representative merged images of the ER (mCh-KDEL) and PBs labeled with three factors of the decapping complex (GFP-Dcp2, GFP-Dcp1a, or GFP-Dcp1b). Insets show movement of the two organelles through space and time over a 2-min time-lapse movie with frames captured every 5 s (Movie 1). PBs labeled with a "1" tracked with ER tubules for less than four consecutive frames, whereas PBs labeled with a "3" tracked with ER tubules for the entire time-lapse movie. (D and E) Thirty cells were imaged for each condition from three biological replicates and quantified for the mean number of PBs per cell (D) and the degree of association between the ER and PBs (E). For (D), statistical significance was determined by one-way analysis of variance (ANOVA) with multiple comparisons, and error bars indicate SEM. For (A) and (C), scale bars are 5 and 2 μ m in the full cell and inset images, respectively. **** $P < 0.0001$.

cells to shift the balance of cisternae and tubules toward more cisternal ER. *RTN4* knockout (KO) cells displayed significantly fewer PBs compared with wild-type U-2 OS cells, even though they expressed PB factors at similar levels to wild-type U-2 OS cells (Fig. 3, G and H). We confirmed that the *RTN4* KO phenotype was due to a loss in Rtn4a function because PB biogenesis could be rescued by

exogenous expression of Rtn4a-mCh into *RTN4* KO cells (fig. S2). Finally, we depleted ER tubules by overexpressing the cisternal ER promoting protein CLIMP63 (36), which led to a significant decrease in PB numbers, reminiscent of *RTN4* KO (Figs. 3, I and J, and 4, C and D). Thus, ER structure affects PB biogenesis in a way that is likely reflective of the translational capacity of the ER.

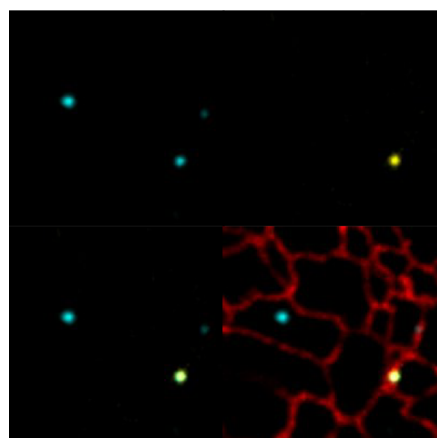
Inhibition of mRNA translation overrides the dependence of PB biogenesis on ER morphology

We next tested whether the dependence of PB biogenesis on ER shape is due to altering ER translational capacity. We restricted translation by inducing an oxidative stress response under cisternal ER-promoting conditions using sodium arsenite (NaAsO_2), which induces a



Movie 2. Resolving ER-PB contact in live cells.

Time-lapse movie corresponding to Fig. 2D, inset 1, showing PBs (cyan) labeled with GFP-Dcp2, ER-PB contact (yellow) labeled with dimerization of RA-Sec61β and GB-Dcp1b, and the ER (red) labeled with BFP-KDEL. Frames were captured every 5 s over the course of 2 min.



Movie 3. Resolving ER-PB contact in live cells.

Time-lapse movie corresponding to Fig. 2D, inset 2, showing PBs (cyan) labeled with GFP-Dcp2, ER-PB contact (yellow) labeled with dimerization of RA-Sec61β and GB-Dcp1b, and the ER (red) labeled with BFP-KDEL. Frames were captured every 5 s over the course of 2 min.

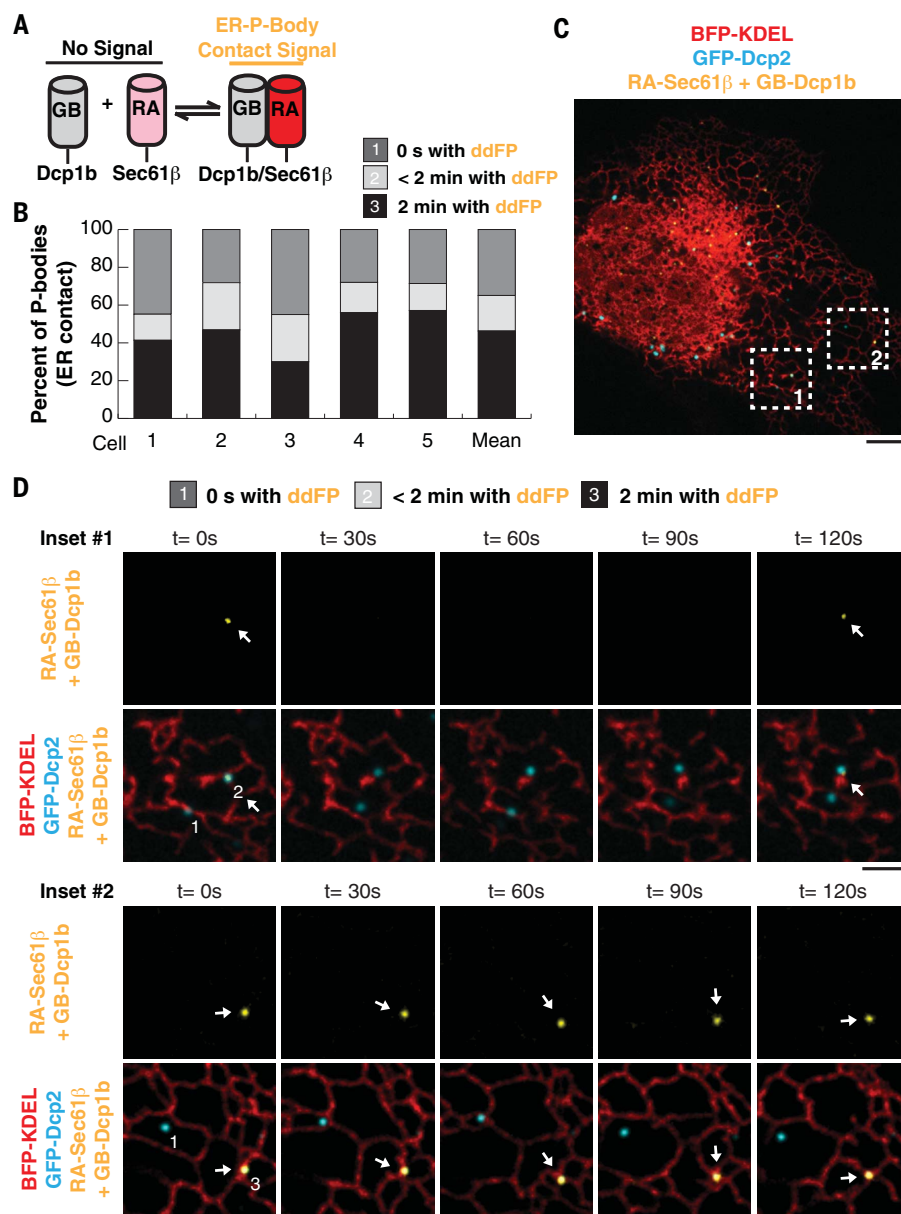
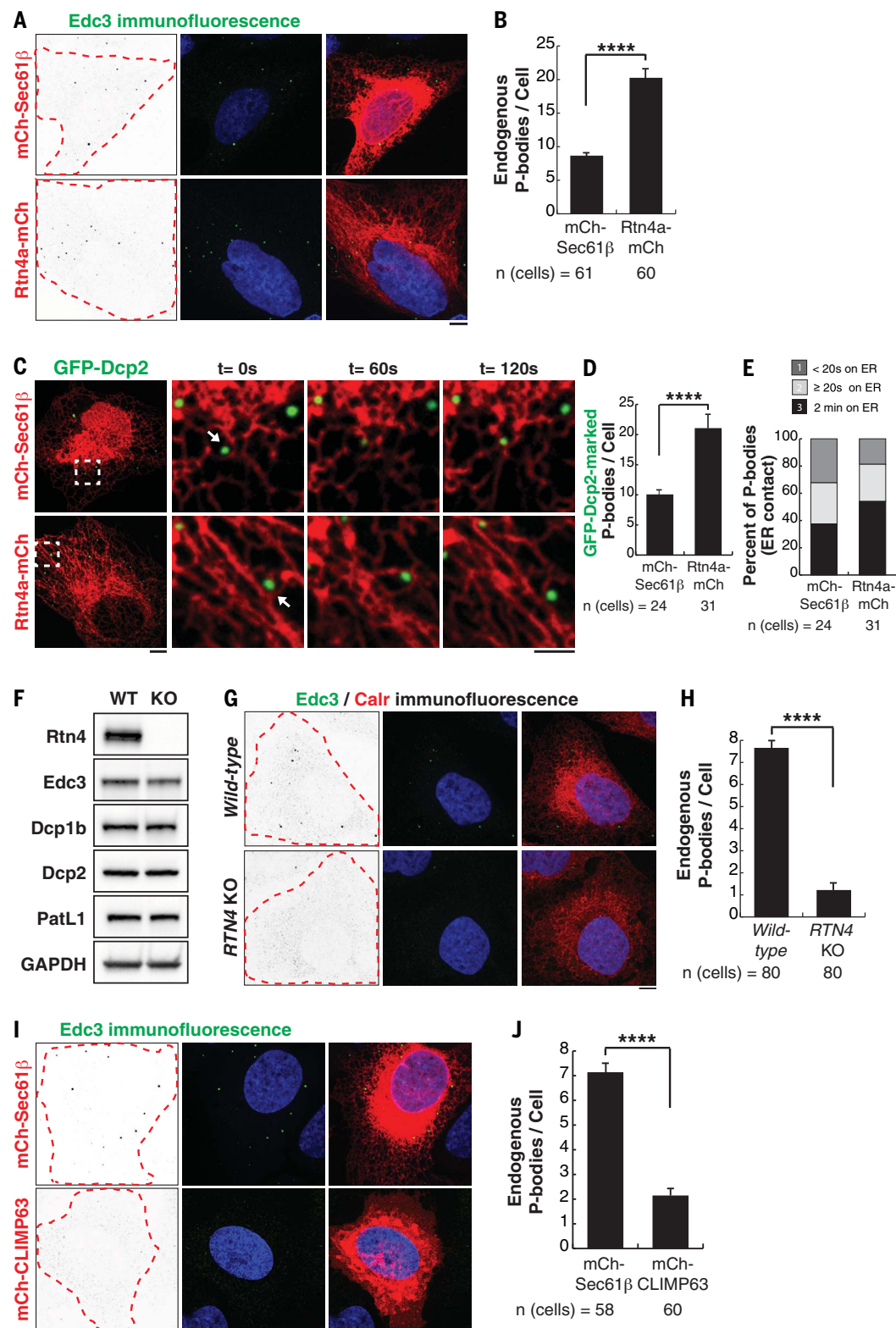


Fig. 2. The ER forms transient and stable contact sites with PBs. (A) Cartoon of ddFP system used to assay ER (RA-Sec61β) and PB (GB-Dcp1b) contact. (B) Quantification of ER contact from five cells together with their mean values ($n = 113$ PBs). PBs were binned into three categories: (i) PBs without ddFP signal, (ii) PBs with ddFP signal for a fraction of the 2-min time-lapse movie, and (iii) PBs with ddFP signal for the entire 2-min time-lapse movie. (C) Representative merged image of Dcp2-marked PBs (cyan), KDEL-labeled ER (red), and ER contact (yellow). The numbered regions indicate the inset areas shown in (D). (D) Inset 1 (Movie 2) and inset 2 (Movie 3) show examples of each PB category. The arrows highlight time points with positive ddFP signal (yellow). Scale bars are 5 μm in (C) and 2 μm in (D).

Fig. 3. The relationship between ER shape and PB biogenesis.

(A) Representative images of Edc3 IF studies performed in U-2 OS cells transiently transfected with mCh-Sec61 β or Rtn4a-mCh. Edc3 IF gray-scale images were inverted to highlight Edc3 puncta (left), Edc3 IF in green merged with the nuclear stain Hoechst in blue (middle), and the middle panels merged with mCh-tagged ER markers in red (right). The dashed lines indicate the cellular boundary as estimated by the outer reaches of ER signal. (B) The mean numbers of endogenous PBs were quantified in U-2 OS cells exogenously expressing mCh-Sec61 β or Rtn4a-mCh from three biological replicates. (C) Representative merged images of U-2 OS cells overexpressing either mCh-Sec61 β or Rtn4a-mCh together with the PB marker GFP-Dcp2. Insets show movement of the two organelles through space and time over a 2-min time-lapse movie with frames captured every 5 s. PBs were binned as in Fig. 1C. The arrows show PBs that maintain contact with the ER for the entire movie. (D and E) Cells were imaged for each condition from three biological replicates and quantified for the mean number of PBs per cell (D) and the degree of association between the ER and PBs (E). (F) Immunoblot analyses of protein expression levels for Rtn4 and PB factors (Edc3, Dcp1b, Dcp2, and PatL1) in whole-cell lysates of wild-type and *RTN4* KO U-2 OS cells. Glyceraldehyde-3-phosphate dehydrogenase (GAPDH) was used as a loading control. (G) Representative images of IF studies performed in wild-type and *RTN4* KO U-2 OS cells against Edc3 and calreticulin (Calr) to label PBs (green) and ER (red), respectively. Edc3 IF gray-scale images were inverted to highlight Edc3 puncta (left), Edc3 IF in green merged with the nuclear stain Hoechst in blue (middle), and the middle panels merged with calreticulin IF in red (right). (H) The mean numbers of PBs were quantified in wild-type and *RTN4* KO U-2 OS cells from three biological replicates. (I) Representative images of Edc3 IF studies performed in U-2 OS cells transiently transfected with mCh-Sec61 β or mCh-CLIMP63. Edc3 IF gray-scale images were inverted to highlight Edc3 puncta (left), Edc3 IF in green merged with the nuclear stain Hoechst in blue (middle), and the middle panels merged with mCh-tagged ER markers in red (right). (J) The mean numbers of endogenous PBs were quantified in U-2 OS cells exogenously expressing mCh-Sec61 β or mCh-CLIMP63 from three biological replicates. In (B), (D), (H), and (J), statistical significance was determined by Student's *t* test, and error bars indicate SEM; *****P* < 0.0001. In (A), (C), (G), and (I), scale bars are 5 and 2 μ m in full cell and inset images, respectively.



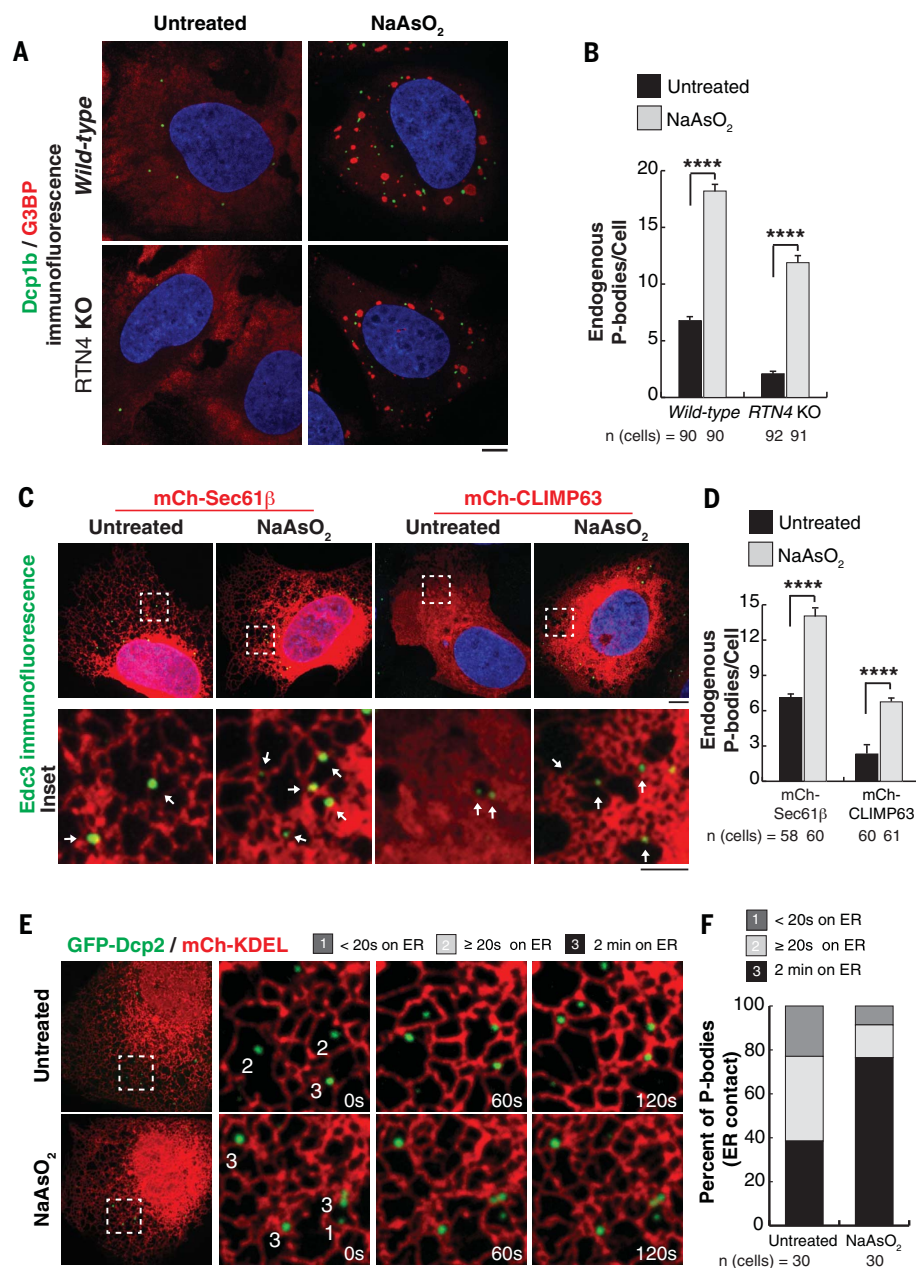


Fig. 4. The relationship between PB biogenesis, ER shape, and oxidative stress-induced mRNA translation inhibition. (A) Representative images of Dcp1b (PB marker, green) and G3BP (stress granule marker, red) IF studies were performed in wild-type and *RTN4* KO U-2 OS cells treated with 0.5 mM NaAsO₂ for 1 hour. Blue indicates the nucleus stained by Hoechst. (B) The mean numbers of endogenous PBs were quantified from three biological replicates. (C) Representative images of Edc3 IF studies performed in U-2 OS cells transiently transfected with mCh-Sec61β or mCh-CLIMP63 treated with 0.5 mM NaAsO₂ for 1 hour. Arrows within insets highlight PBs that overlap with domains of high ER membrane curvature. (D) The mean numbers of endogenous PBs were quantified from three biological replicates in U-2 OS cells exogenously expressing mCh-Sec61β or mCh-CLIMP63 that were either untreated or treated with NaAsO₂. (E and F) Representative merged images of U-2 OS cells exogenously expressing GFP-Dcp2 and mCh-KDEL to label PBs and the ER in live cells, respectively (E). Insets show movement of the two organelles through space and time over a 2-min time-lapse movie with frames captured every 5 s. PBs were binned as in Fig. 1C. Cells were imaged for each condition from three biological replicates and quantified for the degree of association between the ER and PBs (F). In (B) and (D), statistical significance was determined by one-way ANOVA with multiple comparisons, and error bars indicate SEM; *****P* < 0.0001. In (A), (C), and (E), scale bars are 5 and 2 μm in full cell and inset images, respectively.

well-studied translation inhibition and RNP granule biogenesis response (17). We observed a significant increase in PB and stress granule abundance in wild-type cells after NaAsO₂ treatment for 60 min (Fig. 4, A and B). PB abundance also increased significantly after NaAsO₂ treatment under two cisternal ER-promoting conditions, *RTN4* depletion (Fig. 4, A and B) or mCh-CLIMP63 overexpression (Fig. 4, C and D). Furthermore, a closer inspection of PBs induced by NaAsO₂ revealed a localization to ER domains of high membrane curvature, such as tubules, fenestrae, and edges of cisternae (Fig. 4C, insets). Thus, we measured the effect of NaAsO₂ treatment on the percentage of PBs that are bound to ER tubules. ER-PB contact was tracked in live cells expressing GFP-Dcp2 and mCh-KDEL. Translation inhibition induced by NaAsO₂ treatment doubled the percentage of PBs that were tightly associated with the ER in these cells compared with untreated cells (Fig. 4, E and F).

We aimed to complement NaAsO₂-induced RNP granule studies with puromycin to directly target the translation machinery in wild-type and *RTN4* KO cells. Puromycin is an antibiotic that inhibits global translation by disrupting peptide transfer, leading to the release of ribosomes from mRNA. We used a short 15-min treatment and high 200 μM concentration of puromycin that can clear ribosomes off ER membranes (36). The short puromycin treatment also allowed us to minimize any downstream effects that accompany a global translation block.

We observed a significant increase in PB numbers in response to puromycin-induced release of ribosomes from mRNA and ER membranes in both wild-type and *RTN4* KO cells (fig. S3). As expected (22), puromycin did not induce stress granule formation. Thus, the relationship between PB biogenesis and ER shape is dependent on the translational capacity of the ER because inhibiting mRNA translation with NaAsO₂ or puromycin could induce PB biogenesis even when cisternal ER is abundant.

ER stress and the unfolded protein response induce PB disassembly

Cisternal ER and ER translational capacity will also increase when the unfolded protein response (UPR) is evoked during ER stress. The UPR can relieve the burden of misfolded protein accumulation by attenuating general translation and by selectively up-regulating and translating genes encoding for ER resident proteins such as chaperones (37). Thus, we further tested the relationship between ER shape, ER translational capacity, and PB biogenesis by inducing the UPR. Cells were treated with tunicamycin (Tm), which triggers the UPR by blocking N-linked glycosylation of

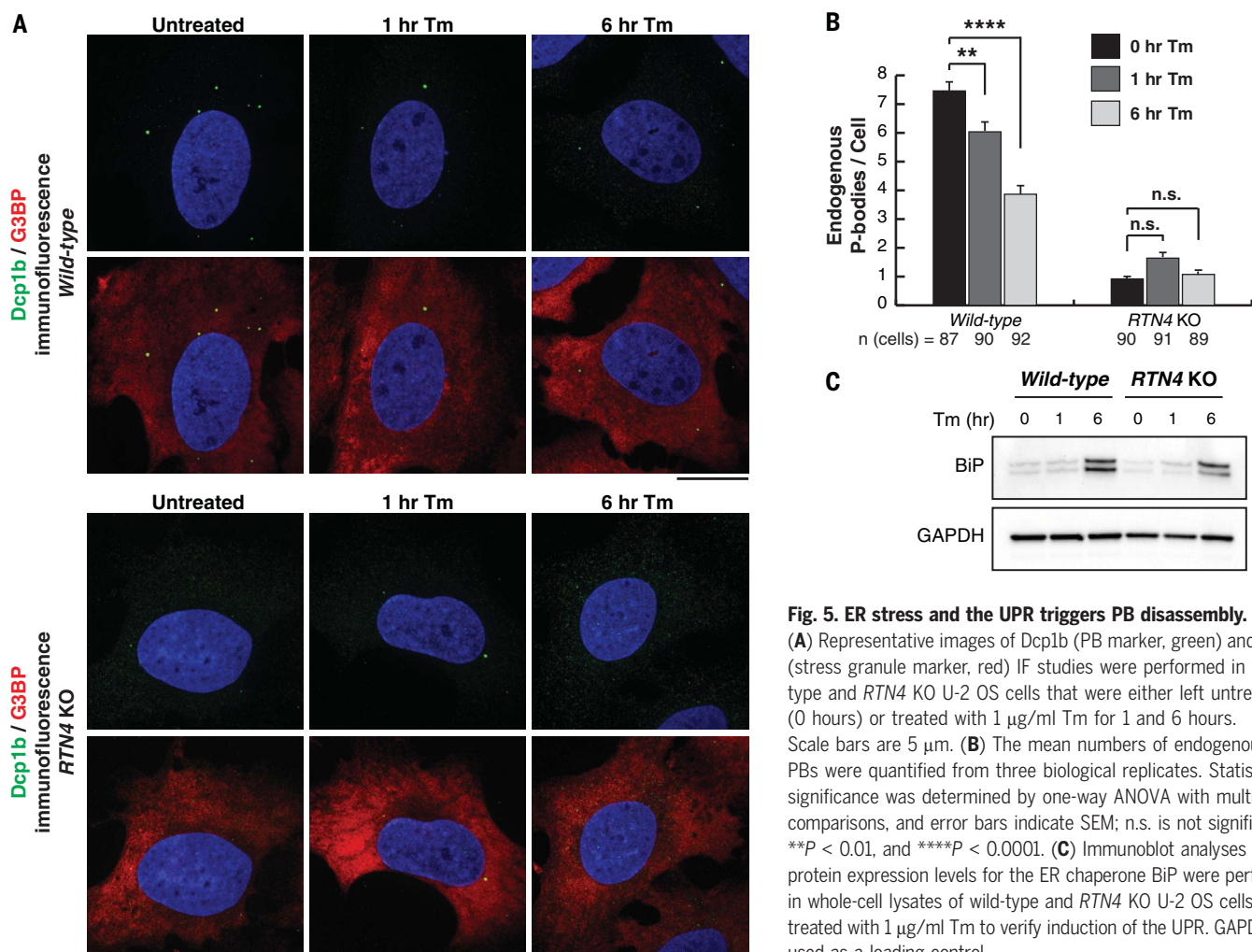


Fig. 5. ER stress and the UPR triggers PB disassembly.

(A) Representative images of Dcp1b (PB marker, green) and G3BP (stress granule marker, red) IF studies were performed in wild-type and *RTN4* KO U-2 OS cells that were either left untreated (0 hours) or treated with 1 μ g/ml Tm for 1 and 6 hours. Scale bars are 5 μ m. (B) The mean numbers of endogenous PBs were quantified from three biological replicates. Statistical significance was determined by one-way ANOVA with multiple comparisons, and error bars indicate SEM; n.s. is not significant, ** $P < 0.01$, and **** $P < 0.0001$. (C) Immunoblot analyses of protein expression levels for the ER chaperone BiP were performed in whole-cell lysates of wild-type and *RTN4* KO U-2 OS cells treated with 1 μ g/ml Tm to verify induction of the UPR. GAPDH was used as a loading control.

nascent proteins in the ER lumen. Wild-type and *RTN4* KO cells were treated with Tm for 1 and 6 hours to resolve any differences between acute pre-UPR and UPR conditions (Fig. 5). We confirmed that the UPR was induced by 6-hour Tm treatment by detecting increased levels of the ER chaperone BiP and expansion of cisternal ER (Fig. 5C and fig. S4).

Induction of the UPR by Tm reduced PB numbers in wild-type cells and had no measurable effect on the already low PB numbers in *RTN4* KO cells (Fig. 5, A and B). Surprisingly, Tm-induced UPR did not trigger stress granule formation in either wild-type or *RTN4* KO cells (Fig. 5A). However, previous studies connecting ER stress to stress granules did so by using thapsigargin, which has effects that extend beyond ER stress owing to the release of calcium from the ER into the cytosol (38).

Taken together, our data show a consistent relationship whereby conditions that increase cisternal ER or ER translational capacity reduce PB numbers, and conversely, conditions that decrease cisternal ER or translational capacity increase PB numbers and increase ER-PB contact. Given that PBs store and

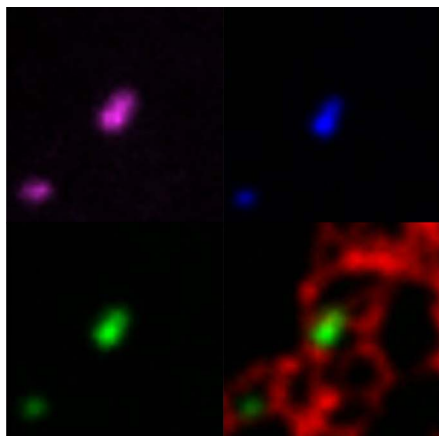
degrade translationally inactive mRNAs, the ability of PBs to form and disassemble in response to changes in ER translational capacity opens up the possibility that ER-PB contact sites are conduits for mRNA exchange between the two organelles.

ER tubules mark the sites of RNP granule fission

The fission and fusion of RNP granules, such as PBs and stress granules, have been observed in live cells (29, 39, 40). It is assumed that these events occur spontaneously given the liquid-like nature of biological condensates (16, 31). However, two observations suggest that RNP granule fission might be a regulated process within cells. First, the observation of PB fission is rare (29), which suggests that it is not energetically favorable for fission to occur spontaneously within cells. Second, the fission rate of stress granules increases dramatically during the disassembly process, which is engaged upon stress removal and restoration of translation initiation (40). Because ER contacts mediate the fission of mitochondria and early and late endosomes (13, 14), we asked

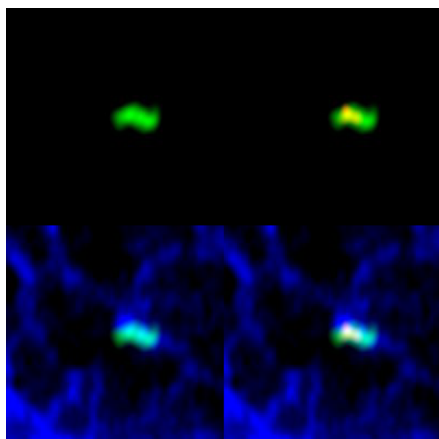
whether these unconventional ER contact sites with RNP granules might also define the position of their fission. We investigated the spatiotemporal relationship between the ER and PB fission by capturing movies of U-2 OS cells expressing an ER marker (mCh-KDEL) together with PB-localized components of the mRNA decapping complex [BFP-Dcp1a, GFP-Dcp1b, and Janelia Fluor (JF)-646-SNAP-Dcp2] (Fig. 6, C and D; Movie 4; and fig. S4, A and B). To assess ER tubule localization, we measured fluorescence intensities across a line drawn along the axis of the PB perpendicular to the fission site (Fig. 6A).

We noticed that ER tubules crossed over the “constricted” neck leading up to PB fission events 100% of the time (Fig. 6, B to D, and fig. S4, A and B). To further dissect the spatiotemporal relationship between ER contact and PB fission, we captured time-lapse super-resolution movies of cells expressing the ddFP ER-PB contact system (from Fig. 2). Notably, ddFP-resolved ER contact was observed at 100% of PB fission events (Fig. 6B). Moreover, we observed fission events that displayed ER contact before the formation of a constricted



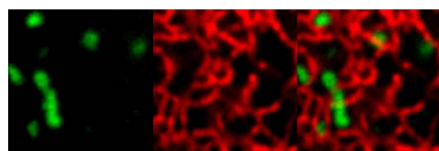
Movie 4. ER tubules mark the site of PB fission.

Time-lapse movie corresponding to Fig. 6C showing the ER (red) labeled with mCh-KDEL and PBs simultaneously labeled with JF646-SNAP-Dcp2 (magenta), BFP-Dcp1a (blue), and GFP-Dcp1b (green). There are 5 s between each frame.



Movie 5. ddFP system resolves the timing of ER contact during PB fission.

Time-lapse movie corresponding to Fig. 6E showing the ER (blue) labeled with BFP-KDEL, PBs (green) labeled with GFP-Dcp2, and ER contact (red) detected by RA-GB dimerization linked to RA-Sec61β and GB-Dcp1b. Images were captured every 3 s using the Zeiss LSM880 confocal laser scanning microscope with Airyscan detectors.



Movie 6. ER tubules mark the site of stress granule fission. Time-lapse movie corresponding to Fig. 6E showing the ER (red) labeled with mCh-KDEL and stress granules (green) labeled with GFP-G3BP. There are 5 s between each frame.

neck, suggesting that the ER might contribute to constriction initiation during the fission process (Fig. 6, E and F; Movie 5; and fig. S5, C and D). This demonstrates a strict correlation between ER tubule–PB interaction at fission events analogous to the percentage of mitochondrial (88%) and endosomal fission (97%) events associated with ER tubules (13, 14).

We also asked whether ER tubules define the position of stress granule fission. Stress granules are not constitutive structures in cells but form within minutes upon exposure to stressors that inhibit translation initiation, such as NaAsO₂. Stress granules are membraneless organelles that traffic, at least in part, by hitchhiking on endosomes or lysosomes (41) and disassemble through fission reactions after the removal of stress and upon reactivation of translation (39, 40). These dynamic properties make stress granules an ideal system for studying membraneless organelle fission and the role of the ER in this process. Thus, we visualized the spatiotemporal relationship between ER tubules and stress granule disassembly during NaAsO₂ washout. Cells expressing ER (mCh-KDEL) and stress granule (GFP-G3BP) markers were treated with 0.5 mM NaAsO₂ for 60 min followed by NaAsO₂ washout for 40 min. Live imaging began at the 40-min washout time point in the presence of 200 nM integrated stress-response inhibitor (ISRIB). ISRIB expedites the stress granule disassembly process by reinitiating mRNA translation by circumventing eIF2α-phosphorylation-induced translation inhibition (38). Time-lapse movies of stress granule disassembly were captured during ISRIB treatment, and line scans were used to assess ER tubule localization during stress granule fission (Fig. 6, G and H, and fig. S5, E and F). Similar to PB fission, ER tubules rearranged across the constriction for 100% of stress granule fission events (Fig. 6, B, G, and H; Movie 6; and fig. S5, E and F).

Discussion

Our observations presented here suggest that contact sites with the ER are not restricted to membrane-bound organelles but also occur with non-membrane-bound organelles in a functional manner. First, a large population of PBs are tethered at molecular distances to the ER in animal cells. Second, there is a relationship between PB composition and ER contact. ER contact sites with membraneless PBs share similarities in how ER MCSs interact with a membrane-bound organelle, the endosome—the percentage of endosomes tethered to the ER increases as endosomes mature. Roughly 50% of early endosomes are tethered to the ER, whereas nearly all late endosomes maintain contact with the ER (42). Thus, it is possible that the ~40 to 50% of PBs tethered to the ER represent a different PB “maturation”

state from untethered PBs, such that PBs can gain contact as their composition is altered, possibly by exchanging Dcp1a and Dcp1b.

Third, our studies reveal an inverse relationship between PB biogenesis and the abundance of ER cisternae, which would be expected to have a higher ribosome density and translational capacity. In complementary experiments, the effect of ER shape on PB abundance was suppressed under conditions that inhibit translation. Given that PBs store and degrade translationally inactive mRNAs, the ability of PBs to form and disassemble in response to changes in ER translational capacity opens up the possibility that ER–PB contact sites are conduits for mRNA and/or protein exchange between the two organelles.

Lastly, our work also provides evidence that RNP granule fission can be an active process and will be mediated by ER contact sites. In particular, dynamic ER tubules defined the position of fission for two different membraneless organelles just like they do for membrane-bound organelles (13, 14). Possible machineries that could be delivered by ER tubules to drive fission of RNP granules would include protein chaperones, RNA helicases, and modification enzymes. Because it has been well documented that membraneless organelles can undergo liquid-to-solid transitions (43), it is an intriguing possibility that the ER can sense and control the physical properties of these organelles through fission. Understanding the role that the ER plays in regulating RNP granules is important because many neurodegenerative disorders are associated with age-related aggregation of RNA granule components (43, 44).

Materials and methods

DNA plasmids and cell lines

GFP-Dcp2, GFP-Dcp1b, and GFP-G3BP1 were a kind gift from R. Buchan (University of Arizona, Tucson, AZ). GFP-Dcp1a was generated by cloning Dcp1a from U-2 OS cDNA and inserted into XhoI/KpnI sites of the pAcGFP-C1 vector (Clontech, Mountain View, CA) and then subcloned into the BFP-C1 vector to generate BFP-Dcp1a. SNAP-Dcp2 was cloned from GFP-Dcp2 and inserted into XhoI/BamHI sites of SNAP-C1 vector. The Janelia Fluor 646 (JF-646) SNAP ligand was a kind gift from L. Lavis (Janelia Farm, Ashburn, VA). mCh-KDEL, mCh-Sec61β, Rtn4a-mCh, and BFP-KDEL were previously described (9, 13, 14). GB-NES (Addgene #61017), GA-NES (Addgene #61018), and RA-NES (Addgene #61019) vectors were a kind gift from D. Buysse and G. Odorizzi (University of Colorado, Boulder, CO). We then generated GA-C1, GB-C1, and RA-C1 vectors by amplifying GA, GB, and RA sequences (without nuclear export sequence) from GA-NES, GB-NES, and RA-NES vectors and inserted them into the NheI/BspEI sites of the pAcGFP-C1 vector to replace the GFP-encoding sequence (Clontech, Mountain View,

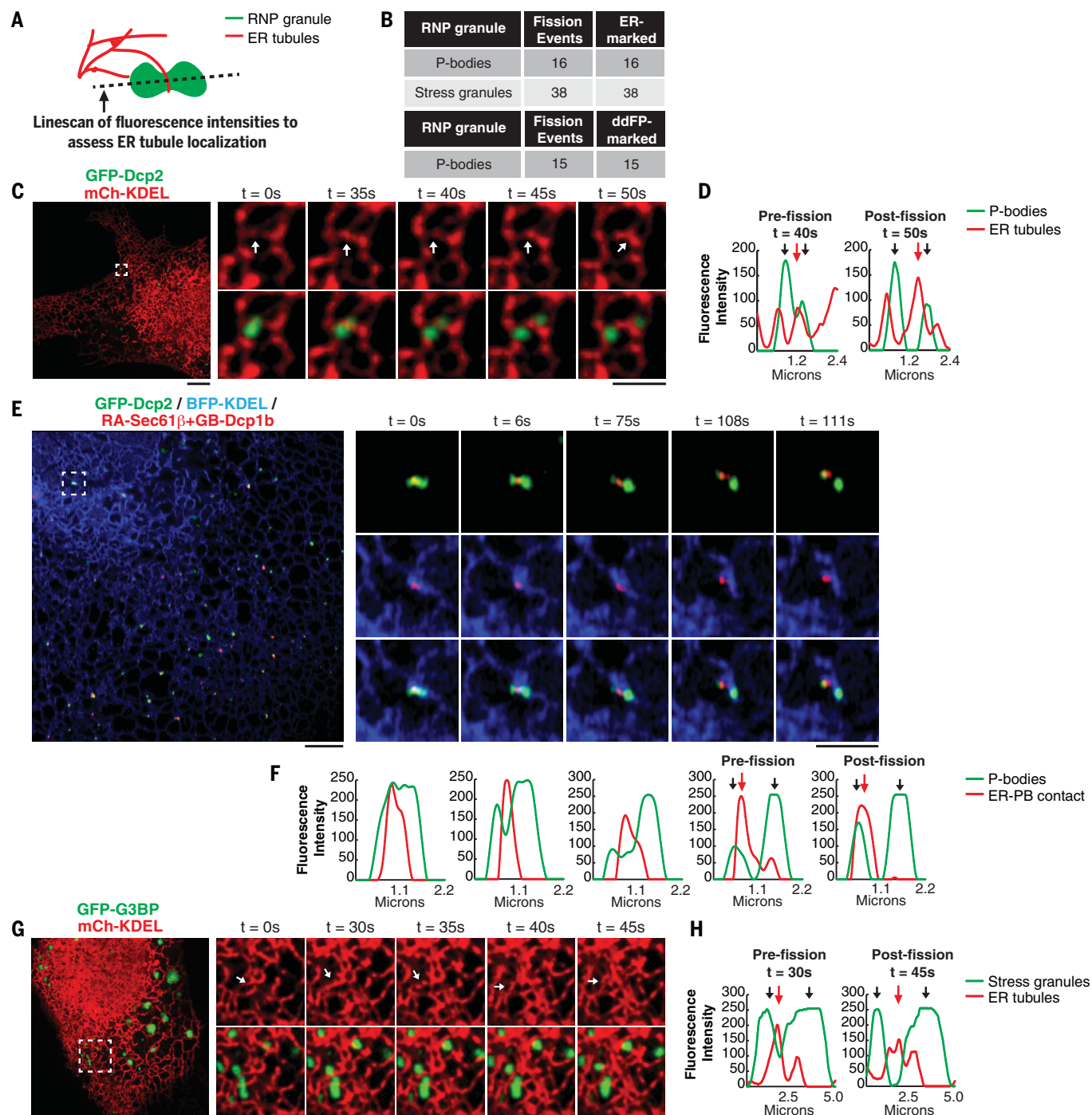


Fig. 6. ER tubules localize to the sites of PB and stress granule fission.

(A) Cartoon depicting line scan positioned perpendicular to RNP granule fission sites to assess ER tubule localization pre- and postfission. (B) Catalog of ER localization to PB and stress granule fission events as well as ddFP resolving of ER contact at PB fission events. (C) Representative merged images of the ER (red) labeled with mCh-KDEL and PBs (green) colabeled with GFP-Dcp1b (shown), BFP-Dcp1a, and JF646-SNAP-Dcp2 in U-2 OS cells. Insets are time-lapse images of the ER alone (top) and ER-PBs merged (bottom). Arrows highlight ER tubules positioned at PB fission sites (Movie 4). (D) Line scan analyses of fluorescence intensities of PBs (green) and the ER (red) pre- and postfission. Red arrows highlight ER tubules localized to the site of PB fission. (E) Representative images of U-2 OS cells expressing general PB (GFP-Dcp2) and ER markers (BFP-KDEL) together with the ddFP pair from Fig. 2 to resolve

ER-PB contact (RA-Sec61β and GB-Dcp1b). Insets are time-lapse merged images of PBs (green) and ER-PB contact (red) (top); the ER (blue) and ER contact (red) (middle); and the ER (blue), PBs (green), and ER-PBs (red) (bottom) (Movie 5). (F) Line scan analyses of fluorescence intensities of PBs (green) and ER-PB contact (red) for each time point. Red arrows highlight ER tubules localized to the site of PB fission. (G) Representative merged images of the ER (red) labeled with mCh-KDEL and stress granules (green) labeled with GFP-G3BP in U-2 OS cells treated with 0.5 mM NaAsO₂ for 60 min followed by 40 min of washout with 200 nM ISRIB. Arrows highlight ER tubules positioned at stress granule fission sites (Movie 6). (H) Line scan analyses of fluorescence intensities of stress granules (green) and the ER (red) pre- and postfission. Red arrows highlight ER tubules localized to the site of stress granule fission. In (C), (E), and (G), scale bars are 5 and 2 μm in full cell and inset images, respectively.

CA). RA-Sec61 β was generated by amplifying the Sec61 β -encoding sequence from GFP-Sec61 β and inserting it into XhoI/KpnI sites of the RA-C1 vector. GB-Dcp1b was generated by subcloning Dcp1b from GFP-Dcp1b and inserting it into XhoI/KpnI sites of the GB-C1 vector.

The *RTN4* KO U-2 OS cell line was generated using CRISPR-Cas9 following a published protocol (45). Briefly, two guide RNAs targeting the *RTN4* gene were cloned into the lentiCRISPR v2 backbone (Addgene plasmid #52961). The two 20-nt regions that are targeted on the *RTN4* gene are CGTTCAAG-TACCACTTCGTG and GGCGCGCCCCTGATGGACTT. LentiCRISPR v2 plasmids containing two *RTN4*-targeting guide sequences (500 ng/ml each) were simultaneously transfected into U-2 OS cells using lipofectamine 3000 following the manufacturer's protocol. Transfected cells were recovered in growth media for 24 hours and then subjected to puromycin (2 μ g/ml) selection for 72 hours (with fresh puromycin every 24 hours). The surviving polyclonal population was diluted into single colonies in 96-well plates. Single clones of KO cells were verified through Western blot (Rtn4A antibody; Cell Signaling) and immunofluorescence (Rtn4A/B antibody; Santa Cruz).

Cell culture, transfection, and drug treatments

Human osteosarcoma U-2 OS cells (ATCC-HTB 96) were tested for Mycoplasma contamination by ATCC at the time of purchase. Cells were grown in McCoy's 5A (modified) medium supplemented with 10% fetal bovine serum (FBS) and 1% penicillin and streptomycin.

Before plating cells for imaging experiments, 35-mm glass-bottom microscope dishes (Cell Vis) were coated with 10 μ g/ml of fibronectin for 5 hours at 37°C. After 5 hours, the fibronectin solution was removed, the microscope dishes were rinsed with PBS to remove excess fibronectin, and U-2 OS cells were seeded at 0.5×10^5 cells/ml about 18 to 24 hours before transfection. DNA plasmid transfections were performed with 2.5 μ l of lipofectamine 3000 (Invitrogen) per 1 ml of OPTI-MEM media (Invitrogen) for ~5 hours followed by a wash and replenishment with full media. Cells were imaged 18 to 24 hours after transfection in prewarmed 37°C Fluorobrite DMEM (Invitrogen) supplemented with 10% FBS and Glutamax (Invitrogen).

For all experiments, the following amounts of DNA were transfected per milliliter: 150 ng mCh-KDEL; 200 ng BFP-KDEL; 200 ng GFP-Dcp2; 200 ng SNAP-Dcp2; 200 ng GFP-Dcp1a; 200 ng BFP-Dcp1a; 200 ng GFP-Dcp1b; 200 ng GB-Dcp1b; 400 ng RA-Sec61 β ; 150 ng GFP-G3BP; 500 ng mCh-Sec61 β ; and 500 ng Rtn4a-mCh.

In ER-PB tracking during oxidative stress experiments, NaAsO₂ was dissolved in dH₂O to yield a 0.5 M stock solution just before treatment. U-2 OS cells expressing GFP-Dcp2

and mCh-KDEL were incubated in imaging media with 0.5 mM NaAsO₂ for 50 min at 37°C. Cells expressing both markers were located and 2-min time-lapse movies with frames were captured every 5 s.

In stress granule disassembly experiments, GFP-G3BP and mCh-KDEL were incubated with 0.5 mM NaAsO₂ for 1 hour. Cells were then washed and replenished with 37°C imaging media and imaged 40 min after wash-out with 200 nM ISRIB added into the imaging media. Two-min time-lapse movies with frames captured every 5 s permitted the capture of stress granule fission during the disassembly process.

In mRNA translation inhibition and ER stress experiments, wild-type and *RTN4* KO cells were treated with 0.5 mM NaAsO₂ for 1 hour (oxidative stress), 200 μ M puromycin for 15 min, or 1 μ g/ml tunicamycin for 1 and 6 hours (ER stress) then fixed with 37°C fixative (4% paraformaldehyde, 4% sucrose in PBS) for 10 min. Cells were then permeabilized and immunolabeled with 1:200 Dcp1b monoclonal rabbit (Cell Signaling Tech) and 1:200 G3BP mouse monoclonal (Abcam) antibodies to simultaneously image PBs and stress granules, or 1:200 Edc3 mouse monoclonal (Santa Cruz) and 1:200 Calreticulin polyclonal rabbit (Abcam) antibodies to simultaneously image PBs and the ER.

Microscopy

Imaging was performed with an inverted fluorescence microscope (TE2000-U; Nikon) equipped with an electron-multiplying charge-coupled device camera (Cascade II; Photometrics) and a Yokogawa spinning disc confocal system (CSU-Xm2; Nikon). Live-cell imaging was performed at 37°C. Images were captured with a 100 \times NA 1.4 oil objective and acquired using the open source microscopy software Micro-Manager. Live-cell super-resolution capture of ddFP-marked ER contact during PB fission was acquired with the Zeiss LSM 880 equipped with Airyscan detectors and 63 \times /1.4-NA plan Apochromat oil objective using Zeiss ZEN software.

Immunofluorescence and analyses of PB number and ER-PB colocalization

U-2 OS cells were seeded at 0.8×10^5 cells/ml on fibronectin-coated coverslips and fixed, 30 hours after plating, with 37°C fixative solution (4% paraformaldehyde, 4% sucrose in PBS) for 10 min. Fixed cells were washed with PBS and permeabilized with 0.1% Triton-X100 followed by blocking with 5% normal donkey serum in PBS. Labeling of PBs and ER was achieved by incubating cells overnight at 4°C with 1:200 Edc3 mouse monoclonal (Santa Cruz) and 1:200 Calreticulin polyclonal rabbit (Abcam) antibodies in blocking serum. Cells were then washed with PBS and fluorescent-

ly labeled with donkey-anti-mouse 488 and donkey-anti-rabbit 594 secondary antibodies (Invitrogen). Cells were then washed and the nuclei labeled with Hoechst. Coverslips were mounted on microscope slides using Prolong glass resin and imaged the following day.

Using a 100 \times objective, Z-stack images of cells from each condition were captured within the same day under identical conditions with respect to laser intensities and exposures. Critically, the standardization of sample preparation and image capture allowed for the standardization of quantification. PB counting was accomplished by first defining the diffuse PB marker signal for each experiment. The first cell captured in the wild-type untreated condition was opened and a ROI was drawn within the cytosol, which excludes bright PB fluorescent foci, and the maximum fluorescence intensity was identified using the measure function in ImageJ. This number was then incorporated into a macros script that subtracts this fluorescence intensity from cells across all conditions followed by Yen-automated thresholding and particle analysis using the "analyze particles" plug-in in ImageJ.

The level of colocalization between PBs and ER tubules was accomplished by selecting ROIs that contained at least one PB and resolvable ER tubules. ROIs were necessary because the ER network is too dense to resolve in regions within the cell, such as the microtubule organizing center. The ROIs were cropped such that the PB was offset from the center to allow for comparison of actual images to rotated images. Segmentation of PBs was accomplished by Otsu thresholding. Segmentation of the ER was accomplished by manual thresholding owing to the broad range of ER labeling intensities throughout the cell and between ROIs. Colocalization between PBs and ER tubules was determined by calculating the Mander's coefficient of the percentage of PBs overlapping with ER tubules ($M1_{PB}$). To determine whether this overlap was due to chance, the ER tubule ROI was rotated 90° clockwise and the Mander's coefficient of the percentage of PBs overlapping with the rotated ER tubule ROI was calculated ($M1_{90}$).

Line scan analyses of PB and stress granule fission events

For PB fission, U-2 OS cells expressing mCh-KDEL, GFP-Dcp1b, BFP-Dcp1a, and SNAP-Dcp2 were incubated with JaneliaFluor 646 in serum-free media for 15 min to conjugate a far-red fluorophore to SNAP-Dcp2, thus permitting live imaging in four channels. Time-lapse videos were acquired over the course of 2 min, with each channel captured every 5 s. Exposure times ranged between 20 and 150 ms in each channel.

The drug treatment and imaging conditions for stress granule fission are detailed above.

Upon identification of PB or stress granule fission during postimaging analysis, a segmented line was drawn perpendicular to the PB or stress granule fission site through the length of the PB or stress granule. The fluorescence intensities of ER and PB or stress granule channels were measured along the length of the line for each time point and plotted. ER-marked fission events were identified by acute decreases in PB or stress granule marker fluorescence that coincided with mCh-KDEL (ER) fluorescence peaks.

REFERENCES AND NOTES

1. L. A. Staehelin, The plant ER: A dynamic organelle composed of a large number of discrete functional domains. *Plant J.* **11**, 1151–1165 (1997). doi: [10.1046/j.1365-3113.1997.11061151.x](https://doi.org/10.1046/j.1365-3113.1997.11061151.x); pmid: [9225461](https://pubmed.ncbi.nlm.nih.gov/9225461/)
2. H. Wu, P. Carvalho, G. K. Voeltz, Here, there, and everywhere: The importance of ER membrane contact sites. *Science* **361**, eaan5835 (2018). doi: [10.1126/science.aan5835](https://doi.org/10.1126/science.aan5835); pmid: [30072511](https://pubmed.ncbi.nlm.nih.gov/30072511/)
3. J. E. Vance, Phospholipid synthesis in a membrane fraction associated with mitochondria. *J. Biol. Chem.* **265**, 7248–7256 (1990). pmid: [2332429](https://pubmed.ncbi.nlm.nih.gov/2332429/)
4. R. Rizzuto et al., Close contacts with the endoplasmic reticulum as determinants of mitochondrial Ca^{2+} responses. *Science* **280**, 1763–1766 (1998). doi: [10.1126/science.280.5370.1763](https://doi.org/10.1126/science.280.5370.1763); pmid: [9624056](https://pubmed.ncbi.nlm.nih.gov/9624056/)
5. B. Kornmann et al., An ER-mitochondria tethering complex revealed by a synthetic biology screen. *Science* **325**, 477–481 (2009). doi: [10.1126/science.1175088](https://doi.org/10.1126/science.1175088); pmid: [19556461](https://pubmed.ncbi.nlm.nih.gov/19556461/)
6. B. Mesmin et al., A four-step cycle driven by PI(4)P hydrolysis directs sterol/PI(4)P exchange by the ER-Golgi tether OSBP. *Cell* **155**, 830–843 (2013). doi: [10.1016/j.cell.2013.09.056](https://doi.org/10.1016/j.cell.2013.09.056); pmid: [24209621](https://pubmed.ncbi.nlm.nih.gov/24209621/)
7. R. Hua et al., VAPs and ACBD5 tether peroxisomes to the ER for peroxisome maintenance and lipid homeostasis. *J. Cell Biol.* **216**, 367–377 (2017). doi: [10.1083/jcb.201608128](https://doi.org/10.1083/jcb.201608128); pmid: [28108526](https://pubmed.ncbi.nlm.nih.gov/28108526/)
8. N. Rocha et al., Cholesterol sensor ORP1L contacts the ER protein VAP to control Rab7-RILP-p150^{Glued} and late endosome positioning. *J. Cell Biol.* **185**, 1209–1225 (2009). doi: [10.1083/jcb.200811005](https://doi.org/10.1083/jcb.200811005); pmid: [19564404](https://pubmed.ncbi.nlm.nih.gov/19564404/)
9. J. R. Friedman, J. R. Dibeneditto, M. West, A. A. Rowland, G. K. Voeltz, Endoplasmic reticulum-endosome contact increases as endosomes traffic and mature. *Mol. Biol. Cell* **24**, 1030–1040 (2013). doi: [10.1091/mbc.e12-10-0733](https://doi.org/10.1091/mbc.e12-10-0733); pmid: [23389631](https://pubmed.ncbi.nlm.nih.gov/23389631/)
10. A. L. Zajac, Y. E. Goldman, E. L. F. Holzbaur, E. M. Ostap, Local cytoskeletal and organelle interactions impact molecular-motor-driven early endosomal trafficking. *Curr. Biol.* **23**, 1173–1180 (2013). doi: [10.1016/j.cub.2013.05.015](https://doi.org/10.1016/j.cub.2013.05.015); pmid: [23770188](https://pubmed.ncbi.nlm.nih.gov/23770188/)
11. C. Raiborg et al., Repeated ER-endosome contacts promote endosome translocation and neurite outgrowth. *Nature* **520**, 234–238 (2015). doi: [10.1038/nature14359](https://doi.org/10.1038/nature14359); pmid: [25855459](https://pubmed.ncbi.nlm.nih.gov/25855459/)
12. B. Knoblach et al., An ER-peroxisome tether exerts peroxisome population control in yeast. *EMBO J.* **32**, 2439–2453 (2013). doi: [10.1038/emboj.2013.170](https://doi.org/10.1038/emboj.2013.170); pmid: [23900285](https://pubmed.ncbi.nlm.nih.gov/23900285/)
13. J. R. Friedman et al., ER tubules mark sites of mitochondrial division. *Science* **334**, 358–362 (2011). doi: [10.1126/science.1207385](https://doi.org/10.1126/science.1207385); pmid: [21885730](https://pubmed.ncbi.nlm.nih.gov/21885730/)
14. A. A. Rowland, P. J. Chitwood, M. J. Phillips, G. K. Voeltz, ER contact sites define the position and timing of endosome fission. *Cell* **159**, 1027–1041 (2014). doi: [10.1016/j.cell.2014.10.023](https://doi.org/10.1016/j.cell.2014.10.023); pmid: [25416943](https://pubmed.ncbi.nlm.nih.gov/25416943/)
15. S. F. Banani et al., Compositional control of phase-separated cellular bodies. *Cell* **166**, 651–663 (2016). doi: [10.1016/j.cell.2016.06.010](https://doi.org/10.1016/j.cell.2016.06.010); pmid: [27374333](https://pubmed.ncbi.nlm.nih.gov/27374333/)
16. S. Boeynaems et al., Protein phase separation: A new phase in cell biology. *Trends Cell Biol.* **28**, 420–435 (2018). doi: [10.1016/j.tcb.2018.02.004](https://doi.org/10.1016/j.tcb.2018.02.004); pmid: [29602697](https://pubmed.ncbi.nlm.nih.gov/29602697/)
17. C. J. Decker, R. Parker, P-bodies and stress granules: Possible roles in the control of translation and mRNA degradation. *Cold Spring Harb. Perspect. Biol.* **4**, a012286 (2012). doi: [10.1101/cshperspect.a012286](https://doi.org/10.1101/cshperspect.a012286); pmid: [22763747](https://pubmed.ncbi.nlm.nih.gov/22763747/)
18. J. Collier, R. Parker, General translational repression by activators of mRNA decapping. *Cell* **122**, 875–886 (2005). doi: [10.1016/j.cell.2005.07.012](https://doi.org/10.1016/j.cell.2005.07.012); pmid: [16179257](https://pubmed.ncbi.nlm.nih.gov/16179257/)
19. C. Kilchert, J. Weidner, C. Prescianotto-Baschong, A. Spang, Defects in the secretory pathway and high Ca^{2+} induce multiple P-bodies. *Mol. Biol. Cell* **21**, 2624–2638 (2010). doi: [10.1091/mbc.e10-02-0099](https://doi.org/10.1091/mbc.e10-02-0099); pmid: [20519435](https://pubmed.ncbi.nlm.nih.gov/20519435/)
20. A. Hubstenberger et al., P-body purification reveals the condensation of repressed mRNA regulons. *Mol. Cell* **68**, 144–157.e5 (2017). doi: [10.1016/j.molcel.2017.09.003](https://doi.org/10.1016/j.molcel.2017.09.003); pmid: [28965817](https://pubmed.ncbi.nlm.nih.gov/28965817/)
21. C. Wang et al., Context-dependent deposition and regulation of mRNAs in P-bodies. *eLife* **7**, e29815 (2018). doi: [10.7554/eLife.41300](https://doi.org/10.7554/eLife.41300)
22. N. Kedersha et al., Dynamic shuttling of TIA-1 accompanies the recruitment of mRNA to mammalian stress granules. *J. Cell Biol.* **151**, 1257–1268 (2000). doi: [10.1083/jcb.151.6.1257](https://doi.org/10.1083/jcb.151.6.1257); pmid: [11121440](https://pubmed.ncbi.nlm.nih.gov/11121440/)
23. A. Khong et al., The stress granule transcriptome reveals principles of mRNA accumulation in stress granules. *Mol. Cell* **68**, 808–820.e5 (2017). doi: [10.1016/j.molcel.2017.10.015](https://doi.org/10.1016/j.molcel.2017.10.015); pmid: [29129640](https://pubmed.ncbi.nlm.nih.gov/29129640/)
24. S. Markmiller et al., Context-dependent and disease-specific diversity in protein interactions within stress granules. *Cell* **172**, 590–604.e13 (2018). doi: [10.1016/j.cell.2017.12.032](https://doi.org/10.1016/j.cell.2017.12.032); pmid: [29373831](https://pubmed.ncbi.nlm.nih.gov/29373831/)
25. G. E. Palade, A small particulate component of the cytoplasm. *J. Biophys. Biochem. Cytol.* **1**, 59–68 (1955). doi: [10.1083/jcb.1.1.59](https://doi.org/10.1083/jcb.1.1.59); pmid: [14381428](https://pubmed.ncbi.nlm.nih.gov/14381428/)
26. G. Palade, Intracellular aspects of the process of protein synthesis. *Science* **189**, 347–358 (1975). doi: [10.1126/science.1096303](https://doi.org/10.1126/science.1096303); pmid: [1096303](https://pubmed.ncbi.nlm.nih.gov/1096303/)
27. C. H. Jan, C. C. Williams, J. S. Weissman, Principles of ER cotranslational translocation revealed by proximity-specific ribosome profiling. *Science* **346**, 1257521 (2014). doi: [10.1126/science.1257521](https://doi.org/10.1126/science.1257521); pmid: [25378630](https://pubmed.ncbi.nlm.nih.gov/25378630/)
28. D. W. Reid, Q. Chen, A. S.-L. Tay, S. Shenolikar, C. V. Nicchitta, The unfolded protein response triggers selective mRNA release from the endoplasmic reticulum. *Cell* **158**, 1362–1374 (2014). doi: [10.1016/j.cell.2014.08.012](https://doi.org/10.1016/j.cell.2014.08.012); pmid: [25215492](https://pubmed.ncbi.nlm.nih.gov/25215492/)
29. N. Kedersha et al., Stress granules and processing bodies are dynamically linked sites of mRNP remodeling. *J. Cell Biol.* **169**, 871–884 (2005). doi: [10.1083/jcb.200502088](https://doi.org/10.1083/jcb.200502088); pmid: [15967811](https://pubmed.ncbi.nlm.nih.gov/15967811/)
30. C. P. Brangwynne et al., Germline P granules are liquid droplets that localize by controlled dissolution/condensation. *Science* **324**, 1729–1732 (2009). doi: [10.1126/science.1172046](https://doi.org/10.1126/science.1172046); pmid: [19460965](https://pubmed.ncbi.nlm.nih.gov/19460965/)
31. S. Alberti, A. Gladfelter, T. Mittag, Considerations and challenges in studying liquid-liquid phase separation and biomolecular condensates. *Cell* **176**, 419–434 (2019). doi: [10.1016/j.cell.2018.12.035](https://doi.org/10.1016/j.cell.2018.12.035); pmid: [30682370](https://pubmed.ncbi.nlm.nih.gov/30682370/)
32. Y. Ding et al., Ratiometric biosensors based on dimerization-dependent fluorescent protein exchange. *Nat. Methods* **12**, 195–198 (2015). doi: [10.1038/nmeth.3261](https://doi.org/10.1038/nmeth.3261); pmid: [25622108](https://pubmed.ncbi.nlm.nih.gov/25622108/)
33. M. West, N. Zurek, A. Hoenger, G. K. Voeltz, A 3D analysis of yeast ER structure reveals how ER domains are organized by membrane curvature. *J. Cell Biol.* **193**, 333–346 (2011). doi: [10.1083/jcb.201011039](https://doi.org/10.1083/jcb.201011039); pmid: [21502358](https://pubmed.ncbi.nlm.nih.gov/21502358/)
34. M. Puhka, M. Joensuu, H. Vihinen, I. Belevich, E. Jokitalo, Progressive sheet-to-tubule transformation is a general mechanism for endoplasmic reticulum partitioning in dividing mammalian cells. *Mol. Biol. Cell* **23**, 2424–2432 (2012). doi: [10.1091/mbc.e10-12-0950](https://doi.org/10.1091/mbc.e10-12-0950); pmid: [22573885](https://pubmed.ncbi.nlm.nih.gov/22573885/)
35. G. K. Voeltz, W. A. Prinz, Y. Shibata, J. M. Rist, T. A. Rapoport, A class of membrane proteins shaping the tubular endoplasmic reticulum. *Cell* **124**, 573–586 (2006). doi: [10.1016/j.cell.2005.11.047](https://doi.org/10.1016/j.cell.2005.11.047); pmid: [16469703](https://pubmed.ncbi.nlm.nih.gov/16469703/)
36. Y. Shibata et al., Mechanisms determining the morphology of the peripheral ER. *Cell* **143**, 774–788 (2010). doi: [10.1016/j.cell.2010.11.007](https://doi.org/10.1016/j.cell.2010.11.007); pmid: [21111237](https://pubmed.ncbi.nlm.nih.gov/21111237/)
37. P. Walter, D. Ron, The unfolded protein response: From stress pathway to homeostatic regulation. *Science* **334**, 1081–1086 (2011). doi: [10.1126/science.1209038](https://doi.org/10.1126/science.1209038); pmid: [22116877](https://pubmed.ncbi.nlm.nih.gov/22116877/)
38. C. Sidrauski, A. M. McGeachy, N. T. Ingolia, P. Walter, The small molecule ISRIB reverses the effects of eIF2 α phosphorylation on translation and stress granule assembly. *eLife* **4**, e05033 (2015). doi: [10.7554/eLife.05033](https://doi.org/10.7554/eLife.05033)
39. S. Jain et al., ATPase-modulated stress granules contain a diverse proteome and substructure. *Cell* **164**, 487–498 (2016). doi: [10.1016/j.cell.2015.12.038](https://doi.org/10.1016/j.cell.2015.12.038); pmid: [26777405](https://pubmed.ncbi.nlm.nih.gov/26777405/)
40. J. R. Wheeler, T. Matheny, S. Jain, R. Abrisch, R. Parker, Distinct stages in stress granule assembly and disassembly. *eLife* **5**, e18413 (2016). doi: [10.7554/eLife.18413](https://doi.org/10.7554/eLife.18413); pmid: [27602576](https://pubmed.ncbi.nlm.nih.gov/27602576/)
41. Y. C. Liao et al., RNA granules hitchhike on lysosomes for long-distance transport, using annexin A11 as a molecular tether. *Cell* **179**, 147–164.e20 (2019). doi: [10.1016/j.cell.2019.08.050](https://doi.org/10.1016/j.cell.2019.08.050); pmid: [31539493](https://pubmed.ncbi.nlm.nih.gov/31539493/)
42. J. R. Friedman, J. R. Dibeneditto, M. West, A. A. Rowland, G. K. Voeltz, Endoplasmic reticulum-endosome contact increases as endosomes traffic and mature. *Mol. Biol. Cell* **24**, 1030–1040 (2013). doi: [10.1091/mbc.e12-10-0733](https://doi.org/10.1091/mbc.e12-10-0733); pmid: [23389631](https://pubmed.ncbi.nlm.nih.gov/23389631/)
43. A. Patel et al., A liquid-to-solid phase transition of the ALS protein FUS accelerated by disease mutation. *Cell* **162**, 1066–1077 (2015). doi: [10.1038/s41586-018-0665-2](https://doi.org/10.1038/s41586-018-0665-2); pmid: [30464263](https://pubmed.ncbi.nlm.nih.gov/30464263/)
44. T. O. Vogler et al., TDP-43 and RNA form amyloid-like myo-fibrils in regenerating muscle. *Nature* **563**, 508–513 (2018). doi: [10.1038/s41586-018-0665-2](https://doi.org/10.1038/s41586-018-0665-2); pmid: [30464263](https://pubmed.ncbi.nlm.nih.gov/30464263/)
45. F. A. Ran et al., Genome engineering using the CRISPR-Cas9 system. *Nat. Protoc.* **8**, 2281–2308 (2013). doi: [10.1038/nprot.2013.143](https://doi.org/10.1038/nprot.2013.143); pmid: [24575458](https://pubmed.ncbi.nlm.nih.gov/24575458/)

ACKNOWLEDGMENTS

We thank A. Khong, B. Van Treeck, E. Zamponi, R. G. Abrisch, B. S. Rao, G. Odorizzi, and D. Buysse for helpful insights and discussion. **Funding:** G.K.V. and R.P. are investigators of the Howard Hughes Medical Institute. J.E.L. and H.W. were supported by a grant to G.K.V. from the NIH (GM13009816). **Author contributions:** J.E.L., G.K.V., and R.P. designed the research plan and interpreted the results. J.E.L., P.I.C., and H.W. performed and analyzed the experiments. J.E.L. wrote and R.P. and G.K.V. edited the manuscript. **Competing interests:** None of the authors have a competing interest. **Data and materials availability:** All data are available in the manuscript or the supplementary materials. The expression plasmids reported in this manuscript are available at Addgene or upon request.

SUPPLEMENTARY MATERIALS

science.sciencemag.org/content/367/6477/eaay7108/suppl/DC1
Figs. S1 to S5

[View/request a protocol for this paper from Bio-protocol.](#)

13 July 2019; resubmitted 4 November 2019

Accepted 4 December 2019

10.1126/science.aay7108

RESEARCH ARTICLE

CELLULAR NEUROSCIENCE

Microglia monitor and protect neuronal function through specialized somatic purinergic junctions

Csaba Cserép^{1*}, Balázs Pósfa^{1,2*}, Nikolett Lénárt¹, Rebeka Fekete^{1,2}, Zsófia I. László^{2,3}, Zsolt Lele³, Barbara Orsolits¹, Gábor Molnár⁴, Steffanie Heindl⁵, Anett D. Schwarcz¹, Katinka Ujvári¹, Zsuzsanna Környei¹, Krisztina Tóth^{1,2}, Eszter Szabadits¹, Beáta Sperlág⁶, Mária Baranyi⁶, László Csiba⁷, Tibor Hortobágyi^{8,9,10}, Zsófia Maglóczy¹¹, Bernadett Martinecz¹, Gábor Szabó¹², Ferenc Erdélyi¹², Róbert Szipócs¹³, Michael M. Tamkun¹⁴, Benno Gesierich⁵, Marco Duering^{5,15}, István Katona³, Arthur Liesz^{5,15}, Gábor Tamás⁴, Ádám Dénes^{1†}

Microglia are the main immune cells in the brain and have roles in brain homeostasis and neurological diseases. Mechanisms underlying microglia–neuron communication remain elusive. Here, we identified an interaction site between neuronal cell bodies and microglial processes in mouse and human brain. Somatic microglia–neuron junctions have a specialized nanoarchitecture optimized for purinergic signaling. Activity of neuronal mitochondria was linked with microglial junction formation, which was induced rapidly in response to neuronal activation and blocked by inhibition of P2Y12 receptors. Brain injury–induced changes at somatic junctions triggered P2Y12 receptor–dependent microglial neuroprotection, regulating neuronal calcium load and functional connectivity. Thus, microglial processes at these junctions could potentially monitor and protect neuronal functions.

Microglia are the main immunocompetent cells of the nervous system and their role in brain development and maintenance of proper neuronal function throughout life is widely recognized (1, 2). Changes in microglial activity are linked with major human diseases, including different forms of neurodegeneration, stroke, epilepsy, and psychiatric disorders (3, 4).

Microglia perform dynamic surveillance of their microenvironment using motile microglial processes that constantly interact with neurons (5, 6). However, the molecular mechanisms of bidirectional microglia–neuron communication are unclear. To date, most studies have focused on the interactions between microglial processes and synaptic elements, including axonal boutons and dendritic spines, which have commonly been perceived as the main form of interaction between microglia and neurons (7, 8). However, neurons are extremely polarized cells with a high degree of functional independence concerning metabolism and signal integration in their dendritic and axonal compartments (9–11). The large-scale structure of neurons (i.e., their cell body and axonal or dendritic branches) in the brain is relatively

stable under most conditions. In comparison, small synaptic structures such as dendritic spines and axonal boutons are often distant from neuronal cell bodies and are highly dynamic. Therefore, the interactions between microglia and synapses may not fully explain how microglia are capable of monitoring and influencing the activity of neurons or how early events of cellular injury in the perisomatic compartment are detected. This may be particularly relevant for the migration and differentiation of neural precursors, cell survival and programmed cell death, adult neurogenesis, and the phagocytosis of damaged neuronal cell bodies (12–15). It is not understood how microglia could monitor neuronal status over years or even decades and discriminate salvageable neurons from irreversibly injured cells mainly on the basis of changes occurring at distant synaptic structures.

To understand the possible mechanisms of effective communication between microglia and neurons, we tested the hypothesis that specialized junctions on neuronal cell bodies may support the dynamic monitoring and assistance of neuronal function by microglia.

Microglial processes contact specialized areas of neuronal cell bodies in mouse and human brains

To visualize microglia together with cortical neurons and to study microglia–neuron interactions in the intact brain in real time, CX3CR1^{+/GFP} microglia reporter mice were electroporated in utero with *pCAG-IRES-tdTomato* plasmid (fig. S1A). In vivo two-photon (2P) imaging revealed microglial processes contacting the cell bodies of cortical layer 2 to 3 neurons in the adult brain (Fig. 1, A and B, and movie S1). Microglial processes preferentially returned to the same areas on the neuronal soma (observed in 23 neurons out of 28 from 3 mice). The average lifetime of somatic microglia–neuron contacts was 25 min; some contacts persisted for >1 hour (fig. S1B), whereas dendritic contacts had a significantly shorter lifetime of 7.5 min (Fig. 1C; $p = 0.00035$; $n = 26$ contacts from 3 mice), similar to that reported for synaptic contacts (16). Post hoc confocal laser scanning microscopy (CLSM) and electron microscopic analysis further validated the direct interaction between microglial processes and the cell bodies of cortical pyramidal neurons (Fig. 1D and fig. S1, C and D), which we named somatic microglial junction. Similar interactions were present on well-characterized interneuron populations, namely type 3 vesicular glutamate transporter–positive (vGluT3⁺) and parvalbumin-expressing (PV⁺) cells in the neocortex and the hippocampus (fig. S1E). Somatic microglia–neuron junctions were also observed in the human neocortex (Fig. 1E). Somatic microglial junctions were present on 93% of cortical pyramidal neurons, 95% of vGluT3⁺ neurons, and 89% of PV⁺ interneurons in mice ($n = 443$ cells from 4 mice). Despite the well-established microglial regulation of neuronal synapses, only 9% of glutamate-releasing and 11% of γ -aminobutyric acid (GABA)–releasing synapses were associated with microglial processes (Fig. 1F and fig. S1F; $n = 1183$ synapses from 4 mice). Eighty-seven percent of neurons in the human neocortex received microglial contact with their cell body (Fig. 1, E and F; $n = 170$ cells from 3 patients). We also tested the possible presence of somatic microglial junctions in subcortical areas. Ninety-eight percent of neurons in the caudate putamen, 91% of neurons in the nucleus reticularis gigantocellularis, and 96% of neurons in the medial septum were contacted by microglial processes

¹Momentum Laboratory of Neuroimmunology, Institute of Experimental Medicine, Budapest, Hungary. ²Szentágotai János Doctoral School of Neuroscience, Semmelweis University, Budapest, Hungary. ³Momentum Laboratory of Molecular Neurobiology, Institute of Experimental Medicine, Budapest, Hungary. ⁴MTA-SZTE Research Group for Cortical Microcircuits of the Hungarian Academy of Sciences, Department of Physiology, Anatomy and Neuroscience, University of Szeged, Szeged, Hungary. ⁵Institute for Stroke and Dementia Research, Ludwig-Maximilians-University, Munich, Germany. ⁶Laboratory of Molecular Pharmacology, Institute of Experimental Medicine, Budapest, Hungary. ⁷MTA-DE Cerebrovascular and Neurodegenerative Research Group, Department of Neurology, University of Debrecen, Debrecen, Hungary. ⁸Institute of Pathology, Faculty of Medicine, University of Szeged, Szeged, Hungary. ⁹Department of Old Age Psychiatry, Institute of Psychiatry, Psychology and Neuroscience, King's College London, London, UK. ¹⁰Centre for Age-Related Medicine, SESAM, Stavanger University Hospital, Stavanger, Norway. ¹¹Human Brain Research Laboratory, Institute of Experimental Medicine, Budapest, Hungary. ¹²Medical Gene Technology Unit, Institute of Experimental Medicine, Budapest, Hungary. ¹³Institute for Solid State Physics and Optics of Wigner RCP, Budapest, Hungary. ¹⁴Department of Biomedical Sciences, Colorado State University, Fort Collins, Colorado, USA. ¹⁵Munich Cluster for Systems Neurology (SyNergy), Munich, Germany.

*These authors contributed equally to this work.

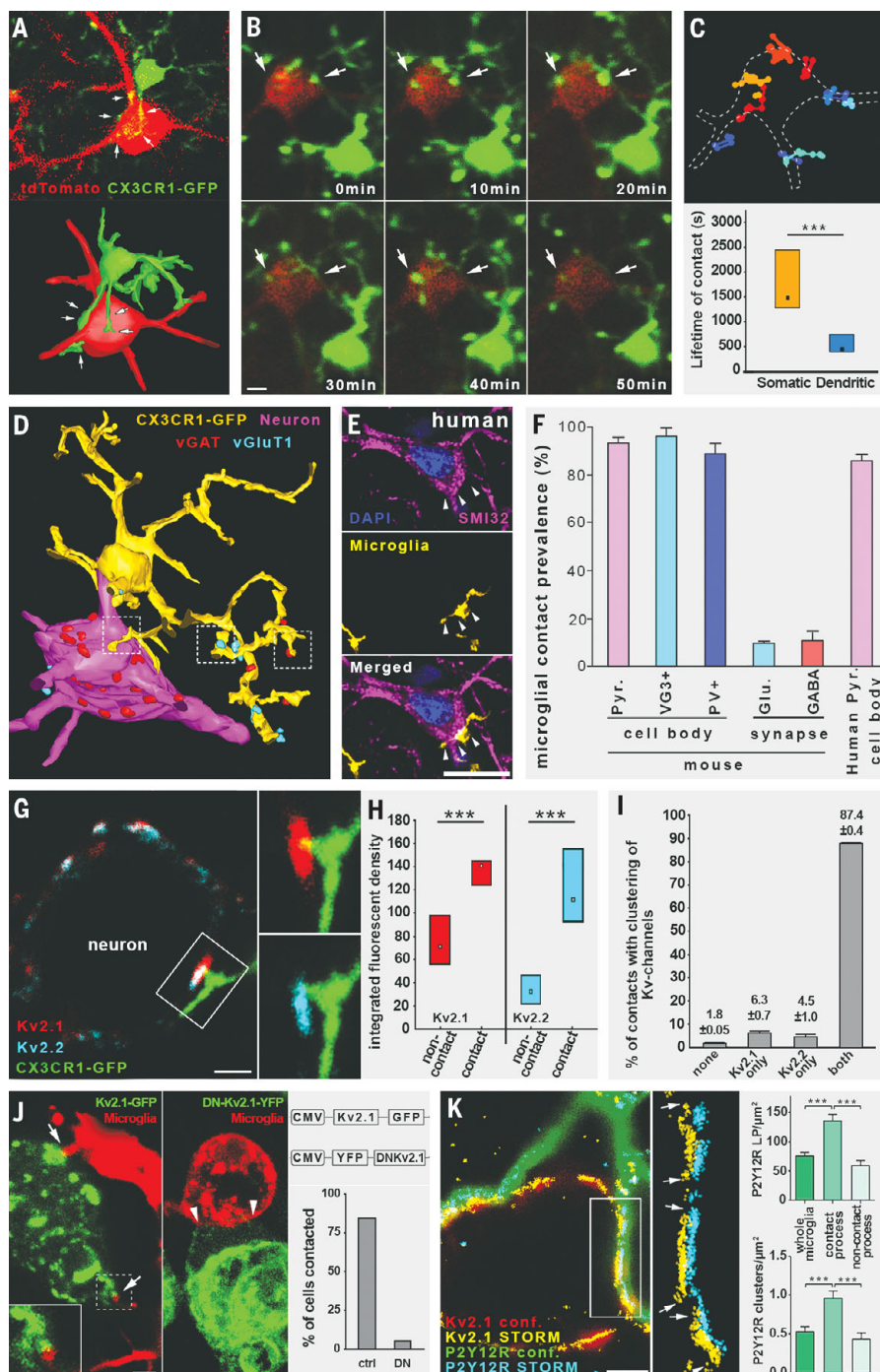
†Corresponding author. Email: denes.adam@koki.mta.hu

($n = 268$ cells from 2 mice). Thus, these contacts are evolutionary conserved and present in all main areas of the brain.

Microglia at somatic junctions may sense changes in neuronal state through signals released by exocytosis. In neurons, clustered Kv2.1 proteins are well known to provide exocytotic surfaces by anchoring vesicle fusion molecules to the neuronal membrane (17, 18). Furthermore, both Kv2.1 and Kv2.2 proteins are involved in forming endoplasmic reticulum (ER)–plasma membrane (PM) junctions (membrane-trafficking

hubs) and in anchoring intracellular organelles to the neuronal PM (19). Microglia contacted neuronal somatic membranes at sites of Kv2.1 and Kv2.2 clustering (Fig. 1G). The integrated density of Kv2.1 signal at these sites was 96% higher and the density of Kv2.2 signal was 254% higher compared with those without microglial contacts (Fig. 1H; $p < 0.0001$ in both cases; $n = 114$ and $n = 107$, respectively, from 3 mice). Eighty-seven percent of all microglia–neuron contacts expressed both types of clusters, 6.3% expressed only Kv2.1

clusters, 4.5% only Kv2.2 clusters, and only 1.8% of contacts were void of any Kv clusters (Fig. 1I; $n = 111$ contacts from 2 mice). Furthermore, 99% of neocortical and 94% of hippocampal CA1-region neurons expressed both Kv2.1 and Kv2.2 channels at the cellular level (fig. S2, A to C). The spatial association between Kv2.1 clusters and microglial processes was also observed on human cortical neurons (fig. S1, G and H; $n = 21$ cells). Because Kv2.1 clusters are implicated in a large number of cellular processes involved in cell-to-cell



communication, we focused on Kv2.1 in our further experiments. Kv2.1 hot spots appeared to define preformed neuronal microdomains because Kv2.1 clusters remained unaltered after selective elimination of microglia by PLX5622 (fig. S1, I and J; 4.71 clusters per cross-section in control versus 6.64 clusters per cross-section in depleted; $n = 59$ cells from 4 mice). To test the functional involvement of Kv2.1 clusters in the formation of somatic junctions, we developed a dominant-negative Kv2.1 mutant construct, DNKv2.1. This construct could not integrate into the PM and blocked the forward trafficking of any endogenous Kv2 proteins that may be expressed. We transfected human embryonic kidney (HEK) 293 cells, which naturally lack Kv2.1 protein (20), with fluorescent protein-coupled Kv2.1 or DNKv2.1 constructs and cocultured these with microglia. Microglial processes contacted Kv2.1-transfected HEK cells preferentially at Kv2.1 clusters and did not contact the DNKv2.1-transfected HEK cells (Fig. 1J and movie S2). Eighty-four percent of Kv2.1-transfected HEK cells received microglial process contacts (97% of these contacts arrived onto Kv2.1 clusters), whereas only 5.4% of DNKv2.1-transfected HEK cells received process contacts ($n = 75$ cells from 3 experiments). Thus, cell surface expression and clustering of Kv2.1 proteins is sufficient to induce contact formation by microglial processes.

Activity-dependent exocytotic adenosine 5'-triphosphate (ATP) or adenosine 5'-diphosphate (ADP) release takes place from neuronal cell bodies under physiological conditions (21, 22). ATP (ADP) is a major chemoattractant for microglial processes through the microglial purinoreceptor P2Y₁₂ receptor (5, 23). We thus asked whether signaling through P2Y₁₂ receptor was also essential for microglia-neuron interactions at these somatic junctions. In fact, all microglia, but no other cells in the brain, including perivascular macrophages, were found to be P2Y₁₂ receptor positive (fig. S3), including their processes recruited to somatic junctions (fig. S3B). The restriction of P2Y₁₂ receptor expression to microglia within the brain agrees with results of earlier single-cell transcriptomics studies (24, 25).

To investigate the nanoscale architecture of P2Y₁₂ receptors at somatic microglia-neuron junctions, we used correlated CLSM and STORM superresolution microscopy, which enables the precise assessment of P2Y₁₂ receptor and Kv2.1 clusters at 20-nm lateral resolution (26). P2Y₁₂ receptors formed dense clusters on microglial processes at somatic junctions directly facing neuronal Kv2.1 clusters (Fig. 1K). Unbiased cluster analysis revealed that P2Y₁₂ receptor localization point density and cluster density were both significantly higher on microglial processes inside the junctions than on processes outside the junctions or on the whole microglial cell (Fig. 1K and fig. S2D; for detailed statistics

and numbers, see table S1). Furthermore, somatic contact-dependent clustering of P2Y₁₂ receptors occurred on both pyramidal cells and interneurons (fig. S2E; for detailed statistics and numbers, see table S1). Contact-dependent molecular clustering, however, could not be observed in the case of the microglial calcium-binding protein Iba1 (fig. S2F). Contact-dependent P2Y₁₂ receptor clustering was specific to somatic junctions, and immunogold density was 62% lower on microglial membranes contacting boutons than on those contacting somata (fig. S2G; $p = 0.0002$; $n = 26$ contacts from 3 mice). Thus, we suggest the existence of a functionally specialized yet ubiquitous communication site between P2Y₁₂ receptor-positive microglial processes and neuronal cell bodies.

Somatic microglia-neuron junctions have a specific nanoarchitecture and molecular fingerprints

To further investigate the ultrastructural features of somatic microglia-neuron junctions, we performed transmission electron microscopy and high-resolution electron tomography with three-dimensional (3D) reconstruction. P2Y₁₂ receptor immunogold labeling confirmed the formation of direct junctions between microglial processes and neuronal somata both in mice (Fig. 2A) and in postmortem human brain tissue (fig. S4A). Microglia-neuron junctions were composed of closely apposed mitochondria, reticular membrane structures, intracellular tethers, and associated vesicle-like membrane structures within the neuronal cell body (Fig. 2A). 3D electron tomography confirmed this nanoarchitecture in neurons (Fig. 2B and movies S3 and S4). These morphological features were not observed in perisomatic boutons contacted by microglia. Furthermore, automated 3D analysis of tomographic volumes showed that P2Y₁₂ receptor density negatively correlated with the distance between microglial and neuronal membranes within the junctions (Fig. 2, C and D, and fig. S4C; $p < 0.001$; $n = 13,055$ points from 3 contacts). We also compared P2Y₁₂ receptor density between microglial membrane surfaces establishing junctions with neuronal somata and adjacent surfaces (within a few micrometers) that contacted boutons or other neuronal elements. We detected a significantly higher P2Y₁₂ receptor density at microglial membranes directly contacting neuronal cell bodies (Fig. 2E and movie S5; $p = 0.00115$; $n = 24$ surfaces). This suggests an important role for purinergic signaling in the formation of somatic microglia-neuron junctions.

We also observed discrete intercellular structures resembling cell-adhesion molecules in the extracellular space that connected the membranes of microglia and neuronal cell bodies (average length 23.5 ± 3.1 nm; $n = 89$ from 3 mice; fig. S4B). This falls in the range of the size of integrins expressed by microglia

(27, 28) or the width of immunological synapses between peripheral immune cells (29). Mitochondria-associated membranes (MAMs, average distance: 19.5 nm; $n = 104$ from 3 mice; fig. S4B) were observed (30) and discrete tethers between mitochondria and MAMs were also visible (movie S4).

We hypothesized that mitochondrial ATP production and changes in neuronal activity could trigger microglial process recruitment. Thus, we investigated the possible enrichment of neuronal mitochondria at microglial junctions on a large sample size using an unbiased, semiautomatic analysis of the outer mitochondrial membrane protein TOM20. TOM20 immunofluorescent intensity was 420% higher at somatic junctions compared with adjacent areas (Fig. 2, F and G; $p < 0.001$; $n = 14$ contacts from 2 mice), confirming the strong accumulation of neuronal mitochondria at the somatic junctions.

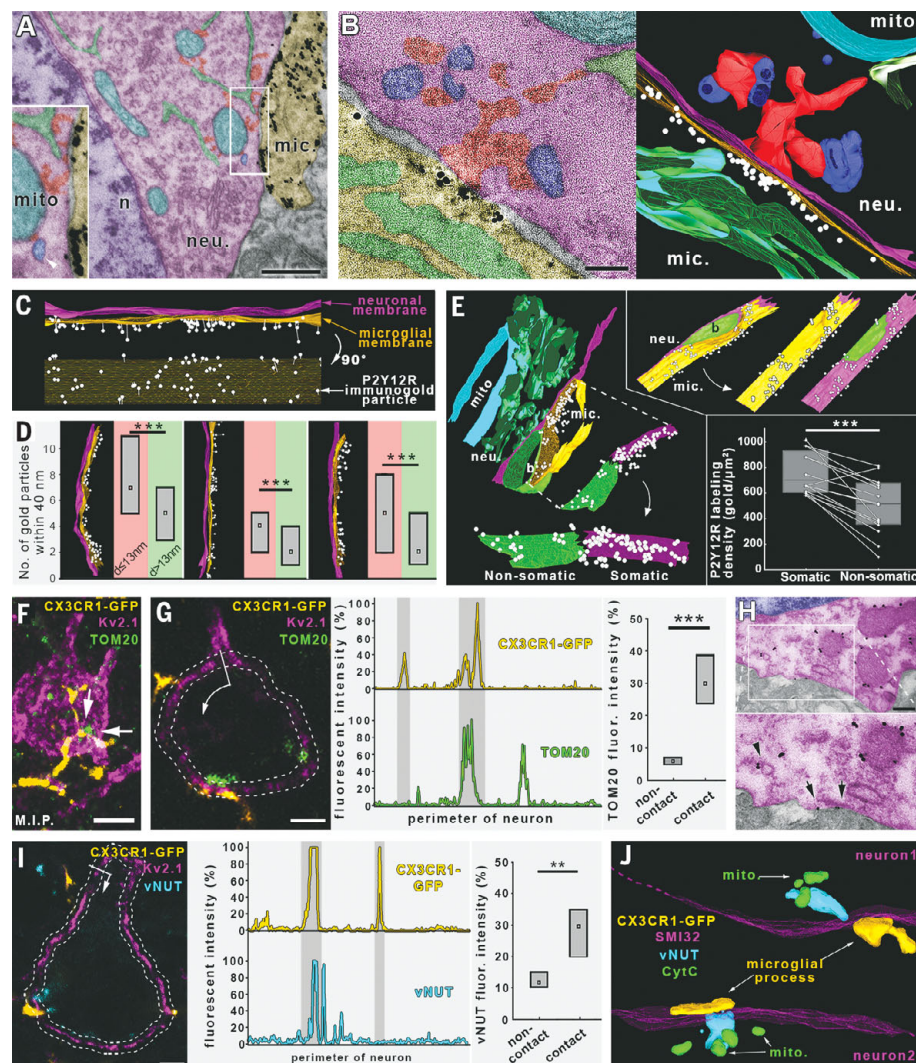
TOM20-positive vesicles were observed between mitochondria and the neuronal membrane in addition to TOM20-negative vesicles (Fig. 2H and fig. S4, E and F). This may suggest trafficking and possible exocytosis of mitochondria-derived vesicles (31) at somatic microglial junctions. Mitochondria-derived vesicles (MDVs) often integrate into the endolysosomal pathway (31), and these vesicles are positive for the lysosomal marker LAMP1 (32). Indeed, LAMP1-positive puncta were closely associated with 83.3% of all Kv2.1 clusters at somatic junctions (fig. S4G; $n = 72$ contacts from 2 mice), suggesting the release of MDVs and lysosomal content at these junctions.

Kv2.1-immunogold clusters were tightly associated with the observed neuronal structures (i.e., closely apposed mitochondria, MAMs, ER, vesicle-like structures, cytoplasmic densities) within these junctions (fig. S4D). Similarly to our CLSM results (fig. S1I), Kv2.1 nanoclustering was not affected by the absence of microglia (fig. S4D). These structures may function as mitochondria-related signaling hubs in neurons that microglia can recognize. Vesicular release of mitochondria-derived ATP from neurons may occur in a vesicular nucleotide transporter (vNUT)-dependent manner (33, 34). Indeed, vNUT signal intensity was 2.5 times higher in the vicinity of the neuronal membranes at somatic microglia-neuron junctions compared with areas outside the junctions (Fig. 2I; $p = 0.002$; $n = 15$ contacts from 2 mice). Neuronal vNUT labeling was concentrated between mitochondria and the microglia-contacted neuronal membranes (Fig. 2J).

Kv2.1 or vNUT signal was not present in perisomatic axon terminals (GABA-releasing synaptic boutons), including those contacted by microglial processes (fig. S4, H and I; $n = 220$ boutons for Kv2.1 and $n = 194$ boutons for vNUT from 2 mice), confirming again that

Fig. 2. Microglia–neuron junctions have a specialized nanoarchitecture and molecular machinery optimized for purinergic cell-to-cell communication.

(A) Transmission electron micrograph showing the area of the neuronal cell body (neu.) contacted by a P2Y12 receptor–immunogold (black grains)–labeled microglial process (mic.). The junction has a specific nanoarchitecture with closely apposed mitochondria (mito., cyan), reticular membrane structures (green), and intracellular tethers (red). A mitochondria-associated vesicle (blue, marked by white arrowhead) is also visible. The nucleus (n) of the neuron is purple. (B) A 0.5-nm-thick virtual section of an electron tomographic volume (left) and 3D model (right) showing the special nanoarchitecture of a somatic microglia–neuron junction [colors represent the same structures as in (A)]. Note the specific enrichment of P2Y12 receptor labeling at the core of the junction. (C and D) P2Y12 receptor density negatively correlates with the distance between microglial and neuronal membranes within the junctions. (E) P2Y12 receptor density is highest at those surfaces of microglial processes that are in direct contact with the neuronal cell bodies (P2Y12 receptor labeling is white; b, bouton). (F) CLSM maximal intensity projection (M.I.P.) showing microglial processes (yellow) contacting neuronal somata (magenta) with adjacent mitochondria (green). (G) Neuronal mitochondria are enriched at microglial junction sites. (H) Transmission electron micrographs showing TOM20–immunogold labeling in neocortical neurons. Immunogold labeling (black grains) is specifically associated with outer mitochondrial membranes, whereas TOM20-positive vesicles can also be observed (arrowheads). Some immunogold particles can be found on the PM of the neurons (arrows), suggesting the exocytosis of mitochondria-derived vesicles. (I) vNUT-labeled vesicles are enriched at microglial junction sites. (J) 3D reconstruction of high-resolution confocal Z-stack showing parts of two neuronal cell bodies (magenta), both contacted by microglial processes (yellow). The vNUT signal (cyan) was concentrated between the junctions and closely positioned mitochondria (green). For statistical details, see the supplementary text for Fig. 2.



these molecular fingerprints were associated with somatic microglia–neuron junctions.

Physiological microglia–neuron communication at somatic junctions is P2Y12 receptor dependent and linked with neuronal mitochondrial activity

Next, we aimed to test whether microglial process recruitment to somatic junctions was functionally linked with the activity of mitochondria in neurons. To this end, CX3CR1^{+/GFP} mice were electroporated in utero with the mitochondria-targeted *CAG-Mito-R-Geco1* reporter construct (fig. S5A). Again, we observed the involvement of somatic mitochondria in microglial junctions (Fig. 3A). In vivo 2P imaging was performed to monitor microglial process recruitment to neuronal mitochondria in the cerebral cortex (Fig. 3B). As expected, recruited microglial processes came into close apposition with neuronal mitochondria. These

processes stayed in the vicinity of neuronal mitochondria for ~29 min in vivo (Fig. 3B and movie S6; $n = 25$ contacts on 19 neurons from 3 mice, median value), closely matching the value measured in tdTomato-electroporated mice (Fig. 1C). To study the functional relationship between microglial junction formation and activity of neuronal mitochondria, we assessed intracellular changes of the metabolic electron carrier nicotinamide adenine dinucleotide (NADH) (35) in coronal slices of visual and somatosensory cortices from CX3CR1^{+/GFP} mice. Intracellular NADH fluorescence showed a granular pattern, indicating a mitochondrial NADH source. Indeed, the NADH signal colocalized with the *Mito-R-Geco1* signal, confirming its mitochondrial origin (fig. S5C). To search for somatic junction formation, we performed 2P imaging, which allowed us to track the movement of microglial processes and monitor cytosolic NADH in viable layer 2/3 neurons

simultaneously (fig. S5D). We detected apparent increases in NADH intrinsic fluorescence (Fig. 3, C and E; $p = 0.024$; $n = 10$ cells) in parallel with the formation of somatic microglial junctions. By contrast, we found no changes in the mean intrinsic NADH fluorescence detected at neuronal somata contacted by microglial processes in P2Y12 receptor^{−/−} tissue (Fig. 3, D and E; $p = 0.3$; $n = 11$ cells). Thus, microglial process recruitment to somatic junctions is linked to the metabolic activity of neuronal mitochondria through a P2Y12 receptor–dependent mechanism.

The molecular machinery and intercellular interactions identified above suggested the involvement of purinergic signaling in these somatic junctions. To test whether neuronal somata could release ATP at these sites, we conducted a series of in vitro experiments. Quinacrine-labeled ATP-containing vesicles localized between neuronal mitochondria and

neuronal membranes were present at sites where microglial processes contacted neuronal Kv2.1 clusters in microglia–neuron cocultures (Fig. 3F). Quinacrine labeling also colocalized with vNUT signal (Fig. 3F), as previously demonstrated for neurons (33).

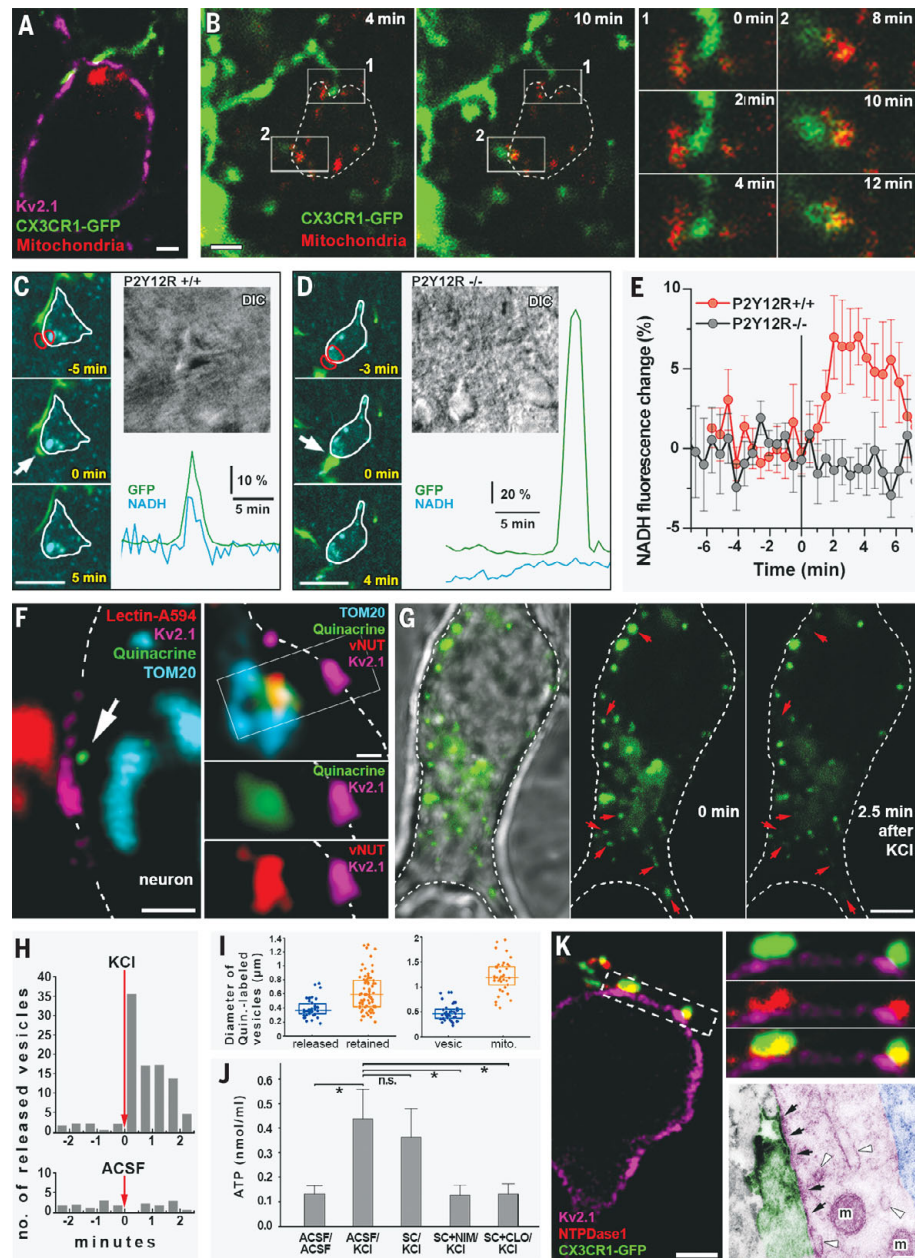
Next, we tested whether neuronal activity could release ATP-containing vesicles from neuronal cell bodies. KCl (40 mM) stimulation induced a rapid membrane depolarization and calcium influx in cultured neurons (fig. S5E; $n = 23$ cells for FluoVolt measurements, $n = 20$ cells for Rhod3 measurements). CLSM in vitro

time-lapse imaging confirmed that quinacrine-labeled (ATP-containing) vesicles were released from neuronal cell bodies after KCl stimulation (Fig. 3, G and H; 880% increase in release events after KCl versus a 27% decrease after vehicle; $n = 13$ cells). Size analysis confirmed that the smaller vesicles were released [Fig. 3I; median diameter of released vesicles was $0.37 \mu\text{m}$ and that for retained vesicles was $0.59 \mu\text{m}$ ($n = 118$ puncta), similar to previous reports (33)]. The larger vesicles were identified as mitochondria by their uniform TOM20 labeling (Fig. 3I; median diameter of vesicle

labeling was $0.45 \mu\text{m}$ and that for mitochondrial labeling was $1.2 \mu\text{m}$; $n = 83$ puncta).

Next, we applied high-sensitivity high-performance liquid chromatography (HPLC) to detect the levels of released ATP in the medium (Fig. 3J). KCl induced a robust ATP release in cultured neurons ($p = 0.0218$; $n = 11$), which was not inhibited by a mixture of the synaptic calcium-channel blockers ω -agatoxin and ω -conotoxin ($p = 0.6532$; $n = 11$), but was almost completely inhibited by the L-type calcium-channel blocker nimodipine [known to be important for somatic vesicular release

Fig. 3. Neuronal mitochondrial activity and purinergic signaling are involved in microglia–neuron communication. (A) CLSM image showing a microglial process (green) contacting Kv2.1 clusters (magenta) on a neuronal soma in the vicinity of a mitochondrion (Mito-R-Geco1, red) in a perfusion-fixed brain. (B) In vivo 2P imaging of CX3CR1^{+/GFP} mice in utero electroporated with CAG-Mito-R-Geco1 construct. Dashed line shows the outline of the neuron. Green microglial processes touch the neuronal cell body where somatic mitochondria are present. Regions of interest 1 and 2 are enlarged to show the development of somatic junctions. (C and D) Representative samples from time-lapse imaging of microglia showing processes extending and contacting neuronal soma in CX3CR1^{+/GFP}/P2Y12 receptor^{+/+} (C) and CX3CR1^{+/GFP}/P2Y12 receptor^{-/-} (D) mice. White arrow indicates the contact site of microglia. Differential interference contrast (DIC) images of the imaged neurons and the fluorescence signal of GFP (green) and NADH (dark cyan) of red outlined areas are shown. (E) Average (and standard deviation) of NADH intrinsic fluorescence of all neurons in P2Y12 receptor^{+/+} (red, $n = 10$) and P2Y12 receptor^{-/-} (black, $n = 11$) mice. (F) CLSM image showing microglial process contacting a neuronal Kv2.1 cluster with closely apposed quinacrine-labeled ATP-containing vesicle and closely localized neuronal mitochondria. Quinacrine labeling colocalizes with the vNUT signal. (G) Images from CLSM in vitro time-lapse imaging showing that quinacrine-labeled ATP-containing vesicles (green) are released (red arrows) from the neuronal cell body (white dashed outline) after KCl stimulation (M.I.P. of Z stack, $2.5 \mu\text{m}$). (H) Number of released quinacrine-positive vesicles plotted as a function of time after KCl or vehicle treatment. (I) Size distribution of quinacrine-labeled puncta. The smaller ones (vesicles) tend to be released and the larger ones (mitochondria) are retained. (J) KCl induces a robust ATP release in cultured neurons, which could not be inhibited by a mixture of the synaptic calcium-channel blockers ω -agatoxin and ω -conotoxin (SC), but was almost completely inhibited by the L-type calcium-channel blocker nimodipine (NIM) or the vNUT inhibitor clodronate (CLO). (K) CLSM image showing robust NTPDase1 expression on microglial processes within the somatic junctions. Electron microscopic insert shows NTPDase1-labeled (dark precipitate) microglial process contacting the neuronal cell body. Neuronal mitochondria (m), vesicles, and membrane structures (white arrowheads) are closely apposed to the contact site (black arrows) where NTPDase1 is expressed on the microglial membrane. For statistical data, see the supplementary text for Fig. 3.



(36); $p = 0.0271$; $n = 10$] or the vNUT inhibitor clodronate ($p = 0.0284$; $n = 10$). These data confirmed the presence of an activity-dependent somatic ATP release from neurons. Because the main ligand for microglial P2Y₁₂ receptors is ADP, we tested the possible presence of nucleosidase expression at microglia–neuron contacts. Using CLSM and electron microscopy, we found robust NTPDase1 expression on 99.6% of all microglial processes within the somatic junctions (Fig. 3K; $n = 275$ contacts from 2 mice). Thus, neuron-derived ATP can readily be converted into ADP and sensed by microglia right within the somatic junctions.

Because microglial processes are in a position at the somatic junctions to sense neuronal activity, we further explored the signaling mechanisms at these sites *in vivo* using 2P imaging in CX3CR1^{+/GFP} microglia reporter mice that were electroporated *in utero* with the neuronal reporter *pCAG-IRES-tdTomato* (Fig. 4, A and B). Intra-cisterna magna administration of the potent and selective P2Y₁₂ receptor inhibitor PSB0739 (PSB) reduced somatic junction lifetime by 45% but did not affect the lifetime of dendritic microglia–neuron contacts (Fig. 4C, control somata versus PSB somata; $p = 0.0331$; $n = 40$). We also tested synapse density after acute intra-cisterna magna administration of vehicle (control) or PSB. PSB treatment did not alter neocortical synapse

numbers (fig. S6G; 0.353 synapses/ μm^2 in control somata and 0.352 synapses/ μm^2 in PSB-injected somata; $n = 423$ appositions from 4 animals). Because the maintenance of somatic microglia–neuron junctions depends on physiological P2Y₁₂ receptor function, we tested whether microglia would react directly to changes in neuronal activity. We induced neuronal activation by using the chemogenetic DREADD (designer receptor exclusively activated by designer drug) approach. pAAV carrying the hSyn-hM3D(Gq)-mCherry construct was injected into the cerebral cortex of P2Y₁₂ receptor^{+/+} and P2Y₁₂ receptor^{-/-} mice that had been crossed with CX3CR1^{+/GFP} mice to visualize microglial responses in the presence or absence of P2Y₁₂ receptor signaling (fig. S5, F and G). After intraperitoneal injection of clozapine-N-oxide (CNO) to induce hM3D(Gq)-DREADD activation, we observed a 234% increase in neuronal cFos signal compared with vehicle treatment (fig. S5H; $p < 0.001$; $n = 100$), confirming a specific and robust neuronal activation.

Chemogenetic neuronal activation resulted in an increased microglial process coverage of the soma of DREADD- and cFos-coexpressing neurons in P2Y₁₂ receptor^{+/+} mice (Fig. 4D; 243% of control, $p = 0.0139$; $n = 101$ neurons from 8 mice), but not in P2Y₁₂ receptor^{-/-} mice (Fig. 4E; 133% of control, $p = 0.7497$; $n =$

85 neurons from 6 mice). We also tested the effect of acute central pharmacological blockade of microglial P2Y₁₂ receptors (Fig. 4F) and found that PSB injected intra-cisterna magna completely abolished the neuronal activity-induced increase in microglial process coverage (Fig. 4G; 72.34% lower process coverage in CNO+PSB than in CNO+vehicle, $p < 0.001$; $n = 124$ neurons from 6 mice). Thus, microglia dynamically react to changes in neuronal activity at somatic microglia–neuron junctions in a P2Y₁₂ receptor-dependent manner, leading to a rapid increase of somatic coverage by microglial processes.

Microglia protect neurons after acute brain injury in a P2Y₁₂ receptor-dependent manner through altered somatic junctions

Because somatic microglia–neuron junctions were abundant in the healthy brain, we next investigated whether these morphofunctional communication sites were altered in response to brain injury. Microglia are known to respond rapidly to changes in neuronal activity in the boundary zone of the infarct after stroke (37). Thus, we performed experimental stroke and delineated the evolving penumbra on the basis of the metabolic activity of the tissue as assessed by the redox indicator tetrazolium chloride coregistered with the immunofluorescent signal for MAP2 and microglia

Fig. 4. Physiological microglia–neuron communication at the somatic junction site is P2Y₁₂ receptor dependent. (A) Outline of acute P2Y₁₂ receptor-blockade experiments. i.c.m., intra-cisterna magna. (B) CLSM images showing examples of the recorded microglia–neuron contacts. Empty arrowheads point to dendritic contacts and full arrowheads mark somatic junctions. (C) Acute intra-cisterna magna administration of PSB significantly reduced somatic junction lifetime, but did not affect the lifetime of dendritic microglia–neuron contacts. n.s., not significant. (D) Neuronal activity induced a robust elevation of microglial process coverage of neuronal cell bodies in CNO-treated animals but not in DREADD⁺/cFos⁻ cells. (E) CNO-triggered neuronal activity could not induce an elevation of microglial process coverage of neuronal cell bodies in P2Y₁₂ receptor^{-/-} mice. (F) Outline of combined chemogenetic and acute P2Y₁₂ receptor-blockade experiments. (G) Acute inhibition of microglial P2Y₁₂ receptors prevented neuronal activity-induced increase of microglial process coverage. For statistical data, see the supplementary text for Fig. 4.

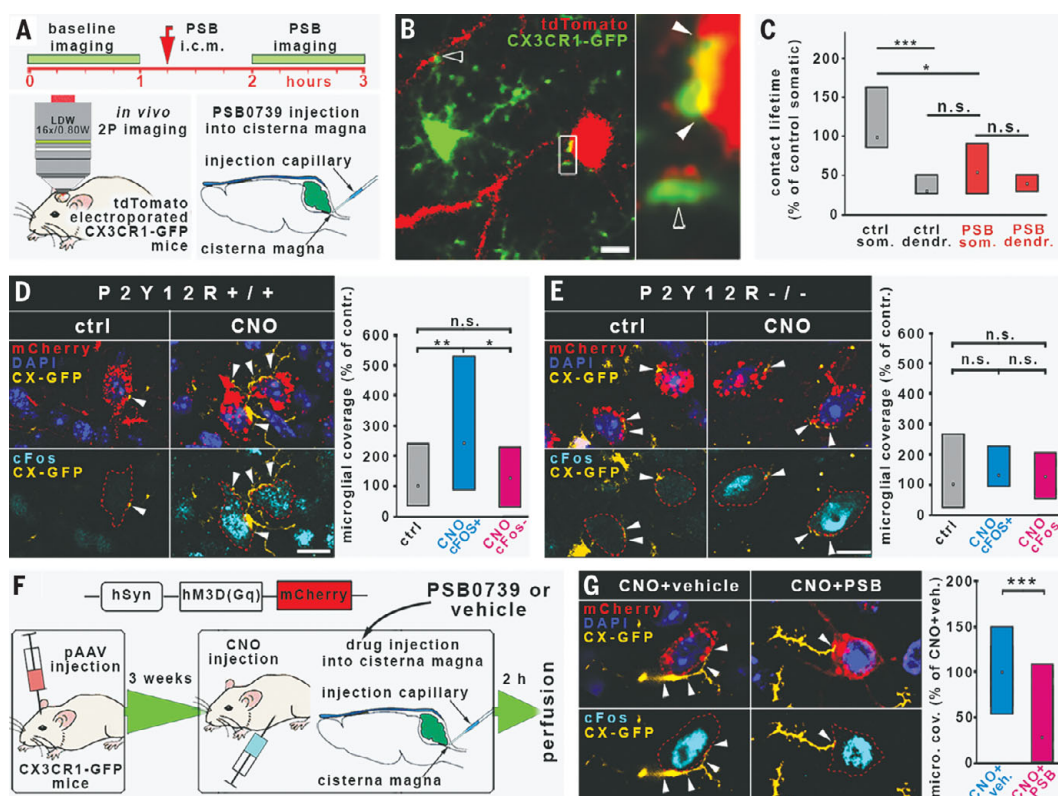


(fig. S6A). We observed the fragmentation of mitochondria (Fig. 5A, 74% decrease of individual mitochondrial area, 46% decrease of mitochondrial major axis; $p < 0.001$ for both; $n = 189$ mitochondria) and an almost complete declustering of Kv2.1 proteins in morphologically intact penumbral neurons (Fig. 5B and fig. S6E, from 4 to 0 median clusters/cross-section and from 0.0947 to 0 clusters/ μm in control and stroke, respectively, $p < 0.001$; $n = 58$ cells). These morphological changes were accompanied by a robust increase in the microglial process coverage of neuronal cell bodies originating from somatic microglia-neuron junctions in both mice and human postmortem brain tissues (Fig. 5, B to E; mouse: 3.8-fold increase, $p < 0.001$; $n = 30$ neurons; human: 1.5-fold increase, $p = 0.007$; $n = 249$ neurons). Acute intra-cisterna magna administration of the P2Y₁₂ receptor inhibitor PSB or preventing mitochondrial injury by using the mitochondrial ATP-sensitive potassium (KATP) channel opener diazoxide (38) completely abolished stroke-induced increases in microglial process coverage around somatic junctions (Fig. 5D, control versus stroke: $p < 0.001$, PSB control versus PSB stroke: $p =$

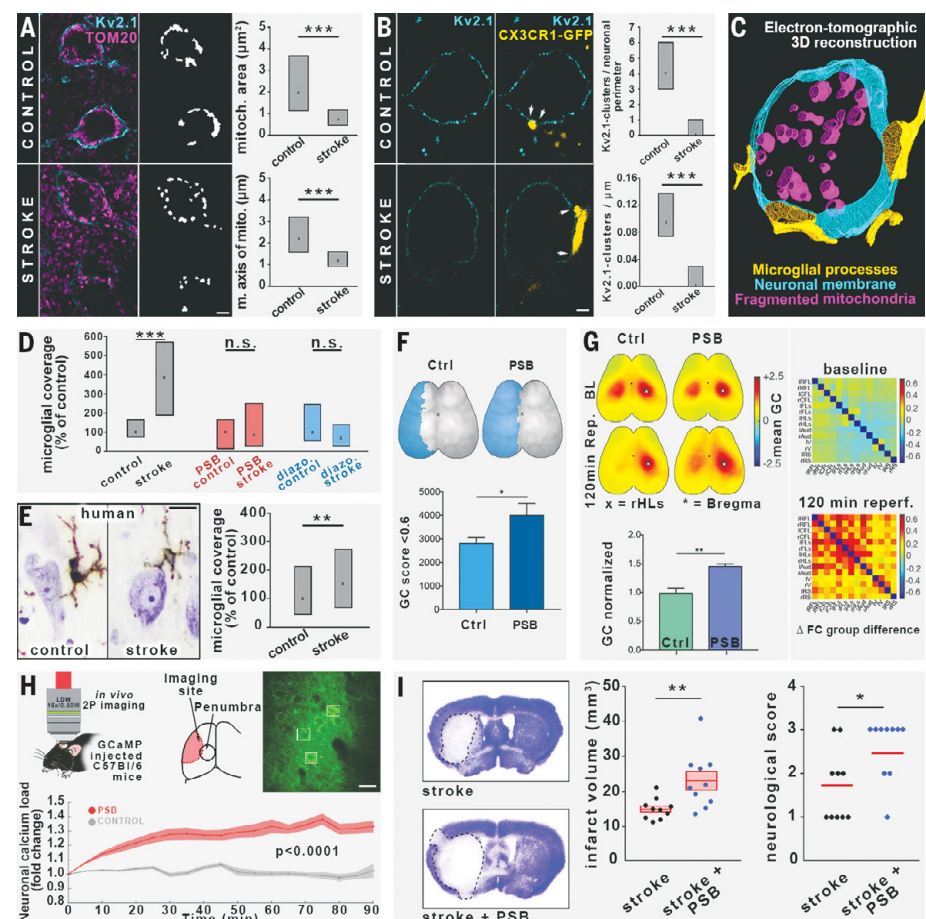
0.792, diazoxide control versus diazoxide stroke: $p = 0.053$; $n = 140$ neurons). The viability of the examined neurons with increased microglial process coverage was confirmed by normal chromatin structure and membrane integrity (fig. S6, B and C). Transmission electron tomography also confirmed increased microglial process coverage and mitochondrial fragmentation of neurons (Fig. 5C).

To test the impact of P2Y₁₂ receptor-dependent microglial functions on neuronal viability in vivo, we investigated pharmacological inhibition of P2Y₁₂ receptor by injection of PSB intra-cisterna magna before middle cerebral artery occlusion (MCAo). Inhibition of microglial P2Y₁₂ receptor prevented increases in microglial process coverage of neuronal cell bodies in the penumbra and altered functional connectivity in the brain as assessed by a widefield-imaging approach in Thyl-GCaMP6s mice (Fig. 5, F and G). An absence of P2Y₁₂ receptor signaling significantly increased the area of functional disconnection (global connectivity < 0.6) in the ipsilateral hemisphere during ischemia, accompanied by a trend toward elevated neuronal calcium load (Fig. 5F and fig. S6F; $p = 0.0439$; $n = 17$ mice). Seed-based

connectivity analysis revealed a significant increase in the contralateral sensory hindlimb area after reperfusion in PSB-treated animals. Moreover, connectivity analysis of 14 functional areas revealed a substantial and widespread increase in connectivity strength in the absence of microglial P2Y₁₂ receptor signaling (Fig. 5G; $p = 0.0077$; $n = 7$ mice).

To examine the effect of P2Y₁₂ receptor inhibition at the single-neuron level in the evolving ischemic penumbra in vivo, we investigated GCaMP6f-injected mice with 2P microscopy. In control mice, neuronal GCaMP6f signal remained unchanged for the first 90 min of reperfusion, whereas blockade of microglial P2Y₁₂ receptors with PSB resulted in a strong elevation in neuronal calcium load (Fig. 5H; $p < 0.0001$; $n = 96$ neurons from 3 mice). This corroborated the findings obtained from the widefield-imaging approach at the cellular level as well. Furthermore, P2Y₁₂ receptor inhibition significantly increased lesion volume at 24 hours reperfusion (Fig. 5I; 54% increase, $p = 0.008$; $n = 20$ mice) and resulted in worse neurological outcome (Fig. 5I; Bederson score, stroke: 1.7 ± 0.26 ; stroke+PSB: 2.5 ± 0.224 , $p = 0.033$; $n = 20$ mice).

Fig. 5. Microglia protect neurons after acute brain injury in a P2Y₁₂ receptor-dependent manner through altered somatic junctions. (A) CLSM images showing that stroke induces the fragmentation of mitochondria (magenta) in neuronal cell bodies (Kv2.1 labeling, cyan) in the penumbra. Mitochondrial area and mitochondrial major axis are both significantly decreased. (B) CLSM images of cortical neurons showing that, in parallel with the declustering of Kv2.1-channels (cyan), microglial coverage (yellow) is significantly increased after stroke in the penumbra. (C) 3D reconstruction from electron tomographic volume showing elevated microglial coverage and fragmentation of neuronal mitochondria. (D) Microglial coverage of neuronal cell bodies is robustly increased after stroke, whereas acute central blockade of P2Y₁₂ receptors or activation of KATP channels completely abolishes the stroke-induced increase of coverage. (E) Stroke induces a 1.5-fold increase in somatic microglia coverage of human cortical neurons. (F) Topographical maps showing the area of pixels with a global connectivity (GC) score < 0.6 after ischemia. The sum of outlined pixels revealed higher dropdown of GC in PSB-treated animals after stroke. (G) Left panel: Topographical maps showing increased region of interest to GC of the contralateral HLs in PSB-treated mice 120 min after stroke. Right panel: Seed-to-seed connectivity is increased in PSB-treated animals after stroke. (H) In vivo 2P calcium imaging revealing a significant increase of neuronal calcium load during reperfusion after acute P2Y₁₂ receptor inhibition with PSB. (I) Infarct volume is increased after acute central P2Y₁₂ receptor inhibition, which is accompanied by a significantly worse neurological outcome. For statistical data, see the supplementary text for Fig. 5.



To investigate the duration of the PSB effect *in vivo*, 2-hour-long imaging sessions were performed with 2P microscopy 1 to 3 hours and 24 to 26 hours after intra-cisterna magna PSB injection ($n = 173$ contacts analyzed from 3 mice). The lifetime of somatic junctions was significantly reduced by up to 3 hours after PSB administration (56.3% of lifetime under baseline conditions, $p = 0.0139$), whereas there was no effect observed 1 day later (93.8% of lifetime under baseline conditions), suggesting an acute effect of intra-cisterna magna PSB (Fig. S6, H and I). The acute effect of PSB was also confirmed by the histological measurements performed 4 hours after MCAo (Fig. 5D). To verify that PSB injected intra-cisterna magna only inhibited microglial P2Y₁₂ receptors, and not those expressed by circulating platelets, we measured ADP-induced platelet activation in plasma samples 1 hour after MCAo, when blood-brain barrier injury is apparent (37, 39, 40). ADP-induced increases in platelet CD62P were not altered in mice treated with intra-cisterna magna PSB compared with vehicle-treated animals (Fig. S5J).

Disintegration of somatic microglia–neuron junctions after neuronal injury triggers increased microglial process coverage of the cell bodies of compromised but potentially viable neurons through P2Y₁₂ receptor and mitochondrial signaling. This could allow the initiation of protective microglial responses that limit brain injury.

Discussion

Here, we describe a form of interaction between microglia and neurons. Under physiological conditions, somatic microglia–neuron junctions were present on most of the neurons in both mice and humans. The junctions appeared to function as communication sites that are rapidly altered in response to brain injury. We propose that microglia constantly monitor neuronal status through these somatic junctions, allowing neuroprotective actions to take place in a targeted manner.

Sites of somatic junctions in neurons were preferentially and repeatedly contacted by microglia. Such interactions had much longer lifetimes compared with the microglial contacts targeting dendrites. In previous studies, the proximity between microglial cell bodies or processes with neuronal somata has been observed in zebrafish and mice (41, 42). However, the formation of direct membrane-to-membrane junctions, the molecular identity of neuronal membranes contacted, activity-dependent recruitment of microglial processes to neuronal cell bodies, the mechanisms of junction formation, and the function of somatic microglia–neuron interactions have not been addressed. Therefore, we took advantage of cutting-edge neuroanatomical approaches and discovered that somatic microglia–neuron junctions

are characterized by specific ultrastructural and molecular composition. These morphological and molecular features are absent in perisomatic boutons contacted by microglia, suggesting that the main form of neuronal quality control by microglial processes is not mediated by interactions between microglia and perisomatic axon terminals.

Mitochondria are the primary energy generators in cells, playing fundamental roles in calcium homeostasis, intracellular signaling (43, 44), and neuronal quality control (45), as well as in determining cellular fate (46). Although neuronal mitochondria are also considered “immunometabolic hubs” involved in antigen presentation and the regulation of innate immune responses (47, 48), changes in mitochondrial function caused by metabolic imbalance, oxidative stress, inflammation, cellular injury, or cell death occur in most neuropathological states (49). MAMs are also considered to be key integrators of metabolic and immunological signals, playing a central role in neurodegeneration and cell-fate decisions (30, 50, 51). Thus, somatic mitochondria and MAMs are ideally positioned to report neuronal status to microglia and to mediate neuronal quality control. Consistent with this, we show that the recruitment of microglial processes to somatic junctions in the vicinity of neuronal mitochondria is linked with mitochondrial activity. This may indicate rapid sensing of mitochondrial activity-associated changes of neurons by microglial processes through the release of ATP and other mediators or the impact of microglia-derived substances on neuronal activity and/or mitochondrial function at somatic junctions. Neurons can execute somatic ATP release through pannexin hemichannels, voltage-dependent anion channels, or activity-dependent vesicle exocytosis (21, 22, 36). vNUT is known to be responsible for somatic vesicular ATP release in neurons (34). In fact, we demonstrated the enrichment of vNUT between neuronal mitochondria and the somatic membranes contacted by microglia and, using time-lapse imaging and HPLC measurements, we confirmed the presence of activity-dependent somatic ATP release from neurons that was blocked by vNUT inhibition. TOM20-positive mitochondria-derived vesicles and other vesicles were also observed within the neuronal cytoplasm at somatic microglia–neuron junctions, together with the enrichment of LAMP1-positive lysosomes, which could, together with the released ATP, provide a constant readout of neuronal activity and mitochondrial function as seen in neurons and other cells (31, 52). The strong enrichment of vNUT in these contacts, the existence of an activity- and vNUT-dependent somatic ATP release, the presence of filamentous cytoplasmic structures connecting vesicles to the core of the junction, the presence of TOM20

immunogold-positive vesicles within the contacts attached to the neuronal PM, the close association of neuronal lysosomes, and the massive accumulation and nanoscale clustering of exocytosis-promoting Kv2.1 proteins within these contact sites collectively indicate the convergence of multiple parallel vesicular exocytotic pathways at somatic microglia–neuron junctions.

Kv2.1 channels are major regulators of neuronal potassium levels. However, they tend to assemble into discrete clusters on the surface of neurons, where they do not function as ion channels, but rather provide sites for intensive membrane trafficking as exocytotic and endocytotic hubs (17, 18, 53). Furthermore, Kv2.1 clusters are known to induce stable ER–PM junctions (53), anchoring MAMs and mitochondria into these morphofunctional units and providing an ideal site for the release of mitochondria-associated messenger molecules (31). The functional importance of these interactions is confirmed by our results showing that Kv2.1 clusters on transfected HEK cells readily induced the formation of microglial process contacts to these clusters, which could not be observed on HEK cells transfected with the dominant-negative mutant Kv2.1. Furthermore, microglial P2Y₁₂ receptor clusters were precisely aligned with neuronal Kv2.1 clusters at somatic junctions.

The activation of P2Y₁₂ receptors was mainly associated with injury or pathological states in previous studies and was considered negligible for physiological microglial surveillance on the basis of *ex vivo* studies (54). Compared with normal extracellular ATP levels in the brain, high levels of ATP (1 mM) were shown to induce P2Y₁₂ receptor-dependent microglial recruitment, similar to that seen during microglial phagocytosis or in models of synaptic plasticity, whereas microglial surveillance is considered to be P2Y₁₂ receptor independent (54, 55). Our *in vivo* results refine this view and highlight the importance of the compartment-dependent effects of P2Y₁₂ receptor on microglial process responses: PSB0739 significantly reduced somatic junction lifetime but did not affect the lifetime of dendritic microglia–neuron contacts, whereas it abolished microglial reactions to altered neuronal activity, confirming P2Y₁₂ receptor dependence of microglial actions under physiological conditions. Furthermore, neuronal mitochondrial activity was also linked with physiological microglial P2Y₁₂ receptor activity at these junctions. It is also possible that P2Y₁₂ receptor-mediated actions are more important for sustaining than for forming somatic junctions during the communication between neuronal somata and microglial processes. The contact-dependent clustering of P2Y₁₂ receptors further confirms their involvement in physiological microglia–neuron interactions at somatic

junctions. Blockade of microglial P2Y₁₂ receptor left cortical synapse numbers completely unchanged and contact-dependent nanoclustering of microglial P2Y₁₂ receptors was not seen when microglia contacted synaptic boutons. Thus, microglia–neuron interactions at these sites are not only P2Y₁₂ receptor dependent, they are also fundamentally different from those seen at synapses.

The failure of most neuroprotection trials in stroke and other brain diseases strongly indicates the importance of understanding the complexity of pathophysiological processes, including microglial actions. Potentially salvageable neurons around the infarct core may show metabolic activity up to 6 to 17 hours after stroke in patients and experimental animals (56, 57). Here, Kv2.1 declustering was observed in compromised neurons of the penumbra as early as 4 hours after brain injury, which paralleled mitochondrial fragmentation in neurons and increased microglial process coverage around somatic microglia–neuron junctions. Thus, P2Y₁₂ receptor-dependent microglial actions protect neurons, whereas blockade of microglial P2Y₁₂ receptor signaling alone impaired cortical network function and increased calcium load and the area of ischemia-induced disconnection within 2 hours after stroke (a clinically relevant time window). This increase in brain injury was similar to that seen after the complete and selective elimination of microglia (37). These protective microglia- and P2Y₁₂ receptor-mediated effects were linked with mitochondrial actions initiated upon neuronal injury because the diazoxide (a KATP channel opener)-abolished increases in microglial process coverage of neurons after stroke were similar to those seen after blockade of P2Y₁₂ receptor signaling.

All of these results unequivocally indicate that microglia continuously monitor neuronal status through somatic junctions, rapidly responding to neuronal changes and initiating neuroprotective actions.

We propose that healthy neurons may constitutively release ATP and other signaling molecules at these junctions, communicating their “well-being” to microglia. In turn, disintegration of these specialized morphofunctional hubs caused by excitotoxicity, energy depletion, or other noxious stimuli may trigger rapid and inherently protective microglial responses, leading to the restoration of neuronal function or the isolation and phagocytosis of dying neurons in case terminal neuronal injury occurs (55). Along with P2Y₁₂ receptor-mediated microglial process recruitment, it is likely that a broad range of signals is integrated at somatic microglial junctions and, through these, microglia may sense products of neuronal exocytosis and changes in the cell membrane (e.g. apoptotic signals) and alter the duration of physical contact or initiate phagocytosis. The most im-

portant open research areas include the clarification of additional signaling mechanisms (vesicular and nonvesicular) involved in neuron-to-microglia communication at these junctions and the mechanisms of microglial neuroprotection (e.g. regulation of neuronal ion fluxes, neuronal calcium dynamics, or the metabolism of neuronal mitochondria). Because the role of microglia–neuron somatic junctions in most brain diseases is completely unknown, microglia–neuron interactions through these sites may differ in different forms of acute and chronic neuropathologies.

REFERENCES AND NOTES

- M. S. Thion, F. Ginhoux, S. Garel, *Science* **362**, 185–189 (2018).
- K. Kierdorf, M. Prinz, *J. Clin. Invest.* **127**, 3201–3209 (2017).
- M. W. Salter, B. Stevens, *Nat. Med.* **23**, 1018–1027 (2017).
- W. M. Song, M. Colonna, *Nat. Immunol.* **19**, 1048–1058 (2018).
- D. Davalos et al., *Nat. Neurosci.* **8**, 752–758 (2005).
- A. Nimmerjahn, F. Kirchhoff, F. Helmchen, *Science* **308**, 1314–1318 (2005).
- Y. Wu, L. Dissing-Olesen, B. A. MacVicar, B. Stevens, *Trends Immunol.* **36**, 605–613 (2015).
- L. Weinhard et al., *Nat. Commun.* **9**, 1228 (2018).
- J.-M. Cioni, M. Koppers, C. E. Holt, *Curr. Opin. Neurobiol.* **51**, 86–94 (2018).
- T. Mischak, T. L. Schwarz, *Neuron* **96**, 651–666 (2017).
- M. Terenzio, G. Schiavo, M. Fainzilber, *Neuron* **96**, 667–679 (2017).
- J. Aarum, K. Sandberg, S. L. B. Haeblerlein, M. A. A. Persson, *Proc. Natl. Acad. Sci. U.S.A.* **100**, 15983–15988 (2003).
- M. Ueno et al., *Nat. Neurosci.* **16**, 543–551 (2013).
- J. L. Marin-Teva, M. A. Cuadros, D. Martín-Oliva, J. Navascués, *Neuron Glia Biol.* **7**, 25–40 (2011).
- A. Sierra et al., *Neural Plast.* **2014**, 610343 (2014).
- H. Wake, A. J. Moorhouse, S. Jinno, S. Kohsaka, J. Nabekura, *J. Neurosci.* **29**, 3974–3980 (2009).
- E. Deutsch et al., *Mol. Biol. Cell* **23**, 2917–2929 (2012).
- L. Feinschreiber, D. Singer-Lahat, U. Ashery, I. Lotan, *Ann. N. Y. Acad. Sci.* **1152**, 87–92 (2009).
- M. Kirmiz, N. C. Vierra, S. Palacio, J. S. Trimmer, *J. Neurosci.* **38**, 7562–7584 (2018).
- B. Jiang, X. Sun, K. Cao, R. Wang, *Mol. Cell. Biochem.* **238**, 69–79 (2002).
- A. Menéndez-Méndez et al., *Front. Pharmacol.* **8**, 951 (2017).
- R. D. Fields, *Semin. Cell Dev. Biol.* **22**, 214–219 (2011).
- S. E. Haynes et al., *Nat. Neurosci.* **9**, 1512–1519 (2006).
- Y. Zhang et al., *J. Neurosci.* **34**, 11929–11947 (2014).
- O. Butovsky et al., *Nat. Neurosci.* **17**, 131–143 (2014).
- B. Dudok et al., *Nat. Neurosci.* **18**, 75–86 (2015).
- I. D. Campbell, M. J. Humphries, *Cold Spring Harb. Perspect. Biol.* **3**, a004994 (2011).
- H. Akiyama, P. L. McGeer, *J. Neuroimmunol.* **30**, 81–93 (1990).
- F. E. McCann et al., *J. Immunol.* **170**, 2862–2870 (2003).
- G. Csordás, D. Weaver, G. Hajnóczky, *Trends Cell Biol.* **28**, 523–540 (2018).
- A. Sugiyama, G.-L. McLelland, E. A. Fon, H. M. McBride, *EMBO J.* **33**, 2142–2156 (2014).
- V. Soubannier et al., *Curr. Biol.* **22**, 135–141 (2012).
- T. Ho et al., *Front. Cell. Neurosci.* **9**, 389 (2015).
- Y. Moriyma, M. Hiasa, S. Sakamoto, H. Omote, M. Nomura, *Purinergic Signal.* **13**, 387–404 (2017).
- A. M. Brennan, J. A. Connor, C. W. Shuttleworth, *J. Cereb. Blood Flow Metab.* **26**, 1389–1406 (2006).
- X. Zhang, Y. Chen, C. Wang, L.-Y. M. Huang, *Proc. Natl. Acad. Sci. U.S.A.* **104**, 9864–9869 (2007).
- G. Szalay et al., *Nat. Commun.* **7**, 11499 (2016).
- J. O. Onukwuor, D. Stevens, C. Kamunde, *J. Exp. Biol.* **219**, 2743–2751 (2016).
- F. Orsini et al., *Arterioscler. Thromb. Vasc. Biol.* **38**, 2678–2690 (2018).
- K. Bekó et al., *J. Thromb. Haemost.* **15**, 1223–1235 (2017).

- Y. Li, X.-F. Du, C.-S. Liu, Z.-L. Wen, J.-L. Du, *Dev. Cell* **23**, 1189–1202 (2012).
- R. D. Stowell et al., *Dev. Neurobiol.* **78**, 627–644 (2018).
- C. N. Hall, M. C. Klein-Flügge, C. Howarth, D. Attwell, *J. Neurosci.* **32**, 8940–8951 (2012).
- N. S. Chandel, *BMC Biol.* **12**, 34 (2014).
- E. I. Rugarli, T. Langer, *EMBO J.* **31**, 1336–1349 (2012).
- A. Kasahara, L. Scorrano, *Trends Cell Biol.* **24**, 761–770 (2014).
- D. Arnoult, F. Soares, I. Tattoli, S. E. Girardin, *EMBO Rep.* **12**, 901–910 (2011).
- G. R. Bantug et al., *Immunity* **48**, 542–555.e6 (2018).
- A. U. Joshi, D. Mochly-Rosen, *Pharmacol. Res.* **138**, 2–15 (2018).
- J. Rieusset, *Biochem. Biophys. Res. Commun.* **500**, 35–44 (2018).
- R. Bravo-Sagua et al., *Curr. Mol. Med.* **13**, 317–329 (2013).
- G.-L. McLelland, S. A. Lee, H. M. McBride, E. A. Fon, *J. Cell Biol.* **214**, 275–291 (2016).
- P. D. Fox et al., *J. Cell Sci.* **128**, 2096–2105 (2015).
- C. Madry et al., *Neuron* **97**, 299–312.e6 (2018).
- R. Fekete et al., *Acta Neuropathol.* **136**, 461–482 (2018).
- G. Marchal et al., *Stroke* **27**, 599–606 (1996).
- J. C. Baron, M. E. Moseley, *J. Stroke Cerebrovasc. Dis.* **9**, 15–20 (2000).

ACKNOWLEDGMENTS

We thank L. Barna and the Nikon Imaging Center at the Institute of Experimental Medicine (IEM) for kindly providing microscopy support, D. Mastronarde at MCDB for his continuous help with IMOD software, and S. Kovács from ETH Zurich for scripting analytic tools. We are also grateful to N. Hájós (IEM), Z. Nusser (IEM), and J. Trimmer (University of California, Davis) for their support and useful comments. We thank the Department of Pathology, St. Borbála Hospital, Tatabánya, and the Human Brain Research Lab at the IEM for providing human brain tissue and D. Gali-Görkei and R. Rácz for excellent technical assistance. We also thank Plexikon for providing PLX5622 and Deltagen for the donation of P2Y₁₂ receptor^{-/-} mice. **Funding:** This work was supported by a Momentum Research Grant from the Hungarian Academy of Sciences (LP2016-4/2016 to A.D.) and ERC-CoG 724994 (A.D.), a János Bolyai Research Scholarship of the Hungarian Academy of Sciences (C.C., and N.L.), and grants UNKP-19-3-I (B.P.) and UNKP-19-4 (C.C.) from the New National Excellence Program of the Ministry for Innovation and Technology. Additionally, this work was funded by H2020-ITN-2018-813294-ENTRAIN (A.D.), the Hungarian Academy of Sciences (G.T.), the National Research, Development and Innovation Office of Hungary (GINOP-2.3.2-15-2016-00018, VKSZ-14-1-2015-0155, G.T.), the Ministry of Human Capacities, Hungary (20391-3/2018/FEKUSTRAT, G.T.), the German Research Foundation (FOR 2879), and ERC-StG 802305 to A.L. I.K. was supported by a Momentum Research Grant from the Hungarian Academy of Sciences (LP2013-54), the Hungarian Scientific Research Fund (OTKA, K 116915), and the National Research, Development and Innovation Office of Hungary (VKSZ-14-1-2015-0155). M.M.T. was supported by National Institutes of Health grant R01GM109888. B.S. and Z.M. were supported by the National Research, Development and Innovation Office of Hungary (K116654 to B.S. and K125436 to Z.M.) and by the National Brain Research Program (2017-1.2.1-NKP-2017-00002). T.H. was supported by the Hungarian Brain Research Program (1.2.1-NKP-2017-00002). G.M. was supported by Hungarian Scientific Research Fund (OTKA, K128863). L.C. was supported by the National Research, Development and Innovation Fund (GINOP-2.3.2-15-2016-00048-Stay Alive). R.S. was supported by Hungarian Scientific Research Fund (OTKA, K 129047). This work was also supported by EFOP-3.6.3-VEKOP-16-2017-00009 from Semmelweis University. **Author contributions:** The project was conceived by C.C., B.P., and A.D. Surgery was performed by N.L. and A.D. Two-photon imaging was performed by R.F. Immunohistochemistry and light microscopy were performed by C.C., B.P., A.D., B.O., A.D.S., and E.S. STORM microscopy was performed by B.O. Electron microscopy was performed by C.C., B.P., E.S., and A.D.S. Electron tomography was performed by C.C. and B.P. In vitro NADH imaging was performed by G.M. under the supervision of G.T. Plasmid engineering and in utero electroporation were performed by Z. L. and Z. I. L. In vitro cell culture transfection and experiments were performed by Z.K., K.T., and Z.I.L. Virus injection was performed by R.F. and B.M. Widefield calcium imaging was performed by S.H. under the supervision of A.L. HPLC measurements were performed by M.B. under the supervision of B.S. Data were analyzed by C.C., B.P., B.O., G.M., S.H., N.L., A.D.S., K.U., A.L., and A.D. Critically important clinical and neuropathological data and materials were contributed by L.C.,

T.H., Z.M. G.S., M.M.T., and F.E. The laser-optical setup for dual wavelength in vitro 2P measurements was optimized by R.S. Resources were provided and essential intellectual contributions were made by I.K., G.T., and A.L., who also revised the manuscript. Funding was obtained and the project supervised by A.D. The paper was written by C.C., B.P., and A.D. with input from all authors. **Competing interests:** The authors declare no competing interests. **Data and materials availability:** PLX5622

was obtained under a material transfer agreement with Plexikon (Berkeley, CA). All data are available in the main text or the supplementary materials.

SUPPLEMENTARY MATERIALS

science.sciencemag.org/content/367/6477/528/suppl/DC1
Materials and Methods
Figs. S1 to S6

Tables S1 to S3
Movies S1 to S7
References (58–67)

12 April 2019; resubmitted 14 October 2019
Accepted 3 December 2019
Published online 12 December 2019
10.1126/science.aax6752

NANOMATERIALS

One-dimensional van der Waals heterostructures

Rong Xiang^{1*†}, Taiki Inoue^{1†}, Yongjia Zheng^{1†}, Akihito Kumamoto², Yang Qian¹, Yuta Sato³, Ming Liu¹, Daiming Tang⁴, Devashish Gokhale^{5‡}, Jia Guo^{1,6}, Kaoru Hisama¹, Satoshi Yotsumoto¹, Tatsuro Ogamoto¹, Hayato Arai¹, Yu Kobayashi⁷, Hao Zhang¹, Bo Hou⁸, Anton Anisimov⁹, Mina Maruyama¹⁰, Yasumitsu Miyata⁷, Susumu Okada¹⁰, Shohei Chiashi¹, Yan Li^{1,6}, Jing Kong¹¹, Esko I. Kauppinen¹², Yuichi Ikuhara², Kazu Suenaga³, Shigeo Maruyama^{1,8*}

We present the experimental synthesis of one-dimensional (1D) van der Waals heterostructures, a class of materials where different atomic layers are coaxially stacked. We demonstrate the growth of single-crystal layers of hexagonal boron nitride (BN) and molybdenum disulfide (MoS₂) crystals on single-walled carbon nanotubes (SWCNTs). For the latter, larger-diameter nanotubes that overcome strain effect were more readily synthesized. We also report a 5-nanometer-diameter heterostructure consisting of an inner SWCNT, a middle three-layer BN nanotube, and an outer MoS₂ nanotube. Electron diffraction verifies that all shells in the heterostructures are single crystals. This work suggests that all of the materials in the current 2D library could be rolled into their 1D counterparts and a plethora of function-designable 1D heterostructures could be realized.

The demonstration of two-dimensional (2D) van der Waals (vdW) heterostructures (1–3)—in which atomic layers are stacked on each other and different 2D crystals are combined beyond symmetry and lattice matching—represents a way of manipulating crystals to enable both the exploration of physics not observable in conventional materials and device applications (4–8). These 2D heterostructures have been fabricated by transferring preprepared layers (transfer approach) (5, 9) or by synthesizing layers onto a base layer (synthesis approach) (10). Whether such artificial materials and interfaces can be fabricated in other dimensions remains an open question. In 1D materials, for example, an ideal vdW heterostructure would be a coaxial structure with different types of nanotubes. Such ideal structures have been investigated in theoretical studies (11, 12) and would appear to require a synthesis approach. However, experimental attempts to fabricate coaxial nanotube structures have yielded only amorphous or very poorly crystallized coatings (13, 14).

We demonstrate the experimental discovery and controlled fabrication of true 1D vdW heteronanotubes. A typical structure was 4 to 5 nm in diameter but contained three different shells: an inner carbon nanotube (CNT), a middle hexagonal boron nitride nanotube (BNNT), and an outer molybdenum disulfide (MoS₂) nanotube. Electron diffraction (ED) and many other characterizations were used to confirm that each shell in this structure was a seamless,

perfect nanotube that realized the heteronanotubes studied in theoretical models. The heterostructures formed through an open-end growth mode that has rarely been observed in previous 1D nanostructure growth. We outline some basic geometric principles that governed the formation of these 1D vdW heterostructure nanotubes, including the absence of structural correlation between inner and outer shells and the requirement of a threshold diameter for MoS₂ nanotubes.

In this study, the base structure, a single-walled carbon nanotube (SWCNT) (15), was chosen as the starting material for several reasons. It is, so far, the best-studied 1D material and can be synthesized in many controlled geometries. Also, a SWCNT can be metallic or semiconducting, which means it could serve as the electrode or channel material for a heteronanotube device. The typical SWCNTs used in this study were 1 to 2 nm in diameter and a few micrometers in length and were self-suspended as a random network (16). Schematics comparing the 2D and 1D vdW heterostructures are presented in Fig. 1, A and B.

Structure analysis of SWCNT-BNNT heterostructure

We present the initial growth step: the formation of the SWCNT-BNNT 1D heterostructure. We used SWCNTs as a template and synthesized additional hexagonal boron nitride (BN) layers by chemical vapor deposition (CVD). Figure 1C shows a representative high-

resolution transmission electron microscope (HRTEM) image of this coaxial heterostructure (additional images are available in fig. S1A). In a conventional HRTEM image, this nanotube is not distinguishable from a triple-walled pure carbon nanotube. The aberration-corrected HRTEM image of a similar tube revealed a contrast of stacking of two perfect nanotubes (Fig. 1, D and E). However, given that the starting material is purely single-walled before we perform a post-BN coating, we expect that the outer wall or walls are BN. This is supported by electron energy-loss spectroscopic (EELS) mapping (Fig. 1F). Because the reaction occurs on the outer surface, unlike previous attempts inside a nanotube (17, 18), we achieve continuous coating and highly crystallized outer BNNTs. The number of outer BNNT walls can be adjusted from a minimum of one to a maximum of five to eight, depending on the duration of BN CVD (fig. S1, B and C). These different layers grow independently, but the first layer is always the longest. The walls of our SWCNT template are very clean, so the nucleation is usually observed at the end of a suspended region, where a SWCNT is connected with another SWCNT or a SWCNT bundle (fig. S2). Occasionally, nucleation also occurs simultaneously at both ends of a suspended SWCNT region. Nucleation from the middle of a SWCNT is rarely observed.

One critical feature of the current structure is that each layer is a single crystal, which distinguishes this study from all previously reported coaxial tubular structures. This perfect crystallization is shown by the ED patterns provided in Fig. 2, A to C, and fig. S1. The perfect SWCNT-BNNT coaxial single crystals could reach a few hundreds of nanometers to ~2 μm and were limited only by the length of individually isolated regions in our starting SWCNTs. The other important feature of the current structure is its small diameter. Many of our SWCNT-BNNT structures are thinner than 2 nm, and the ternary SWCNT-BNNT-MoS₂ are 3 to 5 nm (described in a later section). This small dimension is essential for accessing the distinctive properties of 1D materials, such as confinement of excitons in the 1D crystals.

We characterized these coaxial crystals with several other techniques. X-ray photoelectron spectroscopy (XPS) revealed B–N and C–C bonds in this sample but no apparent peaks of C–N and B–C, which confirmed that BN and carbon moieties were chemically isolated (fig. S3). Optical absorption spectra (fig. S4A) revealed a

¹Department of Mechanical Engineering, The University of Tokyo, Tokyo 113-8656, Japan. ²Institute of Engineering Innovation, The University of Tokyo, Tokyo 113-8656, Japan.

³Nanomaterials Research Institute, National Institute of Advanced Industrial Science and Technology (AIST), Tsukuba 305-8565, Japan. ⁴International Center for Materials Nanoarchitectonics (WPI-MANA), National Institute for Materials Science (NIMS), Namiki 1-1, Tsukuba 305-0044, Japan. ⁵Department of Chemical Engineering, Indian Institute of Technology Madras, Chennai 600036, India. ⁶College of Chemistry and Molecular Engineering, Peking University, Beijing 100871, China. ⁷Department of Physics, Tokyo Metropolitan University, Tokyo 192-0397, Japan. ⁸Energy NanoEngineering Laboratory, National Institute of Advanced Industrial Science and Technology (AIST), Tsukuba 305-8564, Japan. ⁹Canatu Ltd., Helsinki FI-00390, Finland. ¹⁰Graduate School of Pure and Applied Sciences, University of Tsukuba, Tsukuba 305-8571, Japan. ¹¹Department of Electrical Engineering and Computer Science, Massachusetts Institute of Technology, Cambridge, MA 02139, USA. ¹²Department of Applied Physics, Aalto University School of Science, Espoo 15100, FI-00076 Aalto, Finland.

*Corresponding author. Email: xiangrong@photon.tu-tokyo.ac.jp (R.X.); maruyama@photon.tu-tokyo.ac.jp (S.M.) †These authors contributed equally to this work. ‡Present address: Department of Chemical Engineering, Massachusetts Institute of Technology, Cambridge, MA 02139, USA.

peak near 205 nm, and the peak intensity increased with growth time (number of outside BNNT layers). Cathode luminance spectra (fig. S4B) of the sample confirmed the existence of outer BN by emissions in the ultraviolet range. Also, the growth strategy was shown to apply to SWCNTs with different morphologies, including vertical arrays, horizontal arrays, random

networks, and suspended SWCNTs between silicon pillars (fig. S5).

The formation of this SWCNT-BNNT heterostructure follows an open-end growth mechanism (shown schematically in movie S1). In this scenario, the extension of the second layer happened only at the open edge of the BNNT. The third (and beyond) layer followed a sim-

ilar approach but nucleated in a later stage. This pattern is similar to the growth of additional layers in 2D material, but it has very rarely been observed in previous growth of carbon nanotubes (19). The open-edge growth mechanism is supported by the many atomic steps observed in heterostructures with incomplete growth of outer BNNT crystal layers

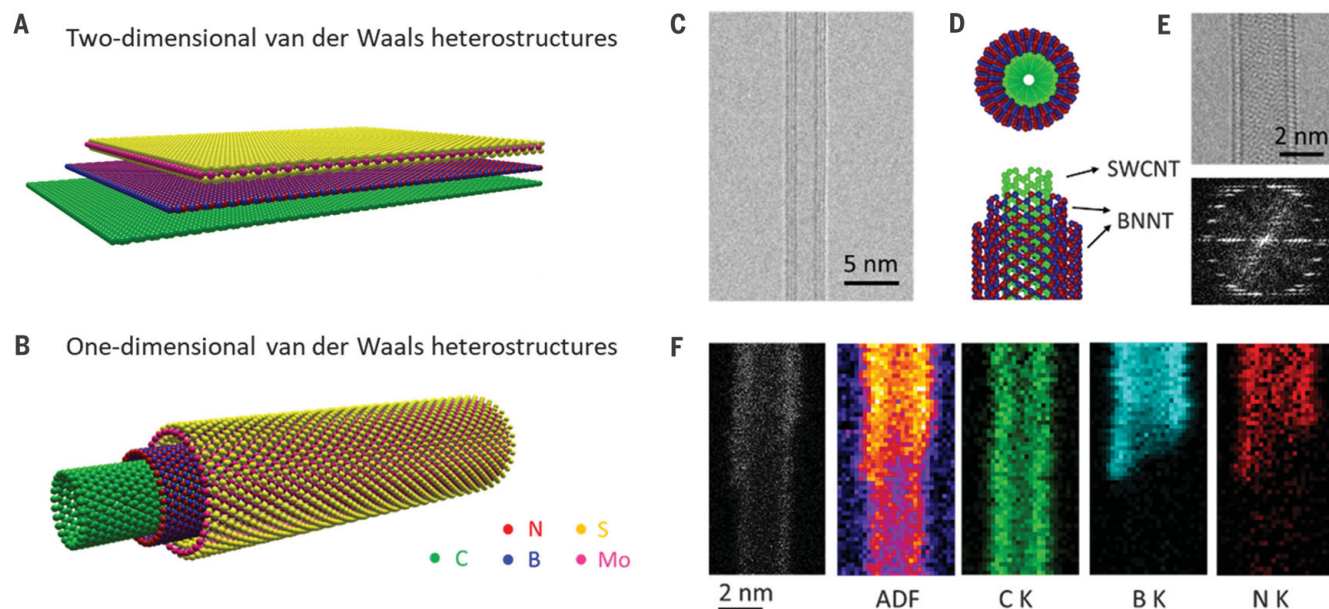


Fig. 1. Overview of 1D vdW heterostructures. (A and B) Atomic arrangement of two-dimensional planar vdW heterostructures (A) and one-dimensional coaxial vdW heterostructures (B). (C and D) TEM image (C) and structure models (D) of a SWCNT wrapped with two layers of BNNT. (E) Aberration-

corrected TEM image of a SWCNT-BNNT and its fast Fourier transform. (F) Annular dark-field (ADF) image and EELS mapping of a SWCNT partially wrapped with BNNT, showing that the inner layer is carbon and the outer layer is BN. C K, K₁ edge of C (green); B K, K₁ edge of B (cyan); N K, K₁ edge of N (red).

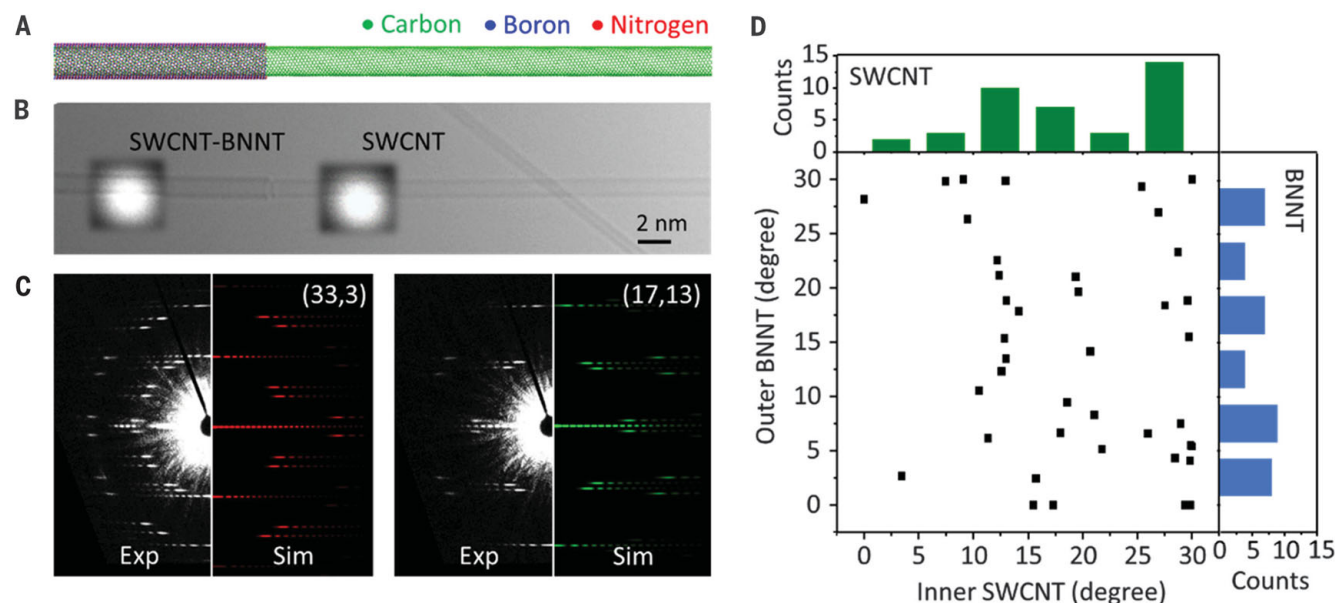


Fig. 2. Structural characterization of SWCNT-BNNT vdW heterostructures. (A and B) Atomic model (A) and TEM image (B) of SWCNT-BNNT atomic steps. (C) Experimental (Exp) and simulated (Sim) ED pattern of the inner (17, 13) SWCNT

and outer (33, 3) BNNT. (D) Plot of chiral angle of inner SWCNT versus the outer BNNT for double-walled SWCNT-BNNT, revealing that as-grown SWCNTs were enriched in the near-armchair form but that the outer BNNT was evenly distributed.

(Fig. 2, A and B). Our starting SWCNTs have an ultraclean surface and our CVD chamber is a clean, low-pressure system, which avoids any atomic impurities on the SWCNT surface or contamination from the chamber that could cause imperfection in the outer nanotube.

The atomic step in composition along the growing nanotube also allowed us to obtain nano-area ED patterns (20) of the pristine SWCNT and the same tube after BNNT growth, which allowed us to assign chirality of each layer. In Fig. 2C, the inside SWCNT is assigned as (17, 13) and the outside BNNT as (33, 3). In another case, a (34, 0) single-walled BNNT formed on the surface of a (16, 14) SWCNT

(fig. S6). Even without these atomic steps, the 2% difference between the lattice constants of SWCNT and BNNT (21) allows us to distinguish them in the ED patterns.

In a collection of 74 SWCNTs and 40 SWCNT-BNNT double-walled nanotubes (details shown in figs. S7 and S8 and table S1), a greater number of SWCNTs were in near-armchair form (Fig. 2D). This near-armchair enrichment was consistent with previous experimental and theoretical analyses (22, 23). However, the outer BNNTs were randomly distributed (with a slight preference for the zigzag conformation). No chiral angle dependence was observed in these SWCNT-BNNT heterostructures, so sym-

metry and lattice matching did not limit our ability to combine materials using our technique (24). This absence of correlation of inner and outer layers differed from what has been observed in CVD fabrication of 2D vdW heterostructures, where the growth layer is usually aligned with the base material. We attribute this difference to the symmetry breaking in 1D materials compared with that in their 2D counterparts.

Optical, thermal, and electronic characterization of SWCNT-BNNT heterostructure

Raman and photoluminescence (PL) spectra of the SWCNT-BNNT showed peaks typical

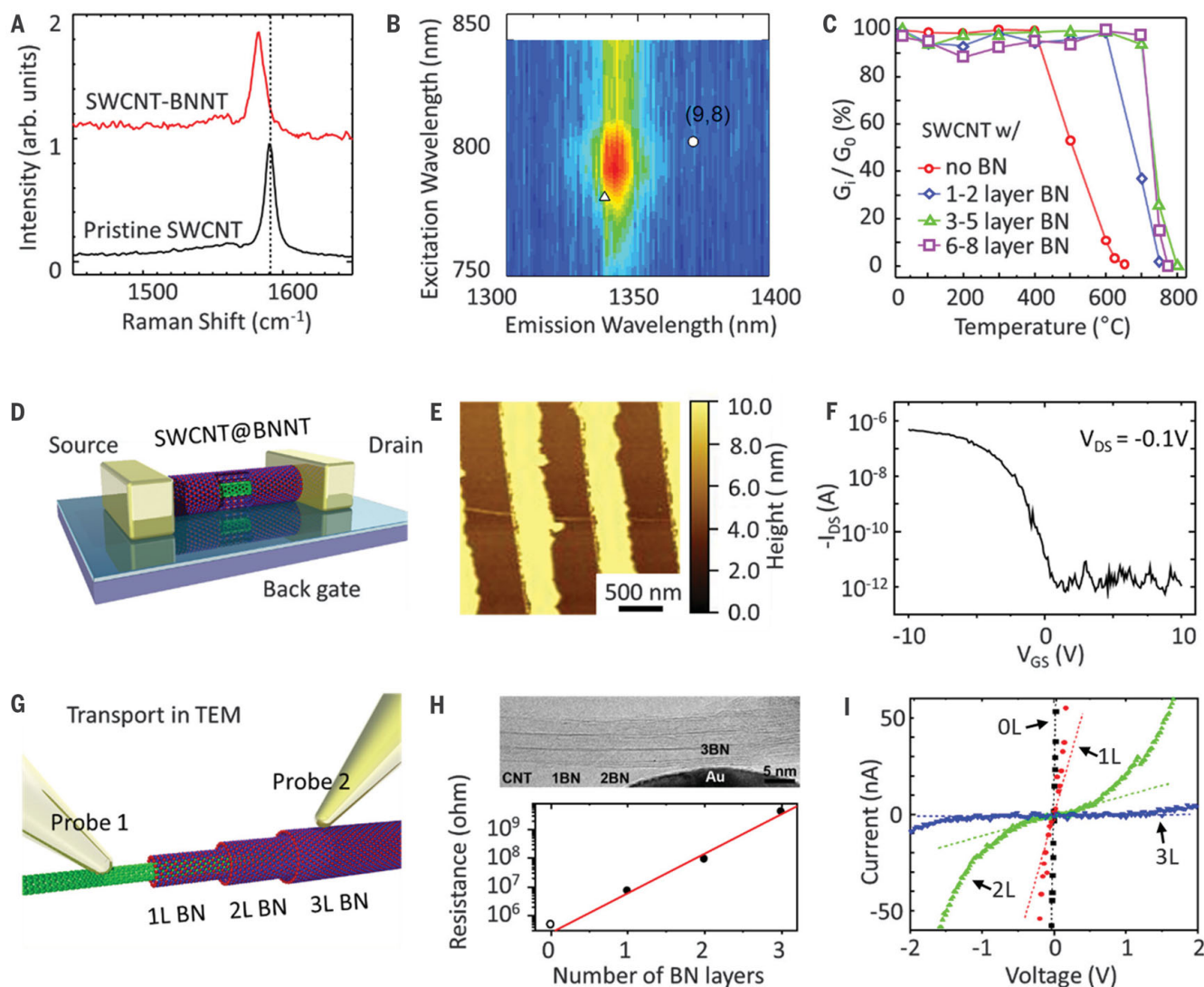


Fig. 3. Optical, thermal, and electronic characterization of SWCNT-BNNT heterostructures. (A) Typical G band of an individual SWCNT before and after BN coating. Arb. units, arbitrary units; dotted line indicates the original G band position at ~1590 cm⁻¹. (B) PL excitation-emission map of suspended (9, 8) SWCNT after BN CVD. Circle and triangle marks indicate the optical transition energy of suspended (9, 8) SWCNT in the ambient atmosphere (38, 39) and in vacuum (40). (C) Thermal stability of SWCNT and SWCNT-BNNT heterostructures obtained in an in situ

Raman reaction cell. The ratio of G-band intensity (G_i) after high-temperature burning to the original G-band intensity (G_0) before burning gives the relative loss of SWCNTs in these samples. (D to F) A schematic (D), AFM image (E), and characteristic transfer curve (F) of a back-gated FET built on a SWCNT-BNNT. I_{DS} , drain current; V_{GS} , gate voltage; V_{DS} , drain voltage. (G) Schematic of the transport measurement inside TEM. (H) Bright-field TEM image (upper) and resistance versus number of BN layers (lower). (I) Typical I - V curve obtained in electronic measurement inside TEM.

of pristine inner SWCNTs, which showed that their structural integrity was preserved (Fig. 3, A and B). However, a G band downshift of 5 to 10 cm^{-1} appeared in both isolated SWCNT-BNNT heterostructures and heterostructure networks. That downshift was a fingerprint for BNNT coating in our experiments. We tentatively attributed this downshift to the thermal strain between SWCNT and BNNT. The difference in thermal expansion during BN synthesis caused a slight distortion for SWCNTs along the tube axis. The outer BN layers acted as a protective coating and protected the inside of the SWCNTs against oxidation. Burning of the SWCNT inside BNNT started at 700°C in air, whereas naked SWCNTs burned at 400°C (Fig. 3C), as measured in a Raman cell. After annealing the heterostructure in oxygen, inside SWCNTs were removed, and clean and crystallized single-walled and few-walled BNNTs were obtained (fig. S9).

The BNNT coating did not change the intrinsic electronic transport of the inner SWCNT. We fabricated a back-gated field-effect transistor (FET) on an individual SWCNT-BNNT heterostructure (Fig. 3D). This SWCNT-BNNT was synthesized from a suspended SWCNT and then transferred onto a Si substrate. The SWCNT-BNNT FET showed performance similar to that of a SWCNT FET and had an on/off ratio of 10^5 (Fig. 3, E and F), which means that the high quality of the SWCNT was preserved. To further investigate the isolation and tunneling of outer BNNT layers, we measured the current through different BNNT layers in a TEM equipped with two probes (Fig. 3G). We distinguished the numbers of BNNT layers on SWCNTs directly from TEM and simultaneously mea-

sured the electron conduction at local positions separated by ~ 10 nm (Fig. 3, H and I). Current-voltage (I - V) curves—measured at the positions of the SWCNT-BNNT with zero, one, two, and three layers of BNNTs (Fig. 3I)—show the exponential increase of the zero-bias resistance with the layer number, indicative of direct tunneling through the insulating BN layers (Fig. 3H, bottom). This characteristic of tunnel current is similar to that of 2D BN layers exfoliated from bulk crystals (25, 26), and it was consistent with the layer quality being comparable to exfoliated crystals. The quality of these structures could allow for the experimental exploration of properties that have been theoretically predicted for 1D heterostructures, such as SWCNT-BNNT being a topological insulator if combined in a proper symmetry (12).

MoS₂-based binary and ternary heterostructures

MoS₂ 2D sheets have been studied intensively as the representative transition metal dichalcogenide material in recent years (27). Multiwalled MoS₂ nanotubes, with diameters usually >20 nm, and their hybrid materials are well known (28–30), but single-walled, single-crystal MoS₂ nanotubes have not been convincingly demonstrated in previous studies. Thus, we explored the growth of MoS₂ on SWCNTs. Figure 4, A to C, shows the atomic structure, TEM, and scanning TEM (STEM) images of SWCNT-MoS₂ coaxial nanotubes obtained after applying our growth strategy. The MoS₂ nanotube has much stronger image contrast than carbon in both TEM and STEM images (additional images and EELS mapping are shown in fig. S10). Single-walled MoS₂ nano-

tubes were predicted to have a direct band gap, in contrast to multiwalled nanotubes that have an indirect band gap (31), and to exhibit strong quantum confinement effects (32).

We observed a strong diameter dependence for the formation of single-walled MoS₂ nanotubes. Unlike BNNT wrapping, the yield of MoS₂ nanotubes was very low (less than 1%), and seamless wrapping was only observed on large-diameter (>3 nm) SWCNTs. We performed simulations of the strain energy of single-walled MoS₂ nanotubes with different diameters, D . A $1/D^2$ relation was obtained (Fig. 4D), which suggests that, in small diameter range, strain energy was much higher than for SWCNTs and BNNTs (31, 33, 34). This difference can be simply attributed to the thickness of a single layer of MoS₂, containing three atomic planes and becoming unstable when rolled into a tubular structure. This also explains why MoS₂ nanotubes were only seen previously as multiwalled or on multiwalled CNTs (14, 28). Thus, the minimum diameter of a single-walled MoS₂ nanotube should be much larger than that of SWCNTs. The MoS₂ nanotubes (fig. S10, C to F) have diameters ranging from 3.9 to 6.8 nm and formed only on SWCNTs with diameters of at least 3 nm. Because most of our starting SWCNTs were thinner than 3 nm, the yield of SWCNT-MoS₂ heterostructures was low.

Finally, we grew a ternary, SWCNT-BN-MoS₂ coaxial nanotube (Fig. 5, A to D). This 5-nm-diameter structure consisted of an inner SWCNT, a middle three layers of BNNT, and a single outer layer of MoS₂. The elemental information was visualized by EELS mapping (Fig. 5D). Typical ED patterns in Fig. 5E reveal diffractions from all three crystal layers, with MoS₂

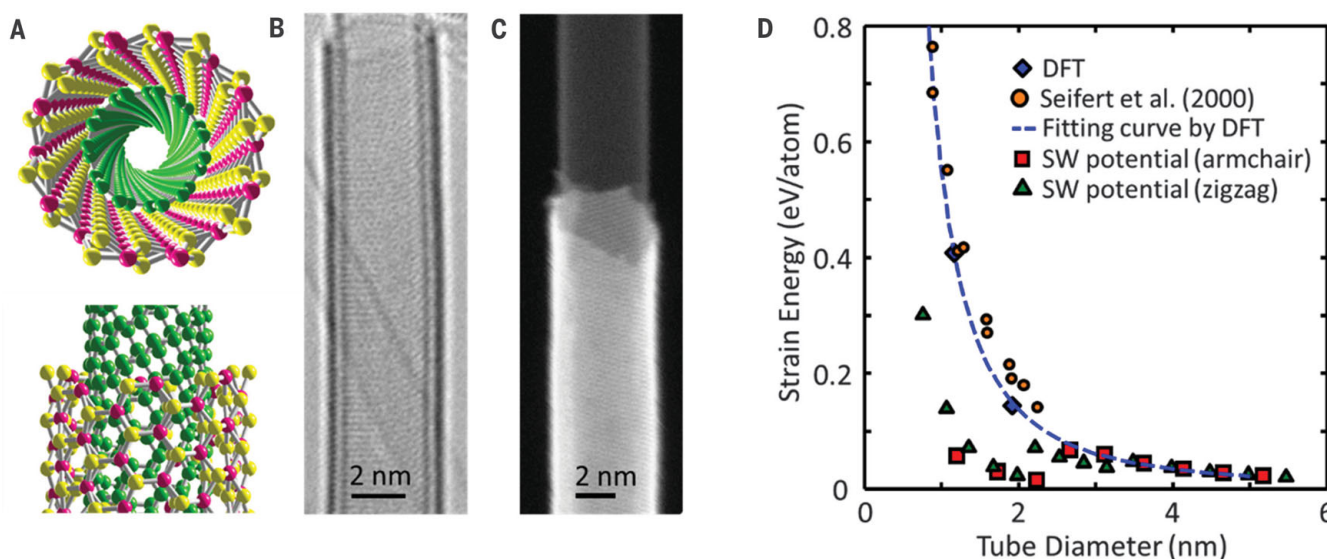


Fig. 4. SWCNT-MoS₂ 1D vdW heterostructure. (A to C) Atomic model (A), HRTEM image (B), and high-angle annular dark field (HAADF) STEM image (C) of a single-walled MoS₂ nanotube grown on a SWCNT. (D) Strain energy of a single-walled MoS₂ nanotube as a function of tube diameter, calculated by a modified Stillinger-Weber (SW) potential and density functional theory (DFT) simulation.

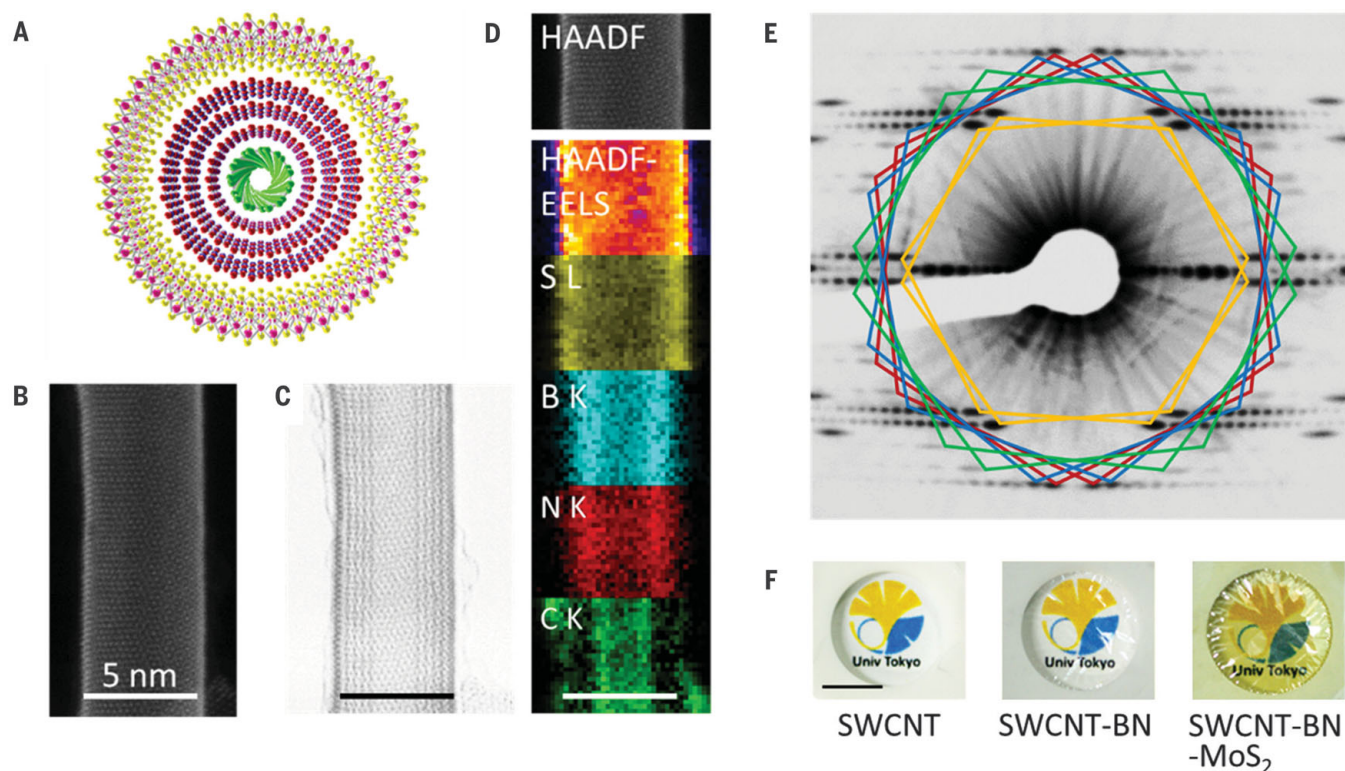


Fig. 5. SWCNT-BNNT-MoS₂ 1D vdW heterostructures. (A to D) Atomic model (A), HAADF-STEM image (B), annular bright field (ABF)-STEM image (C), and EELS mapping (D) of a 5-nm-diameter ternary 1D vdW heterostructure, consisting of one layer of carbon, three layers of BN, and one layer of MoS₂. Scale bars, 5 nm; S L, L_{2,3} edge of S (yellow). (E) An almost-ideal experimental

ED pattern of a SWCNT-BNNT-MoS₂ heterostructure, with different colors distinguishing the diffractions from different layers (L1 green, SWCNT; L2 blue, BNNT1; L3 red, BNNT2; and L4 yellow, MoS₂ nanotube). (F) Optical images of SWCNT, SWCNT-BNNT, and SWCNT-BNNT-MoS₂ films against a printed logo of the University of Tokyo. Scale bar, 10 mm.

having the strongest intensity and SWCNT and BNNT showing weaker but distinguishable contrast. The unidirectional distribution of the patterns also supports the coaxial feature. The four sets of hexagonal pairs with different colors indicate the orientation of atomic arrangement in the upper and lower surfaces to the electron beam.

Because the nanotube diameter increased from 2 to >3 nm after BNNT coating, the synthesis of an additional MoS₂ nanotube became much easier, and the yield of the SWCNT-BNNT-MoS₂ heterostructure reached ~10% after 20 min of MoS₂ CVD. A rough count of the yield of heterostructure versus CVD time is provided in fig. S11. The coating can be produced on the centimeter-length scale, and the difference can be observed between the original SWCNT, SWCNT-BNNT, and SWCNT-BNNT-MoS₂ films even with the naked eye (Fig. 5F). The optical absorption spectrum (fig. S12) of the sample revealed the photon absorption from three different layers.

We noticed that the innermost SWCNT and outermost MoS₂ in a SWCNT-BNNT-MoS₂ heterostructure are electronically coupled. This is supported by the different PL intensities of the SWCNT-BNNT-MoS₂ and BNNT-MoS₂ heterostructures. In the former case, PL of MoS₂ was

markedly quenched by the existence of SWCNT (fig. S13). In the latter case, however, PL of MoS₂ was 10 times as high. We calculated the band alignment of a graphene, BN, and MoS₂, and the Dirac point of graphene was found to be −4.26 eV, only 0.1 eV below the conduction band edge of MoS₂ (fig. S14). This calculation suggests that, if the starting SWCNT could be a small-diameter, semiconducting SWCNT, the SWCNT-BNNT-MoS₂ heterostructure is a type II junction. Interlayer excitons probably exist, even though electrons and holes are spatially separated by few layers of BNNT.

Discussion

We have extended the concept of vdW heterostructures to 1D materials. In these coaxial heteronanotubes, both cores and shells are single crystalline and form a seamless structure. We showed the controlled fabrication of SWCNT-BNNT and SWCNT-BNNT-MoS₂ coaxial structures with diameters <5 nm. We also developed some basic rules governing the fabrication of 1D heterostructures, including the absence of shell-shell epitaxial structure correlation and the requirement of a threshold diameter for MoS₂ nanotubes. This approach is likely extendable to other layered materials (35–37) and yields a large number of combinations, and

1D vdW heterostructures could host distinctive physics arising from curvature and diameter confinement.

REFERENCES AND NOTES

1. A. K. Geim, I. V. Grigorieva, *Nature* **499**, 419–425 (2013).
2. K. S. Novoselov, A. Mishchenko, A. Carvalho, A. H. Castro Neto, *Science* **353**, aac9439 (2016).
3. Y. Liu et al., *Nat. Rev. Mater.* **1**, 16042 (2016).
4. X. Hong et al., *Nat. Nanotechnol.* **9**, 682–686 (2014).
5. T. Georgiou et al., *Nat. Nanotechnol.* **8**, 100–103 (2013).
6. C. H. Lee et al., *Nat. Nanotechnol.* **9**, 676–681 (2014).
7. B. Hunt et al., *Science* **340**, 1427–1430 (2013).
8. F. Withers et al., *Nat. Mater.* **14**, 301–306 (2015).
9. K. Kang et al., *Nature* **550**, 229–233 (2017).
10. W. Yang et al., *Nat. Mater.* **12**, 792–797 (2013).
11. A. Sengupta, *J. Mater. Sci.* **52**, 8119–8131 (2017).
12. C. Hu, V. Michaud-Roux, W. Yao, H. Guo, *Nano Lett.* **19**, 4146–4150 (2019).
13. L. L. Chen, H. H. Ye, Y. Gogotsi, *J. Am. Ceram. Soc.* **87**, 147–151 (2004).
14. W. K. Hsu et al., *Appl. Phys. Lett.* **77**, 4130–4132 (2000).
15. S. Iijima, T. Ichihashi, *Nature* **363**, 603–605 (1993).
16. A. G. Nasibulin et al., *ACS Nano* **5**, 3214–3221 (2011).
17. R. Nakanishi et al., *Sci. Rep.* **3**, 1385 (2013).
18. R. Arenal, A. Lopez-Bezanilla, *ACS Nano* **8**, 8419–8425 (2014).
19. Y. Yao, C. Feng, J. Zhang, Z. Liu, *Nano Lett.* **9**, 1673–1677 (2009).
20. J. M. Zuo et al., *Microsc. Res. Tech.* **64**, 347–355 (2004).
21. C. R. Dean et al., *Nat. Nanotechnol.* **5**, 722–726 (2010).
22. F. Ding, A. R. Harutyunyan, B. I. Yakobson, *Proc. Natl. Acad. Sci. U.S.A.* **106**, 2506–2509 (2009).
23. Y. Magnin, H. Amara, F. Ducastelle, A. Loiseau, C. Bichara, *Science* **362**, 212–215 (2018).
24. A. Koma, *Thin Solid Films* **216**, 72–76 (1992).

25. G. H. Lee *et al.*, *Appl. Phys. Lett.* **99**, 243114 (2011).
26. L. Britnell *et al.*, *Nano Lett.* **12**, 1707–1710 (2012).
27. A. Splendiani *et al.*, *Nano Lett.* **10**, 1271–1275 (2010).
28. Y. Wang *et al.*, *Adv. Mater.* **28**, 10175–10181 (2016).
29. Y. Feldman, E. Wasserman, D. J. Srolovitz, R. Tenne, *Science* **267**, 222–225 (1995).
30. R. Tenne, *Nat. Nanotechnol.* **1**, 103–111 (2006).
31. G. Seifert, H. Terrones, M. Terrones, G. Jungnickel, T. Frauenheim, *Phys. Rev. Lett.* **85**, 146–149 (2000).
32. M. Ghorbani-Asl *et al.*, *Sci. Rep.* **3**, 2961 (2013).
33. D. B. Zhang, T. Dumitrică, G. Seifert, *Phys. Rev. Lett.* **104**, 065502 (2010).
34. E. Hernández, C. Goze, P. Bernier, A. Rubio, *Phys. Rev. Lett.* **80**, 4502–4505 (1998).
35. J. Zhou *et al.*, *Nature* **556**, 355–359 (2018).
36. L. Li *et al.*, *Nat. Nanotechnol.* **9**, 372–377 (2014).
37. L. Tao *et al.*, *Nat. Nanotechnol.* **10**, 227–231 (2015).
38. J. Lefebvre, P. Finnie, *Phys. Rev. Lett.* **98**, 167406 (2007).
39. K. Liu *et al.*, *Nat. Nanotechnol.* **7**, 325–329 (2012).
40. S. Chiashi, S. Watanabe, T. Hanashima, Y. Homma, *Nano Lett.* **8**, 3097–3101 (2008).

ACKNOWLEDGMENTS

We thank Y. Kato and K. Otsuka for the helpful discussion.

Funding: Part of this work is financially supported by JSPS KAKENHI grant nos. JP25107002, JP15H05760, JP15K17984, JP19K05223, JP16H06333, JP17K14601, JP18H05329, and

JP19H02543; IRENA Project by JST-EC DG RTD; Strategic International Collaborative Research Program, SICORP; JSPS-NSFC scientific cooperation program; and by the “Nanotechnology Platform” (project no. 12024046) of the Ministry of Education, Culture, Sports, Science and Technology (MEXT), Japan. This research also received funding from projects 286546 (DEMEC), 292600 (SUPER), and 316572 (CNTstress), supported by the Academy of Finland, as well as projects 3303/31/2015 (CNT-PV) and 1882/31/2016 (FEDOC), supported by TEKES/Business Finland. Y.Q. is supported by JSPS DC fellowship (JP19J12932). D.T. acknowledges the support from the World Premier International (WPI) Center for Materials Nanoarchitectonics (MANA) and the TEM station of the National Institute for Materials Science (NIMS). **Author contributions:** R.X., T.I., and S.M. conceived and designed the experiments. E.I.K. and A.A. synthesized the SWCNT film. T.I., Y.Z., and M.L. performed the BN CVD. Y.Q. performed the CVD growth of MoS₂ nanotubes using powder precursors. Y.M. and Y.K. performed the MOCVD growth of MoS₂ nanotubes. R.X. took the HRTEM images of heterostructures. A.K. took the EELS mapping of SWCNT-BN. Y.S. took the aberration-corrected HRTEM image of SWCNT-BN, STEM image, and EELS mapping of SWCNT-MoS₂. A.K. and R.X. took the STEM image and EELS mapping of the SWCNT-BN-MoS₂ heterostructure. R.X. took the ED patterns of the SWCNT-BNNT. R.X. and D.G. assigned the chirality of SWCNT-BN. D.G. analyzed the chiral angle distribution. A.K. simulated the ED pattern. R.X. took and analyzed the ED patterns of the SWCNT-BNNT-MoS₂ nanotubes. Y.Z. and R.X. counted the yield

of SWCNT-BNNT and SWCNT-MoS₂. T.I. fabricated the FET device and measured the transfer curve. D.T. measured the electrical conduction of SWCNT-BNNT inside TEM. H.A. synthesized the suspended SWCNTs. S.Y. and T.O. measured the PL emission. J.G. studied the thermal stability of SWCNT-BNNT. T.I. measured and analyzed the XPS. M.L. burned SWCNT out of BNNT and measured the PL spectra of MoS₂-based heterostructures. Y.Z. and R.X. measured the cathodoluminescence. R.X. built the atomic structure of heterostructures. K.H. performed the molecular dynamics and DFT calculation of structure stability. M.M. and S.O. performed the DFT calculation of band alignment. R.X. wrote the manuscript. All authors joined the discussion and commented on the manuscript. **Competing interests:** None declared. **Data and materials availability:** All data needed to evaluate the conclusions in the paper are present in the paper or the supplementary materials.

SUPPLEMENTARY MATERIALS

science.sciencemag.org/content/367/6477/537/suppl/DC1
Materials and Methods

Figs. S1 to S15

Table S1

References (41–52)

Movie S1

26 August 2019; accepted 10 December 2019
10.1126/science.aaz2570

CATALYSIS

Highly active cationic cobalt(II) hydroformylation catalysts

Drew M. Hood¹, Ryan A. Johnson¹, Alex E. Carpenter², Jarod M. Younker², David J. Vinyard³, George G. Stanley^{1*}

The cobalt complexes $\text{HCo}(\text{CO})_4$ and $\text{HCo}(\text{CO})_3(\text{PR}_3)$ were the original industrial catalysts used for the hydroformylation of alkenes through reaction with hydrogen and carbon monoxide to produce aldehydes. More recent and expensive rhodium-phosphine catalysts are hundreds of times more active and operate under considerably lower pressures. Cationic cobalt(II) bisphosphine hydrido-carbonyl catalysts that are far more active than traditional neutral cobalt(I) catalysts and approach rhodium catalysts in activity are reported here. These catalysts have low linear-to-branched (L:B) regioselectivity for simple linear alkenes. However, owing to their high alkene isomerization activity and increased steric effects due to the bisphosphine ligand, they have high L:B selectivities for internal alkenes with alkyl branches. These catalysts exhibit long lifetimes and substantial resistance to degradation reactions.

Hydroformylation, or the oxo reaction, is one of the highest-volume homogeneously catalyzed industrial processes today, converting alkenes, H_2 , and CO into aldehydes (and related products) at a rate of more than 10 million metric tons per year (1). The four most common industrial catalyst technologies are summarized in Table 1 (1–3), along with the cationic Co(II) bisphosphine system reported here. Although these major industrial catalyst systems exhibit distinctive strengths and perform optimally under specific conditions, a long-standing challenge has been to access the feed tolerance and robustness of so-called high-pressure systems [i.e., $\text{HCo}(\text{CO})_4$] under mild conditions with base metals.

The first hydroformylation catalyst, cobalt complex $\text{HCo}(\text{CO})_4$, was accidentally discovered by Otto Roelen in 1938; its currently accepted mechanism was proposed by Heck and Breslow in 1960 (4, 5). The $\text{HCo}(\text{CO})_4$ -catalyzed process is commonly referred to as the high-pressure system because CO partial pressure must be increased drastically as the temperature rises in order to inhibit decomposition of the catalyst to cobalt metal (6).

The phosphine-modified cobalt catalyst system, $\text{HCo}(\text{CO})_3(\text{PR}_3)$, was discovered and commercialized by Slauch and Mullineaux in the 1960s (7, 8). The electron-donating alkylated phosphine improves catalyst stability by increasing π -backbonding to the carbonyl ligands, which stabilizes the catalyst relative to $\text{HCo}(\text{CO})_4$, allowing it to be run at lower pressures. The stronger Co–CO bonding, however, substantially slows the catalyst, necessitating higher operating temperatures and unusually high

catalyst concentrations (Table 1). The donating phosphine ligand increases the hydrogenation activity of the catalyst for aldehyde-to-alcohol (desired) and alkene-to-alkane (undesired) conversion.

In the early 1970s, rhodium catalysts were discovered to be hundreds of times more active than cobalt for the hydroformylation of linear 1-alkenes (9, 10). However, these systems perform comparatively poorly with branched or otherwise complex olefin streams. Although $\text{HRh}(\text{CO})_4$ is the most active hydroformylation catalyst known, as well as an active alkene isomerization catalyst, it readily forms inactive Rh-carbonyl clusters (1, 11) and requires very high operating pressures. The industry standard for low-pressure hydroformylation is $\text{HRh}(\text{CO})(\text{PPh}_3)_2$ (1, 12). However, facile dissociation of the PPh_3 ligand requires excess PPh_3 (e.g., 0.4 to 1.6 M PPh_3 with 1 mM Rh catalyst) to maintain the most regioselective, albeit lower-activity, bisphosphine catalyst. The high cost and low abundance of rhodium requires low-loss catalyst recycling technologies (1, 6, 12).

Our laboratory previously reported a highly active and selective dicationic dirhodium hydroformylation catalyst bearing a tetraphosphine ligand, $(\text{Et}_2\text{PCH}_2\text{CH}_2)(\text{Ph})\text{PCH}_2\text{P}(\text{Ph})\text{CH}_2\text{CH}_2\text{PEt}_2$, that bridges and chelates the two rhodium centers (13, 14). The chiral diastereomer (used as a racemic mixture) of this catalyst showed high activity and selectivity for the hydroformylation of 1-hexene, while the meso diastereomer was a very poor catalyst. The activity of the chiral diastereomer is a function of bimetallic cooperativity, which is blocked for the meso diastereomer. The localized cationic charges on the metal centers play an important role to compensate for the electron-donating alkylated phosphine ligands that produce poor monometallic rhodium hydroformylation catalysts. Unfortunately, the dicationic dirhodium catalyst suffers from degradation pathways that

lead to catalyst deactivation. A tetraphosphine ligand with a far stronger chelate effect was synthesized, and studies with model nickel complexes using both ligand diastereomers demonstrated the enhanced stability toward phosphine ligand dissociation (15).

The strong chelate effect of this newly synthesized tetraphosphine ligand prompted us to prepare and study a dicationic dicobalt(II) catalyst precursor, $[\text{Co}_2(\text{acac})_2(\text{P4-phenylene})](\text{BF}_4)_2$ [acac, acetoacetate; P4-phenylene, $(\text{Et}_2\text{P})(1,2\text{-C}_6\text{H}_4)\text{P}(\text{Ph})\text{CH}_2\text{P}(\text{Ph})(1,2\text{-C}_6\text{H}_4)(\text{PEt}_2)$], for hydroformylation activity (Fig. 1). This system proved to be quite active for hydroformylation, but both the chiral and meso diastereomers exhibited similar activity and selectivity (supplementary materials, table S1). This observation indicated that the dicobalt catalyst was functioning as two independent monometallic catalysts, because from the dirhodium catalysis only the chiral diastereomer can effectively promote bimetallic cooperativity. This prompted the study of much simpler monometallic cationic Co(II) bisphosphine precursors.

A class of cationic monometallic cobalt catalysts

The monometallic catalyst precursor, $[\text{Co}(\text{acac})(\text{DPPBz})](\text{BF}_4)$ (Fig. 1), proved to be even more active than the dicobalt complexes for hydroformylation under exceptionally mild conditions for cobalt. Table 2 shows the role of temperature and pressure for the hydroformylation of 1-hexene using $[\text{Co}(\text{acac})(\text{DPPBz})](\text{BF}_4)$ as the catalyst precursor (average of three catalytic runs). Activity increased with temperature up to 170°C at 50 bar of 1:1 H_2 :CO, at which point catalyst decomposition commenced. This cationic Co(II) catalyst showed high alkene isomerization activity, similar to Co(I) systems. The low linear-to-branched (L:B) selectivity observed for the aldehyde products demonstrates that the cationic cobalt catalyst can coordinate internal alkenes formed through isomerization and hydroformylate them (full analysis of the branched aldehyde and alkene products is given in table S2). The highest alkene isomerization activity occurred at relatively high temperatures and low pressures (160°C and 30 bar), which is consistent with most hydroformylation catalysts (1, 6, 12). Hydrogenation of aldehyde product to alcohol was occasionally observed despite using a 1:1 H_2 :CO gas ratio that does not favor hydrogenation. Alcohol production was more prevalent with the more electron-donating bisphosphine ligands at higher temperatures (e.g., 160°C) in the 30- to 60-bar pressure regime once the aldehyde concentration built up (tables S1 and S6). Hydrogenation of alkene to alkane was usually <3%.

The observed CO pressure effect (Table 2) appears notable. As the H_2 :CO pressure increased, the catalyst activity also increased. The initial turnover frequency (TOF) for the

¹Department of Chemistry, Louisiana State University, Baton Rouge, LA 70803, USA. ²ExxonMobil Chemical Company, Baytown, TX 77520, USA. ³Department of Biological Sciences, Louisiana State University, Baton Rouge, LA 70803, USA.

*Corresponding author. Email: gstanley@lsu.edu

cobalt-DPPBz-based catalyst essentially doubled from 52.5 min⁻¹ (30 bar) to 103.2 min⁻¹ (90 bar). Hydroformylation catalysts generally exhibit a negative [CO] order rate dependence (e.g., -0.6 to -1) beyond a critical CO pressure (1, 6, 12) owing to the inhibition noted above.

However, preliminary kinetic data using 3,3-dimethylbutene as an alkene that cannot be isomerized showed that reaction rates are first order in cobalt catalyst and alkene, approximately +0.6 in H₂, and -1 in CO (table S3). The drastic increase in TOF with increasing H₂:CO pressure for 1-hexene shown in Table 2 is due to the lower alkene isomerization reaction at higher pressures, which increases the amount of the most-active 1-alkene present relative to the considerably less reactive internal alkenes formed from alkene isomerization.

Electron-rich bisphosphine ligands lead to more active cationic Co(II) hydroformylation catalysts at lower to medium H₂:CO pressures (table S4). The most electron-rich Et₂PCH₂CH₂PEt₂ (depe) ligand generates a catalyst that is 46% more active compared with the DPPBz system at 51.7 bar and 140°C (table S4). This is very unusual, as electron-donating phosphines, especially chelating bisphosphines, are well known to substantially lower the activity of both rhodium and cobalt monometallic hydroformylation catalysts. The more electron-donating phosphine-based Co(II) catalysts do show a stronger CO inhibitor effect at higher pressures. The (Et₂P)₂-1,2-C₆H₄ (DEPBz) ligand-based cationic cobalt catalyst, for example, has an initial TOF of 61.5 min⁻¹ at 50 bar and 140°C, but that rate

slows to 36.7 min⁻¹ at 70 bar and 21.7 min⁻¹ at 90 bar (table S5).

High activity at low pressure

The higher activity of the more electron-rich cationic Co(II) bisphosphine catalysts allows operation at the low pressures typical of rhodium catalysis. Using [Co(acac)(depe)](BF₄) under our standard conditions (1 mM catalyst, 1 M 1-hexene, dimethoxytetraglyme solvent), the catalyst was activated at 140°C under 34 bar of 1:1 H₂:CO for 5 min. The autoclave temperature and pressure were then reduced to 100°C and 10 bar, followed by pressure injection of 1-hexene to initiate catalysis. Sixty-eight turnovers (TOs) to aldehyde [gas chromatography-mass spectrometry (GC-MS) analysis] were observed after 1 hour and 619 TOs after 29 hours, with a

Table 1. Comparison of industrial hydroformylation catalysts and the cationic Co(II) bisphosphine system. TOF, turnover frequency; L:B, product linear-to-branched ratio.

Properties	Unmodified Co(I)	Phosphine-modified Co(I)	Unmodified Rh(I)	Phosphine-modified Rh(I)	Cationic Co(II) bisphosphine
Catalyst	HCo(CO) ₄	HCo(CO) ₃ (PR ₃)	HRh(CO) ₄	HRh(CO)(PPh ₃) ₂	[HCo(CO) _n (P ₂)] ⁺
Typical alkene feed	Branched and/or internal olefins	Linear alkenes (α or internal)	Branched and/or internal olefins	Shorter-chain α-olefins and specialty substrates	Branched and/or internal olefins
Temperature (°C)	140–200	180–200	100–150	80–130	100–160
Pressure (bar)	100–300	50–150	100–300	8–20	10–50
Ligand:metal ratio	—	2:1	—	400–1600:1	1:1
Ligand type	—	Alkyl phosphine	—	PPh ₃ (most common)	Diphosphine
Catalyst loading (ppm metal)	500–1500	1000–2500	1–10	10–250	60–600
H ₂ :CO ratio	1:1	2:1	1:1	12:1	1:1
Typical TOF (min ⁻¹) for α-olefins	5–20	0.2–0.5	>150	40–600	10–60
L:B (n:iso)	1–4:1	8–10:1	1–2:1	10–20:1	1–2:1
Alkene isomerization	High	Moderate	Low to moderate	Low	High
By-product formation	High (up to 30% alcohols, paraffin, acetals, etc.)	20–30% paraffin	Low	Very low	Low

Table 2. Temperature- and pressure-dependent studies for the hydroformylation of 1-hexene with [Co(acac)(DPPBz)](BF₄). DPPBz, (Ph₂P)₂-1,2-C₆H₄. Catalysis conditions: 1 mM catalyst (61 ppm Co), 1 M 1-hexene, 0.1 M heptane standard, dimethoxytetraglyme solvent, 1:1 H₂:CO, 1000 revolutions per minute stirring under constant pressure. TOF based on a sample taken at 2 min. Other results based on sampling after 1 hour.

Temperature (°C)	Pressure (bar)	Initial TOF (min ⁻¹)	Aldehyde (%)	Aldehyde L:B	Alkane (%)	Isomerization (%)
120*	50	26.5	59.4	1.7	0	7.6
140*	50	43.6	71.3	1.3	0.3	17.9
160	50	66.0	76.8	1.1	1.4	18.9
Pressure (bar)	Temperature (°C)	Initial TOF (min ⁻¹)	Aldehyde (%)	Aldehyde L:B	Alkane (%)	Isomerization (%)
30†	160	52.5	49.0	0.94	1.4	45.7
50	160	66.0	76.8	1.1	1.4	18.9
70	160	94.8	84.0	1.3	1.2	12.1
90	160	103.2	87.3	1.4	1.0	9.1

*The reaction mixture was heated to 160°C for 5 min to activate the catalyst, then cooled to operating temperature before alkene injection.

†Some catalyst decomposition was noted by black cobalt metal deposition.

L:B aldehyde ratio of 0.8, no detectable alkane or alcohol production, and 15.1% alkene isomerization. The cationic Co(II) bisphosphine catalyst is far faster than the recently reported $\text{H}_2\text{Fe}(\text{CO})_2(\text{PPh}_3)_2$ catalyst, which underwent only 95 TOs with 1-octene over 24 hours at 100°C and 20 bar with 2:1 L:B aldehyde regioselectivity (16).

Direct rate comparisons between the cationic cobalt(II) bisphosphine catalysts reported here and industrial cobalt systems are difficult because of the higher pressure or temperature conditions used in industry and differences in catalyst stability. The high-pressure $\text{HCo}(\text{CO})_4$ catalyst, for example, decomposes to cobalt metal under the medium-pressure conditions reported in Table 1 (table S6). The phosphine-modified $\text{HCo}(\text{PR}_3)(\text{CO})_3$ catalyst is run industrially at higher temperatures and rather high catalyst and phosphine ligand concentrations relative to our 1 mM [61 parts per million (ppm) Co] catalyst conditions. After 10 minutes, catalytic runs using 1-hexene with a model Co(I) catalyst using PBu_3 under industrial conditions [2400 ppm Co, 75% 1-hexene, 25% tetrahydrofuran (THF), 200°C, 69 bar, 2:1 H_2 :CO] produced 13 TOs to aldehyde (6.4:1 L:B), 41 TOs to alcohol, 35.9% alkene isomerization, and 3.7%

hydrogenation of alkene to alkane. Therefore, the cationic cobalt DPPBz catalyst is at least 30 to 60 times faster than typical phosphine-modified neutral Co(I) catalyst systems.

Table 3 shows hydroformylation results using 3,3-dimethylbutene as the alkene substrate with four different cationic cobalt(II) bisphosphine catalysts and two rhodium-based catalysts using triphenylphosphine (PPh_3) and the bulky, chelating bisphosphite ligand biphenphos (Fig. 1). The Rh-biphenphos-type catalyst is one of the most active and selective hydroformylation catalysts but suffers from facile phosphite degradation reactions that lead to shorter catalyst lifetimes (1, 17–19). We chose 3,3-dimethylbutene as the substrate for these studies to allow a direct comparison of the intrinsic hydroformylation reaction rates between the cationic cobalt bisphosphine and rhodium-based catalysts. The cobalt catalysts are very active at alkene isomerization, which competes with hydroformylation and produces internal alkenes that hydroformylate more slowly. Because of its tertiary carbon center, 3,3-dimethylbutene is not susceptible to alkene isomerization, thus allowing a direct comparison for the hydroformylation activity of these catalysts.

The data in Table 3 demonstrate that the more active cationic cobalt catalysts based on the stronger σ -donating ethyl-substituted bisphosphine ligands (depe and DEPBz) (Fig. 1) are within a factor of 10 of the rhodium catalysts on the basis of the observed rate constant k_{obs} . The reactions with cobalt catalysts were run at a higher temperature and pressure, with the higher temperature probably having more influence on the rate. Therefore, the cobalt catalyst rates are within a factor of ~20 of these rhodium catalysts, although rhodium is >4000 times more expensive than cobalt on a molar basis (20). The increased activity of the cationic Co(II) bisphosphine catalyst system with more electron-donating alkylated phosphines, once again, is very unusual, as both Co(I) and especially Rh(I) hydroformylation catalysts are drastically slowed by electron-donating phosphine ligands owing to stronger metal-carbonyl π -backbonding.

The utility of this cationic cobalt(II) catalyst system is most evident with respect to internal, branched alkenes that are more challenging to hydroformylate (21). The hydroformylation of internal and internal branched alkenes makes up ~20% of the commercial marketplace, using mainly the high-pressure $\text{HCo}(\text{CO})_4$ and $\text{HRh}(\text{CO})_4$ catalyst systems. Table 4 shows the results after 6 hours for three internal branched alkenes using $\text{HCo}(\text{CO})_4$, $[\text{HCo}(\text{CO})_x(\text{depe})](\text{BF}_4)^-$, Rh: PPh_3 (1:400), and Rh:biphenphos (1:3) catalysts. As might be expected, $\text{HCo}(\text{CO})_4$ has the highest activity for these sterically hindered alkenes, which is why it is used in industry along with the high-pressure $\text{HRh}(\text{CO})_4$ catalyst system. Note, however, that $\text{HCo}(\text{CO})_4$ is running at 90 bar and would slowly decompose to cobalt metal at lower pressures. The $[\text{Co}:\text{depe}]^+$ cationic catalyst is almost as active as $\text{HCo}(\text{CO})_4$ but is operating at a pressure of only 30 bar and would run substantially faster at higher pressures and temperatures (Table 1). The cationic Co(II) catalyst system, like the $\text{HCo}(\text{CO})_4$ system, is selective toward the more valuable linear aldehyde products.

Phosphine-modified rhodium hydroformylation catalysts perform poorly with internal branched alkenes, as seen in Table 4. Neither Rh: PPh_3 nor the highly active rhodium-bisphosphite catalyst systems can hydroformylate 2,3-dimethyl-2-butene (tetramethylethylene), and Rh:biphenphos barely works with 4,4-dimethyl-2-pentene, with only 0.8% conversion after 6 hours. Rh:biphenphos can hydroformylate 4-methyl-2-pentene with excellent selectivity (28:1 L:B), but it completely decomposed and stopped hydroformylating 3 hours into the run. Rh: PPh_3 converted more 4-methyl-2-pentene relative to $[\text{Co}:\text{depe}]^+$, 62.0 versus 54.7% conversion to aldehyde, but with low L:B selectivity (0.4:1 versus 4.4:1).

Stability is a key criterion for judging the overall quality of a catalyst system. For example,

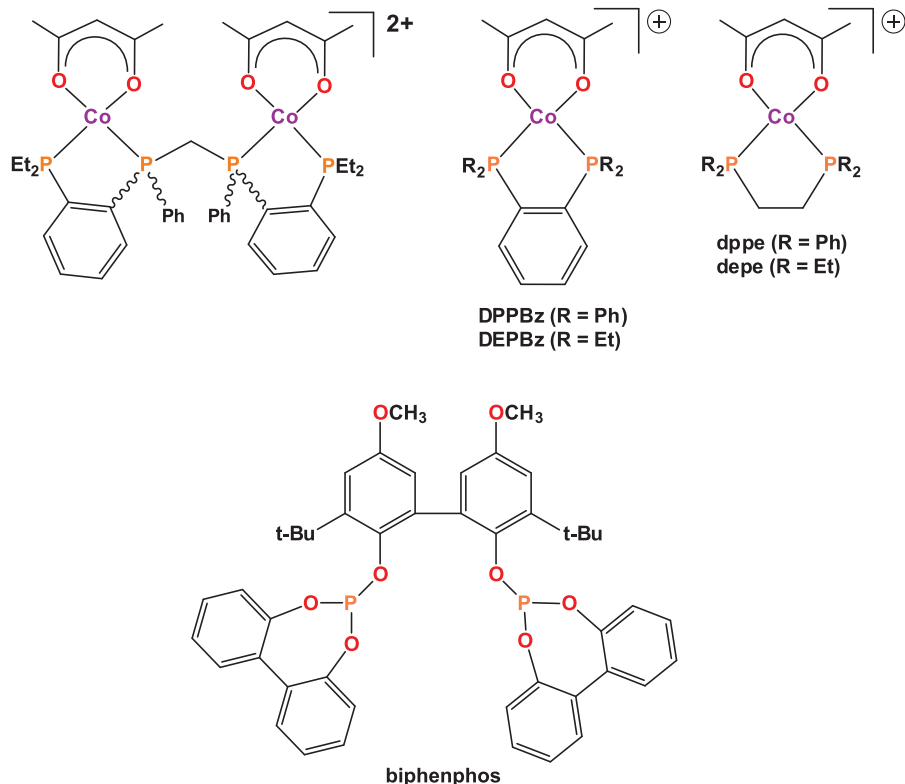


Fig. 1. Structures of the cobalt catalyst precursors and biphenphos ligand in this study. (Top, left to right) $[\text{Co}_2(\text{acac})_2(\text{P4-phenylene})]^{2+}$, $[\text{Co}(\text{acac})(\text{R}_2\text{P-1,2-C}_6\text{H}_4)]^+$, and $[\text{Co}(\text{acac})(\text{R}_2\text{PCH}_2\text{CH}_2\text{PR}_2)]^+$ (R = Et or Ph). BF_4^- counteranions are present for each complex. Bisphosphine ligand abbreviations are shown. The biphenphos ligand (bottom) was used for the rhodium catalyst comparison. Et, ethyl; Ph, phenyl; t-Bu, *tert*-butyl.

Rh:PPh₃ catalyst systems operate with a large excess of PPh₃ to minimize Rh-induced phosphine fragmentation reactions that lead to catalyst deactivation (22, 23). Unsaturated rhodium centers are quite active for phosphine P-phenyl, P-benzyl, or P-OR group oxidative addition reactions that initiate several possible catalyst decomposition pathways.

The cationic cobalt bisphosphine catalysts reported here, however, show prolonged stability at moderate temperatures (140° to 160°C) and pressures (50 bar). Unlike for all other known phosphine-modified cobalt and rhodium catalysts, it is not necessary to add excess phosphine ligand to stabilize this cationic cobalt(II) catalyst system. The bisphosphines based on the 1,2-phenylene chelate (DPPBz

and DEPBz) are powerful chelates and appear to generate the most-robust cationic cobalt(II) catalysts.

Three extended high-TO number hydroformylation runs were used to demonstrate the stability of the cationic cobalt(II) catalyst in a batch autoclave environment using very low catalyst loadings (table S10). The longest and highest TO run used 3 μM (0.24 ppm Co) [Co(acac)(DPPBz)](BF₄) and 6 M 1-hexene (45.45 g, 68 ml, 2 million equivalents) in 18 ml of dimethoxytetraglyme solvent. The reaction was run at 160°C under 50 bar of 1:1 H₂:CO for 14 days (336 hours). During this time, 1.2 million TOs to aldehyde product were performed with an average TOF of 59.5 min⁻¹. The product distribution at the end was 2% 1-hexene, 1.2%

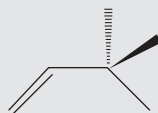
alkane, 40.8% isohexenes, 33.4% aldehyde (of which >50% was 2-methylhexanal), 1.1% alcohol, and 21.5% condensed aldehydes (mostly dimers, with some trimers). The catalyst was still operating after 336 hours, and the rate of hydroformylation at this point (55 TOs/min, GC-MS analysis) indicated excellent catalyst stability. With the exception of passing the 1-hexene through a short alumina column to remove peroxide impurities, no special purifications of the solvent, catalyst, or reaction gases were undertaken.

Evidence for a 19e⁻ intermediate

In situ Fourier-transform infrared (FTIR) studies using a Mettler Toledo ReactIR system with a high-pressure cell and a SiComp

Table 3. Hydroformylation of 3,3-dimethylbutene by cobalt and rhodium catalysts. All reactions were run with 1.0 M 3,3-dimethylbutene, 1.0 mM catalyst, 0.1 M heptane as internal standard, and 1:1 H₂:CO. Results are based on three runs with standard deviations given in parentheses; cobalt catalysts were run for 2 hours, and the rhodium catalysts were run for 20 min. The k_{obs} values were determined by gas consumption analysis under constant

pressure conditions. Cobalt precatalysts were introduced as the BF₄ salts in dimethoxytetraglyme solvent and activated at 160°C for 5 min, then cooled to operating temperature before the alkene was injected. Rh(acac)(CO)₂ was used as the catalyst precursor and run in toluene with the following excess phosphine:Rh ratios: 3:1 for the chelating biphenphos ligand and 400:1 for PPh₃:Rh. No excess phosphine was used for the cobalt runs.



Catalyst	Temperature (°C)	Pressure (bar)	Time (min)	Aldehyde (%)	Aldehyde L:B	Alkane (%)	$k_{\text{obs}} \times 10^{-4} \text{ (M s}^{-1}\text{)}$
[Co:DPPBz] ⁺	140	30	120	60.0 (3.8)	58	0.8 (0.02)	1.4 (2)
[Co:dppe] ⁺	140	30	120	64.1 (3.5)	57	1.0 (0.1)	1.5 (1)
[Co:depe] ⁺	140	30	120	77.1 (1.0)	54	1.2 (0.05)	2.1 (1)
[Co:DEPBz] ⁺	140	30	120	84.8 (1.7)	51	1.2 (0.1)	2.6 (1)
Rh:biphenphos	120	15	20	96.4 (0.2)	All linear	3.3 (0.06)	25 (1)
Rh:PPh ₃	120	10.3	20	91.1 (2.1)	34	0.3 (0.04)	21 (2)

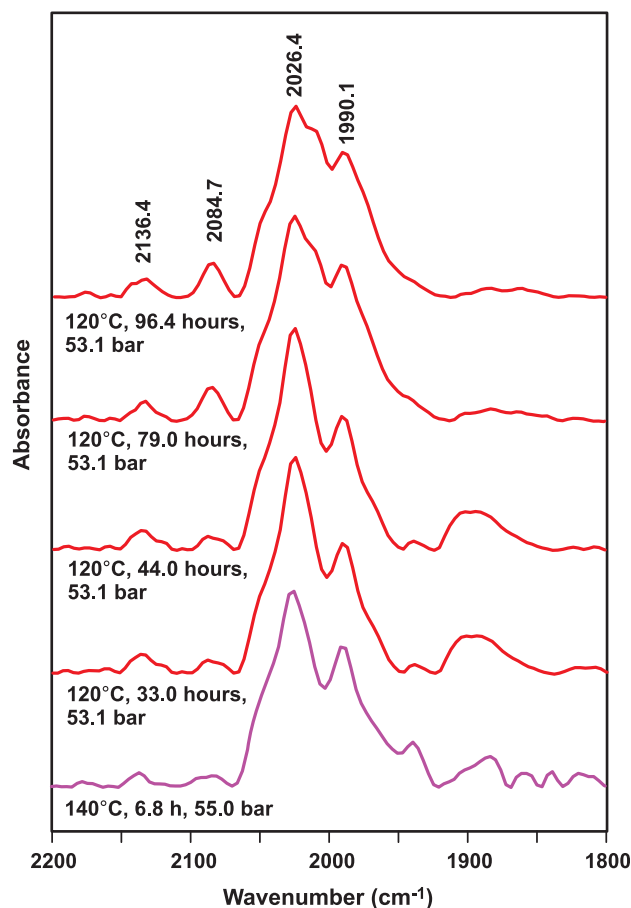
Table 4. Hydroformylation results for internal branched alkenes. All reactions were run for 6 hours with 1.0 M alkene, 1.0 mM catalyst, 0.1 M heptane as internal standard, and 1:1 H₂:CO. Results are an average of two runs. Co₂(CO)₈ or Co(hexanoate)₂ was used to generate HCo(CO)₄, and the cobalt reactions were run in dimethoxytetraglyme solvent. Rh(acac)(CO)₂ was used as the catalyst precursor and run in toluene with the following excess phosphine:Rh ratios: 3:1 for the chelating biphenphos ligand and 400:1 for PPh₃:Rh. No alcohol production was observed.

Alkene	Catalyst	Temperature (°C)	Pressure (bar)	Aldehyde (%)	Aldehyde L:B	Alkane (%)	Isomer (%)
	HCo(CO) ₄	140	90	36.5	All linear	–	4.8
	[Co:depe] ⁺	140	30	24.9	All linear	–	10.0
	Rh:biphenphos	120	15	0	–	–	–
	Rh:PPh ₃	120	10.3	0	–	–	–
	HCo(CO) ₄	140	90	28.6	All linear	2.2	14.2
	[Co:depe] ⁺	140	30	26.9	All linear	3.7	33.5
	Rh:biphenphos	120	15	0.8	All linear	–	2.8
	Rh:PPh ₃	120	10.3	0	–	–	–
	HCo(CO) ₄	140	90	77.7	6.2	–	10.4
	[Co:depe] ⁺	140	30	54.7	4.4	–	32.1
	Rh:biphenphos*	120	15	81.7*	28	1.9	14.8
	Rh:PPh ₃	120	10.3	62.0	0.4	–	8.4

*The Rh:biphenphos catalyst decomposed and stopped hydroformylating after 3 hours, as indicated by the absence of additional H₂:CO gas uptake.

Fig. 2. In situ FTIR studies of [Co(acac)(DPPBz)](BF₄). A

101-hour study of the cationic cobalt catalyst (10 mM) in dimethoxytetraglyme. The proposed catalyst complexes, [HCo(CO)_x(DPPBz)]⁺ (*x* = 1 to 3), have carbonyl bands at 2085, 2046 (shoulder), 2026, 2011 (shoulder), 1990, and 1974 cm⁻¹ (shoulder). The monometallic cationic cobalt-bisphosphine catalyst shows only minor changes in the carbonyl region upon stirring at 120°C and 53 bar for 65 hours. The band at 2136 cm⁻¹ is free CO dissolved in the solvent.



probe provided insight into the nature of the active catalyst and its high stability. Figure 2 shows representative FTIR spectra of the metal-carbonyl region between 120° and 140°C over the course of a 101-hour study for a 10 mM sample of [Co(acac)(DPPBz)](BF₄) in dimethoxytetraglyme solvent reacting with 1:1 H₂:CO. The catalyst precursor underwent hydrogenolysis at 120°C (more slowly at lower temperatures of 80° to 100°C) to lose acacH and generate the proposed mixture of cationic Co(II) hydrides: [HCo(CO)_x(DPPBz)]⁺, where *x* = 1 (15e⁻), 2 (17e⁻), and 3 (19e⁻). The formally 19e⁻ tricarbonyl complex is assigned to the highest-frequency coordinated carbonyl band observed at 2085 cm⁻¹, along with two other carbonyl bands in the 2046- to 2000-cm⁻¹ region [fig. S16 and density functional theory (DFT) assignments in table S12]. This species is most clearly observed in the IR at lower temperatures with enough dissolved CO present. All three monomeric catalyst species are in equilibrium across the temperature range studied, with terminal CO bands in the 2085- to 1980-cm⁻¹ range.

A similar cationic 17e⁻ Co(II) complex, [HCo(CO)₂(dippf)]⁺ [dippf, 1,1'-bis(diisopropylphosphino)ferrocene], has been prepared using electrochemical oxidation from the neutral

Co(I) species. Carbonyl bands are observed at 2051 and 2024 cm⁻¹ (24). The dippf ligand has a much larger chelate bite angle relative to DPPBz, so the structures of [HCo(CO)₂(dippf)]⁺ and [HCo(CO)₂(DPPBz)]⁺, neither of which have been determined, are expected to be different. One of our carbonyls is proposed to be trans to a phosphine ligand, which should result in a lower CO stretching frequency relative to that seen for [HCo(CO)₂(dippf)]⁺, which should not have any carbonyls trans to phosphine ligands. The higher frequency positions of the terminal bands are consistent between both cationic Co(II) complexes. [HCo(CO)₂(dippf)]⁺ disproportionates under the spectroelectrochemical conditions to eliminate H₂ and form the Co(I) complex [Co(CO)₂(dippf)]⁺.

High-pressure ¹H, ³¹P, and ⁵⁹Co nuclear magnetic resonance (NMR) studies (25, 26) of our catalyst (23° to 120°C, 27 bar, 1:1 H₂:CO) did not show any hydride, ³¹P, or ⁵⁹Co NMR resonances, which is consistent with the catalyst species being paramagnetic Co(II). No diamagnetic cobalt species were observed in the high-pressure NMR studies of the catalyst, which considerably reduces the likelihood that traditional Co(I) hydroformylation catalysts are involved. The high activity and medium-to-low pressure stability of this cationic catalyst system clearly argue against

HCo(CO)₄ or HCo(CO)₃(PR₃) catalyst formation or participation. Electron paramagnetic resonance (EPR) studies (fig. S9) demonstrate that the [Co(acac)(DPPBz)](BF₄) catalyst precursor is low-spin Co(II) with clear hyperfine coupling to one cobalt and two equivalent phosphorus centers, indicating a square planar geometry. This structure has been confirmed by x-ray crystallography (fig. S10) with a coordinated THF.

The in situ FTIR study summarized in Fig. 2 demonstrates that there are only minor changes in the carbonyl region of the catalyst at 120°C and 53 bar between the 33- and 96-hour spectra. After cooling and depressurization of the IR cell, the catalyst solution was transferred to an autoclave and was fully active for the hydroformylation of 1-hexene (140°C, 50 bar), giving the same catalytic results as a fresh catalyst precursor sample. This observation demonstrates very good catalyst stability under reaction conditions with no alkene substrate present. A simple industrial stability test for rhodium-phosphine hydroformylation catalysts involves stirring in an autoclave under 1:1 H₂:CO at the reaction temperature in the absence of alkene. All rhodium-phosphine catalysts with P-OR, P-phenyl, or P-benzyl linkages deactivate under these conditions via Rh-induced phosphine fragmentation reactions within 24 hours (usually less). The lower activity of our cobalt catalyst relative to rhodium appears to protect it from metal-induced phosphine ligand and catalyst degradation reactions. This, combined with a strong chelate effect that minimizes phosphine dissociation, produces a robust catalyst that does not require excess phosphine ligand for stability.

A proposed mechanism for this class of cationic Co(II) bisphosphine catalysts is shown in Fig. 3. The fundamental reaction steps are essentially the same as those for known hydroformylation catalysts: alkene coordination, migratory insertion of hydride to form the alkyl, and migratory insertion of CO with the alkyl to form an acyl-like species. Owing to the cationic charge and Co(II) oxidation state, the hydrogen reaction with the cobalt-acyl is proposed to be a heterolytic cleavage to eliminate aldehyde product and regenerate the cationic cobalt-hydride catalyst, as an oxidative addition of H₂ to form a cationic Co(IV) dihydride complex is unlikely.

Alkene coordination to the cobalt center is proposed to occur almost exclusively via the equatorial coordination site that is trans to the bisphosphine ligand. The axial coordination sites are less accessible to sterically hindered alkenes, such as those shown in Table 4. DFT calculations of the association of tetramethylethylene to the free coordination site favor equatorial over axial sites by ~4 kcal/mol (table S16). The most sterically accessible coordination site on the cobalt center is the equatorial

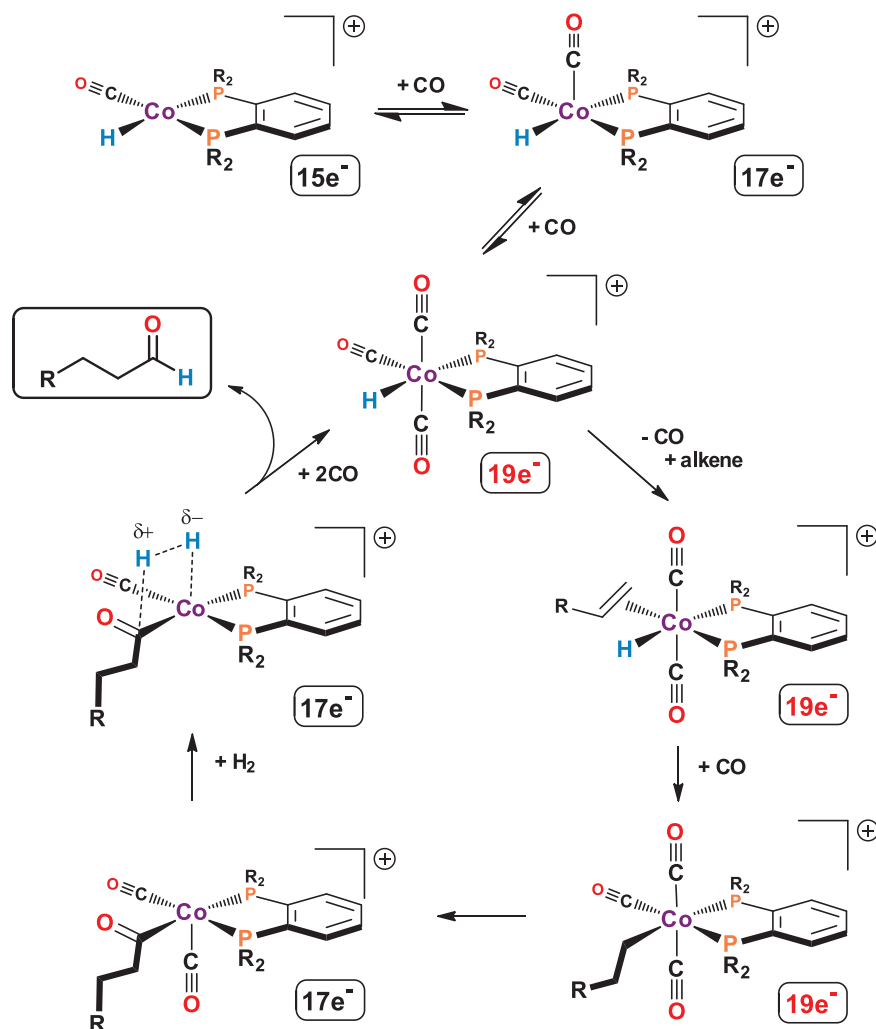


Fig. 3. Proposed hydroformylation mechanism involving $19e^-$ catalyst species. Most of the proposed reaction steps are entirely consistent with what is known for cobalt and rhodium hydroformylation catalysts. A distinctive key feature is the capacity to form $19e^-$ complexes via CO coordination, which helps weaken and dissociate the equatorial CO ligand, the strongest bound CO in the proposed alkene coordination site. The equatorial coordination site is the most likely binding site for sterically hindered alkenes. Although single reaction arrows are shown for clarity, each step is in equilibrium. δ^+ , partial positive charge; δ^- , partial negative charge.

carbonyl, but this is also the strongest CO binding site.

The coordination of a third CO ligand to form a 6-coordinate $19e^-$ complex helps weaken all the metal-ligand bonds, but especially the equatorial CO ligand that must dissociate to make room for an incoming alkene ligand. There is a much lower energy cost to form a $19e^-$ versus a $20e^-$ complex. Shi and colleagues demonstrated that the carbonyl substitution chemistry for $17e^-$ $V(CO)_6$ radical proceeds 10^{10} times faster than for $18e^-$ $Cr(CO)_6$ (27). The phosphine substitution reaction with the $17e^-$ $V(CO)_6$ radical was shown to be associative and extremely facile, proceeding through a $19e^-$ transition state. The $18e^-$ $[V(CO)_6]^-$ anion, in marked contrast, is inert toward phosphine substitution reactions. DFT calculations show that the $19e^-$

$[HCo(CO)_3(DPPBz)]^+$ complex is ~ 9 kcal/mol higher in free energy than the $17e^-$ complex at 115°C , indicating that its formation is energetically accessible (table S15).

The other important rate-enhancing effect is the cationic charge localized on the cobalt center, which compensates for the two donating phosphine ligands. Our work on the dicationic dirhodium tetraphosphine hydroformylation catalyst system has clearly shown the importance of having a localized cationic charge on the metal center to compensate for the electron-donating property of the two phosphine ligands (28). As seen for the neutral $Co(I)$ $HCo(CO)_3(PR_3)$ catalyst system, the electron-donating phosphine ligand enhances electron density at Co, which contributes to CO π -backbonding. This, in turn, increases the Co–CO bond strength, which stabilizes the catalyst with

respect to decomposition to cobalt metal but also substantially slows catalysis.

The $17e^-$ dicarbonyl complex, $[HCo(CO)_2(\text{bisphosphine})]^+$, may also coordinate alkene to the equatorial coordination site after CO dissociation to initiate hydroformylation. But the observed ligand effects on hydroformylation and observation of proposed $19e^-$ carbonyl complexes in the FTIR indicate that $19e^-$ intermediates likely play an important role in catalysis. This cationic $Co(II)$ -bisphosphine catalyst, for example, shows increased activity with more electron-donating phosphines at medium CO partial pressures (Table 3 and table S4). This observation further supports the proposed $19e^-$ intermediate that helps labilize the equatorial Co–CO bond, allowing alkene coordination to initiate hydroformylation.

The high-energy carbonyl band around 2085 cm^{-1} is assigned to the $19e^-$ $[HCo(CO)_3(\text{bisphosphine})]^+$ complex. This band increases in intensity for the more electron-donating phosphine ligands studied (fig. S15). The more electron-rich bisphosphine ligands favor the $19e^-$ tricarboxyl complex at lower CO partial pressures, which in turn helps labilize the equatorial carbonyl ligand under those conditions. As the CO partial pressure increases, the free CO in solution starts to compete with the alkene for coordination to the more electron-rich metal center, leading to the CO inhibition effect appearing sooner relative to the more electron-deficient bisphosphine ligands. Temperature also plays an important role in labilizing the Co–CO ligands.

Monodentate phosphines (PBu_3 , PPh_3) do not generate effective hydroformylation catalysts under these medium-pressure conditions (table S8). Sterically bulky chelating bisphosphines such as $(iPr)_2PCH_2CH_2P(iPr)_2$ generate cationic $Co(II)$ hydroformylation catalysts that are considerably less active than the bisphosphine ligands reported here (table S9). One explanation is that the more hindered phosphine ligands inhibit addition of two axial CO ligands to form the key $19e^-$ $[HCo(CO)_3(P_2)]^+$ catalyst species that favors equatorial CO dissociation. The increased steric bulk of the bisphosphine isopropyl or cyclohexyl groups has little effect on the aldehyde L:B ratio (table S9 and figs. S17 and S18), which supports the proposed equatorial coordination of the alkene into the least sterically hindered metal coordination site. The bisphosphine R groups are pointed away from the equatorial plane and most affect axial ligand coordination. This is another piece of evidence supporting the $19e^-$ catalyst species as an important player in the catalytic mechanism.

Outlook

Relatively little research into new cobalt-based hydroformylation catalysts has occurred since the introduction of the phosphine-modified

catalyst system in the late 1960s. The combination of relatively high pressures and temperatures needed, along with the assumption that industry had explored most alternative cobalt hydroformylation catalysts, strongly inhibited research in this area. The discovery of this highly active cationic Co(II) hydroformylation catalyst system was therefore quite surprising. That this catalyst system appears to have exceptional stability with respect to cobalt-induced phosphine degradation reactions or decomposition to cobalt metal opens doors for medium-pressure hydroformylation technology in both academic and industrial settings.

REFERENCES AND NOTES

1. A. Börner, R. Franke, *Hydroformylation: Fundamentals, Processes, and Applications in Organic Synthesis* (Wiley-VCH, 2016).
2. I. Wender, P. Pino, *Organic Syntheses via Metal Carbonyls*, vol. 2 (Wiley, 1977), pp. 47–197.
3. F. Hebrard, P. Kalck, *Chem. Rev.* **109**, 4272–4282 (2009).
4. R. F. Heck, D. S. Breslow, *J. Am. Chem. Soc.* **82**, 4438–4439 (1960).
5. R. F. Heck, D. S. Breslow, *J. Am. Chem. Soc.* **83**, 4023–4027 (1961).
6. B. Cornils, in *New Syntheses with Carbon Monoxide*, J. Falbe, Ed. (Springer-Verlag, 1980).
7. L. H. Slaugh, R. D. Mullineaux, *J. Organomet. Chem.* **13**, 469–477 (1968).
8. L. H. Slaugh, R. D. Mullineaux, Hydroformylation of olefins, U.S. Patent 3,448,157 (1969).
9. D. Evans, J. A. Osborn, G. Wilkinson, *J. Chem. Soc. A* **1968**, 3133–3142 (1968).
10. R. L. Pruett, J. A. Smith, *J. Org. Chem.* **34**, 327–330 (1969).
11. C. Li, L. Guo, M. Garland, *Organometallics* **23**, 2201–2204 (2004).
12. P. W. N. M. van Leeuwen, C. P. Casey, G. T. Whiteker, in *Rhodium Catalyzed Hydroformylation*, P. W. N. M. van Leeuwen, C. Claver, Eds. (Kluwer, 2000).
13. M. E. Broussard *et al.*, *Science* **260**, 1784–1788 (1993).
14. D. A. Aubry, N. N. Bridges, K. Ezell, G. G. Stanley, *J. Am. Chem. Soc.* **125**, 11180–11181 (2003).
15. W. J. Schreiter *et al.*, *Inorg. Chem.* **53**, 10036–10038 (2014).
16. S. Pandey *et al.*, *J. Am. Chem. Soc.* **140**, 4430–4439 (2018).
17. E. Billig, A. G. Abatjoglou, D. R. Bryant, Transition metal complex catalyzed processes, U.S. Patent 4,668,651 (1988).
18. B. Moasser, W. L. Gladfelder, D. C. Roe, *Organometallics* **14**, 3832–3838 (1995).
19. G. W. Parshall, W. H. Knoth, R. A. Schunn, *J. Am. Chem. Soc.* **91**, 4990–4995 (1969).
20. Rhodium and cobalt metal prices: www.dailymetalprice.com.
21. P. W. N. M. van Leeuwen, C. F. Roobeek, *J. Organomet. Chem.* **258**, 343–350 (1983).
22. A. G. Abatjoglou, E. Billig, D. R. Bryant, *Organometallics* **3**, 923–926 (1984).
23. A. G. Abatjoglou, D. R. Bryant, *Organometallics* **3**, 932–934 (1984).
24. M. J. Krafft *et al.*, *Angew. Chem. Int. Ed.* **52**, 6781–6784 (2013).
25. R. J. Klingler, J. W. Rathke, *J. Am. Chem. Soc.* **116**, 4772–4785 (1994).
26. M. J. Chen, R. J. Klingler, J. W. Rathke, K. W. Kramarz, *Organometallics* **23**, 2701–2707 (2004).
27. Q.-Z. Shi, T. G. Richmond, W. C. Troglor, F. Basolo, *J. Am. Chem. Soc.* **106**, 71–76 (1984).
28. R. C. Matthews *et al.*, *Angew. Chem. Int. Ed.* **35**, 2253–2256 (1996).

ACKNOWLEDGMENTS

We thank D. P. Young (LSU Physics) for collecting magnetic susceptibility data on [Co(acac)(DEPBz)](BF₄) and [Co(acac)(DPPBz)](BF₄). **Funding:** The authors gratefully acknowledge the following financial support, which led to this research: prior support from U.S. National Science Foundation grant CHE-01-11117, Dow Chemical, Louisiana Board of Regents LEQSF(2014-17)-RD-B-02, and LSU LIFT²; and current support from ExxonMobil

Chemical Company. **Author contributions:** D.M.H. designed and prepared all the original catalyst precursors; performed catalytic testing and high-pressure in situ NMR studies; and assisted with the high-pressure FTIR studies and low- and high-pressure EPR sample preparation. R.A.J. independently tested the catalysts, collected data with different substrates, and assisted with the high-pressure FTIR studies. A.E.C. independently prepared and tested the cationic cobalt catalyst and performed x-ray crystallographic studies. J.M.Y. performed DFT calculations on low- and high-spin variants of the cationic cobalt(II) catalysts. D.J.V. collected and interpreted all the EPR data on the [Co(acac)(DPPBz)](BF₄) catalyst precursor and activated catalyst under low- and high-pressure H₂/CO conditions. G.G.S. designed the cationic catalyst concept for hydroformylation; performed the high-pressure FTIR experiments and separate DFT studies on the catalyst species; and contributed to the interpretation of the results and primary drafting of the paper. **Competing interests:** D.M.H. and G.G.S. are inventors on PCT patent application PCT/US19/36194 submitted by Louisiana State University, which covers this and related catalyst systems. A.E.C. and J.M.Y. are employees of ExxonMobil Chemical Company. **Data and materials availability:** Crystallographic data for [Co(acac)(THF)(DPPBz)](BF₄) are freely available from the Cambridge Crystallographic Data Centre under CCDC-1957261. Full synthetic and catalytic details, including preparative procedures and spectroscopic data for catalyst precursors, along with additional catalytic results, can be found in the supplementary materials. Optimized DFT geometries and energetics are provided as a separate zipped tarball (DFT_structures.tar.gz; see supplementary materials).

SUPPLEMENTARY MATERIALS

science.sciencemag.org/content/367/6477/542/suppl/DC1
Materials and Methods
Figs. S1 to S19
Tables S1 to S16
References (29–50)
DFT Geometries

5 August 2019; accepted 23 December 2019
10.1126/science.aaw7742

NEUROSCIENCE

Local D2- to D1-neuron transmodulation updates goal-directed learning in the striatum

Miriam Matamales^{1*}, Alice E. McGovern^{2,3}, Jia Dai Mi⁴, Stuart B. Mazzone^{2,3}, Bernard W. Balleine^{1†}, Jesus Bertran-Gonzalez^{1†*}

Extinction learning allows animals to withhold voluntary actions that are no longer related to reward and so provides a major source of behavioral control. Although such learning is thought to depend on dopamine signals in the striatum, the way the circuits that mediate goal-directed control are reorganized during new learning remains unknown. Here, by mapping a dopamine-dependent transcriptional activation marker in large ensembles of spiny projection neurons (SPNs) expressing dopamine receptor type 1 (D1-SPNs) or 2 (D2-SPNs) in mice, we demonstrate an extensive and dynamic D2- to D1-SPN transmodulation across the striatum that is necessary for updating previous goal-directed learning. Our findings suggest that D2-SPNs suppress the influence of outdated D1-SPN plasticity within functionally relevant striatal territories to reshape volitional action.

In changing environments, it is adaptive for humans and other animals flexibly to adjust their actions to maximize reward. Extinction learning allows individuals to withhold instrumental actions when their consequences change. Rather than erasing such actions from one's repertoire, current views propose that extinction generates new inhibitory learning that, when incorporated into previously acquired behavior, acts selectively to reduce instrumental performance (1).

Associative learning theory identifies the negative prediction errors produced by the absence of an anticipated reward as the source of the inhibitory learning underlying instrumental extinction (2). Such signals are thought to involve pauses in dopamine (DA) activity, and this pattern is well suited to alter plasticity in the posterior dorsomedial striatum (DMS), a key structure encoding the action-outcome associations necessary for goal-directed learning (3). Nevertheless, the way complex DA signals (4) alter postsynaptic circuits in the DMS to shape goal-directed learning remains unknown.

Within the DMS, the plasticity associated with goal-directed learning involves glutamate release timed to local DA activity to alter intracellular cyclic adenosine monophosphate (cAMP)-dependent pathways in postsynaptic neurons, a function that involves slow temporal scales (5) and that leads to gene transcription necessary for learning (6). This activity is distributed across two major subpopulations of spiny projection neurons (SPNs)—the prin-

cipal targets of DA (7). These are completely intermixed within the striatum and express distinct DA receptor subtypes that respond to DA in an opposing manner: Half express type 1 receptors and trigger powerful cAMP signaling in DA-rich states (D1-SPNs), whereas the other half express type 2 receptors and show robust signaling in DA-lean states (D2-SPNs) (8). Given that positive and negative prediction errors during appetitive learning are known to influence DA release (4, 9), we hypothesized that prediction errors during reward and extinction learning generate distinctive molecular activation patterns in D1- and D2-SPNs across the striatum to provide a molecular signature identifying those regions most relevant for plasticity.

Nucleosomal response in SPNs captures goal-directed learning

We first established whether intracellular signaling in SPNs undergoes functional reorganization across the striatum during goal-directed learning. We trained mice to acquire rewarded instrumental actions, where a lever press (action) was either briefly or more extensively associated with the delivery of food (outcome) (Fig. 1, A and B). In group Novice, initial acquisition was marked by a spontaneous increase in lever press frequency during the first session of training, which was used to flag the approximate time at which the action-outcome contingency was first experienced (fig. S1, A and B). By contrast, mice in group Expert received 19 days of additional training (Fig. 1B), clearly increasing lever pressing across days (fig. S1C and table S1).

We next assessed whether the different levels of training were represented in the signaling patterns in striatal SPNs. We used immunodetection of phosphorylated histone H3 on serine 10 (P-H3), a ubiquitous transcriptional activation marker that is rapidly induced in

SPNs in response to different DA states (6, 8). We found a robust P-H3 signal in the nucleus of striatal neurons that colabeled with DARPP-32, a marker of SPNs (Fig. 1C), suggesting that projection neurons—relative to other types of striatal neurons—were transcriptionally active under these conditions. Wide-field, high-resolution mapping identified different levels of transcriptionally active SPNs (taSPNs) across groups, with clear territorial differences in their distribution (Fig. 1D). Compared to Non Contingent controls—exposed to the lever and receiving as many rewards but noncontingently—Novice mice showed a high density of taSPNs concentrated in the DMS, consistent with the role of this region in action-outcome encoding (3). By contrast, when compared to their Yoked controls, group Expert showed an increase in taSPN density that distributed laterally, in support of the functional lateralization expected from extensively trained actions (Fig. 1D) (10). Critically, we found a clear dissociation between taSPN density and the extent of overall performance (i.e., lever presses and magazine checks) (Fig. 1, D and E, and table S1). This allowed us to link goal-directed learning with the induction of DA-promoted transcriptional activity in SPNs. The nuclear P-H3 signal was detected in D1- as well as D2-SPN subtypes (Fig. 1F), indicating that both neuronal systems were sensitive to the DA states underpinning goal-directed learning. D1 neurons were more transcriptionally active than D2 neurons in all training groups (Fig. 1G), and taD1/taD2-SPN ratios remained constant (fig. S1D and table S1).

Regional overlap of activated taSPN subpopulations predicts extinction learning

To compare the activation patterns of D2- and D1-neurons in the striatum during instrumental and extinction learning, we mapped and classified large numbers of taSPNs in whole striatal sections of *drd2-eGFP* (enhanced green fluorescent protein) mice (fig. S2). We trained two groups of mice on an increasing fixed ratio (FR) reinforcement schedule where access to each food outcome relied on a predictable instrumental effort (Fig. 2A). The groups showed indistinguishable performance with very similar increases in lever press rate across training (fig. S3A and table S2). On day 16, group Extinction underwent an altered training session in which lever pressing activated the food dispenser, but no outcomes were delivered. This manipulation generated vigorous responding for “no-reward” (Ø) that was comparable to that of nonextinguished mice (Instrumental controls) for almost half of the session, at which point their cumulative performance decayed (Fig. 2B, fig. S3B, and table S2).

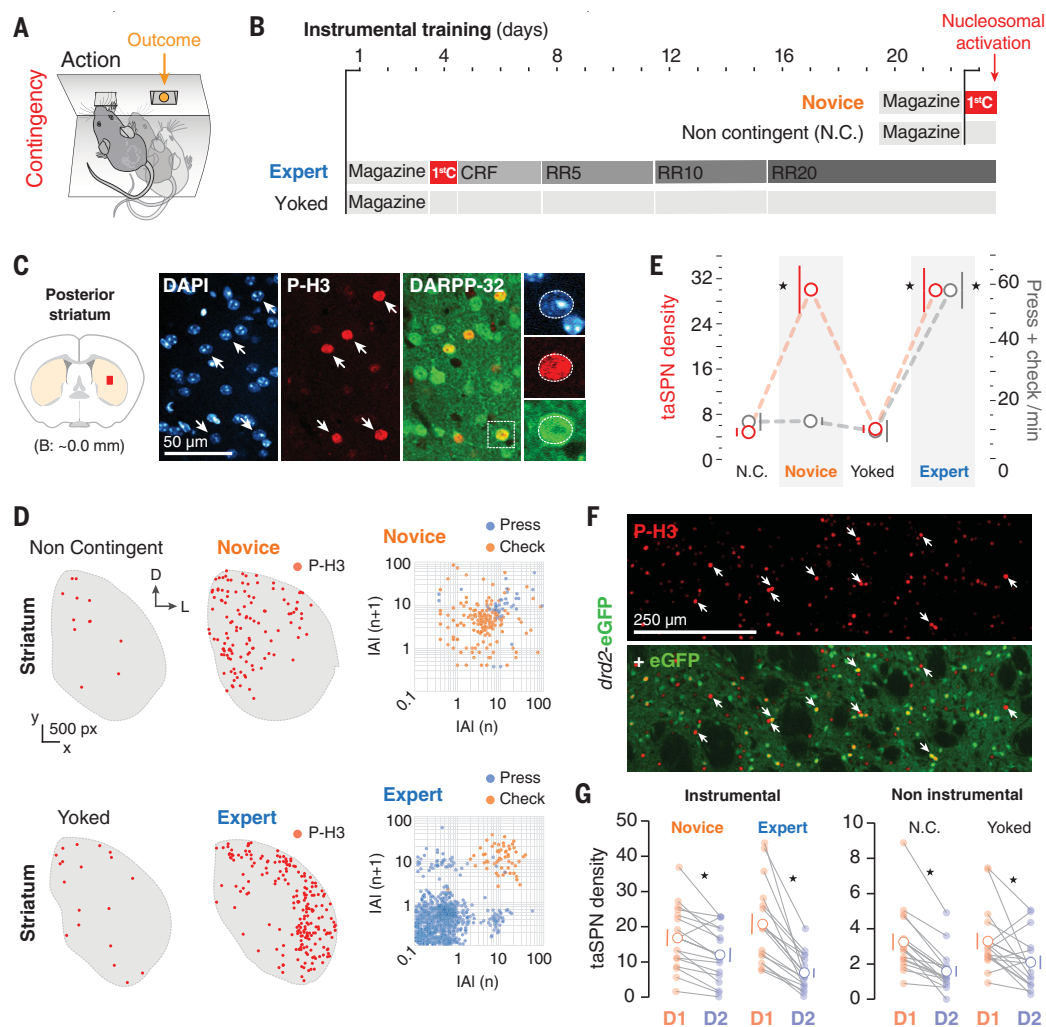
Mapping of taSPNs in entire striatal sections revealed that overall densities of taD2- and taD1-SPNs were similar in Instrumental and

¹Decision Neuroscience Laboratory, School of Psychology, University of New South Wales, Sydney, NSW, Australia. ²Department of Anatomy and Neuroscience, University of Melbourne, Melbourne, VIC, Australia. ³School of Biomedical Sciences, University of Queensland, St Lucia, QLD, Australia. ⁴Department of Women and Children's Health, Faculty of Life Sciences and Medicine, King's College London, London SE1 7EH, UK.

*Corresponding author: Email: m.matamales@unsw.edu.au (M.M.); j.bertran@unsw.edu.au (J.B.G.) †These authors contributed equally to this work.

Fig. 1. Nucleosomal response mapping reveals learning-related territories in the striatum. (A) Mice were trained to associate an action (lever press) with an outcome (food pellet).

(B) Four groups of eight mice received different levels of instrumental conditioning. 1stC, first Contingency. (C) Immunodetection of phosphorylated nucleosomes (phospho-Ser₁₀-histone H3; P-H3) identifies transcriptionally active (ta) neurons in the posterior striatum. P-H3 immunoreactivity was specifically detected in the nuclei (DAPI⁺) of SPNs (DARPP-32⁺). (D) Digitized reconstruction of taSPNs throughout the striatum in “Novice,” “Expert,” and their control groups (4362 SPNs mapped). Right panels: return maps of inter-action-intervals (IAIs) for lever presses (blue) and magazine checks (orange). Each data point represents the time delay to its preceding (x) and succeeding (y) behavioral element. (E) taSPN density (cells/mm²) and overall action rate in the different training groups (eight mice per group, both striata). (F) Identification of taSPNs in the striatum of a trained *drd2*-eGFP mouse. Arrows: taD2-SPNs (downward) and taD1-SPNs (upward). (G) P-H3⁺ nuclei densities of each neuronal type in the striatum of the different training groups. Note the different scale on the y axes. *, simple effects (table S1).



Extinction groups (fig. S3, C and D, and table S2). However, density-based cluster analysis showed that taD2- and taD1-SPNs followed characteristic spatial distributions across the posterior striatum in each group (Fig. 2C). In mice undergoing a rewarded session, each system tended to occupy nonoverlapping areas in the DMS, with taD1-SPNs segregated to lateral territories (Fig. 2C, top). In animals undergoing extinction, we found a high level of convergence in DMS areas, with very few neurons detected laterally (Fig. 2C, bottom). Extinction mice exhibited a marked increase in the proportion of taD2-SPN territories that overlapped with functional D1-SPN areas specifically in the DMS (Fig. 2, D and E), as well as a higher proportion of taD1-SPN clusters sharing space with taD2-SPNs in this same region (Fig. 2, D and F, and table S2).

D2-SPNs in the DMS are required to encode extinction learning

We hypothesized that recruiting activated D2-SPNs in the DMS is directly related to inhibitory learning during extinction. We selectively

removed D2-SPNs from the DMS where we had observed high taD2- and taD1-SPN confluence (Fig. 2D) through genetic ablation in adult *adorea2a-Cre::drd2*-eGFP hybrid mice (Fig. 2G and fig. S4A). After instrumental training, Lesioned and Sham mice were given a 10-min extinction learning session (day 16) followed by an extinction test 24 hours later (Fig. 2H). This protocol was aimed at detecting differences on test due to deficient integration of extinction learning 24 hours earlier. D2-SPN ablation had no effect on the initial acquisition of instrumental contingencies; both groups showed very similar levels of performance across sessions (Fig. 2I, left) and an indistinguishable response structure on day 15 (Fig. 2I, right, and table S2). Likewise, both groups similarly reduced lever press performance during the 10-min extinction learning session (Fig. 2J and table S2), although performance differed 24 hours later: Lesioned mice accumulated a higher number of presses across the session and showed a higher average level of pressing and a steeper linear regression slope (Fig. 2K and table S2). This increase in performance

was not due to an overall increase in lever press rates but rather to recurrent and persistent performance during the extinction session (Fig. 2L; fig S4, B to D; and table S2).

We then analyzed the distribution of taD2- and taD1-SPNs that accumulated in the posterior striatum during the 20-min test on day 17. We again found an increased confluence of taD2- and taD1-SPNs in the DMS of Sham mice, which still displayed substantial overlap despite being assessed on the second day of extinction (Fig. 2M and table S2). Conversely, the absence of D2-SPNs in Lesioned mice was associated with a high density of taD1-SPNs in the DMS (Fig. 2, M and N, and table S2). Density analysis in the DMS revealed that taD2- and taD1-SPNs followed opposing density patterns in Sham and Lesioned mice: Higher densities of taD2-SPNs predicted low densities of taD1-SPNs and vice versa (Fig. 2O and table S2).

D2-SPNs spatially rearrange D1-SPN plasticity

We sought to establish whether D2- and D1-SPNs functionally interact within convergent striatal territories using pharmacological

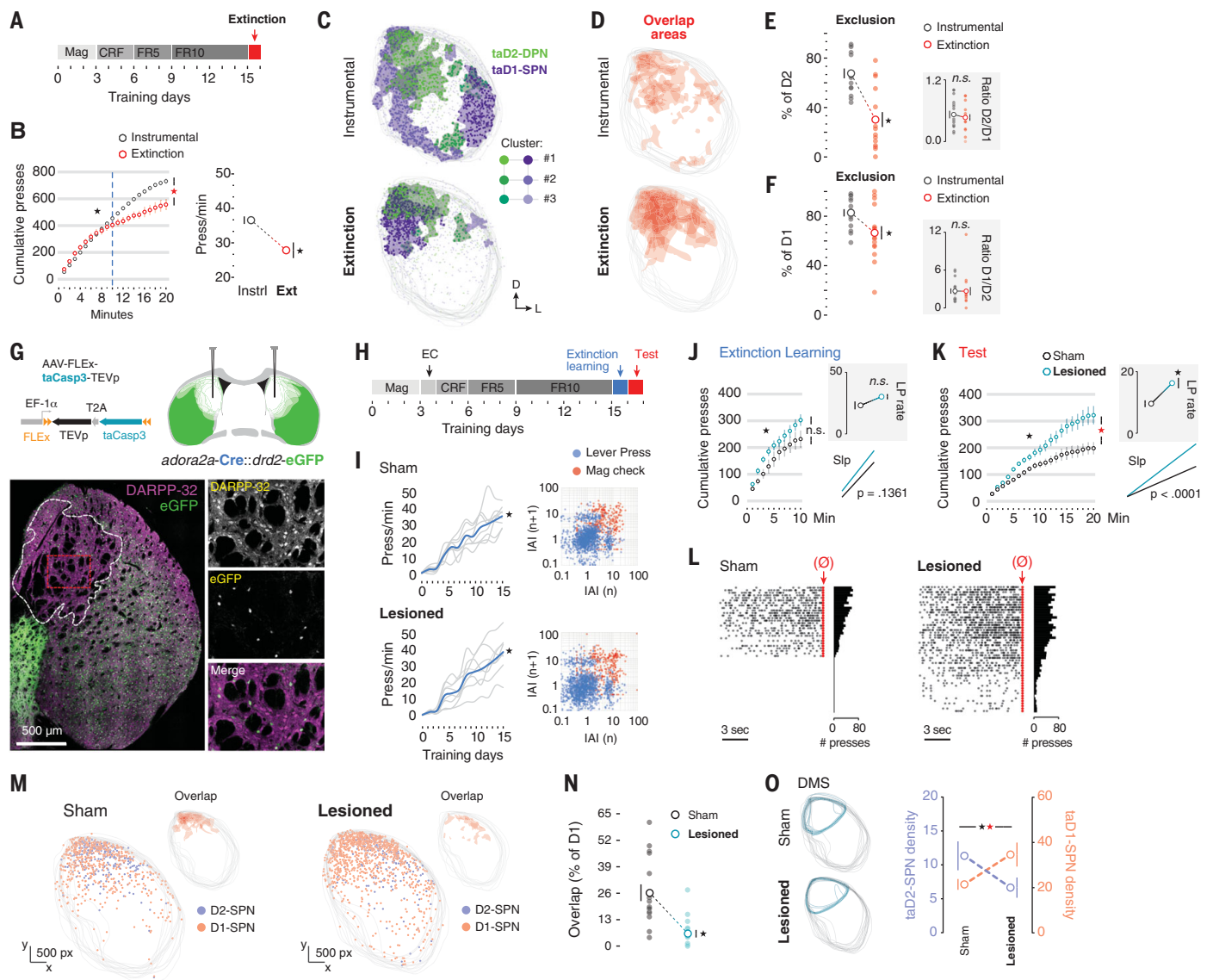


Fig. 2. Functional confluence of projection systems in the striatum promotes extinction of learned actions. (A) Mice (eight per group) were trained on increasing fixed ratio (FR) reinforcement schedules prior to extinction (day 16). (B) Cumulative and average lever press performance during instrumental (control) and extinction sessions (day 16). (C) Distribution of taD2- and taD1-SPNs in the posterior striatum of mice in (B). Plots show up to three density clusters from aligned hemisections in each group (4044 SPNs mapped). (D) Reconstruction of taD2- and taD1-SPN overlapping territories in the striatum. (E and F) Extent of taD2- and taD1-SPN territory exclusion. Data are percentages of taD2-SPN territories segregated from taD1-SPNs (E) and vice versa (F). Insets: overall D2/D1 (E) and D1/D2 (F) P-H3⁺ SPN ratios. (G) Genetic lesion of D2-SPNs in the DMS through AAV-FLEX-taCasp3-TEVp system. DARPP-32⁺eGFP⁺ SPNs remained intact (fig. S4A). (H) Sham and

Lesioned mice were trained as in (A) but underwent additional extinction testing on day 17. (I) Lever press performance in both groups across instrumental training. Right: return maps of collective IAI on day 15. (J and K) Cumulative presses per minute on days 16 (J) and 17 (K). Insets: average press performance (top) and linear regression slope (Slp) analysis (bottom). (L) Raster plots and frequency histograms of pooled lever press data preceding the delivery of each pseudoreward (red). (M) Digitized reconstruction of taD2- and taD1-SPNs after test. Insets: taD2- and taD1-SPN overlapping territories. (N) Extent of taD2- and taD1-SPN territory overlap (% of D1). (O) P-H3⁺ nuclei density in D2-SPNs (left axis, purple) and D1-SPNs (right axis, orange) in the DMS. Left: regions quantified in each group. [(E), (F), (N), and (O)]: Two hemisections per mouse, eight mice per group; *, overall/simple effect (black) and interaction (red). n.s., not significant (table S2).

compounds known to induce robust and widespread intracellular signaling in each system (8). Systemic injection of raclopride (RAC; a D2-receptor antagonist) to *drd2*-eGFP mice induced a strong nucleosomal response mostly in D2-SPNs that extended throughout the posterior striatum, whereas GBR12783 (GBR; a DA-

transporter inhibitor) induced an even stronger activation with similar distribution but mostly in D1-SPNs (Fig. 3A). We injected four groups of *drd2*-eGFP mice with different combinations of vehicle, RAC ($t = 0$), and GBR ($t = 15$) and recorded their ambulatory locomotor activity in an open field arena prior to perfusion

($t = 30$) (Fig. 3B). GBR injection strongly increased locomotion in both groups that received it, irrespective of the RAC injection (Fig. 3, C to G, and table S3). In RAC-treated mice, taD2-SPNs dominated most of the striatal space (Fig. 3, H and I), whereas a reverse pattern was observed after GBR treatment (Fig. 3, H

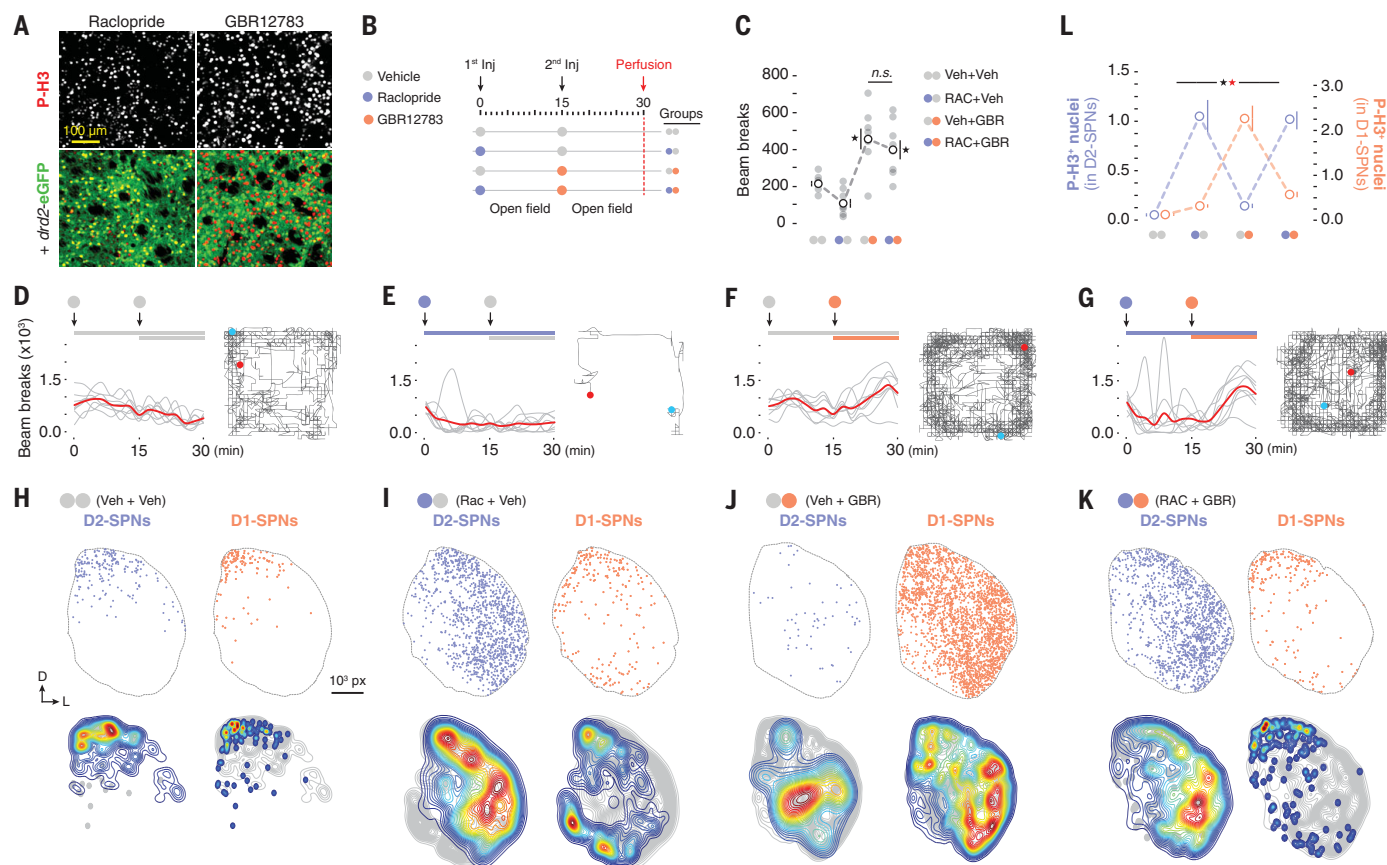


Fig. 3. Overstimulated SPN systems compete for space in the striatum.

(A) Confocal micrographs showing the effects of D2R blockade (Raclopride, 0.3 mg/kg) and dopamine transporter inhibition (GBR12783, 15 mg/kg) on taSPNs. (B) Two-injection experimental design applied to each group prior to perfusion (eight mice per group). Ambulation was measured in an open field. (C) Ambulation (beam breaks) recorded after the second injection (min 15 to 30). (D to G) Ambulatory activity per minute. Right: ambulatory trajectory (start: blue; finish: red) in one example mouse after the second

injection. (H to K) Top: maps of taD2- and taD1-SPNs in the striatum of an example mouse. Bottom: distribution contour plots delimiting regions of increasing P-H3⁺ nuclear density in D2- (left) and D1- (right) SPN systems separately. Isodensity curves are pseudocolored from low (blue) to high (red) relative densities (31,542 taD1-SPNs and 29,100 taD2-SPNs mapped). (L) Quantification of P-H3⁺ nuclei (counts $\times 10^3$) distributed in D2- and D1-SPNs in each group (9 to 12 sections per group). *, significant overall/simple effect (black) and interaction (red). n.s., not significant (table S3).

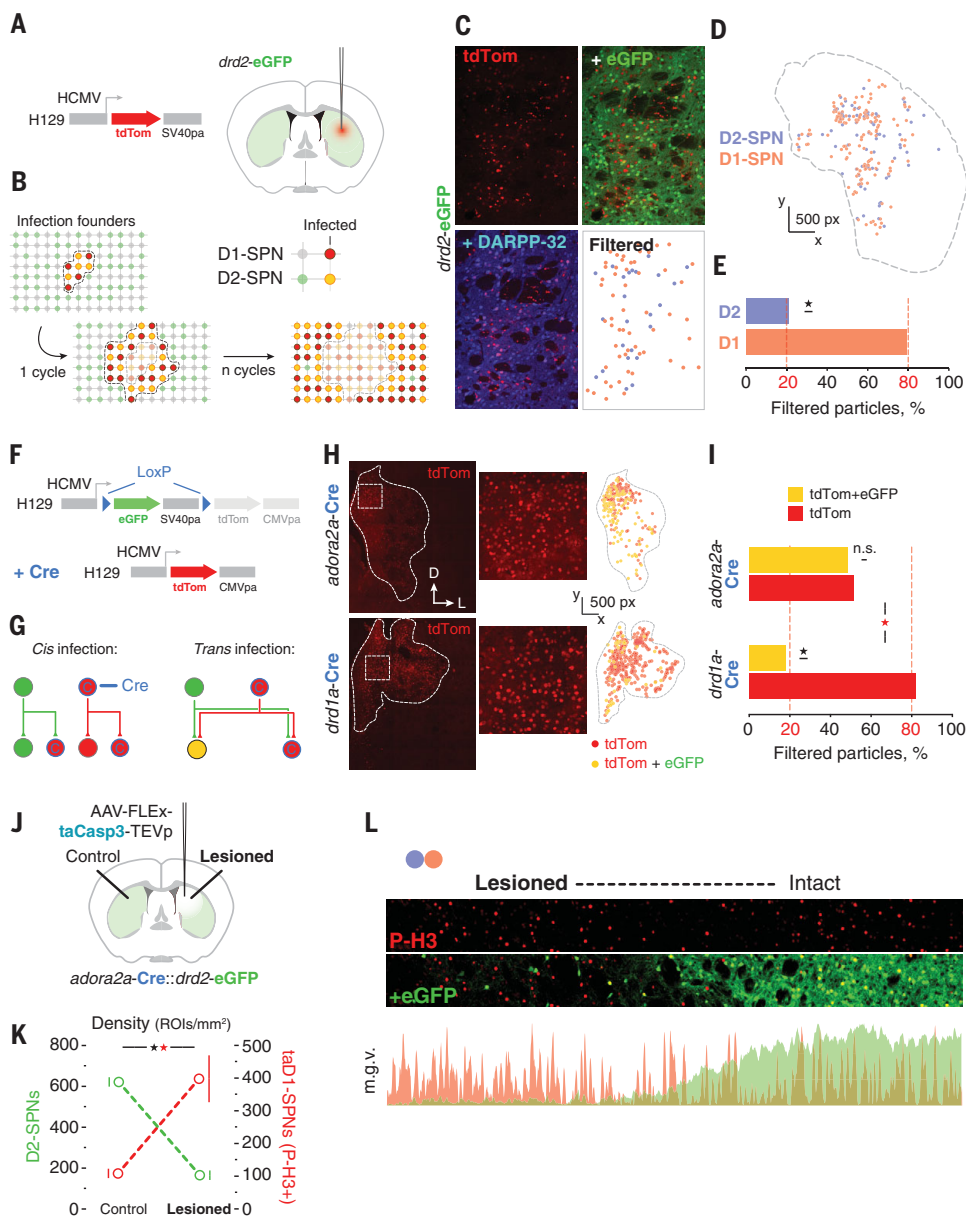
and J). The combination of both drugs, however, resulted in a high density of taD2-SPNs and a low density of taD1-SPNs throughout the posterior striatum, indicating that prior injection of RAC prevented the effects of GBR on D1-SPN nuclear activity (Fig. 3K). This large-scale D2-to-D1 suppression was reproduced when RAC was combined with a full D1 agonist (fig. S5). Moreover, the distribution of taD2 and taD1-SPN peak density areas tended to occupy spatially distinct regions of the striatum in all groups, regardless of the pharmacological cocktail received (Fig. 3, H to K, lower panels). This opposition was supported by a strong overall treatment \times neuron interaction (Fig. 3L and table S3). Paradoxically, animals with D2-dominated (and D1-inhibited) SPN signaling (Fig. 3K) showed unaltered GBR-induced hyperlocomotion (Fig. 3G), again suggesting that nuclear activity in SPNs can be dissociated from behavioral performance (compare Fig. 1E).

Broad connectivity of the local striatal network supports an extensive D2- to D1-SPN transmodulation

We reasoned that the local network in the striatum may reflect large-scale connectivity biases consistent with the magnitude of the D2-to-D1 modulation reported above. To investigate this, we used a quantitative network-level approach to measure connectivity biases using unilateral injections of the herpes simplex virus 1 (HSV1) H129^{tdTomato} in the posterior striatum of *drd2-eGFP* mice (Fig. 4A). Because this virus moves along synaptically connected neurons in the anterograde direction (11), we mapped transduced tdTomato⁺ SPNs across large territories to reveal the broad connectivity patterns established within the striatum (Fig. 4B and fig. S6A). Only ~20% of the transduced SPNs were D2-SPNs, whereas up to ~80% were D1-SPNs (Fig. 4, C to E, and table S4). These numbers were similar across all areas of infection, regardless of whether they were ipsi-

or contralateral to the initial injection (fig. S6, B to D, and table S4). Injection of the virus in the prelimbic cortex (i.e., one upstream synapse) provided very similar weights of transduced D1- (~80%) and D2- (~20%) SPNs (fig. S6, E to G, and table S4).

To confirm that the enhanced connectivity in D1-SPNs was influenced by a D2-to-D1 drive, we infected the striatum with HSV1 H129^{Floxed} virus, an anterograde tracing approach in which transsynaptic labeling switches from green to red in the presence of Cre (12) (Fig. 4F and fig. S7, A to C). This method allowed us to quantify cross-system connectivity by assessing the proportion of (non-Cre-expressing) neurons that received dual green and red infection within a critical temporal window (Fig. 4G). Intrastriatal injection in *adora2a-Cre* mice revealed equal proportions of single (tdTom)- and double (tdTom + eGFP)-labeled SPNs (Fig. 4, H and I, and table S4). By contrast, infection in *drd1a-Cre* mice produced a much lower proportion



of double-labeled SPNs (Fig. 4, H and I, and table S4). The percentages of double- and single-labeled neurons in *drd1a-Cre* mice matched those previously observed with the nonswitchable virus in *drd2-eGFP* (i.e., 20 and 80%; compare Fig. 4, E and I). Again, these same proportions were consistently found across all infected striatal areas analyzed, irrespective of the area of spread (fig. S7, C to E). The two major projection systems in the striatum establish very different local connectivity, with D2-SPNs making substantial connections with D1-SPNs but not vice versa. The magnitude of this asymmetry provides full neuroanatomical support for the large-scale D2- to D1-SPN transmodulation observed in this study.

To address the functional relevance of this connectivity bias, we evaluated the effects of RAC and GBR cocktail on striata where D2-SPNs had been genetically ablated in the DMS (fig. S8, A and B). After recovery, mice with unilateral D2-SPN depletions (Fig. 4J) were treated with RAC and GBR prior to perfusion (as in Fig. 3B), and patterns of transcriptional activation were contrasted between control and lesioned sides. The density of taD1-SPNs was inversely proportional to the density of D2-SPNs in control and lesioned sides (Fig. 4K and table S4). Analysis of P-H3⁺ nuclei across contiguous striatal territories spanning lesioned and intact areas revealed that the identity of the transcriptionally active neurons transitioned from D2-SPNs (in intact territories) to D1-

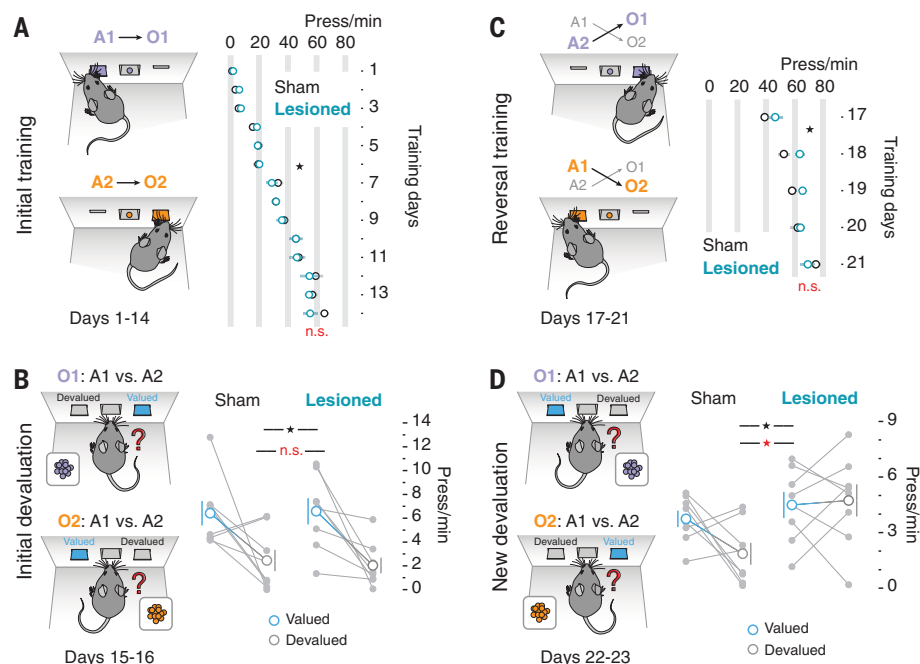
SPNs (in D2-ablated territories) (Fig. 4L). Similarly, D2-SPN removal in the DMS opened windows of uncontrolled D1-SPN activation (fig. S8C).

D2-SPNs shape other sources of flexibility in goal-directed learning

Thus far, our results suggest that D2-SPNs shape the changes in striatal plasticity necessary for flexible encoding of goal-directed learning. In the case of inhibitory learning during extinction, this process is compatible with the role ascribed to DA in negative prediction error scenarios: A sustained pause of phasic DA in defined striatal territories may lead to recruitment of D2-SPNs and, with it, the D2-to-D1 transmodulation reported here. We next sought

Fig. 5. D2-SPNs control the updating of learning.

Bilateral genetic lesions of D2-SPNs were performed in the DMS of *adora2a*-Cre::*drd2*-eGFP hybrid mice (fig. S8, D and E) (eight mice per group). Initial learning: (A) Sham and Lesioned mice were trained to two action–outcome (A–O) contingencies, resulting in increased performance (press/min) across days. (B) Initial devaluation test: a choice (A1 versus A2) was presented after having sated the mice on one or the other outcome (O1/O2) over consecutive days. Graph shows performance on the valued (blue: provides nonsated O) and devalued (gray: provides sated O) levers. Additional learning: (C) Mice were then trained to the reversed A–O contingencies, which rapidly increased press/min performance. (D) A new round of devaluation and choice tests were presented [as in (C)]. *, significant overall effect (black) and interaction (red). n.s., not significant (table S5).



to evaluate the role of D2-SPNs in flexible learning that should not overtly depend on a negative reward prediction error. We induced subtle changes in the identity predictions of preexisting action–outcome relationships by reversing the outcome congruence between pairs of action–outcome associations. We trained mice with bilateral D2-SPN ablations in the DMS (fig. S8, D and E) and their sham controls on two action–outcome associations (A1–O1 and A2–O2), which generated identical performance in both groups (Fig. 5A and table S5). We then verified whether both A–O contingencies had been correctly encoded by giving the mice an outcome-specific devaluation test, which evaluated the effect of sensory-specific satiety on one or the other outcome on choice between the two trained actions (13) (Fig. 5B). Both groups correctly encoded the initial contingencies (i.e., A1–O1 and A2–O2); satiety on one of the outcomes (e.g., O1) reduced performance of the action associated with that outcome in training (A1; devalued) relative to the other, still valued, action (A2; valued) (Fig. 5B and table S5). We then explored whether these mice could incorporate new information by training them with the outcome identities reversed for 5 days (i.e., A1–O2 and A2–O1) (Fig. 5C and table S5) prior to a second outcome-specific devaluation test (Fig. 5D). Whereas Sham mice were able to show flexible encoding and could adjust their choice according to the new A–O associations, mice with D2-SPN ablation failed to do so (Fig. 5D and table S5).

Discussion

One of the most intriguing characteristics of the striatum is the random spatial distribution

and high degree of intermingling between its D1 (direct) and D2 (indirect) projection systems, a feature that is actively promoted developmentally (14) and that has been retained throughout evolution (15). The result is a highly entropic binary mosaic that extends through an expansive and homogeneous space and that is mostly devoid of histological boundaries (16). Such organization is unusual in the brain and can be seen as an adaptation to provide an optimal postsynaptic scaffold for the integration of regionally meaningful neuromodulatory signals (17). In such a plain, borderless environment, the rules established locally by D1 and D2-SPNs are likely to be critical in defining functional territories throughout the striatum, and this, we propose, is the key process shaping striatal-dependent learning.

Our study suggests that the striatum takes full advantage of this “one-to-one” binary mosaic structure, in which activated D2-SPNs access and modify developing behavioral programs encoded by regionally defined ensembles of transcriptionally active D1-SPNs (what we call D2-to-D1 transmodulation). We propose that this process is slow, as it depends on the molecular integration of additive neuromodulatory signals (5), but could, with time, create the functional boundaries necessary to identify and shape specific learning in the striatum. A good example of this sort of dynamic, persistent neuromodulation is the recently described “wave-like” motion of DA signals throughout the mediolateral axis of the striatum (17). Beyond offering a broad solution to the credit assignment problem, recurrent waves of neuromodulatory activity in defined striatal areas could provide the kind of unbiased signal that, in

the context of the molecular dichotomies established by D1 and D2 receptors (8), shape the striatal mosaic into meaningful transcriptional motifs. In the case of extinction learning, as observed here, noisy alternations between DA-rich and DA-lean states within the DMS appear to generate a mixed population of activated SPNs comprising both D1 and D2 systems. This regional overlap lays the groundwork for the local one-to-one modulation that shapes and integrates new learning, limiting outdated D1-SPN function in the case of extinction learning, and segregating new and existing territories of plasticity in the case of action–outcome identity reversal.

REFERENCES AND NOTES

1. M. E. Bouton, *Psychopharmacology* **236**, 7–19 (2019).
2. M. E. Bouton, B. W. Balleine, *Behav. Anal.* **19**, 202–212 (2019).
3. B. W. Balleine, *Neuron* **104**, 47–62 (2019).
4. A. Mohebi et al., *Nature* **570**, 65–70 (2019).
5. P. Greengard, *Science* **294**, 1024–1030 (2001).
6. A. Stipanovich et al., *Nature* **453**, 879–884 (2008).
7. C. R. Gerfen, D. J. Surmeier, *Annu. Rev. Neurosci.* **34**, 441–466 (2011).
8. J. Bertran-Gonzalez et al., *J. Neurosci.* **28**, 5671–5685 (2008).
9. M. J. Wanat, I. Willuhn, J. J. Clark, P. E. M. Phillips, *Curr. Drug Abuse Rev.* **2**, 195–213 (2009).
10. H. H. Yin et al., *Nat. Neurosci.* **12**, 333–341 (2009).
11. A. E. McGovern et al., *J. Neurosci. Methods* **209**, 158–167 (2012).
12. A. E. McGovern et al., *J. Neurosci.* **35**, 7041–7055 (2015).
13. B. W. Balleine, A. Dickinson, *Neuropharmacology* **37**, 407–419 (1998).
14. A. Tinterri et al., *Nat. Commun.* **9**, 4725 (2018).
15. S. Grillner, B. Robertson, *Curr. Biol.* **26**, R1088–R1100 (2016).
16. G. Gangarossa et al., *Front. Neural Circuits* **7**, 124 (2013).
17. A. A. Hamid, M. J. Frank, C. I. Moore, *bioRxiv* 729640 [Preprint] (2019).

ACKNOWLEDGMENTS

We thank Z. Skrbis for technical assistance. **Funding:** This work was supported by the Australian Research Council (Grants DE160101275 to J.B.-G., DP19010251 to J.B.-G. and M.M. and DP150104878 to B.W.B.) and by a Fellowship from the NHMRC of Australia to B.W.B. (GNT1079561). **Author contributions:** M.M., B.W.B. and J.B.-G.

conceived the study and designed the experiments. M.M. and J.B.-G. performed behavioral experiments. J.B.-G. performed surgeries and viral manipulations. A.E.M. and S.B.M. designed and produced the HSV viruses. A.E.M. and J.D.M. performed the experiments with HSV viruses. M.M. performed quantitative imaging analyses. M.M. and J.B.-G. performed statistical analyses. M.M., B.W.B., and J.B.-G. wrote the paper. **Competing interests:** The authors declare no competing interests. **Data and materials availability:** All source data supporting the conclusions of the study are published in Figshare data repository

(<https://figshare.com/s/6dd880046d1d5d3a1100>). AAV vectors and transgenic mouse lines were obtained under material transfer agreements with Addgene, the University of North Carolina, Jackson Laboratories and the Rockefeller University.

SUPPLEMENTARY MATERIALS

science.sciencemag.org/content/367/6477/549/suppl/DC1
Materials and Methods

Figs. S1 to S8
Tables S1 to S5
References (18–25)

[View/request a protocol for this paper from Bio-protocol.](#)

20 September 2019; accepted 19 December 2019
10.1126/science.aaz5751

REPORT

THERMAL CONDUCTIVITY

Ultrahigh thermal conductivity in isotope-enriched cubic boron nitride

Ke Chen^{1*}, Bai Song^{1*†‡}, Navaneetha K. Ravichandran^{2*}, Qiye Zheng^{3§}, Xi Chen^{4¶}, Hwijong Lee⁴, Haoran Sun⁵, Sheng Li⁶, Geethal Amila Gamage Udalamatta Gamage⁵, Fei Tian⁵, Zhiwei Ding¹, Qichen Song¹, Akash Rai³, Hanlin Wu⁶, Pawan Koirala⁶, Aaron J. Schmidt¹, Kenji Watanabe⁷, Bing Lv⁶, Zhifeng Ren⁵, Li Shi^{4,8}, David G. Cahill³, Takashi Taniguchi⁷, David Broido^{2‡}, Gang Chen^{1‡}

Materials with high thermal conductivity (κ) are of technological importance and fundamental interest. We grew cubic boron nitride (cBN) crystals with controlled abundance of boron isotopes and measured κ greater than 1600 watts per meter-kelvin at room temperature in samples with enriched ^{10}B or ^{11}B . In comparison, we found that the isotope enhancement of κ is considerably lower for boron phosphide and boron arsenide as the identical isotopic mass disorder becomes increasingly invisible to phonons. The ultrahigh κ in conjunction with its wide bandgap (6.2 electron volts) makes cBN a promising material for microelectronics thermal management, high-power electronics, and optoelectronics applications.

Ultrahigh thermal conductivity (κ) materials are desirable for thermal management and have long been a subject of both fundamental and applied interest (1). Despite decades of effort, only a few materials are known to have an ultrahigh thermal conductivity, which we define as exceeding $1000 \text{ W m}^{-1} \text{ K}^{-1}$ at room temperature (RT) (2). In metals, free electrons conduct both charge and heat. Therefore, the best electrical conductors, such as silver and copper, also have the highest κ for metals. In semiconductors and insulators, phonons carry the heat. The intricate interplay between lattice dynamics, anharmonicity, and defects dictates thermal transport. Despite the large number of materials that have phonon-dominated heat transport, diamond has been recognized since 1953 as the most thermally conductive bulk material at RT (3). Besides diamond, a set of

nonmetallic crystals with high κ was systematically identified by Slack in 1973 (4), including silicon carbide (SiC), boron phosphide (BP), and the cubic, zincblende polymorph of boron nitride (cBN) (5). In addition, Slack (4) proposed guidelines for searching for crystals with high κ , suggesting that candidates should be composed of a strongly bonded light element or elements arranged in a simple lattice with low anharmonicity. These guidelines were established with approximate models but captured the essential need for high-phonon group velocity and low-phonon scattering rates.

Since Slack's work, the κ of diamond ($\sim 2000 \text{ W m}^{-1} \text{ K}^{-1}$ with natural carbon isotopes at RT) (6, 7) has not been surpassed among bulk materials. High thermal conductivities of up to $490 \text{ W m}^{-1} \text{ K}^{-1}$ and $768 \text{ W m}^{-1} \text{ K}^{-1}$ were reported for BP and cBN (8–12), respectively, benefiting from progress in crystal growth and thermal characterization techniques. Unlike cBN and BP, boron arsenide (BAs) has the much heavier arsenic element and was originally estimated to have a room-temperature κ (κ_{RT}) of $200 \text{ W m}^{-1} \text{ K}^{-1}$ (4). In 2013, Lindsay, Broido, and Reinecke (13, 14) showed with ab initio simulations that BAs should have a κ_{RT} rivaling that of diamond because of a dramatic reduction in the strength of the lowest-order processes giving intrinsic thermal resistance, three-phonon scattering. Several experiments in 2018 demonstrated a κ_{RT} of $\sim 1200 \text{ W m}^{-1} \text{ K}^{-1}$ (11, 15, 16), making BAs one of the most thermally conductive materials and consistent with modified predictions that included four-phonon scattering (16, 17).

Apart from the unusual BAs, cBN was predicted to have a κ_{RT} exceeding $2000 \text{ W m}^{-1} \text{ K}^{-1}$ upon isotopic enrichment of the boron atoms by using theories that ignored four-phonon

scattering (13, 18, 19). We combined experimental characterizations with ab initio simulations that include four-phonon scattering to revisit heat transport in cBN, using synthetic crystals with natural ($^{\text{nat}}\text{B}$) and controlled abundance of boron isotopes. We demonstrated experimentally that $^{\text{c}^{\text{nat}}}\text{BN}$ crystals can have a κ_{RT} over $850 \text{ W m}^{-1} \text{ K}^{-1}$ and that enriched ^{10}B (or ^{11}B) N can reach over $1600 \text{ W m}^{-1} \text{ K}^{-1}$. The ultrahigh κ we measured was consistent with our first-principles calculations, which showed relatively weak effects of higher-order anharmonic phonon-phonon interactions on κ in cBN. Furthermore, the $\sim 90\%$ enhancement of κ_{RT} upon boron isotope enrichment qualitatively supported prior calculations (13, 18, 19) and represents a very large RT isotope effect. For isotope-controlled BP and BAs, we only calculated a 31 and 12% increase in κ_{RT} , respectively, which agreed with the small isotope effect we measured. We used simulations to discover the differences between these boron pnictides which can only be understood by considering the subtle interplay between the mutual interactions involving phonons and isotopic disorder.

We prepared four sets of cBN crystals combining natural nitrogen (99.6% ^{14}N and 0.4% ^{15}N) with different boron isotope compositions, including $^{\text{nat}}\text{B}$ (21.7% ^{10}B and 78.3% ^{11}B), enriched (99.3%) ^{10}B , enriched (99.2%) ^{11}B , and a roughly equal mix of ^{10}B and ^{11}B ($^{\text{eq}}\text{B}$, 53.1% ^{10}B and 46.9% ^{11}B). The $^{\text{c}^{\text{nat}}}\text{BN}$ crystals were obtained by means of a conventional process by using commercial hexagonal boron nitride (hBN, with $^{\text{nat}}\text{B}$) crystals as a starting material (20–22). Because no boron isotope-controlled hBN crystals were commercially available, we grew the other cBN crystals with a metathesis reaction of $\text{Na}^{\text{m}}\text{BH}_4 + \text{NH}_4\text{Cl}$ under high pressure, where $^{\text{m}}\text{B}$ is ^{10}B or ^{11}B (22). By controlling the mixing ratio of $\text{Na}^{10}\text{BH}_4$ and $\text{Na}^{11}\text{BH}_4$, we achieved the desired boron isotope ratios. We obtained nearly colorless $^{\text{c}^{\text{nat}}}\text{BN}$ crystals with the conventional process, whereas the isotope-controlled cBN crystals from the metathesis reaction generally were a light amber color (Fig. 1A and fig. S1). We made single-crystal x-ray diffraction (XRD) measurements on a ^{10}B BN sample (Fig. 1B and fig. S1) and found a cubic structure with the $F\bar{4}3m$ space group with a refined lattice constant of $3.6165 \pm 0.0005 \text{ \AA}$, which is in good agreement with literature values (5). We observed peaks corresponding to different crystallographic directions, indicating the presence of multiple crystallites (22). We measured the isotope compositions of the cBN crystals using time-of-flight secondary ion mass spectrometry (TOF-SIMS) (Fig. 1C). We also characterized impurities using TOF-SIMS (fig. S2) and found that they mainly consisted of carbon and oxygen, which is consistent with previous results (27). In addition, we used Raman

¹Department of Mechanical Engineering, Massachusetts Institute of Technology, Cambridge, MA 02139, USA.

²Department of Physics, Boston College, Chestnut Hill, MA 02467, USA.

³Department of Materials Science and Engineering and Materials Research Laboratory, University of Illinois at Urbana-Champaign, Urbana, IL 61801, USA.

⁴Materials Science and Engineering Program, Texas Materials Institute, The University of Texas at Austin, Austin, TX 78712, USA.

⁵Department of Physics and Texas Center for Superconductivity, University of Houston, Houston, TX 77204, USA.

⁶Department of Physics, The University of Texas at Dallas, Richardson, TX 75080, USA.

⁷National Institute for Materials Science, Namiki 1-1, Tsukuba, Ibaraki 305-0044, Japan.

⁸Department of Mechanical Engineering, The University of Texas at Austin, Austin, TX 78712, USA.

*These authors contributed equally to this work.

†Corresponding author. Email: songbai@pku.edu.cn (B.S.);

broido@bc.edu (D.B.); gchen2@mit.edu (G.C.)

‡Present address: Department of Energy and Resources Engineering, and Beijing

Innovation Center for Engineering Science and Advanced Technology,

Peking University, Beijing 100871, China.

§Present address: Lawrence Berkeley National Laboratory, and Department of

Mechanical Engineering, University of California, Berkeley, CA 94720,

USA.

¶Present address: Department of Electrical and Computer Engineering, University of California, Riverside, CA 92521, USA.

spectroscopy to identify the isotope compositions (Fig. 1D). As the average mass of boron increases from $c^{10}\text{BN}$ to $c^{11}\text{BN}$, the characteristic Raman peaks for the optical phonons at the Brillouin zone-center red-shift noticeably, scaling with the square root of the reciprocal reduced mass and in good agreement with simulations (fig. S27 and table S1).

We subsequently selected cBN crystals with flat facets of $\sim 200\ \mu\text{m}$ lateral dimension (Fig. 1A) for thermal transport measurements using the laser pump-probe techniques of time- and frequency-domain thermoreflectance (TDTR and FDTR, respectively) (Fig. 2, figs. S3 to S19, and table S4) (11, 15, 16, 22). The $c^{\text{eq}}\text{BN}$ crystals yielded the lowest κ_{RT} of $810 \pm 90\ \text{W m}^{-1}\text{K}^{-1}$, with 53.1% ^{10}B and 46.9% ^{11}B . A higher κ_{RT} of $880 \pm 90\ \text{W m}^{-1}\text{K}^{-1}$ was found for the $c^{\text{nat}}\text{BN}$ crystals, with 78.3% ^{11}B , which was also higher than previously reported measurements (Fig. 3C) (11, 12). As we further enriched the ^{11}B isotope to 99.2%, we observed a κ_{RT} of $1660 \pm 170\ \text{W m}^{-1}\text{K}^{-1}$ in the $c^{11}\text{BN}$ crystals. Likewise, we measured an ultrahigh κ_{RT} of $1650 \pm 160\ \text{W m}^{-1}\text{K}^{-1}$ in the $c^{10}\text{BN}$ crystals with 99.3% ^{10}B , which we confirmed using a different TDTR platform

that gave a κ_{RT} of $1600 \pm 170\ \text{W m}^{-1}\text{K}^{-1}$ (Fig. 3, inset). We found no substantial effect from the metal transducer layer by using both gold and aluminum (Fig. 2C and table S4) and no dependence of κ_{RT} on the pump modulation frequency from 2 to 12 MHz (fig. S16) within the experimental uncertainty. We also performed FDTR measurements (Fig. 2B) on the same set of samples to verify the results and obtained κ_{RT} of $800 \pm 50\ \text{W m}^{-1}\text{K}^{-1}$, $850 \pm 60\ \text{W m}^{-1}\text{K}^{-1}$, $1620 \pm 100\ \text{W m}^{-1}\text{K}^{-1}$, and $1580 \pm 100\ \text{W m}^{-1}\text{K}^{-1}$ for $c^{\text{eq}}\text{BN}$, $c^{\text{nat}}\text{BN}$, $c^{11}\text{BN}$, and $c^{10}\text{BN}$, respectively.

We quantify the isotope effect as $P = (\kappa_{\text{enr}} / \kappa_{\text{nat}} - 1) \times 100\%$, where κ_{enr} and κ_{nat} denote the κ of enriched and natural isotope abundances, respectively. We observed an unusually high ($P \approx 90\%$) isotope effect on heat transport in cBN at RT, which is qualitatively consistent with the modeling result of Morelli *et al.* (18) and a first-principles prediction that included three-phonon and phonon-isotope scattering but ignored four-phonon scattering (13, 19). In comparison, previous experimental efforts only reported a small to moderate isotope effect on other materials. For example, the effect was $P \approx 10\%$ for Si (23), 20% for Ge (24), 5% for GaAs

(25), 15% for GaN (26), and 50% for diamond (27). Isotope effects of 43 and 58% were measured for hBN (28) and graphene (29), respectively. However, first principles calculations for hBN (28) and graphene (30, 31) found much smaller isotope effects of only $\sim 15\%$. Furthermore, the smaller theory values for graphene were within the range of the large error bars in experiment (29).

To understand the high thermal conductivity and large isotope effect we observed in cBN, we used the unified ab initio theory we developed for phonon-mediated thermal transport in solids (22, 32, 33). Briefly, we obtained the required phonon properties and anharmonic interatomic force constants within the density functional theory framework (Quantum ESPRESSO) and acquired the thermal conductivity by solving the Peierls-Boltzmann equation (PBE) for phonon transport, including three- and four-phonon scattering, phonon-isotope, and phonon-impurity scattering. Our approach accounts for the distinction between normal and Umklapp scattering and can accurately predict the thermal and thermodynamic properties of materials from low to high temperatures, from weak to strong anharmonicity, and without any adjustable parameters (22, 32, 33).

We computed the thermal conductivity of ideal cBN crystals versus the percentage of ^{10}B and compared them with the measured values (for three $c^{10}\text{BN}$, two $c^{11}\text{BN}$, one $c^{\text{nat}}\text{BN}$, and two $c^{\text{eq}}\text{BN}$ crystals) (Fig. 3A and table S4). The overall agreement is very good, although some of the measured values for the isotope-enriched cBN samples were noticeably smaller. In order to track down this discrepancy, we computed the influence of carbon and oxygen substitution impurities for boron or nitrogen and found that the defect of oxygen substituting on the boron site (O_B) can substantially reduce thermal conductivity (22). A realistic O_B concentration around 10^{18} to $10^{20}\ \text{cm}^{-3}$ (21) could potentially explain the difference between experiment and theory (Fig. 3A, gray bars), along with the variation across multiple samples and measurements (22). Our simulations predict a high κ for crystals of all boron isotope compositions owing to the shared high-phonon frequencies and group velocities (figs. S22 and S23). A modestly enriched isotope composition such as 98% of either ^{10}B or ^{11}B is sufficient for achieving a κ_{RT} greater than $1400\ \text{W m}^{-1}\text{K}^{-1}$ for cBN. This greatly eases the requirement for boron isotope enrichment, which is important for facilitating potential applications of isotopically enriched cBN. Unlike BAs (11, 13–16), the effect of four-phonon scattering is weak for cBN at all boron isotope compositions because three-phonon scattering dominates over the entire frequency range (Fig. 3B).

We theoretically and experimentally determined the isotope effect for κ_{RT} in BP and BAs,

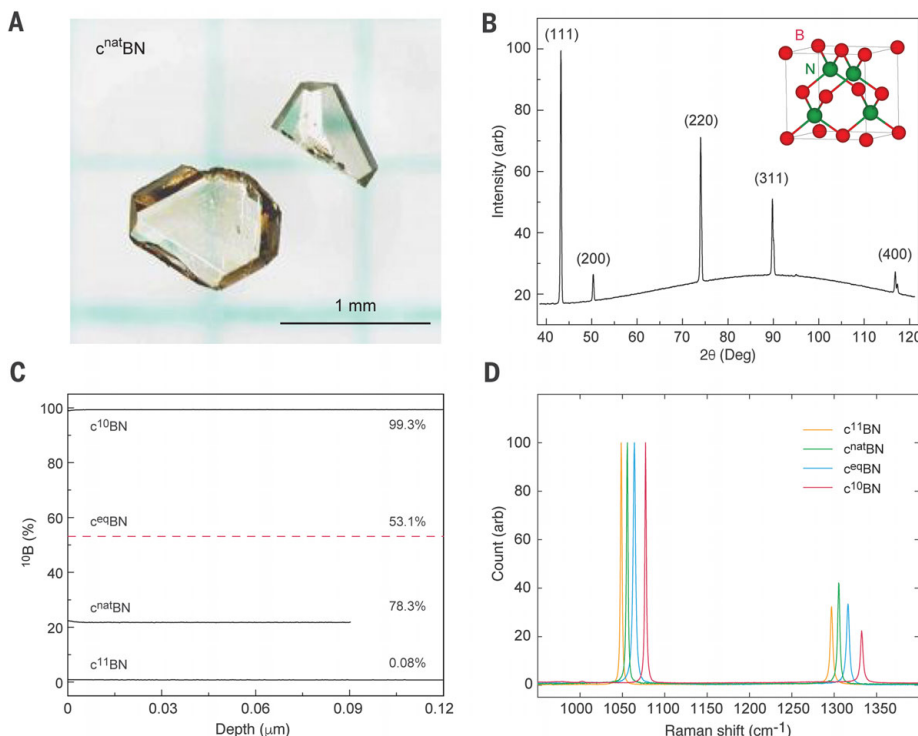


Fig. 1. Structure and composition of homegrown cBN crystals. (A) Optical image of two typical $c^{\text{nat}}\text{BN}$ crystals. (B) XRD pattern from a $c^{10}\text{BN}$ crystal, indicating a zinc-blende structure (inset) with a lattice constant of $3.6165 \pm 0.0005\ \text{\AA}$. Moreover, there appear to be a few crystallites within the sample. Crystals from the same growth batch were used for thermal measurement. (C) Boron isotope concentrations measured with TOF-SIMS. Because no large $c^{\text{eq}}\text{BN}$ crystal was available for an accurate TOF-SIMS measurement, the dashed red line shows an estimation based on the characteristic Raman peaks (fig. S27 and table S1). (D) Raman peak positions as signatures of boron isotope compositions. Representative room-temperature spectra were normalized to the highest peak for better peak-shift visualization.

in order to compare with cBN (22). We found reasonable agreement within uncertainty between our measured, calculated κ and reference κ (Fig. 3A, bottom) (9–11, 15, 16). The κ we measured were 600 ± 90 , 540 ± 50 , and $490 \pm 50 \text{ W m}^{-1} \text{ K}^{-1}$ for ^{10}BP (96% ^{10}B), ^{11}BP (96% ^{11}B), and $^{\text{nat}}\text{BP}$ (19.9% ^{10}B and 80.1% ^{11}B), respectively, and were 1210 ± 130 , 1180 ± 130 , and $1240 \pm 130 \text{ W m}^{-1} \text{ K}^{-1}$ for ^{10}BAs (96% ^{10}B), ^{11}BAs (99% ^{11}B), and $^{\text{nat}}\text{BAs}$ (19.9% ^{10}B and 80.1% ^{11}B), respectively (figs. S20 and S21). The phonon-isotope scattering had much smaller effects on BP and BAs (Fig. 3A). Quantitatively, the κ_{RT} we computed for cBN, BP, and BAs increased by up to $P = 108$, 31, and 12%, respectively, as the boron isotopes became 100% purified. Such dramatic variation in the isotope effect on these boron pnictides seems puzzling because boron dictates the isotope disorder in all of them, whereas the pnictogens either have a negligible isotopic impurity (N) or are isotopically pure (P and As). A key difference, however, lies in the pnictogen-to-boron mass ratios, which vary from ~ 1.3 for cBN, to 2.8 for BP, and 6.8 for BAs.

The strong inverse correlation between the isotope effect on κ and the atomic mass ratio is driven largely by the decreasing phonon-isotope scattering rates going from cBN to BP and BAs (Fig. 3B). In all three compounds, heat is carried mainly by acoustic phonons. The large relative mass difference between ^{10}B and ^{11}B contributes to considerable mass fluctuations in $^{\text{c}^{10}}\text{BN}$, $^{\text{c}^{10}}\text{BP}$, and $^{\text{c}^{10}}\text{BAs}$ (22). With increasing pnictogen-to-boron mass ratio, the vibration amplitudes of the isotopically mixed B atoms decrease sharply for acoustic phonons throughout the Brillouin zone (fig. S25). In BP and BAs, the heavier pnictogens dictate the acoustic phonons, whereas the mass fluctuation on the B sites becomes increasingly invisible, leading to weak phonon-isotope scattering (Fig. 3B). In cBN, the small mass difference between B and N results in large displacements on the B sites for acoustic phonons, which substantially increases the phonon-isotope scattering strength, leading to shorter phonon lifetimes and lower thermal conductivity (Fig. 3B and figs. S25 and S26). The small isotope effect for BAs results not only from the weak phonon-isotope scattering but

also from a competition with four-phonon scattering (Fig. 3B). With only three-phonon scattering, a 40% isotope enhancement of κ was calculated for BAs (13), in contrast with the

much smaller P of 12% upon including four-phonon scattering.

We studied the temperature dependence of the thermal conductivity of cBN from 250 to 500 K, which is important for high-power electronics. The thermal conductivities we measured decreased with increasing temperature (Fig. 3C) and agreed well with our ab initio calculations for the measured boron isotope compositions, except for a small deviation around 250 K. The thermal conductivities of isotope-enriched cBN lie between those of BAs and diamond, with a rate of decrease smaller than that of BAs but similar to that of diamond. The more rapid decrease of κ in BAs reflects the important role played by four-phonon scattering. In fact, the κ of $^{\text{c}^{10}}\text{BN}$ can exceed that of $^{\text{nat}}\text{BAs}$ at elevated temperatures (Fig. 3C and fig. S26), in contrast to previous calculations that did not include four-phonon scattering and found the opposite behavior (13).

We computed the κ accumulation with phonon mean free path (MFP) (34) for cBN at 100, 300, and 500 K (Fig. 3D). Above RT, κ saturates beyond a phonon MFP of $\sim 4 \mu\text{m}$. However, at 100 K, more than 35% ($^{\text{c}^{10}}\text{BN}$) and up to 52% ($^{\text{c}^{10}}\text{BN}$) of the thermal conductivity is contributed by phonons with a MFP longer than $100 \mu\text{m}$. Considering the small size of our isotope-engineered samples (~ 100 to $200 \mu\text{m}$) (Fig. 2B and fig. S1) and the potential existence of multiple crystallites therein (Fig. 1B and fig. S1), we estimated that phonon-boundary scattering could happen at a length scale of $10 \mu\text{m}$ and therefore substantially limit thermal transport at low temperatures. This may explain the discrepancy between the experiment and calculation at 250 K (Fig. 3C and fig. S28), especially for $^{\text{c}^{10}}\text{BN}$ and $^{\text{c}^{11}}\text{BN}$, in which long-MFP phonons have a larger relative contribution to κ and therefore experience a stronger size effect.

Cubic-BN has high hardness and chemical resistance and is important for machining under conditions in which diamond tools may fail (20, 21). Cubic-BN also has a very wide bandgap (6.2 eV), which makes it particularly attractive for ultraviolet optoelectronics (35, 36). We demonstrated a high thermal conductivity of over $1600 \text{ W m}^{-1} \text{ K}^{-1}$ in isotopically enriched cBN crystals.

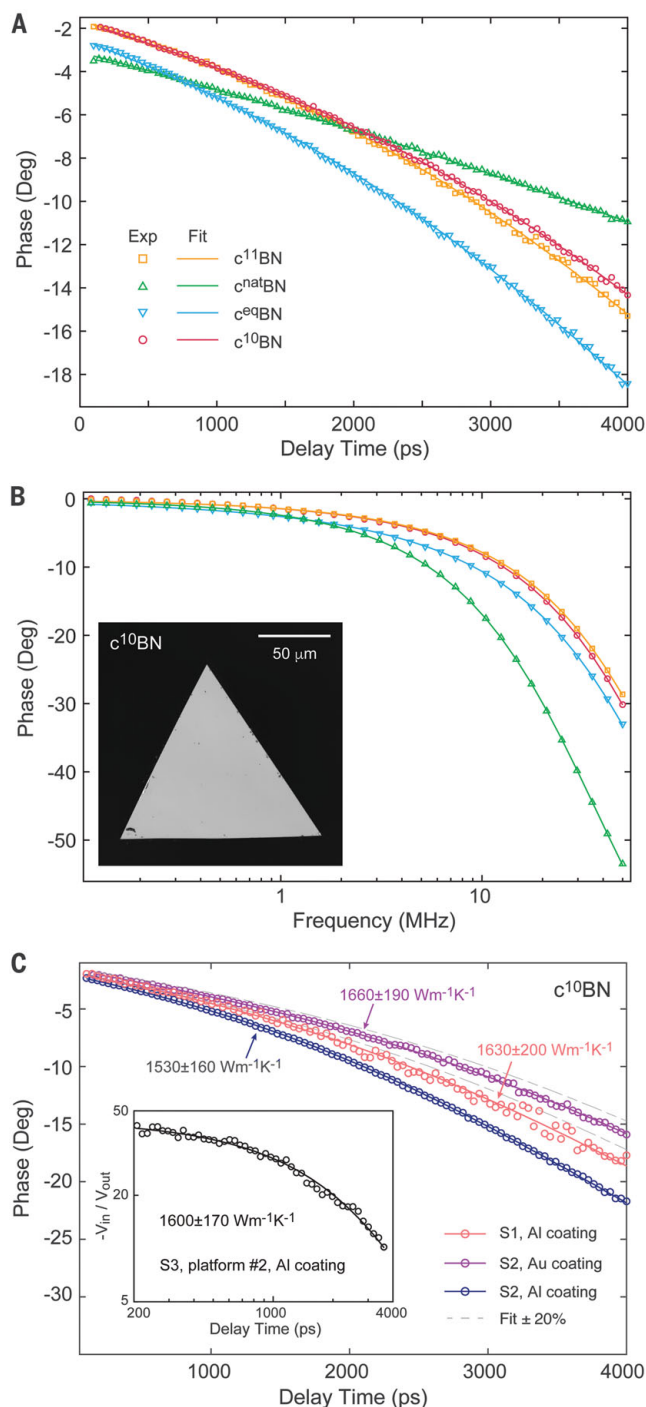


Fig. 2. Heat transport measurement with TDTR and FDTR. (A) TDTR and **(B)** FDTR phase signals measured at RT at the Massachusetts Institute of Technology (MIT) from the same set of cBN crystals together with the fitted curves. (Inset) The flat and clean surface of a $^{\text{c}^{10}}\text{BN}$ crystal imaged with laser confocal scanning microscopy (LCSM). **(C)** TDTR signals measured at MIT on two $^{\text{c}^{10}}\text{BN}$ crystals and with different metal coatings. (Inset) Results for a third $^{\text{c}^{10}}\text{BN}$ crystal measured at the University of Illinois at Urbana-Champaign (UIUC) on a second TDTR platform with different settings (22).

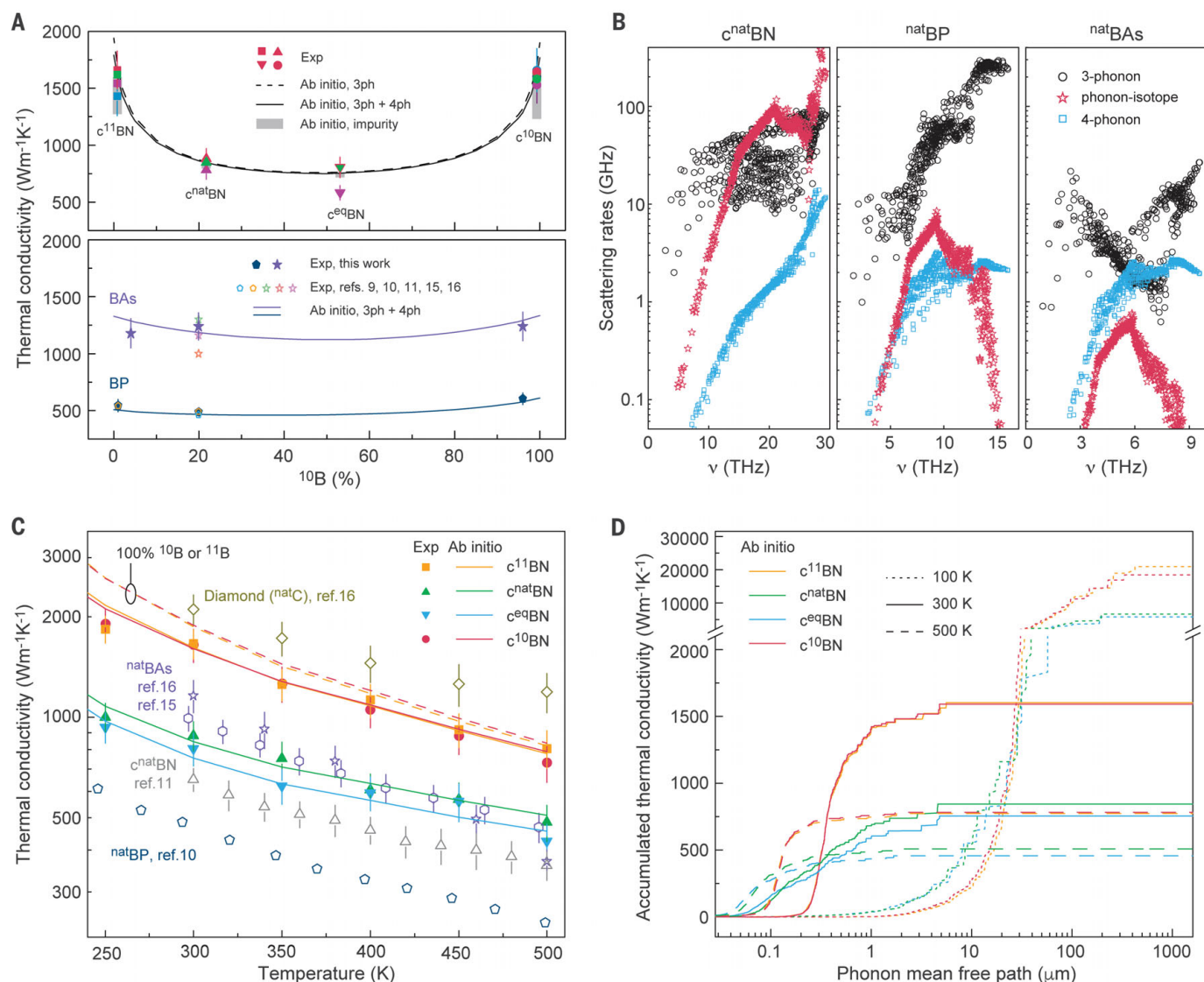


Fig. 3. Isotope effect and temperature dependence of heat transport in cubic boron pnictides. (A) Computed thermal conductivities κ of ideal (top) cBN and (bottom) BAs and BP crystals, compared with measured values (table S4) as a function of isotope composition for three c¹¹BN, two c¹⁰BN, one c^{nat}BN, and two c^{eq}BN crystals. For cBN, the effect of oxygen impurities is indicated with the gray bars. **(B)** Comparison of various phonon scattering rates in cBN, BP, and BAs with natural B at 300 K obtained from ab initio simulations. Phonon-isotope scattering rates are inversely correlated with the pnictogen-to-boron mass ratio.

Four-phonon scattering is weaker than both three-phonon and phonon-isotope scattering in cBN but exceeds phonon-isotope scattering at all frequencies of interest in BAs. **(C)** Measured and calculated κ of cBN crystals versus temperature. The solid lines are calculations for the measured B isotope compositions shown in Fig. 1C, and the dashed lines are for 100% ^{10}B or ^{11}B . Literature data for cBN, BP, BAs, and diamond with natural isotopes are also plotted. **(D)** Calculated κ accumulation with phonon MFP for cBN at 100, 300, and 500 K.

This ultrahigh thermal conductivity was achieved by removing the strong phonon-isotope scattering that occurs in natural cBN. Ab initio calculations reveal that the strong isotope effect we observed was due to the large relative mass difference in boron isotopes combined with weak three- and four-phonon scattering processes. Our measurements and calculations show that the isotope effect found in cBN was sharply reduced in BP and BAs as the isotopic mass disorder becomes increasingly invisible to the heat-carrying acoustic phonons with increasing pnictogen mass. Our

findings demonstrate isotope engineering as one potentially effective method for achieving high thermal conductivity and highlights the potential of isotopically enriched cBN in critical thermal management applications involving high power, high temperature, and high photon energy.

REFERENCES AND NOTES

1. S. L. Shindé, J. Goela, *High Thermal Conductivity Materials* (Springer, 2006).
2. C. Dames, *Science* **361**, 549–550 (2018).
3. R. Berman, F. E. Simon, J. M. Ziman, *Proc. R. Soc. London Ser. A* **220**, 171–183 (1953).

4. G. A. Slack, *J. Phys. Chem. Solids* **34**, 321–335 (1973).
5. R. H. Wentorf Jr., *J. Chem. Phys.* **26**, 956 (1957).
6. J. R. Olson et al., *Phys. Rev. B Condens. Matter* **47**, 14850–14856 (1993).
7. L. Wei, P. K. Kuo, R. L. Thomas, T. R. Anthony, W. F. Banholzer, *Phys. Rev. Lett.* **70**, 3764–3767 (1993).
8. Y. Kumashiro et al., *J. Appl. Phys.* **65**, 2147–2148 (1989).
9. J. S. Kang, H. Wu, Y. Hu, *Nano Lett.* **17**, 7507–7514 (2017).
10. Q. Zheng et al., *Adv. Funct. Mater.* **28**, 1805116 (2018).
11. J. S. Kang, M. Li, H. Wu, H. Nguyen, Y. Hu, *Science* **361**, 575–578 (2018).
12. N. V. Novikov et al., *Dopov. Akad. Nauk Ukr. RSR, Ser. A*, 72–75 (1983).
13. L. Lindsay, D. A. Broido, T. L. Reinecke, *Phys. Rev. Lett.* **111**, 025901 (2013).
14. D. A. Broido, L. Lindsay, T. L. Reinecke, *Phys. Rev. B Condens. Matter Mater. Phys.* **88**, 214303 (2013).

15. S. Li *et al.*, *Science* **361**, 579–581 (2018).
16. F. Tian *et al.*, *Science* **361**, 582–585 (2018).
17. T. Feng, L. Lindsay, X. Ruan, *Phys. Rev. B* **96**, 161201 (2017).
18. D. T. Morelli, J. P. Heremans, G. A. Slack, *Phys. Rev. B Condens. Matter Mater. Phys.* **66**, 195304 (2002).
19. L. Lindsay, D. A. Broido, T. L. Reinecke, *Phys. Rev. B Condens. Matter Mater. Phys.* **88**, 144306 (2013).
20. T. Taniguchi, S. Yamaoka, *J. Cryst. Growth* **222**, 549–557 (2001).
21. T. Taniguchi, K. Watanabe, *J. Cryst. Growth* **303**, 525–529 (2007).
22. Materials and methods are available as supplementary materials.
23. A. V. Inyushkin, A. N. Taldenkov, A. M. Gibin, A. V. Gusev, H.-J. Pohl, *Phys. Status Solidi, C Conf. Crit. Rev.* **1**, 2995–2998 (2004).
24. V. I. Ozhogin *et al.*, *JETP Lett.* **63**, 490–494 (1996).
25. A. V. Inyushkin *et al.*, *Semicond. Sci. Technol.* **18**, 685–688 (2003).
26. Q. Zheng *et al.*, *Phys. Rev. Mater.* **3**, 014601 (2019).
27. T. R. Anthony *et al.*, *Phys. Rev. B Condens. Matter* **42**, 1104–1111 (1990).
28. C. Yuan *et al.*, *Commun. Phys.* **2**, 1–8 (2019).
29. S. Chen *et al.*, *Nat. Mater.* **11**, 203–207 (2012).
30. G. Fugallo *et al.*, *Nano Lett.* **14**, 6109–6114 (2014).
31. L. Lindsay *et al.*, *Phys. Rev. B Condens. Matter Mater. Phys.* **89**, 155426 (2014).
32. N. K. Ravichandran, D. Broido, *Phys. Rev. B* **98**, 085205 (2018).
33. N. K. Ravichandran, D. Broido, *Nat. Commun.* **10**, 827 (2019).
34. C. Dames, G. Chen, in *Thermoelectrics Handbook: Macro to Nano*, D. M. Rowe, Ed. (Taylor and Francis, 2006), pp. 42–1–42–16.
35. K. Watanabe, T. Taniguchi, H. Kanda, *Phys. Status Solidi* **201**, 2561–2565 (2004).
36. Y. Kubota, K. Watanabe, O. Tsuda, T. Taniguchi, *Science* **317**, 932–934 (2007).

ACKNOWLEDGMENTS

We thank Y. Zhou and A. Dolocan for assistance with the thermal and TOF-SIMS measurement, respectively. **Funding:** This work was supported by the Office of Naval Research under Multidisciplinary University Research Initiative grant N00014-16-1-2436. Synthesis of the cBN crystals was supported by the Elemental Strategy Initiative conducted by the Ministry of Education, Culture, Sports, Science and Technology, Japan, and the Japan Society for the Promotion of Science KAKENHI grant 18K19136. The FDTR platform was supported by the National Science Foundation under award CBET 1851052. The TOF-SIMS instrument was purchased through the NSF grant DMR-0923096 at Texas Materials Institute, University of Texas, Austin. **Author contributions:** T.T. and K.W. grew the cBN crystals. H.S., G.A.G.U.G., F.T., and Z.R. grew the BAS

crystals. S.L., H.W., P.K., and B.L. grew the BP crystals. K.C., B.S., and Q.S. performed thermal measurements using TDTR and FDTR at MIT. A.J.S. developed the FDTR platform. B.S. wrote the TDTR data analysis code. K.C. and B.S. performed the analysis. Q.Z., A.R., and D.G.C. performed TDTR measurements at UIUC. B.S. and K.C. measured the Raman spectra, LCSM, and atomic force microscopy images of cBN. X.C., H.L., and L.S. performed TOF-SIMS and XRD characterizations of cBN. N.K.R. and D.B. performed all the ab initio computations of thermal conductivity. Z.D. calculated the Raman peaks. B.S., K.C., N.K.R., D.B., and G.C. wrote the paper. All authors contributed to the writing of the manuscript. The project was directed and supervised by B.S., D.B., and G.C. **Competing interests:** None declared. **Data and materials availability:** All data are available in the manuscript and supplementary materials.

SUPPLEMENTARY MATERIALS

science.sciencemag.org/content/367/6477/555/suppl/DC1
Materials and Methods
Figs. S1 to S30
Tables S1 to S4
References (37–50)

24 September 2019; accepted 20 December 2019
Published online 9 January 2020
10.1126/science.aaz6149

ORGANIC CHEMISTRY

Catalyst-controlled doubly enantioconvergent coupling of racemic alkyl nucleophiles and electrophiles

Haohua Huo, Bradley J. Gorsline, Gregory C. Fu*

Stereochemical control in the construction of carbon-carbon bonds between an alkyl electrophile and an alkyl nucleophile is a persistent challenge in organic synthesis. Classical substitution reactions via S_N1 and S_N2 pathways are limited in their ability to generate carbon-carbon bonds (inadequate scope, due to side reactions such as rearrangements and eliminations) and to control stereochemistry when beginning with readily available racemic starting materials (racemic products). Here, we report a chiral nickel catalyst that couples racemic electrophiles (propargylic halides) with racemic nucleophiles (β -zincated amides) to form carbon-carbon bonds in doubly stereoconvergent processes, affording a single stereoisomer of the product from two stereochemical mixtures of reactants.

Transition metal catalysts for the construction of aryl-aryl bonds have revolutionized organic synthesis (1, 2), particularly in the pharmaceutical industry, where these reactions have enabled the straightforward diversification of lead structures and thereby greatly facilitated drug development. Nevertheless, there is growing recognition in medicinal chemistry that, to improve the prospect for clinical success, it may be advantageous to incorporate more sp^3 -hybridized carbons and more stereocenters into drug candidates (3, 4). Furthermore, from a broader perspective, alkyl-alkyl bonds are even more pervasive in organic molecules than are aryl-aryl bonds.

A particularly straightforward strategy for the construction of alkyl-alkyl bonds is the nucleophilic substitution reaction of an alkyl electrophile with an alkyl nucleophile. Unfortunately, classical pathways for nucleophilic substitution (S_N1 and S_N2 reactions) are effective for only a very small subset of the possible electrophiles and nucleophiles, with side reactions such as elimination (loss of H-X; X, leaving group) or rearrangement often intervening instead (5). Furthermore, products of alkyl-alkyl coupling often bear a stereocenter at one or both carbons of the new bond, whereas uncatalyzed S_N1 and S_N2 reactions typically produce racemic products from racemic reactants.

Recently, we and others have demonstrated that transition metals, in particular earth-abundant nickel, can catalyze nucleophilic substitution reactions of alkyl electrophiles and address key shortcomings (reactivity and stereoselectivity) of classical S_N1 and S_N2 pathways for the construction of alkyl-alkyl bonds (6–12). Because the simultaneous control of two stereocenters in reactions between two

racemic partners is an especially challenging goal (Fig. 1A, iii), efforts have until now focused on the two individual components of this ultimate objective, specifically, enantioconvergent substitution reactions of either racemic electrophiles or racemic nucleophiles, each with achiral reaction partners (Fig. 1A, i and ii, respectively). To date, a range of examples of enantioconvergent substitutions of racemic electrophiles have been described (Fig. 1A, i) (6, 7), whereas in the case of alkyl-alkyl couplings of racemic nucleophiles (Fig. 1A, ii), success has been restricted to a single nucleophile, 2-zincated-*N*-Boc-pyrrolidine (13–15).

Here, we describe progress in addressing the two key stereochemical challenges remaining in such alkyl-alkyl bond formations (Fig. 1A, ii and iii). First, we develop a catalyst that effects enantioconvergent substitutions of achiral alkyl electrophiles by a family of racemic nucleophiles (Fig. 1B, i). Then, building on this foundation, we establish that doubly enantioconvergent substitution reactions of racemic electrophiles by racemic nucleophiles can be accomplished, whereby the chiral catalyst achieves alkyl-alkyl bond formation while simultaneously controlling the stereochemistry at both termini of the newly formed bond (Fig. 1B, ii).

The catalytic enantioselective synthesis of carbonyl compounds that bear a β,β -dialkyl stereocenter is a topic of substantial interest, owing to the presence of such subunits in a variety of bioactive molecules (e.g., valnoctamide) (16, 17). Unfortunately, one particularly powerful strategy for the generation of such targets, the conjugate addition of carbon nucleophiles to α,β -unsaturated carbonyl compounds, requires comparatively reactive nucleophiles (Grignard reagents) in the case of α,β -unsaturated amides, because of their relatively low electrophilicity (18). Because Grignard reagents have somewhat poor functional-group

compatibility, the development of complementary approaches to the direct catalytic asymmetric synthesis of amides that bear such β stereocenters is a worthwhile objective.

In the initial phase of this program, we determined that a chiral nickel/(pyridine-oxazoline) catalyst can achieve enantioconvergent substitution reactions of achiral alkyl iodides by racemic β -zincated amides with good enantioselectivity and yield (Fig. 2). Thus, under our optimized conditions, a β -zincated pentanamide coupled with *n*-hexyl iodide in 90% enantiomeric excess (ee) and 95% yield (entry 1). The ee and yield values together establish that the catalyst is providing enantioselectivity not via a simple kinetic resolution of the racemic nucleophile but instead by selective conversion of both enantiomers of the nucleophile into a single enantiomer of the product.

A wide array of primary alkyl iodides served as suitable electrophiles in this nickel-catalyzed enantioconvergent substitution reaction by a racemic nucleophile (Fig. 2, entries 1 to 17). Substitution proceeded with good ee and yield with electrophiles that varied in steric demand (entries 1 to 4) and bore a broad range of functional groups (entries 5 to 17: an olefin, a silyl ether, a trifluoromethyl group, an acetal, an ester, a ketone, a nitrile, an alkyl chloride, an alkyl bromide, an imide, an amide, and a thiophene). Furthermore, through additive studies (see table S3), we determined that groups such as an aldehyde, an aryl bromide, an aryl chloride, a benzofuran, an epoxide, an indole, and a tertiary amine are compatible with the method.

To achieve the challenging goal of catalyst-controlled doubly enantioconvergent couplings of racemic electrophiles with racemic nucleophiles (Fig. 1A, iii), it is necessary for secondary electrophiles to undergo substitution by secondary nucleophiles; to date, examples of metal-catalyzed secondary-secondary couplings are still scarce (13, 14, 19–22), with the exception of allylation reactions (23). When the conditions developed for nickel-catalyzed enantioconvergent substitution reactions of primary alkyl iodides (conditions 1 in Fig. 2) were applied to cyclohexyl iodide, good enantioselectivity but moderate yield were observed (93% ee, 49% yield at 52% conversion). Small modifications of the reaction conditions (conditions 2 in Fig. 2) led to improved yield with essentially identical enantioselectivity (entry 18: 87% yield, 92% ee). With this method, the chiral nickel/(pyridine-oxazoline) catalyst achieved the enantioconvergent substitution of a range of secondary alkyl iodides, including saturated oxygen and nitrogen heterocycles, by the racemic nucleophile with good ee and yield (entries 18 to 23).

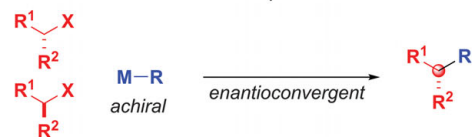
As described above, a single racemic alkyl nucleophile (2-zincated *N*-Boc-pyrrolidine) has previously been shown to engage in enantioconvergent substitution reactions with alkyl

Division of Chemistry and Chemical Engineering, California Institute of Technology, Pasadena, CA 91125, USA.

*Corresponding author. Email: gcfu@caltech.edu

A Catalyst-controlled stereoselectivity: Previous work

- i At the carbon originating from the electrophile (●):
A number of families of electrophiles



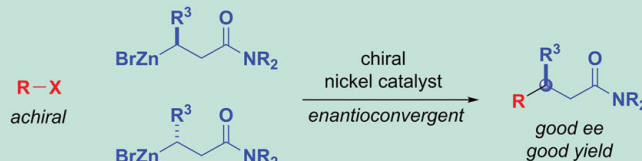
- ii At the carbon originating from the nucleophile (○):
A single nucleophile



- iii At both carbons (●○) of the new carbon–carbon bond:
No examples

**B Catalyst-controlled stereoselectivity: This study**

- i At the carbon originating from the nucleophile (○):
A family of nucleophiles



- ii At both carbons (●○) of the new carbon–carbon bond

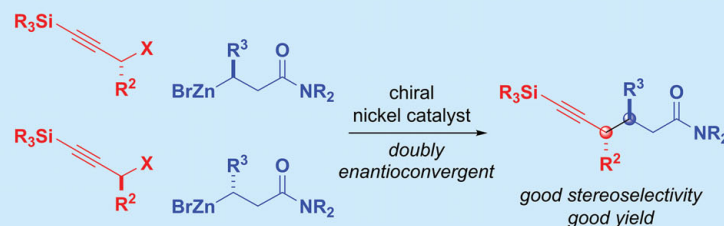


Fig. 1. Alkyl-alkyl bond formation. (A) Catalyst-controlled stereoselectivity—previous work. (B) Catalyst-controlled stereoselectivity—this study. ee, enantiomeric excess; M, metal; R, substituent; X, leaving group.

electrophiles (Fig. 1A, ii) (13, 14). In contrast, the present method is effective for nucleophilic substitutions by a family of racemic nucleophiles, with both primary and secondary alkyl iodides as electrophiles (Fig. 2, entries 24 to 38). For example, the R^3 substituent of the nucleophile can vary in size or bear a functional group, and good enantioselectivities were consistently observed (entries 24 to 33). Furthermore, the standard conditions can be applied to a variety of amides, including Weinreb amides (24) (entries 34 to 38).

Turning next to doubly enantioconvergent alkyl-alkyl bond formation (Fig. 1A, iii), we hypothesized that we might enhance the likelihood for success if we focused our efforts on the use of electrophiles and nucleophiles that have successfully participated in the individual dimensions of this challenge (Fig. 1A, i and ii). We therefore examined the coupling of a racemic propargylic electrophile (25) with a racemic β -zincated amide. Although the nickel/(pyridine-oxazoline)-based conditions that we developed to control one stereocenter with a racemic β -zincated amide (Fig. 2) could not be applied directly to the doubly enantioconvergent substitution reaction, we were able to achieve our goal with a related nickel/(pyridine-oxazoline)-based method (Fig. 3).

Under these conditions, the chiral nickel catalyst coupled a 1.0:1.0 mixture of a racemic electrophile and a racemic nucleophile to provide the substitution product with good enantioselectivity, diastereoselectivity, and yield

[Fig. 3, entry 1: 92% ee, 98:2 diastereomeric ratio (dr), 74% yield]. Together, the values for stereoselectivity and yield establish that this substitution reaction is indeed a doubly enantioconvergent process, whereby the catalyst is transforming both enantiomers of the two racemic starting materials into a particular stereoisomer of the desired product with good stereoselectivity.

On a gram scale, the doubly enantioconvergent substitution reaction illustrated in entry 1 of Fig. 3 proceeded with essentially identical stereoselectivity and yield as for a reaction conducted on a 0.5-mmol scale. A higher turnover number but a lower yield were observed when half of the standard loading of the nickel catalyst was used. The method was not highly sensitive to traces of moisture or air—the addition of 0.1 equivalent of water or 0.5 ml of air led to similar stereoselectivity and only a modest drop in yield.

The scope of the method proved fairly broad with respect to both the propargylic halide and the β -zincated amide. In the case of the propargylic halide, the R^2 substituent could vary in steric demand (Fig. 3, entries 1 to 4) and bear functional groups such as an ether, an acetal, an alkyne, an alkene, an ester, an alkyl chloride, and a furan (entries 5 to 15). Furthermore, a variety of silicon substituents on the alkyne were tolerated (entries 16 to 18).

Similarly, good stereoselectivity and yield were observed with a variety of β -zincated amides. For example, the β substituent (R^3) could range in size and include a variety of

functional groups (Fig. 3, entries 21 to 30). Furthermore, different substituents on the nitrogen of the amide [including a Weinreb amide (24)] were tolerated (entries 19 and 20).

Although we have not yet carried out in-depth mechanistic studies of this process, we have determined that no EPR-active species were observed during a reaction in progress, which is consistent with our previous mechanistic investigations of nickel-catalyzed enantioconvergent coupling reactions of racemic electrophiles, wherein a diamagnetic organonickel(II) complex was suggested to be the primary resting state of nickel during catalysis (26, 27). Furthermore, when a coupling was conducted in the presence of TEMPO (2,2,6,6-tetramethyl-1-piperidinyloxy), adducts derived from both the electrophile and the nucleophile were observed, consistent with the generation of organic radicals from each reaction partner (Fig. 3, mechanistic data); the intermediacy of organic radicals provides a pathway for enantioconvergence of the two racemic reactants. In order for the chiral nickel catalyst to achieve good stereoselectivity in the case of the nucleophile, it must distinguish between two alkyl substituents (R^3 and CH_2CONR_2 in Fig. 3), which can be challenging in asymmetric synthesis. We hypothesize that bidentate **L2**, rather than a tridentate ligand [e.g., a pybox (7)], is effective, because the lower coordination number of the ligand facilitates complexation of the oxygen of the amide to nickel in the stereochemistry-determining step, thereby enabling differentiation of the alkyl groups.

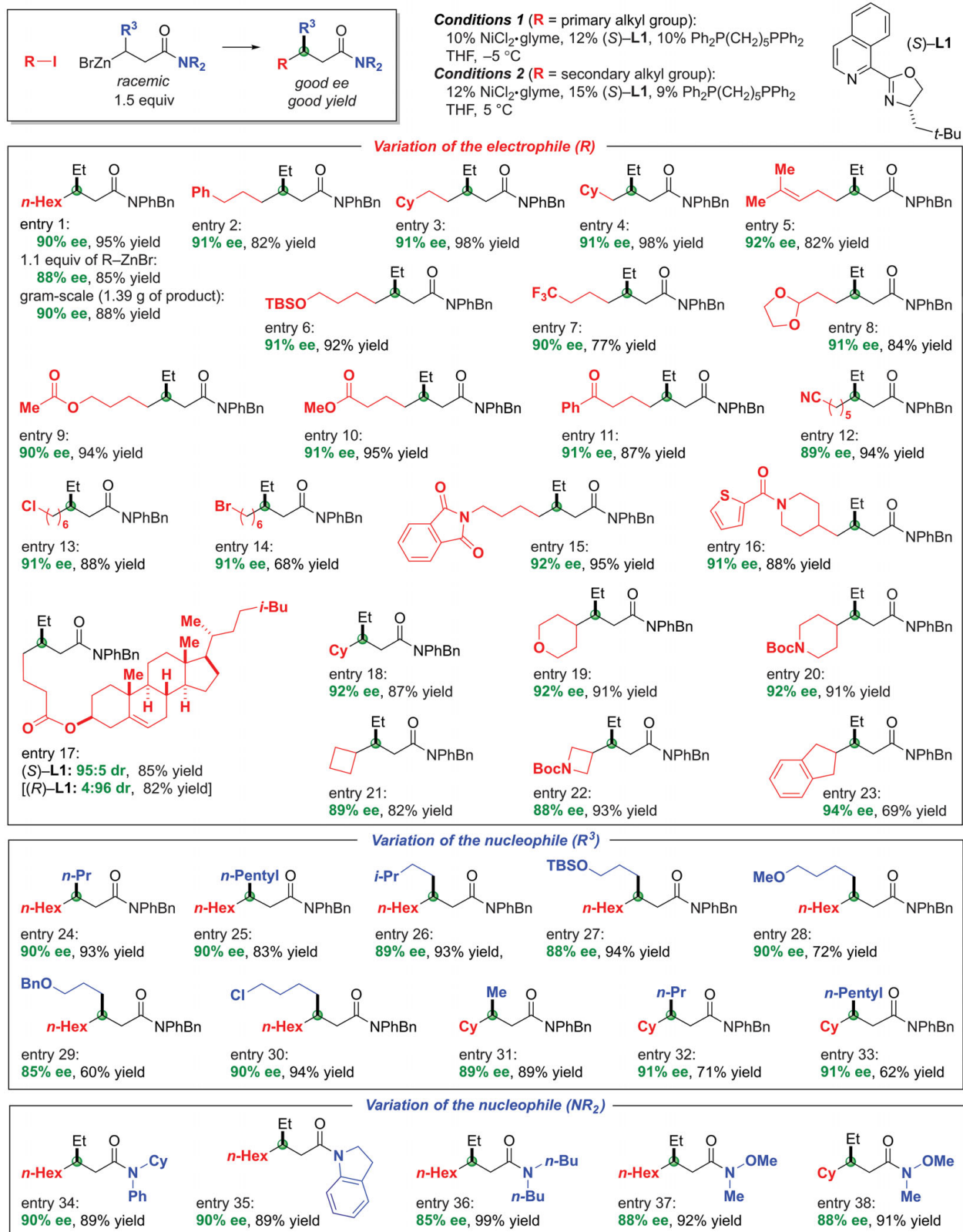


Fig. 2. Enantioconvergent substitution reactions of racemic nucleophiles. Couplings were generally conducted using 0.6 mmol of the electrophile. All data represent the average of two experiments. The percent yield represents purified product. Bn, benzyl; Boc, *tert*-butoxycarbonyl; *i*-Bu, isobutyl; *t*-Bu, *tert*-butyl; Cy, cyclohexyl; Et, ethyl; *n*-Hex, *n*-hexyl; Me, methyl; Ph, phenyl; *i*-Pr, isopropyl; *n*-Pr, *n*-propyl; TBS, *tert*-butyldimethylsilyl.

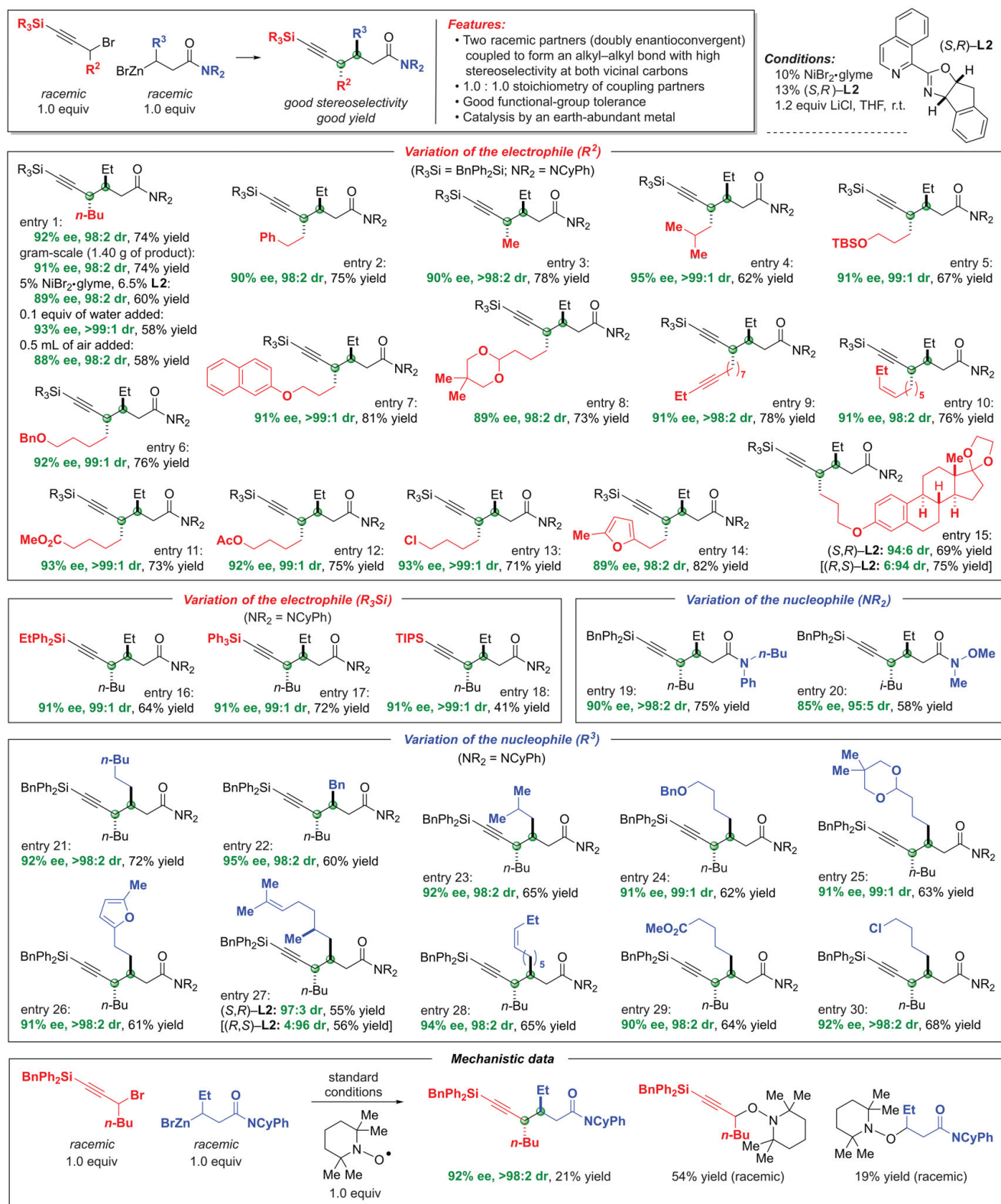


Fig. 3. Doubly enantioconvergent substitution reactions of racemic electrophiles by racemic nucleophiles. Couplings were generally conducted using 0.5 mmol of the electrophile. All data represent the average of two experiments. The percent yield represents purified product. dr, diastereomeric ratio; Ac, acetyl; TIPS, triisopropylsilyl.

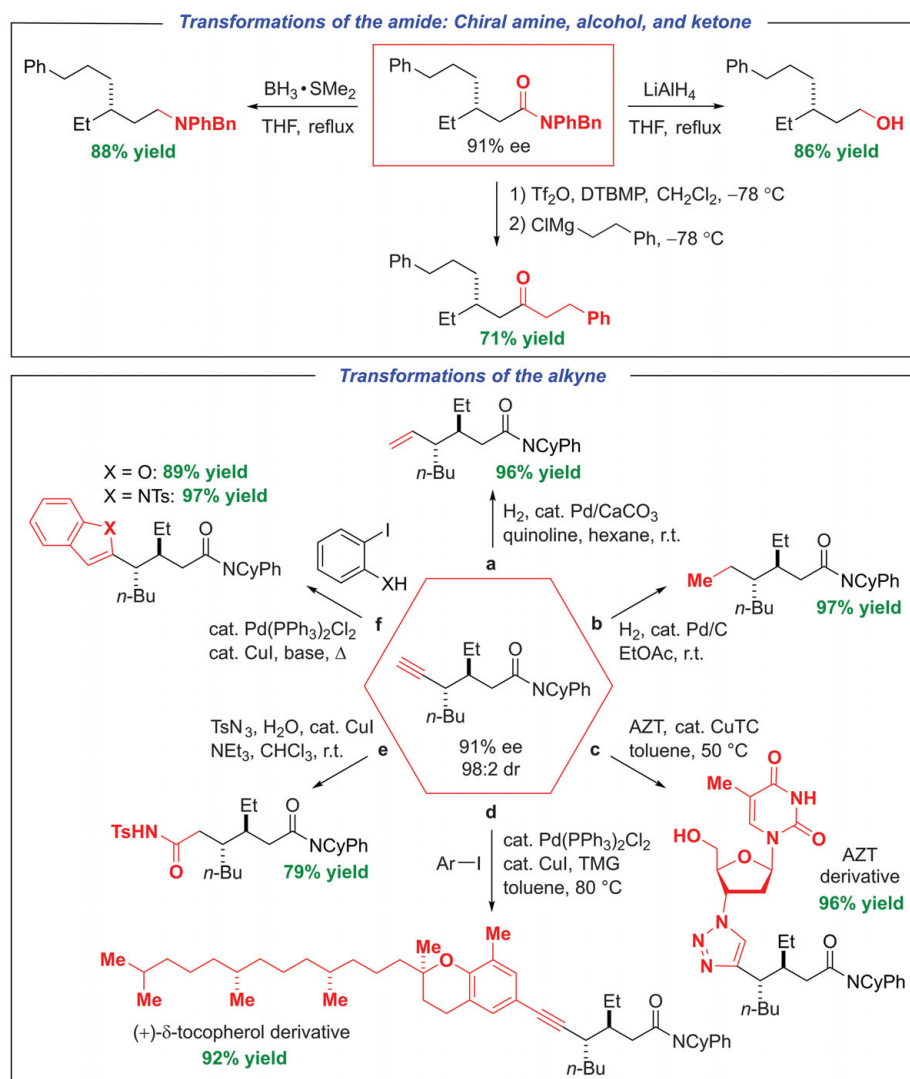


Fig. 4. Transformations into other useful families of enantioenriched compounds. The percent yield represents purified product (average of two experiments). Tf, triflate; DTBMP, 2,6-di-*t*-butyl-4-methylpyridine; AZT, azidothymidine; TC, thiophene-2-carboxylate; TMG, 1,1,3,3-tetramethylguanidine.

The products of these enantioconvergent couplings were readily converted into other useful families of enantioenriched compounds (Fig. 4). For example, *N*-aryl-*N*-alkylamides could be directly transformed in good yield without racemization into tertiary amines, primary alcohols, and dialkylketones (28). Furthermore, alkynes are highly versatile synthetic handles that are suitable for elaboration into a wide variety of useful functional groups (29). Thus, the terminal alkyne (removal of the silicon protecting group: tetra-*n*-butylammonium fluoride, tetrahydrofuran, room temperature; 91% yield) could be reduced to an alkene or an alkane (Fig. 4, reactions a and b, respectively); engaged in an azide cycloaddition (reaction c) (30, 31) or a Sonogashira reaction (reaction d); or converted into an amide (reaction e) (32), an indole, or a benzofuran (reaction f) (33).

Future studies will focus on expanding the scope of these doubly enantioconvergent alkyl-alkyl couplings to include a wide range of activated and unactivated electrophiles, as well as a broad array of conjugated and nonconjugated nucleophiles. Success in these endeavors could transform the enantioselective synthesis of organic compounds.

REFERENCES AND NOTES

- A. Suzuki, *Angew. Chem. Int. Ed.* **50**, 6722–6737 (2011).
- E. Negishi, *Angew. Chem. Int. Ed.* **50**, 6738–6764 (2011).
- F. Lovering, J. Bikker, C. Humblet, *J. Med. Chem.* **52**, 6752–6756 (2009).
- F. Lovering, *MedChemComm* **4**, 515–519 (2013).
- S. R. Hartshorn, *Aliphatic Nucleophilic Substitution* (Cambridge Univ. Press, 1973).
- J. Choi, G. C. Fu, *Science* **356**, eaaf7230 (2017).
- G. C. Fu, *ACS Cent. Sci.* **3**, 692–700 (2017).
- A. Kaga, S. Chiba, *ACS Catal.* **7**, 4697–4706 (2017).
- T. Iwasaki, N. Kambe, *Top. Curr. Chem.* **374**, 66 (2016).

- E. Geist, A. Kirschning, T. Schmidt, *Nat. Prod. Rep.* **31**, 441–448 (2014).
- S. P. Pitre, N. A. Weires, L. E. Overman, *J. Am. Chem. Soc.* **141**, 2800–2813 (2019).
- A. E. Wendlandt, P. Vangal, E. N. Jacobsen, *Nature* **556**, 447–451 (2018).
- C. J. Cordier, R. J. Lundgren, G. C. Fu, *J. Am. Chem. Soc.* **135**, 10946–10949 (2013).
- X. Mu, Y. Shibata, Y. Makida, G. C. Fu, *Angew. Chem. Int. Ed.* **56**, 5821–5824 (2017).
- T. Hayashi, M. Tajika, K. Tamao, M. Kumada, *J. Am. Chem. Soc.* **98**, 3718–3719 (1976).
- T. Shekh-Ahmad, N. Hen, J. H. McDonough, B. Yagen, M. Bialer, *Epilepsia* **54**, 99–102 (2013).
- A. Cordova, Ed., *Catalytic Asymmetric Conjugate Reactions* (Wiley-VCH, 2010).
- M. Rodríguez-Fernández, X. Yan, J. F. Collados, P. B. White, S. R. Harutyunyan, *J. Am. Chem. Soc.* **139**, 14224–14231 (2017).
- C. F. Malosh, J. M. Ready, *J. Am. Chem. Soc.* **126**, 10240–10241 (2004).
- S. W. Smith, G. C. Fu, *Angew. Chem. Int. Ed.* **47**, 9334–9336 (2008).
- C.-T. Yang et al., *J. Am. Chem. Soc.* **134**, 11124–11127 (2012).
- J. T. Binder, C. J. Cordier, G. C. Fu, *J. Am. Chem. Soc.* **134**, 17003–17006 (2012).
- U. Kazmaier, Ed., *Transition Metal Catalyzed Enantioselective Allylic Substitution in Organic Synthesis* (Springer, 2012).
- S. Balasubramaniam, I. S. Aidhen, *Synthesis* **23**, 3707–3738 (2008).
- S. W. Smith, G. C. Fu, *J. Am. Chem. Soc.* **130**, 12645–12647 (2008).
- N. D. Schley, G. C. Fu, *J. Am. Chem. Soc.* **136**, 16588–16593 (2014).
- H. Yin, G. C. Fu, *J. Am. Chem. Soc.* **141**, 15433–15440 (2019).
- P.-Q. Huang, Y. Wang, K.-J. Xiao, Y.-H. Huang, *Tetrahedron* **71**, 4248–4254 (2015).
- B. M. Trost, C.-J. Li, Eds., *Modern Alkyne Chemistry: Catalytic and Atom-Economic Transformations* (Wiley-VCH, 2015).
- V. V. Rostovtsev, L. G. Green, V. V. Fokin, K. B. Sharpless, *Angew. Chem. Int. Ed.* **41**, 2596–2599 (2002).
- C. W. Tornøe, C. Christensen, M. Meldal, *J. Org. Chem.* **67**, 3057–3064 (2002).
- S. H. Cho, E. J. Yoo, I. Bae, S. Chang, *J. Am. Chem. Soc.* **127**, 16046–16047 (2005).
- R. F. Schumacher, A. Honrad, C. Bolm, *Eur. J. Org. Chem.* **2012**, 3737–3741 (2012).

ACKNOWLEDGMENTS

We thank S. H. Jungbauer, S. C. Virgil, L. M. Henling, D. G. Vander Velde, H. Yin, D. J. Freas, W. Zhang, and Z. Yang for assistance and discussions. **Funding:** Support has been provided by the National Institutes of Health (National Institute of General Medical Sciences, R37-GM62871). H.H. thanks the Resnick Sustainability Institute at Caltech for fellowship support. **Author contributions:** H.H. and B.J.G. performed all experiments. H.H. and G.C.F. wrote the manuscript. All authors contributed to the analysis and the interpretation of the results. **Competing interests:** The authors declare no competing interests. **Data and materials availability:** The data that support the findings of this study are available in the paper, in its supplementary materials (experimental procedures and characterization data), and from the Cambridge Crystallographic Data Centre (CCDC) (www.ccdc.cam.ac.uk/structures; crystallographic data are available free of charge under CCDC reference numbers 1935944 and 1935945).

SUPPLEMENTARY MATERIALS

science.sciencemag.org/content/367/6477/559/suppl/DC1
Materials and Methods
Supplementary Text
Figs. S1 and S2
Tables S1 to S5
Spectral Data
References (34–40)

4 September 2019; accepted 26 November 2019
10.1126/science.aaz3855

CRYSTALLOGRAPHY

Crystal symmetry determination in electron diffraction using machine learning

Kevin Kaufmann¹, Chaoyi Zhu^{2*}, Alexander S. Rosengarten^{1*}, Daniel Maryanovsky³, Tyler J. Harrington², Eduardo Marin¹, Kenneth S. Vecchio^{1,2†}

Electron backscatter diffraction (EBSD) is one of the primary tools for crystal structure determination. However, this method requires human input to select potential phases for Hough-based or dictionary pattern matching and is not well suited for phase identification. Automated phase identification is the first step in making EBSD into a high-throughput technique. We used a machine learning–based approach and developed a general methodology for rapid and autonomous identification of the crystal symmetry from EBSD patterns. We evaluated our algorithm with diffraction patterns from materials outside the training set. The neural network assigned importance to the same symmetry features that a crystallographer would use for structure identification.

Identifying structure is a crucial step for the analysis of proteins (1–3), micro- (4, 5) and macromolecules (6), pharmaceuticals (7), geological specimens (8), synthetic materials (9–11), and many other types of materials. Crystal structure plays an important role in the material properties exhibited (12, 13). Determining the crystal symmetry, lattice parameters, and atom positions of the crystal phases is a challenging task, especially for low-symmetry phases and multiphase materials. The most common techniques involve either x-ray diffraction (XRD) or transmission electron microscopy (TEM)–based convergent beam electron diffraction (CBED) (14–16). XRD requires only a sample powder or a polished bulk sample and in most cases only a few hours to collect diffraction intensities over a range of angles. Researchers must refine diffraction patterns to match the experimentally collected pattern to one in a database or from a theoretical model. This process has drawbacks because structural misclassification can occur as a result of lattice parameter shifts, overlapping XRD peaks in multiphase samples, texture effects, and the matching thresholds set by researchers. TEM studies that use CBED are more precise than XRD in their ability to pinpoint the location of individual crystals, produce singular diffraction patterns for a given phase, and capture subtle symmetry information. However, sample preparation, data collection rates, data analysis rates, and the requirement of substantial operator experience limit the throughput for CBED-based studies (17–19).

A scanning electron microscope (SEM) equipped with an electron backscatter diffrac-

tion (EBSD) system has become important for the characterization of crystalline materials and geological samples (8). Nishikawa and Kikuchi discovered EBSD patterns in 1928 (20). Early research by Alam *et al.* (21), Venables *et al.* (22), and Dingley (23) led to the emergence of commercial EBSD systems. The development of fully automated image analysis methods occurred in the early 1990s (24, 25). After the introduction of automated EBSD, commercial software and hardware have evolved to capture more than 3000 patterns per second, which expands the applicability of the technique to assist researchers with more complex problems (26). For example, the high-throughput capability of a modern EBSD system enables determination of fine-scale grain structures, sample texture, point-to-point crystal orientation, residual stress or strain, geometrically necessary dislocation densities, and other information (27–31). The relative ease of sample preparation compared with TEM samples and the larger sample area analysis in less time makes SEM-EBSD an attractive technique for studies of location-specific orientation with high precision (~2°), high misorientation resolution (0.2°), and high spatial resolution (~40 nm) (32). One of the most common applications of EBSD in multiphase samples is phase differentiation along with orientation determination. A user selects the phases presumed to be in the sample, and a program finds the best-fit phase and orientation to the diffraction pattern (33). Selected libraries of simulated diffraction patterns of phases can be used in a dictionary indexing approach to assist with phase differentiation, including when working with deformed or fine-grained materials (34). Phase identification is possible when combined with other analytical techniques such as energy-dispersive x-ray spectroscopy (EDS) or wavelength-dispersive x-ray spectroscopy (WDS) (33, 35, 36). This requires that the chemical and structural information of the phase exists in a theoretical model or crystal

database, such as the Inorganic Crystal Structure Database. A method was developed to determine the crystal structure using EBSD without EDS data, but this requires hand-drawn lines to be overlaid with a high degree of accuracy on individual Kikuchi bands (35, 37). This method is slow and tedious, as it requires manual annotation of each individual pattern. In general, EBSD has been limited to elucidating the orientation of user-defined crystal structures.

Recently, the materials science field has begun to embrace the big data revolution (38). Researchers have shown the ability to predict new compositions for bulk metallic glasses (39), shape-memory alloys (40), Heusler compounds (41, 42), and ultra-incompressible superhard materials (43). Other groups are developing machine-learning methods to establish structure-property linkages (44–46) or to predict the crystal stability of new materials (47). Holm and colleagues (48, 49) have demonstrated the classification of optical microscopy images into one of seven groups with greater than 80% accuracy (48), as well as microconstituent segmentation using the PixelNet convolutional neural network (CNN) architecture trained on manually annotated micrographs of ultrahigh-carbon steel (49). These machine learning–driven analysis techniques represent important developments in the materials science toolbox. Previous studies have attempted crystal symmetry identification using deep neural networks and TEM diffraction; however, the developed model's practical use is hindered by the choice to use images simulated in RGB color, whereas real TEM diffraction patterns are captured in grayscale (50). Another study used full XRD pattern images for single-phase materials (51). These techniques only provide point (TEM) or global (XRD) information about the sample; by contrast, EBSD's mapping capabilities can provide spatially relevant crystallographic information across many length scales. Here, we demonstrate a hybrid methodology, EBSD coupled with a machine-learning algorithm, to identify the Bravais lattice or space group of a bulk sample from diffraction patterns. The trained machine-learning model is subsequently applied to a distinct set of materials it was not trained on, but which contain the same crystal symmetry, and it identifies the correct Bravais lattice or space group with a high degree of accuracy.

We used two CNNs in this work. The two image classification model architectures are ResNet50 (52) and Xception (53) (Fig. 1). We started by constructing a convolution layer, where a learnable filter is convolved across the image. We computed the scalar product between the filter and the input at every position, or “patch,” to form a feature map. Next,

¹Department of NanoEngineering, University of California, San Diego, La Jolla, CA 92093, USA. ²Materials Science and Engineering Program, University of California, San Diego, La Jolla, CA 92093, USA. ³Department of Cognitive Science, University of California, San Diego, La Jolla, CA 92093, USA.

*These authors contributed equally to this work.

†Corresponding author. Email: kvecchio@eng.ucsd.edu

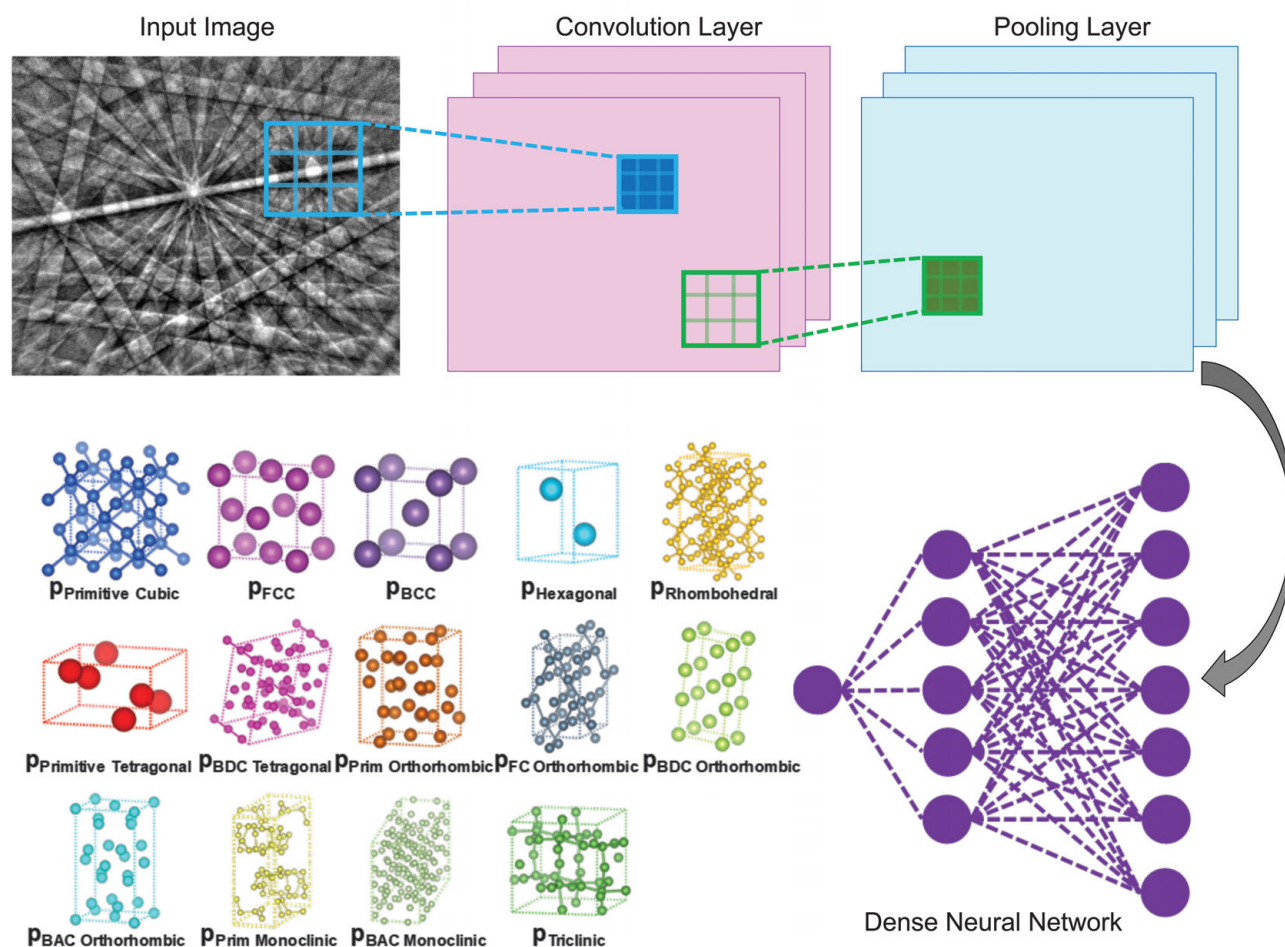


Fig. 1. Illustration of the inner workings of a convolutional neural network. Convolutional neural networks (CNNs) are composed of a series of alternating convolutional and pooling layers. Each convolutional layer extracts features from its preceding layer, using filters (or kernels) learned from training the model, to form feature maps. These feature

maps are then downsampled by a pooling layer to exploit data locality. A traditional dense neural network, a simple type of classification network, is placed as the last layer of the CNN, where the probability that the input diffraction pattern belongs to a given class (e.g., Bravais lattice or space group) is computed.

we sequentially stacked a series of alternating convolutional and pooling layers. We organized the feature maps with the units in a convolutional layer and connected each feature map to local patches in the previous layer through a set of weights called a filter bank. All units in a feature map shared the same filter banks (also called kernels), whereas different feature maps in a convolutional layer used different filter banks. We placed pooling layers after convolutional layers to downsample the feature maps. This produced coarse-grained representations and spatial information about the features in the data. The trained layers of feature detection nodes are “learned” from the data as the algorithm finds motifs encoding the underlying crystallographic symmetry present in the diffraction patterns.

We found that both ResNet50 and Xception (53) CNNs performed similarly well at classifying EBSD patterns. We applied the trained

model to diffraction patterns that were “new” to the algorithm. This means that the patterns were not part of the training set but rather a random mix of orientations that may or may not be similar to the training patterns. Both the ResNet50 (Fig. 2) and Xception (fig. S1) architectures correctly classified nearly 300,000 diffraction patterns with >90% overall accuracy for each architecture. Specifically, this means that no user input was required for the algorithm to identify which of the 14 Bravais lattices each individual EBSD pattern belonged to. The main crystal structure misclassification was jadeite, a monoclinic mineral often assigned to structures containing the same symmetry elements (fig. S1, A and C). This specific misclassification resulted in an overall decrease of the algorithm’s performance. An in-depth analysis of this misclassification type was performed to understand the cause. The model displayed much higher accuracy on all other

materials, typically greater than 95% for individual materials.

We collected 50,000 EBSD patterns from nine completely different materials for blind testing of our algorithms’ crystal symmetry identification. Each architecture correctly classified the Bravais lattice of the unknown material with 93.5% (Fig. 2B) and 91.2% (fig. S2) overall accuracy for ResNet50 and Xception, respectively. The base-centered monoclinic crystal structure has a propensity to be incorrectly classified as primitive orthorhombic or rhombohedral. The base-centered monoclinic, primitive orthorhombic, and rhombohedral Bravais lattices used in training belong to the $2/m$, mmm , and $3m$ point groups, respectively. The $2/m$ and mmm point groups each only have two-fold axis symmetry, mirror plane symmetry, and inversion center symmetry in different multiplicity (table S1). The rhombohedral $3m$ point group shares these same

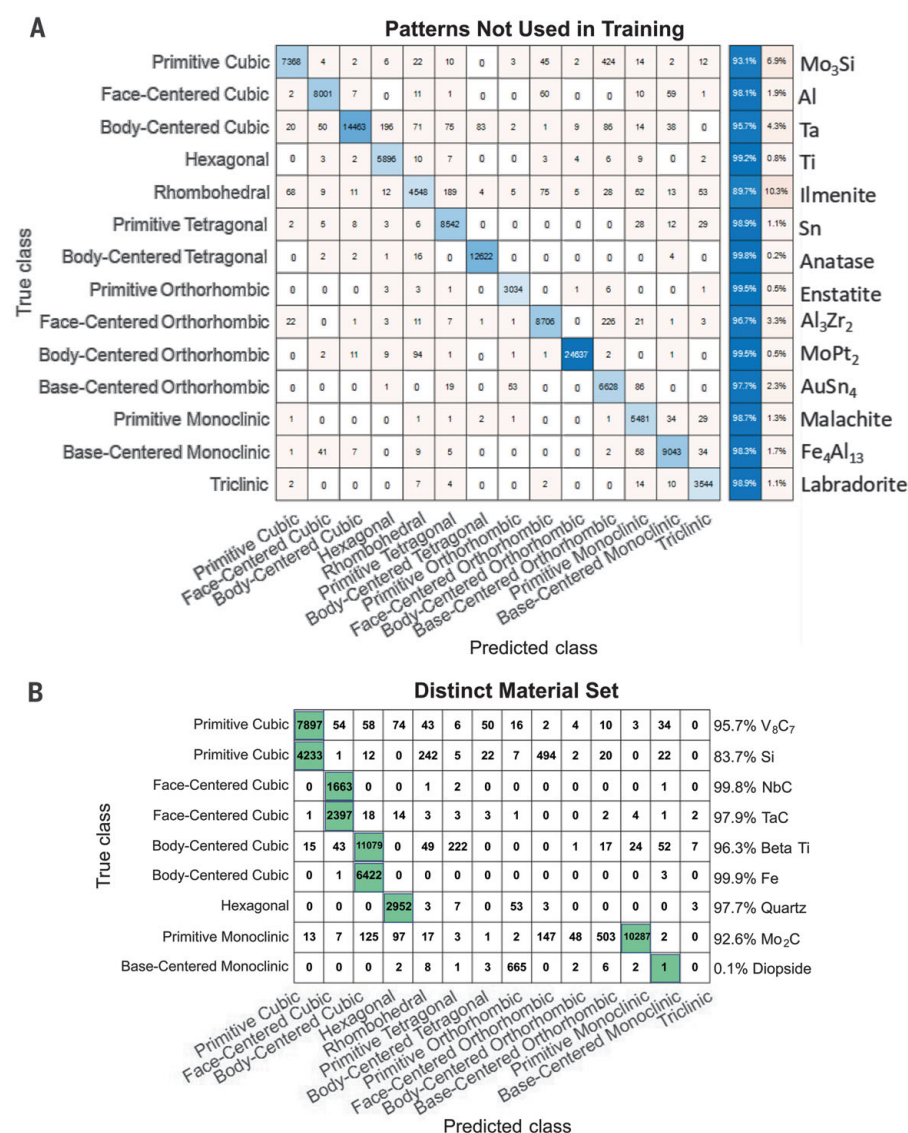


Fig. 2. Confusion matrix displaying the ResNet50 algorithm's classification results. (A) The trained algorithm classifies a second set of diffraction patterns from 14 of the materials. The diagonal (blue shaded boxes) represents the successful matching of the CNN predictions to the true Bravais lattices of the sample. **(B)** The algorithm classifies electron backscatter diffraction patterns collected from materials not used during training of the model. Correct classification is identified by the green squares instead of along the diagonal.

symmetry elements, with the addition of one three-fold axis symmetry. Of the misclassification to these two point groups, the model displays a lesser degree of misclassification to the $\bar{3}m$ point group containing the extra symmetry element, as expected for a well-fit model. This sort of misclassification event presents itself as a potential source of error, especially in a low-symmetry phase, where one pattern from the Kikuchi sphere may not contain enough symmetry elements for the best possible classification.

We also used our method to classify the small changes in atomic arrangement that distinguish space groups within the $4/m, \bar{3},$

$2/m$ (cubic) point group (fig. S3) at a rate of 1 pattern per second. We found that the ResNet50 and Xception algorithms only misclassified a small portion of our as-collected dataset between the selected cubic space groups.

Walking through a specific example of feature identification by the algorithm helps us to understand how it arrives at a correct classification. We start with diffraction patterns of nickel and aluminum with similar crystallographic orientation (Fig. 3). The importance of features in each image is determined by the learned filter banks in the algorithm. The importance of local regions in the image is

elucidated using the trained neural network architecture and a set of tools called Grad-CAM (54). After the algorithm computes the “importance” of these local regions, Grad-CAM maps the normalized weights from 0 (dark blue) to 1 (dark red). These heat maps are similar for nickel and aluminum and show an intense interest of the network in symmetry located at the zone axes. The regions of greatest interest are the $[1\bar{1}2]$ and $[112]$ zone axes (two-fold symmetry). The machine-learning algorithm couples this information with the presence of the $[001]$ (four-fold symmetry) and $[013]$ (two-fold symmetry) zone axes and their spatial relationship, owing to pooling layers, to correctly identify the Bravais lattice as face-centered cubic. We observed a similar interest in information nearest the zone axes for the other materials.

We determined heat maps for the 28 materials we used in the training set (fig. S4). This allowed us to investigate where the algorithm has difficulty with identifications. We used Grad-CAM to investigate the misidentification of diopside (fig. S5). The base-centered monoclinic and primitive orthorhombic class both result in similar activations, with interest centered around the only “x-fold” symmetry present in diopside, the two-fold symmetry $[112]$ zone axis. Because the base-centered monoclinic and primitive orthorhombic structures differ only on the number of two-fold axes and do not possess higher-symmetry elements, the algorithm has difficulty distinguishing between the structures. We observed that the area of greatest interest is not always centered around the bright spot of a zone axis, as for Cr₃Si or Sn, and instead favors the side with other zone axes nearby in the diffraction pattern.

Our algorithm reduced the amount of prior sample knowledge required for crystal structure identification. A common approach for crystal identification is to run the diffraction images through a Hough transform, which helps to extract diffraction maxima at Kikuchi band intersections. This method can lead to misclassification of similar crystal structures that have similar diffraction maxima (55–57). In contrast, our algorithm autonomously uses all the information in each diffraction pattern. To demonstrate how this helps with a multiphase sample, we used rutiled quartz (Fig. 4), which contains a phase that was not in our training set. Our machine learning-generated phase map is nearly identical to the one generated by the Hough-transform method. Of the seven errors, five are located where the traditional method could not index the structure.

Our methodology enables high-throughput and autonomous determination of crystal symmetry in electron backscatter diffraction. We found that the CNN identifies specific

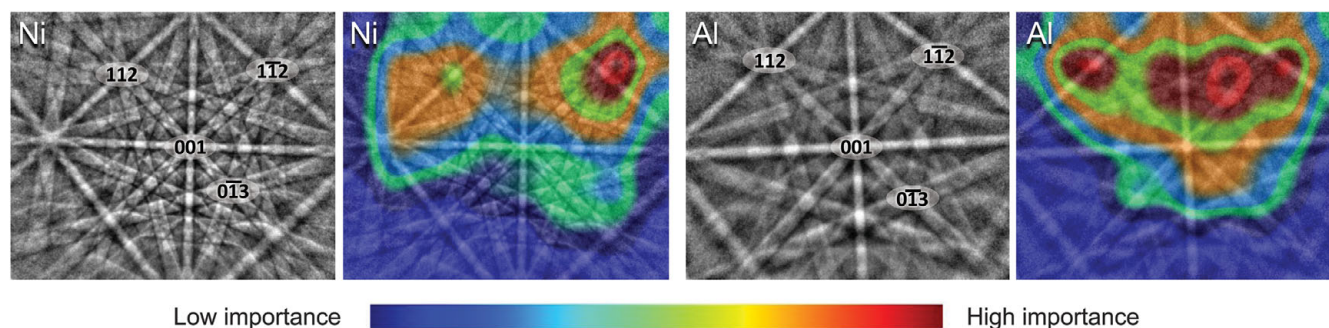


Fig. 3. Visualizing the features used for classification of a diffraction pattern as face-centered cubic (fcc). Electron backscatter diffraction patterns from nickel (Ni) and aluminum (Al) were selected from nearly identical orientations. In the diffraction patterns, four of the zone axes present in each are labeled. The corresponding heat maps

display the importance of information in the image for correctly classifying it as fcc. Note that for each of these two images, the symmetry information near the $[1\bar{1}2]$ zone axis produces the highest activation, followed by the $[112]$ zone axis and the symmetry shared by the $[001]$ and $[0\bar{1}3]$ zone axes.

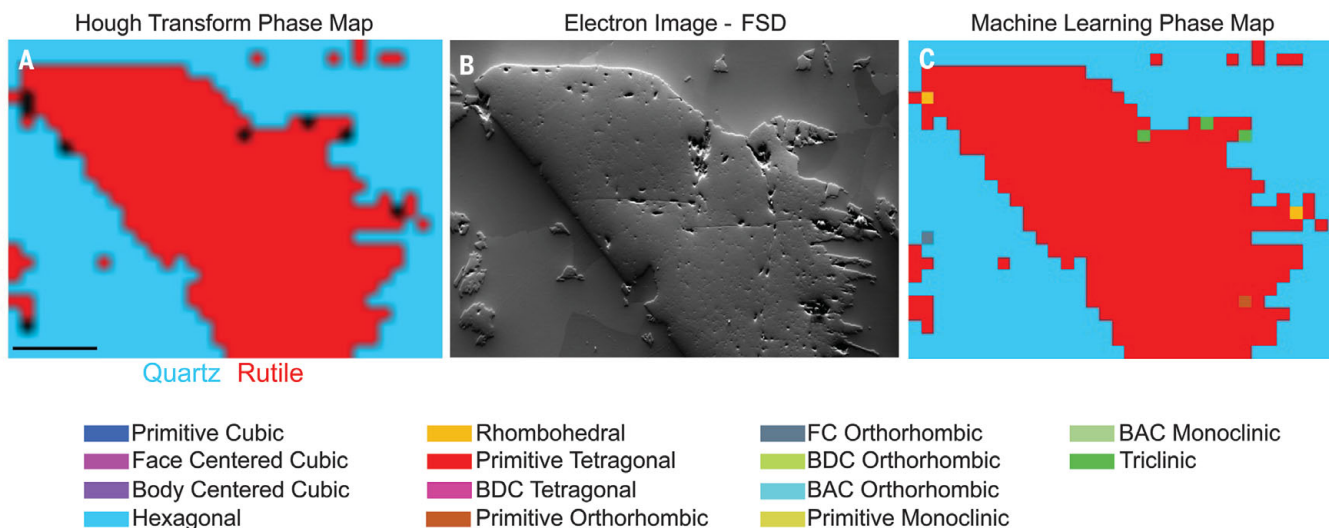


Fig. 4. Comparison of phase-mapping techniques. (A) Phase map generated by traditional Hough-transform EBSD, where the user had to select quartz and rutile as the two specific phases present in the sample. Black pixels could not be identified. (B) Electron image of the region of the sample from

which the diffraction patterns were collected. The quartz appears recessed and rutile emerges above the surface. (C) Phase map generated via machine-learning determination of the Bravais lattice for each diffraction pattern. Scale bar in (A), 100 μm .

features resulting from unique crystal symmetry operations within the diffraction pattern images. The method can potentially be expanded to encompass a multi-tiered model to determine the complete crystal structure. Improvements building on our methodology include neural network architectures specifically designed for specific multiphase samples or through incorporating other data (e.g., phase chemistry) into the algorithm. We believe that a wide range of research areas including pharmacology, structural biology, and geology would benefit by using automated algorithms that reduce the amount of time required for structural identification.

REFERENCES AND NOTES

1. I. M. Abrams, J. W. McBain, *Science* **100**, 273–274 (1944).
2. T. Walz *et al.*, *Nature* **387**, 624–627 (1997).
3. J. A. Rodriguez *et al.*, *Nature* **525**, 486–490 (2015).
4. K. Hedberg *et al.*, *Science* **254**, 410–412 (1991).
5. C. I. Blaga *et al.*, *Nature* **483**, 194–197 (2012).
6. S. W. Hui, D. F. Parsons, *Science* **184**, 77–78 (1974).
7. L. Palatinus *et al.*, *Science* **355**, 166–169 (2017).
8. M. Bestmann, S. Piazzolo, C. J. Spiers, D. J. Prior, *J. Struct. Geol.* **27**, 447–457 (2005).
9. W. J. Huang *et al.*, *Nat. Mater.* **7**, 308–313 (2008).
10. P. A. Midgley, R. E. Dunin-Borkowski, *Nat. Mater.* **8**, 271–280 (2009).
11. S. Curtarolo, D. Morgan, K. Persson, J. Rodgers, G. Ceder, *Phys. Rev. Lett.* **91**, 135503 (2003).
12. J. F. Nye, *Physical Properties of Crystals: Their Representation by Tensors and Matrices* (Clarendon, 1985).
13. J. C. Tan, A. K. Cheetham, *Chem. Soc. Rev.* **40**, 1059–1080 (2011).
14. B. Ollivier, R. Retoux, P. Lacorre, D. Massiot, G. Férey, *J. Mater. Chem.* **7**, 1049–1056 (1997).
15. J. E. Post, D. R. Veblen, *Am. Mineral.* **75**, 477–489 (1990).
16. S. J. Andersen *et al.*, *Acta Mater.* **46**, 3283–3298 (1998).
17. K. S. Vecchio, D. B. Williams, *Metall. Trans. A* **19**, 2885–2891 (1988).
18. K. S. Vecchio, D. B. Williams, *Acta Metall.* **35**, 2959–2970 (1987).
19. D. B. Williams, A. R. Pelton, R. Gronsky, Eds., *Images of Materials* (Oxford Univ. Press, 1991).
20. S. Nishikawa, S. Kikuchi, *Nature* **122**, 726 (1928).
21. M. N. Alam, M. Blackman, D. W. Pashley, *Proc. R. Soc. A* **221**, 224–242 (1954).
22. J. A. Venables, C. J. Harland, *Philos. Mag.* **27**, 1193–1200 (1973).
23. D. J. Dingley, *Scan. Electron Microsc.* **4**, 273–286 (1981).
24. B. L. Adams, S. I. Wright, K. Kunze, *Metall. Trans. A* **24**, 819–831 (1993).

25. N. C. Krieger Lassen, D. Juul Jensen, K. Conradsen, *Scanning Microsc.* **6**, 115–121 (1992).
26. J. Goulden, P. Trimby, A. Bewick, *Microsc. Microanal.* **24** (S1), 1128–1129 (2018).
27. A. J. Schwartz, M. Kumar, B. L. Adams, D. P. Field, Eds., *Electron Backscatter Diffraction in Materials Science* (Springer, 2009).
28. V. Randle, O. Engler, O. Engler, *Introduction to Texture Analysis* (CRC Press, 2014).
29. C. Zhu et al., *Int. J. Plast.* **92**, 148–163 (2017).
30. C. Zhu, T. Harrington, G. T. Gray III, K. S. Vecchio, *Acta Mater.* **155**, 104–116 (2018).
31. C. Zhu, T. Harrington, V. Livescu, G. T. Gray III, K. S. Vecchio, *Acta Mater.* **118**, 383–394 (2016).
32. D. Chen, J. C. Kuo, W. T. Wu, *Ultramicroscopy* **111**, 1488–1494 (2011).
33. M. M. Nowell, S. I. Wright, *J. Microsc.* **213**, 296–305 (2004).
34. F. Ram, M. De Graef, *Acta Mater.* **144**, 352–364 (2018).
35. D. J. Dingley, S. I. Wright, in *Electron Backscatter Diffraction in Materials Science*, A. J. Schwartz, M. Kumar, B. L. Adams, D. P. Field, Eds. (Springer, 2009), pp. 97–107.
36. R. P. Goehner, J. R. Michael, *J. Res. Natl. Inst. Stand. Technol.* **101**, 301–308 (1996).
37. L. Li, M. Han, *J. Appl. Crystallogr.* **48**, 107–115 (2015).
38. A. A. White, *MRS Bull.* **38**, 594–595 (2013).
39. F. Ren et al., *Sci. Adv.* **4**, eaq1566 (2018).
40. D. Xue et al., *Nat. Commun.* **7**, 11241 (2016).
41. A. O. Oliynyk et al., *Chem. Mater.* **28**, 7324–7331 (2016).
42. S. Sanvito et al., *Sci. Adv.* **3**, e1602241 (2017).
43. A. Mansouri Tehrani et al., *J. Am. Chem. Soc.* **140**, 9844–9853 (2018).
44. T. Xie, J. C. Grossman, *Phys. Rev. Lett.* **120**, 145301 (2018).
45. J. Jung, J. I. Yoon, H. K. Park, J. Y. Kim, H. S. Kim, *Comput. Mater. Sci.* **156**, 17–25 (2019).
46. O. Isayev et al., *Nat. Commun.* **8**, 15679 (2017).
47. W. Ye, C. Chen, Z. Wang, I.-H. Chu, S. P. Ong, *Nat. Commun.* **9**, 3800 (2018).
48. B. L. DeCost, E. A. Holm, *Comput. Mater. Sci.* **110**, 126–133 (2015).
49. B. L. DeCost, T. Francis, E. A. Holm, arXiv 1805.08693 [cs.CV] (4 February 2019).
50. A. Ziletti, D. Kumar, M. Scheffler, L. M. Ghiringhelli, *Nat. Commun.* **9**, 2775 (2018).
51. F. Oviedo et al., *Npj Comput. Mater.* **5**, 60 (2019).
52. K. He, X. Zhang, S. Ren, J. Sun, in *Proceedings of the IEEE International Conference on Computer Vision* (2016), pp. 770–778.
53. F. Chollet, in *Proceedings of the IEEE International Conference on Computer Vision* (2017), pp. 1251–1258; http://openaccess.thecvf.com/content_cvpr_2017/papers/Chollet_Xception_Deep_Learning_CVPR_2017_paper.pdf.
54. R. R. Selvaraju et al., *Int. J. Comput. Vis.* 10.1007/s11263-019-01228-7 (2019).
55. T. Karthikeyan, M. K. Dash, S. Saroja, M. Vijayalakshmi, *J. Microsc.* **249**, 26–35 (2013).
56. C. L. Chen, R. C. Thomson, *J. Alloys Compd.* **490**, 293–300 (2010).
57. S. McLaren, S. M. Reddy, *J. Struct. Geol.* **30**, 1229–1241 (2008).

ACKNOWLEDGMENTS

We thank E. Chin of the Scripps Institute of Oceanography and her students for their assistance collecting and identifying mineral and geological samples. **Funding:** Supported by the U.S. Department of Defense (DoD) [through the National Defense Science and Engineering Graduate Fellowship (NDSEG) Program] and the ARCS Foundation, San Diego Chapter (K.K.); the Joint DoD/Department of Energy Munitions Technology Development Program and the Dynamic Materials Science Campaign at LANL (C.Z.); and the Oerlikon Group (K.S.V.). **Author contributions:** K.K. assisted in developing the idea, performed the bulk of the experimental work, worked on later versions of the neural network python code, and prepared the initial draft of the manuscript and figures; C.Z. assisted with the development of the idea into a scientific study, contributed his

knowledge of EBSD, assisted with the figures, and developed MATLAB code for phase-mapping the machine-learning predictions and pattern database management; A.S.R. developed the initial python code for implementing the neural networks; A.S.R. and D.M. managed the deployment of Grad-CAM tools and assisted in the analysis of the results from the deep learning models; T.J.H. assisted K.K. with materials selection, fabrication, and processing; T.J.H. helped focus the research direction; E.M. assisted K.K. with materials fabrication, processing, and analysis; K.S.V. led the development of the idea, guided the focus of the project, and reviewed and revised the manuscript; and all authors participated in analyzing and interpreting the final data and contributed to the discussions and revisions of the manuscript. **Competing interests:** The authors declare no competing interests. **Data and materials availability:** All data and models generated during and/or analyzed during the current study are available from the corresponding author upon reasonable request. The python code for implementing these models with Keras and Tensorflow is available at <https://github.com/krkaufma/Electron-Diffraction-CNN>, Zenodo (DOI: 10.5281/zenodo.3564937) and from the corresponding author upon request. The diffraction patterns analyzed during the current study have not yet been deposited in a publicly available repository because of the sheer size of the library (nearly 3 terabytes). This is an ongoing effort and until then, they are available upon reasonable request.

SUPPLEMENTARY MATERIALS

science.sciencemag.org/content/367/6477/564/suppl/DC1
Materials and Methods
Supplementary Text
Table S1
Figs. S1 to S10
References (58–65)

6 June 2019; accepted 23 December 2019
10.1126/science.aay3062

HUMAN GENETICS

Genetics of schizophrenia in the South African Xhosa

S. Gulsuner¹, D. J. Stein², E. S. Susser^{3,4}, G. Sibeko², A. Pretorius², T. Walsh¹, L. Majara⁵, M. M. Mndini², S. G. Mqulwana², O. A. Ntola², S. Casadei¹, L. L. Ngqengelele², V. Korchina⁶, C. van der Merwe⁵, M. Malan², K. M. Fader³, M. Feng^{3,4}, E. Willoughby⁷, D. Muzny⁶, A. Baldinger², H. F. Andrews^{3,4}, R. C. Gur⁸, R. A. Gibbs⁶, Z. Zingela^{9,10}, M. Nagdee^{9,10}, R. S. Ramesar⁵, M.-C. King^{1*}, J. M. McClellan¹

Africa, the ancestral home of all modern humans, is the most informative continent for understanding the human genome and its contribution to complex disease. To better understand the genetics of schizophrenia, we studied the illness in the Xhosa population of South Africa, recruiting 909 cases and 917 age-, gender-, and residence-matched controls. Individuals with schizophrenia were significantly more likely than controls to harbor private, severely damaging mutations in genes that are critical to synaptic function, including neural circuitry mediated by the neurotransmitters glutamine, γ -aminobutyric acid, and dopamine. Schizophrenia is genetically highly heterogeneous, involving severe ultrarare mutations in genes that are critical to synaptic plasticity. The depth of genetic variation in Africa revealed this relationship with a moderate sample size and informed our understanding of the genetics of schizophrenia worldwide.

Schizophrenia is a disabling neurodevelopmental disorder characterized by aberrant perceptions, thought, and social connectivity. An evolutionary perspective is particularly valuable for understanding the genetic origins of the disorder (1). Because fewer children are born to persons with schizophrenia, mutations underlying the illness are under negative selection. Therefore, the genetic architecture of schizophrenia is characterized

by damaging mutations that are very recent or de novo and thus individually extremely rare (2–5). Common variants with individually small effects on schizophrenia have also been reported (6). Genes implicated by both common and rare alleles operate in pathways that are essential to brain development, including histone modification, neuronal migration, transcriptional regulation, immune function, and synaptic integrity (3–6).

Until now, nearly all genetic studies of schizophrenia have been based in populations of European or Asian ancestries. The goal of the present study was to identify and characterize genetic influences on schizophrenia in the Xhosa population of South Africa. The study was undertaken not because the Xhosa have an unusual prevalence of schizophrenia, but because African populations harbor the greatest wealth of human genetic diversity (7). Nearly 99% of human evolution after the chimpanzee-human divergence 5 to 6 million years ago took place before human migrations from Africa to Eurasia 50,000 to 100,000 years ago. Because relatively small numbers of individuals migrated (8), a very large number of alleles remained on the African continent, creating an African-specific tranche of human genetic variation. Alleles of the African tranche are more rare than the common single-nucleotide polymorphisms (SNPs) shared by all populations and more common than recent mutations that appeared subsequently in all populations. In the absence of studies of ancestral African populations, alleles of the African tranche are missing from our understanding of human disease.

The Xhosa trace their history to the migration of Bantu people from the Great Lakes region of eastern Africa to southern Africa centuries ago. Until the arrival of these migrants, southern Africa was occupied exclusively by San peoples, who diverged from

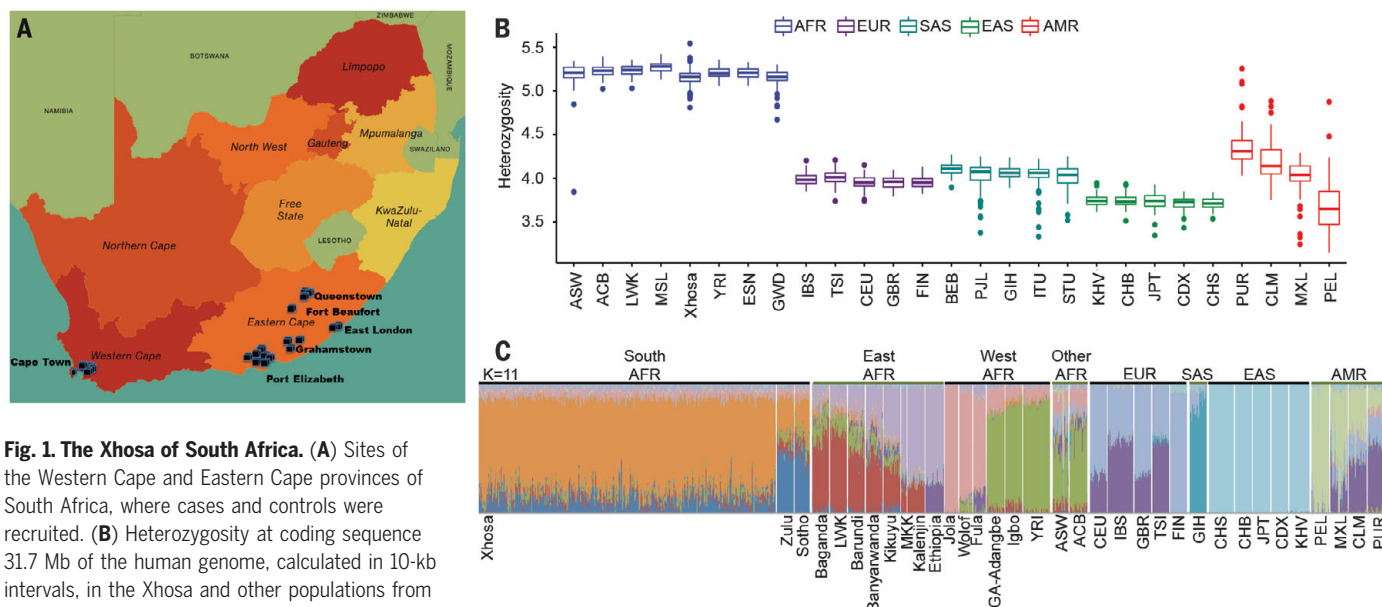


Fig. 1. The Xhosa of South Africa. (A) Sites of the Western Cape and Eastern Cape provinces of South Africa, where cases and controls were recruited. (B) Heterozygosity at coding sequence 31.7 Mb of the human genome, calculated in 10-kb intervals, in the Xhosa and other populations from all continents. (C) Population structure of the Xhosa with respect to other world populations, evaluated by using ADMIXTURE version 1.3.0 with $K = 6$. Genotypes from populations other than the Xhosa are from the African Genome Variation Project and the 1000 Genomes Project. Sources and abbreviations for all populations are listed in the materials and methods.

¹Department of Medicine, Department of Genome Sciences, and Department of Psychiatry, University of Washington, Seattle, WA, USA. ²Department of Psychiatry and Mental Health, University of Cape Town, Cape Town, South Africa. ³Mailman School of Public Health, Columbia University, New York, NY, USA. ⁴New York State Psychiatric Institute, New York, NY, USA. ⁵Division of Human Genetics, University of Cape Town, Cape Town, South Africa. ⁶Human Genome Sequencing Center, Baylor College of Medicine, Houston, TX, USA. ⁷Department of Psychology, University of Minnesota, Minneapolis, MN, USA. ⁸Department of Psychiatry, University of Pennsylvania, Philadelphia, PA, USA. ⁹Department of Psychology, Rhodes University, Makhanda (Grahamstown), South Africa. ¹⁰Department of Psychiatry and Human Behavioral Sciences, Walter Sisulu University, Mthatha, South Africa.

*Corresponding author. Email: mcking@u.washington.edu

other modern humans at least 100,000 years ago (9). Archaeological, linguistic, and DNA evidence indicate that the Xhosa people are descended from the admixture of these Bantu and San populations (10–12). The Xhosa now live throughout South Africa and are the largest population of the Eastern Cape region.

For this project, participants with schizophrenia (cases) were recruited from psychiatric inpatient units and outpatient health clinics in the Eastern Cape Province and Western Cape Province (Fig. 1A). Controls were recruited from the same locales, including patients presenting with conditions not related to mental health. Cases and controls were matched for age, gender, education, and region of recruitment (13).

A total of 2092 individuals, all self-identifying as Xhosa, enrolled in the study. The final cohort for genetic analysis was 1826 individuals, comprising 909 cases and 917 controls. More detailed information regarding sampling strategy, consent, and clinical and demographic features of the cohort is provided in tables S1 and S2 (13). DNA from participants was evaluated by whole-exome sequencing, with quality control and variant interpretation being based on established experimental and bioinformatics methods (figs. S1 to S5) (13).

As expected, genetic variation among the Xhosa (regardless of case-control status) was far greater than among non-Africans (Fig. 1B). Analysis of the Xhosa vis-a-vis other African populations suggested the closest genetic relationship to the Zulu and Sotho populations, their geographic neighbors (Fig. 1C and figs. S6 to S10).

To characterize the genetic architecture of schizophrenia in the Xhosa population, we evaluated contributions from both rare alleles and common alleles. We first compared the numbers of cases versus controls carrying at least one private damaging variant in a gene that was intolerant to such mutations (table S3) (13). A “private variant” was defined as a variant that appeared in only one case or only one control among our participants and that was absent from other population databases (13). “Damaging variants” were defined as nonsense mutations, frameshift mutations, and splice-disrupting and missense mutations that were predicted to be damaging by multiple criteria (13).

Definition of private damaging variants in mutation-intolerant genes yielded “case genes,” which harbored such mutations only in cases, and “control genes,” which harbored such mutations only in controls. For example, *CNTNAPI* was a case gene, harboring four different private damaging variants in cases and none in controls, whereas *MUC5B* was a control gene, harboring seven different private damaging variants in controls and none in cases. Analyses were carried out for minimum thresholds of one, two, or three different private damaging mutations per case gene or per control gene.

Comparisons of cases and controls yielded four significant results. First, cases were significantly more likely than controls to harbor private damaging mutations in case genes or control genes that were intolerant to such mutations (Fig. 2A). Results were similar for thresholds of one, two, and three private dam-

aging mutations per gene and were robust to definitions of intolerance (table S4). These results paralleled those of our prior study of exclusively de novo events in schizophrenia cases and controls (4). As a control for this approach, we compared the numbers of cases versus controls harboring at least one private

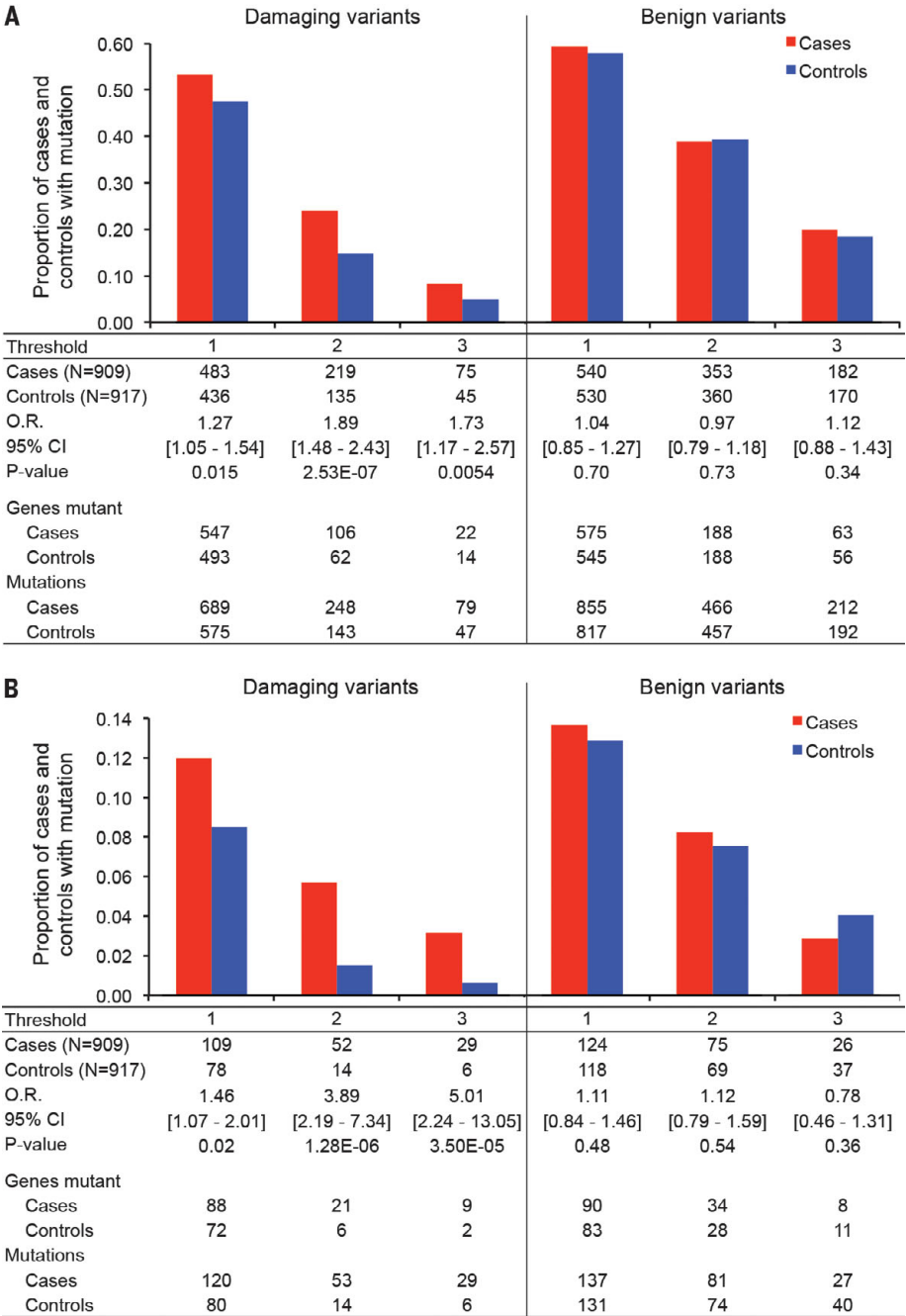


Fig. 2. Distributions of damaging mutations in cases and controls. Histograms indicate the proportions of cases and controls with private damaging mutations in genes with such mutations only in cases (case genes) or only in controls (control genes). Thresholds indicate the minimum number of private damaging mutations that define a case gene or a control gene. (A) Proportions of cases and controls with either private damaging or benign mutations in all case genes or control genes. O.R., odds ratio. (B) Proportions of cases and controls with either private damaging or benign mutations in synaptic genes (15).

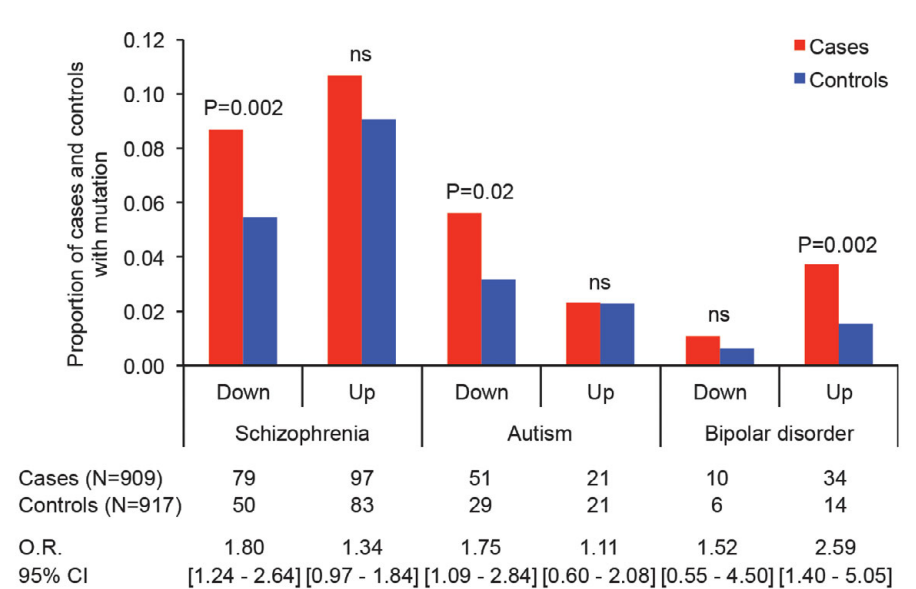


Fig. 3. Proportions of cases and controls with mutations in genes that are dysregulated in severe mental illness. Previous studies evaluated differential gene expression in the postmortem brain of genes from individuals with schizophrenia, autism, and bipolar disorder (16). Integrating these data with mutational profiles of cases and controls reveals that cases were significantly more likely than controls to carry private damaging mutations in genes that are downregulated in schizophrenia or autism or upregulated in bipolar disorder. ns, not significant.

benign mutation in mutation-intolerant genes (13). There were no significant differences between cases and controls for these benign events (Fig. 2A).

Differences in mutation distributions in cases versus controls were consistent with an oligogenic model; that is, the hypothesis that the illness may be caused by one or a few severe damaging variants. Case status was significantly associated with more private damaging mutations per individual [Firth logistic regression, $P = 0.0002$ (13)]. The odds ratio representing the increased risk of being a case associated with each additional mutation was 1.25 [95% confidence interval (CI), 1.11–1.41] (table S5).

Second, cases were significantly more likely than controls to carry private damaging mutations, specifically in genes that are highly expressed in brain (14) (table S6) and in genes that are involved in synaptic functioning (15) (Fig. 2B). Increasingly strong effects were found for subsets of synaptic genes harboring two or three private damaging mutations (Fig. 2B). Again, as a control for the approach, we compared the numbers of cases versus controls harboring at least one private benign mutation in mutation-intolerant synaptic genes. There were no significant differences between cases and controls.

Proportions of HIV-positive individuals differed by case-control status and by gender (table S1). To determine whether HIV status was a confounder for the genomics analyses,

we recalculated all comparisons in two ways: by using HIV status as a covariate in regression and excluding all HIV-positive individuals. Results did not differ from those reported above (table S7).

Third, integration of gene dysregulation profiles from analysis of postmortem brain tissues from individuals with schizophrenia, autism, or bipolar disorder (16) with mutational profiles of Xhosa cases and controls revealed that Xhosa cases were significantly more likely than controls to carry private damaging mutations in genes that are downregulated in schizophrenia or autism, or up-regulated in bipolar disorder (Fig. 3). By contrast, controls were not enriched for damaging mutations in any set of genes that are dysregulated in these illnesses.

The possibility that individual genes were enriched for rare variants in cases versus controls was evaluated by using SKAT (sequence kernel association test) (17). No single gene was significant after multiple-comparison adjustment, although marginal results may prove significant in future studies with larger sample sizes (13) (table S8 and fig. S11).

To evaluate the African tranche of variation, we compared distributions of African-specific exonic variants of frequency 0.01 to 0.10 in cases versus controls by logistic regression, adjusting for covariates (13). In addition, common exonic variants (defined as minor allele frequency MAF ≥ 0.01 in the Xhosa, regardless of frequency in other populations) were eval-

uated by using the same methods. Q-Q plots and Manhattan plots for these analyses are shown in fig. S12. With the caveat that sample size was low for an exome-wide association design, one SNP was significant after exome-wide multiple-comparison adjustment (table S9): rs12600437 in the 3' untranslated region of zinc finger protein ZFP3 had a higher minor allele frequency in controls than in cases.

Cases and controls were assessed for copy number variants (CNVs) in 15 genomic regions enriched for CNVs in schizophrenia and other psychiatric disorders (18). Of the 904 cases and 912 controls with exome data that could be evaluated for CNVs (19), three cases and one control carried a deletion at chromosome 15q11.2, three cases carried a duplication at chromosome 16p13.11, and one control carried a duplication at chromosome 16p11.2 (fig. S13). In addition, one control had karyotype XXY, and one control had karyotype XYY.

Fourth, to determine whether results for the Xhosa generalized to non-African populations, we evaluated data from a case-control study of schizophrenia in the Swedish population (3) using the same methods. We applied our quality control criteria to the Swedish dataset, yielding data from 4436 cases and 5713 controls, then selected random subsets of 909 Swedish cases and 909 Swedish controls 10,000 times, matching for critical covariates (13). For each Swedish subset, we counted the numbers of cases and controls harboring qualifying private mutations, using the same criteria as for the Xhosa cases and controls, then calculated P values from the median numbers of cases and controls for each threshold (table S10). As with the Xhosa, Swedish cases were significantly more likely than controls to harbor private damaging mutations in case genes or control genes that are intolerant to such mutations.

Results for the Xhosa yielded generally larger effect sizes than did the results for the Swedes, reflecting the greater depth of genetic variation of the Xhosa population and hence more rigorous definitions of case-only and control-only genes. For the same number of cases and controls, greater genetic variation in Africa provides more power to detect relationships of genes to phenotypes. The concordance of analyses of the Xhosa and Swedish populations is important, because many findings in genetic studies of schizophrenia do not replicate across populations (20). Results from both populations support disruptions in synaptic signaling and plasticity as being critical to the development of schizophrenia.

We can make some inferences about the causes of schizophrenia given these results. In the Xhosa, private damaging mutations in genes that are critical to synaptic plasticity and neural circuitry were enriched in participants with schizophrenia, with one or a few severe

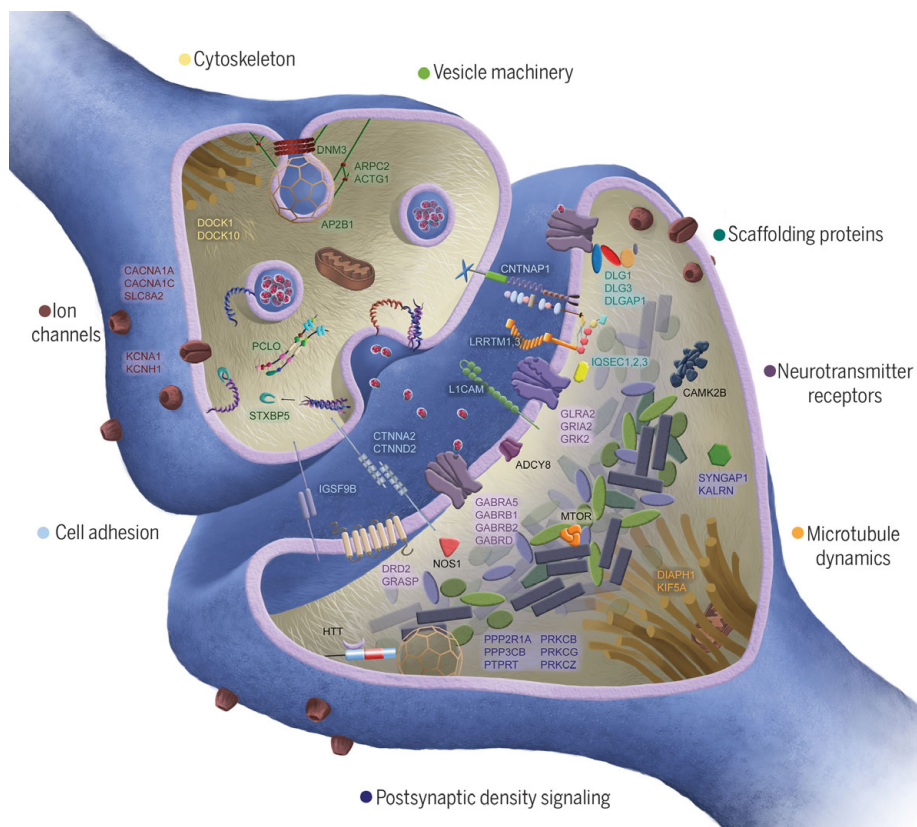


Fig. 4. Synaptic genes harboring damaging mutations in Xhosa persons with schizophrenia. Proteins shown in the figure are encoded by genes that are mutant in at least one individual with schizophrenia. Synaptic genes collectively harbor a significantly greater burden of private damaging mutations in cases compared with controls. No single gene is significantly enriched for private damaging events in cases; most genes have a private damaging variant in one case and no controls.

mutations in each affected individual. Human brain circuitry comprises some 100 million neurons interconnected by synapses, which are the communication hubs for transmitting and processing information. Dynamic changes in dendritic structure and synaptic organization are choreographed by complex signaling cascades involving thousands of proteins, including scaffolds, channels, receptors, kinases, adhesion molecules, signaling enzymes, and cytoskeleton components. These changes are ultimately responsible for learning, memory, and brain function (21).

Genes encoding synaptic proteins are well conserved, intolerant of mutations, and enriched for de novo mutations associated with neurodevelopmental disorders, including intellectual disability, autism, and schizophrenia (15). Among Xhosa cases, synaptic genes harboring private damaging mutations included glutamate (*GRIA2*), γ -aminobutyric acid (*GABRB1*, *GABRB2*, *GABRA5*, and *GABRD*), dopamine (*DRD2*), and glycine (*GLRA2*) receptors; voltage-gated calcium channels (*CACNA1A* and *CACNA1C*); scaffold proteins (*DLG1*, *DLG3*, and *DLGAP1*); cell adhesion molecules (*CNTNAP1*, *CTNND1*, *CTNNA2*, and

CTNND2); and multiple postsynaptic density signaling proteins, kinases, and phosphatases (Fig. 4). Synaptic genes that are disrupted by private damaging mutations in multiple cases include *CACNA1C*, *DLGAP1*, and huntingtin (*HTT*) and its associated kinase kalirin (*KALRN*), each of which was mutant in three cases, and *CNTNAP1*, which was mutant in four cases.

In both African and non-African populations, a causal role for private damaging mutations in genes that are important to brain development is consistent with the nature of schizophrenia and with selection against it. Although schizophrenia is highly heritable, most cases are sporadic, and affected individuals have significantly fewer children, all of which are consistent with a critical role for de novo and recent ultrarare mutations (1). As a result, schizophrenia is characterized by extreme genetic heterogeneity, with no single gene explaining schizophrenia in more than a small number of patients (22).

Advances in treatments for schizophrenia depend on characterizing shared mechanisms underlying the illness. Results from African and European cohorts converge, both implicating disruptions in synaptic architecture

and plasticity. Current antipsychotic medications generally act as antagonists and/or agonists at neurotransmitter receptors, mostly targeting dopamine, serotonin, and adrenergic receptors (23). These agents broadly affect neurotransmitter firing in neuronal circuits throughout the central nervous system, rather than narrowly targeting specific molecular pathways. Although helpful for reducing psychotic symptoms, these agents are not curative and generally do not address the neurocognitive and social difficulties inherent to the disorder (23). The synaptic genes that are disrupted in our cases encode structural components of neurotransmitter and ion channel receptors, cell adhesion proteins, scaffolding proteins, and postsynaptic density signaling molecules (27). Interventions designed to remediate disruptions in synaptic structural organization and intracellular signaling pathways potentially offer more specific therapeutic benefits.

Private damaging mutations in genes that are critical to brain function also appear in controls. For this study, controls were recruited from health clinics, which is a conservative bias because damaging mutations in controls may confer susceptibility to conditions that share genetic influences with schizophrenia. Whether a person harboring a severe mutation in a critical gene develops schizophrenia depends on the biology of the gene, the consequences of the mutation for gene function, and secondary events. For many patients, schizophrenia may be oligogenic, involving a few severe germline mutations and/or brain-specific severe somatic events, either genetic or epigenetic (1, 24). Secondary events may also include nongenetic brain injury during development. To the extent that these secondary events are stochastic, a damaging mutation in a critical gene may not lead to schizophrenia in the person in whom it first appears, but only in subsequent generations.

Finally, the infrastructure, capacity building, and research cohorts currently being established by H3Africa offer enormous promise for gene discovery for complex human phenotypes (25). Human biology is universal, and the study of human genomics in Africa provides an invaluable scientific opportunity to better detect and define genes that are critical for health worldwide.

REFERENCES AND NOTES

1. J. McClellan, M. C. King, *Cell* **141**, 210–217 (2010).
2. A. Ganna et al., *Am. J. Hum. Genet.* **102**, 1204–1211 (2018).
3. G. Genovese et al., *Nat. Neurosci.* **19**, 1433–1441 (2016).
4. S. Gulsuner et al., *Cell* **154**, 518–529 (2013).
5. M. Fromer et al., *Nature* **506**, 179–184 (2014).
6. Schizophrenia Working Group of the Psychiatric Genomics Consortium, *Nature* **511**, 421–427 (2014).
7. J. M. McClellan, T. Lehner, M. C. King, *Cell* **171**, 261–264 (2017).
8. L. L. Cavalli-Sforza, P. Menozzi, A. Piazza, *The History and Geography of Human Genes* (Princeton Univ. Press, 1994).
9. E. R. Chimusa et al., *PLOS Genet.* **11**, e1005052 (2015).
10. J. B. Peires, *The House of Phalo: A History of the Xhosa People in the Days of Their Independence* (Univ. of California Press, 1982).

11. J. L. Newman, *The Peopling of Africa: A Geographic Interpretation* (Yale Univ. Press, 1995).
12. D. W. Phillipson, *African Archaeology* (Cambridge Univ. Press, ed. 3, 2005).
13. Materials and methods are available as supplementary materials.
14. A. Wells et al., *Nucleic Acids Res.* **43**, 10804–10820 (2015).
15. F. Koopmans et al., *Neuron* **103**, 217–234.e4 (2019).
16. M. J. Gandal et al., *Science* **362**, eaat8127 (2018).
17. I. Ionita-Laza, S. Lee, V. Makarov, J. D. Buxbaum, X. Lin, *Am. J. Hum. Genet.* **92**, 841–853 (2013).
18. C. R. Marshall et al., *Nat. Genet.* **49**, 27–35 (2017).
19. N. Krumm et al., *Genome Res.* **22**, 1525–1532 (2012).
20. D. Curtis, *Psychiatr. Genet.* **28**, 85–89 (2018).
21. J. Li et al., *Sci. Signal.* **9**, rs8 (2016).
22. T. Singh et al., *Nat. Neurosci.* **19**, 571–577 (2016).
23. S. J. Kaar, S. Natesan, R. McCutcheon, O. D. Howes, *Neuropharmacology*, 107704 (2019).
24. W. C. Huang, K. Bennett, C. Gregg, *Trends Neurosci.* **41**, 925–937 (2018).
25. C. Rotimi et al., *Science* **344**, 1346–1348 (2014).

ACKNOWLEDGMENTS

This study owes its success to African scientists and medical personnel and the grace of the Xhosa community. Institutional review committees at the University of Cape Town, Walter Sisulu University, Rhodes University, the University of Washington, and Columbia University approved the study. B. Malagas (University of Cape Town data verification officer) audited and reconciled the database. **Funding:** This work was supported by NIH grants U01MH096754 (D.J.S.), U01MH096756 (E.S.S.), U01MH096844 (M.-C.K., J.M.M., and T.W.), and UM1HG008898 with supplementary funding from the National Institute of Mental Health (R.A.G.), the South African Medical Research Council (D.J.S. and R.A.G.), and a NARSAD grant (to S.G.). **Author contributions:** S.G., D.J.S., E.S.S., T.W., R.C.G., R.S.R., M.-C.K., and J.M.M. designed the study. D.J.S., E.S.S., G.S., A.P., M.M.M., S.G.M., O.A.N., L.L.N., A.B., R.C.G., Z.Z., and M.N. designed interview instruments and interviewed and enrolled participants. S.G., T.W., L.M., S.C., V.K., C.v.d.M., D.M., R.C.G., R.A.G., R.S.R., M.-C.K., and J.M.M. performed experiments and evaluated genomic data. A.P., M.M., K.M.F., M.F., A.B., H.F.A., R.C.G., and J.M.M. curated and validated data. S.G., E.W., M.-C.K., and J.M.M. drafted the manuscript and figures.

All authors critically reviewed the manuscript. **Competing interests:** D.J.S. receives research grants and honoraria from Lundbeck Pharmaceuticals and from Sun Pharmaceuticals IndustriesLtd. T.W. is a consultant to Color Genomics. R.A.G. receives payment for genetic testing from Baylor Genetics. All other authors declare no competing interests. **Data and materials availability:** Exome data from consenting participants have been deposited to dbGaP (accession no. phs000959.v1).

SUPPLEMENTARY MATERIALS

science.sciencemag.org/content/367/6477/569/suppl/DC1
Materials and Methods
Tables S1 to S10
Figs. S1 to S13
References (26–50)

[View/request a protocol for this paper from Bio-protocol.](#)

29 July 2019; accepted 18 December 2019
10.1126/science.aay8833

BEE HEALTH

Engineered symbionts activate honey bee immunity and limit pathogens

Sean P. Leonard^{1,2}, J. Elijah Powell¹, Jiri Perutka², Peng Geng², Luke C. Heckmann¹, Richard D. Horak¹, Bryan W. Davies², Andrew D. Ellington², Jeffrey E. Barrick^{2*}, Nancy A. Moran^{1*}

Honey bees are essential pollinators threatened by colony losses linked to the spread of parasites and pathogens. Here, we report a new approach for manipulating bee gene expression and protecting bee health. We engineered a symbiotic bee gut bacterium, *Snodgrassella alvi*, to induce eukaryotic RNA interference (RNAi) immune responses. We show that engineered *S. alvi* can stably recolonize bees and produce double-stranded RNA to activate RNAi and repress host gene expression, thereby altering bee physiology, behavior, and growth. We used this approach to improve bee survival after a viral challenge, and we show that engineered *S. alvi* can kill parasitic *Varroa* mites by triggering the mite RNAi response. This symbiont-mediated RNAi approach is a tool for studying bee functional genomics and potentially for safeguarding bee health.

Honey bees (*Apis mellifera*) are dominant crop pollinators worldwide and a model organism for studying development, behavior, and learning. Recently, high honey bee colony mortality (1), attributed largely to synergistic interactions between parasitic mites (*Varroa destructor*) and RNA viruses (2), has become a critical problem for agriculture and the maintenance of natural biodiversity. Despite the importance of honey bees, studies of honey bee biology are limited by bees' unusual social structure and reproductive biology. New genetic tools and methods for deterring pathogens are vital for understanding and protecting honey bees.

Honey bees possess the molecular machinery for RNA interference (RNAi) (3), a eukaryotic antiviral immune system in which double-stranded RNA (dsRNA) triggers degradation of other RNAs with similar sequences. RNAi can be induced by feeding or injecting dsRNA, and this has been used to knock down expression of bee genes and to impair replication of RNA viruses, including deformed wing virus (DWV) (4–8). dsRNA administered to bees is transmitted to their eukaryotic parasites and can induce parasite RNAi responses. This approach has been used to suppress *Varroa* (9) and *Nosema* (10) by using dsRNAs that silence essential parasite genes. However, use of dsRNA for sustained manipulation of bee gene expression or control of bee pests has proven difficult. Even administration of dsRNA to individual bees yields patchy and transient gene knockdown (11), and dsRNA can have off-target effects (12–14). There are even greater obstacles to using dsRNA to defend entire hives located in the field against pathogens,

as dsRNA is expensive to produce and degrades rapidly in the environment.

Here, we describe successful efforts to engineer *Snodgrassella alvi* wkB2, a symbiotic bacterium found in bee guts, to continuously produce dsRNA to manipulate host gene expression and protect bees against pathogens and parasites.

S. alvi is a core member of the conserved gut microbiota of honey bees (15). To test whether engineered *S. alvi* robustly colonizes bees, we inoculated newly emerged, antibiotic-treated bees en masse with *S. alvi* transformed with a plasmid expressing green fluorescent protein (GFP) and then monitored bacterial colonization (Fig. 1). Even at a dose of 500 colony-forming units (CFU), engineered *S. alvi* establishes within worker bees, grows to $\sim 5.0 \times 10^7$ CFU after 5 days (Fig. 1A), and persists stably throughout the life span of bees reared in the lab (Fig. 1B). Most engineered *S. alvi* cells remained functional throughout our 15-day experiments, although some bees contained cells that lost fluorescence at the final time point (Fig. 1C). We also confirmed that, 11 days after colonization, engineered *S. alvi* was found along the gut wall with the same localization as the wild-type strain (Fig. 1, D to F) (15).

To test whether *S. alvi* can deliver dsRNA in situ, we designed a modular platform to assemble plasmids that produce dsRNA from an inverted arrangement of two promoters (fig. S1). First, we assessed whether *S. alvi* produced dsRNA during colonization and whether there was a general bee immune response to symbiont production of dsRNA. We inoculated bees with *S. alvi* wkB2 transformed with either a plasmid that expressed no dsRNA (pNR) or a plasmid that expressed dsRNA corresponding to the GFP coding sequence (pDS-GFP). At 5, 10, and 15 days after inoculation, we sampled and dissected bees to measure RNA levels in different body regions. We detected GFP RNA in the head, gut,

and hemolymph of bees colonized with dsRNA-producing bacteria at all sampling times (fig. S2). The presence of GFP RNA in the hemolymphs and heads of bees, where no bacteria reside, suggests that RNA is transported throughout their bodies, as previously reported (8). We also detected up-regulation and differential expression of immune pathway genes in the bees colonized with *S. alvi* bearing the pDS-GFP plasmid, and for some genes this up-regulation correlated with the amount of dsRNA produced in the gut (fig. S2). The up-regulated genes included *DDX52* and *DHX33*, which encode RNA helicases previously implicated in the bee immune response to dsRNA (8). Other up-regulated genes included *cact1* and *cact2* (in abdomens), which remained up-regulated for the entire 15-day trial; *cact1* and *cact2* were previously shown to be up-regulated after injection of dsRNA, but only for a few hours (8). The RNAi components *dicer* and *argonaute* were not consistently up-regulated, but *dicer* expression in abdomens did increase 5 to 10 days after colonization, as reported for *dicer* shortly after dsRNA injection (8). Thus, engineered *S. alvi* persistently produces dsRNA in situ, and the bee host responds by activating immune pathway genes.

Next, we tested whether symbiont-produced dsRNA can be used to silence specific host genes. The insulin/insulin-like growth factor signaling pathway controls bee feeding behavior and development, including the transition of worker bees from nurses to foragers (16). We built a dsRNA plasmid targeting the insulin receptor *InR1* (pDS-InR1) (Fig. 2A and fig. S3), transformed this plasmid into *S. alvi*, and assayed its effects on bees. Compared with the pDS-GFP off-target control, we saw significantly lower expression of *InR1* over multiple days and in all tested body regions (Fig. 2B). In contrast, previous studies found that direct injections of dsRNA into honey bee brains cause only transient (<1 day) knockdown (17). Bees colonized by bacteria harboring the pDS-InR1 plasmid showed increased sensitivity to low concentrations of sucrose (Fig. 2C) and gained more weight over time in each of two independent trials (Fig. 2D and fig. S4). *InR1*-suppressing bacteria led to significantly heavier bees at 10 and 15 days after colonization, likely a product of increased feeding behavior. Thus, symbiont-mediated RNAi systemically silences bee genes and can lead to persistent behavioral and physiological changes.

Next, we tested whether symbiont-produced dsRNA can protect bees against a common viral pathogen. We designed three dsRNA-producing plasmids targeting different sections of the DWV genome (pDS-DWV1 to pDS-DWV3) (fig. S5) and then initially assessed whether *S. alvi* with these plasmids could help bees resist DWV infection (fig. S6). We orally inoculated bees with DWV and 48 hours later assessed viral

¹Department of Integrative Biology, The University of Texas at Austin, Austin, TX 78712, USA. ²Department of Molecular Biosciences, The University of Texas at Austin, Austin, TX 78712, USA.

*Corresponding author. Email: nancy.moran@austin.utexas.edu (N.A.M.); jbarrick@cm.utexas.edu (J.E.B.)

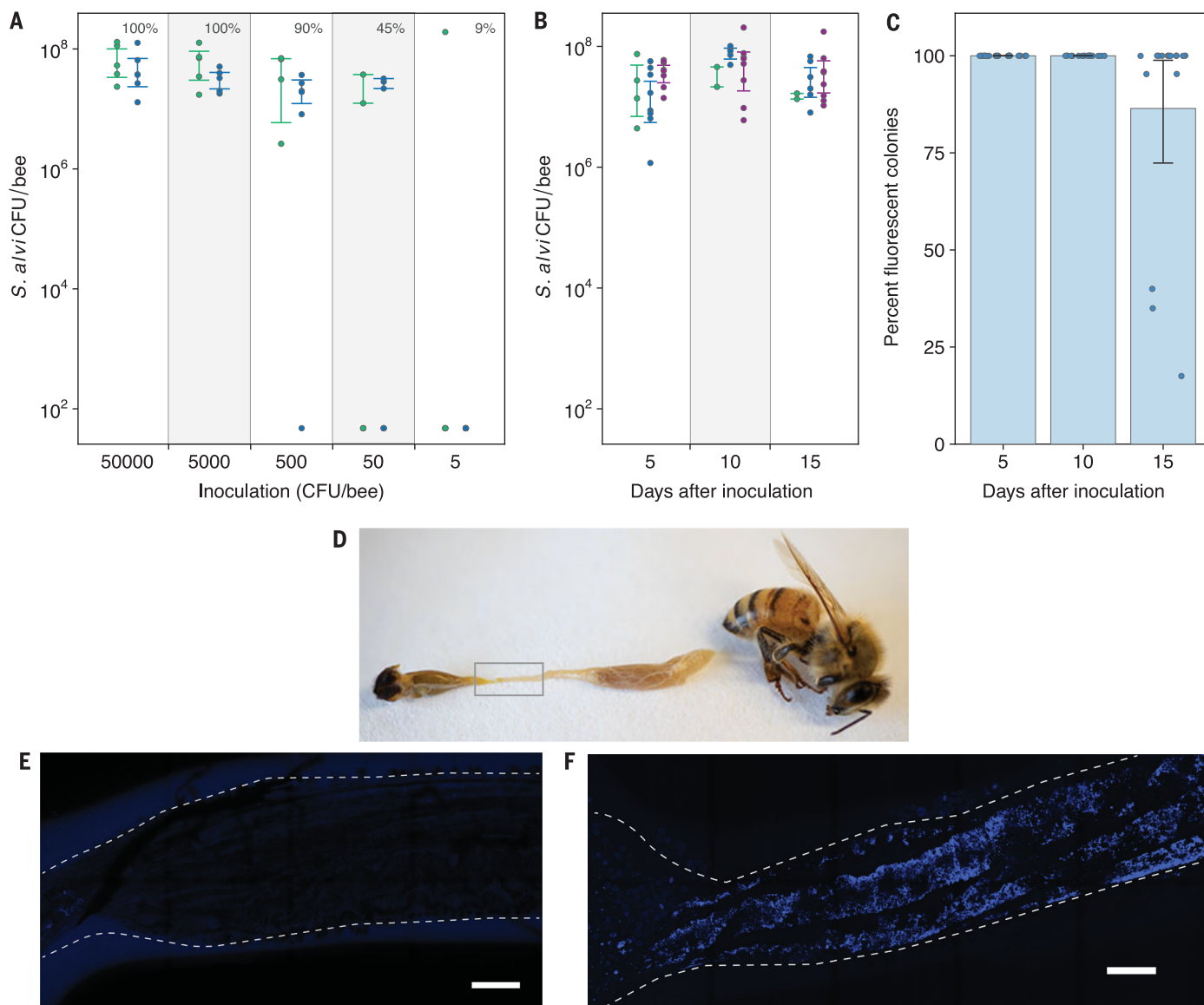


Fig. 1. Engineered *S. alvi* colonizes and functions in bee guts. (A) Colonization of newly emerged honey bees by different inoculum sizes. The percentage of bees colonized in each treatment is annotated above the inoculation dose. $N = 53$ bees from two hives. (B) Stability of *S. alvi* colonization over time. $N = 48$ bees from three hives. Colors in (A) and (B) correspond to different source hives. (C) Stability of GFP expression by engineered *S. alvi* over time. (D) Photograph of dissected bee. *S. alvi* resides in the ileum (gray box). (E and F) Ile of bees 11 days after colonization with nonfluorescent (E) or fluorescent (F) *S. alvi*. E2-Crimson fluorescence from engineered *S. alvi* is blue. Scale bars, 150 μm . Error bars in (A) to (C) are 95% bootstrap confidence intervals.

replication in the hemolymph using a quantitative polymerase chain reaction assay. DWV levels were lower, on average, in bees colonized by *S. alvi* with any dsRNA-producing plasmid, including the off-target pDS-GFP control (figs. S6A and S7). The *dicer* gene was also up-regulated in bees inoculated with most dsRNA-producing plasmids after virus exposure (fig. S6B). These results suggest some nonspecific induction of an immune response in bees colonized with *S. alvi* expressing dsRNA. However, only the pDS-DWV2 plasmid significantly increased survival in a separate experiment in which bees were injected with purified virus (fig. S6C).

To validate the latter finding, we performed a larger experiment to assess whether dsRNA-producing bacteria improved survival after DWV injection. This procedure mimics the natural route of DWV transmission via *Varroa* mites feeding on bees (2). We injected cohorts of 7-day-old bees with DWV and monitored their survival over 10 days (Fig. 3). After DWV injection, bees with bacteria bearing pNR died rapidly. Likewise, pDS-GFP provided no significant protection. In contrast, pDS-DWV2 significantly improved survival of virus-injected bees. Thus, symbiont-mediated RNAi can protect honey bees from DWV, and it does so in a targeted, sequence-specific manner.

Finally, we tested whether symbiont-produced dsRNA can protect bees against *Varroa* mites. When *Varroa* mites parasitize bees, they feed on fat bodies (18) and ingest dsRNA present in that tissue, triggering their own RNAi response. Using mite RNAi to target essential mite genes results in mite death or lowered reproduction (8). We designed a dsRNA-producing plasmid with 14 concatenated sequences from essential genes previously shown to kill *Varroa* (pDS-VAR) (Fig. 4A and fig. S8) (8). We inoculated bees with *S. alvi* bearing pNR, pDS-GFP, or pDS-VAR; introduced adult *Varroa* mites 5 days later; and monitored mite survival for 10 days. Mites that fed on bees colonized with pDS-VAR

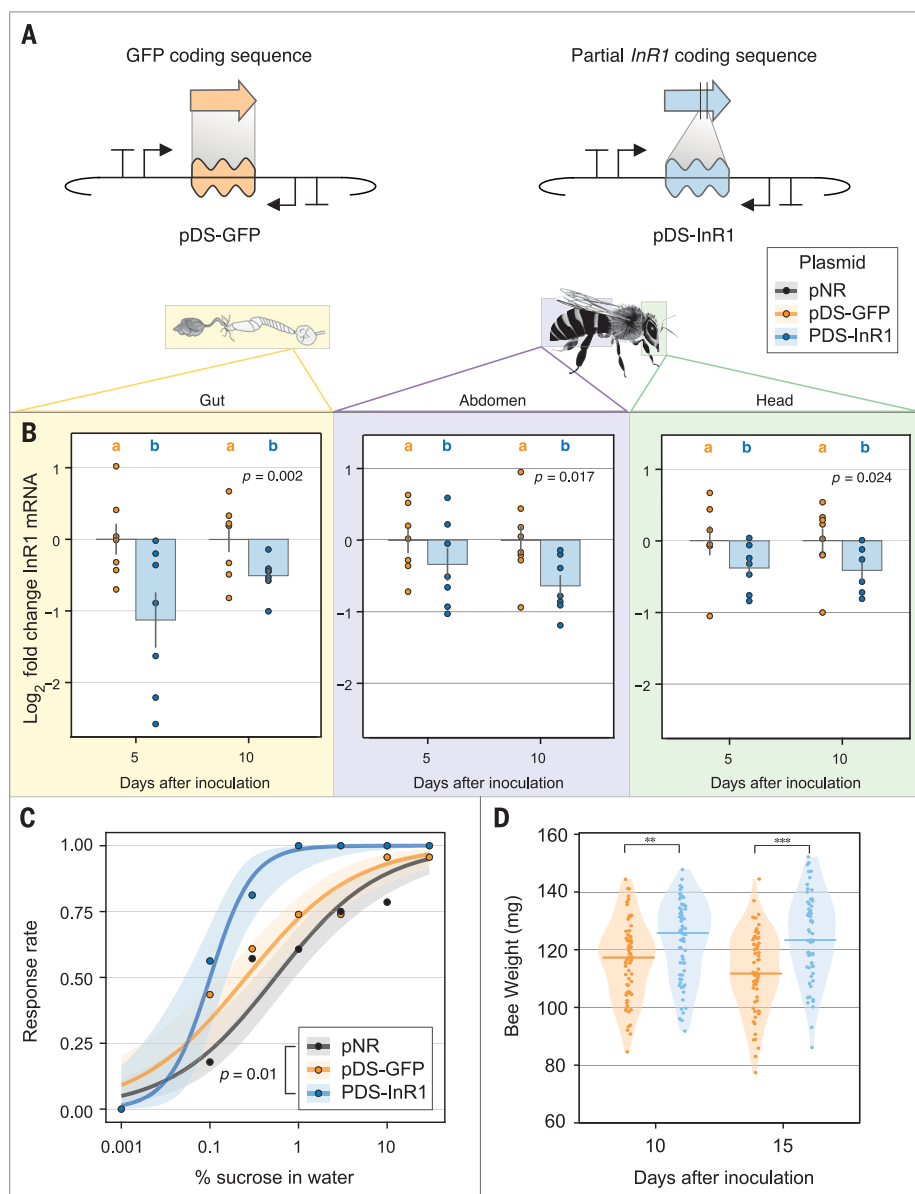


Fig. 2. Symbiont-mediated RNAi reduces expression of a specific host gene and alters feeding behavior and physiology. (A) Plasmid design for off-target dsRNA control plasmid (pDS-GFP) and *InR1* knockdown plasmid (pDS-InR1). (B) Bees colonized with engineered *S. alvi* expressing *InR1* dsRNA (pDS-InR1 plasmid) show reduced expression of *InR1* throughout body regions for 10 days compared to bees colonized with off-target dsRNA control (pDS-GFP). Total *N* = 29 bees from one hive. (C) pDS-InR1 plasmid increases host feeding activity (sucrose sensitivity response), measured 5 days after inoculation. Curves are a binomial family generalized linear model fit to the response data for *N* = 67 bees from two hives. (D) pDS-InR1 plasmid significantly increases bee weight, measured 10 and 15 days postinoculation (Mann-Whitney *U* test). Total *N* = 135 bees from one hive. See fig. S4 for data from an additional trial. Error bars and shading represent SEs. ***P* < 0.01; ****P* < 0.001.

bacteria died more quickly than mites that fed on control bees (Fig. 4B).

Determining whether engineered symbiotic bacteria can improve whole hive health will require further testing. It is promising that inoculating bees with dsRNA-producing strains alone has no negative effect on their survival (fig. S9). Ongoing within-hive transmission could increase the effectiveness of this treatment by

promoting the persistence and spread of engineered strains to new bees. Natural transmission of *S. alvi* and other bee gut symbionts occurs through direct social contact within hives (15), and engineered *S. alvi* strains are transferred between cohoused bees in the lab (fig. S10), suggesting that within-hive transmission is likely. Less is known about between-hive transmission of the bee gut

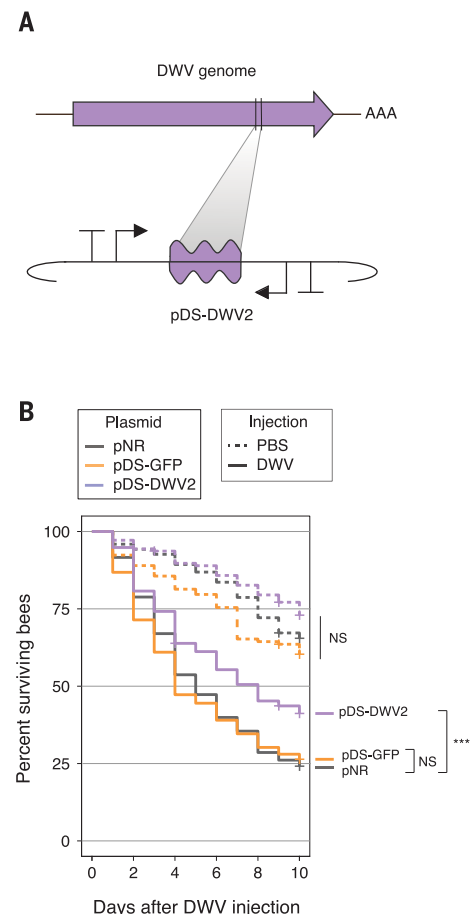


Fig. 3. Symbiont-produced RNAi can improve honey bee survival after viral injection.

(A) Design of the DWV knockdown construct pDS-DWV2. (B) Survival curves of bees monitored for 10 days after injection with DWV or the phosphate-buffered saline (PBS) control. Bees inoculated with pNR, pDS-GFP, or pDS-DWV2 and then injected with PBS showed no significant change in survival (dotted lines). When injected with DWV, bees inoculated with pDS-DWV2 showed increased survival compared with bees inoculated with pNR (no dsRNA control) or pDS-GFP (off-target dsRNA control). ****P* < 0.001 (Wald test); NS, not significant. Total *N* = 980 bees, sourced from three separate hives.

microbiota. Use of this approach outside of the laboratory would require an understanding of these processes and the necessary biocontainment safeguards.

The degree of protection of bees that we observed in our experiments could likely be improved by further optimizing this symbiont-mediated RNAi delivery system. The specific dsRNA sequence chosen will affect the efficacy of targeted RNAi knockdown, as has been shown for suppression of DWV by oral delivery of RNAi (19). Engineering *S. alvi* to deliver more dsRNA to bees (e.g., by reducing

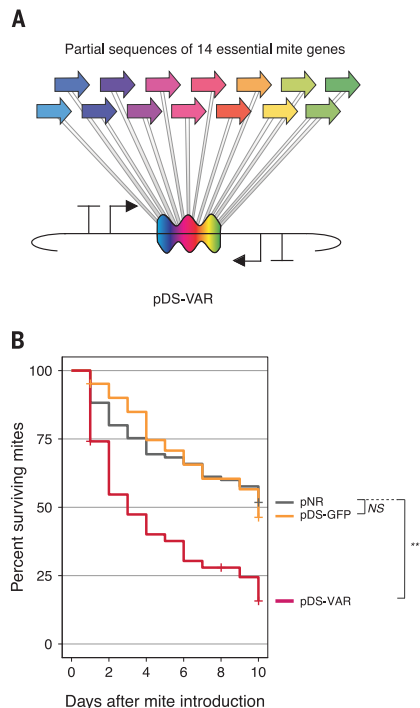


Fig. 4. Symbiont-produced RNAi kills *Varroa* mites feeding on honey bees. (A) Design of pDS-VAR plasmid targeting essential *Varroa* genes. (B) Survival curves for *Varroa* mites that fed on bees colonized with engineered *S. alvi*. Total $N = 253$ mites. All mites came from a single infested hive. Bees were sourced from three separate hives. $**P < 0.01$ (Wald test); NS, not significant.

ribonuclease III activity) could also improve efficacy (20). The deleterious effects of *Varroa* mites and viruses for which the mites act as vectors are interdependent (2); both types of pests could be targeted simultaneously by symbiont-mediated RNAi, which might lead to synergistic improvements in bee health or more robust protection in the context of the fluctuating biotic interactions within hives.

For example, co-infecting viruses that encode RNAi suppressors may limit the efficacy of symbiont-mediated RNAi (21); thus, a strategy that exploits the RNAi machinery of both bees and mites could ensure more consistent benefits to bee health.

We have shown that microbiome engineering can increase resistance to pathogens, a strategy proposed for humans (22) and honey bees (23, 24). Insect-associated microbes have been engineered to interfere with mosquito transmission of malaria (25) and to kill crop pests (26), but not to improve pollinator health. Our results imply movement of symbiont-produced dsRNA from the gut lumen into bee cells but do not identify the mechanism of transfer. Possibly, lysis of *S. alvi* cells releases dsRNA to be taken up through the same route as orally administered dsRNA. Alternatively, symbiont-mediated dsRNA delivery may co-opt an uncharacterized interaction of *S. alvi* with its bee host, such as outer membrane vesicle production (27) or direct RNA export (28). Symbiont-mediated RNAi provides a new tool to study bee biology and to improve resilience against current and future challenges to honey bee health.

REFERENCES AND NOTES

1. S. G. Potts et al., *Trends Ecol. Evol.* **25**, 345–353 (2010).
2. F. Nazzi et al., *PLOS Pathog.* **8**, e1002735 (2012).
3. L. M. Brutscher, M. L. Flenniken, *J. Immunol. Res.* **2015**, 941897 (2015).
4. G. V. Arndam, K. Norberg, R. E. Page Jr., J. Erber, R. Scheiner, *Behav. Brain Res.* **169**, 201–205 (2006).
5. S. D. Desai, Y. J. Eu, S. Whyard, R. W. Currie, *Insect Mol. Biol.* **21**, 446–455 (2012).
6. E. Maori et al., *Insect Mol. Biol.* **18**, 55–60 (2009).
7. W. Hunter et al., *PLOS Pathog.* **6**, e1001160 (2010).
8. L. M. Brutscher, K. F. Daughenbaugh, M. L. Flenniken, *Sci. Rep.* **7**, 6448 (2017).
9. Y. Garbian, E. Maori, H. Kalev, S. Shafir, I. Sela, *PLOS Pathog.* **8**, e1003035 (2012).
10. N. Paldi et al., *Appl. Environ. Microbiol.* **76**, 5960–5964 (2010).
11. J. G. Scott et al., *J. Insect Physiol.* **59**, 1212–1221 (2013).
12. C. L. Mogren, J. G. Lundgren, *PeerJ* **5**, e4131 (2017).
13. A. Jarosch, R. F. Moritz, *Apidologie* **43**, 128–138 (2012).
14. F. M. F. Nunes et al., *Insects* **4**, 90–103 (2013).

15. W. K. Kwong, N. A. Moran, *Nat. Rev. Microbiol.* **14**, 374–384 (2016).
16. S. A. Amment, M. Corona, H. S. Pollock, G. E. Robinson, *Proc. Natl. Acad. Sci. U.S.A.* **105**, 4226–4231 (2008).
17. X. Guo, Y. Wang, I. Sinakevitch, H. Lei, B. H. Smith, *J. Insect Physiol.* **111**, 47–52 (2018).
18. S. D. Ramsey et al., *Proc. Natl. Acad. Sci. U.S.A.* **116**, 1792–1801 (2019).
19. E. V. Ryabov et al., *PLOS Biol.* **17**, e3000502 (2019).
20. L. Timmons, D. L. Court, A. Fire, *Gene* **263**, 103–112 (2001).
21. D. Yang et al., *Front. Genet.* **9**, 384 (2018).
22. K. J. Chua, W. C. Kwok, N. Aggarwal, T. Sun, M. W. Chang, *Curr. Opin. Chem. Biol.* **40**, 8–16 (2017).
23. A. Rangberg, D. B. Diep, K. Rudi, G. V. Arndam, *Integr. Comp. Biol.* **52**, 89–99 (2012).
24. A. Rangberg, G. Mathiesen, G. V. Arndam, D. B. Diep, *Benef. Microbes* **6**, 513–523 (2015).
25. S. Wang et al., *Science* **357**, 1399–1402 (2017).
26. M. M. A. Whitten et al., *Proc. R. Soc. B* **283**, 20160042 (2016).
27. J. A. Tsatsaronis, S. Franch-Arroyo, U. Resch, E. Charpentier, *Trends Microbiol.* **26**, 401–410 (2018).
28. A. Ghosal et al., *MicrobiologyOpen* **4**, 252–266 (2015).

ACKNOWLEDGMENTS

We thank K. Hammond for laboratory support and work on figures and H. Ochman for useful discussion. **Funding:** This work was supported by DARPA BRICS HR0011-15-C-0095, DARPA HR0011-16-2-0019, and U.S. NIH award R01GM108477. **Author contributions:** Conceptualization, S.P.L., B.W.D., A.D.E., J.E.B., and N.A.M.; Methodology, S.P.L., J.E.P., J.P., J.E.B., and N.A.M.; Investigation, S.P.L., J.E.P., P.G., L.C.H., and R.D.H.; Resources, B.W.D., A.D.E., J.E.B., and N.A.M.; Supervision, J.E.B. and N.A.M.; Writing – original draft, S.P.L., J.E.B., and N.A.M.; Writing – review and editing, S.P.L., J.E.P., J.P., P.G., L.C.H., R.D.H., B.W.D., A.D.E., J.E.B., and N.A.M. **Competing interests:** S.P.L., J.E.B., and N.A.M. have filed a patent application (62/529,754) on the commercial use of engineered gut bacteria to improve honey bee health. J.E.B. is the owner of Evolvomics LLC. **Data and materials availability:** All data are available in the main text or the supplementary materials. Bacterial strains and plasmids used in the research are available from N.A.M. under a material transfer agreement.

SUPPLEMENTARY MATERIALS

science.sciencemag.org/content/367/6477/573/suppl/DC1
Materials and Methods
Figs. S1 to S11
Tables S1 to S4
References (29–37)

[View/request a protocol for this paper from Bio-protocol.](#)

6 May 2019; resubmitted 24 October 2019
Accepted 5 December 2019
10.1126/science.aax9039

GRAVITATION

Lense–Thirring frame dragging induced by a fast-rotating white dwarf in a binary pulsar system

V. Venkatraman Krishnan^{1,2*}, M. Bailes^{1,3}, W. van Straten⁴, N. Wex², P. C. C. Freire², E. F. Keane^{1,5}, T. M. Tauris^{6,7,2}, P. A. Rosado^{1,†}, N. D. R. Bhat⁸, C. Flynn¹, A. Jameson¹, S. Osłowski¹

Radio pulsars in short-period eccentric binary orbits can be used to study both gravitational dynamics and binary evolution. The binary system containing PSR J1141–6545 includes a massive white dwarf (WD) companion that formed before the gravitationally bound young radio pulsar. We observed a temporal evolution of the orbital inclination of this pulsar that we infer is caused by a combination of a Newtonian quadrupole moment and Lense–Thirring (LT) precession of the orbit resulting from rapid rotation of the WD. LT precession, an effect of relativistic frame dragging, is a prediction of general relativity. This detection is consistent with an evolutionary scenario in which the WD accreted matter from the pulsar progenitor, spinning up the WD to a period of <200 seconds.

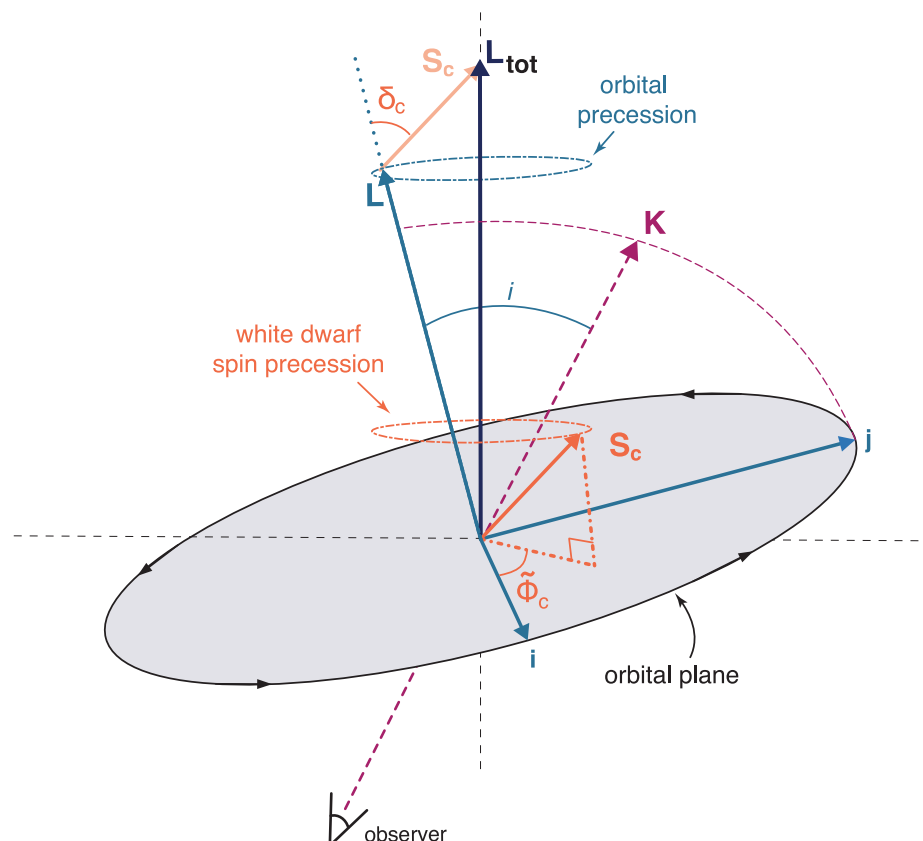
In general relativity (GR), the mass–energy current of a rotating body induces a gravitomagnetic field, so called because it has formal similarities with the magnetic field generated by an electric current (I). This gravitomagnetic interaction drags inertial frames in the vicinity of a rotating mass. The strength of this drag is proportional to the body's intrinsic angular momentum (spin). Frame dragging in a binary system causes a precession of the orbital plane called Lense–Thirring (LT) precession (2). The effect has been detected in the weak-field regime by

satellite experiments in the gravitational field of the rotating Earth (3, 4). Frame dragging is also a plausible interpretation for x-ray spectra of accreting black holes because it affects photon propagation and the properties of the accretion disk, which in some cases allows the determination of the black hole spin (5).

In binary pulsar systems [systems containing both a rotating magnetized neutron star (NS), the radio emission of which is visible from Earth as a pulsar, and an orbiting companion star], relativistic frame dragging caused

by the spin of either the pulsar or its companion is expected to contribute to spin–orbit coupling. These relativistic effects are seen in addition to Newtonian contributions from a mass–quadrupole moment (QPM) induced by the rotation of the body (6). Both contributions cause precession of the position of the periastron (ω ; the point in the pulsar orbit that is closest to its companion) and precession of the orbital plane, changing the orbital inclination (i ; see Fig. 1). If these precessional effects are induced by the NS rotation, then they are dominated by LT, whereas in the case of a rotating main-sequence companion star, they are dominated by QPM interactions (6, 7). Fast-rotating white dwarf (WD) companions with spin periods of a few minutes fall between

Fig. 1. Definition of the orbital geometry. Diagram illustrating the orbital geometry of the system following the “DT92” convention (10) with all vectors shifted to the origin. \mathbf{L} is the angular momentum of the orbit, which is perpendicular to the orbital plane and inclined at an angle i to the line-of-sight vector, \mathbf{K} . The plane containing the vectors \mathbf{L} and \mathbf{K} intersects the orbital plane, defining the orbital plane's unit vector \mathbf{j} and its perpendicular counterpart \mathbf{i} . \mathbf{S}_c is the spin angular momentum of the WD companion, which is misaligned from \mathbf{L} by an angle δ_c . The vector sum of \mathbf{L} and \mathbf{S}_c forms the total angular momentum vector \mathbf{L}_{tot} , which is invariant, whereas \mathbf{L} and \mathbf{S}_c precess. $\tilde{\Phi}_c$ is the angle that the projection of \mathbf{S}_c on the orbital plane subtends with respect to \mathbf{i} and is related to the precession phase of the WD (Φ_c) as $\tilde{\Phi}_c = \Phi_c - 270^\circ$. The precessions of \mathbf{L} and \mathbf{S}_c form precession cones around \mathbf{L}_{tot} as labeled. The precession of \mathbf{S}_c causes Φ_c to sweep through 360° , whereas its rate of advance is modulated by the precession of \mathbf{L} , which induces small oscillations to the position of \mathbf{j} and thus in \mathbf{i} . Some angles and vector magnitudes in the figure are exaggerated for clarity. In practice, $|\mathbf{L}| \gg |\mathbf{S}_c|$; even if the WD is spinning at its breakup speed, the angle between \mathbf{L} and \mathbf{L}_{tot} is at most 0.74° . A more detailed version of this diagram is shown in fig. S1.



¹Centre for Astrophysics and Supercomputing, Swinburne University of Technology, Melbourne, Victoria 3122, Australia.

²Max-Planck-Institut für Radioastronomie, D-53121 Bonn, Germany. ³Australian Research Council Centre of Excellence for Gravitational Wave Discovery (OzGrav), Swinburne University of Technology, Melbourne, Victoria 3122, Australia.

⁴Institute for Radio Astronomy and Space Research, Auckland University of Technology, Auckland 1142, New Zealand. ⁵Square Kilometer Array Organisation, Jodrell Bank Observatory, Macclesfield SK11 9DL, UK. ⁶Aarhus Institute of Advanced Studies, Aarhus University, 8000 Aarhus C, Denmark. ⁷Department of Physics and Astronomy, Aarhus University, 8000 Aarhus C, Denmark. ⁸International Centre for Radio Astronomy Research, Curtin University, Bentley, Western Australia 6102, Australia.

*Corresponding author. Email: vkrishnan@mpifr-bonn.mpg.de

†Present address: Holaluz-Clidom S.A., Passeig de Joan de Borbó 99-101, 4a Planta, 08039 Barcelona, Spain.

these two extremes and are expected to yield similar contributions from both effects (8). Although QPM spin-orbit interaction has already been observed in some binary pulsars [e.g., PSR J0045–7319 (7)], no binary pulsar orbit has been shown to experience a measurable contribution from LT drag.

The times of arrival (TOAs) of the radio pulses from pulsars can be measured with high precision, with uncertainties that are often more than three orders of magnitude smaller than their spin periods. This allows pulsars to be monitored for decades without losing rotational phase information. This “pulsar-timing” methodology can provide precise measurements of the pulsar’s spin and astrometric parameters (9). For pulsars in binary systems, pulsar timing also provides precise measurements of the binary orbit: five parameters describing the nonrelativistic (Keplerian) parameters and, for some binaries, relativistic effects that affect both the orbit and the propagation of the radio signals (10). These relativistic effects are typically parameterized using theory-independent post-Keplerian (PK) parameters (11, 12). Measurements of two PK parameters can be used to obtain the mass of the pulsar (M_p) and of the companion (M_c) by assuming a theory of gravity, such as GR, whereas three or more PK parameters can be used to perform self-consistency tests of that theory. An alternative formalism assumes a theory of gravity such as GR, which allows direct model fitting of the component masses. The latter is preferred if the goal is to understand the properties and dynamics of the system under that theory, rather than testing the theory itself. We adopt this approach and assume that GR adequately describes the system.

PSR J1141–6545 is a radio pulsar with a spin period of ~394 ms in an ~4.74-hour eccentric orbit with a massive WD companion (13, 14). It is one of only two confirmed NS–WD binary systems (the other being PSR B2303+46, a much wider-orbit binary) in which the WD is known to have formed first and is thus older than the NS. This requires an unusual evolution of the stellar pair (15, 16). The initially more massive (primary) star must have formed the older massive WD. Forming a NS requires a higher stellar mass, so the initially (slightly) less massive secondary star must have accreted sufficient mass from the primary star to explode in a supernova (SN), producing the pulsar. Before exploding, the secondary would have undergone an expansion leading to mass transfer back to the primary star, by that point already a WD.

Because the primary was already a WD, there cannot have been subsequent mass accretion onto the newly formed pulsar. Thus, unlike most other pulsars with WD companions, PSR J1141–6545 and PSR B2303+46 were not spun

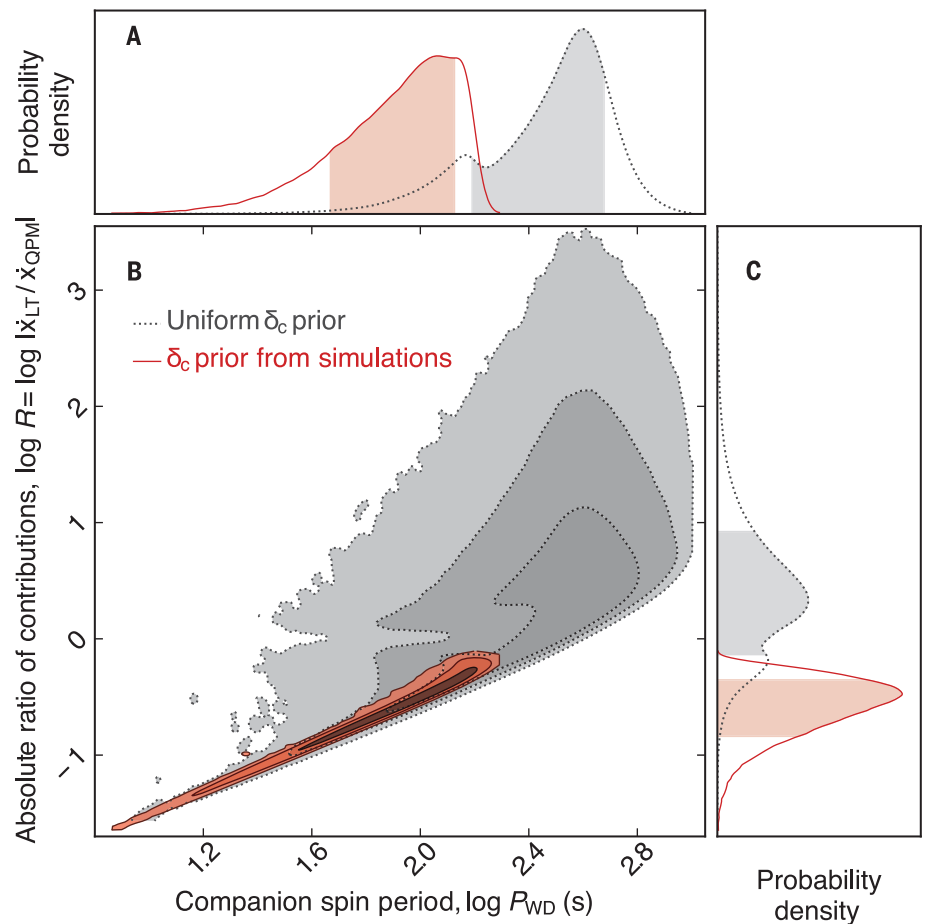


Fig. 2. Contributions to orbital precession from WD rotation. The absolute ratio of the contributions to \dot{x}_{SO} from \dot{x}_{LT} and \dot{x}_{QPM} , $R = |\dot{x}_{LT} / \dot{x}_{QPM}|$, is plotted as a function of P_{WD} . (A and C) Marginalized posterior distributions with their 68% confidence intervals shaded, defined as the combination of the two 34% confidence regions on either side of the 2D maximum of the likelihood function. (B) Two-dimensional probability distribution with contours defining the 68%, 95%, and 99% likelihood confidence intervals. The gray-shaded regions and dotted contours are constraints using only the radio observations of the pulsar, whereas the red regions and solid contours include additional binary evolutionary constraints from simulations (8). Numerical values are provided in Table 2.

up by mass transfer; they still have the large magnetic field strengths typical of young pulsars, as inferred from their spin evolution. The pulsar spin axes, which are expected to have started at a random orientation with respect to the orbital plane after the SN explosion, were therefore not aligned with the orbital angular momentum by an accretion process. For a compact system, such a misalignment can result in observable relativistic spin precession of the pulsar (17). This has been observed in PSR J1141–6545 as precession led to temporal evolution of the pulse profile, providing constraints on the system’s geometry (18, 19).

PSR J1141–6545 has been observed since 2000, allowing the determination of several PK parameters including the advance of periastron ($\dot{\omega}$), relativistic time dilation, gravitational wave damping, and the Shapiro delay.

These are all in agreement with GR (8), justifying our assumption of the theory. We seek the measurement of an additional PK parameter, the temporal evolution of the observed projected semimajor axis (x_{obs}), which to necessary precision can be written as $x_{obs} = (a_p \sin i/c) + A$, where a_p is the semimajor axis of the pulsar’s orbit, i its inclination, c is the speed of light, and A is the first “aberration” parameter, which describes how the aberration of the pulsar signal affects our measurement of x (8, 10).

Timing observations of PSR J1141–6545 have been undertaken using the 64-m Parkes and the UTMOST radio telescopes (20). Our data recording and TOA extraction followed standard pulsar data acquisition and reduction methods (8). The timing data were analyzed using the DDGR model (21), which describes the timing of the pulsar using GR. The measured

and derived parameters of the system are provided in Table 1.

We measure the temporal evolution of x for this system, $\dot{x}_{\text{obs}} = (1.7 \pm 0.3) \times 10^{-13} \text{ s s}^{-1}$. This value may include contributions from different physical and geometric effects depending on whether there is a corresponding change in a_p , i , or A . We find (8) only two appreciable contributions to \dot{x}_{obs} : The largest is a change in i that is due to the precession of the orbital plane caused by the spin of the WD (\dot{x}_{SO}), with a smaller contribution arising from a change in A caused by geodetic precession of the pulsar (10). The magnitude of the latter contribution was computed from the precessional con-

straints on the system's geometry (8, 19); we find that it contributes $<21\%$ of \dot{x}_{obs} at 99% confidence. The remainder is caused by \dot{x}_{SO} , the largest contribution, which corresponds to an average increase of i of 1.7 arc sec per year. All other contributions are several orders of magnitude smaller (8).

Both QPM and LT effects induced by the WD spin (and only these effects) provide non-negligible contributions to \dot{x}_{SO} : The QPM contribution (\dot{x}_{QPM}) is inversely proportional to the square of the WD spin period (P_{WD}), whereas the LT contribution (\dot{x}_{LT}) is inversely proportional to P_{WD} . These effects also contribute to $\dot{\omega}$, but for this system the contribution is

expected to be smaller than our observational uncertainties. The LT contribution to $\dot{\omega}$ is potentially detectable in compact double-NS systems such as the double pulsar, PSR J0737–3039A (22).

Both \dot{x}_{QPM} and \dot{x}_{LT} are modulated by the spin misalignment angle (δ_c) and the precession phase (Φ_c^0 ; see Fig. 1) of the WD at our reference epoch (T_0 ; see Table 1). Both of these angles are unknown, so we performed Markov Chain Monte Carlo (MCMC) computations to obtain a distribution for the individual contributions and used Bayesian statistics to marginalize over the parameter space of δ_c and Φ_c^0 . From this, we infer the maximum allowable P_{WD} consistent with the observed \dot{x}_{obs} (8).

Figure 2 shows the absolute ratio of the contributions from \dot{x}_{LT} and \dot{x}_{QPM} , $R = |\dot{x}_{\text{LT}}/\dot{x}_{\text{QPM}}|$, as a function of P_{WD} (fig. S2 shows a full correlation plot). This demonstrates that we can constrain $P_{\text{WD}} < 900 \text{ s}$ with 99% confidence. For known isolated WDs, their spin periods are known to range from a few hours to a few tens of hours (23, 24); the fastest rotating isolated WD known (SDSS J0837+1856), which also has a mass similar to the WD in the PSR J1141–6545 system [~ 0.9 solar masses (M_\odot)], has a spin period of ~ 1.13 hours (24). Our upper limit on P_{WD} is thus a confirmation of WD spin-up caused by an earlier episode of mass transfer. If $P_{\text{WD}} > 270 \text{ s}$, LT is the dominant contributor to \dot{x}_{SO} . R never reaches zero (see also fig. S2), so for all allowed values of $\{\delta_c, \Phi_c^0\}$, \dot{x}_{LT} never vanishes. Thus, we detect the action of LT drag in the motion of this binary pulsar.

Taking these results as confirmation of the evolutionary history discussed above, we use binary evolution simulations to constrain δ_c and place further constraints on P_{WD} (8). We find that the mass-transfer phase lasts for $\sim 16,000$ years before the resulting pulsar progenitor star undergoes an “ultrastripped” SN event (25–27). If the mass-accretion rate of the $\sim 1.02 M_\odot$ WD is restricted by the Eddington limit (i.e., the maximum rate of accretion before photon pressure blocks further accretion), which is $\sim 4 \times 10^{-6} M_\odot$ per year for this WD, then it would accrete $\sim 0.06 M_\odot$ in this time. We choose an initial orbital period and mass of the pulsar progenitor star to reproduce the most probable pre-SN binary parameters using 70 million simulations of post-SN orbital parameters of systems resembling PSR J1141–6545 (8).

These simulations allow us to estimate a lower limit on P_{WD} of $\sim 20 \text{ s}$, although this depends on the interactions between the accreted material and the magnetosphere of the WD, which is not known. The angular velocity at which the WD would break up provides a firmer lower limit on P_{WD} of 7 s. The value of δ_c obtained from simulations is $<50^\circ$ at 99% confidence. This means that the WD spin is prograde, i.e., still rotating in the same

Table 1. Model parameters for PSR J1141–6545. Shown are postfitting model parameter values for PSR J1141–6545 with the DDGR timing model. The glitch parameters apply to a previously known pulsar glitch that occurred in 2008 (8).

Dataset and model fit quality	
Modified Julian date (MJD) range	51,630.8 to 58,214.5 (18.03 years)
No. of TOAs	20,861
Weighted root mean square timing residual (μs)	95.6
Reduced χ^2 value	1.0004
Fixed quantities	
Reference epoch (MJD)	54,000
Glitch epoch (MJD)	54,272.7
Measured quantities	
Right ascension, α (J2000 equinox)	$11^{\text{h}}41^{\text{m}}07.007^{\text{s}} \pm 0.003^{\text{s}}$
Declination, δ (J2000 equinox)	$-65^\circ45'19.14'' \pm 0.1''$
Pulse frequency, ν (s^{-1})	$2.5387230404 \pm 1 \times 10^{-10}$
First derivative of pulse frequency, $\dot{\nu}$ (s^{-2})	$-2.76800 \times 10^{-14} \pm 1 \times 10^{-19}$
Dispersion measure, DM (pc cm^{-3})	115.98 ± 0.03
Orbital period, P_b (d)	$0.19765096149 \pm 3 \times 10^{-11}$
Epoch of periastron, T_0 (MJD)	$53999.9960283 \pm 2 \times 10^{-7}$
Projected semimajor axis of orbit, \dot{x}_{obs} (s)	$1.858915 \pm 3 \times 10^{-6}$
Longitude of periastron, ω_0 (degrees)	$80.6911 \pm 6 \times 10^{-4}$
Orbital eccentricity, e	$0.171876 \pm 1 \times 10^{-6}$
First derivative of x , \dot{x}_{obs} (s s^{-1})	$(1.7 \pm 0.3) \times 10^{-13}$
First derivative of e , \dot{e} (s^{-1})	$(-2 \pm 8) \times 10^{-15}$
Companion mass, M_c (M_\odot)	1.02 ± 0.01
Total mass, M_{TOT} (M_\odot)	$2.28967 \pm 6 \times 10^{-5}$
Glitch phase	1.0011 ± 0.0001
Glitch-induced step change in ν (Hz)	$(1.49508 \pm 0.0001) \times 10^{-6}$
Glitch-induced step change in $\dot{\nu}$ (Hz s^{-1})	$-(8.7 \pm 0.2) \times 10^{-17}$
Derived quantities	
Pulsar mass, M_p (M_\odot)	1.27 ± 0.01
Orbital inclination, i (degrees)	71 ± 2 or 109 ± 2

Table 2. Confidence intervals (68%) from Fig. 2. Shown are the 68% confidence intervals of the companion spin period and the absolute ratio of contributions to \dot{x}_{SO} from \dot{x}_{LT} and \dot{x}_{QPM} .

Parameter	Uniform δ_c prior	δ_c prior from simulations
Companion spin period [P_{WD} (s)]	397_{-242}^{+78}	116_{-70}^{+17}
Absolute ratio of contributions to \dot{x}_{SO} [$R = \dot{x}_{\text{LT}}/\dot{x}_{\text{QPM}} $]	$2.13_{-1.41}^{+6.18}$	$0.33_{-0.19}^{+0.11}$

direction as the orbit (before the SN, the WD spin was most probably aligned with the orbit, $\delta_c \sim 0^\circ$, caused by accretion of matter from the pulsar's progenitor). We use the distribution of δ_c from simulations as a prior for additional MCMC computations, obtaining tighter constraints for the distribution of R and P_{WD} shown in Fig. 2 (see also fig. S3 for a full correlation plot). We find that P_{WD} is < 200 s with 99% confidence. This is because, for $\delta_c < 50^\circ$, \dot{x}_{QPM} is positive whereas \dot{x}_{LT} is negative. To obtain the net positive \dot{x}_{SO} that we observe, the WD needs to spin substantially faster so the excess from QPM ($\dot{x}_{\text{QPM}} - \dot{x}_{\text{SO}}$) compensates for the negative \dot{x}_{LT} . Table 2 provides the 68% confidence limits on R and P_{WD} with and without binary evolution simulations. These WD spin constraints correspond to an angular momentum between 2 and $20 \times 10^{48} \text{ g cm}^2 \text{ s}^{-1}$. This is one to two orders of magnitude larger than the range observed among the recycled pulsars in double-NS systems, 0.03 to $0.4 \times 10^{48} \text{ g cm}^2 \text{ s}^{-1}$, which also likely experienced accretion onto the first-formed NS (26).

In summary, measurement of the relativistic effects in the PSR J1141–6545 system have enabled us to determine the masses of its WD and NS components, the orbital inclination, and its variation. This variation is dominated by contributions from both the Newtonian quadrupole spin–orbit coupling and the LT precession caused by the rapidly spinning WD. LT precession is required for any orbital orientation and is the dominant term if $P_{\text{WD}} > 270$ s after marginalizing over the system's geometry. For prograde rotation of the WD, which is indicated by binary evolution simulations, $P_{\text{WD}} < 200$ s and LT precession has an opposite sign to the quadrupolar term. PSR J1141–6545 therefore exhibits another manifestation of Einstein's general theory of relativity: LT frame dragging.

REFERENCES AND NOTES

1. I. Ciufolini, J. A. Wheeler, *Gravitation and Inertia* (Princeton Univ. Press, 1995).
2. J. Lense, H. Thirring, *Phys. Z.* **19**, 156 (1918).
3. I. Ciufolini, E. C. Pavlis, *Nature* **431**, 958–960 (2004).
4. C. W. F. Everitt *et al.*, *Phys. Rev. Lett.* **106**, 221101 (2011).
5. C. S. Reynolds, *New Astron.* **3**, 41–47 (2019).
6. N. Wex, *Class. Quantum Gravity* **12**, 983–1005 (1995).
7. V. M. Kaspi, M. Bailes, R. N. Manchester, B. W. Stappers, J. F. Bell, *Nature* **381**, 584–586 (1996).
8. Materials and methods are available as supplementary materials.
9. D. R. Lorimer, M. Kramer, *Handbook of Pulsar Astronomy* (Cambridge Univ. Press, 2012).
10. T. Damour, J. H. Taylor, *Phys. Rev. D Part. Fields* **45**, 1840–1868 (1992).
11. T. Damour, N. Deruelle, *Ann. Inst. Henri Poincaré Phys. Théor.* **43**, 107–132 (1985).
12. T. Damour, N. Deruelle, *Ann. Inst. Henri Poincaré Phys. Théor.* **44**, 263–292 (1986).
13. V. M. Kaspi *et al.*, *Astrophys. J.* **543**, 321–327 (2000).
14. J. Antoniadis, C. G. Bassa, N. Wex, M. Kramer, R. Napiwotzki, *Mon. Not. R. Astron. Soc.* **412**, 580–584 (2011).
15. T. M. Tauris, T. Sennels, *Astron. Astrophys.* **355**, 236 (2000).
16. R. P. Church, S. J. Bush, C. A. Tout, M. B. Davies, *Mon. Not. R. Astron. Soc.* **372**, 715–727 (2006).
17. B. M. Barker, R. F. O'Connell, *Phys. Rev. D Part. Fields* **12**, 329–335 (1975).
18. A. W. Hotan, W. van Straten, R. N. Manchester, *Astron. Soc. Aust.* **21**, 302–309 (2004).
19. V. Venkatraman Krishnan *et al.*, *Astrophys. J.* **873**, L15 (2019).
20. M. Bailes *et al.*, *Astron. Soc. Aust.* **34**, e045 (2017).
21. J. H. Taylor, J. M. Weisberg, *Astrophys. J.* **345**, 434 (1989).
22. M. S. Kehl, N. Wex, M. Kramer, K. Liu, in *Fourteenth Marcel Grossmann Meeting–MG14* (2018), pp. 1860–1865.
23. S. D. Kawaler, in *19th European Workshop on White Dwarfs*, P. Dufour, P. Bergeron, G. Fontaine, eds. (2015), vol. 493 of *Astronomical Society of the Pacific Conference Series*, p. 65.
24. J. J. Hermes *et al.*, *Astrophys. J.* **841**, L2 (2017).
25. T. M. Tauris *et al.*, *Astrophys. J.* **778**, L23 (2013).
26. T. M. Tauris, N. Langer, P. Podsiadlowski, *Mon. Not. R. Astron. Soc.* **451**, 2123–2144 (2015).
27. K. De *et al.*, *Science* **362**, 201–206 (2018).
28. V. Venkatraman Krishnan *et al.*, Data and software release for: Lense–Thirring frame dragging induced by a fast-rotating white dwarf in a binary pulsar system, Zenodo (2019); <https://doi.org/10.5281/zenodo.3555380>.

ACKNOWLEDGMENTS

We thank the referees and the editor for a thorough reading of the manuscript and for suggesting helpful improvements; J. Antoniadis, M. Kramer, L. Lentati, D. Reardon, R. M. Shannon, and S. Stevenson for discussions on this paper; N. Langer for the

use of his binary evolution (BEC) code; and L. Toomey, J. Hurley, and E. Ali for help with the data release. Data reduction and analysis were performed on the gSTAR and OzSTAR national supercomputing facilities at Swinburne University of Technology. This research has made extensive use of NASA's Astrophysics Data System (<https://ui.adsabs.harvard.edu/>) and includes archived data obtained through the CSIRO Data Access Portal (<http://data.csiro.au>). **Funding:** This research was primarily supported by the Australian Research Council Centre of Excellence for All-sky Astrophysics (CAASTRO; project no. CE110001020). The gSTAR and OzSTAR supercomputers are funded by Swinburne and the Australian Government's Education Investment Fund. V.V.K., N.W., and P.C.C.F. acknowledge continuing support from the Max Planck Society. M.B., C.F., and S.O. acknowledge Australian Research Council grants OzGrav (CE170100004) and a laureate fellowship (FL150100148). P.C.C.F. acknowledges financial support from the European Research Council (ERC) starting grant BEACON (contract no. 279702). T.M.T. acknowledges an AIAS-COFUND Senior Fellowship funded by the European Union's Horizon 2020 Research and Innovation Programme (grant no. 754513) and the Aarhus University Research Foundation. P.A.R. acknowledges support from the Australian Research Council (Discovery Project no. DP140102578). N.D.R.B. acknowledges support from a Curtin Research Fellowship (CRF12228). The Parkes radio telescope is funded by the Commonwealth of Australia for operation as a National Facility managed by CSIRO. The Molonglo Observatory is owned and operated by the University of Sydney with support from the School of Physics and the University. **Author contributions:** V.V.K. led the analysis; wrote software for data reduction, analysis, and interpretation; and led writing of the manuscript. V.V.K., M.B., W.v.S., and N.D.R.B. performed all observations with the Parkes telescope. V.V.K., M.B., C.F., A.J., and S.O. performed all observations with the UTMOST telescope. V.V.K., W.v.S., and S.O. performed robust polarization calibration and profile evolution modeling. V.V.K., E.F.K., and P.A.R. performed bootstrap ToA analysis and red noise modeling. V.V.K., M.B., N.W., and P.C.C.F. interpreted the results and analyzed precessional contributions to the observed values. T.M.T. performed and interpreted the binary evolution and SN simulations. **Competing interests:** The authors declare no competing interests. **Data and materials availability:** Our observational data and analysis software, including links to the software dependencies and each observational dataset, are available at Zenodo (28).

SUPPLEMENTARY MATERIALS

science.sciencemag.org/content/367/6477/577/suppl/DC1
Materials and Methods
Supplementary Text
Figs. S1 to S11
Table S1
References (29–64)

10 May 2019; accepted 3 December 2019
10.1126/science.aax7007

MOLECULAR BIOLOGY

N⁶-methyladenosine of chromosome-associated regulatory RNA regulates chromatin state and transcription

Jun Liu^{1,2*}, Xiaoyang Dou^{1,2*}, Chuanyuan Chen^{3,4*}, Chuan Chen⁵, Chang Liu^{1,2}, Meng Michelle Xu⁶, Siqi Zhao^{3,4}, Bin Shen⁷, Yawei Gao^{5†}, Dali Han^{3,4,8,9†}, Chuan He^{1,2,10†}

N⁶-methyladenosine (m⁶A) regulates stability and translation of messenger RNA (mRNA) in various biological processes. In this work, we show that knockout of the m⁶A writer *Mettl3* or the nuclear reader *Ythdc1* in mouse embryonic stem cells increases chromatin accessibility and activates transcription in an m⁶A-dependent manner. We found that METTL3 deposits m⁶A modifications on chromosome-associated regulatory RNAs (carRNAs), including promoter-associated RNAs, enhancer RNAs, and repeat RNAs. YTHDC1 facilitates the decay of a subset of these m⁶A-modified RNAs, especially elements of the long interspersed element-1 family, through the nuclear exosome targeting-mediated nuclear degradation. Reducing m⁶A methylation by METTL3 depletion or site-specific m⁶A demethylation of selected carRNAs elevates the levels of carRNAs and promotes open chromatin state and downstream transcription. Collectively, our results reveal that m⁶A on carRNAs can globally tune chromatin state and transcription.

N⁶-methyladenosine (m⁶A) is an abundant modification on most eukaryote mRNAs (1, 2), regulated mainly by writer, eraser, and reader proteins (3). The mRNA m⁶A modification is installed by METTL3 (4) and can be removed by demethylases FTO and ALKBH5 (5, 6). Readers, including the YTH domain family and HNRNP proteins, directly or indirectly recognize the m⁶A-marked transcripts and affect mRNA metabolism (4, 7–9).

m⁶A plays critical roles in diverse biological processes, including the self-renewal and differentiation of embryonic and adult stem cells (3, 4). In mouse embryonic stem cells (mESCs), transcripts encoding pluripotency factors tend to be m⁶A-methylated and subjected to YTHDF2-mediated decay in cytoplasm, which affects their turnover during differentiation

(10–12). However, m⁶A appears to also exhibit YTHDF2-independent regulations during early development, given that *Ythdf2* knockout (KO) mice can survive to late embryonic developmental stages but *Mettl3* KO results in early embryonic lethality (11, 13). Notably, mouse KO of the nuclear m⁶A reader *Ythdc1* exhibits similar early mouse embryonic lethality to the *Mettl3* KO (14). These observations imply that m⁶A could play additional roles in the nucleus that affect cell survival and differentiation. Previous studies have also suggested that m⁶A methylation on chromatin modifier transcripts or the chromosome binding of methyltransferase may affect transcription (15–17).

We investigated two independent *Mettl3* KO mESC lines (*Mettl3*^{−/−}-1 and *Mettl3*^{−/−}-2) (10) and analyzed newly transcribed RNA levels. *Mettl3* KO mESCs displayed marked increases in nascent transcripts synthesis compared with control wild-type (WT) mESCs (Fig. 1A). We generated stable rescue cell lines that express WT METTL3 or an inactive mutant METTL3 (fig. S1A). The increased transcription of nascent transcripts upon *Mettl3* KO was reversed with WT but not mutant METTL3 (Fig. 1B).

We next asked if the global chromatin state is affected by *Mettl3* deletion. We performed deoxyribonuclease (DNase) I-treated terminal deoxynucleotidyl transferase-mediated deoxyuridine triphosphate nick end labeling (TUNEL) assay and observed a notable increase in chromatin accessibility in *Mettl3* KO mESCs compared with wild type. Moreover, expression of WT but not mutant METTL3 reversed the increased chromatin accessibility, suggesting m⁶A dependence (Fig. 1, C and D).

We constructed conditional knockout (CKO) *Ythdc1* (fig. S1B) and *Ythdf2* (fig. S1C) mESCs. *Ythdc1* CKO showed a similar increase in tran-

scription and chromatin openness as *Mettl3* KO (fig. S1, D and F), whereas *Ythdf2* CKO showed minimal differences (fig. S1, E and G). The changes observed in *Ythdc1* CKO mESCs were reversed by expressing WT but not mutant YTHDC1 (fig. S1, B, D, and F). Consistently, both H3K4me3 and H3K27ac, two histone marks associated with active transcription, were elevated upon *Mettl3* and *Ythdc1* depletion (fig. S1, H and I). Together, these data suggested a nuclear regulatory role for RNA m⁶A.

We next isolated nonribosomal RNAs from soluble nucleoplasmic and chromosome-associated fractions and quantified m⁶A/A by liquid chromatography–tandem mass spectrometry (LC-MS/MS) (fig. S2A). The m⁶A/A ratio in nonribosomal chromosome-associated RNAs (carRNAs) decreased the most (>50%) upon *Mettl3* KO (Fig. 2A and fig. S2B), suggesting an effect of m⁶A on carRNAs. We immunoprecipitated ribosomal-RNA–depleted, m⁶A-containing carRNAs and performed high-throughput sequencing (methylated RNA immunoprecipitation sequencing, MeRIP-seq) in *Mettl3* KO and WT mESCs. The m⁶A levels showed a global decrease after *Mettl3* KO (fig. S2C), consistent with LC-MS/MS analysis (Fig. 2A). We identified ~40,000 peaks in each sample; both m⁶A levels (fig. S2D) and peaks (fig. S2E) were fully reproducible. Compared with wild type, *Mettl3* KO samples showed more hypomethylated peaks (fig. S2F), with the largest reduction found at intergenic regions (fig. S2, G and H).

We analyzed three types of carRNAs with potential regulatory functions: promoter-associated RNA (paRNA), enhancer RNA (eRNA), and RNA transcribed from transposable elements (repeat RNA), which we termed chromosome-associated regulatory RNAs (carRNAs). The m⁶A levels of these carRNAs were markedly decreased in *Mettl3* KO mESCs (Fig. 2B). Approximately 15 to 30% of all carRNAs contain m⁶A in mESCs, ~60% of which are regulated by METTL3 (fig. S3A). These m⁶A peaks contain GAC and AAC motifs, similar to those of the coding mRNAs (fig. S3, B and C). We categorized carRNAs into m⁶A-marked and non-m⁶A subgroups and found that the abundances of m⁶A-marked transcripts, but not non-m⁶A RNAs, were significantly elevated upon *Mettl3* KO (Fig. 2C and fig. S3D). Additionally, changes in m⁶A levels negatively correlated with changes in expression levels for all three carRNA groups upon *Mettl3* KO (fig. S3E). Together, these data suggest that m⁶A methylation destabilizes these carRNAs.

Previous work has uncovered that YTHDC1 associates with components of the nuclear exosome targeting (NEXT) complex, which is responsible for degradation of certain non-coding nuclear RNAs (18). We confirmed that YTHDC1 interacts with the NEXT components RBM7 and ZCCHC8 (fig. S4A). Because

¹Department of Chemistry and Institute for Biophysical Dynamics, University of Chicago, Chicago, IL 60637, USA.

²Howard Hughes Medical Institute, University of Chicago, Chicago, IL 60637, USA.

³Key Laboratory of Genomic and Precision Medicine, Beijing Institute of Genomics, Chinese Academy of Sciences, Beijing 100101, China.

⁴College of Future Technology, Sino-Danish College, University of Chinese Academy of Sciences, Beijing 100049, China.

⁵Institute for Regenerative Medicine, Shanghai East Hospital, Shanghai Key Laboratory of Signaling and Disease Research, Frontier Science Center for Stem Cell Research, School of Life Sciences and Technology, Tongji University, Shanghai 200120, China.

⁶Department of Basic Medical Sciences, School of Medicine, Institute for Immunology, Beijing Key Laboratory for Immunological Research on Chronic Diseases, THU-PKU Center for Life Sciences, Tsinghua University, Beijing 100084, China.

⁷State Key Laboratory of Reproductive Medicine, Department of Histology and Embryology, Nanjing Medical University, Nanjing 211166, China.

⁸China National Center for Bioinformation, Beijing 100101, China.

⁹Institute for Stem Cell and Regeneration, Chinese Academy of Sciences, Beijing 100101, China.

¹⁰Department of Biochemistry and Molecular Biology, University of Chicago, Chicago, IL 60637, USA.

*These authors contributed equally to this work.

†Corresponding author. Email: chuanhe@uchicago.edu (C.H.); handl@big.ac.cn (D.H.); gaoyawei@tongji.edu.cn (Y.G.)

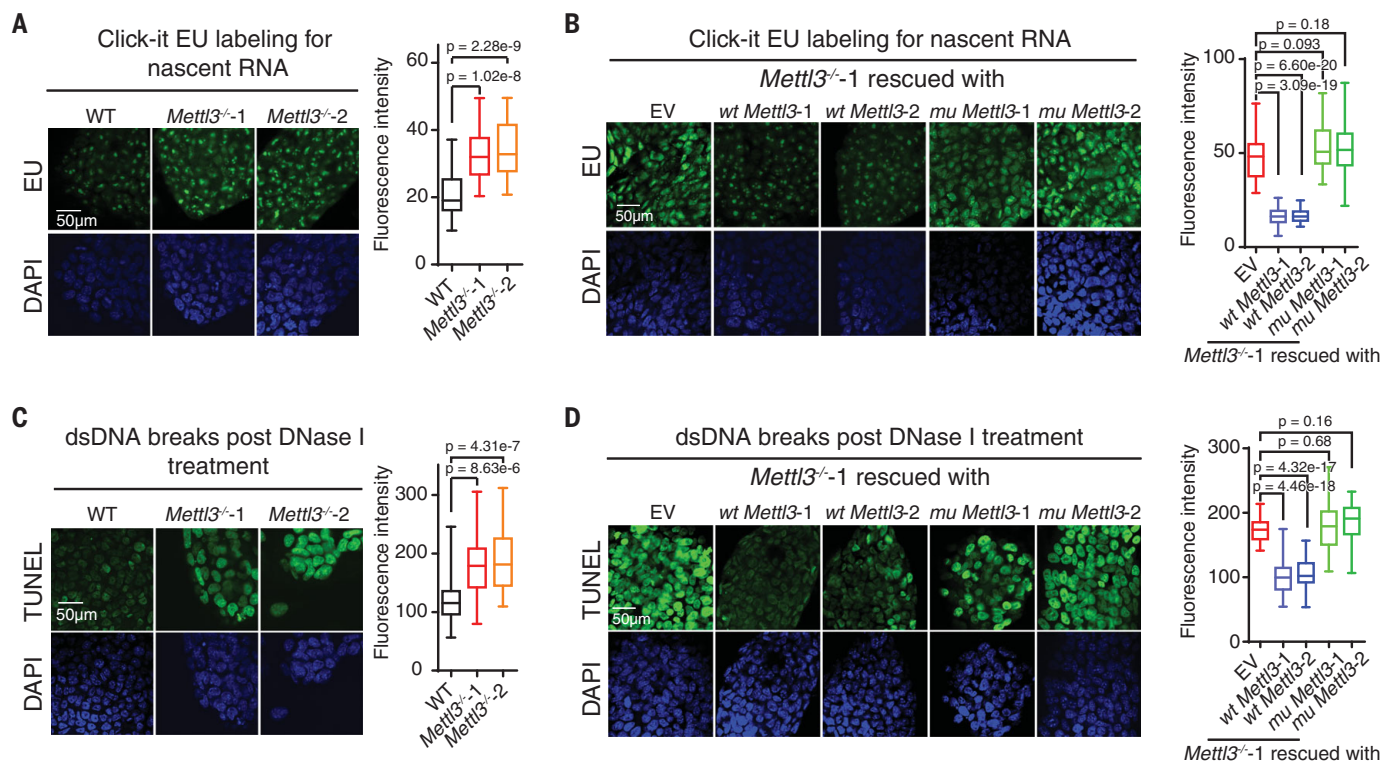


Fig. 1. *Mettl3* KO in mESCs leads to increased nascent RNA transcription and chromatin accessibility.

(A and B) Analysis of nascent RNA synthesis in WT or *Mettl3*^{-/-} mESCs [(A), *Mettl3*^{-/-1} and -2 are two independently generated KO lines], and *Mettl3*^{-/-} mESCs rescued with WT or an inactive mutant *Mettl3* (B). Nascent RNA synthesis was detected by using a click-it RNA Alexa fluor 488 imaging kit. EU, 5-ethynyl uridine;

DAPI, 4',6-diamidino-2-phenylindole. (C and D) Analysis of chromatin accessibility in WT or *Mettl3*^{-/-} mESCs (C), and *Mettl3*^{-/-} mESCs rescued with WT or mutant *Mettl3* (D). DNase I-treated TUNEL assay was performed. For (A) to (D), the nucleus is counterstained by DAPI. EV (empty vector) refers to *Mettl3*^{-/-} mESCs when transfected with empty vector plasmid. dsDNA, double-stranded DNA.

YTHDC1 is a known m⁶A reader and *Ythdc1* CKO induced transcription up-regulation (fig. S1D), we hypothesized that YTHDC1 recognizes a subset of m⁶A-marked carRNAs and triggers their decay through NEXT in mESCs. Consistently, depletion of *Ythdc1* or *Zcchc8*, but not of *Ythdf2*, increased the m⁶A/A ratio of carRNAs (fig. S4B). We subsequently performed MeRIP-seq of nonribosomal carRNAs and observed consistently increased m⁶A levels after *Ythdc1* depletion (fig. S4, C to E). We identified more hypermethylated peaks in *Ythdc1* CKO mESCs compared with controls (fig. S4F). The distribution of m⁶A peaks on mRNA was not notably altered (fig. S4G); however, the proportion of m⁶A peaks at intergenic regions increased upon *Ythdc1* CKO (fig. S4H). These observations suggest that YTHDC1, like METTL3, affects carRNAs transcribed mostly from intergenic regions.

We examined carRNAs and observed markedly increased m⁶A for repeat RNAs upon YTHDC1 depletion (fig. S5A). Specifically, ~20 to 30% of m⁶A-marked paRNAs and eRNAs and >60% of m⁶A-marked repeat RNAs are affected by YTHDC1 depletion, indicating a main role of YTHDC1 in affecting the stability of repeat RNAs in mESCs (fig. S5B). These m⁶A peaks

in different regions share similar motifs to those we detected previously (fig. S5, C and D). Moreover, we correlated m⁶A fold changes on three carRNA groups separately and observed distinct negative correlations in all cases between *Mettl3* and *Ythdc1* depletion (fig. S5E), which further indicates that YTHDC1 promotes decay of a portion of these carRNAs. We next performed nuclear RNA decay assays and observed notably increased half lifetimes for all three groups of carRNAs upon *Ythdc1* CKO (Fig. 2D and fig. S5F). Moreover, the m⁶A-marked RNAs from all three carRNA groups showed greater increases in half lifetime compared with those of non-m⁶A RNAs after *Ythdc1* CKO (Fig. 2E and fig. S5G).

We then ranked repeats families according to their m⁶A peak enrichment fold changes in response to *Mettl3* or *Ythdc1* depletion and identified the long interspersed element-1 (LINE1) family as one of the most responsive in both cases (fig. S6, A and B). LINE1 elements are the most abundant class of mouse retrotransposon, transcribed in early embryos, and they play critical roles in development—particularly in remodeling chromatin structure and regulating transcription (19, 20). We observed that m⁶A levels of each subfamily of

LINE1 negatively correlate with their divergence: younger LINE1 contains higher m⁶A levels (fig. S6, C and D) and shows more significant methylation fold changes (fig. S6, E and F) upon *Mettl3* or *Ythdc1* depletion. We next verified that the decay of L1Md_F, a representative young subfamily of LINE1, is regulated by YTHDC1 and METTL3 in an m⁶A-dependent manner (supplementary text and figs. S6G and S7).

paRNAs, eRNAs, and repeat RNAs, such as LINEs, can regulate transcription by affecting chromatin architecture at corresponding genomic loci. Because *Mettl3* KO increases both transcription and chromatin accessibility (Fig. 1), we next examined whether these changes are regulated by methylation of these carRNAs. We performed time-course RNA sequencing of nascent transcripts as well as total nuclear RNAs and conducted mammalian native elongating transcript sequencing (mNET-seq) (21, 22) in *Mettl3* KO and WT mESCs. Both the global expression level (Fig. 3, A and B) and transcription rate (Fig. 3, C and D, and fig. S8, A and B) increased upon *Mettl3* KO. Genes that were up-regulated in *Mettl3* KO mESCs tended to have upstream carRNAs marked with m⁶A more frequently than those that were

Fig. 2. Transcript turnover of carRNAs is regulated by m⁶A.

(A) LC-MS/MS

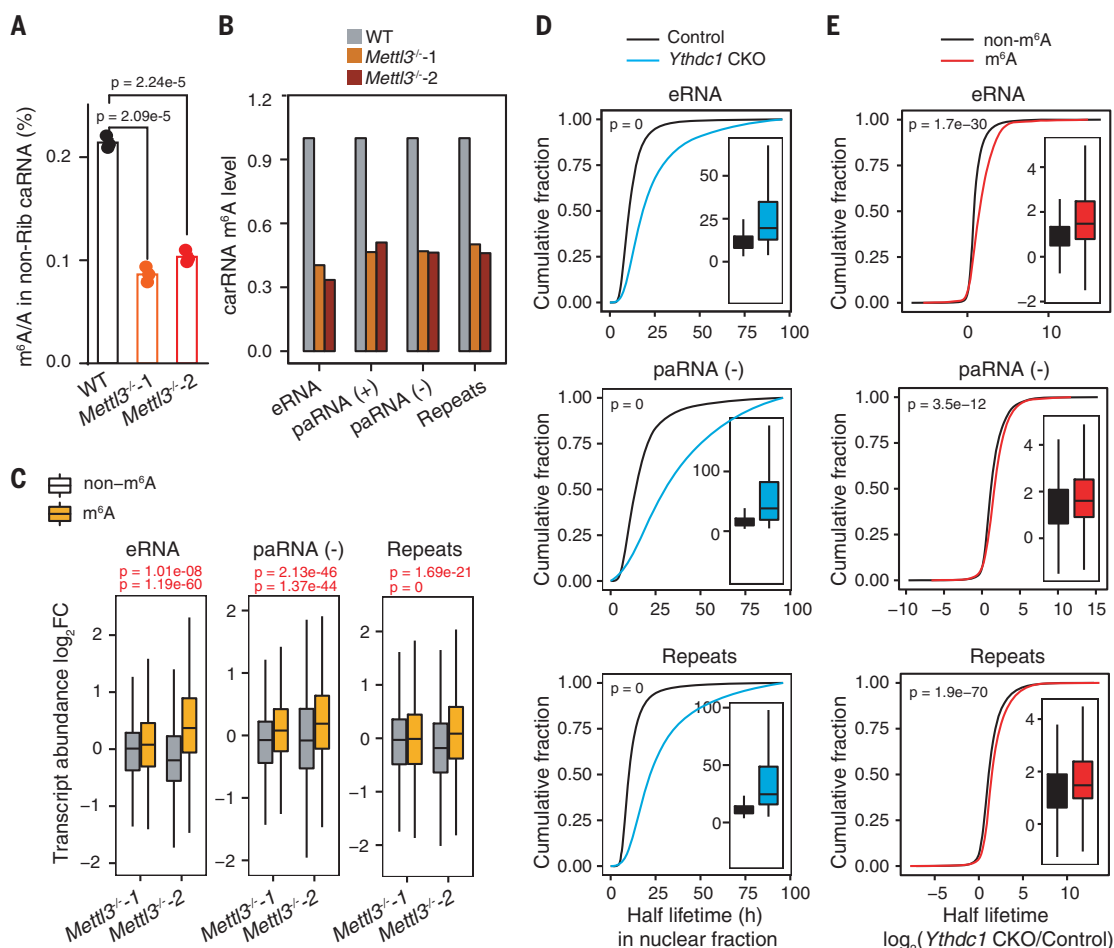
quantification of the m⁶A/A ratio in nonribosomal (non-Rib) carRNAs (including pre-mRNA) extracted from WT or *Mettl3*^{-/-} mESCs.

n = 3 biological replicates; error bars indicate means ± SEM. **(B)** m⁶A level changes on carRNAs were quantified through normalizing m⁶A sequencing results with spike-in between WT and *Mettl3* KO mESCs. *n* = 2 biological replicates.

(C) carRNAs were divided into methylated (m⁶A) or nonmethylated (non-m⁶A) groups. The boxplot shows greater increases in transcript abundance fold changes of the m⁶A group versus the non-m⁶A group upon *Mettl3* KO over WT mESCs. For (A) and (C), *P* values were determined by two-tailed *t* test. **(D)** Cumulative distribution and boxplots (inside) of nuclear carRNA half lifetime changes in CKO *Ythdc1* and control mESCs.

(E) Cumulative distributions and boxplots (inside) of the half lifetime changes of carRNAs upon *Ythdc1* CKO. carRNAs were divided into methylated (m⁶A) or nonmethylated (non-m⁶A) groups.

Depletion of YTHDC1 led to greater half lifetime increases of m⁶A-marked carRNAs than non-m⁶A-marked ones. For (D) and (E), *P* values were calculated by a nonparametric Wilcoxon-Mann-Whitney test. h, hours.



down-regulated (Fig. 3, A and B). Moreover, genes with m⁶A-marked upstream carRNAs attained higher increases in transcription rate than those with non-m⁶A-marked upstream carRNAs. The same is true when sorting genes with their precursor mRNAs (pre-mRNAs) not subjected to m⁶A methylation (Fig. 3, E to F, and fig. S8, C to E), which indicates that the reduced m⁶A methylation of these carRNAs upon *Mettl3* KO activates the transcription of downstream genes.

Notably, we found that all m⁶A-dependent genes that showed reduced upstream carRNA methylation upon *Mettl3* depletion (~6584 genes) exhibited increased transcription rates (Fig. 3G). We identified a subset of these genes that demonstrated transcription rate differences >1 upon *Mettl3* KO (fig. S9A) and found that these genes are mainly involved in transcription regulation, chromatin modification, and stem cell population maintenance (fig. S9B). Hence, the reduced m⁶A methylation of carRNAs not only promotes downstream transcription but may activate genes involved

in chromatin opening, initiating a positive feedback loop. We further analyzed *Prdm9*, *Kmt2d* (encoding two H3K4me3 methyltransferases), *Esrrb*, and *Ranbp17* (related with differentiation), all of which possess upstream carRNAs with reduced m⁶A level upon *Mettl3* KO (fig. S10). Consistently, the half lifetime of these carRNAs and the transcription rate of their downstream genes both increased upon *Mettl3* KO, and these changes could be rescued by WT but not mutant METTL3 (fig. S11).

The interactions between super-enhancers and their target genes are known to be affected by transcription of exosome-regulated transcripts in mESCs (23). We examined super-enhancers and found that ~80% of super-enhancer RNAs (seRNAs) contain m⁶A peaks (Fig. 3H and fig. S12A). The m⁶A methylation level of seRNAs decreased (fig. S12, B and C) and the m⁶A-marked seRNAs showed a greater increase in abundances compared with non-m⁶A-marked ones upon *Mettl3* KO (Fig. 3I). seRNAs that showed reduced m⁶A level upon *Mettl3* KO were associated with increased transcription

rates at downstream genes (Fig. 3J); genes with transcription rate differences larger than one were mainly involved in transcription regulation, chromatin modification, and stem cell maintenance (fig. S12, D and E), consistent with results obtained from other carRNAs (fig. S9). Moreover, we found that genes regulated by m⁶A-marked upstream seRNAs tended to exhibit greater increases in transcription rate than those regulated by m⁶A-marked upstream typical eRNAs upon *Mettl3* KO (fig. S12F).

We next investigated chromatin state changes affected by altered carRNA methylation. We performed chromatin immunoprecipitation sequencing (ChIP-seq) and observed global increases of these two active marks, H3K4me3 and H3K27ac, upon *Mettl3* KO (fig. S13, A and B), consistent with the Western blot results (fig. S1H). Moreover, genes with m⁶A-marked upstream carRNAs showed greater increases in H3K4me3 and H3K27ac than genes with non-m⁶A upstream carRNAs in *Mettl3* KO mESCs (Fig. 4A). Likewise, *Mettl3* KO mESCs showed obvious increases in both marks at

regions that flank METTL3-enriched DNA loci (fig. S13, C and D). These data suggested that stabilizing the upstream carRNAs in *Mettl3* KO mESCs could increase the deposition of active histone marks.

We suspect that carRNAs could recruit proteins, such as CBP/EP300 and YY1, to promote open chromatin and activate transcription (24, 25). In fact, YY1 was identified as one of the top enriched transcription factors (TFs) at genomic regions that harbor m⁶A-marked carRNAs (fig. S14A). Our ChIP-seq experiments revealed global increases of EP300 and YY1 binding in *Mettl3* KO mESCs (Fig. 4, B and C), which correlated well with higher nearby eRNAs or paRNAs abundances (fig. S14, B and C). Moreover, both EP300 and YY1 binding negatively correlate with the m⁶A level of nearby carRNAs (Fig. 4, D and E), and *Mettl3* KO leads to elevated EP300 and YY1 binding at regions that lose m⁶A (Fig. 4, F and G). The genomic regions with both m⁶A-marked carRNAs and binding of EP300 or YY1 showed the greatest increase in H3K27ac compared with regions with just m⁶A or just EP300/YY1 binding upon *Mettl3* KO (Fig. 4H). We also performed ChIP-seq of JARID2, a component of the polycomb repressive complex 2 (PRC2), because RNA transcripts could repel PRC2 binding to maintain chromatin openness (26). We observed a globally decreased JARID2 binding, correlating well with the abundance increases of eRNAs and repeats transcripts upon *Mettl3* KO (fig. S14, D and E). Furthermore, JARID2 tends to bind to regions with high m⁶A methylation of carRNAs (fig. S14F), with a positive correlation between the m⁶A level on carRNA and local JARID2 binding changes upon *Mettl3* KO (fig. S14G). Therefore, these m⁶A-regulated carRNAs may stabilize the open chromatin state by not only recruiting active TFs but also repelling repressive factors, such as PRC2, upon loss of methylation.

Lastly, elevated LINE1 may also modulate global chromatin accessibility (19). We blocked LINE1 RNA in *Mettl3*^{-/-} mESCs and observed an overall reduction in chromatin accessibility (Fig. 4I) (20). We employed a fused CRISPR-dCas13b system (27) with either WT or inactive mutant FTO (fig. S15A). Only when targeting LINE1 by guide RNA (gRNA) with dCas13b-*wt* FTO, but not dCas13b-*mu* FTO, did we observe decreased m⁶A level and increased half lifetime for LINE1, together with a globally increased chromatin accessibility (fig. S15, B to E). We then applied the dCas13b-FTO system to genes that harbor m⁶A-marked upstream carRNAs (fig. S16). When targeting carRNAs using gRNAs and dCas13b-*wt* FTO, we observed site-specific methylation reduction, with little methylation change observed using dCas13b-*mu* FTO or negative control gRNAs (Fig. 4J and fig. S17). We also observed increased half lifetime of these carRNAs, up-regulation of

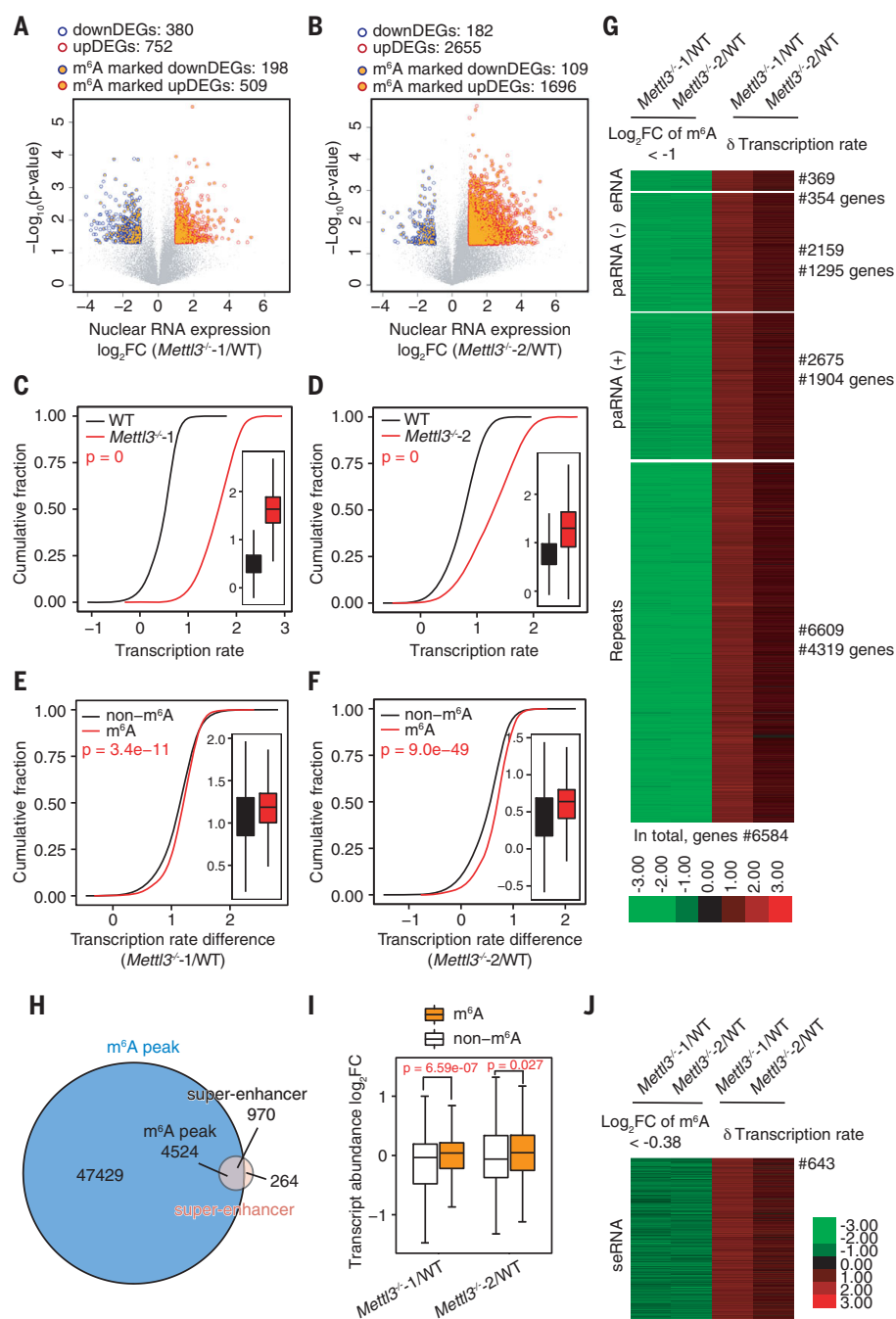


Fig. 3. The m⁶A level of carRNAs affects downstream gene expression and transcription rate.

(A and B) Volcano plot of genes with differential expression levels in *Mettl3*^{-/-}1 (A) or *Mettl3*^{-/-}2 (B) versus WT mESCs [$P < 0.05$ and $|\log_2\text{FC}| > 1$ (FC, fold change)]. Genes with upstream, m⁶A-marked carRNAs are shown with orange circles. Gene expression level was normalized to ERCC spike-in with linear regression method. DEG, differentially expressed gene. (C and D) Cumulative distribution and boxplot (inside) of gene transcription rate in *Mettl3*^{-/-}1 (C) or *Mettl3*^{-/-}2 (D) versus WT mESCs. (E and F) Cumulative distribution and boxplot (inside) of transcription rate difference between *Mettl3*^{-/-}1 (E) or *Mettl3*^{-/-}2 (F) versus WT mESCs. Genes were categorized into two subgroups according to whether their upstream carRNAs contain m⁶A (m⁶A) or not (non-m⁶A). For (C) to (F), P values were calculated by a nonparametric Wilcoxon-Mann-Whitney test. (G) Heatmap showing the m⁶A level fold changes ($\log_2\text{FC} < -1$) on carRNAs and downstream gene transcription rate difference between *Mettl3* KO and WT mESCs. (H) Venn diagram showing the overlap between the m⁶A peaks and super-enhancer peaks in mESCs. (I) Boxplot showing fold changes of the abundance of m⁶A-marked and non-m⁶A-marked seRNAs between *Mettl3*^{-/-} and WT mESCs. For (A), (B), and (I), P values were determined by two-tailed t test. (J) Heatmap showing fold change ($\log_2\text{FC} < -0.38$) of m⁶A level of seRNAs and transcription rate difference of their downstream genes between *Mettl3* KO and WT mESCs.

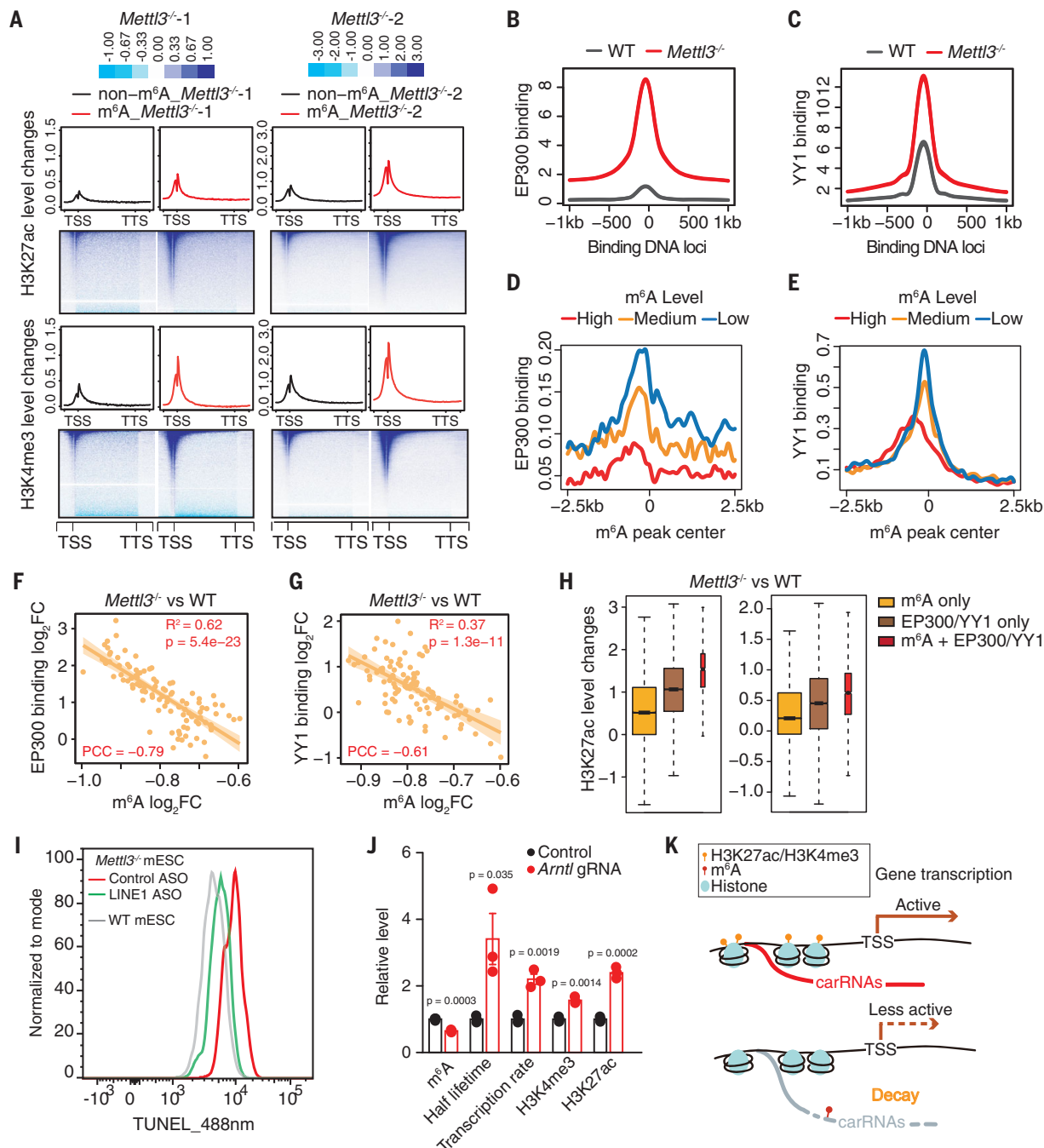


Fig. 4. The m⁶A level of carRNAs affects local chromatin state and downstream transcription. (A) Profiles of H3K27ac (top) and H3K4me3 (bottom) level changes on gene body together with 2.5 kb upstream of the TSS (transcription start site) and 2.5 kb downstream of the TTS (transcription termination site) in WT and *Mettl3* KO mESCs. Genes were categorized into two groups according to whether they harbor upstream m⁶A-marked carRNAs (m⁶A) or not (non-m⁶A). (B and C) Profiles of EP300 (B) or YY1 (C) DNA binding at their peak center and flanking 2.5 kb regions in WT and *Mettl3* KO mESCs. (D and E) Profiles of EP300 (D) and YY1 (E) DNA binding at the center of m⁶A peaks overlapped with carRNAs and its flanking 2.5 kb regions in WT mESCs. m⁶A peaks were categorized into highly (high), moderately (medium), or lowly (low) methylated groups, according to their m⁶A levels in WT mESCs. (F and G) The correlation between changes in m⁶A level of the carRNAs and changes in EP300 (F) or YY1 (G) DNA binding at genomic regions that show m⁶A differences with *Mettl3* KO. The genomic regions were

categorized into 100 bins on the basis of fold change rank of m⁶A level upon *Mettl3* KO. (H) Barplots showing H3K27ac level changes at genomic regions that are m⁶A methylated (m⁶A only, without EP300 and YY1 binding), bound by EP300 or YY1 (EP300/YY1 only, without m⁶A carRNA), and m⁶A methylated with EP300 and YY1 binding (m⁶A + EP300/YY1). The last group showed the highest increase upon *Mettl3* KO. (I) Analysis of chromatin accessibility in *Mettl3* KO mESCs treated with control or LINE1 antisense oligos (ASOs). DNase I-treated TUNEL assay was performed. (J) A dCas13b-FTO (WT or inactive mutant) construct with gRNA targeting the seRNA of *Arntl* was used to reduce the m⁶A level of *Arntl* seRNA. After treatment, increased half lifetime of the target seRNA, elevated local H3K27ac and H3K4me3 levels, and increased *Arntl* transcription rate were observed, accompanied by the decreased seRNA m⁶A level. (K) A schematic model showing how m⁶A affects transcription by regulating the decay of upstream carRNAs stability and chromatin state.

downstream gene transcription, and elevated local H3K4me3 and H3K27ac levels (Fig. 4J and fig. S18). Together, these results strongly support our discovery that m⁶A methylation of carRNAs controls carRNA stability and downstream gene transcription.

To explore functional relevance of this m⁶A-mediated regulation, we modulated the LINE1 RNA level in WT and *Mettl3* KO mESCs. LINE1 abundance was elevated in *Mettl3* KO mESCs (fig. S19A) (11). Blocking LINE1 elevated differentiation capacity and decreased cell renewal in *Mettl3* KO mESCs (fig. S19, B to D). In contrast, targeting LINE1 using gRNA with dCas13b-*wt* FTO resulted in decreased differentiation capacity and increased cell renewal in WT mESCs but not with Cas13b-*mu* FTO (fig. S19, B to D). We also confirmed regulatory functions of m⁶A-marked carRNAs in endometrial cancer progression, in which down-regulation of METTL3 increases cell proliferation, migration, and tumor growth (supplementary text and figs. S20 to S23) (28).

In this work, we report that carRNAs can be m⁶A methylated by METTL3. A subset of these m⁶A-marked carRNAs (mainly LINE1 repeats) is destabilized by YTHDC1 via the NEXT complex. We show that m⁶A serves as a switch to affect abundances of these carRNAs, thus tuning nearby chromatin state and downstream transcription (Fig. 4K). Effects of m⁶A methylation on carRNAs could vary; m⁶A may stabilize modified carRNAs in different cell types.

In mESCs, the transcription activation induced by m⁶A depletion is coupled with the increased chromatin accessibility, enrichment of certain TFs, and elevated histone marks, revealing a direct cross-talk between carRNA m⁶A methylation and chromatin state. Our findings demonstrate an additional layer of regulatory effect of carRNA m⁶A on transcription.

REFERENCES AND NOTES

1. D. Dominissini *et al.*, *Nature* **485**, 201–206 (2012).
2. K. D. Meyer *et al.*, *Cell* **149**, 1635–1646 (2012).
3. M. Frye, B. T. Harada, M. Behm, C. He, *Science* **361**, 1346–1349 (2018).
4. I. A. Roundtree, M. E. Evans, T. Pan, C. He, *Cell* **169**, 1187–1200 (2017).
5. G. Jia *et al.*, *Nat. Chem. Biol.* **7**, 885–887 (2011).
6. G. Zheng *et al.*, *Mol. Cell* **49**, 18–29 (2013).
7. X. Wang *et al.*, *Nature* **505**, 117–120 (2014).
8. X. Wang *et al.*, *Cell* **161**, 1388–1399 (2015).
9. W. Xiao *et al.*, *Mol. Cell* **61**, 507–519 (2016).
10. P. J. Batista *et al.*, *Cell Stem Cell* **15**, 707–719 (2014).
11. S. Geula *et al.*, *Science* **347**, 1002–1006 (2015).
12. Y. Wang *et al.*, *Nat. Cell Biol.* **16**, 191–198 (2014).
13. I. Ivanova *et al.*, *Mol. Cell* **67**, 1059–1067.e4 (2017).
14. S. D. Kasowitz *et al.*, *PLOS Genet.* **14**, e1007412 (2018).
15. Y. Wang *et al.*, *Nat. Neurosci.* **21**, 195–206 (2018).
16. I. Barbieri *et al.*, *Nature* **552**, 126–131 (2017).
17. B. Slobodin *et al.*, *Cell* **169**, 326–337.e12 (2017).
18. M. Lubas *et al.*, *Mol. Cell* **43**, 624–637 (2011).
19. J. W. Jachowicz *et al.*, *Nat. Genet.* **49**, 1502–1510 (2017).
20. M. Percharde *et al.*, *Cell* **174**, 391–405.e19 (2018).
21. A. Mayer *et al.*, *Cell* **161**, 541–554 (2015).
22. T. Nojima *et al.*, *Cell* **161**, 526–540 (2015).
23. E. Pefanis *et al.*, *Cell* **161**, 774–789 (2015).
24. D. A. Bose *et al.*, *Cell* **168**, 135–149.e22 (2017).
25. A. A. Sigova *et al.*, *Science* **350**, 978–981 (2015).
26. X. Wang *et al.*, *Nat. Struct. Mol. Biol.* **24**, 1028–1038 (2017).
27. S. Rauch, C. He, B. C. Dickinson, *J. Am. Chem. Soc.* **140**, 11974–11981 (2018).
28. J. Liu *et al.*, *Nat. Cell Biol.* **20**, 1074–1083 (2018).

ACKNOWLEDGMENTS

We thank H. Chang for *Mettl3* KO mESCs and J. Tauler and A. Andersen from Life Science Editor for editing. **Funding:** This study was supported by the National Institute of Health HG008935 to C.H.; Strategic Priority Research Program XDA16010506 to D.H.; National Key R&D Program of China 2018YFA0109700 to D.H.; National Institute of Health ES030546 to C.H.; National Key R&D Program of China 2016YFA0100400 to Y.G. and Chuan C.; the China Scholarship Council (CSC) for the visit of Y.G. to the University of Chicago; National Science Fund for Excellent Young Scholars 31922017 to D.H.; and the CAS Hundred Talent Program to D.H. The Mass Spectrometry Facility of the University of Chicago is funded by the National Science Foundation (CHE-1048528). C.H. is an investigator of the Howard Hughes Medical Institute. **Author contributions:** C.H., J.L., and Y.G. conceived the original idea and designed original studies. J.L. performed most experiments with help from Y.G., Chuan C., C.L., and M.M.X. X.D. performed most computational analyses with initial discovery of carRNA methylation by Chuanyuan C., S.Z., and D.H. B.S. constructed most mESC lines. J.L., X.D., and C.H. wrote the manuscript with input from all authors. **Competing interests:** C.H. is a scientific founder and a member of the scientific advisory board of Accent Therapeutics, Inc. **Data and materials availability:** All sequencing data have been deposited in Gene Expression Omnibus (GSE133600 and GSE140561). All other data are available in the manuscript or the supplementary materials.

SUPPLEMENTARY MATERIALS

science.sciencemag.org/content/367/6477/580/suppl/DC1
Materials and Methods
Supplementary Text
Figs. S1 to S23
Tables S1 and S2
References (29–44)

[View/request a protocol for this paper from Bio-protocol.](#)

2 July 2019; resubmitted 20 November 2019
Accepted 30 December 2019
Published online 16 January 2020
10.1126/science.aay6018

CANCER

Therapeutic targeting of preleukemia cells in a mouse model of *NPM1* mutant acute myeloid leukemia

Hannah J. Uckelmann^{1,2}, Stephanie M. Kim^{1,2}, Eric M. Wong^{1,2}, Charles Hatton^{1,2}, Hugh Giovino^{1,2}, Jayant Y. Gadrey^{1,2}, Andrei V. Krivtsov^{1,2}, Frank G. Rücker³, Konstanze Döhner³, Gerard M. McGeehan⁴, Ross L. Levine⁵, Lars Bullinger⁶, George S. Vassiliou^{7,8}, Scott A. Armstrong^{1,2,*}

The initiating mutations that contribute to cancer development are sometimes present in premalignant cells. Whether therapies targeting these mutations can eradicate premalignant cells is unclear. Acute myeloid leukemia (AML) is an attractive system for investigating the effect of preventative treatment because this disease is often preceded by a premalignant state (clonal hematopoiesis or myelodysplastic syndrome). In *Npm1c/Dnmt3a* mutant knock-in mice, a model of AML development, leukemia is preceded by a period of extended myeloid progenitor cell proliferation and self-renewal. We found that this self-renewal can be reversed by oral administration of a small molecule (VTP-50469) that targets the MLL1-Menin chromatin complex. These preclinical results support the hypothesis that individuals at high risk of developing AML might benefit from targeted epigenetic therapy in a preventative setting.

Nucleophosmin (*NPM1*) mutant acute myeloid leukemia (AML) is one of the most common types of AML (1–3). Despite its high prevalence, the mechanism of leukemogenesis is still poorly understood, and targeted therapy options are lacking (4). *NPM1* gene mutations (*NPM1c*) induce cytoplasmic localization of NPM1 and often co-occur with other mutations in genes such as *DNA methyltransferase 3A* (*DNMT3A*^{R882H}). *NPM1c* leukemias express a distinctive stem cell-like gene expression pattern that includes homeobox cluster A and B (*HOXA/B*) genes and their DNA-binding cofactor MEIS1 (5–8). In humans, *DNMT3A* mutations are detected in the most primitive hematopoietic stem cell compartment, often long before the development of leukemia, a condition often referred to as clonal hematopoiesis of indeterminate potential (CHIP) (9). *NPM1* mutations are found in committed progenitors and differentiated myeloid cells in AML but are absent from the stem cell and lymphoid compartments (9, 10). This suggests that *NPM1c* may induce self-renewal in myeloid progenitors as a critical step in the development of AML and that this aberrant progenitor self-renewal may represent a critical step in the progression from CHIP to AML.

To identify the leukemia-initiating cellular population in *NPM1c* AML, we used previously developed mouse models with an inducible Cre recombinase (*MxCre*) and heterozygous conditional knock-in of the humanized *Npm1* mutation (*Npm1*^{fllox-cA/+}; hereafter called *Npm1c* mutant mice), alone or in combination with *Dnmt3a*^{R878H} mutation (*Dnmt3a*^{R878H/+}; hereafter called *Dnmt3a* mutant mice) (5, 11). We confirmed *Hox* gene up-regulation in different hematopoietic stem and progenitor populations of *Npm1c*, *Dnmt3a*, and *Npm1c/Dnmt3a* mutant mice 16 weeks after induction of the knock-in allele by polyinosinic: polycytidylic acid (pIpC) injection (Fig. 1A). At this time, mutant mice showed no signs of leukemia and had normal blood counts, and only the double mutant showed a slight increase in granulocyte-macrophage progenitor (GMP) frequencies (fig. S1, A and B). Sorted wild-type (WT) and *Dnmt3a* single-mutant cells showed a stepwise decrease of *Hoxa9* mRNA expression from long-term hematopoietic stem cells (LT-HSCs) to GMPs, which coincides with their loss of self-renewal properties (Fig. 1A). *Npm1c* or *Npm1c/Dnmt3a* mutant cells maintained inappropriately high levels of *Hoxa9* across the different progenitor cell types (Fig. 1A). RNA sequencing (RNA-seq) analysis 4 weeks after activation of the *Npm1c* allele revealed that half of the top 20 up-regulated genes in *Npm1c* GMPs were *Hoxa/b* genes. The HSC-enriched Lin[−], Sca1⁺, Kit⁺ population (LSK) showed much lower fold changes owing to their high baseline expression of *Hoxa/b* genes (Fig. 1B and table S1). The gene expression programs induced in *Npm1c* mutant GMPs were also enriched for LT-HSC and human *NPM1c* mutant AML signatures, which include *Hoxa/b* genes and *Meis1* (fig. S1, C to I). On the basis of these gene expression data, we con-

clude that *Npm1c* supports the inappropriate expression of genes associated with normal stem cell self-renewal, such as *Hoxa/b* cluster genes, throughout myeloid differentiation.

We next investigated whether *Npm1c* can induce stem cell-associated gene expression de novo in committed progenitor cells, which lack self-renewal and have low levels of *Hox* and *Meis1* expression. For this, we sorted Cre-negative *Npm1c*, *Dnmt3a*, and *Npm1c/Dnmt3a* mutant GMPs and LSK cells and then used retroviral Cre overexpression to induce the mutant knock-in alleles in vitro (Fig. 1C). *Npm1c* expression induced *Hoxa9* expression in GMPs in vitro, suggesting that the *Npm1c*-driven stem cell-associated program can be turned on at different stages of myeloid differentiation (Fig. 1C). Induction of *Dnmt3a*^{R878H} knock-in alone did not induce or enhance the *Hoxa9* induction activated by *Npm1c* in progenitors, indicating that mutant *Npm1c* and not *Dnmt3a* is responsible for the observed up-regulation of stem cell-associated genes.

Our gene expression data suggest that *Npm1c* induces stem cell properties in non-stem cells. To examine whether these transcriptional changes coincide with functional self-renewal properties in *Npm1c* progenitors, we first performed colony-forming unit (CFU) assays. *Npm1c* mutant GMPs displayed increased in vitro self-renewal capacity, as shown by their ability to replat up to four rounds in CFU assays (fig. S2, A and B). Transplantation experiments performed using in vivo pIpC-induced and in vitro Cre-transduced mutant GMPs demonstrated that *Npm1c* enhances engraftment and self-renewal of GMPs (Fig. 1D and fig. S2C). Although some of the initially engrafted GMPs were depleted over time, about half of the mice retained self-renewing GMPs for >12 weeks (Fig. 1E). These long-term engrafting GMPs (LT-GMPs) showed CD11b⁺Gr1⁺ peripheral blood engraftment, and recipient mice showed no signs of leukemia for more than 6 months (fig. S2D). These experiments demonstrate that self-renewal properties induced by *Npm1c* in myeloid progenitors are sufficient to give rise to a preleukemic population that stably engrafts long term.

To determine whether these preleukemic *Npm1c* mutant clones would progress to leukemia, we performed secondary transplants of LT-GMPs (Fig. 2A). Secondary recipients of *Npm1c* single-mutant or *Npm1c/Dnmt3a* double-mutant LT-GMPs developed AML 3 to 5 months after secondary transplant similar to mice that received mutant LSK cells (Fig. 2B). LSK- and GMP-derived secondary transplanted mice presented with high white blood cell counts, enlarged spleens, and extramedullary hematopoiesis, suggesting that *Npm1c* is sufficient to give GMPs enough self-renewal capacity to ultimately generate AML (Fig. 2, C and D, and fig. S3, A and B). The long latency indicates

¹Department of Pediatric Oncology, Dana-Farber Cancer Institute, and Division of Hematology/Oncology, Boston, MA, USA. ²Boston Children's Hospital and Harvard Medical School, Boston, MA, USA. ³Department of Internal Medicine III, University Hospital of Ulm, Ulm, Germany. ⁴Syndax Pharmaceuticals, Inc., Waltham, MA, USA. ⁵Center for Hematologic Malignancies, Memorial Sloan Kettering Cancer Center, New York, NY, USA. ⁶Department of Hematology, Oncology and Tumor Immunology, Charité University Medicine, Berlin, Germany. ⁷Wellcome-MRC Cambridge Stem Cell Institute, University of Cambridge, Cambridge, UK. ⁸Wellcome Trust Sanger Institute, Cambridge, UK.

*Corresponding author. Email: scott_armstrong@dfci.harvard.edu

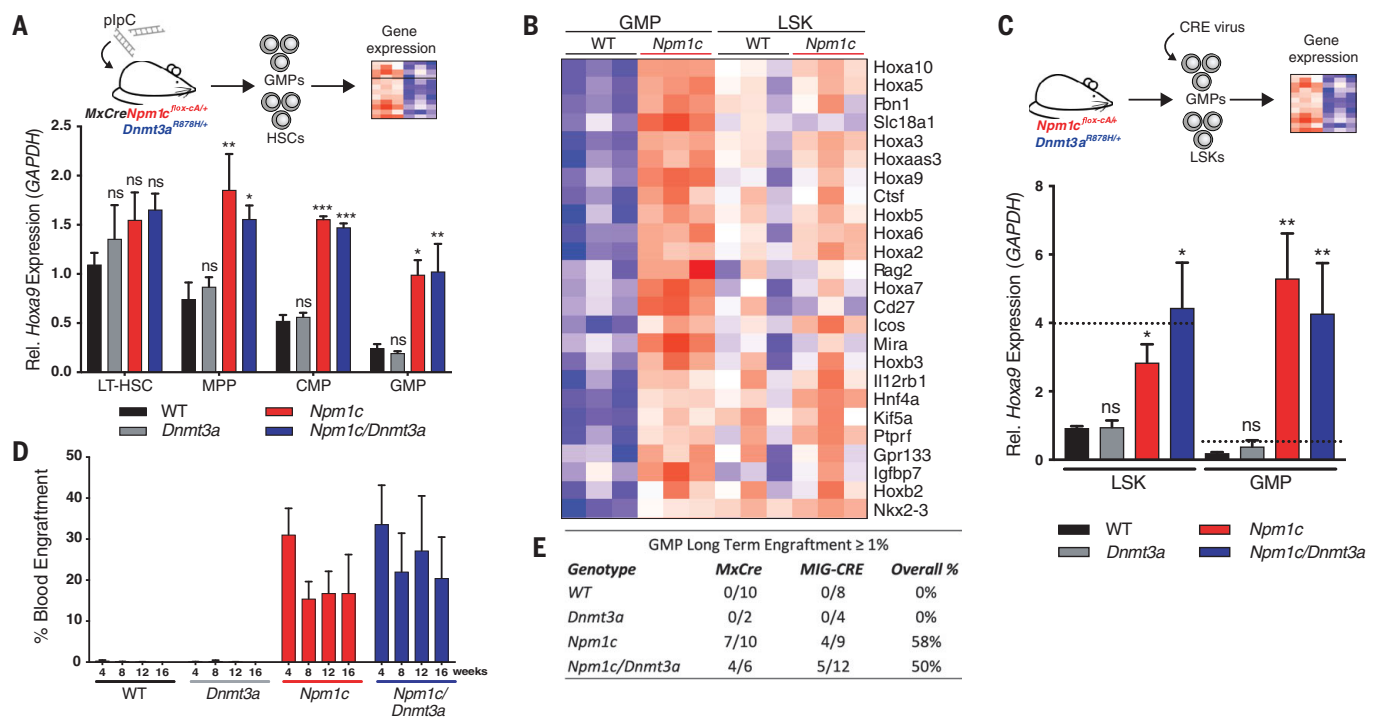


Fig. 1. *Npm1c* induces self-renewal properties in myeloid progenitor cells. (A) *Hoxa9* gene expression in *Npm1c*, *Dnmt3a*, and *Npm1c/Dnmt3a* mutant LT-HSCs, multipotential progenitors (MPPs), common myeloid progenitors (CMPs), and GMPs 16 weeks after plpC injection ($n \geq 3$ mice per group; error bars indicate mean \pm SD). Rel., relative; GAPDH, glyceraldehyde 3-phosphate dehydrogenase. (B) Heatmap showing the top 25 up-regulated genes in *Npm1c* versus WT LSK cells and GMPs, 4 weeks after plpC treatment ($n = 3$ mice per group). (C) Relative expression of *Hoxa9*

3 days after in vitro *Cre* transduction ($n \geq 4$ mice per group; error bars indicate mean \pm SEM). The dotted lines indicate *Hoxa9* expression level from freshly isolated LSK cells and GMPs. (D) Peripheral blood percentage CD45.2 engraftment of WT and *Npm1c*, *Dnmt3a*, and *Npm1c/Dnmt3a* mutant GMPs sorted 4 weeks after plpC induction, transplanted into lethally irradiated recipients. Error bars indicate mean \pm SEM. (E) Summary table of GMP-transplanted mouse numbers and percentages engrafted $\geq 1\%$ for >12 weeks. *MIG-CRE*, MSCV-CRE-IRES-GFP retrovirus. ns, not significant; * $P < 0.05$; ** $P < 0.01$; *** $P < 0.001$.

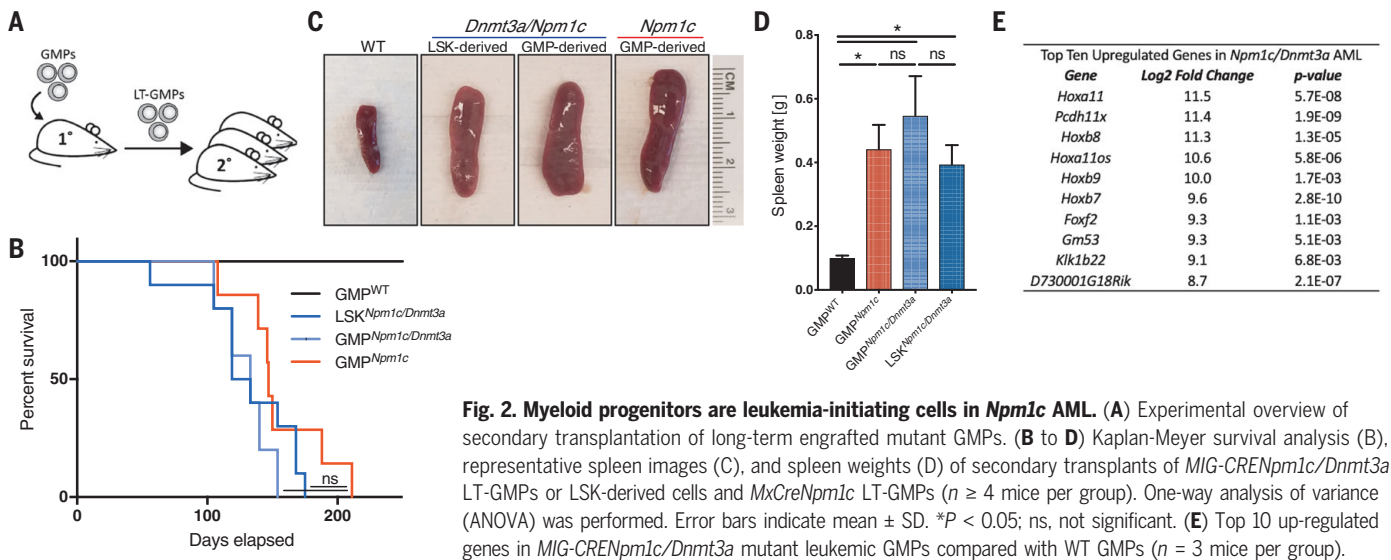


Fig. 2. Myeloid progenitors are leukemia-initiating cells in *Npm1c* AML. (A) Experimental overview of secondary transplantation of long-term engrafted mutant GMPs. (B to D) Kaplan-Meier survival analysis (B), representative spleen images (C), and spleen weights (D) of secondary transplants of *MIG-CRE**Npm1c/Dnmt3a* LT-GMPs or LSK-derived cells and *MxCre**Npm1c* LT-GMPs ($n \geq 4$ mice per group). One-way analysis of variance (ANOVA) was performed. Error bars indicate mean \pm SD. * $P < 0.05$; ns, not significant. (E) Top 10 up-regulated genes in *MIG-CRE**Npm1c/Dnmt3a* mutant leukemic GMPs compared with WT GMPs ($n = 3$ mice per group).

that *Npm1c* mutant LT-GMPs may acquire further mutations over time, which has been shown to occur in this and other *Npm1c* knock-in mouse models (7, 12). Furthermore, mouse *Npm1c/Dnmt3a* mutant leukemia cells showed highly up-regulated *Hoxa/b* expression, which

resembled expression patterns observed in human *NPM1c* AML and other *HOX*-associated AMLs such as *MLL*-AF9 AML (Fig. 2E and fig. S3, C and D). These results confirm that pre-leukemic *Npm1c* mutant LT-GMPs eventually give rise to leukemia.

We have previously shown that inhibition of the interaction between the histone methyltransferase *MLL1* and adaptor protein *Menin* reverses leukemogenic gene expression in the *NPM1c* AML cell line *OCI-AML3* (13). *Menin*-*MLL* interaction inhibitors were originally developed

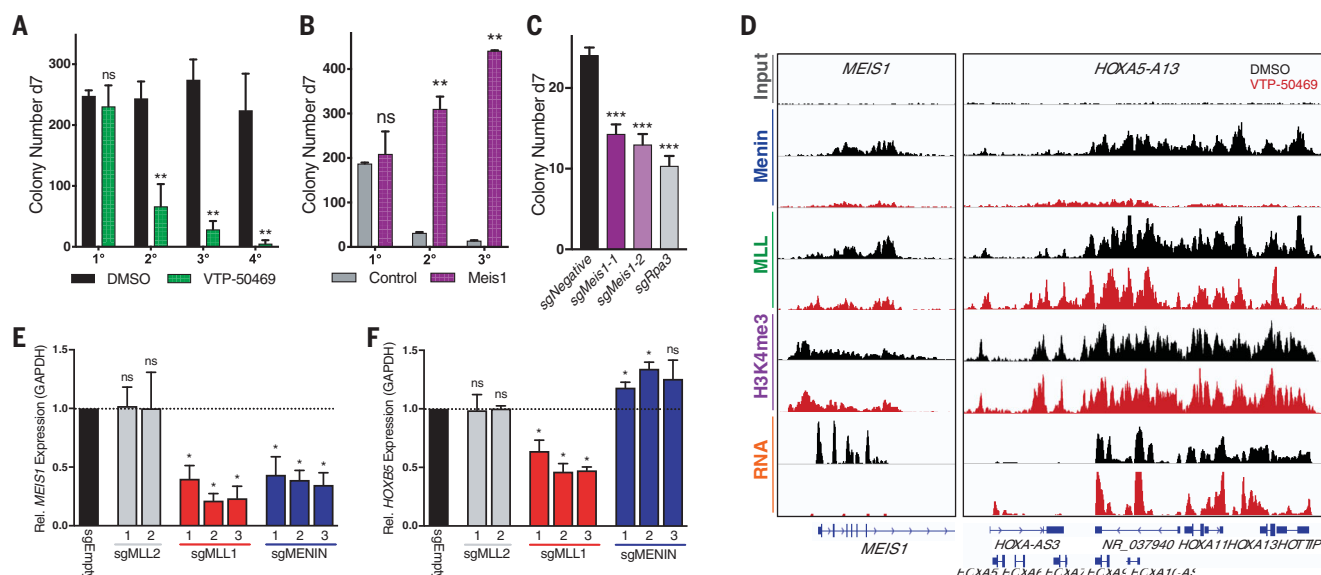


Fig. 3. Meis1, Menin, and MLL1 are essential for maintaining self-renewal program.

(A) CFU serial replating assay of mouse MIG-CRE/*Npm1c*/*Dnmt3a* mutant cell line (SIIL12) with dimethyl sulfoxide (DMSO) or VTP-50469. Data represent the mean of three independent experiments. d7, day 7. (B) CFU assay of mouse SIIL12 cells transduced with MSCV-PURO control (left) or *Meis1*-PURO (right) virus and grown in the presence of 10 nM VTP-50469. Data represent the mean of three independent experiments. (C) CFU assay of SIIL12 cells electroporated with control or *Meis1*- or *Rpa3*-targeting single guide RNAs (sgRNAs) for Cas9-mediated KO. Data

represent the mean of three independent experiments. (D) Chromatin immunoprecipitation sequencing (ChIP-seq) density plots showing changes in chromatin occupancy of Menin, MLL, and H3K4me3 and changes in mRNA expression in response to VTP-50469 in OCI-AML3 cells at the *MEIS1* and *HOXA* loci.

(E and F) *MEIS1* (E) and *HOXB5* (F) gene expression in OCI-AML3 cells transduced with control, sgMLL1, sgMLL2, and sgMenin. Data represent the mean of three independent experiments. One-way ANOVA was performed. Error bars indicate mean \pm SD. ns, not significant; * P < 0.05; ** P < 0.01; *** P < 0.001.

to target the oncogenic MLL-fusion complexes by directly disrupting the oncogene complex from assembling on chromatin. Our findings, however, suggest that the WT MLL1-Menin interaction is essential to maintain *NPM1c*-driven leukemia. To test this, we used an orally bioavailable inhibitor of the Menin-MLL1 interaction (VTP-50469). This compound has been used to treat established disease in models of MLL-rearranged AML and B cell acute lymphoblastic leukemia [see (14) for details on the chemical synthesis of VTP-50469]. We assessed whether *Npm1c* mutant mouse cells respond to Menin inhibition in serial CFU replating assays of double- and single-mutant cell lines (Fig. 3A and fig. S4A). Menin inhibition led to a rapid loss of replating capacity and up-regulation of myeloid differentiation marker CD11b with no significant increase in apoptosis (fig. S4, B and C). Gene expression analysis of *Npm1c*/*Dnmt3a* mutant mouse cells after Menin inhibition revealed a rapid repression of stem cell genes, including *Meis1* and *Pbx3* (fig. S5A, left). *Meis1* and *Pbx3* are important cofactors of *Hoxa/b* transcription factors and play essential roles in *Hoxa9*-driven leukemogenesis and maintenance of leukemic stem cell gene expression programs (15–17). Even though many *Npm1c*-induced genes, including *Hoxa/b*, remained highly expressed, the loss of essential cofactors such as *Meis1* could account for the loss of self-renewal observed upon Menin inhibition.

To confirm that reduced *Meis1* expression is crucial for the drastic differentiation of *Npm1c*/*Dnmt3a* mutant cells observed after VTP-50469 treatment, we first attempted to rescue the VTP-50469-induced loss of leukemic stem cell gene expression by retroviral overexpression of *Meis1*. Maintaining *Meis1* expression rescued the replating capacity of *Npm1c*/*Dnmt3a* mutant cells in the presence of Menin inhibitor and increased the median inhibitory concentration (IC_{50}) values significantly (Fig. 3B and fig. S5B). Whereas control cells lost essential components of their self-renewal program in response to VTP-50469, *Meis1*-expressing cells showed increased expression of a group of stem cell-associated genes, including *Mecom* and *Pbx3*, and retained them in the presence of Menin inhibitor (fig. S5, B to G). Conversely, Cas9-mediated knockout (KO) of *Meis1* led to a rapid loss of out-of-frame edited cells in culture as well as a reduction in CFU replating capacity, confirming *Meis1* as a dependency in *NPM1c* mutant AML (Fig. 3C and fig. S5H). These data confirm the essential role of *Meis1* in maintaining leukemic stem cell programs.

Next, we confirmed that human *NPM1c* mutant leukemia cell line OCI-AML3 also responds to VTP-50469. OCI-AML3 cells were highly sensitive to Menin-MLL inhibition, as demonstrated by their low IC_{50} value (3 nM on day 6) and rapid down-regulation of *MEIS1* and *PBX3* upon VTP-50469 treatment (fig. S6,

A to C). In contrast to previously published Menin inhibitor molecules such as MI-2-2 and MI-503 that were shown to reduce expression of *HOXA/B* cluster genes as well as *MEIS1*, *HOX* genes were not repressed in response to VTP-50469 in OCI-AML3 cells (fig. S6, B and C). In mouse cells, a modest repressive effect on some *Hox* genes was observed, whereas others were up-regulated (figs. S7, D and E, and S10, A to D) (18, 19). Furthermore, we observed a reduction of Menin and MLL1 chromatin occupancy at the *MEIS1* and *PBX3* transcriptional start sites (TSSs), whereas MLL1 binding at *HOXA/B* TSSs was retained in regions where Menin was depleted (Fig. 3D, fig. S6E, and table S2). Globally, Menin chromatin occupancy was decreased, whereas MLL1 and trimethylated histone H3 lysine 4 (H3K4me3) were lost only at specific sites that were highly enriched for genes down-regulated in response to Menin inhibition (figs. S6, F to H, and S7, A to C). To verify that MLL1 loss is responsible for the observed loss of stem cell-associated gene expression, we generated Cas9-mediated OCI-AML3 KO cell lines of *MLL1*, *MLL2*, and *Menin* (fig. S8, A to C, and table S4). *Menin* KO mimicked the expression changes observed upon VTP-50469 treatment, with reduced *MEIS1* and *PBX3* expression and up-regulation of *HOXB5* and *HOXA5* (Fig. 3, E and F, and fig. S8, D and E). Loss of *MLL1*, however, also resulted in a reduction in *HOX* expression, whereas *MLL2*

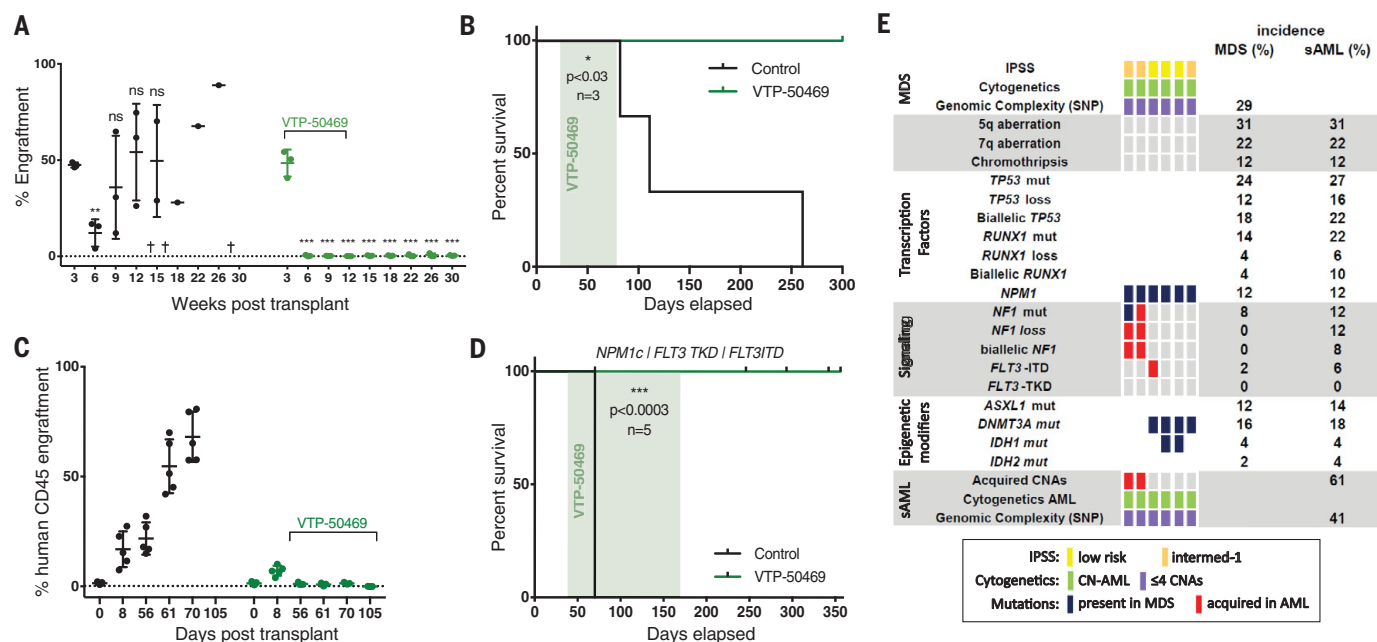


Fig. 4. Preleukemic *Npm1c* LT-GMPs and human AML cells can be eradicated by Menin inhibition. (A and B) Percent engraftment of CD45.2 in peripheral blood (A) and Kaplan-Meier survival analysis (B) of mice transplanted with *Npm1c/Dnmt3a* LT-GMPs receiving control or 0.1% VTP-50469-spiked chow for 9 weeks (one-way ANOVA; $n = 3$ mice per group; error bars indicate mean \pm SD). (C and D) Percent engraftment of hCD45 in peripheral blood (C) and Kaplan-Meier survival analysis (D) of *NPM1c*, *FLT3ITD*, *FLT3TKD*-transplanted PDX mice receiving control or

0.1% VTP-50469-spiked chow for 129 days (patient 1, table S5; $n = 5$ mice per group; error bars indicate mean \pm SD). (E) Mutational screening of 49 paired MDS and sAML patient samples for *RUNX1*, *TP53*, *NPM1*, *FLT3*, *ASXL1*, *DNMT3A*, *IDH1*, and *IDH2* mutations revealed six patients with persistent *NPM1* mutations detected in MDS samples before AML development. IPSS, International Prognostic Scoring System; SNP, single-nucleotide polymorphism; CN-AML, cytogenetically normal AML; CNAs, copy number alterations. ns, not significant; $**P < 0.01$; $***P < 0.001$.

disruption showed no or only minor effects on *HOX* and *MEIS1* (Fig. 3F and fig. S8E). In agreement with this, *Menin* and *MLL1* KO cells were rapidly depleted in competition assays, whereas *MLL2* KO cells were not (fig. S8F). Our findings confirm *MLL1* as the main driver of oncogenic *HOX* and *MEIS1* gene expression in *NPM1c* mutant AML and show that only a subset of *MLL1* target genes are also Menin dependent.

DNMT3A mutations are frequently found in patients with CHIP and are associated with increased risk for hematologic malignancies (9, 20–23). By contrast, *NPM1c* mutations have not been reported in CHIP, suggesting that their acquisition is rapidly followed by leukemic progression. This was demonstrated in at least one patient with *IDH2* mutant CHIP that developed AML shortly after *NPM1c* was detected (8, 24). Our mouse model of preleukemic *Npm1c/Dnmt3a* LT-GMPs allowed us to test whether we can interrupt leukemia progression by means of eradication of *Npm1c* mutant preleukemic clones. We evaluated the in vivo efficacy of VTP-50469 using secondary transplants of *Npm1c* single-mutant and *Npm1c/Dnmt3a* double-mutant LT-GMPs (fig. S9A). Engraftment was confirmed 3 weeks after transplant, and mice were treated with 0.1% VTP-50469-spiked chow for 9 weeks (fig. S9,

B and C). In control animals, we observed an expansion of LT-GMP engraftment and eventually mice succumbed to AML (Fig. 4, A and B, and fig. S9D). Notably, no relapse of LT-GMPs was observed more than 6 months after the treatment was discontinued, and VTP-50469-treated groups showed prolonged survival of more than 9 months versus an average of 5 months in the untreated groups (Fig. 4B and fig. S9E). Furthermore, when VTP-50469-treated mice were sacrificed 300 days after transplant, no *Npm1c* mutant cells were detected in bone marrow, spleen, or liver (fig. S9, F to H). WT stem cell self-renewal was not affected by VTP-50469 treatment, as demonstrated by stable engraftment of WT HSCs (fig. S9I). Repression of *Meis1* and *Pbx3* and other stem cell-associated genes was validated by RNA-seq analysis of sorted *Npm1c/Dnmt3a* LT-GMPs after 5 days of in vivo treatment (fig. S10, A to D). VTP-50469 was well tolerated even when administered for long periods (9 weeks continuously), which could potentially be extended to ensure complete clearance of *NPM1c* mutant cells if needed. These data indicate that we can specifically eradicate preleukemic *Npm1c* mutant self-renewing myeloid progenitor cells

using targeted epigenetic therapy without having detrimental effects on either normal HSCs or hematopoiesis.

We next investigated whether *NPM1c* mutant cells remained sensitive to Menin-MLL inhibition after progression to AML. Menin-MLL inhibitors have been shown to be effective targeting *MLL*-fusion leukemias in vivo, but whether they will be similarly effective in the more common *NPM1c* mutant AML was less clear. To this end, we used patient-derived xenograft (PDX) assays of untreated and relapsed *NPM1c* AML harboring *FLT3*, *DNMT3a*, and *IDH1* co-mutations (table S5). Inhibiting *MLL1*-Menin dramatically reduced tumor burden in blood, spleen, and bone marrow of three different PDX models treated for 30 to 43 days (fig. S11, A to I). The few detectable human cells expressed high levels of the differentiation marker CD11b (fig. S11, J and K). VTP-50469 treatment significantly prolonged survival in two independent *NPM1c* PDX models (Fig. 4, C and D, and fig. S12, A and B). Gene expression analysis of *NPM1c* PDX cells isolated 10 days after in vivo Menin inhibitor treatment confirmed reduced expression of *MEIS1* and *PBX3*, as observed in our mouse model, whereas *HOX* genes were slightly increased (fig. S12C). Furthermore, Menin inhibition was effective in PDX mice with high tumor burden [40 to 80% human CD45

(hCD45)] (fig. S13A). A reduction of blood leukemia burden was observed after 3 weeks of VTP-50469 treatment. Except for one mouse that expired after 10 days of treatment, the three remaining VTP-50469-treated mice survived more than 150 days after transplant with hCD45 engraftment of <1% (fig. S13, B and C). Our data suggest that Menin-MLL inhibition is highly effective not just in the preleukemic setting but also in fully developed aggressive human *NPM1c* mutant AMLs.

To determine the feasibility of detecting preleukemic *NPM1* mutant clones in patients, we screened 49 paired myelodysplastic syndrome (MDS) and secondary AML (sAML) samples for AML-associated mutations (*NPM1*, *DNMT3A*, *RUNX1*, *TP53*, *NF1*, *ASXL1*, *IDH1*, and *IDH2*). *NPM1c* was detected in six (12%) of MDS and paired sAML samples, whereas co-occurring signaling mutations *NF1* and *FLT3* were mostly acquired during progression to sAML in these samples (Fig. 4E). Half of these *NPM1c* mutant MDS patients rapidly developed leukemia within 1 to 2 months, whereas the remaining three patients (or the other half of patients) progressed more slowly (5 to 6.5 months) (table S6). *NPM1c* can therefore be detected in a preleukemic setting and may act as a marker for progression to AML, making it an ideal target for preventative therapy. In the context of screening and monitoring, this may plausibly be extended to individuals with large *DNMT3A* or *IDH1/2* mutant CHIP clones, which is predictive of high AML risk (9).

In summary, this study shows that eliminating preleukemic cells with targeted therapy is

a potentially promising approach; specifically, we present evidence in a mouse model of AML that early intervention is possible with molecules that target chromatin regulators. Combined with improved long-term monitoring of patients with high-risk CHIP or MDS for appearance of an *NPM1c* preleukemic clone, disease prevention could become a realistic possibility in the future.

REFERENCES AND NOTES

- B. Falini et al., *N. Engl. J. Med.* **352**, 254–266 (2005).
- R. F. Schlenk et al., *N. Engl. J. Med.* **358**, 1909–1918 (2008).
- E. Papaemmanuil et al., *N. Engl. J. Med.* **374**, 2209–2221 (2016).
- H. Döhner, D. J. Weisdorf, C. D. Bloomfield, *N. Engl. J. Med.* **373**, 1136–1152 (2015).
- G. S. Vassiliou et al., *Nat. Genet.* **43**, 470–475 (2011).
- L. Brunetti et al., *Cancer Cell* **34**, 499–512.e9 (2018).
- O. M. Dovey et al., *Blood* **130**, 1911–1922 (2017).
- T. J. Ley et al., *N. Engl. J. Med.* **368**, 2059–2074 (2013).
- S. Jaiswal et al., *N. Engl. J. Med.* **371**, 2488–2498 (2014).
- L. I. Shlush et al., *Nature* **506**, 328–333 (2014).
- O. A. Guryanova et al., *Nat. Med.* **22**, 1488–1495 (2016).
- M. A. Loberg et al., *Leukemia* **33**, 1635–1649 (2019).
- M. W. M. Kühn et al., *Cancer Discov.* **6**, 1166–1181 (2016).
- A. V. Krivtsov et al., *Cancer Cell* **36**, 660–673.e11 (2019).
- Z. Li et al., *Cancer Res.* **76**, 619–629 (2016).
- G. G. Wang, M. P. Pasillas, M. P. Kamps, *Mol. Cell. Biol.* **26**, 3902–3916 (2006).
- Z. Li et al., *Blood* **121**, 1422–1431 (2013).
- J. Grembecka et al., *Nat. Chem. Biol.* **8**, 277–284 (2012).
- D. Borkin et al., *Cancer Cell* **27**, 589–602 (2015).
- T. McKerrell et al., *Cell Rep.* **10**, 1239–1245 (2015).
- M. Xie et al., *Nat. Med.* **20**, 1472–1478 (2014).
- G. Genovese et al., *N. Engl. J. Med.* **371**, 2477–2487 (2014).
- S. Abelson et al., *Nature* **559**, 400–404 (2018).
- P. Desai et al., *Nat. Med.* **24**, 1015–1023 (2018).

ACKNOWLEDGMENTS

We thank Z. Feng and all members of the Armstrong Lab for their help; A. Cremer and J. Perry for critically reading the manuscript;

F. Perner for the *Menin* sgRNA constructs; and Y. Soto-Feliciano for the ipUSEPR sgRNA expression plasmid. **Funding:** S.A.A. was supported by NIH grants CA176745, CA204639, CA066996, and CA206963 and by grants from Wicked Good Cause and Cookies for Kids' Cancer. K.D. and L.B. were supported by SFB 1074 project B3. H.J.U. was supported by the German Research Foundation (DFG, UC77/1-1). R.L.L. was supported by NIH grants P30 CA008748 and U54 OD020355-04. G.S.V. is funded by a Cancer Research UK Senior Fellowship (C22324/A23015). **Author contributions:** H.J.U. and S.A.A. conceived the study and wrote the manuscript; H.J.U., S.M.K., E.M.W., H.G., A.V.K., and J.Y.G. conducted experiments; C.H. analyzed RNA-seq and ChIP-seq data; G.M.M. provided MLL1-Menin inhibitor VTP-50469; R.L.L. and G.S.V. provided the *Dnmt3a* and *Npm1* mutant knock-in mice used in this study; and F.G.R., K.D., and L.B. provided primary MDS and sAML data. **Competing interests:** S.A.A. has been a consultant and/or shareholder for Vitae/Allergan Pharmaceuticals, Epizyme Inc., Imago Biosciences, Cyteir Therapeutics, C4 Therapeutics, Syros Pharmaceuticals, OxStem Oncology, Accent Therapeutics, and Mana Therapeutics. S.A.A. has received research support from Janssen, Novartis, and AstraZeneca. R.L.L. is on the supervisory board of Qiagen and is a scientific advisor to Loxo, Imago, C4 Therapeutics, and Isoplexis, which each include an equity interest. He receives research support from and consulted for Celgene and Roche, he has received research support from Prelude Therapeutics, and he has consulted for Incyte, Novartis, Astellas, Morphosys, and Janssen. He has received honoraria from Lilly and Amgen for invited lectures and from Gilead for grant reviews. G.S.V. is a consultant for Oxstem and a consultant for and minor stockholder in Kyma. H.G. owns stock in Theravance Biopharma. **Data and materials availability:** VTP-50469 can be obtained by means of a MTA from G.M.M. through Syndax. All data of this study are deposited in the NCBI Gene Expression Omnibus (GEO) under accession number GSE129638.

SUPPLEMENTARY MATERIALS

science.sciencemag.org/content/367/6477/586/suppl/DC1
Materials and Methods

Figs. S1 to S13

Tables S1 to S6

References (25–32)

[View/request a protocol for this paper from Bio-protocol.](#)

23 April 2019; accepted 27 December 2019
10.1126/science.aax5863

Overseas **Chinese Scholars'** Visit to Top Chinese Universities

Check the Details from www.edu.cn/zgx

- 10,000+ academic job vacancies in China
- Free one-to-one consultation service

Send your CV to consultant@acabridge.edu.cn

海外学者
中国行



烟台大学
YANTAI UNIVERSITY



上海立信会计金融学院
SHANGHAI LIXIN UNIVERSITY OF ACCOUNTING AND FINANCE



西安交通大学
XI'AN JIAOTONG UNIVERSITY



10 ways that Science Careers can help advance your career

1. Register for a free online account on **ScienceCareers.org**.
2. Search thousands of job postings and find your perfect job.
3. Sign up to receive e-mail alerts about job postings that match your criteria.
4. Upload your resume into our database and connect with employers.
5. Watch one of our many webinars on different career topics such as job searching, networking, and more.
6. Download our career booklets, including Career Basics, Careers Beyond the Bench, and Developing Your Skills.
7. Complete an interactive, personalized career plan at “my IDP.”
8. Visit our Employer Profiles to learn more about prospective employers.
9. Research graduate program information and find a program right for you.
10. Read relevant career advice articles from our library of thousands.

Visit **ScienceCareers.org**
today — all resources are free



Science Careers

FROM THE JOURNAL SCIENCE  AAAS

SCIENCECAREERS.ORG



myIDP:
A career plan customized for you, by you.

For your career in science, there's only one **Science**

Features in myIDP include:

- Exercises to help you examine your skills, interests, and values.
- A list of 20 scientific career paths with a prediction of which ones best fit your skills and interests.

 Visit the website and start planning today!
myIDP.sciencecareers.org

ScienceCareers In partnership with:



Assistant/Associate Professor of Medicine/ Nephrology

The Division of **NEPHROLOGY AND HYPERTENSION AT STONY BROOK MEDICINE** is recruiting a full-time Physician Scientist reporting directly to the Chief of Nephrology. The Assistant/Associate Professor will be responsible for research, patient care, and teaching. The selected incumbent will be expected to develop an independent research program supported by extramural funding.

Required Qualifications: MD or equivalent. Board Certified in Internal Medicine. Board Certified/Eligible in Nephrology. Experience in clinical care and clinical, translational or basic research. Eligible for tenure-track position.

Preferred Qualifications: Physician Scientist candidates with a demonstrated publication and active funding track record in clinical, translational, and/or basic research in nephrology are preferred. The ideal candidate will have exhibited a strong commitment to advancing scientific knowledge of the field of nephrology, as well as demonstrate a strong commitment to clinical, educational, and academic excellence.

To qualify for an appointment as Associate Professor or Professor, the candidate must meet the School of Medicine's criteria for Appointment, Promotion and Tenure located at: <http://medicine.stonybrookmedicine.edu/facultysenate/committees/apt>

For a full position description, or application procedures, visit: www.stonybrook.edu/jobs (Ref. # 57424)

Stony Brook University is an Affirmative Action/ Equal Opportunity employer. We encourage protected veterans, individuals with disabilities, women and minorities to apply.

Where Science Gets Social.

AAAS.ORG/COMMUNITY



Member COMMUNITY
AAAS

AMERICAN ASSOCIATION FOR THE ADVANCEMENT OF SCIENCE

ADELPHI UNIVERSITY

Assistant Professor of Biology

Adelphi University invites applications for a tenure-track position in biology to begin fall 2020. A Ph.D is required and postdoctoral experience is highly preferred. Teaching responsibilities will include graduate physiology, human anatomy & physiology, and could include courses such as animal behavior, pathophysiology, introductory biology, and/or additional specialty courses in the applicant's area of expertise. The successful applicant will have a commitment to teaching students from diverse cultural backgrounds and excellent potential as a teacher, plus a record of significant research accomplishment and the potential to develop a fundable independent research program involving undergraduate and master's students.

For more information about the department, visit <http://biology.adelphi.edu/>. We are strongly committed to achieving excellence through cultural diversity. Adelphi is a private university with the spirit of a liberal arts college, committed to combining teaching and scholarship, and located in suburban Long Island within easy reach of New York City. More detailed descriptions of the position and application are available through.

Deadline for applications: February 17, 2020.

To apply, please visit:
<https://apptrkr.com/1780509>

By Jaivime Evaristo

Avoiding immigration limbo

Banks won't give a mortgage loan to someone who is only going to be in the country for 1 year," declared the real estate agent. His remark shocked me. I was a tenure-track faculty member at the time, but I was deemed unworthy to receive a line of credit because of my visa situation. I'm a citizen of the Philippines, and the visa that my U.S. institution obtained for me had to be renewed each year. So, on paper it looked as though I only had permission to be in the country for 1 year. My wife and I encountered many such hurdles because of my visa—and they ultimately drove me to quit my faculty position and leave the country.

In hindsight, I didn't take the visa application process seriously enough when I was negotiating my job offer. I was so excited about landing a tenure-track position that I didn't take time to think through what kind of visa and accommodations I would need to make my personal life work. I also assumed that the university had a system in place to deal with foreign hires. I said yes to the job offer and signed on the dotted line.

The first sign of trouble came when I tried to buy a house in our new city. I had moved there ahead of my wife and 1-year-old daughter so that I could look for a neighborhood where we could settle down. But as the real estate agent predicted, mortgage lenders didn't want to gamble on someone with a 1-year visa. I signed a lease for an apartment instead.

After my wife joined me, we needed a car because our sprawling community didn't have a strong public transportation system. But we had trouble securing credit for that, too. In the end, we had to put down more than \$3000 as a down payment.

The third, and final, straw came when my wife wanted to return to her work as a nurse after her maternity leave. Prior to our move, she had obtained a license to practice nursing in the United States. But she couldn't apply for jobs because of legal restrictions associated with my visa. That left her feeling frustrated and isolated, unable to establish a professional life in a new country.

Stress ran high in our small one-bedroom apartment. The logical fix to our problems was for me to secure permanent residency status, otherwise known as a green card. But that just brought more problems. I pleaded with my department chair, dean, and provost to support my green card application. But it took 6 months for the university



**“Don’t sign ... until you know
that you’ll have what
you need in your new country.”**

to agree to sponsor my application, and I didn't know how long the review and approval process would take on top of that.

Exasperated by the entire ordeal, I applied for jobs in countries that I thought would be more supportive of foreign workers and their families. I was offered a faculty job in the Netherlands and, within 3 months, my family and I moved across the Atlantic.

That was 1 year ago, and we've been much happier ever since. My wife, who is allowed to work in the Netherlands, is completing a course toward a nursing certification while our daughter, now 3 years old, is at government-subsidized day care. We are renting a nice house and are looking for one to buy. And we've been helped by a

government policy that grants a 30% tax exemption for foreign hires for a period of 5 years.

I'm glad we've ended up where we are. But when I look back, I wish that I'd been more prepared and proactive when negotiating my first faculty position. I could have asked the university to apply for a multiyear visa—which, I later learned, is what human resources staff had done for other faculty hires. I could have also requested a guarantee that the university would sponsor my application for permanent residency within a certain period of time and would pay for some immigration-related expenses, such as green card application fees.

I hope that other immigrant scientists take heed from my tale. If you land a job, don't sign on the dotted line until you know that you'll have what you need in your new country. ■

Jaivime Evaristo is an assistant professor at Utrecht University in the Netherlands. Do you have an interesting career story to share? Send it to SciCareerEditor@aaas.org.

ILLUSTRATION: ROBERT NEUBECKER